NANOMATERIALS FOR SENSING AND OPTOELECTRONIC APPLICATIONS

Edited by
M. K. Jayaraj
Subha P. P.
Shibi Thomas

ELSEVIER

Micro & Nano Technologies Series

NANOMATERIALS FOR SENSING AND OPTOELECTRONIC APPLICATIONS

NANOMATERIALS FOR SENSING AND OPTOELECTRONIC APPLICATIONS

Edited by

M. K. JAYARAJ
Cochin University of Science and Technology, Kochi, India;
University of Calicut, Malappuram, India

SUBHA P. P.
Cochin University of Science and Technology, Kochi,
Kerala, India

SHIBI THOMAS
Department of Physics, Bharata Mata College,
Thrikkakara, Kochi, India

ELSEVIER

Elsevier
Radarweg 29, PO Box 211, 1000 AE Amsterdam, Netherlands
The Boulevard, Langford Lane, Kidlington, Oxford OX5 1GB, United Kingdom
50 Hampshire Street, 5th Floor, Cambridge, MA 02139, United States

Notices

Knowledge and best practice in this field are constantly changing. As new research and experience broaden our understanding, changes in research methods, professional practices, or medical treatment may become necessary.

Practitioners and researchers must always rely on their own experience and knowledge in evaluating and using any information, methods, compounds, or experiments described herein. In using such information or methods they should be mindful of their own safety and the safety of others, including parties for whom they have a professional responsibility.

To the fullest extent of the law, neither the Publisher nor the authors, contributors, or editors, assume any liability for any injury and/or damage to persons or property as a matter of products liability, negligence or otherwise, or from any use or operation of any methods, products, instructions, or ideas contained in the material herein.

ISBN: 978-0-12-824008-3

Publisher: Matthew Deans
Acquisitions Editor: Edward Payne
Editorial Project Manager: Isabella C. Silva
Production Project Manager: Kamesh Ramajogi
Cover Designer: Miles Hitchen

Typeset by Aptara, New Delhi, India

Contents

Contributors

M. Alonso Cotta
Instituto de FÃ-sica Gleb Wataghin, Universidade Estadual de Campinas, 13083-859 Campinas, SÃ£o Paulo, Brazil.

R. Anjana
Cochin University of Science and Technology, Kochi, India; Department of Physics, St. Albert's College (Autonomous), Ernakulam, India

K.S. Anju
Cochin University of Science and Technology, Kochi, India

A.S. Asha
Cochin University of Science and Technology, Kochi, India; Centre of Excellence in Advanced Materials, Cochin University of Science and Technology, Kochi, India

P.A. Aswathy
Cochin University of Science and Technology, Kochi, India; Department of Physics, St. Stephen's College, Kollam, India

Maneesh Chandran
Department of Physics, National Institute of Technology Calicut, Calicut, India

A. Irzhak
Institute of Microelectronics Technology, Russian Academy of Sciences, Chernogolovka, 142432, Russia

M.K. Jayaraj
Cochin University of Science and Technology, Kochi, India; University of Calicut, Malappuram, India

V. Koledov
Kotelnikov Institute of Radio Engineering and Electronics of the Russian Academy of Sciences, Moscow, Russia

T.K. Krishnapriya
Cochin University of Science and Technology, Kochi, India

P. Lega
Magnetic Phenomena Laboratory, Kotelnikov Institute of Radio Engineering and Electronics, Russian Academy of Sciences, Mokhovaya 11-7, 125009, Moscow, Russia

P.S. Midhun
Cochin University of Science and Technology, Kochi, India

A.M.V. Mohan
Electrodics & Electrocatalysis Division, CSIR-Central Electrochemical Research Institute (CECRI), Karaikudi, India

P. Mymoona
Electroplating and Metal Finishing Division (EMFD), Council of Scientific and Industrial Research (CSIR)-Central Electrochemical Research Institute (CECRI), Karaikudi, India; Academy of Scientific and Innovative Research (AcSIR)-CSIR, Ghaziabad, India

Subha P.P.
Department of Physics, Cochin University of Science and Technology, Kochi, Kerala, India

M.J. Priya
Centre of Excellence in Advanced Materials, Cochin University of Science and Technology, Kochi, Kerala, India

Biji Pullithadathil
Nanosensor Laboratory, PSG Institute of Advanced Studies, Coimbatore, India

K.K. Rajeev
Department of Instrumentation, Cochin University of Science and Technology, Kochi, India; Centre of Excellence in Advanced Materials, Cochin University of Science and Technology, Kochi, India

J.V. Rival
Smart Materials Lab, Department of Nanoscience and Technology, University of Calicut, Kerala, India

K.J. Saji
International School of Photonics, Cochin University of Science and Technology, Kochi, India; Centre of Excellence in Advanced Materials, Cochin University of Science and Technology, Kochi, India

V. Sampath
Indian Institute of Technology Madras, Chennai-600 036, India

Manu Shaji
Cochin University of Science and Technology, Kochi, India

E.S. Shibu
Smart Materials Lab, Department of Nanoscience and Technology, University of Calicut, Kerala, India

Z. Song
International Research Centre for Nano Handling & Manufacturing of China, Changchun University of Science and Technology, Changchun 130022, China

A.M. Starvin
Department of Chemistry, Christian College, Kattakada, Thiruvananthapuram, India

P.S. Subin
Centre of Excellence in Advanced Materials, Cochin University of Science and Technology, Kochi, Kerala, India

Navami Sunil
Nanosensor Laboratory, PSG Institute of Advanced Studies, Coimbatore, India

Shibi Thomas
Department of Physics, Bharata Mata College, Thrikkakara, Kochi, India

S. von Gratowski
Laboratory of Spectroscopy and Millimeter and Submillimeter Wave Measurements, Kotelnikov Institute of Radio Engineering and Electronics, Russian Academy of Sciences, Fryazino Branch, FIRE RAS, Vvedenski Sq.1, Fryazino, Moscow Region, 141190, Russia

Preface

This book on "Nanomaterials for sensing and optoelectronic applications" is designed for postgraduate and research students. Nanomaterials are defined by their nanoscale dimensions, where surface or interface qualities take precedence over bulk features. The large surface area of nanomaterials gives rise to novel physical and chemical properties, which make them suitable for developing devices and instruments for a variety of applications in fields of life sciences, chemical industry, pharmaceuticals, energy conversion and storage, electronics, photonics, aviation and space, food safety, and information technology. This book leans more toward experimental methods and practical applications rather than detailing the fundamental principles. We believe that the framework of this book will better benefit a novice researcher. This book brings together reviews, recent studies, and knowledge on nanomaterials for sensing and optoelectronic applications.

Developing sensors with a high response, improved selectivity, and a faster recovery time are the prime goals for researchers working on sensors. A nanostructured design helps the miniaturization of the sensing device with improved performance, paving the way for portable sensors. Such sensors can be a breakthrough in various fields, including biomedical research and environmental monitoring. Intriguing results using metal oxide semiconductor–based and thin-film transistor–based gas sensors have been reported in recent years. Metal oxide semiconductors with exposed high-energy facets have been reported to have improved gas sensing performance. The first three chapters provide an overview of nanostructured gas sensors using metal oxide semiconductors and two-dimensional transition metal dichalcogenides. Chapter 4 details the significance of developing nanostructures with interesting features using template-assisted synthesis. Chapter 5 gives an introduction to biosensors and the phenomenon of luminescence, as well as various types of luminescent nanoparticles employed in bioimaging, which are thoroughly explained in Chapter 6. The major challenges in bioimaging and the use of luminescent nanoparticles as a bioimaging probe are also discussed. Early, fast, accurate disease diagnosis is the most demanding need from biomedicine, the first step toward fighting against diseases. Chapter 7 details the different nanophotonic techniques that can be used for disease diagnosis. Precision nanoclusters have been used for a broad spectrum of applications, such as molecular/metal ion sensing, device fabrication, green energy harvesting, photocatalysis,

and in the biomedical field. The use of atomically precise nanoclusters in these applications is discussed in Chapter 8. Surface-enhanced Raman spectroscopy (SERS) has evolved as a unique sensing technique since it combines molecular fingerprint specificity with single-molecule sensitivity. Recent advancements in developing core–shell nanostructures for the development of SERS substrates are also discussed in Chapter 9. SERS is also a label-free technique for monitoring biomarkers in biological matrices at trace-level concentrations. The recent advances in the field of SERS-based sensors for biomarker detection in body fluids such as sweat, saliva, and tear with an emphasis on the analysis of biomarkers, fabrication techniques, and potential real-time applications for biochemical sensing are included in Chapter 10. There is always growing demand for flexible and skin-interfaced sensors capable of the real-time monitoring of relevant biomarkers from human body fluids, like sweat, saliva, tear, and interstitial fluid. The design of nanomaterials-based electrochemical sensors enhances the sensitivity of detection, and Chapter 11 discusses nanomaterials-based flexible electrochemical sensors for healthcare monitoring. Artificial synaptic devices are one of the most far-fetched applications of nanostructured materials. Artificial neural networks based on resistive switching (RS) devices are considered one of the most straightforward and cost-effective ways of realizing this technology. Apart from that, RS has found immense applications in semiconductor electronics as well. The mechanism of RS in nanostructures and its numerous applications are discussed in Chapter 12. Shape memory alloys (SMAs) are smart materials that exhibit the unique property of a shape change upon exposure to a change in temperature. The combination of nanomaterials and SMAs helps to tailor the properties and to fabricate several nanodevices based on individual nanoobjects. One of the emerging technologies of nanotweezers based on shape memory composite materials and their application for manipulating real nanoobjects like nanotubes and nanowires is discussed in Chapter 13. The final chapter of this book elaborates on the outstanding physical and chemical properties of diamond. Various techniques for the growth of diamond in the form of thin films on different substrates and their characteristics are explained.

It is very exciting to finally publish this book on “Nanomaterials for sensing and optoelectronic applications.” There are many people to whom we are grateful for their valuable contributions. We extend our sincere thanks to Ms. Priya, M. J., Mr. Manu, S., Mr. Midhun, P. S., Ms. Krishnapriya, T. K., Ms. Anju, K. S., Mr. Subin, P. S., Ms. Navami, S., Mr. Jose, V. R., Dr. Anjana, R., Dr. Pillai, A. M., Dr. Saji, K. J., Dr. Asha, A. S., and present and former researchers at Nanophotonic and Optoelectronic Devices Laboratory (NPOED), Department of Physics, Cochin University of Science and Technology. They have

contributed their research results meticulously for each chapter of this book. We also take this opportunity to thank with due regards, Prof. Kumar, K. R., Department of Instrumentation, Cochin University of Science and Technology; Dr. Shibu, E. S., Department of Nanoscience and Technology, University of Calicut; Dr. Biji, P., Department of Chemistry and Nanoscience and Technology, PSG Institute of Advanced Studies; Dr. Vinu, M. V. M., CSIR-Central Electrochemical Research Institute (CECRI), Karaikudi; Prof. Sampath, V., Indian Institute of Technology Madras, India; Von Gratowski, S. and Koledov, V., Kotelnikov Institute of Radio Engineering and Electronics of the Russian Academy of Sciences, Moscow, Russia; and Dr. Chandran, M., Department of Physics, National Institute of Technology, India, for their contribution.

It was a pleasant experience to work with the Elsevier Editorial team, who have enabled the timely publication of this book.

Dr. M.K. Jayaraj
Dr. P.P. Subha
Dr. T. Shibi

1

Facet-dependent gas sensing properties of metal oxide nanostructures

M.J. Priya [a], Subha P.P. [b] and M.K. Jayaraj [b,c]

[a] Centre of Excellence in Advanced Materials, Cochin University of Science and Technology, Kochi, Kerala, India. [b] Cochin University of Science and Technology, Kochi, India. [c] University of Calicut, Malappuram, India

1.1 Introduction

Recently, nanostructured metal oxides have attracted much attention in many industrial and domestic applications for the detection of toxic, flammable, and explosive gases due to their high sensitivity, flexibility in production, small size, low cost, and ability to detect both reducing and oxidizing gases (Miller et al., 2014; Wang et al., 2010). The sensing properties of these nanomaterials strongly depend on their size, structure, shape, surface-to-volume ratio, and physical and chemical properties. With the increasing demand for selective and sensitive gas sensors, researchers are following different strategies to improve the gas sensing properties of the metal oxide semiconductor (MOS)–based gas sensors, such as changing the morphology of nanostructures (Gurlo, 2011; Shouli et al., 2010; Sun et al., 2012), noble metal doping (Luo et al., 2017; Sarkar et al., 2015), the formation of hierarchical nanostructures (Miller et al., 2014; Walker et al., 2019), core–shell (CS) structures (Yan et al., 2018), hollow heteronanostructures (Guo et al., 2019), and exposing high energy crystal facets (Jia et al., 2014; Liang et al. 2019a; Liu, et al., 2012). Among these strategies, scientists are more interested in the development of nanostructures with selectively exposed high-energy facets.

The numbers of dangling bonds (unsaturated bonds), number of active site for gas adsorption, and the arrangement of surface atoms are important factors that play a crucial role in gas sensing properties since gas sensing processes occur on the surface. Different crystal facets with distinctive surface atomic arrangements possess different gas sensing properties. High-energy facets possess a large number of

Nanomaterials for Sensing and Optoelectronic Applications. DOI: https://doi.org/10.1016/B978-0-12-824008-3.00015-1

dangling bonds, atomic steps, and edges, which leads to more active sites for gas adsorption; hence sensing materials exposed with high-energy facets show greater reactivity than those exposed with the low-energy facets (Gao & Zhang, 2018; Kuang et al., 2014; Pal & Pal, 2015; Shang & Guo, 2015).

This chapter gives a basic idea regarding MOS-based sensors, including their gas sensing mechanism, the design of the gas sensor, the design of the gas sensing measurement unit, different performance parameters, and different strategies adopted for the improvement of the performance of MOS gas sensors. The importance of MOSs with exposed high-energy facets in the improvement of gas sensing performance has been discussed in detail. Also, the effects of dangling bond density on gas sensing properties have been discussed. According to the research and calculation, surface engineering by selectively exposing high-energy facets provides an effective way to obtain MOS gas-sensitive materials with superior performance. The understanding of the facet-dependent properties of MOS will lead to the fabrication of more effective gas sensors in the future.

1.2 Metal oxide–based gas sensors

1.2.1 Gas sensing mechanism

The fundamental principle of MOS–based chemoresistive sensors is the change in the conductivity of the MOS due to the oxygen adsorption and desorption reactions on the metal oxide surface. In the case of an n-type MOS-based gas sensor the sensing mechanism is as follows: in ambient air atmosphere, oxygen adsorbed on the surface of the sensing layer by extracting electrons from the conduction band of the MOS, which results in the formation of a Schottky potential barrier in MOS (Shankar et al., 2016). The adsorption of oxygen on the surface of MOS depends on the operating temperature of the sensor. At lower temperatures (<150°C), oxygen molecules are adsorbed in the form of molecular oxygen ions (O_2^-) via the trapping of a comparably fewer number of electrons; however, at higher temperatures (>150°C), more electrons are trapped by the adsorbed oxygen and form atomic oxygen species (O^- and O_2^-) (Kashif et al., 2013). The processes involved in the adsorption of oxygen on the metal oxide surface can be described as follows:

$$O_2\,(\text{gas}) \rightarrow O_2\,(\text{ads}) \tag{1.1}$$

$$O_2\,(\text{ads}) + e^- \rightarrow O_2^-\,(\text{ads}),\ T < 150^\circ\text{C} \tag{1.2}$$

$$O_2^-\,(\text{ads}) + e^- \rightarrow 2O^-(\text{ads}),\ \ T > 150^\circ\text{C} \tag{1.3}$$

$$O^-\,(\text{ads}) + e^- \rightarrow O^{2-}\,(\text{ads}),\ T > 150^\circ\text{C} \tag{1.4}$$

The extracted electrons from the conduction band (E_c) leave behind positively charged ions, resulting in upward band bending and the formation of an electron-depletion region or a space-charge layer in the MOS, as shown in Fig. 1.1. The height and depth of the band bending depend on the amount and type of adsorbed oxygen. Due to the formation of the electron depletion region, an increase in the resistance of the MOS can be observed. When this surface is exposed to reducing gases such as acetone and ammonia, the adsorbed oxygen ions interact with the target gases and the trapped electrons are released back onto the MOS surface. The amount of oxygen removed from the surface is proportional to the concentration of the reducing gas. Thus the height and depth of band bending and the resistance of the MOS decrease (Ananya, 2018; Shankar et al., 2016; Wang et al., 2010). The oxygen desorption from the MOS surface in the presence of a reducing gas (say, R) can be described as follows:

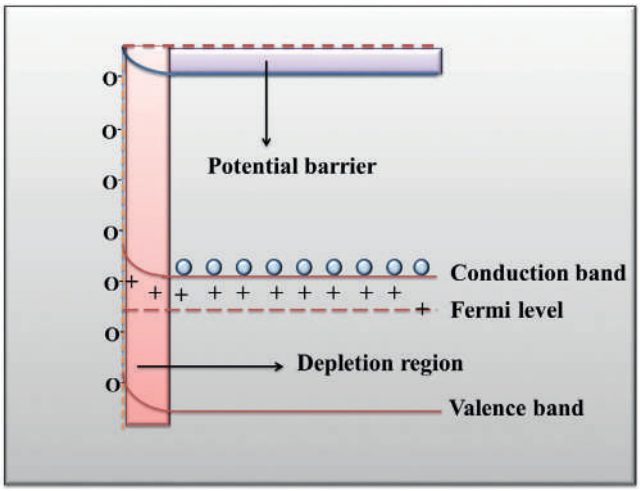

Figure 1.1. Schematic representation of band bending after the adsorption of oxygen species (Priya et al., 2021).

$$R + nO^- \rightarrow a\ CO_2 + b\ H_2O + ne^- \tag{1.5}$$

These electrons are released back onto the MOS surface and the produced gas and water molecule are released into the atmosphere. On the other hand, an oxidizing gas depletes the charge carriers, leading to an increase in resistance. Similarly, in the case of p-type MOS, where positive holes are the majority charge carriers, a decrease in the resistance is observed in the presence of an oxidizing gas and an increase in the resistance in the case of a reducing gas (Barsan et al., 2012; Neri, 2015; Subha & Jayaraj, 2019). Table 1.1 clearly summarizes the response of n- and p-type MOS toward reducing and oxidizing gases.

1.2.2 Design of MOS gas sensors

The commonly available configurations for the design of semiconductor-based gas sensors are (1) sintered pellet gas sensors (Kazemi et al., 2016), (2) thick-film gas sensors (Arshak & Gaidan, 2005), and (3) thin-film gas sensors (Mirzaei et al., 2019). The disadvantage with the use of sintered pellet gas sensors is their relatively low gas response due to the limited surface area (Mirzaei et al., 2019). Therefore researchers are more interested in the use of thin- or thick-film gas sensors either in the tubular or planar configuration, as shown in Fig. 1.2.

Table 1.1 Change in the resistance of n- and p-type MOS when exposed to reducing and oxidizing gases.

Type of MOS	When exposed to reducing gases	When exposed to oxidizing gases
n-type	Resistance decrease	Resistance increase
p-type	Resistance increase	Resistance decrease

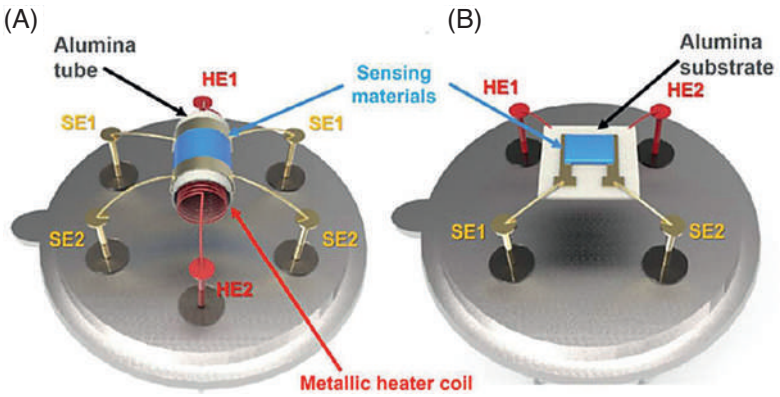

Figure 1.2. Schematic diagram of metal oxide gas sensor configurations: (A) tubular and (B) planar (SE and HE represent the sensor electrode and heater electrode, respectively). Reproduced with permission from (Lee, 2018), Copyright 2018, Elsevier.

Thin- or thick-film sensors are prepared by depositing a sensitive layer on an insulating substrate such as alumina (Al_2O_3) and Si/SiO_2 wafer. The metal oxide powder is ground together with suitable solvents like ethanol and terpineol using an agate mortar to form a slurry for the tubular configuration. Then the slurry is coated on an alumina tube, on which a pair of Au electrodes had been printed previously, followed by drying and subsequent annealing at high temperatures. Finally, a small Ni–Cr alloy coil is inserted into the tube as a heater so as to adjust and optimize the working temperature of the gas sensor. The tubular configuration is shown in Fig. 1.2A. Si/SiO_2 or alumina substrate with preprinted interdigitated gold electrodes is commonly used for the fabrication of planar sensors (Fig. 1.2B). A schematic diagram of the interdigitated pattern is shown in Fig. 1.3. The use of platinum electrodes is limited due to their high cost. In such cases Au electrodes are more preferred. The working temperature is obtained by placing the device on the external heater or with the help of an internal heater printed at the back of the substrate. The planar configuration is more

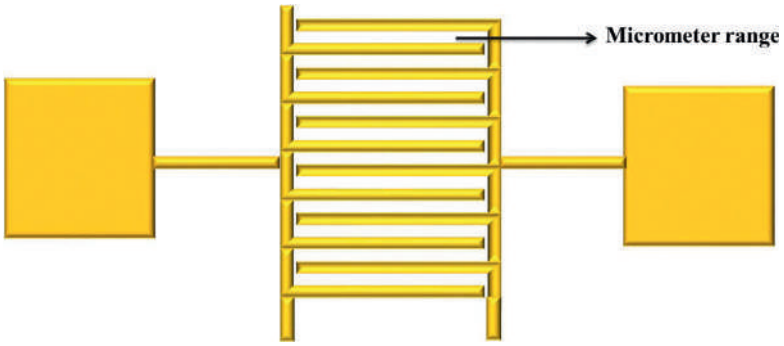

Figure 1.3. Schematic diagram of the interdigitated electrode pattern.

preferred for large-scale production due to the improved fabrication productivity and quality of the sensor (Lee, 2018; Mirzaei et al., 2019).

When we consider the substrate material, alumina is the best available substrate material due to its high thermal conductivity and stability, low thermal expansion coefficients, high mechanical strength, and low electrical conductivity (Lee, 2018). The high thermal stability of alumina is an important feature since most MOS-based sensors work at relatively higher temperatures. However, for the fabrication of electrodes in the micrometer range ($<10\ \mu m$), microfabrication techniques such as UV or electron-beam lithography has to be employed, which leads to the preference of a Si/SiO_2 wafer as the substrate material over the alumina substrate due to the surface roughness of alumina substrate.

Plastic foils can also be used as supporting materials due to the increasing demand for flexible gas sensors. The advantages of plastic foils are their foldable and wearable design, lightweight, transparency, and mass productivity due to roll-to-roll printing processes. Polymers such as polyimide (PI), with relatively high thermal stability, have been widely used as supporting materials for flexible sensors operating at a relatively higher temperature. However, the operation of MOS sensors above 400°C is difficult using PI substrates (Wang et al., 2016).

1.2.3 Gas sensing measurement system

Generally, two types of measurement systems are commonly used for studying the gas sensing properties of the device: static and dynamic. Fig. 1.4 shows the schematic diagram of a static measurement system. The system consists of a transparent gas chamber of a defined volume with a gas inlet. The sample is placed inside the chamber under a controlled temperature and humidity. The operating temperature of the sample can be adjusted by varying the heating voltage. During the measurement, a fixed amount of analyte gas is injected through the gas

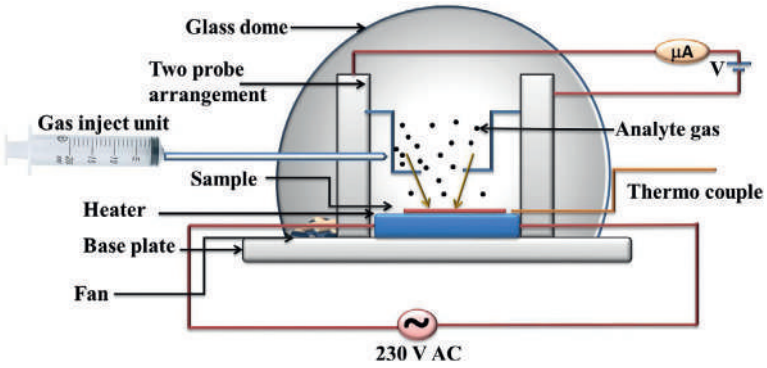

Figure 1.4. Schematic diagram of the static gas sensing measurement system (Mirzaei et al., 2018, 2019; Patil, 2007).

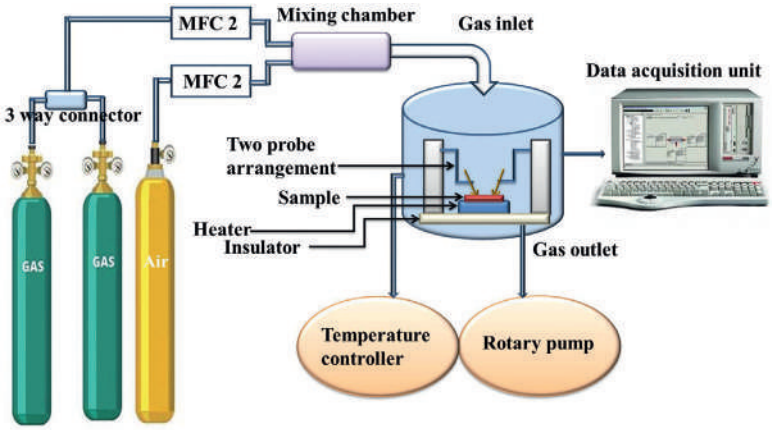

Figure 1.5. Schematic diagram of the dynamic gas sensing measurement system.

inlet with the help of a syringe. To uniformize the distribution of the injected test gas, an electrical fan is installed inside the chamber. The concentration of analyte gas is calculated with the ratio of the volume of the injected gas to the volume of air under standard atmospheric pressure. After reaching saturation in the current, the chamber is opened to recover to the initial current in the air atmosphere. The procedure is repeated for different analyte gases at different conditions (Mirzaei et al., 2018, 2019).

A dynamic system consists of gas cylinders with a known concentration, mass flow controllers (MFCs), a test chamber with a gas inlet and outlet, heating arrangement, electrical measurement arrangements, and data acquisition systems, as shown in Fig. 1.5. With the help of MFCs, the flow rate of analyte gases and synthetic air can be controlled. The concentration of analyte gases can be changed by mixing properly with synthetic air or nitrogen in a mixing chamber connected prior to the test chamber. Then the mixed volume of gas

is passed into the test chamber through the gas inlet. The sample is placed on an external heater and the working temperature can be controlled with a temperature controller. The sample is connected to a measurement unit to record the current variation continuously. During measurement, the current through the sample in air and in the presence of analyte gas at different temperatures is recorded. Finally, after the measurement, the gas from the test chamber is removed with the help of a rotary pump arrangement.

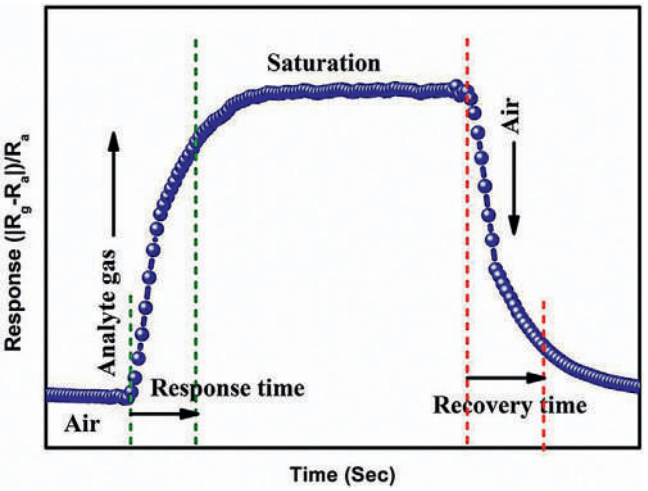

Figure 1.6. Typical response curve of an MOS-based gas sensor.

1.2.4 Performance parameters

The gas-sensing performance of sensors is evaluated using the following important parameters (Balaguru 2004; Tonezzer et al., 2015; Tshabalala et al., 2016).

1.2.4.1 Gas response and sensitivity

Generally, the response of a semiconductor-based gas sensor is defined as follows:

$$\text{Response} = \frac{|R_g - R_a|}{R_a} \tag{1.6}$$

where R_a and R_g represent the resistances of the gas sensor in the presence of air and target gas, respectively. A typical response curve is shown in Fig. 1.6. Sensitivity is the change in measured resistance (ΔR) with a change in analyte concentration (ΔC), i.e., the slope of a calibration graph: $\mathrm{S} = S = {}^{\Delta R}/_{\Delta C}$.

1.2.4.2 Selectivity

It is the ability of a sensor to differentiate a specific target gas from a mixture of gases. A good sensor will detect a particular gas while remaining insensitive to other gases. The selectivity coefficient (K) of a gas sensor can be written as

$$K = \frac{S_I}{S_{II}} \tag{1.7}$$

where S_I and S_{II} are the sensing responses of the sensor toward two different gases, I and II, respectively.

1.2.4.3 Stability

Stability is defined as the reproducibility of the device in the sensing measurement after long use. To avoid the effects of nonrepeatability

after repeated use, the materials are subjected to a thermal pretreatment.

1.2.4.4 Response time and recovery time

Response time is defined as the time taken for the sensor to reach 90% of the maximum response and recovery time is the time taken for the sensor to reach back to 10% of the maximum response after the removal of analyte gas. For practical applications, rapid response and short recovery times are always preferred for the efficient detection of toxic or explosive target gases.

1.2.4.5 Operating temperature

Generally, the working temperature of metal oxide gas sensors is in the range of 30°C–500°C. The response is limited at low temperatures because of the slow rates of the chemical reactions, and it is limited at high temperatures due to the high diffusion rate of gas molecules. The optimum temperature should be chosen to get maximum sensor response and short response time and recovery time etc.

1.2.4.6 Limit of detection (LoD)

The detection limit is defined as the lowest concentration of gas that can be detected by the sensor and is expressed as follows:

$$\mathrm{LoD} = \frac{3 \times \mathrm{noise_{rms}}}{\mathrm{Slope}} \tag{1.8}$$

where noise_{rms} represents the standard deviation of the sensor response, and the slope is the first derivative of the response vs. the gas concentration curve.

1.3 Strategies for improving the performance of metal oxide–based gas sensors

1.3.1 Changing the sensing layer morphology

The morphology of the sensing materials plays a critical role in the sensing performance of metal oxide gas sensors (Dong et al., 2020). Exposed surface area and porosity are different for different morphologies; thus the number of active sites for gas adsorption is also different, which affects the gas sensing performance. Investigations are carried out on different dimensional nanostructures to get an enhanced sensing response (Lin et al., 2017). Fig. 1.7 shows the ethanol sensing properties of SnO_2 sensors with different morphologies. From the figure, it

is clear that SnO_2 nanosheets show the best sensing performances with the largest surface area and a porous structure that has large number of active sites for gas adsorption than the other morphologies (Zeng et al., 2013).

Zero-dimensional (0D) nanoparticles are used in the field of gas sensors but the agglomeration of such particles limits its application in this field. One-dimensional (1D) nanostructures such as nanotubes, nanorods, nanowires, and nanofibers have a high aspect ratio and hence a large surface-to-volume ratio, thus having enhanced gas sensing properties. Also for 1D structures, electrons flow along the axial direction, which increases the speed of charge transfer, thus further enhancing the sensing performance. Two-dimensional (2D) nanostructures have also garnered interest due to their large surface area. Also, they can be used as building blocks for three-dimensional (3D) hierarchical structures. 3D hierarchical nanostructures are potential candidates as sensing materials compared to 0D, 1D, and 2D nanostructures because of their large surface area, abundance of active sites, high porosity, a less agglomerated configuration, and fast interfacial transport. For porous nanostructures, analyte gas interacts with the surface; also the gas penetrates into the sensing material, which improves the sensing response (Lin et al., 2017; Németh et al., 2007; Zeng et al., 2013). Hollow nanostructures show a better response than solid nanostructures. In the case of hollow structures analyte gas can be adsorbed on the inner and outer surfaces of the sensing materials, which facilitates the superior performance of sensors. For example, Guo et al. studied the ethanol sensing properties of Cu_2O hollow and solid sphere sensors (Guo et al., 2019). Fig. 1.8(A&B) shows the scanning electron microscope (SEM) images of Cu_2O solid and hollow spheres. The hollow spheres show superior gas sensing performance over solid spheres, as shown in Fig. 1.8C. The enhanced performance is due to their unique hollow structure, which provides plenty of active sites on both the inner and outer surfaces.

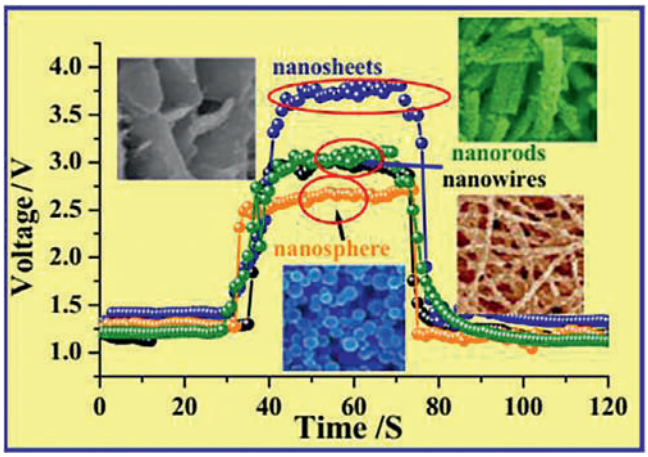

Figure 1.7. Response–recovery characteristics of the SnO_2 sensors with different morphologies at 340°C toward 100 ppm ethanol. Reproduced with permission from (Zeng et al., 2013), Copyright 2013, Elsevier.

1.3.2 Doping with noble metals

Noble metals such as Pt, Pd, Au, and Ag are widely used as doping materials for metal oxide–based sensors due to their catalytic activities. They can reduce the activation energy and hence increase the adsorption on the MOS surface. This will lead to fast response and

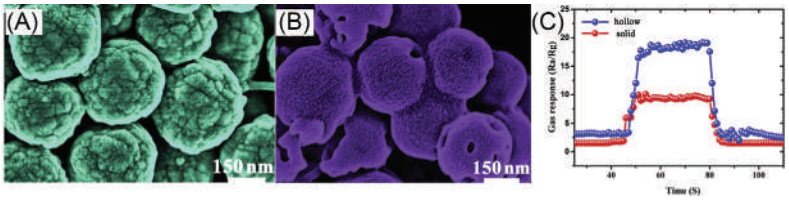

Figure 1.8. SEM images of (A) solid Cu_2O microspheres and (B) hollow Cu_2O microspheres. (C) Response–recovery characteristics of hollow and solid sphere Cu_2O sensors at 350°C toward 200 ppm ethanol. Reproduced with permission from (Guo et al., 2019), Copyright 2019, Elsevier.

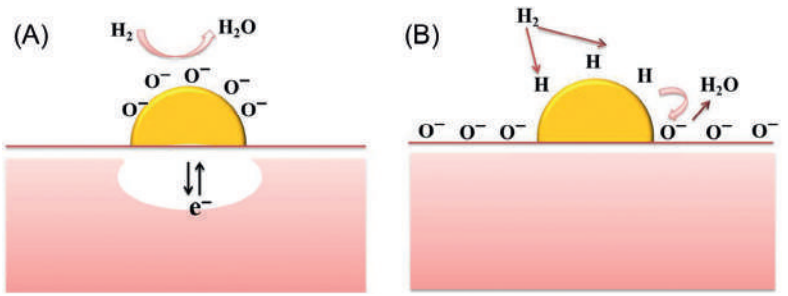

Figure 1.9. Sensitization mechanisms of noble metal–doped metal oxide surface by (A) Fermi-level control and (B) spillover effect (Degler et al., 2019; Franke et al., 2006).

recovery times and lower the operating temperature (Luo et al., 2017). Also, they can produce more active sites on the surface. Analyte gas can be adsorbed on the noble metal and then spilled into the MOS. For example, noble metals can dissociate H atom from H_2, which then spills over and is adsorbed on the surface of metal oxide, as shown in Fig. 1.9. The role of a noble metal is to bring down the reaction activation energy. Generally, the work function of noble metals is more than that of semiconductors; hence the Fermi level of a noble metal lies below that of MOS. Due to the work function difference, the electrons from the semiconductor flow into the noble metals to equal the Fermi levels, as shown in Figs. 1.9 and 1.10. This electron transfer generates the Schottky barrier at the interface and energy bands in the MOS are bent upward due to positive charge, which makes the material more sensitive to analyte gases, as shown in Fig. 1.10 (Degler et al., 2019; Sarkar et al., 2015).

1.3.3 Forming hierarchical structures

For a better gas sensing response, heterostructures have been synthesized from two different metal oxides having different Fermi levels. The metal oxides can be either p-type or n-type. By the combination of these metal oxides, p–p, n–n, and p–n junctions can be formed. During the formations of heterostructures, due to the difference in Fermi level, electrons flow from areas of higher Fermi level to areas of lower Fermi level until the two Fermi levels are equal, as explained before. This charge transfer creates a depletion region at the interface of the two metal oxides and increases the resistance of the materials.

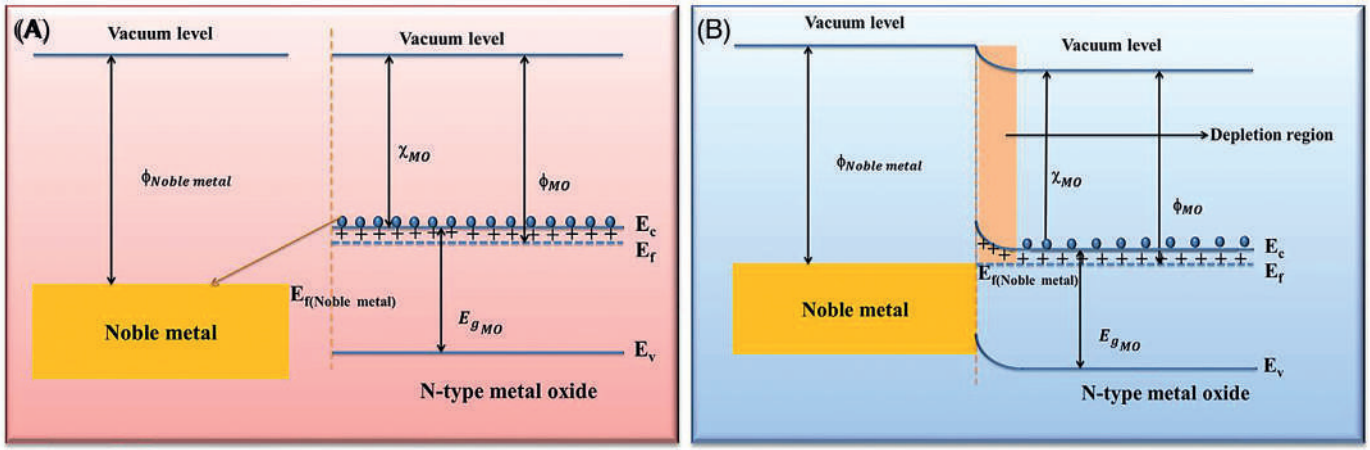

Figure 1.10. Schematic diagram showing the possible band structures at the Schottky junction (A) before and (B) after thermal equilibrium.

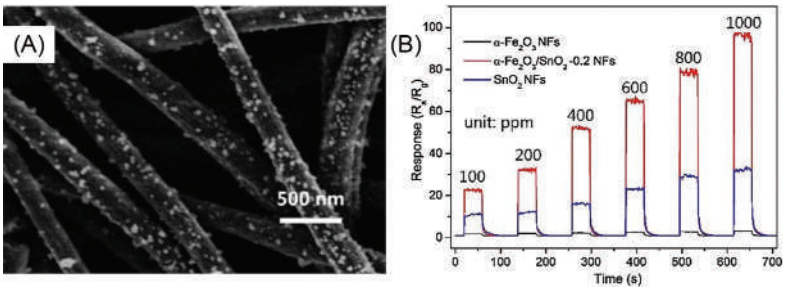

Figure 1.11. (A) SEM images of α-Fe_2O_3/SnO_2 nanofibers and (B) dynamic response curves of α-Fe_2O_3, α-Fe_2O_3/SnO_2 and SnO_2 nanofibers toward 100–1000 ppm ethanol at 300°C. Reproduced with permission from (Yan et al., 2018), Copyright 2018, Elsevier.

The increased resistance makes the sensing material more sensitive to the analyte gases (Alenezi et al., 2014; Chang et al., 2020; Gao et al., 2019; Qin et al., 2020). For example, Yan et al. synthesized hierarchical α-Fe_2O_3/SnO_2 nanofibers by using the electrospinning method (Yan et al., 2018). The SEM image of hierarchical nanofibers is shown in Fig. 1.11A. Compared to pure α-Fe_2O_3 and SnO_2 nanofibers, the hierarchical structure exhibits an enhanced ethanol sensing response, as shown in Fig. 1.11B. The better sensing response of α-Fe_2O_3/SnO_2 heterostructure nanofibers is due to the heterojunctions constructed between the two MOSs.

1.3.4 Exposing high-energy facets

Due to the different atomic arrangements of two nonequivalent lattice planes of a crystal, the faceting process is widely used for many interesting applications. In gas sensing applications the surface properties of the sensing material are critical factors in determining its performance. Controlling crystal facet growth is one of the basic strategies to improve the surface properties and enhance both the sensitivity and the selectivity of the sensors. But unfortunately, high-energy facets are rapidly dominated by lower-energy facets during crystal growth processes, which makes the facet engineering process more difficult. For example, in the case of SnO_2, crystal planes such as {221} and {111} having a higher relative surface energy (2.28 Jm^{-2} and 2.209 Jm^{-2}) than that of generally obtained stable low-index facets such as {110} (1.401 Jm^{-2}), {101} (1.554 Jm^{-2}), and {100} (1.648 Jm^{-2}) (Han et al., 2009; Wang et al., 2012). Usually, the crystal tends to expose these low-surface-energy crystal planes during growth. But under optimal conditions, the crystal can be grown in a direction favorable for the exposure of high-energy facets.

As explained before, the gas sensing mechanism of the MOSs can be described as the change in the electrical conductivity arising from the chemical interaction between the analyte gas and the chemisorbed

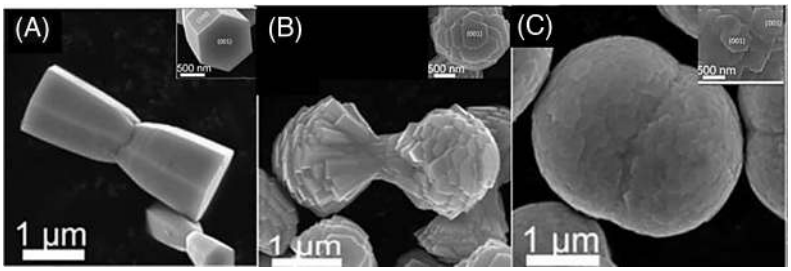

Figure 1.12. FESEM images of ZnO: (A) prism, (B) dumbbell, and (C) twin sphere (Insets: Corresponding enlarged vertical images). Reproduced with permission from (Gong et al., 2018), Copyright 2018, Elsevier.

oxygen species on the metal oxide surface. These chemical interactions involve the gas adsorption, charge transfer, and gas desorption occurring on the surface of metal oxide nanostructures. The ability to adsorb oxygen species (such as O_2^-, O^{2-}, and O^-) and target molecules depends on the exposed crystal facet of the surface since the high-index crystal facets of materials can significantly affect their surface properties, especially the surface adsorptivity, by providing a large number of active sites for adsorption. The chemical activity of such materials is very high due to the presence of high densities of atom steps, ledges, kinks, and dangling bonds. For example, on the {0001} surface, Zn atoms are usually coordinative unsaturated, located in twofold-coordinated sites with two dangling bonds and threefold-coordinated sites with one dangling bond. However, on the {1010} surface, most of the Zn atoms are fourfold coordinated and only a small part of them are threefold coordinated with one dangling bond. Obviously, more dangling bonds are presented on the {0001} surface than the {1010}surface, which increases the oxygen adsorption on th {0001} surface, resulting in an improved sensing performance (Xu et al., 2017). Another reason for the improved sensitivity of the facet-dependent gas sensors is the single-crystalline nature. The single-crystalline structure could reduce the grain boundary barriers and provide better electronic transporting ability, which may lead to an increase in sensitivity compared to the polycrystalline structure (Chang et al., 2013).

One of the important advantages of the specific facets of semiconductor nanocrystals is the selective adsorption to certain gas molecules. Therefore the sensing properties of metal oxide nanocrystals can be tuned toward a particular analyte gas depending on their exposed crystal facets. It is reported that sensors made of zinc oxide (ZnO) prisms exposed with {100} facets show selective response to H_2S gas, whereas ZnO twin-spheres exposed with {001}facets show selective response to acetone. The intermediate ZnO dumbbell structure between the prisms and twin-spheres exposed with both facets show similar sensing capabilities to H_2S and acetone (Gong et al., 2018). The microstructures are shown in Fig. 1.12.

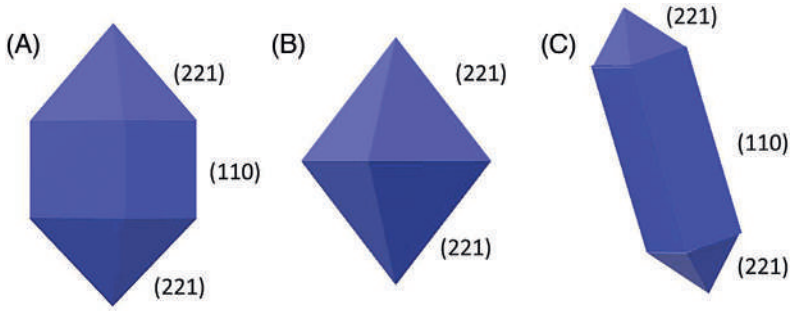

Figure 1.13. Schematic model of different SnO_2 nanoparticles: (A) elongated octahedral, (B) octahedral, and (C) lance-shaped nanoparticles prepared via hydrothermal synthesis in the acidic medium of HCl at 200°C for 12 h (Han et al., 2009).

1.4 General synthesis routes of high-energy crystal facet–exposed metal oxides

The hydrothermal route is one of the most convenient methods for the synthesis of facet-exposed nanostructures. The reaction dynamics can be controlled by choosing suitable precursors, the medium, and experimental conditions. Additionally, some surfactant agents such as polyvinylpyrrolidone (PVP) and formamide may be used, which can selectively adsorb onto specific facets to enhance the growth in a particular direction only. For example, during a typical synthesis of SnO_2 octahedra particles by Han et al., a small amount of HCl was added along with the PVP for the predominant exposure of the high-energy {221} facets (Han et al., 2009). SnO_2 octahedra particles with different morphologies enclosed within {221} surfaces were formed according to the variation of the volume of HCl, as shown in Fig. 1.13. The formation of octahedral SnO_2 particles is the result of the coordinative effect of H^+ and Cl^- ions. Through the specific adsorption of Cl^- ions, we can kinetically control the shape of the SnO_2 nanocrystals. In an aqueous solution, tin(IV) ions can be easily hydrolyzed to produce extremely small SnO_2 particles. But the growth of SnO_2 nanocrystals can be slowed down by adding the HCl solution, which can inhibit the hydrolysis of Sn^{4+} ions to a certain extent. The acidity is crucial at pH 0.4 since the higher concentration of HCl will completely inhibit the hydrolysis of Sn^{4+}. The PVP surfactant plays a key role in dispersing the SnO_2 particles rather than in morphology control. For the synthesis of octahedral SnO_2 particles enclosed by high-energy {111} facets, a basic medium of tetramethylammonium hydroxide (TMAH) can also be used (Wang et al., 2012). In a similar way, PVP can also be used for the synthesis of p-type Cu_2O nanostructures with exposed {111} facets (Wang et al., 2017) and {111} faceted ultrathin NiO single-crystalline porous nanosheets (Liang et al., 2019a). Fluoride ions from NaF, HF, and NH_4F are known to preserve high-energy facets in metal oxide systems through selective capping (Wang et al., 2013). NaCl, Na_2SO_4, K_2SO_4, and formamide have also become well known recently for their

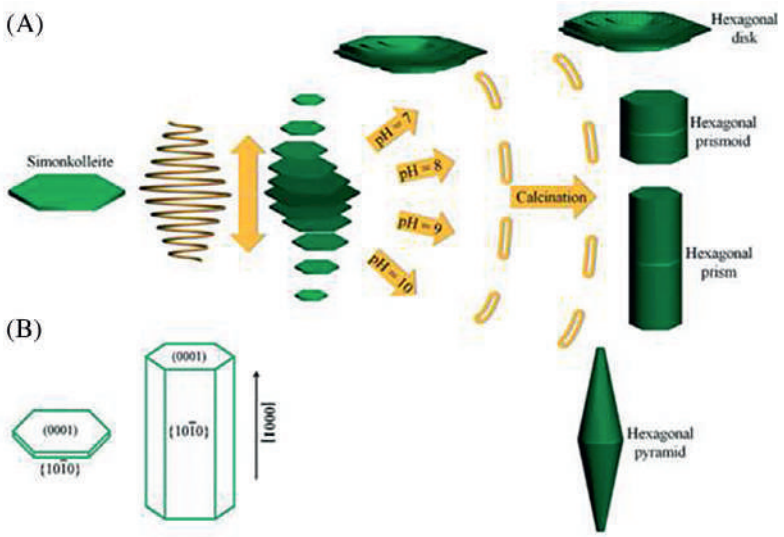

Figure 1.14. Illustration of (A) the formation mechanism of various hexagonal ZnO structures and (B) the crystal facets in hexagonal ZnO structures. Reproduced with permission from (Qin et al., 2014), Copyright 2014, Royal Society of Chemistry.

use as capping agents for the synthesis of a high-energy facet–exposed metal oxide system (Jia et al., 2014).

In the case of anatase TiO_2 nanoparticles hydrofluoric acid or other fluorine-containing species were used as capping agents for synthesizing samples exposed with a large percentage of reactive {001} facets (Majumder & Roy, 2017). These routes are not environmentally friendly as fluorine-containing compounds generate toxic and corrosive substances at high temperatures. Therefore the development of a novel synthesis strategy is needed with fluorine-free chemicals as the capping agent. A few reports are available in the literature on the successful growth of {001} faceted TiO_2 nanostructures using cetyltrimethylammonium bromide (CTAB) (Majumder & Roy, 2017), urea (Liang et al., 2019b; Yang et al., 2015), etc. ZnO nanostructures with exposed highly reactive facets can be synthesized through hydrothermal routes with and without the help of surfactants like CTAB or by adjusting the pH of the precursor solution (Qin et al., 2014). The structural variation or the percentage variation of the particular facets by adjusting the pH of the precursor solution is clearly shown in Fig. 1.14.

1.5 Facet-dependent gas sensing properties of zinc oxide gas sensors

Here, the sensing properties of ZnO nanostructures with exposed high-energy facets are discussed. Kaneti et al synthesized two types of ZnO nanostructures, namely, nanoplates and nanorods with exposed {0001} and {10$\bar{1}$0} crystal facets through facile solvothermal methods (Kaneti et al., 2014). In the gas sensing results the response of ZnO nanoplates toward ethanol was two times higher than that of the ZnO

nanorods at an optimum operating temperature of 300°C. The bond lengths corresponding to O–H, C–H, C–O, and C–C bonds for free ethanol molecules obtained from density functional theory (DFT) calculation were 0.977, 1.098, 1.438, and 1.513 Å, respectively. When the ethanol gas is exposed to the ZnO surface, the O atom from the ethanol molecule forms a hydrogen bond with the surface Zn atom and the H atom with the adsorbed O^-. The DFT calculations proved that the O–H bond distance of the ethanol molecule increases during the interactions with the surface Zn atoms and the greatest elongation is observed for the {0001} crystal plane, which leads to the stronger adsorption of ethanol molecule on {0001} surface. In addition, the C–C–O and C–O–H angles of the ethanol molecule also change significantly when the ethanol molecule is adsorbed on the {0001} crystal plane compared to the free ethanol molecule. The above analysis reveals that the strongest ethanol interaction occurs on the {0001} surface compared to the other ZnO surfaces, and thus the highest ethanol response is obtained.

Similarly, Tian et al synthesized a ZnO sensor by using the solution process that exhibits three times higher ethanol response than an unprocessed sensor at an operating temperature range of 240°C–420°C, probably because of the higher exposed {0001} facet for oxygen adsorption (Tian et al., 2012). Such a gas sensor exhibits a steadier and lower initial resistance and a clearer and faster resistance change to 1 ppm ethanol and thus can be used to detect the ethanol even at low concentrations. Chang et al. synthesized ZnO porous 3D nanostructures with an exposed {0001} facet that showed enhanced NO_2 sensing response than the commercially available ZnO sensor (Chang et al., 2013). Alenezi et al. studied the ethanol sensing properties of ZnO nanostructures exposed with {0001} and $\{10\bar{1}0\}$ facets (Alenezi et al., 2013). The {0001} facets gave better results than the $\{10\bar{1}0\}$ facets. Xu et al. synthesized ZnO nanosheets with exposed {0001} facets that showed superior ethanol sensing properties than those with $\{10\bar{1}0\}$ facets (Xu et al., 2017). A higher acetone selectivity could be achieved with surface-tuned ZnO nanosheets with exposed {100} facet sensors synthesized by Xiao et al. (2012). An additional surface modification using Pd nanoparticles could impose only a slight change in the interaction with the acetone and thus in the response value. Qin et al. studied the ethanol sensing properties of different ZnO nanostructures (Qin et al., 2014). At a working temperature of 330°C, the ZnO disk with the most exposed {0001} facet showed the highest gas response toward ethanol, which was nearly two, three, and six times higher than those of prismoid, prism, and pyramid structures with a lesser amount of {0001} facet-exposed, respectively.

Gong et al studied the gas sensing selectivity of different ZnO nanostructures such as a prism, dumbbell, and twin-sphere (Gong et al., 2018). Specifically, the sensors made with ZnO prisms mainly exposed with {100} facets showed the highest response to

H_2S compared to the other synthesized shapes such as dumbbell and twin-sphere among the reducing gases, including acetonitrile, chlorobenzene, benzene, methylbenzene, ethanol, formaldehyde, acetone, ammonia, and methanol (Fig. 1.15A). In contrast, twin-sphere devices covered with {001} facets produced the highest response to acetone (Fig. 1.15C). Also, the sensors exposed with both the facets (dumbbell shape) exhibit similar responses to acetone and H_2S and therefore show poor selectivity to the gases (Fig. 1.15B). Here, the acetone and H_2S responses of the sensors linearly increase and decrease, respectively, with increasing the coverage of {001} facets on the ZnO surface. The adsorption energies (E_a) of acetone and H_2S molecules onto ZnO crystals closely depend on the facets of their surfaces and it is 1.40 eV for H_2S and 1.17 eV for acetone onto {100} facets of ZnO crystal. This means that the {100} facets of ZnO crystals could absorb and sense H_2S more when compared to acetone. However, the adsorption energy of H_2S and acetone to {001} planes are 0.48 and 0.77 eV, respectively, which is favorable for the selective detection of acetone.

Along with the enhanced gas sensing responses, this surface morphology tuning strategy can be used for the selective adsorption and detection of a particular gas, increasing the demand for developing a high-energy facet–exposed metal oxide nanostructure. The ongoing works in this field are proving improved properties such as response and recovery time, stability, reversibility, and repeatability, which will demand the high production of facet-exposed gas sensors.

1.6 Challenges and approaches

From the discussed examples, it is clear that the exposed facets are the key factor that determines their sensing ability to certain gases. For the same type of MOS, either the surface morphology or the surface area does not totally affect the sensing properties; while the exposed crystal planes plays a crucial role in tuning the sensing properties. The literature proves the crucial role of surface engineering by exposing high-energy facets in enhancing the gas sensing properties of MOS materials. The production of many unsaturated dangling bonds in the exposed crystal surface is the most promising approach to realize the superior gas sensing performance, which can provide more active sites for the adsorption of gas molecules, resulting in excellent gas sensing properties of MOS. However, there are still some challenges that remain in several aspects:

- The controlled synthesis of MOS nanomaterials with exposed high-energy facets is challenging since the facets having high surface energy usually grow rapidly and finally vanish. Although there have been several successful reported syntheses, we still need a detailed study on their growth mechanism.

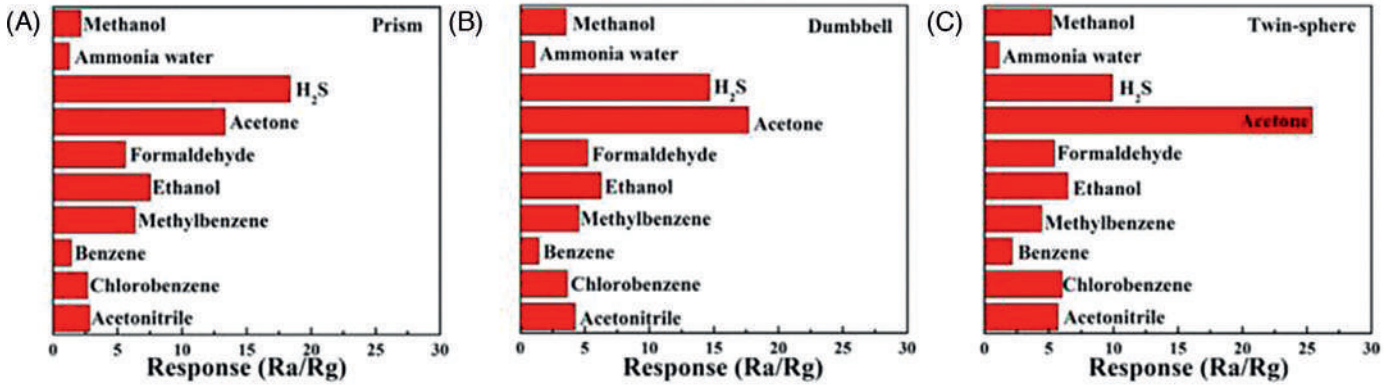

Figure 1.15. (A–C) Selectivity of the different nanocrystals upon exposure to 100 ppm of various gases. Reproduced with permission from (Gong et al., 2018), Copyright 2018, Elsevier.

- The long-term stability of high-energy facets during the gas sensing process has not been reported yet. The stability of the gas sensors is an important property for potential biomedical applications.
- For achieving the selective detection of biomarkers such as acetone and ammonia, the gas sensing mechanism between the analyte material and the gas should be well known, which further demands a deep investigation in this field.
- The challenge in the use of the gas sensor as a breath analyzer is in developing highly sensitive and selective gas sensors since it involves the analysis of a mixture of VOCs, and their concentration in the breath is very low.

The sensing material exposed with high-energy crystal surfaces have superior physical and chemical properties favorable for gas sensing application. However, we still requires further experiments and research for the large scale production of facet-exposed gas sensors for the real time measurements.

1.7 Application

One of the important applications of gas sensors in the medical field is the early diagnosis of diseases by examining exhaled breath. Exhaled human breath mainly consists of nitrogen, oxygen, CO_2, water, inert gases, and traces of volatile organic compounds (VOCs). The concentration of VOCs is very low in the ppm range. There are more than 1000 types of VOCs present in the exhaled breath, which are closely related to certain kinds of diseases. They are known as breath markers since they correlate to specific diseases such as ammonia with kidney disease, carbon monoxide with lung inflammation, and dimethyl sulfide with liver disease etc. If this breath print is analyzed correctly, the current health status of a person could be identified easily. For example, among the different gas biomarkers, acetone is considered to be the key factor that reflects the progress or the therapeutic effect of diabetes mellitus. The acetone level in the exhaled breath of a healthy individual is reported as 300–900 ppb, while it is increased to more than 1.8 ppm in the case of a diabetic patient. Therefore the detection of gas biomarkers in exhaled breath is rapidly emerging, and it has been developed as an effective and noninvasive tool for diagnosing and monitoring the physiological conditions of the human body (Güntner et al., 2019; Lin et al., 2019; Righettoni et al., 2015; Yoon & Lee, 2017).

1.8 Summary

In this chapter a basic idea regarding MOS-based sensors, including their gas sensing mechanism, design of the gas sensor, design of the gas sensing measurement unit, and performance parameters, was

provided. Strategies for improving the performance of metal oxide–based gas sensors such as through a change in morphology, doping with a noble metal, formation of hierarchical structure, and exposed high-energy facets were also discussed. The gas sensing properties of high-energy facet–exposed MOS gas sensors were discussed in detail.

References

Alenezi, M.R., Alshammari, A.S., Jayawardena, K.D.G.I., Beliatis, M.J., Henley, S.J., Silva, S.R.P., 2013. Role of the exposed polar facets in the performance of thermally and UV activated ZnO nanostructured gas sensors. J. Phys. Chem. C 117 (34), 17850–17858. https://doi.org/10.1021/jp4061895.

Alenezi, M.R., Henley, S.J., Emerson, N.G., Silva, S.R.P., 2014. From 1D and 2D ZnO nanostructures to 3D hierarchical structures with enhanced gas sensing properties. Nanoscale 6 (1), 235–247. https://doi.org/10.1039/c3nr04519f.

Ananya, D., 2018. Semiconductor metal oxide gas sensors: A review. Materials Science and Engineering: B 206–217. https://doi.org/10.1016/j.mseb.2017.12.036.

Arshak, K., Gaidan, I., 2005. Development of a novel gas sensor based on oxide thick films. Materials Science and Engineering B: Solid-State Materials for Advanced Technology 118 (1–3), 44–49. https://doi.org/10.1016/j.mseb.2004.12.061.

Balaguru, R.J.B., Jeyaprakash, B.G., 2004. Mimic of a Gas sensor, Metal Oxide Gas Sensing Mechanism, Factors Influencing the Sensor Performance and Role of nanomaterials based gas sensors. NPTEL–Electrical Electron. Eng. Nanodevices 1–30.

Barsan, N., Weimar, U., Chemistry, T. (2012). Fundamentals of metal oxide gas sensors. In: IMCS 2012 - The 14th International Meeting on Chemical Sensors (pp. 618–621). https://doi.org/10.5162/IMCS2012/7.3.3.

Chang, J., Ahmad, M.Z., Wlodarski, W., Waclawik, E.R., 2013. Self-assembled 3D ZnO porous structures with exposed reactive {0001} facets and their enhanced gas sensitivity. Sensors (Switzerland) 13 (7), 8445–8460. https://doi.org/10.3390/s130708445.

Chang, X., Qiao, X., Li, K., Wang, P., Xiong, Y., Li, X., Xia, F., Xue, Q., 2020. UV assisted ppb-level acetone detection based on hollow ZnO/MoS_2 nanosheets core/shell heterostructures at low temperature. Sens. Actuators B 317. https://doi.org/10.1016/j.snb.2020.128208.

Degler, D., Weimar, U., Barsan, N., 2019. Current understanding of the fundamental mechanisms of doped and loaded semiconducting metal-oxide-based gas sensing materials. ACS Sensors 4 (9), 2228–2249. https://doi.org/10.1021/acssensors.9b00975.

Dong, C., Zhao, R., Yao, L., Ran, Y., Zhang, X., Wang, Y., 2020. A review on WO_3 based gas sensors: Morphology control and enhanced sensing properties. J. Alloys Compd. 820. https://doi.org/10.1016/j.jallcom.2019.153194.

Franke, M.E., Koplin, T.J., Simon, U., 2006. Metal and metal oxide nanoparticles in chemiresistors: does the nanoscale matter? small 2, 36–50. doi:10.1002/smll.200500261.

D.R. Patil, D.R., Patil, L.A., Patil, P.P., et al., 2007. Cr_2O_3-activated ZnO thick film resistors for ammonia gas sensing operable at room temperature. Sens Act B 126, 368374. doi:10.1016/j.snb.2007.03.028.

Gao, X., Ouyang, Q., Zhu, C., Zhang, X., Chen, Y., 2019. Porous MoO_3/SnO_2 nanoflakes with n-n junctions for sensing H_2S. ACS Applied Nano Materials 2 (4), 2418–2425. https://doi.org/10.1021/acsanm.9b00308.

Gao, X., Zhang, T., 2018. An overview: Facet-dependent metal oxide semiconductor gas sensors. Sens. Actuators B 277, 604–633. https://doi.org/10.1016/j.snb.2018.08.129.

Gong, F., Peng, L., Zhang, Y., Cao, Y., Jia, D., Li, F., 2018. Selectively sensing H_2S and acetone through tailoring the facets exposed on the surfaces of ZnO supercrystals. Mater. Lett. 218, 106–109. https://doi.org/10.1016/j.matlet.2018.01.116.

Güntner, A.T., Abegg, S., Königstein, K., Gerber, P.A., Schmidt-Trucksäss, A., Pratsinis, S.E., 2019. Breath sensors for health monitoring. ACS Sensors 4 (2), 268–280. https://doi.org/10.1021/acssensors.8b00937.

Guo, Q., Li, Y., Zeng, W., 2019. Synthesis of Cu_2O microspheres with hollow and solid morphologies and their gas sensing properties. Physica E 114. https://doi.org/10.1016/j.physe.2019.113564.

Gurlo, A., 2011. Nanosensors: Towards morphological control of gas sensing activity. SnO_2, In_2O_3, ZnO and WO_3 case studies. Nanoscale 3 (1), 154–165. https://doi.org/10.1039/c0nr00560f.

Han, X., Jin, M., Xie, S., Kuang, Q., Jiang, Z., Jiang, Y., Xie, Z., Zheng, L., 2009. Synthesis of tin dioxide octahedral nanoparticles with exposed high-energy {221} facets and enhanced gas-sensing properties. Angew. Chemie. 121, 9344–9347. https://doi.org/10.1002/ange.200903926.

Jia, Q.Q., Ji, H.M., Wang, D.H., Bai, X., Sun, X.H., Jin, Z.G., 2014. Exposed facets induced enhanced acetone selective sensing property of nanostructured tungsten oxide. J. Mater. Chem. A 2 (33), 13602–13611. https://doi.org/10.1039/c4ta01930j.

Kaneti, Y.V., Zhang, Z., Yue, J., Zakaria, Q.M.D., Chen, C., Jiang, X., Yu, A., 2014. Crystal plane-dependent gas-sensing properties of zinc oxide nanostructures: Experimental and theoretical studies. Phys. Chem. Chem. Phys. 16 (23), 11471–11480. https://doi.org/10.1039/c4cp01279h.

Kashif, M., Ali, M.E., Ali, S.M.U., Hashim, U., Hamid, Abd, S., B, 2013. Impact of hydrogen concentrations on the impedance spectroscopic behavior of Pd-sensitized ZnO nanorods. Nanoscale Res. Lett. 8 (1), 1–9. https://doi.org/10.1186/1556-276X-8-68.

Kazemi, N., Hashemi, B., Mirzaei, A., 2016. Promotional effect of nitric acid treatment on CO sensing properties of SnO_2/MWCNT nanocomposites. Processing and Application of Ceramics 10 (2), 97–105. https://doi.org/10.2298/PAC1602097K.

Kuang, Q., Wang, X., Jiang, Z., Xie, Z., Zheng, L., 2014. High-energy-surface engineered metal oxide micro- and nanocrystallites and their applications. Acc. Chem. Res. 47 (2), 308–318. https://doi.org/10.1021/ar400092x.

Lee, J.H., 2018. Technological realization of semiconducting metal oxide-based gas sensors. Gas Sensors Based on Conducting Metal Oxides: Basic Understanding, Technology and Applications. Elsevier, pp. 167–216.

Liang, Y., Yang, Y., Zhou, H., Zou, C., Xu, K., Luo, X., Yu, T., Liu, Y., Ding, M., Yuan, C., 2019a. Active {1 1 1}-faceted ultra-thin NiO single-crystalline porous nanosheets supported highly dispersed Pt nanoparticles for synergetic enhancement of gas sensing and photocatalytic performance. Appl. Surf. Sci. 471, 124–133. https://doi.org/10.1016/j.apsusc.2018.12.012.

Liang, Y., Yang, Y., Zhou, H., Zou, C., Xu, K., Luo, X., Yu, T., Zhang, W., Liu, Y., Yuan, C., 2019b. A systematic study on the crystal facets-dependent gas sensing properties of anatase TiO_2 with designed {010}, {101} and {001} facets. Ceram. Int. 45 (5), 6282–6290. https://doi.org/10.1016/j.ceramint.2018.12.110.

Lin, T., Lv, X., Hu, Z., Xu, A., Feng, C., 2019. Semiconductor metal oxides as chemoresistive sensors for detecting volatile organic compounds. Sensors (Switzerland) 19 (2). https://doi.org/10.3390/s19020233.

Lin, T., Lv, X., Li, S., Wang, Q., 2017. The morphologies of the semiconductor oxides and their gas-sensing properties. Sensors (Switzerland) 17 (12). https://doi.org/10.3390/s17122779.

Liu, X., Zhang, J., Wu, S., Yang, D., Liu, P., Zhang, H., Wang, S., Yao, X., Zhu, G., Zhao, H., 2012. Single crystal α-Fe_2O_3 with exposed {104} facets for high performance gas

sensor applications. RSC Adv. 2 (15), 6178–6184. https://doi.org/10.1039/c2ra20797d.

Luo, Y., Zhang, C., Zheng, B., Geng, X., Debliquy, M., 2017. Hydrogen sensors based on noble metal doped metal-oxide semiconductor: A review. Int. J. Hydrogen Energy 42 (31), 20386–20397. https://doi.org/10.1016/j.ijhydene.2017.06.066.

Majumder, D., Roy, S., 2017. Non-fluorinated synthesis of anatase TiO_2 with dominant {001} facets: Influence of faceted structures on formaldehyde sensitivity. New J. Chem. 41 (15), 7591–7597. https://doi.org/10.1039/c7nj00648a.

Miller, D.R., Akbar, S.A., Morris, P.A., 2014. Nanoscale metal oxide-based heterojunctions for gas sensing: A review. Sens. Actuators B 204, 250–272. https://doi.org/10.1016/j.snb.2014.07.074.

Mirzaei, A., Kim, S.S., Kim, H.W., 2018. Resistance-based H_2S gas sensors using metal oxide nanostructures: A review of recent advances. J. Hazard. Mater. 357, 314–331. https://doi.org/10.1016/j.jhazmat.2018.06.015.

Mirzaei, A., Lee, J.H., Majhi, S.M., Weber, M., Bechelany, M., Kim, H.W., Kim, S.S., 2019. Resistive gas sensors based on metal-oxide nanowires. J. Appl. Phys. 126 (24). https://doi.org/10.1063/1.5118805.

Németh, A., Horváth, E., Lábadi, Z., Fedák, L., Bársony, I., 2007. Single step deposition of different morphology ZnO gas sensing films. Sens. Actuators B 127 (1), 157–160. https://doi.org/10.1016/j.snb.2007.07.091.

Neri, G., 2015. First fifty years of chemoresistive gas sensors. Chemosensors 3 (1), 1–20. https://doi.org/10.3390/chemosensors3010001.

Pal, J., Pal, T., 2015. Faceted metal and metal oxide nanoparticles: Design, fabrication and catalysis. Nanoscale 7 (34), 14159–14190. https://doi.org/10.1039/c5nr03395k.

Priya, M.J., Subha, P.P., Aswathy, P.M., Merin, K.W., Jayaraj, M.K., Rajeev Kumar, K., 2021. Selective detection of hydrogen sulphide from the background of low concentration reducing gases. Mater. Chem. Phys. 260, 124038. https://doi.org/10.1016/j.matchemphys.2020.124038.

Qin, N., Xiang, Q., Zhao, H., Zhang, J., Xu, J., 2014. Evolution of ZnO microstructures from hexagonal disk to prismoid, prism and pyramid and their crystal facet-dependent gas sensing properties. CrystEngComm 16 (30), 7062–7073. https://doi.org/10.1039/c4ce00637b.

Qin, S., Tang, P., Feng, Y., Li, D., 2020. Novel ultrathin mesoporous ZnO-SnO_2 n-n heterojunction nanosheets with high sensitivity to ethanol. Sens. Actuators B 309. https://doi.org/10.1016/j.snb.2020.127801.

Righettoni, M., Amann, A., Pratsinis, S.E., 2015. Breath analysis by nanostructured metal oxides as chemo-resistive gas sensors. Mater. Today 18 (3), 163–171. https://doi.org/10.1016/j.mattod.2014.08.017.

Sarkar, D., Xie, X., Kang, J., Zhang, H., Liu, W., Navarrete, J., Moskovits, M., Banerjee, K., 2015. Functionalization of transition metal dichalcogenides with metallic nanoparticles: Implications for doping and gas-sensing. Nano Lett. 15 (5), 2852–2862. https://doi.org/10.1021/nl504454u.

Shang, Y., Guo, L., 2015. Facet-controlled synthetic strategy of Cu_2O-based crystals for catalysis and sensing. Advanced Science 2 (10). https://doi.org/10.1002/advs.201500140.

Shankar, P., Bosco, J., Rayappan, B. Gas sensing mechanism of metal oxides: The role of ambient atmosphere, type of semiconductor and gases-A review Preparation of nanostructured ZnO using Pulsed laser ablation View project Image Steganography View project. https://www.researchgate.net/publication/270587471.

Shouli, B., Liangyuan, C., Dianqing, L., Wensheng, Y., Pengcheng, Y., Zhiyong, L., Aifan, C., Liu, C.C., 2010. Different morphologies of ZnO nanorods and their sensing property. Sens. Actuators B 146 (1), 129–137. https://doi.org/10.1016/j.snb.2010.02.011.

Subha, P.P., Jayaraj, M.K., 2019. Enhanced room temperature gas sensing properties of low temperature solution processed ZnO/CuO heterojunction. BMC Chemistry 13 (3). https://doi.org/10.1186/s13065-019-0519-5.

Sun, Y.F., Liu, S.B., Meng, F.L., Liu, J.Y., Jin, Z., Kong, L.T., Liu, J.H., 2012. Metal oxide nanostructures and their gas sensing properties: A review. Sensors 12 (3), 2610–2631. https://doi.org/10.3390/s120302610.

Tian, S., Yang, F., Zeng, D., Xie, C., 2012. Solution-processed gas sensors based on ZnO nanorods array with an exposed (0001) facet for enhanced gas-sensing properties. J. Phys. Chem. C 116 (19), 10586–10591. https://doi.org/10.1021/jp2123778.

Tonezzer, M., Dang, T.T.L., Bazzanella, N., Nguyen, V.H., Iannotta, S., 2015. Comparative gas-sensing performance of 1D and 2D ZnO nanostructures. Sens. Actuators B 220, 1152–1160. https://doi.org/10.1016/j.snb.2015.06.103.

Tshabalala, Z.P., Motaung, D.E., Mhlongo, G.H., Ntwaeaborwa, O.M., 2016. Facile synthesis of improved room temperature gas sensing properties of TiO_2 nanostructures: Effect of acid treatment. Sens. Actuators B 224, 841–856. https://doi.org/10.1016/j.snb.2015.10.079.

Walker, J.M., Akbar, S.A., Morris, P.A., 2019. Synergistic effects in gas sensing semiconducting oxide nano-heterostructures: A review. Sens. Actuators B 286, 624–640. https://doi.org/10.1016/j.snb.2019.01.049.

Wang, C., Yin, L., Zhang, L., Xiang, D., Gao, R., 2010. Metal oxide gas sensors: Sensitivity and influencing factors. Sensors 10 (3), 2088–2106. https://doi.org/10.3390/s100302088.

Wang, H., Dou, K., Teoh, W.Y., Zhan, Y., Hung, T.F., Zhang, F., Xu, J., Zhang, R., Rogach, A.L., 2013. Engineering of facets, band structure, and gas-sensing properties of hierarchical Sn^{2+}-Doped SnO_2 nanostructures. Adv. Funct. Mater. 23 (38), 4847–4853. https://doi.org/10.1002/adfm.201300303.

Wang, L., Zhang, R., Zhou, T., Lou, Z., Deng, J., Zhang, T., 2017. P-type octahedral Cu_2O particles with exposed {111} facets and superior CO sensing properties. Sens. Actuators B 239, 211–217. https://doi.org/10.1016/j.snb.2016.08.013.

Wang, T., Guo, Y., Wan, P., Zhang, H., Chen, X., Sun, X., 2016. Flexible transparent electronic gas sensors. Small (Weinheim an Der Bergstrasse, Germany), 12 (28), 3748–3756. https://doi.org/10.1002/smll.201601049.

Wang, X., Han, X., Xie, S., Kuang, Q., Jiang, Y., Zhang, S., Mu, X., Chen, G., Xie, Z., Zheng, L., 2012. Controlled synthesis and enhanced catalytic and gas-sensing properties of tin dioxide nanoparticles with exposed high-energy facets. Chemistry—A European Journal 18 (8), 2283–2289. https://doi.org/10.1002/chem.201103280.

Xiao, Y., Lu, L., Zhang, A., Zhang, Y., Sun, L., Huo, L., Li, F., 2012. Highly enhanced acetone sensing performances of porous and single crystalline ZnO nanosheets: High percentage of exposed (100) facets working together with surface modification with Pd nanoparticles. ACS Appl. Mater. Interfaces 4 (8), 3797–3804. https://doi.org/10.1021/am3010303.

Xu, J., Xue, Z., Qin, N., Cheng, Z., Xiang, Q., 2017. The crystal facet-dependent gas sensing properties of ZnO nanosheets: Experimental and computational study. Sens. Actuators B 242, 148–157. https://doi.org/10.1016/j.snb.2016.09.193.

Yan, S., Xue, J., Wu, Q., 2018. Synchronous synthesis and sensing performance of A-Fe_2O_3/SnO_2 nanofiber heterostructures for conductometric C_2H_5OH detection. Sens. Actuators B 275, 322–331. https://doi.org/10.1016/j.snb.2018.07.079.

Yang, Y., Liang, Y., Wang, G., Liu, L., Yuan, C., Yu, T., Li, Q., Zeng, F., Gu, G., 2015. Enhanced gas-sensing properties of the hierarchical TiO_2 hollow microspheres with exposed high-energy {001} crystal facets. ACS Appl. Mater. Interfaces 7 (44), 24902–24908. https://doi.org/10.1021/acsami.5b08372.

Yoon, J.W., Lee, J.H., 2017. Toward breath analysis on a chip for disease diagnosis using semiconductor-based chemiresistors: Recent progress and future perspectives. Lab Chip 17 (21), 3537–3557. https://doi.org/10.1039/c7lc00810d.

Zeng, W., Miao, B., Zhou, Q., Lin, L., 2013. Hydrothermal synthesis and gas sensing properties of variety low dimensional nanostructures of SnO_2. Physica E. Low-Dimensional Systems and Nanostructures 47, 116–121. https://doi.org/10.1016/j.physe.2012.10.026.

2

Metal oxide semiconductor thin-film transistors for gas sensing applications

Manu Shaji [a], **K.J. Saji** [b,c] **and M.K. Jayaraj** [a,d]

[a] Cochin University of Science and Technology, Kochi, India. [b] International School of Photonics, Cochin University of Science and Technology, Kochi, India. [c] Centre of Excellence in Advanced Materials, Cochin University of Science and Technology, Kochi, India. [d] University of Calicut, Malappuram, India

2.1 Introduction

Oxide electronics is a diverse and active field including materials such as dielectrics, ferroelectrics, magnetics, piezoelectrics, multiferroics, high-temperature superconductors, and epitaxial oxides. These materials find interesting applications across a large variety of devices, including displays, memory devices, and sensors. Transparent conducting oxide (TCO), transparent semiconducting oxide (TSO), and amorphous conducting oxide (ACO) materials have been widely studied for a variety of applications in recent years. Unlike conventional materials, they have an interesting combination of having high conductivity and high transparency in the visible regime, which makes them perfect candidates for smart electronics. Metal oxide materials had been studied before the silicon (Si) era. However, later developments in modern electronics and display technology, dominated by Si technology, put a setback to the research in metal oxide semiconductors (MOSs) and devices (Fortunato et al., 2012; Wager et al., 2014). Thin-film transistor (TFT) technology revolutionized display technology in the modern era. They are widely used in flat panel displays, including television, computers, smartphones, and also flexible and foldable displays. The dominant technology in flat panel display consists of hydrogenated amorphous silicon (a-Si:H) and low-temperature polysilicon (LTPS) TFTs for driving the pixels. The replacement of Si-based TFTs has been crucial for realizing flexible, transparent electronic devices and displays, as the integration of Si TFTs with flexible displays is challenging.

Nanomaterials for Sensing and Optoelectronic Applications. DOI: https://doi.org/10.1016/B978-0-12-824008-3.00004-7

Sensing technology has received increasing interest in recent years, driven by its applicability in various industries, biomedical devices and research, indoor and outdoor air quality supervision, and environmental studies. The miniaturization of gas sensors is essential for applications demanding device portability in areas like disease diagnosis, food quality control, and air quality monitoring. The most common gas sensors commercially available are two-terminal resistive-type gas sensors based on metal oxides, including SnO, SnO_2, tungsten oxide, and ZnO (Baratto et al., 2004; Franke et al., 2006).

2.2 Various types of gas sensors

Sensor research has come a long way from the hot platinum wire–based sensor, the first commercial sensor produced in 1923 (Yunusa et al., 2014). Researchers have made efforts to improve the sensitivity, selectivity, and stability of sensors, leading to the research and development of a wide variety of materials suitable for sensor applications. Different gas sensors with various sensing elements and sensing mechanisms have extensively been studied during the past few decades. The technique used in sensors can be classified into types such as acoustic, piezoelectric, optical, chemiluminescence, and electrochemical. The different types of sensing materials include conducting polymers, 2D materials, organic materials, and MOSs.

Three-terminal field-effect transistors (FETs) are considered worthwhile alternatives after the successful demonstration of an n-channel Pd-gated transistor as a hydrogen sensor in 1975, which was able to detect 10 ppm of hydrogen at 150°C (Lundström et al., 1975). The underlying mechanism of gas detection using FET sensors is the change in channel current due to channel conductance modulation either by the adsorbed gas species or by the gating effect. Various materials such as carbon nanotubes, organic semiconductors, porous silicon, silicon nanowires, metal oxide thin films, and nanowires have been used as sensing (channel) layers. FETs' sensing response can be further improved by combining them with a ring oscillator circuit and other adaptive amplifier circuits (Crone et al., 2002).

2.2.1 Semiconducting metal oxide materials as gas sensors

The gas sensing market has been dominated by MOS-based two-terminal chemiresistive-type gas sensors since the report of the ZnO-based sensor by Seiyama in 1963, which operates at an elevated temperature of 485°C. Sensing properties were investigated by measuring the change in resistance of the sensing layer upon gas adsorption (Tetsuro et al., 1963). The demand for high-performance gas sensors

with high sensitivity, response, and selectivity, together with low power consumption, accelerated the efforts to develop new sensing materials. MOS is the most common sensing material because of its advantages like low cost, high sensitivity, and ease of fabrication. Generally, metal oxides can be classified into two types: transition metal oxides (TiO_2, Fe_2O_3, etc.) and non–transition metal oxides (ZnO, CuO, etc.). Transition metal oxides can exist in different oxidation states and form different oxides and are hence more sensitive to the oxygen environment. Non–transition metal oxides are considered to be inert because of high energy requirements to form other oxidation states. More precisely, metal oxides having a d^0 and d^{10} electronic configuration can be used for gas sensing applications (Liu et al., 2012; Wang et al., 2010). Most of the MOSs, sensitive to gas species, are of n-type, and only a few reports on p-type are available because of the unavailability of p-type MOSs with electrical properties comparable to those of n-type MOSs. Generally, an increase in the concentration of the reducing gas decreases the resistivity of n-type MOSs and increases that of p-type MOSs, whereas an increase in the concentration of the oxidizing gas results in the opposite effect. MOS-based sensors received wide acceptance because of their ability to detect the analyte gas by simply measuring the resistance change between two electrodes (Pantò et al., 2018). However, limited room temperature sensitivity, poor selectivity, and high-temperature operation, ranging from 200°C to 400°C, to ensure fast operation made them power hungry and not suitable for portable device applications. Also, high-temperature operation leads to the fast degradation of the sensing material, causing reliability and durability issues (Park et al., 2019). In Chapter 1 resistive-type metal oxide gas sensors have been discussed in detail.

TFTs, having better sensitivity and capability of room-temperature operation, emerged as a better alternative to the two-terminal gas sensors (see Section 2.3.1 for TFT structure). The conductivity modulation of the semiconducting channel/sensing layer in the TFT using the applied gate voltage allows them to detect a very small change in the conductivity of the sensing layer and thereby detect a very low concentration of gases (Hong et al., 2016; Jeong et al., 2019). Current TFT-based gas sensor technology is mostly based on TFTs with the organic channel as an active layer. They provide high sensitivity, ease of fabrication, low-temperature operation, good selectivity, etc. However, the stability of the semiconducting organic layer is a limiting factor (Wu et al., 2020).

2.3 Metal oxide TFT–based gas sensors

TFTs have many advantages over conventional two-terminal resistive-type sensors from an operational point of view. Unlike

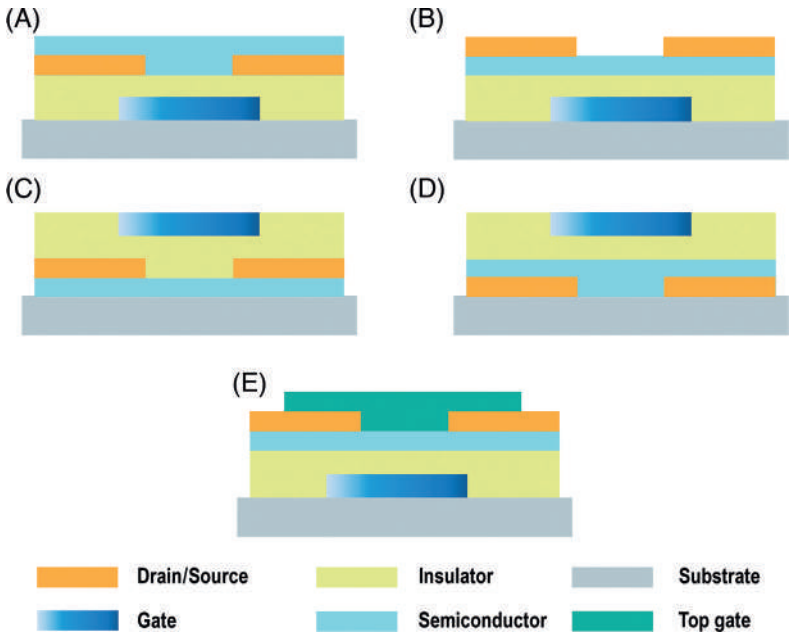

Figure 2.1. Cross-section of TFT structures: (A) coplanar bottom gate, (B) staggered bottom gate, (C) coplanar top gate, (D) staggered top gate, and (E) dual gate.

chemoresistors, which only give the conductivity change upon the exposure of the analyte, the capability of the gate-induced modulation of the electrical performance of the active layer gives a number of readily extractable parameters such as threshold voltage (V_{TH}), mobility (μ), and on/off ratio (I_{ON}/I_{OFF}) (see Section 2.3.1). So an extracted data set can provide a fingerprint of the analyte (Torsi et al., 2000). Most MOS TFTs aim to achieve better electrical and performance parameters comparable to Si since they have promising display applications. However, in the case of sensors we are looking for analyte species–induced change in electrical performance. So TFTs with moderate electrical properties might perform as good gas sensors since we are only interested in the variations in the performance matric. In principle, transistor-based sensors are more selective and more power efficient and have better sensitivity and detection limits because of the gate-controlled amplification of the signals. Furthermore, TFT sensors have a simple structure, so they have more advantages in miniaturization and chip integration.

2.3.1 TFT—structure, basics, and parameters

Fig. 2.1 shows the schematic cross-sections of different types of TFTs. A TFT consists of three components: an insulating dielectric layer, a semiconducting channel, and three electrodes (drain, source, and gate). TFT is a three-terminal field-effect device and works

according to the same principle of metal oxide semiconductor field-effect transistor (MOSFET). The gate and channel are separated by using an insulating dielectric material, which is quite similar to the MOS structure. The basic principle of a field-effect device is to control the flow of electrons (or holes) between the source and drain electrodes via the modulation of a semiconducting channel. This modulation is achieved by accumulating carriers near the semiconductor/dielectric interface through the voltage applied on the gate electrode, which forms a parallel-plate capacitor structure along with the gate dielectric semiconductor. In MOSFET the substrate is a semiconducting Si wafer and the device fabrication is very complex and expensive. TFTs can even be fabricated over insulating substrates like glass and each of the layers is deposited using a different deposition technique (mostly by high vacuum techniques). Compared to MOSFET, TFT fabrication is a comparatively simple and low-temperature process (<650°C). In working as well, these two FETs differ. In MOSFET the substrate acts as the active layer through the formation of an inversion layer of charges near the semiconductor/dielectric interface (if the substrate is n-type, the inversion layer consists of holes and is called a p-MOSFET) and the applied gate voltage modulates the charges in the inversion layer. On the other hand, in TFTs channel conductance is achieved through the modulation of an accumulation layer of charges. (If the active layer is n-type, then the accumulation layer consists of electrons, hence called n-TFT.)

Depending on the three electrodes' position, the TFT can be classified into two types: coplanar and staggered. Based on the fabrication process and application, a suitable device structure can be selected. When the semiconducting layer needs a high processing temperature or needs an active layer with a high-quality crystal structure, a top gate structure is used. Bottom gate structures, especially staggered, are most commonly used for semiconducting channel layer studies and display applications because of the ease of fabrication. For most research purposes, staggered bottom gate structures based on the commercially available substrate/insulator structures such as indium tin oxide (ITO)/antimony-doped tin oxide (ATO) or silicon (Si)/silicon dioxide (SiO_2) substrates are used to study the channel properties (Fig. 2.1B). In the case of hydrogenated amorphous silicon (a-Si:H) TFTs, which are used in LCD displays, the instability caused by backlight illumination can be avoided by using the bottom gate structure. In the sensing application the interaction of the semiconducting layer with sensing gas is crucial and this makes the bottom gate structure suitable for the use of TFT-based gas sensors. The TFT's basic principle is to modulate the conducting channel formed between the drain and source electrodes through the injection of carries near the semiconductor/dielectric interface using appropriate gate bias. The applied gate voltage modulates

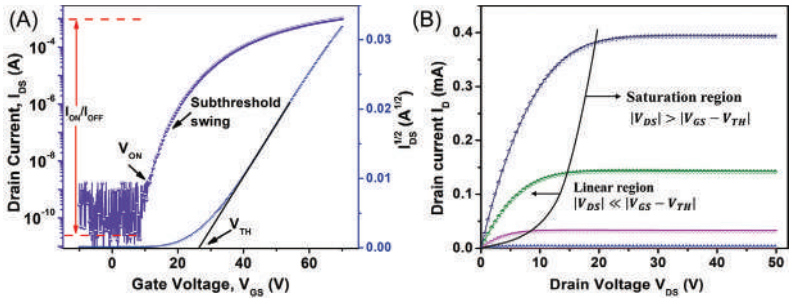

Figure 2.2. (A) Transfer and (B) output characteristics of an n-type TFT.

the accumulation layer in the semiconducting channel, and it helps to turn on and off the device. Based on working, TFTs are of two types:

- Enhancement mode (EM) TFT
- Depletion mode (DM) TFT

EM TFTs are at the OFF state under zero gate bias. These TFTs are produced by using a channel layer with low carrier density, and hence a gate bias is needed to form an accumulation layer of charges in the semiconductor/dielectric interface. In the case of DM TFTs, they are always at the ON state due to the channel with higher conductance, and a gate bias is required to switch off the device. EM mode TFTs are preferred for most applications as they consume less power compared to DM TFTs.

The static characteristics of TFTs can be evaluated by using their output and transfer characteristics, as shown in Fig. 2.2 (the transfer and output characteristics of an n-type EM TFT). The output characteristics can be obtained by measuring the drain to source current (I_{DS}) as a function of drain–source voltage (V_{DS}) for various fixed gate–source voltages (V_{GS}). The transfer curve is obtained by sweeping V_{GS} at a constant V_{DS}. At zero gate bias, there is no charge accumulation at the channel/dielectric interface and hence the current is very low. For a positive gate bias (for n-TFT), the electrons accumulate in the channel/semiconductor interface, and the current flows upon applying an appropriate drain–source bias. The magnitude of the current is proportional to the accumulated charge carrier density and carrier mobility. According to the value of V_{DS}, output characteristics (Fig. 2.2B) have two regions.

1. Linear region – Also known as the pre-pinch off region, the accumulated channel layer is uniformly distributed throughout the channel layer and the TFT behaves as a resistor. A linear increment can be seen in I_{DS} with respect to V_{DS}. We can say that the TFT is in pre-pinch off when $|V_{DS}| \ll |V_{GS} - V_{TH}|$, and I_{DS} is given in Eq. (2.1), where μ_{FE} is the field-effect mobility, C_{ox} is the gate dielectric capacitance per unit area, and W and L are the channel width and length, respectively.

2. Saturation region – Also called the pinch-off region, in this region the drain voltage is higher than the applied gate voltage. This causes the carriers to spread out from the narrow channel region and the current flows through a broader region than just the semiconductor/dielectric interface. A region devoid of charge carriers formed near the drain electrode results in the depletion of charges in the accumulation layer and is called the pinch-off. At this regime, $|V_{DS}| > |V_{GS} - V_{TH}|$, and I_{DS} is given by Eq. (2.2), where μ_{sat} is the saturation mobility.

$$I_{DS} = -\mu_{FE} C_{ox} \frac{W}{L}\left[(V_{GS} - V_{TH})V_{DS} - \frac{1}{2}V_{DS}^2\right] \tag{2.1}$$

$$I_{DS} = -\mu_{sat} C_{ox} \frac{W}{2L}(V_{GS} - V_{TH})^2 \tag{2.2}$$

The different TFT performance parameters that can be extracted from the transfer/output curves are discussed below.

2.3.1.1 On/off ratio

This is defined as the ratio of the maximum to the minimum drain current (I_D). The minimum I_D, which is generally given by the measuring equipment's noise level or by the gate leakage current (I_G), depends on the semiconductor material. An on/off ratio of above 10^6 is needed for display applications. The minimum OFF current depends on the measuring instrument's noise level and leakage current through the gate dielectric.

2.3.1.2 Threshold voltage (V_{TH})

This is the minimum gate voltage required to accumulate charge carriers between drain/source terminals. V_{TH} is defined as the value of V_{GS} when the conductive channel (or an accumulation layer near the dielectric/semiconductor interface) just begins to connect the source and drain electrodes. In n-type TFTs if V_{TH} is negative (positive), the devices are designated to operate in depletion (enhancement) mode. V_{TH} can be identified by the linear extrapolation of the $I_D - V_{GS}$ plot (for the linear regime) or the $I_D^{\frac{1}{2}} - V_{GS}$ plot (for saturation regime) (Fig. 2.2A).

2.3.1.3 Subthreshold swing (S)

It is the inverse of the maximum slope of the transfer characteristic, which indicates the necessary V_{GS} to increase I_D by one decade. It gives an idea about how fast the TFT responds to the applied gate voltage and a value of $S << 1$ is preferred for various practical applications. A lower

value means higher speed and lower power consumption.

$$S = \left(\frac{d\log(I_{DS})}{dV_{GS}}\right)^{-1}$$

2.3.1.4 Mobility (μ)

It is the efficiency of the majority carrier transport in a semiconducting material. In a material μ is affected by several scattering mechanisms, such as lattice vibrations, ionized impurities, grain boundaries, and other structural defects. The most common ones used in the TFT community are the effective mobility (μ_{eff}), the field-effect mobility (μ_{FE}), and the saturation mobility (μ_{sat}).

2.3.1.5 Field-effect mobility (μ_{FE})

It is considered the correct estimation of μ, which includes the V_{GS} effect. It is determined by the conductance at low V_{DS} and can be calculated from the slope of the V_{DS}–I_D curve at small V_{DS} using the following equation:

$$\mu_{FE} = \frac{\text{slope}}{C_{ox}(W/L)V_{DS}}.$$

2.3.1.6 Saturation mobility (μ_{sat})

The determination of this parameter is also common in TFTs and it describes a situation when the effective length is smaller than the actual channel length (L). Saturation mobility can be calculated at high V_{DS} and can be extracted from the slope in the linear region of the V_{DS}–$I_D^{\frac{1}{2}}$ curve

$$\mu_{sat} = \frac{\text{slope}^2}{(1/2)C_{ox}(W/L)}.$$

In TFT-based gas sensing either the active layer or the gate (Fig. 2.1E) can be exposed to the analyte gas. In dual gate TFTs the second gate acts as the sensing layer, and the change in the top gate affects the active channel properties. Usually, the dual-gate configuration is used in the organic TFT-based sensor, where the top organic layer acts as a second gate and its potential changes with gas exposure. This change in potential affects the electrical properties of the underlying active channel layer. Here we discuss more about bottom gate TFTs, in which the active layer and the analyte gas are in direct contact. Upon analyte gas exposure, the above-discussed parameters of a TFT will change depending on the type of gaseous species (oxidizing or reducing) in contact with the active layer. Through the interaction between the analyte molecule and the sensing layer, the conductivity, carrier density, and mobility of the active layer change, which in turn reflects

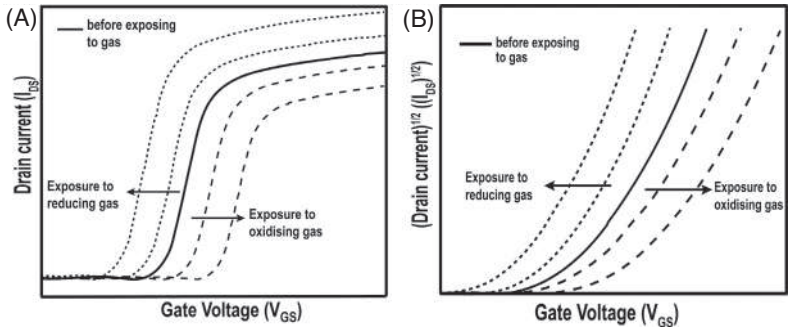

Figure 2.3. Variation in (A) transfer curve and (B) threshold voltage curve upon exposure to reducing and oxidizing gas for an n-type TFT.

in the transistor properties (i.e., in the transfer and output characteristics curves). Different methods have to be adopted to quantify the changes in TFT performance induced by the analyte. One of the methods is to analyze the variation in I_D upon exposure to the analyte with time. This method is similar to the measurement method of resistive-type gas sensors. The most used method is by analyzing the variation in V_{TH}. The shift in V_{TH} gives a direct implication of the type of analyte gas, whether it is oxidizing or reducing in nature. V_{TH} shifts only with applied gate bias, and the drain bias has no influence on it. Fig. 2.3 shows a representation of the shift in the transfer curve and V_{TH} with exposure to different types of gases in an n-type TFT. When an oxidizing gas comes in contact with the n-type active layer, it draws electrons from the channel layer through the reaction with adsorbed oxygen species and reduces the carriers available for charge transport. This reduction in carriers reduces the channel conductance and shifts the transfer curve in the positive direction with a reduction in drain current. The extracted V_{TH} curve also shows a positive directional shift, indicating the reduction in channel conductance. If the channel layer is exposed to reducing gas, it releases electrons to the active layer by reacting with the adsorbed oxygen species. This causes an increase in carrier density and conductivity of the channel layer. Hence the transfer curve shows a negative shift with increased drain current. Here the V_{TH} curve shows a reduction in V_{TH} compared to the actual curve. Mobility also changes during the gas exposure; the oxidizing gas reduces the channel mobility while the reducing gas improves it. Variation in mobility is another parameter that can be taken into account for the detection of various gases.

Metal oxide TFTs have become an intensive research topic after the successful demonstration of ZnO and indium gallium zinc oxide (IGZO)-based TFTs, which exhibited excellent electrical properties and ease of processing methods (Nomura et al., 2004; Prins et al., 1996). In the initial stage, a run toward the realization of flexible and wearable electronics, most of the research concentrated on developing and

integrating metal oxide TFTs for display applications. The ZnO films were polycrystalline even when deposited at room temperature. So the grain boundaries deteriorated the performance, stability, and uniformity of the TFT characteristics. Following ZnO, other binary oxides such as In_2O_3, Ga_2O_3, and SnO_2 were studied extensively (Lavareda et al., 2006; Matsuzaki et al., 2006). Metal oxide TFTs require high-temperature postannealing treatments to achieve excellent electrical properties. Multicomponent amorphous oxides exhibit considerably better TFT performance than binary compounds.

2.3.2 Binary metal oxide TFT gas sensors

Various kinds of n-type binary oxides such as SnO_2, ZnO, In_2O_3, WO_3, and Fe_2O_3 have been studied as chemoresistive two-terminal gas sensors after the report of the first patented gas sensor based on SnO_2 in 1975. TFTs based on binary metal oxides were mostly studied for display applications. From 2003 onward, MOSs gained increasing interest due to the development of the zinc oxide–based TFT by Hoffman et al., which possesses a high mobility of 1 $cm^2\ V^{-1}\ s^{-1}$ (Carcia et al., 2003; Hoffman et al., 2003; Hossain et al., 2003). Usually, metal oxides require high-temperature postannealing to achieve the desired electrical properties. However, attempts to fabricate an MO–TFT operating at room temperature were made due to its high stability compared to the organic TFTs. The ZnO nanowire TFT shows adequate oxygen sensing properties. Exposing the device to oxygen showed a reduction in mobility and conductivity of the nanowire, which was due to the formation of oxygen ions (O^-, O^{2-}) and the subsequent decrease of the conductance of the channel in the nanowire. A further increase in the oxygen pressure results in the widening of the depletion layer and a reduction in carrier density, which was evident from the positive shift in V_{TH} from the transfer curve. As ZnO is sensitive to UV light, UV illumination can reverse the device's performance to its initial state. Upon UV exposure, the oxygen ions combine with the photogenerated holes in the ZnO nanowire, resulting in oxygen desorption (Li et al., 2004). A ZnO-based real-time sensor was fabricated by Andringa et al. to detect a lower concentration of 40-ppb NO_2 with good selectivity at 200°C (Andringa et al., 2013). Since NO_2 is an oxidizing gas, the V_{TH} shift method was adopted for the detection. The mechanism behind the V_{TH} shift can be explained as charge trapping mediated by NO_2 (Fig. 2.4). Upon applying positive gate bias, the carriers accumulate in the channel layer, and some of the accumulated charges get trapped in the defect sites. They do not contribute to the channel current, but they contribute to the electrostatic charge that shields the gate voltage and causes the shift in V_{TH}. When the trapped charges completely compensate the gate bias, no current will flow (Andringa et al., 2012,

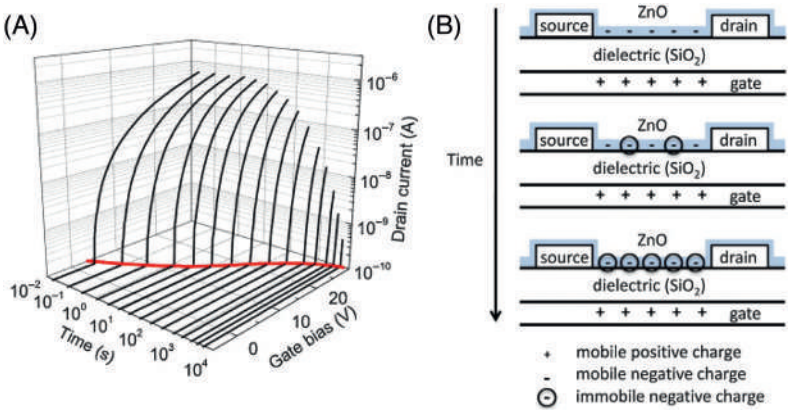

Figure 2.4. (A) Transfer curves of a ZnO transistor exposed to 320-ppb NO_2 as a function of time under a continuously applied gate bias of 30 V. The linear transfer curves, represented by the black lines, were measured at a source–drain bias of 2 V. The red line presents the threshold voltage as a function of stress time. The threshold voltage is empirically taken as the onset of current flow. The threshold voltage starts at about 0 V and shifts with time toward the applied gate bias of 30 V. (B) Schematic representation of the charge trapping process in a transistor. With time, mobile electrons are trapped until the steady state is reached. The gate bias is then completely compensated by immobile trapped charges. Reproduced with permission from (Andringa et al., 2012). Copyright 2012, Elsevier.

2014). Recovery of the trapped carriers is not possible at room temperature.

P-type MOS-based TFTs have received little attention compared to n-type. One reason for the less interest in p-type TFTs is their poor electrical properties, which stems from their electronic band structure (Kamiya & Hosono, 2010). As a gas sensor, p-type MOS has certain advantages: better humidity resistance, ability to chemisorb a higher concentration of oxygen, and good catalytic effect (Zhang et al., 2015). Moreover, the p-MOS gas sensor's response is equal to the square root of the response of the n-MOS gas sensor to the same gas for identical sensor configuration (Hübner et al., 2011). The first report on a p-type MOS–TFT sensor used a sputtered SnO_X as the sensing layer, and the device was highly sensitive and selective toward NO_2 (Fig. 2.5). As NO_2 is an oxidizing gas, upon exposure, the transfer curve shows a positive shift because of the increased hole concentration due to the oxidation of the channel surface. SnO_x TFT gas sensor shows a better response value of 19.4 for 10 ppm of NO_2 and recovery time at room temperature compared to the SnO_x thin-film gas sensor (Jeong et al., 2019).

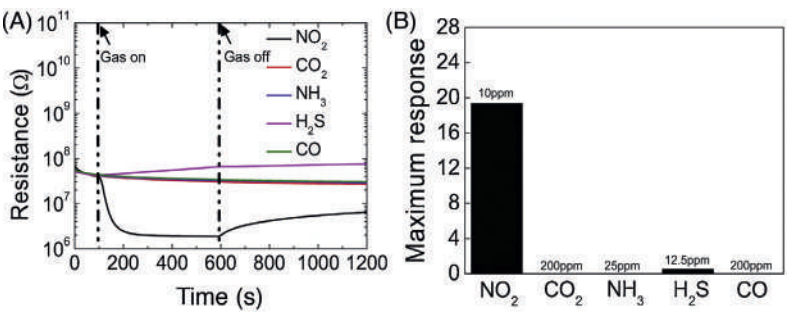

Figure 2.5. (A) Transient resistance behavior (resistance of the p-MOS decreases with exposure to oxidizing gas) and (B) maximum response values of the fabricated SnO_x TFT gas sensor to various target gases obtained at room temperature. Reproduced with permission from (Jeong et al., 2019). Copyright 2019, Elsevier.

2.3.3 Multinary metal oxide TFT gas sensors

Multicomponent amorphous oxides, in general, have considerably better TFT performance than binary compounds. In amorphous oxides carrier transport is mostly influenced by the potential barriers located around the conduction band minimum (CBM), associated with structural randomness, which can easily be improved by properly processing the film. Zn-based multicomponent oxides show high electron mobility. Zinc-doped indium oxide (IZO) has suitable electrical parameters, but a lack of stability under visible light operation renders them unsuitable for device applications (Barquinha et al., 2006). The difficulty in controlling the background carriers down to low values, preferably less than 10^{15} cm^{-3}, and high light sensitivity made researchers work on new multicomponent oxides like IGZO (Nomura et al., 2004). A single-crystalline IGZO transparent TFT with a field-effect mobility of 80 cm^2 V^{-1} s^{-1} was reported by Nomura et al. (2003). However, the device fabrication temperature was 700°C.

Amorphous oxide semiconductor (AOS)–based TFTs possess many advantages, including high electron mobility, low operating voltage, low processing temperature, excellent uniformity, ease of fabrication and low leakage current, and high signal-to-noise ratio. Also, they have a wide processing window and different choices of gate insulators to obtain good TFT performance (Kamiya & Hosono, 2010). An amorphous IGZO (a-IGZO) TFT with a mobility >10 cm^2 V^{-1} s^{-1} at room temperature on a flexible substrate was first developed by Nomura et al. (2004). a-IGZO shows mobility in the range of 5 to 39 cm^2 V^{-1} s^{-1}, with varying amounts of indium, gallium, and oxygen. Gallium acts as a carrier suppressor and stabilizer in a-IGZO, and an increased amount of gallium decreases the conductivity and mobility of the TFT (Kumomi et al., 2008). a-IGZO satisfies the properties needed for the application of TFT-based gas sensors. Because of the amorphous phase, IGZO-based TFT gas sensors have advantages in terms of reproducibility and large area uniformity. A Zn-based AOS is considered sensitive to humidity and oxygen partial pressure, affecting the turn-on voltage, mobility, V_{TH}, and off current. Kang et al. reported the possible use of an a-IGZO TFT as an oxygen pressure sensor. By increasing the oxygen partial pressure from 8.5×10^{-6} to 760 Torr, a shift in turn-on voltage from -54 to -7 V was observed. This shift is associated with oxygen adsorption and desorption on the IGZO surface (Kang et al., 2007). Exposure to water shows a behavior contrary to that upon oxygen exposure because on the IGZO active layer, oxygen acts as an electron acceptor and water molecule acts as an electron donor. Also, the water molecules make deep-level acceptors like traps, and these traps contribute to the change in electrical performance. Also, the active layer thickness is an essential parameter for trap creation (Fig. 2.6),

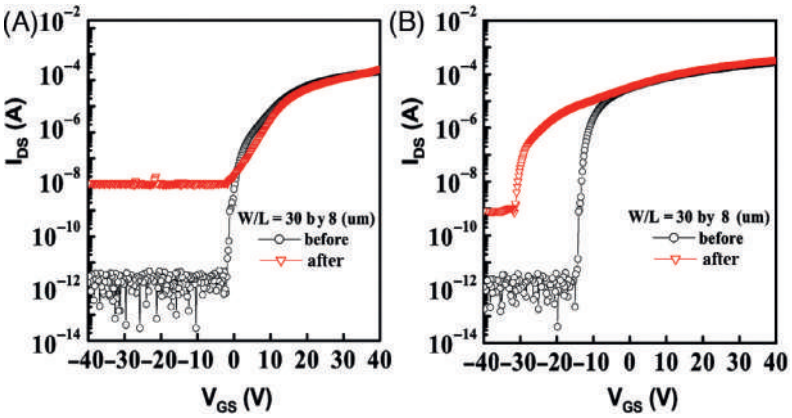

Figure 2.6. The comparison of the transfer curves before and after water exposure for the device with a (A) 35-nm-thick and (B) 150-nm-thick channel, respectively. As the channel layer thickness decreases, acceptor-like traps overwhelm the donor concentration. If the channel thickness is greater than the screening length, the traps will not respond to the change in gate bias and the subthreshold swing value shows less degradation. Reproduced with permission from (Park et al., 2008). Copyright (2008), American Institute of Physics.

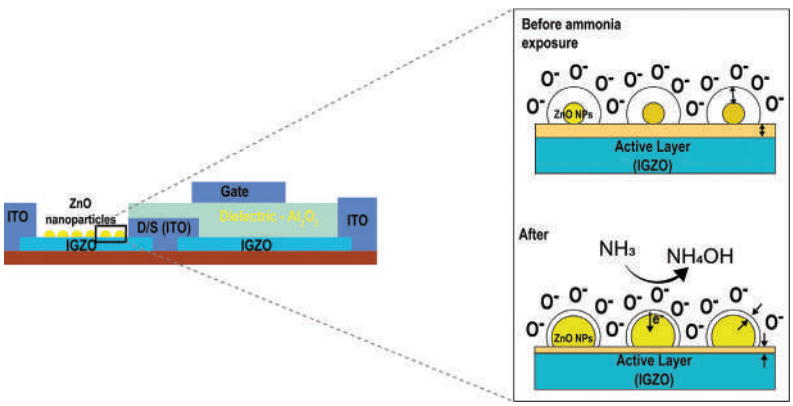

Figure 2.7. Schematic of the IGZO TFT coupled with ZnO nanoparticles, and the enlarged portion shows the change in depletion layer width before and after exposure to ammonia gas.

as trap density decreases with an increase in channel thickness (Park et al., 2008). Nevertheless, for the abovementioned experiments, the recovery process after exposure to oxygen and moisture was very slow. So a temperature-mediated process was needed for fast recovery. An all-oxide transparent, flexible, highly sensitive humidity sensor using a-IGZO showed sensitivity $>10^3$ at a low voltage of $V_G = -1$ to 2 V and $V_D = 1$ V (Kim et al., 2017). The a-IGZO TFT showed an excellent response to gases like H_2 and NO_2 with a detection limit of 12.5 ppm (at 350°C) and 5 ppm (at 200°C), respectively. The device showed an acceptable recovery time only at elevated temperatures (Yang et al., 2012).

To achieve device portability, low power operation and low-temperature or room-temperature operation of gas sensors are needed. This requires modification in the conventional device architecture and smart ways to modify the device performance under a gaseous environment. The improved device architecture of the IGZO TFT coupled with ZnO nanoparticles (Fig. 2.7) reduced the operating

temperature to 150°C (Yun et al., 2017). Using this structure, the reducing gas NH_3 was sensed at a comparatively low temperature of 150°C. The sensing mechanism is quite different from other TFT-based sensors. The sensing and readout elements have different roles in gas detection. When NH_3 comes in contact with the sensing element (ZnO nanoparticles), the reaction with adsorbed oxygen leads to the formation of NH_4OH as a by-product, and the trapped electrons are released to the conduction band of ZnO nanoparticles. This decrease in conduction bandwidth causes an increase in conductivity and, in turn, causes the modulation in drain current in the coupled TFT to be kept at a fixed V_{GS} and V_{DS}. UV illumination is a nonthermal mode of activation of IGZO TFT–based NO_2 sensors. Under UV light, there is an increase in charge carriers due to the photogenerated electron and hole pairs, which result in a negatively shifted transfer curve with an increase in drain current. Through exposure to NO_2 gas, the drain current decreases with a positive shift in the transfer curve. When NO_2 comes in contact with the sensing layer, it acts as an electron acceptor and reduces the number of free carriers, leading to a positive shift in the transfer curve and decreased drain current. NO_2 amounts as low as 2 ppm were able to be detected by using this method. Moreover, the sensor response is relatively slow, and the UV light makes the device unfit for portable uses (Knobelspies et al., 2018).

The variations in the drain current in an a-IGZO TFT strictly originate from the oxidation or reduction reaction between the channel surface and the analyte gas molecules, as the amorphous channel layer does not possess any active reaction sites or grain boundaries. Because of this, enhancement mode (EM) and depletion mode (DM) TFTs were fabricated for the sensing of NO_2 gas at concentrations $\leq$ 10 ppm and $\geq$ 10 ppm, respectively, at a temperature of 100°C (Kim et al., 2018). In EM mode a low concentration of NO_2 is sufficient for the change in drain current due to the low carrier density, and the current variation can be detected easily. However, for DM TFTs, a high amount of NO_2 is required to make an observable change in the drain current. The EM TFT shows fast response and selectivity compared to DM mode TFT (Kim et al., 2018).

The prebiasing measurement method was proposed as a way to improve the performance of a Si-based FET-type gas sensor (Wu et al., 2017). Also, for IGZO and zinc tin oxide (ZTO) TFT–based oxygen sensors, the applied electric field plays the role of a catalyst for the chemisorption of oxygen by reducing the activation energy for adsorption (Chen et al., 2012). A similar technique was implemented to improve the NO_2 sensing property of an a-IGZO TFT. The application of a positive prebias voltage to the gate electrode dramatically reduced the response time and operating temperature for NO_2 sensing. The improved sensing performance was attributed to the electric

field–induced chemisorption of NO_2 on the active channel layer and the reduced activation energy for the surface reaction of NO_2. Fig. 2.8 represents a chemical reaction model of NO_2 adsorption onto an IGZO TFT. NO_2 gas becomes NO_2^- via the extraction of electrons from the MOS layer. This decrease in electron density in the active layer causes a shift in the transfer curve toward the positive direction. A reduced activation energy by the induced electric field accelerates the NO_2 adsorption rate and causes a more positive shift in the transfer curve. But a negative prebias voltage on the gate degrades the TFT performance. The device shows a response value of 475 at an operating temperature of 90°C for 10 ppm of NO_2 (Park et al., 2019). The effect of gate bias voltage was more significant with an increase in pulse amplitude and width. As the prebias time increases, the sensing performance is improved. The device showed optimum sensing performance with a prebias voltage of 5 V for 20 s at a temperature ranging from 60°C to 90°C, which indicates the effectiveness of a positive prebiasing technique at low temperatures. An amorphous zinc tin oxide TFT–based oxygen sensor uses visible light illumination of the TFT to reduce the recovery time without any heat treatment (Chen et al., 2012). However, incorporating such a light source will affect the cost-effective fabrication and miniaturization of the sensor.

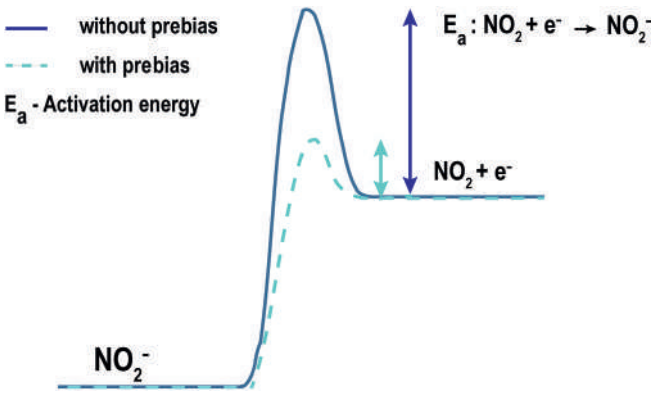

Figure 2.8. Chemical reaction model for NO_2 adsorption onto an IGZO TFT with and without application of positive pre-bias voltage on the gate electrode.

2.4 Hybrid TFT sensors

It is essential to combine various material qualities to fabricate a highly sensitive and selective gas sensor. Hybrid TFTs combine the properties of organic, 2D materials and metal oxides to achieve better sensor response. It was reported that organic layer capped bottom gate a-IGZO-based hybrid TFT sensors could operate at room temperature. When a gas (oxidizing or reducing) interacts with the organic sensing layer (OSL), the oxidation or reduction reaction causes a change in the potential of the OSL. Hence we can treat the OSL as a floating top gate, and the potential variations affect the current in the IGZO TFT. When the device, with poly(3-hexylthiophene) (P3HT) as the OSL, was exposed to ammonia, a reducing gas, a negative potential formed on the OSL through the injection of electrons, causing a current drop in the IGZO TFT. If the same device is exposed to an oxidizing gas like NO, a positive potential forms in the OSL and causes an increase in the TFT current. The device showed a sensitive reversible response to

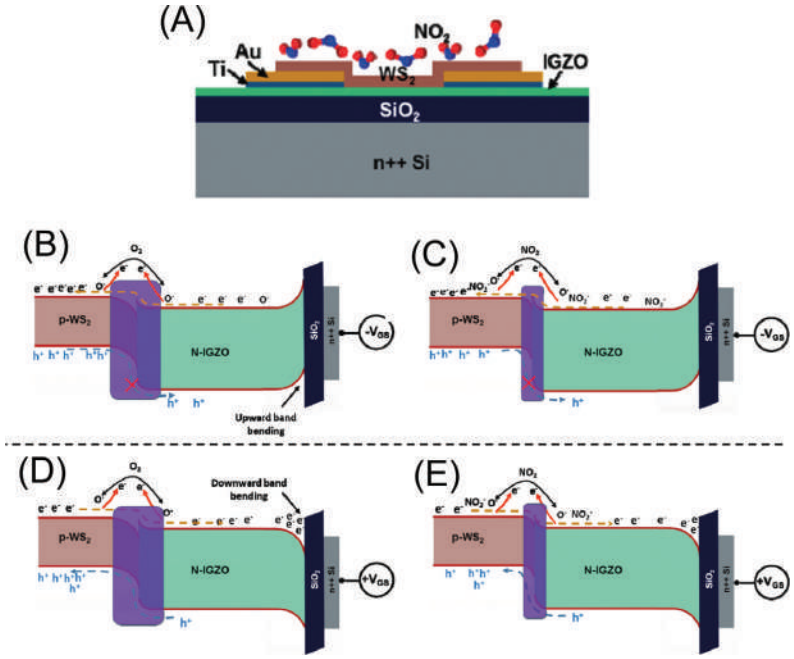

Figure 2.9. (A) Structure of WS_2/IGZO heterojunction TFT and the band diagram of WS_2/IGZO TFT after applying negative gate voltage (V_{GS}) (B) in air and (C) in an NO_2 atmosphere. After applying a positive V_{GS} the band diagram (D) in air and (E) in NO_2 atmosphere. Reproduced with permission from (Tang et al., 2019). Copyright 2019, American Chemical Society.

100-ppb ammonia (with P3HT capping) and 100-ppb acetone (with copper phthalocyanine [CuPc] capping) at room temperature (Zan et al., 2011). CuPc-capped IGZO TFTs have high sensitivity toward acetone, an index gas in the breath of patients with diabetes mellitus that is used to distinguish between healthy ($\leq$900 ppb) and diabetes patients ($\geq$1800 ppb).

A p–n heterojunction TFT with IGZO and 2D-WS_2 (tungsten disulfide) shows a better response to NO_2 gas at room temperature with sensitivity values of 6820 for 5 ppm of NO_2 concentration (Fig. 2.9A). Here a CVD-grown monolayer WS_2 is transferred to the bottom-gated IGZO TFT and forms a p–n heterojunction sensing layer (Tang et al., 2019). The depletion layer formed at the p–n heterojunction interface of WS_2/IGZO limits carrier diffusion and causes the low conductivity of the device in the air. When the sensor is exposed to air, adsorbed oxygen molecules form ionic oxygen species (O^- or O_2^-) by trapping free electrons from the conduction band. When the sensor is exposed to NO_2, the oxidizing NO_2 reacts with the ionic oxygen and adsorbed gas. NO_2 becomes an ionic species by attracting electrons from the heterojunction and decreasing the conductivity. This affects the equilibrium state of the built-in field and induces holes to accumulate at the surface of WS_2 and reduces the depletion layer thickness. The band shape and depletion layer width of the heterojunction can be modulated by applying an external back gate voltage (Figs. 2.9B-E). There were two possible mechanisms to explain NO_2 sensing depending on

the concentration of the exposed gas. At a low NO_2 concentration (0 to 10 ppm), when the adsorption sites are sufficient for gas molecule detection, the Schottky barrier builds up between the WS_2–IGZO junction, and the electrodes changes. Thereby, a change in V_{TH} and subthreshold slope can be seen. NO_2 adsorption is more favorable in the metal/electrode interface, and it modulates the Schottky barrier. Moreover, the higher binding energy of these sites leads to difficulty in desorption. Therefore sensor recovery at a low gas concentration is difficult. At higher gas concentrations (more gas molecules than the active adsorption sites), the predominant sensing mechanism is the doping of transistor channels in addition to the Schottky barrier change. When NO_2 concentration increases, WS_2 becomes more p-type, and more charges are transferred to the p–n heterojunction. This causes an ultrahigh response toward NO_2 under an appropriate gate bias.

2.5 Summary

Electrical stability, large-scale uniformity, and simple and cost-effective fabrication methods make MOS TFTs promising candidates for various optoelectronic applications. The gate-controlled modulation of active channel conductance gives TFT-based gas sensors an upper hand over conventional resistive-type MOS sensors. A number of readily extractable TFT parameters help the sensors to achieve more sensitivity and selectivity toward different gases. Binary MOS TFTs show good sensing toward various oxidizing and reducing gases, but a temperature-mediated process is needed to recover the sensor because the recovery of trapped carriers is not possible at room temperature. P-type MOS TFT sensors were less studied because of their inadequate sensing response. Multicomponent amorphous oxides are another class of MOS showing better gas sensing properties. As the amorphous channel layer does not possess any active reaction sites, the variation in the TFT parameters is originated from the reaction of analyte gas with the channel layer. Sensing response and selectivity can be improved by modifying the device structure. Improved measurement methods like applying a prebias voltage to the gate terminal will effectively reduce the activation energy for the surface reaction of gases and improve sensitivity. Hybrid and p–n junction TFTs combine the properties of organic and 2D materials with MOS to achieve better response, selectivity, and room-temperature operation.

References

Andringa, A.M., Piliego, C., Katsouras, I., Blom, P.W.M., Leeuw, D.M.D., 2014. NO_2 detection and real-time sensing with field-effect transistors. Chem. Mater. 26 (1), 773–785. https://doi.org/10.1021/cm4020628.

Andringa, A.M., Smits, E.C.P., Klootwijk, J.H., De Leeuw, D.M., 2013. Real-time NO_2 detection at ppb level with ZnO field-effect transistors. Sens. Actuators B 181, 668–673. https://doi.org/10.1016/j.snb.2013.01.026.

Andringa, A.M., Vlietstra, N., Smits, E.C.P., Spijkman, M.J., Gomes, H.L., Klootwijk, J.H., Blom, P.W.M., De Leeuw, D.M., 2012. Dynamics of charge carrier trapping in NO_2 sensors based on ZnO field-effect transistors. Sens. Actuators B 171–172, 1172–1179. https://doi.org/10.1016/j.snb.2012.06.062.

Baratto, C., Sberveglieri, G., Onischuk, A., Caruso, B., Di Stasio, S., 2004. Low temperature selective NO_2 sensors by nanostructured fibres of ZnO. Sens. Actuators B 100 (1–2), 261–265. https://doi.org/10.1016/j.snb.2003.12.045.

Barquinha, P., Pimentel, A., Marques, A., Pereira, L., Martins, R., Fortunato, E., 2006. Effect of UV and visible light radiation on the electrical performances of transparent TFTs based on amorphous indium zinc oxide. J. NonCryst. Solids 352 (9–20), 1756–1760. https://doi.org/10.1016/j.jnoncrysol.2006.01.068.

Carcia, P.F., McLean, R.S., Reilly, M.H., Nunes, G., 2003. Transparent ZnO thin-film transistor fabricated by rf magnetron sputtering. Appl. Phys. Lett. 82 (7), 1117–1119. https://doi.org/10.1063/1.1553997.

Chen, Y.C., Chang, T.C., Li, H.W., Chung, W.F., Wu, C.P., Chen, S.C., Lu, J., Chen, Y.H., Tai, Y.H., 2012. High-stability oxygen sensor based on amorphous zinc tin oxide thin film transistor. Appl. Phys. Lett. 100 (26). https://doi.org/10.1063/1.4731773.

Crone, B.K., Dodabalapur, A., Sarpeshkar, R., Gelperin, A., Katz, H.E., Bao, Z., 2002. Organic oscillator and adaptive amplifier circuits for chemical vapor sensing. J. Appl. Phys. 10140. https://doi.org/10.1063/1.1476084.

Fortunato, E., Barquinha, P., Martins, R., 2012. Oxide semiconductor thin-film transistors: A review of recent advances. Adv. Mater. 24 (22), 2945–2986. https://doi.org/10.1002/adma.201103228.

Franke, M.E., Koplin, T.J., Simon, U., 2006. Metal and metal oxide nanoparticles in chemiresistors: Does the nanoscale matter? Small 2 (1), 36–50. https://doi.org/10.1002/smll.200500261.

Hoffman, R.L., Norris, B.J., Wager, J.F., 2003. ZnO-based transparent thin-film transistors. Appl. Phys. Lett. 82 (5), 733–735. https://doi.org/10.1063/1.1542677.

Hong, Y., Kim, C.H., Shin, J., Kim, K.Y., Kim, J.S., Hwang, C.S., Lee, J.H., 2016. Highly selective ZnO gas sensor based on MOSFET having a horizontal floating-gate. Sens. Actuators B 232, 653–659. https://doi.org/10.1016/j.snb.2016.04.010.

Hossain, F.M., Nishii, J., Takagi, S., Ohtomo, A., Fukumura, T., Fujioka, H., Ohno, H., Koinuma, H., Kawasaki, M., 2003. Modeling and simulation of polycrystalline ZnO thin-film transistors. J. Appl. Phys. 94 (12), 7768–7777. https://doi.org/10.1063/1.1628834.

Hübner, M., Simion, C.E., Tomescu-Stănoiu, A., Pokhrel, S., Bârsan, N., Weimar, U., 2011. Influence of humidity on CO sensing with p-type CuO thick film gas sensors. Sens. Actuators B 347–353. https://doi.org/10.1016/j.snb.2010.10.046.

Jeong, H.S., Park, M.J., Kwon, S.H., Joo, H.J., Kwon, H.I., 2019. Highly sensitive and selective room-temperature NO_2 gas-sensing characteristics of SnOX-based p-type thin-film transistor. Sens. Actuators B 288, 625–633. https://doi.org/10.1016/j.snb.2019.03.046.

Kamiya, T., Hosono, H., 2010. Material characteristics and applications of transparent amorphous oxide semiconductors. NPG Asia Materials 2 (1), 15–22. https://doi.org/10.1038/asiamat.2010.5.

Kang, D., Lim, H., Kim, C., Song, I., Park, J., Park, Y., Chung, J., 2007. Amorphous gallium indium zinc oxide thin film transistors: Sensitive to oxygen molecules. Appl. Phys. Lett. 90 (19). https://doi.org/10.1063/1.2723543.

Kim, K.S., Ahn, C.H., Jung, S.H., Cho, S.W., Cho, H.K., 2018. Toward adequate operation of amorphous oxide thin-film transistors for low-concentration gas detection. ACS Appl. Mater. Interfaces 10 (12), 10185–10193. https://doi.org/10.1021/acsami.7b18657.

Kim, K.S., Ahn, C.H., Kang, W.J., Cho, S.W., Jung, S.H., Yoon, D.H., Cho, H.K., 2017. An all oxide-based imperceptible thin-film transistor with humidity sensing properties. Materials 10 (5). https://doi.org/10.3390/ma10050530.

Knobelspies, S., Bierer, B., Daus, A., Takabayashi, A., Salvatore, G.A., Cantarella, G., Perez, A.O., Wöllenstein, J., Palzer, S., Tröster, G., 2018. Photo-induced room-temperature gas sensing with a-IGZO based thin-film transistors fabricated on flexible plastic foil. Sensors (Switzerland) 18 (2). https://doi.org/10.3390/s18020358.

Kumomi, H., Nomura, K., Kamiya, T., Hosono, H., 2008. Amorphous oxide channel TFTs. Thin. Solid. Films 516 (7), 1516–1522. https://doi.org/10.1016/j.tsf.2007.03.161.

Lavareda, G., Nunes de Carvalho, C., Fortunato, E., Ramos, A.R., Alves, E., Conde, O., Amaral, A., 2006. Transparent thin film transistors based on indium oxide semiconductor. J. NonCryst. Solids 352 (23–25), 2311–2314. https://doi.org/10.1016/j.jnoncrysol.2006.03.031.

Li, Q.H., Liang, Y.X., Wan, Q., Wang, T.H., 2004. Oxygen sensing characteristics of individual ZnO nanowire transistors. Appl. Phys. Lett. 85 (26), 6389–6391. https://doi.org/10.1063/1.1840116.

Liu, X., Cheng, S., Liu, H., Hu, S., Zhang, D., Ning, H., 2012. A survey on gas sensing technology. Sensors (Switzerland) 12 (7), 9635–9665. https://doi.org/10.3390/s120709635.

Lundström, K.I., Shivaraman, M.S., Svensson, C.M., 1975. A hydrogen-sensitive Pd-gate MOS transistor. J. Appl. Phys. 46 (9), 3876–3881. https://doi.org/10.1063/1.322185.

Matsuzaki, K., Yanagi, H., Kamiya, T., Hiramatsu, H., Nomura, K., Hirano, M., Hosono, H., 2006. Field-induced current modulation in epitaxial film of deep-ultraviolet transparent oxide semiconductor Ga_2O_3. Appl. Phys. Lett. 88 (9). https://doi.org/10.1063/1.2179373.

Nomura, K., Ohta, H., Takagi, A., Kamiya, T., Hirano, M., Hosono, H., 2004. Room-temperature fabrication of transparent flexible thin-film transistors using amorphous oxide semiconductors. Nature 432 (7016), 488–492. https://doi.org/10.1038/nature03090.

Nomura, K., Ohta, H., Ueda, K., Kamiya, T., Hirano, M., Hosono, H., 2003. Thin-film transistor fabricated in single-crystalline transparent oxide semiconductor. Science 300 (5623), 1269–1272. https://doi.org/10.1126/science.1083212.

Pantò, F., Leonardi, S.G., Fazio, E., Frontera, P., Bonavita, A., Neri, G., Antonucci, P., Neri, F., Santangelo, S., 2018. CO_2 sensing properties of electro-spun Ca-doped ZnO fibres. Nanotechnology 29 (30). https://doi.org/10.1088/1361-6528/aac27c.

Park, J.S., Jeong, J.K., Chung, H.J., Mo, Y.G., Kim, H.D., 2008. Electronic transport properties of amorphous indium-gallium-zinc oxide semiconductor upon exposure to water. Appl. Phys. Lett. 92 (7). https://doi.org/10.1063/1.2838380.

Park, M.J., Jeong, H.S., Joo, H.J., Jeong, H.Y., Song, S.H., Kwon, H.I., 2019. Improvement of NO_2 gas-sensing properties in InGaZnO thin-film transistors by a pre-biasing measurement method. Semicond. Sci. Technol. 34 (6). https://doi.org/10.1088/1361-6641/ab2155.

Prins, M.W.J., Grosse-Holz, K.O., Müller, G., Cillessen, J.F.M., Giesbers, J.B., Weening, R.P., Wolf, R.M., 1996. A ferroelectric transparent thin-film transistor. Appl. Phys. Lett. 68 (25), 3650–3652. https://doi.org/10.1063/1.115759.

Tang, H., Li, Y., Sokolovskij, R., Sacco, L., Zheng, H., Ye, H., Yu, H., Fan, X., Tian, H., Ren, T.L., Zhang, G., 2019. Ultra-high sensitive NO_2 gas sensor based on tunable

polarity transport in CVD-WS_2/IGZO p-N heterojunction. ACS Applied Materials and Interfaces, 11 (43), 40850–40859. https://doi.org/10.1021/acsami.9b13773.

Tetsuro, S., Kiyoshi, F., Masanoai, N., Akio, K., 1963. A new detector for gaseous components using zinc oxide thin films. The Journal of the Society of Chemical Industry, Japan 652–655. https://doi.org/10.1246/nikkashi1898.66.5_652.

Torsi, L., Dodabalapur, A., Sabbatini, L., Zambonin, P.G., 2000. Multi-parameter gas sensors based on organic thin-film-transistors. Sens. Actuators B 67 (3), 312–316. https://doi.org/10.1016/S0925-4005(00)00541-4.

Wager, J. F., Yeh, B., Hoffman, R. L., & Keszler, D. A. (2014). An amorphous oxide semiconductor thin-film transistor route to oxide electronics. Current Opinion in Solid State and Materials Science, 18(2), 53–61. https://doi.org/10.1016/j.cossms.2013.07.002

Wang, C., Yin, L., Zhang, L., Xiang, D., Gao, R., 2010. Metal oxide gas sensors: Sensitivity and influencing factors. Sensors 10 (3), 2088–2106. https://doi.org/10.3390/s100302088.

Wu, M., Hou, S., Yu, X., Yu, J., 2020. Recent progress in chemical gas sensors based on organic thin film transistors. J. Mater. Chem. C 8 (39), 13482–13500. https://doi.org/10.1039/d0tc03132a.

Wu, M., Kim, C.H., Shin, J., Hong, Y., Jin, X., Lee, J.H., 2017. Effect of a pre-bias on the adsorption and desorption of oxidizing gases in FET-type sensor. Sens. Actuators B 245, 122–128. https://doi.org/10.1016/j.snb.2017.01.110.

Yang, D.J., Whitfield, G.C., Cho, N.G., Cho, P.S., Kim, I.D., Saltsburg, H.M., Tuller, H.L., 2012. Amorphous $InGaZnO_4$ films: Gas sensor response and stability. Sens. Actuators B 171–172, 1166–1171. https://doi.org/10.1016/j.snb.2012.06.057.

Yun, D.J., Seo, G.H., Lee, W.H., Yoon, S.M., 2017. Improvement in sensing responses to ammonia gas for gas sensors with separately designed sensing element using ALD-grown ZnO nanoparticles and read-out element of top-gate In-Ga-Zn-O thin-film transistor. IEEE Trans. Electron Devices 64 (5), 2350–2356. https://doi.org/10.1109/TED.2017.2679239.

Yunusa, Z., Hamidon, M.N., Kaiser, A., Awang, Z., 2014. Gas sensors: A review. Sensors and Transducers 168 (4), 61–75. http://www.sensorsportal.com/HTML/DIGEST/New_Digest.htm.

Zan, H.W., Li, C.H., Yeh, C.C., Dai, M.Z., Meng, H.F., Tsai, C.C., 2011. Room-temperature-operated sensitive hybrid gas sensor based on amorphous indium gallium zinc oxide thin-film transistors. Appl. Phys. Lett. 98 (25). https://doi.org/10.1063/1.3601488.

Zhang, J., Zeng, D., Zhu, Q., Wu, J., Xu, K., Liao, T., Zhang, G., Xie, C., 2015. Effect of grain-boundaries in NiO nanosheet layers room-temperature sensing mechanism under NO_2. J. Phys. Chem. C 119 (31), 17930–17939. https://doi.org/10.1021/acs.jpcc.5b04940.

3

Recent developments in 2D MoS_2 thin films for gas sensing applications

P.S. Midhun[a], **K.J. Saji**[b,c] **and M.K. Jayaraj**[a,d]

[a] *Cochin University of Science and Technology, Kochi, India.* [b] *International School of Photonics, Cochin University of Science and Technology, Kochi, India.* [c] *Centre of Excellence in Advanced Materials, Cochin University of Science and Technology, Kochi, India.* [d] *University of Calicut, Malappuram, India*

3.1 Introduction

Two-dimensional (2D) materials have brought a revelation in scientific research, owing to their excellent chemical, mechanical, electrical, and optical properties, making them a strong candidate for various device applications. On top of their exceptional properties, novel 2D materials possess certain structural precedences such as their high surface-to-volume ratio and the ability of their surface to decorate species or functional groups, making them attractive candidates as gas sensing materials that can detect low levels of various gases exposed at low temperatures (Li et al., 2012; Park et al., 2018; Perkins et al., 2013; Sarkar et al., 2014). Among the family of 2D materials, graphene is the most popular and widely used 2D material, owing to its outstanding properties. But the absence of intrinsic bandgap limits the use of graphene on certain device applications. The search for novel 2D materials similar to graphene has triggered the exploration of a wide range of materials such as transition metal dichalcogenides (TMDCs). Among the TMDCs, 2D MoS_2 emerged as a promising semiconducting material by virtue of its extraordinary properties such as high mobility, high flexibility, high breaking strength, and low power consumption (Bertolazzi et al., 2011; P. et al., 2016; Park et al., 2018; Radisavljevic et al., 2011). These features, along with its structural modifications and functionalization with metals or metal oxides, make MoS_2 an efficient sensing material (Cho et al., 2015b, 2015d; Park et al., 2018; Sarkar et al., 2015; Sharma et al., 2018; Zhang et al., 2010). The dimensionality of

Nanomaterials for Sensing and Optoelectronic Applications. DOI: https://doi.org/10.1016/B978-0-12-824008-3.00008-4

the material plays a major role in gas sensing applications, and 2D materials are more promising because of their ultrathin structure and the high surface area associated with it. The high surface area of the material leads to high sensitivity toward adsorbed gas molecules. Theoretically, we assume that the whole surface is exposed to the target gas in the case of monolayer 2D materials such as TMDCs; hence they promise high sensitivity (Neri, 2017; Sun et al., 2014). Also, in monolayer 2D structures the surface atoms are unsaturated due to low coordination numbers. Mostly the adsorption of gas molecules happens on the low coordinated areas of the solid surface, such as edges, steps, terraces, kinks, and corner atoms. Hence the number of chemisorbed gas molecules is high. Since atomically thin 2D TMDCs have numerous low coordinated sites, they are expected to show enhanced sensing properties compared to their bulk counterparts (Liu et al., 2017; Neri, 2017). Besides their structural advantage, 2D TMDCs have a unique electronic band structure with bandgap varying with the thickness of the material. Hence their bandgap can be modulated by tuning the number of layers and thereby the sensing properties of the material. Also, the intrinsic charge transport characteristics can be studied by analyzing the electronic structures of such thin 2D TMDCS, which is essential to understanding the sensing behavior of the material. Substantial changes in the electronic structure may occur in monolayer materials due to the changes in the interlayer coupling, the degree of quantum confinement, and symmetry element. Since the changes in the electronic structure of single-layer materials are strongly influenced by the adsorbed gas species, the sensing properties of the material also improve compared to other bulk materials. 2D TMDCs show remarkable enhancement in sensing properties as the thickness of the material is decreased mainly due to the quantum confinement effect (Kim et al., 2016; Neri, 2017). Also, 2D TMDC–based sensors require less power at even low operating temperatures, thereby increasing the lifetime of the device. This is attributed to the physisorption charge transfer sensing mechanism in 2D TMDC sensors, which require very low power (Neri, 2017; Zhang et al., 2016). These features of 2D TMDCs make them a promising candidate for use as high-performance gas sensors compared to other sensing materials.

3.2 Sensing mechanism in 2D-based gas sensors

A typical metal oxide–based gas sensor uses surface-adsorbed oxygen ions in order to sense target gases. The surface of metal oxides adsorbs negative oxygen ions (O_2^-, O^-, and O^{2-}) at an operating temperature higher than 100°C. When target gases are exposed to

metal oxides, they interact with the negative oxygen ions, resulting in a change in the conductivity of the metal oxides. If the target gas is reducing in nature, the conductivity of metal oxides increases, while exposure to an oxidizing gas decreases the conductivity of metal oxides (Barsan & Weimar, 2001; Jiménez-Cadena et al., 2007; Yang et al., 2017).

In the case of 2D material–based gas sensors (graphene and related inorganic analogs) the sensing mechanism is related to the charge transfer processes, where the sensing material accepts or donates charge to the chemical species to be detected. Upon exposure to various target gases, there occurs a charge transfer reaction between the adsorbed gas molecules and the sensing material. This is followed by different transfer directions and quantities of charges leading to different changes to the resistance of the sensing material. If air is then exposed to the sensing material, desorption of gas molecules occurs, and resistance of the material goes back to the initial state. If an n-type (electron donor) sensing material is exposed to an oxidizing gas, the electrical resistance of the material increases while it decreases when the material interacts with a reducing gas. The reverse process occurs for a p-type (electron acceptor) sensing material (Vargas-Bernal, 2019; Yang et al., 2017).

A theoretical account for the charge transfer mechanism of n-type monolayer MoS_2 was given by Yue et al. using first-principles calculations. The adsorption of H_2, O_2, H_2O, NH_3, NO, NO_2, and CO on monolayer MoS_2 was considered. The charge density difference plot of the interaction of monolayer MoS_2 and the adsorbed gases is shown in Fig. 3.1. The green sector in the figure represents the charge depletion, while charge accumulation is shown in the red sector.

The exposure of oxidizing gases such as H_2, O_2, H_2O, NO, NO_2, and CO with MoS_2 results in the transfer of electron charge from MoS_2 to the adsorbing gases. As a consequence, the electron charge density of MoS_2 decreases, leading to an increase in the resistance of monolayer MoS_2. But when MoS_2 is exposed to NH_3 (a reducing gas), electron charge transfers from MoS_2 to NH_3 molecules cause an increase in the electron charge density of MoS_2 and a decrease in its resistance (Yang et al., 2017; Yue et al., 2013). Measuring the change in the photoluminescence of the sensing material before and after exposure to target gases can prove the charge transfer mechanism in 2D gas sensors.

3.3 2D-based gas sensing devices

A traditional gas sensor detects the target gas when the electrical, electronic, or optical characteristics of the sensing material are changed upon exposure to different target gases. This change in properties of the sensing material can be termed as the sensing signal.

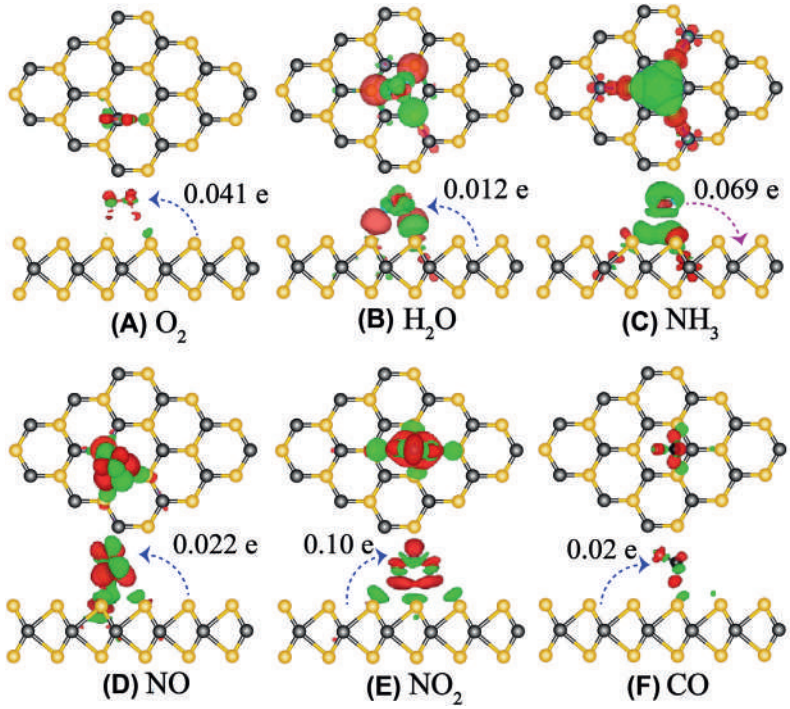

Figure 3.1. Charge density difference plots for (A) O_2, (B) H_2O, (C) NH_3, (D) NO, (E) NO_2, and (F) CO interacting with monolayer MoS_2 (Yue et al., 2013).

Various types of conventionally used 2D-based gas sensors are listed below.

3.3.1 Field-effect transistors

A field-effect transistor (FET) can be used as an effective, low-cost, and portable gas sensor with sensitive detection. A typical FET gas sensor comprises a semiconducting channel (sensing material) with metal electrodes at either end that act as the source and drain. The conductance of the device can be controlled by the application of various bias voltages on the gate electrode through a thin layer of dielectric material. For gas sensing in a FET, the changes in the drain–source current at a constant voltage are measured before and after exposure to the target gas. When the target gas is adsorbed by the sensing material, its electronic structure changes, which results in the change in conductance of the semiconducting channel. A FET gas sensor can be used to detect a variety of target gases. A typical example of a 2D FET sensor using a layer of chemically reduced graphene oxide (rGO) as the semiconducting channel in a back-gated configuration is shown in Fig. 3.2A. The SEM image of the device is shown in Fig. 3.2B. The drain–source current (I_{ds}) is measured by applying a

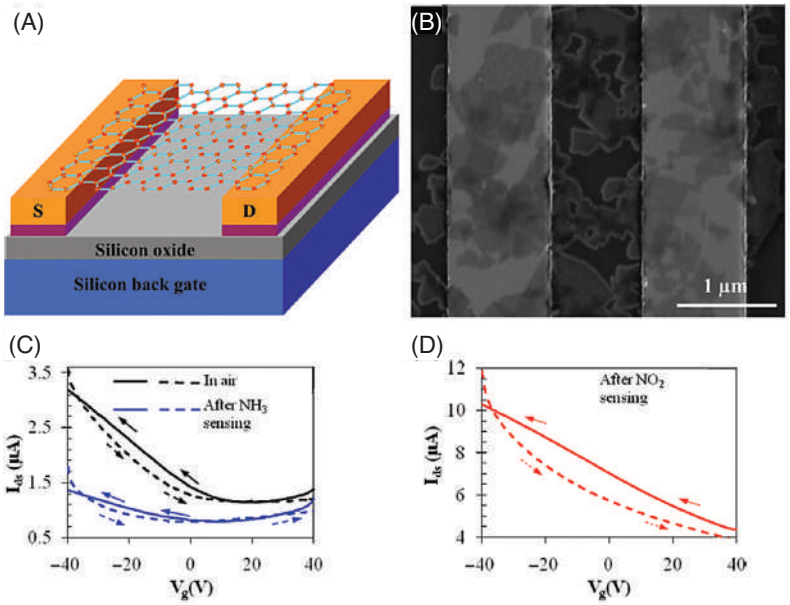

Figure 3.2. (A) Schematic illustration of a FET sensor based on reduced graphene oxide; (B) SEM image of the device, the brightest regions are the metal electrodes; (C) I_{ds} versus V_g curves before (black curve) and after (blue curve) exposure to NH_3; (D) I_{ds} versus V_g curve after NO_2 exposure (Lu et al., 2011). Reprinted with permission from (Lu et al., 2011). Copyright (2011) American Chemical Society.

drain–source voltage of 0.1 V and varying and the gate voltage (V_g) between −40 V and +40 V. The I_{ds}–V_g curve of the device upon exposing the device to air and NH_3 gas is shown in Fig. 3.2C. Before exposure to NH_3, the device shows a typical p-type behavior, while after sensing NH_3, it shows ambipolar characteristics. This can be attributed to the n-type doping effect of the NH_3 gas molecule, which decreases the hole density of rGO, thereby diminishing its conductance. However, exposure to NO_2 gas makes the device completely p-type (I_{ds} slope is higher than in air) and furthermore increases its conductance significantly, as shown in Fig. 3.2D. Being an oxidizing gas, NO_2 extracts electrons from rGO, which increases the hole density in rGO and enhances its conductivity (Donarelli & Ottaviano, 2018; Lu et al., 2011; Yang et al., 2017).

3.3.2 Chemiresistors

Chemiresistors are among the most favored gas sensors, attributed to their cheap production cost, simple mode of operation, ease of fabrication, and ability to reuse. The working mechanism of a chemiresistor is that when the sensing material adsorbs a target gas molecule, the electrical resistance of the sensing material changes. The target gas can be identified by measuring the induced resistance change. In a typical chemiresistor the sensing material is deposited between two interdigitated electrodes supported by an insulating substrate. A

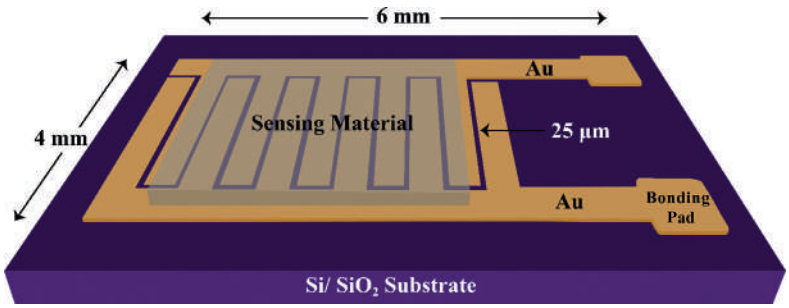

Figure 3.3. Schematic diagram of a G-PANI chemiresistor (Wu et al., 2013).

2D-based chemiresistor gas sensor using drop cast graphene/polyaniline (G-PANI) as the sensing material is shown in Fig. 3.3. Interdigitated gold electrodes spaced at 25 μm were deposited onto a SiO_2 substrate, to which G-PANI was drop cast. The device succeeded at sensing NH_3 in a 1–6400 ppm range. The response of the device is calculated using Eq. 3.1.

$$\text{Response} = \frac{R_G - R_{air}}{R_{air}} \times 100\% \tag{3.1}$$

where R_G is the resistance of the device after NH_3 exposure and R_{air} its resistance in air (Donarelli & Ottaviano, 2018; Wu et al., 2013).

3.3.3 Optical gas sensors

In traditional gas sensors changes in the electrical properties of the sensing material are measured to identify the target gas. But in an optical gas sensor the variations in the optical characteristics, such as fluorescence, reflectivity, and absorbance, of the sensing material are used to sense the target gases.

Gold nanoparticles (AuNPs)–coupled graphene oxide sensor is such a 2D-based optical gas sensor developed by Cittadini et al. that detects target gases by measuring the changes in the relative absorbance of rGO. When the devices is exposed to H_2 (a reducing gas), the absorbance of rGO/AuNPs increases while it decreases upon exposure to NO_2 (an oxidizing gas), as shown in Fig. 3.4 (Barsan & Weimar, 2001; Vargas-Bernal, 2019).

Another sensor that uses the optical properties of a sensing material is a surface plasmon resonance (SPR) sensor. When a light beam is an incident on a material, the surface plasmons get excited, and the diffracted/reflected light is collected by a detector. For SPR excitation, the characteristics of the incident light change if there is a change in the refractive index of the sensing material. 2D materials such as graphene, graphene oxide, and MoS_2 are among the popular sensing materials

used to fabricate SPR sensors (Donarelli & Ottaviano, 2018; Piliarik & Homola, 2009; Zeng et al., 2014, 2015; Zhang et al., 2013).

3.3.4 Impedance Sensors

An impedance sensor, as its name suggests, works on the basis of the change in the impedance of the material, where the impedance is computed in the frequency domain by measuring the current corresponding to an applied sinusoidal voltage (Rheaume & Pisano, 2011). An impedance sensor consists of sensing material deposited between two metal electrodes. A sinusoidal voltage ranging from subhertz to megahertz is applied between two electrodes, and the sensing response is measured using solid-state impedance spectroscopy (Peter et al., 2007). One of the major advantages of impedance sensors is that they can detect very low concentrations (sub-ppm) of hydrocarbons, CO, NO_x, and humidity.

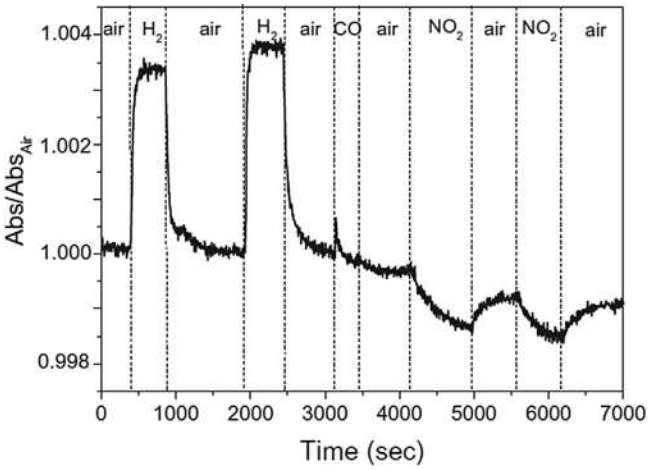

Figure 3.4. https://doi.org/10.1016/j.carbon.2013.12.048. Time-resolved tests for AuH-rGO sample achieved at 528 nm upon exposure to H_2, CO, and NO_2. Reprinted from Carbon, Volume 69, Michela Cittadini, Marco Bersani, Francesco Perrozzi, Luca Ottaviano, Wojtek Wlodarski, Alessandro Martucci, Graphene oxide coupled with gold nanoparticles for localized surface plasmon resonance based gas sensor, 452–459, Copyright (2013), with permission from Elsevier.

3.4 MoS_2-based gas sensors

MoS_2 is a TMDC consisting of Mo and S atoms with strong in-plane covalent bonds, while the vertically stacked layers are linked via weak van der Waals forces between the layers in its bulk form (Fig. 3.5A) (Radisavljevic et al., 2011). MoS_2, like other TMDCs, can exist as a hexagonal (2H), octahedral (1T), and distorted octahedral (1T′) crystal structure (Duerloo et al., 2014). Even though all these phases consist of a molybdenum atom layer sandwiched between two atomic layers of sulfur, only the 2H phase is semiconducting, while other phases are metallic. Hence the 2H phase has been widely studied for electronic device applications. The most commonly occurring and thermodynamically stable crystal structure for MoS_2 is hexagonal (2H), which has a 2D-layered structure with D_{6h} point group symmetry (Ataca et al., 2012). A monolayer of MoS_2 consists of a single sheet of Mo plane sandwiched between two planes of S atoms forming a 2D hexagonal crystal structure with a trigonal prismatic arrangement and D_{3h} point group symmetry (Fig. 3.5B and C). Monolayer MoS_2 has a thickness of ≈6.5 Å with the upper and lower sulfur atoms about 3.2 Å apart (Lu et al., 2011). MoS_2 monolayer has lattice constants reported to be ≈3.22 Å with a S–Mo–S bond angle of ≈80.56° and a covalent bond length of Mo–S of 2.43 Å (Ataca et al., 2011, 2012; Ganatra & Zhang, 2014;

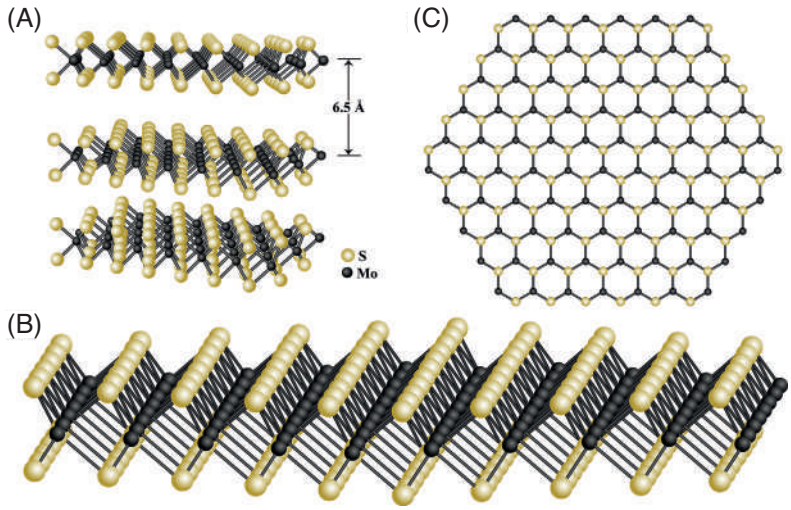

Figure 3.5. (A) 3D form of bulk MoS_2; (B), (C) side and top views of 2D hexagonal layouts of single-layer MoS_2 (Radisavljevic et al., 2011).

P. et al., 2016). Another intriguing feature of 2D MoS_2 is that its surface is free from dangling bonds.

Since 2D-layered MoS_2 is held together by weak van der Waals forces, monolayer MoS_2 can be easily synthesized using exfoliation methods (mechanical and chemical), just as with graphene. Also, it can be grown in large areas using techniques such as chemical vapor deposition (CVD) and physical vapor deposition (pulsed laser deposition and sputtering). Unlike graphene, MoS_2 has a definite bandgap exhibiting both direct (1.89 eV) and indirect (1.2 eV) transitions in its monolayer and bulk forms, respectively. This intriguing nature can be attributed to a combined effect of quantum confinement, long-range Coulombic effects, and a change in the hybridization between p_z orbitals in S atoms and d orbitals in Mo atoms (Mak et al., 2010; Splendiani et al., 2010). Also, monolayer MoS_2 exhibits strong photoluminescence with two excitonic peaks corresponding to 1.9 eV and 2.05 eV. These peaks appear to originate from the direct excitonic transitions at the K zone, with the energy splitting ($\approx$0.15 eV) as a result of the combined effect of interlayer coupling and valence band spin-orbit coupling (Ganatra & Zhang, 2014; Kadantsev & Hawrylak, 2012; P. et al., 2016).

The in-plane stiffness of a monolayer of MoS_2 is about 180 $\pm$ 60 Nm^{-1}, with an effective Young's modulus of 270 $\pm$ 100 GPa, which is higher compared to that of bulk MoS_2 crystal ($\approx$240 GPa) as well as that of steel ($\approx$205 GPa) (Bertolazzi et al., 2011; Castellanos-Gomez et al., 2012). Monolayer MoS_2 has a high breaking strength of 22 $\pm$ 4 GPa, which is between 6% and 11% of its Young's modulus, and consequently, the monolayer MoS_2 can be deformed and bent to a curvature of a radius of 0.75 mm by upholding its innate properties

(Allen et al., 2010; Barvat et al., 2017; Ramana et al., 2008). Because of these extraordinary mechanical features, MoS_2 can be used in flexible electronic and optoelectronic devices. The piezoelectric properties shown by MoS_2 can be exploited for sensitive mechanical transducers applications (Duerloo et al., 2012). Nanomechanical resonators based on MoS_2 could operate in HF (high-frequency, 3–30 MHz) and VHF (very-high-frequency, 30–300 MHz) bands with good performance and exhibit a very high figure of merit of about 2×10^{10} Hz, even at room temperature (Lee et al., 2013a). Single-layer MoS_2 exhibits exceptional electrical properties, which is evident from the first transistor made using MoS_2 as the channel layer. The device exhibited a high mobility of up to 200 cm^2 $(V\ s)^{-1}$ along with a high on/off ratio of $\approx 10^8$ at room temperature (P. et al., 2016; Radisavljevic et al., 2011). Along with these outstanding electrical and optical properties, the high surface-to-volume ratio of mono- and few-layered MoS_2 makes them promising sensing materials.

FET devices were among the first-developed gas sensors using MoS_2 as the sensing material channel. Mechanically exfoliated MoS_2 was used to fabricate single- as well as multilayered (1–4L) MoS_2-based FETs in order to detect NO gas. Even though FET using monolayer MoS_2 showed rapid response toward NO, it was less stable, while multilayered (2L, 3L, and 4L) MoS_2-based FET sensors exhibited both sensitivity and stable response with a detection limit of 0.8 ppm (Li et al., 2012). Similarly, micromechanically exfoliated MoS_2 FET sensors using one- to five-layered MoS_2 were used to sense NO_2, NH_3, and water vapor. The device exhibited an n-type behavior with an increase in resistance during NO_2 (electron acceptor) exposure and a decrease in resistance when exposed to NH_3 (electron donor), as shown in Fig. 3.6C and D, respectively. Surprisingly, five-layered MoS_2 FET sensors were more sensitive compared to bilayer MoS_2 devices, while single-layered MoS_2 FETs turned out to be unstable. The better sensing performance of multilayered MoS_2 FET sensors is because of the fact that the electronic structure of layered MoS_2 is thickness dependent. First-principles calculation using density functional theory (DFT) confirmed the transfer of charge between the MoS_2 semiconducting channel and the exposed gas molecule (Late et al., 2013).

FET gas sensors fabricated using CVD-grown monolayer MoS_2 with Schottky contacts showed a strong response toward NO and NH_3. The device detected NO_2 at 20 ppb and NH_3 at 1 ppm with a conductance change of more than 20% and 40%, respectively. The main reason for this highly improved sensitivity of the device is the Schottky barrier modulation at the MoS_2–metal electrode junctions along with the charge transfer between the gas molecules and MoS_2 monolayer (Liu et al., 2014).

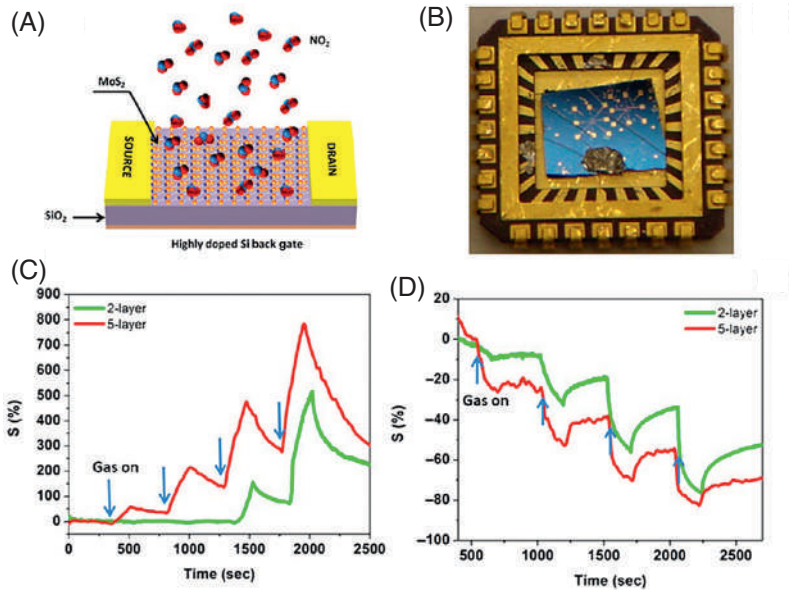

Figure 3.6. (A) Schematics of MoS_2 FET–based NO_2 sensor (Late et al., 2013), (B) optical photograph of the MoS_2 FET sensor mounted on the chip, and comparative (C) two- and (D) five-layer MoS_2 cyclic sensing performances with NO_2 and NH_3, respectively (Late et al. 2013). Reprinted with permission from (Late et al., 2013). Copyright (2013) American Chemical Society.

Resistive gas sensors based on MoS_2 are also widely used for the detection of several target gases. High-concentration aqueous dispersion of MoS_2 nanosheets synthesized using a combination of grinding and sonication were used to sense NH_3 gas. The device was fabricated by inkjet printing MoS_2 nanosheets onto the microelectrode, which was already prepared. The resistance measurements of the sensor corresponding to the exposed NH_3 showed decent sensitivity, which is attributed to the high-concentration aqueous dispersions of MoS_2 nanosheets along with their large surface-to-volume ratio and robust adsorbability (Yao et al., 2013). A CVD-grown MoS_2-based chemiresistor was developed by Lee et al., which can sense NH_3 at a concentration of up to 200 ppm under an N_2 environment at room temperature with a poor recovery below this limit (Lee et al., 2013b). Another resistive-type gas sensor was developed using liquid-exfoliated MoS_2 flakes deposited on prepatterned Si_3N_4 substrates, which can detect both oxidizing (NO_2) and reducing (relative humidity and H_2) gases. Two devices were made, with one annealed at 150°C and the other at 250°C in air. The device annealed in air at 150°C exhibited p-type conductivity when exposed to NO_2 and 50% relative humidity. Conversely, the device annealed in air at 250°C exhibited n-type conductivity when exposed to NO_2, relative humidity, and H_2 gases, sensing both oxidative and reducing gases with a measured detection limit of 20 ppb and response intensity equal to 5.80 at 1 ppm. This outstanding performance of the device is attributed to the partial

oxidation of the MoS_2 surface and increased sulfur vacancies due to annealing in air at 250°C (Donarelli et al., 2015).

A bifunctional sensor using CVD-grown trilayered MoS_2 as a sensing material was developed, which not only senses gas molecules but also detects photons. The device turned out to be an excellent gas sensor with high selectivity and sub-ppm-level detection for NO_2 with a stable cycling behavior in dark conditions compared to that with NH_3, H_2, and H_2S. Even in the presence of light, the device detected NO_2 and NH_3 but with less response compared to that in dark conditions. The possible reason for this behavior is the increase in desorption of the target gases. The sensor also acts as a capable photosensor with moderate photoresponsivity (~71 mA/W), reliable photoresponse, and rapid photoswitching within 500 ms (Cho et al., 2015a).

Apart from the large surface-to-volume ratio and its semiconducting behavior, MoS_2 also possesses numerous active sites, which makes it a good sensing material. In order to study the effect of active sites during sensing MoS_2 aligned in three different ways was used by Cho et al.: horizontally aligned MoS_2, a mixture of horizontally aligned MoS_2 and vertically aligned layer, and vertically aligned MoS_2, grown by means of CVD. The resistive sensors based on vertically aligned MoS_2 showed a five-times higher response to NO_2 when compared to the horizontally aligned MoS_2 device. This can be attributed to the high adsorption energy on the MoS_2 edge sites compared to the MoS_2 films' basal plane. The experimental result was confirmed by DFT calculations, using which the binding energy of NO_2 near the edge sites of MoS_2 was computed and multiple configurations in which it is much stronger than those at the basal plane of the MoS_2 were found (Cho et al., 2015d).

The sensing capabilities of MoS_2 gas sensors can be enhanced by activating efficient charge transfer between the target gas molecules and MoS_2. This can be achieved by the surface functionalization of MoS_2 with the nanomaterial of metal oxides and noble metals as functional (Yang et al., 2017). Such a robust and high-performance gas sensor with flexible thin film transistor (TFT) arrays based on MoS_2 was fabricated by He et al. for the detection of NO_2 gas. They used rGO as the electrode and functionalized MoS_2 thin film with Pt NPs, which increased the sensitivity of the sensor by a factor of three and achieved a detection limit of 2 ppb. This increase in sensitivity is probably attributed to the change of the Schottky barrier between the semiconducting MoS_2 thin-film channel layer and Pt NPs upon the adsorption of NO_2 gas molecules (He et al., 2012). Apart from NO_2 detection, Pt-decorated MoS_2 works as a very efficient humidity sensor as well. Berman et al. developed an ultrasensitive humidity sensor by drop-coating Pt-decorated few-layered MoS_2 nanoflakes on interdigitated Au electrodes. The device recorded a very high response of 4000 times

at 85% relative humidity with excellent stability, making it a suitable sensing layer in a portable, low-power humidity sensor (Burman et al., 2018). The effect of functionalization/doping on MoS_2 by metallic NPs and the sensing behavior of functionalized MoS_2 FET sensors were studied by Sarkar and his group. They doped MoS_2 with noble metals such as Au, Ag, Pd, and Pt, as well as low-work-function metals such as Sc and Y and made monolayer MoS_2 FETs in a back-gated configuration functionalized by Pd NPs in order to detect H_2 gas. Without Pd functionalization, the sensor showed a negligible change in current upon exposure to 3-ppm H_2 gas, while there was a substantial increase in current on the Pd NP–functionalized MoS_2 FET sensor. This is due to the decrease in the work function of Pd NPs upon hydrogen adsorption resulting in the decrease in p-type doping and thus an increase in the current of n-type MoS_2 FET. Also, they obtained a sensitivity of 5 for Pd NP–functionalized MoS_2 FET sensors upon 3-ppm H_2 exposure at room temperature, which was less than 1 for a bulk MoS_2 FET sensor under the same conditions (Sarkar et al., 2015).

Similar to metal NPs, decorating metal oxide NPs on a 2D MoS_2 gas sensor may enhance the sensing characteristics of the device. High-sensitivity SnO_2 nanocrystals decorated on MoS_2 nanosheet–based gas sensors with excellent repeatability and selectivity toward NO_2 gas were fabricated by Cui et al. SnO_2 acted as a strong p-type dopant, which create a p-type channel in the MoS_2 nanosheet. Though the sensing device based on pure MoS_2 nanosheets was unstable, gas sensors made of MoS_2/SnO_2 nanohybrid structures exhibited a stable nature at room temperature. This high stability was the result of incorporating SnO_2 nanocrystals, which increases its work function, and creating a passivation layer to prevent the interaction between the oxygen and the MoS_2. The device exhibited a low detection limit of 0.5 ppm (Cui et al., 2015). In a similar work Yan and coworkers decorated the surface of MoS_2 nanosheets with SnO_2 NPs to form a SnO_2@MoS_2 composite. The SnO_2@MoS_2 composite gas sensor showed a better response to ethanol gas than the device made of pure SnO_2. The better performance of the SnO_2@MoS_2 composite gas sensor is attributed to three major reasons. Primarily, MoS_2 nanosheets exhibit a high surface-to-volume ratio, which prevents SnO_2 NPs aggregation, thereby facilitating the reaction of ethanol with surface-adsorbed oxygen. Also, the active sites provided by MoS_2 nanosheets, along with excellent interaction between SnO_2 NPs and MoS_2 nanosheets, improve the rate of electron transfer and thereby enhance the gas sensing performance of the device. Finally, a p–n junction is formed at the interface between SnO_2 NPs and MoS_2 nanosheets, and when the device is exposed to ethanol gas at high temperatures, the generated electrons get transferred to the conduction band of SnO_2 NPs, thus enhancing the

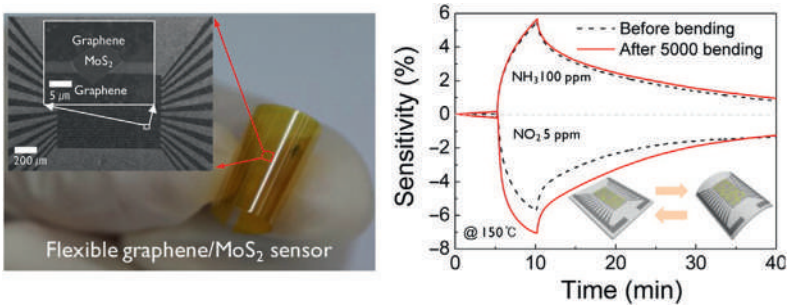

Figure 3.7. (A) Optical image of a MoS_2/graphene heterostructured device on a bent polyimide substrate. (B) Comparison of the gas response characteristics of the flexible heterostructured device before/after the bending cycle test; (inset) 3D schematic images showing the bending test condition (Cho et al., 2015c). Reprinted with permission from (Cho et al., 2015c). Copyright (2015) American Chemical Society.

sensing performance of the device (Yan et al., 2015). MoS_2 nanosheets were also decorated with ZnO NPs, and the ZnO@MoS_2 composite gas sensor showed better gas sensing performance toward ethanol gas than ZnO NPs alone (Yan et al., 2016a).

Apart from functionalization by metal and metal oxide NPs, the hybrid/heterostructures of MoS_2 with other 2D materials were also found to have an immense effect on the sensing behavior of corresponding gas sensors. An atomically thin, flexible MoS_2/graphene heterostructure-based resistive gas sensor developed by Cho and his group is shown in Fig. 3.7A. The flexible sensor was able to successfully detect NH_3 and NO_2 gases at 150°C, and it maintained response to both gases without major degradation even after 5000 bending cycles, as shown in Fig. 3.7B (Cho et al., 2015c). They also investigated the changes in gas sensing properties of MoS_2 heterostructures on flexible substrates when decorated with metal NPs. The flexible MoS_2/graphene hybrid gas sensor was decorated with Pd and Al NPs, and it was found that metal NPs can modulate selectivity by tuning the electronic properties of the 2D sensor. When exposed to NH_3 and NO_2 gases, the device decorated with Pd NPs showed more sensitivity toward NH_3 gas while sensitivity to NO_2 was enhanced by Al NPs (Cho et al., 2015b).

The hydrothermal synthesis of MoS_2 often leads to the formation of hierarchical nanostructures, which may add to the improved sensing capabilities of 2D MoS_2 gas sensors. Such a gas sensor was fabricated by incorporating AuNPs on MoS_2 hierarchical nanostructures, and the device was able to sense NH_3 gas at low temperatures (Yan et al., 2016b). MoS_2/SnO_2 hierarchical p–n heterojunctions, which were the first of their kind, acted as a bifunctional device showing incredible gas sensing performance along with exceptional catalytic property. The device achieved fantabulous performance by tuning the amount of MoS_2. A low amount of MoS_2 made the device an excellent TEA (triethanolamine) sensor with superior selectivity, very high sensitivity, and stability at a relatively low working temperature. By increasing the

amount of MoS_2, the device exhibited excellent catalytic activity for the reduction of 4-nitrophenol. These enhanced bifunctional properties of the device may be ascribed to the synergic effect of hierarchical structures along with the exposure or more active sites (Qiao et al., 2018). The improvement in the gas sensing performance by controlling the surface structure at the atomic level was ascertained from the elevated gas sensing abilities of hierarchical hollow MoS_2 microspheres–based gas sensors fabricated via the hydrothermal method. The device succeeded at detecting H_2S, NH_3, C_2H_5OH, C_5H_8, CO_2, NO_2, SO_2, and NO and showed a higher response toward NO_2 gas at a relatively lower temperature (150°C). The hierarchical MoS_2 hollow sphere possesses more active sites and increased specific surface area, which results in its increased gas sensing performance (Li et al., 2019).

3.5 Summary

2D MoS_2 thin films have emerged as a very promising sensing material for the detection of a wide range of gases, which can be attributed to their extraordinary electrical, optical, mechanical, and chemical properties. 2D MoS_2 FET sensors showed tunable sensing behavior by modulating the thickness of the MoS_2 this film. These sensors are capable of detecting various target gases even at room temperature with low power consumption, making them durable gas sensors. Even after bending for 5000 cycles, the flexible MoS_2-based gas sensor showed a promising response without much degradation. The sensing performance of the 2D MoS_2 FET sensors can be enhanced by functionalizing MoS_2 thin film by metal and metal oxide NPs as well as forming heterostructures and composites of MoS_2 and other 2D counterparts like graphene, rGO, and h-BN. The coupling of these 2D materials seems to have an enhanced effect on the gas sensing properties of the device. The structural orientation of MoS_2 thin films has also had a significant contribution in the sensing behavior, with the vertically aligned MoS_2 FET gas sensor showing a five-times better sensing response compared to the horizontally aligned counterpart. Apart from structural orientation, the formation of the MoS_2 hierarchical structure has also been shown to improve the gas sensing properties mainly because of an increase in the number of active sites along with high specific surface area. Another advantage of the MoS_2-based gas sensor is that it can be used as a bifunctional device that acts as both a gas sensor and a photodetector simultaneously. Even though the MoS_2-based gas sensor has shown very promising development in recent years, there is still a need for improvement in areas such as detection limit and selectivity of the target gas molecules, which hopefully will be solved in the near future.

References

Allen, M.J., Tung, V.C., Kaner, R.B., 2010. Honeycomb carbon: A review of graphene. Chem. Rev. 110 (1), 132–145. https://doi.org/10.1021/cr900070d.

Ataca, C., Şahin, H., Ciraci, S., 2012. Stable, single-layer MX_2 transition-metal oxides and dichalcogenides in a honeycomb-like structure. J. Phys. Chem. C 116 (16), 8983–8999. https://doi.org/10.1021/jp212558p.

Ataca, C., Topsakal, M., Aktürk, E., Ciraci, S., 2011. A comparative study of lattice dynamics of three- and two-dimensional MoS2. J. Phys. Chem. C 115 (33), 16354–16361. https://doi.org/10.1021/jp205116x.

Barsan, N., Weimar, U., 2001. Conduction model of metal oxide gas sensors. J. Electroceram. 7 (3), 143–167. https://doi.org/10.1023/A:1014405811371.

Barvat, A., Prakash, N., Satpati, B., Singha, S.S., Kumar, G., Singh, D.K., Dogra, A., Khanna, S.P., Singha, A., Pal, P., 2017. Emerging photoluminescence from bilayer large-area 2D MoS_2 films grown by pulsed laser deposition on different substrates. J. Appl. Phys. 122 (1). https://doi.org/10.1063/1.4991490.

Bertolazzi, S., Brivio, J., Kis, A., 2011. Stretching and breaking of ultrathin MoS_2. ACS Nano 5 (12), 9703–9709. https://doi.org/10.1021/nn203879f.

Burman, D., Santra, S., Pramanik, P., Guha, P.K., 2018. Pt decorated MoS_2 nanoflakes for ultrasensitive resistive humidity sensor. Nanotechnology 29 (11). https://doi.org/10.1088/1361-6528/aaa79d.

Castellanos-Gomez, A., Poot, M., Steele, G.A., Van Der Zant, H.S.J., Agraït, N., Rubio-Bollinger, G., 2012. Elastic properties of freely suspended MoS_2 nanosheets. Adv. Mater. 24 (6), 772–775. https://doi.org/10.1002/adma.201103965.

Cho, B., Kim, A.R., Park, Y., Yoon, J., Lee, Y.J., Lee, S., Yoo, T.J., Kang, C.G., Lee, B.H., Ko, H.C., Kim, D.H., Hahm, M.G., 2015a. Bifunctional sensing characteristics of chemical vapor deposition synthesized atomic-layered MoS_2. ACS Appl. Mater. Interfaces 7 (4), 2952–2959. https://doi.org/10.1021/am508535x.

Cho, B., Yoon, J., Lim, S.K., Kim, A.R., Choi, S.Y., Kim, D.H., Lee, K.H., Lee, B.H., Ko, H.C., Hahm, M.G., 2015b. Metal decoration effects on the gas-sensing properties of 2D hybrid-structures on flexible substrates. Sensors (Switzerland) 15 (10), 24903–24913. https://doi.org/10.3390/s151024903.

Cho, B., Yoon, J., Lim, S.K., Kim, A.R., Kim, D.H., Park, S.G., Kwon, J.D., Lee, Y.J., Lee, K.H., Lee, B.H., Ko, H.C., Hahm, M.G., 2015c. Chemical sensing of 2D graphene/MoS_2 Heterostructure device. ACS Appl. Mater. Interfaces 7 (30), 16775–16780. https://doi.org/10.1021/acsami.5b04541.

Cho, S.Y., Kim, S.J., Lee, Y., Kim, J.S., Jung, W.B., Yoo, H.W., Kim, J., Jung, H.T., 2015d. Highly enhanced gas adsorption properties in vertically aligned MoS_2 layers. ACS Nano 9 (9), 9314–9321. https://doi.org/10.1021/acsnano.5b04504.

Cui, S., Wen, Z., Huang, X., Chang, J., Chen, J., 2015. Stabilizing MoS_2 nanosheets through SnO_2 nanocrystal decoration for high-performance gas sensing in air. Small 11 (19), 2305–2313. https://doi.org/10.1002/smll.201402923.

Donarelli, M., Ottaviano, L., 2018. 2D materials for gas sensing applications: A review on graphene oxide, MoS_2, WS_2 and phosphorene. Sensors (Switzerland) 18 (11). https://doi.org/10.3390/s18113638.

Donarelli, M., Prezioso, S., Perrozzi, F., Bisti, F., Nardone, M., Giancaterini, L., Cantalini, C., Ottaviano, L., 2015. Response to NO_2 and other gases of resistive chemically exfoliated MoS_2-based gas sensors. Sens. Actuators B 602–613. https://doi.org/10.1016/j.snb.2014.10.099.

Duerloo, K.A.N., Li, Y., Reed, E.J., 2014. Structural phase transitions in two-dimensional Mo-and W-dichalcogenide monolayers. Nat. Commun. 5. https://doi.org/10.1038/ncomms5214.

Duerloo, K.A.N., Ong, M.T., Reed, E.J., 2012. Intrinsic piezoelectricity in two-dimensional materials. J. Phys. Chem. Lett. 3 (19), 2871–2876. https://doi.org/10.1021/jz3012436.

Ganatra, R., Zhang, Q., 2014. Few-layer MoS_2: A promising layered semiconductor. ACS Nano 8 (5), 4074–4099. https://doi.org/10.1021/nn405938z.

He, Q., Zeng, Z., Yin, Z., Li, H., Wu, S., Huang, X., Zhang, H., 2012. Fabrication of flexible MoS_2 thin-film transistor arrays for practical gas-sensing applications. Small 8 (19), 2994–2999. https://doi.org/10.1002/smll.201201224.

Jiménez-Cadena, G., Riu, J., Rius, F.X., 2007. Gas sensors based on nanostructured materials. Analyst 132 (11), 1083–1099. https://doi.org/10.1039/b704562j.

Kadantsev, E.S., Hawrylak, P., 2012. Electronic structure of a single MoS_2 monolayer. Solid State Commun. 152 (10), 909–913. https://doi.org/10.1016/j.ssc.2012.02.005.

Kim, Y.H., Kim, K.Y., Choi, Y.R., Shim, Y.S., Jeon, J.M., Lee, J.H., Kim, S.Y., Han, S., Jang, H.W., 2016. Ultrasensitive reversible oxygen sensing by using liquid-exfoliated MoS_2 nanoparticles. J. Mater. Chem. A 4 (16), 6070–6076. https://doi.org/10.1039/c6ta01277a.

Late, D.J., Huang, Y.K., Liu, B., Acharya, J., Shirodkar, S.N., Luo, J., Yan, A., Charles, D., Waghmare, U.V., Dravid, V.P., Rao, C.N.R., 2013. Sensing behavior of atomically thin-layered MoS_2 transistors. ACS Nano 7 (6), 4879–4891. https://doi.org/10.1021/nn400026u.

Lee, J., Wang, Z., He, K., Shan, J., Feng, P.X.L., 2013a. High frequency MoS_2 nanomechanical resonators. ACS Nano 7 (7), 6086–6091. https://doi.org/10.1021/nn4018872.

Lee, K., Gatensby, R., McEvoy, N., Hallam, T., Duesberg, G.S., 2013b. High-performance sensors based on molybdenum disulfide thin films. Adv. Mater. 25 (46), 6699–6702. https://doi.org/10.1002/adma.201303230.

Li, Y., Song, Z., Li, Y., Chen, S., Li, S., Li, Y., Wang, H., Wang, Z., 2019. Hierarchical hollow MoS_2 microspheres as materials for conductometric NO_2 gas sensors. Sens. Actuators B 282, 259–267. https://doi.org/10.1016/j.snb.2018.11.069.

Li, H., Yin, Z., He, Q., Li, H., Huang, X., Lu, G., Fam, D.W.H., Tok, A.I.Y., Zhang, Q., Zhang, H., 2012. Fabrication of single- and multilayer MoS_2 film-based field-effect transistors for sensing NO at room temperature. Small 8 (1), 63–67. https://doi.org/10.1002/smll.201101016.

Liu, B., Chen, L., Liu, G., Abbas, A.N., Fathi, M., Zhou, C., 2014. High-performance chemical sensing using Schottky-contacted chemical vapor deposition grown monolayer MoS_2 transistors. ACS Nano 8 (5), 5304–5314. https://doi.org/10.1021/nn5015215.

Liu, C., Lu, H., Zhang, J., Yang, Z., Zhu, G., Yin, F., Gao, J., Chen, C., Xin, X., 2017. Abnormal p-type sensing response of TiO_2 nanosheets with exposed {001} facets. J. Alloys Compd. 705, 112–117. https://doi.org/10.1016/j.jallcom.2017.02.118.

Lu, G., Park, S., Yu, K., Ruoff, R.S., Ocola, L.E., Rosenmann, D., Chen, J., 2011. Toward practical gas sensing with highly reduced graphene oxide: A new signal processing method to circumvent run-to-run and device-to-device variations. ACS Nano 5 (2), 1154–1164. https://doi.org/10.1021/nn102803q.

Mak, K.F., Lee, C., Hone, J., Shan, J., Heinz, T.F., 2010. Atomically thin MoS_2: A new direct-gap semiconductor. Phys. Rev. Lett. 105 (13). https://doi.org/10.1103/PhysRevLett.105.136805.

Neri, G., 2017. Thin 2D: The new dimensionality in gas sensing. Chemosensors 5 (3). https://doi.org/10.3390/chemosensors5030021.

P., V.S.Y., J., S.K., A., T, 2016. Atomically thin MoS_2 : A versatile nongraphene 2D material. Adv. Funct. Mater. 2046–2069. https://doi.org/10.1002/adfm.201504202.

Park, J., Mun, J., Shin, J.S., Kang, S.W., 2018. Highly sensitive two dimensional MoS_2 gas sensor decorated with Pt nanoparticles. R. Soc. Open Sci. 5 (12). https://doi.org/10.1098/rsos.181462.

Perkins, F.K., Friedman, A.L., Cobas, E., Campbell, P.M., Jernigan, G.G., Jonker, B.T., 2013. Chemical vapor sensing with monolayer MoS_2. Nano Lett. 13 (2), 668–673. https://doi.org/10.1021/nl3043079.

Peter, M.L., Y., W.L., S., G.R, 2007. Impedancemetric NO_x sensing using YSZ electrolyte and YSZ/Cr_2O_3 composite electrodes. J. Electrochem. Soc. J97. https://doi.org/10.1149/1.2430646.

Piliarik, M., Homola, J., 2009. Surface plasmon resonance (SPR) sensors: Approaching their limits? Opt. Express 17 (19), 16505–16517. https://doi.org/10.1364/OE.17.016505.

Qiao, X.Q., Zhang, Z.W., Hou, D.F., Li, D.S., Liu, Y., Lan, Y.Q., Zhang, J., Feng, P., Bu, X., 2018. Tunable MoS_2/SnO_2 P-N heterojunctions for an efficient trimethylamine gas sensor and 4-nitrophenol reduction catalyst. ACS Sustainable Chemistry and Engineering 6 (9), 12375–12384. https://doi.org/10.1021/acssuschemeng.8b02842.

Radisavljevic, B., Radenovic, A., Brivio, J., Giacometti, V., Kis, A., 2011. Single-layer MoS_2 transistors. Nat. Nanotechnol. 6 (3), 147–150. https://doi.org/10.1038/nnano.2010.279.

Ramana, C.V., Becker, U., Shutthanandan, V., Julien, C.M., 2008. Oxidation and metal-insertion in molybdenite surfaces: Evaluation of charge-transfer mechanisms and dynamics. Geochem. Trans. 9. https://doi.org/10.1186/1467-4866-9-8.

Rheaume, J.M., Pisano, A.P., 2011. A review of recent progress in sensing of gas concentration by impedance change. Ionics 17 (2), 99–108. https://doi.org/10.1007/s11581-010-0515-1.

Sarkar, D., Liu, W., Xie, X., Anselmo, A.C., Mitragotri, S., Banerjee, K., 2014. MoS_2 field-effect transistor for next-generation label-free biosensors. ACS Nano 8 (4), 3992–4003. https://doi.org/10.1021/nn5009148.

Sarkar, D., Xie, X., Kang, J., Zhang, H., Liu, W., Navarrete, J., Moskovits, M., Banerjee, K., 2015. Functionalization of transition metal dichalcogenides with metallic nanoparticles: Implications for doping and gas-sensing. Nano Lett. 15 (5), 2852–2862. https://doi.org/10.1021/nl504454u.

Sharma, S., Kumar, A., Kaur, D., 2018. Room temperature ammonia gas sensing properties of MoS_2 nanostructured thin film. In: AIP Conference Proceedings. American Institute of Physics Inc. (Vol. 1953).

Splendiani, A., Sun, L., Zhang, Y., Li, T., Kim, J., Chim, C.Y., Galli, G., Wang, F., 2010. Emerging photoluminescence in monolayer MoS_2. Nano Lett. 10 (4), 1271–1275. https://doi.org/10.1021/nl903868w.

Sun, Z., Liao, T., Dou, Y., Hwang, S.M., Park, M.S., Jiang, L., Kim, J.H., Dou, S.X., 2014. Generalized self-assembly of scalable two-dimensional transition metal oxide nanosheets. Nat. Commun. 5. https://doi.org/10.1038/ncomms4813.

Vargas-Bernal, R., 2019. Electrical properties of two-dimensional materials used in gas sensors. Sensors (Switzerland) 19 (6). https://doi.org/10.3390/s19061295.

Wu, Z., Chen, X., Zhu, S., Zhou, Z., Yao, Y., Quan, W., Liu, B., 2013. Enhanced sensitivity of ammonia sensor using graphene/polyaniline nanocomposite. Sens. Actuators B 178, 485–493. https://doi.org/10.1016/j.snb.2013.01.014.

Yan, H., Song, P., Zhang, S., Yang, Z., Wang, Q., 2015. Dispersed SnO_2 nanoparticles on MoS_2 nanosheets for superior gas-sensing performances to ethanol. RSC Advances, 5 (97), 79593–79599. https://doi.org/10.1039/c5ra15019a.

Yan, H., Song, P., Zhang, S., Yang, Z., Wang, Q., 2016a. Facile synthesis, characterization and gas sensing performance of ZnO nanoparticles-coated MoS_2 nanosheets. J. Alloys Compd. 662, 118–125. https://doi.org/10.1016/j.jallcom.2015.12.066.

Yan, H., Song, P., Zhang, S., Zhang, J., Yang, Z., Wang, Q., 2016b. A low temperature gas sensor based on Au-loaded MoS_2 hierarchical nanostructures for detecting ammonia. Ceram. Int. 42 (7), 9327–9331. https://doi.org/10.1016/j.ceramint.2016.02.160.

Yang, S., Jiang, C., Wei, S.h., 2017. Gas sensing in 2D materials. Appl. Phys. Rev. 4 (2). https://doi.org/10.1063/1.4983310.

Yao, Y., Tolentino, L., Yang, Z., Song, X., Zhang, W., Chen, Y., Wong, C.P., 2013. High-concentration aqueous dispersions of MoS_2. Adv. Funct. Mater. 23 (28), 3577–3583. https://doi.org/10.1002/adfm.201201843.

Yue, Q., Shao, Z., Chang, S., Li, J., 2013. Adsorption of gas molecules on monolayer MoS_2 and effect of applied electric field. Nanoscale Res. Lett. 8 (1), 1–7. https://doi.org/10.1186/1556-276X-8-425.

Zeng, S., Baillargeat, D., Ho, H.P., Yong, K.T., 2014. Nanomaterials enhanced surface plasmon resonance for biological and chemical sensing applications. Chem. Soc. Rev. 43 (10), 3426–3452. https://doi.org/10.1039/c3cs60479a.

Zeng, S., Hu, S., Xia, J., Anderson, T., Dinh, X.Q., Meng, X.M., Coquet, P., Yong, K.T., 2015. Graphene-MoS_2 hybrid nanostructures enhanced surface plasmon resonance biosensors. Sens. Actuators B 207, 801–810. https://doi.org/10.1016/j.snb.2014.10.124.

Zhang, J., Liu, X., Neri, G., Pinna, N., 2016. Nanostructured materials for room-temperature gas sensors. Adv. Mater. 28 (5), 795–831. https://doi.org/10.1002/adma.201503825.

Zhang, H., Sun, Y., Gao, S., Zhang, J., Zhang, H., Song, D., 2013. A novel graphene oxide-based surface plasmon resonance biosensor for immunoassay. Small 9 (15), 2537–2540. https://doi.org/10.1002/smll.201202958.

Zhang, Y., Xu, J., Xu, P., Zhu, Y., Chen, X., Yu, W., 2010. Decoration of ZnO nanowires with Pt nanoparticles and their improved gas sensing and photocatalytic performance. Nanotechnology 21 (28). https://doi.org/10.1088/0957-4484/21/28/285501.

4

Template-assisted nanostructures for gas sensing applications

P.M. Aswathy [a,b] **and M.K. Jayaraj** [a,c]

[a] *Cochin University of Science and Technology, Kochi, India.* [b] *Department of Physics, St. Stephen's College, Kollam, India.* [c] *University of Calicut, Malappuram, India*

4.1 Introduction

Nanotechnology has proved its possibilities in almost all realms of modern living. Researchers are therefore getting self-motivated in finding novel ways to develop nanomaterials with interesting functionalities. Among the wide niche of applications of nanotechnology, nanostructured gas sensors have attracted ample interest due to the escalating changes in our ecosystem, especially our immediate atmosphere. Upon a wide literature survey, we would come across two common strategies that have been proposed to improve the properties of gas sensors. The generally accepted strategy is to control the growth of nanomaterials by suitably modulating the dimensions, properties, and morphology since the properties of gas sensors are highly dependent on their surface-to-volume ratio. The growth of nanostructures through the unidirectional crystallization of solid-state structures is found to be achieved via various mechanisms such as the use of templates with nanostructure morphologies, inherently anisotropic crystallographic structures for nanowire (NW) morphology, the use of a liquid/solid interface to reduce the symmetry of a seed, and the appropriate use of surfactants or capping agents to control the growth rates of facets of a seed (Yogeswaran & Chen, 2008). The next best strategy to improve sensing performance is through surface modification with noble metals, including silver, platinum, rhodium, and gold. Gas sensing performance can be improved significantly because of the high catalytic activity of noble metals toward the test gases (Guo et al., 2014; Kaneti et al., 2015; Kim et al., 2015; Vallejos et al., 2011; Yan et al., 2016a).

Nanomaterials for Sensing and Optoelectronic Applications. DOI: https://doi.org/10.1016/B978-0-12-824008-3.00003-5

In the case of pure metal nanostructures a number of techniques are in practice, such as inert gas condensation, plasma processing, physical and chemical vapor deposition (CVD), electrodeposition, rapid solidification, sol–gel synthesis, microemulsion, spark erosion, mechanical alloying, and severe plastic deformation (Suryanarayana, 2002). The nucleation of nanostructures depends upon the lattice of the substrate used, adhesion energy, crystal lattice orientation of the electrode surface, specific free surface energy, and lattice mismatch at the interface boundary of the nucleus and substrate. Nanostructures for specific applications can be developed using the surface of the cathode as a template. Such template-assisted electrodeposition processes are mainly of two types: active template-assisted and restrictive template-based electrodeposition (Milchev, 2002; Milchev et al., 1974). Hierarchically assembled structures have also turned out to be very effective for gas sensing due to their less agglomerated configurations, more effective transfer of charge carriers, and chances of better gas diffusion, which leads to high gas response and a fast response speed (Lee, 2009).

4.2 Templated nanostructures: synthesis techniques and applications

Templating against colloidal particles has been accorded as an effective approach for the synthesis of hollow spherical nanostructures. There are several reports on ceramic hollow spheres grown using colloidal particles on the nanoscale with gold, silver, or CdS particles and on mesoscale silica or polymer beads (Correa-Duarte et al., 1998; Walsh & Mann, 1995). Typically, a thin coating of the material (or its precursor) is formed on the template to create a core–shell composite; subsequently, the template is removed by calcination at elevated temperatures or selective etching in an appropriate solution. The inner diameter of these hollow spheres is determined by the template size. For coating, the template with a thin shell of the desired material; controlled adsorption; and/or reactions such as precipitation, grafted polymerization, or sol–gel condensation are adopted on the surfaces of template particles (Garg & Matijević, 1988; Guo & Dong, 1999). However, maintaining the homogeneity and thickness of the coating is trickier, with very high odds for clumping and heterocoagulation. Recent research has developed two techniques for the homogeneous, dense, thin coatings of silica on various types of templates. One technique focuses on the modification of the template surface with an appropriate primer that could enhance the coupling of silica monomers or oligomers to this surface (Liz-Marzán et al., 1996). The second technique is building a shell structure around the surface-functionalized

template particle through layer-by-layer (LBL) adsorption of polyelectrolytes and charged nanoparticle. The subsequent removal of the core can yield hollow spheres with a varied range of dimensions (Caruso et al., 1998).

4.2.1 Template-assisted hollow nanostructures

Hollow nanospheres have been proven to be a preferred structure due to their large surface area, efficient catalytic activity, and structural stability (Gyger et al., 2010; Ma et al., 2013; Yang et al., 2007). Besides, the use of noble metal particles or heterojunction has also been reported to improve sensing properties (Ju et al., 2014; Miller et al., 2014). Zhong et al. had described a facile method that generates mesoscale hollow spheres of TiO_2 and SnO_2 by templating their sol–gel precursor solutions against crystalline arrays of monodisperse polystyrene beads. The diameter of the polystyrene template determines the hollow sphere void size and the ceramic wall thickness could be effortlessly modulated in the range of 30–100 nm by using sol–gel precursor solutions with different concentrations (Zhong et al., 2000). Li et al. (2005) employed the core–shell technique in which hollow spheres were prepared by controlled adsorption, involving precipitation reaction, sol–gel condensation, and LBL deposition of the desired material onto the surface of an appropriately modified colloidal template (usually a polymer) and the subsequent removal of the template through thermal and/or chemical treatments (Decher, 1997; Zhong et al., 2000). p–n heterojunctions with n-type SnO_2 hollow spheres and p-type NiO nanoparticles have also been reported to be efficient triethylamine (TEA) gas sensors with high response and selectivity (Ju et al., 2015). Here, the hollow spheres of SnO_2 were synthesized by using a template-assisted hydrothermal method. NiO nanoparticles were deposited using the pulsed laser deposition (PLD) process onto the surface of the SnO_2 hollow sphere to form NiO/SnO_2 p–n junction sensors, with a response of 48.6 for 10-ppm TEA gas with a detection limit as low as 2 ppm-level.

Coaxial- or core–shell-type oxide-based electrospun nanofibers such as CuO–SnO_2, ZnO–CuO, TiO_2–ZnO, NiO–SnO_2, ZnO–In_2O_3, In_2O_3–WO_3, La_2O_3–WO_3, SnO_2–CeO_2, SnO_2–In_2O_3, and $In_{2-x}Ni_xO_3$ have been reported to be excellent gas sensors (Du et al., 2012; Feng et al., 2012, 2015a, 2015b; Kalantar-Zadeh et al., 2015; Katoch et al., 2014a, 2014b; Lee et al., 2013; Park et al., 2009; Qin et al., 2013; Wang et al., 2010; Zhang & Qiao, 2012). Coaxial electrospinning has also been found to be beneficial for the otherwise nonelectrospinnable core materials since the reduced surface tension at the boundary of two fluids and the elasticity of the shell fluid delay or suppress the Rayleigh instability of the core fluid (Merkle et al., 2013). Choi et al. have reported thin

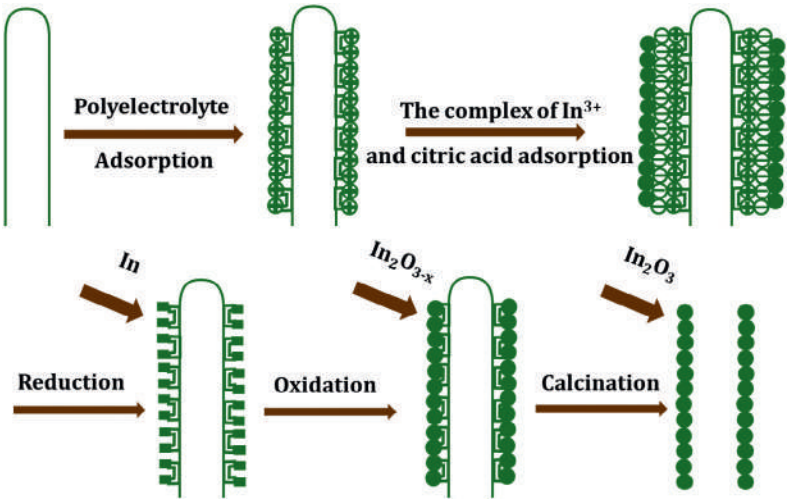

Figure 4.1. Schematic diagram for the growth process of In_2O_3 nanotubes.

(0.5–1 m) layers of non-aligned or quasialigned hollow ZnO fibers by sputtering ZnO onto sacrificial templates, i.e., polyvinyl acetate fibers deposited by electrospinning on silicon or alumina substrates (Choi et al., 2009). As compared to the reference ZnO thin film specimens, the hollow ZnO fibers were more sensitive and exhibited a twofold increase in their surface-to-volume ratio. The sensitivity enhancement upon exposure to residual concentrations (2–10 ppm) of NO_2 in the air at elevated temperatures (200–400°C) was even more. Besides the electrospinning technique, a few metal oxides such as Ga_2O_3, In_2O_3, TiO_2, and Fe_2O_3 in nanotubular morphology have been fabricated through nanoporous alumina template-assisted approaches (Chen et al., 2005; Cheng & Samulski, 2001; Imai et al., 1999). Carbon nanotubes (CNTs) have also been considered to be an ideal template for the synthesis of metal oxide nanotubes of ZrO_2, Al_2O_3, V_2O_5, SiO_2, and MoO_3 using a metal alkoxide–based sol–gel process followed by calcination (Satishkumar et al., 1997). Ample efforts have been made to synthesize metal oxide nanotubes (Fig. 4.1) with CNTs as the skeletal template through different routes such as the supercritical fluid approach, CVD, chemical precipitation method, and LBL assembly (Du et al., 2007; Han & Zettl, 2003; Katoch et al., 2014a; Sun et al., 2005; Zhang et al., 2002).

Template-assisted synthesis routes can utilize both hard templates (Breen et al., 2001; Dai et al., 2002; Xiong et al., 2002; Yang et al., 2003) and soft templates (Yang & Zeng, 2004). Soft templates such as surfactants tend to self-assemble to form micelles with desired structures (Chen et al., 2004). These aggregated micelles are unstable in certain solvents, failing to act as efficient templates. In this view

complex surfactant systems are promoted for the synthesis of hollow structures (Qi et al., 2002; Zhang et al., 2002). A complex surfactant such as poly(ethylene oxide)-block-poly(methacrylic acid)–sodium dodecyl sulfate (PEO-b-PMAA-SDS) micelles as templates could hold Ca^{2+} ions and assist with the precipitation of $CaCO_3$ (Qi et al., 2002). The large steric hindrance of the surfactant polymer PEO-b-PMAA-SDS fails to limit the size of the precipitate to the nanometer regime. However, simple coordination agents or surfactants such as terephthalic acid can effectively hold Sn^{2+} ions without a large steric hindrance and yield SnO_2 hollow nanospheres from a micelle system made up of terephthalic acid and sodium dodecyl benzene sulfonate (SDBS) in an ethanolic solution. The as-prepared hollow nanospheres showed good room-temperature sensitivity to ethanol vapors up to a detection limit of 10 ppm (Zhao et al., 2006).

The functionalization of metal–organic framework (MOF)–derived synergistic catalysts on metal oxides–based hollow nanofibers is another technique for developing gas sensors. The nanoscale catalysts decorated on hollow structures can effectively promote surface reactions; however, they reduce their surface energy at high operating temperatures, leading to the degradation of response and the delay of recovery (Lee, 2009). With an aim for the development of gas sensors having high sensitivity, superior selectivity, and fast responding speed, particularly in a highly humid atmosphere, a facile and effective catalyst loading route was developed by Koo et al. (2017). They used a nanoscale palladium nanoparticles (~2 nm)–loaded Zn-based zeolite imidazole framework (~80 nm) as a catalyst loading platform for the effective functionalization of a PdO@ZnO catalyst onto metal oxide nanotubes. Even rare earth metals such as cerium have been tried as effective defects on metal oxide hollow nanospheres for acetone sensing (Song et al., 2012).

The use of spherical templates is also a facile approach to attain hollow morphology. Several reports have discussed coating polystyrene spheres with Fe precursors and subsequent conversion of the precursor layer into metal oxide (Caruso et al., 2001; Ding et al., 2006; Ohnishi et al., 2006; Shiho & Kawahashi, 2000). The core templates are removed by thermal decomposition.

4.2.2 Anodic aluminum oxide as a template for nanostructures

Various approaches have been developed to generate the branched nanostructures, mainly including vapor-phase (Jung et al., 2007; Wang et al., 2003; Yun et al., 2006), solution-phase (Dong et al., 2007; Kuno et al., 2006; Wan et al., 2008), and template-assisted methods (Li et al., 1998; Meng et al., 2005; Papadopoulos et al., 2000). The

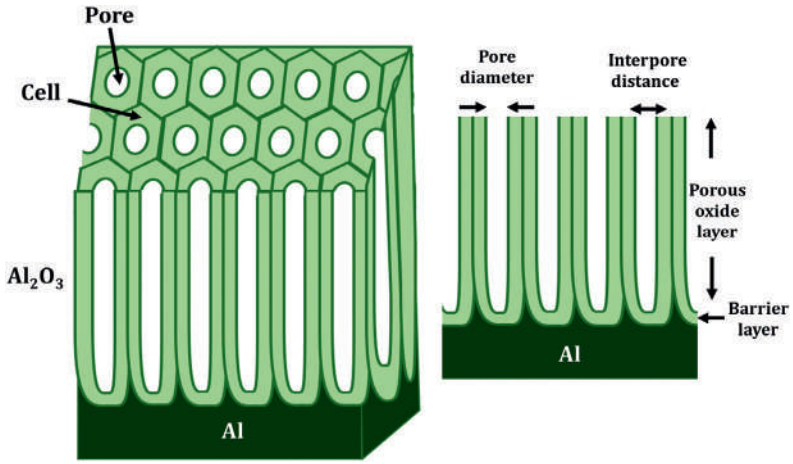

Figure 4.2. AAO structure prepared via the electrochemical oxidation of Al.

template-assisted method has its own advantages, such as precisely controlling the morphology and dimension of the nanostructures. Anodic aluminum oxide (AAO) has been generally used as a template with an aim to realize specific characteristics such as tunable pore shapes, dimensions, and lengths and good mechanical and thermal stability (Jessensky et al., 1998; Li et al., 1998). Anodization of aluminum is a technique in which a layer of porous alumina is formed (Zhang et al., 2006) on the surface of aluminum, thicker than the native oxide usually formed on the aluminum surface for natural anticorrosive protection. These nanoporous AAO can be used as templates since the condition of the anodization process can be modulated to tune the depth and diameter of the nanopores. The most cited early reports on AAO membranes show perfectly parallel pores, ordered hexagonally using a two-step anodization technique (Fig. 4.2) (Martin, 1994; Masuda & Fukuda, 1995). Anodic aluminum membranes or templates are being widely used in research fields such as optoelectronics, energy conversion and storage, high-density magnetic storage devices, and biotechnology. There are a few reviews on anodic alumina and its large-scale use in designing functional and patterned nanostructures for all applications that demand large-surface-area and available adsorption sites (Lee & Park, 2014; Zhao et al., 2018).

AAO templates with branched nanochannels have been applied to generate various branched nanostructures, such as CNTs (Lee et al., 2006; Jani et al., 2013) and semimetal NWs (Tian et al., 2004). Nanowire structured gold and polypyrrole developed using AAO with predesigned nanochannels as templates building have been reported to be promising for integrated nanocircuits and nanoelectronics (Xu et al., 2009). Polyaniline (PANI) NWs electropolymerized using AAO membranes have also exhibited superior electrochemical properties

and a large surface-to-volume ratio fit for gas sensing (Yu et al., 2009). AAO has been extensively used as a nanoporous template for synthesizing nanotubular forms of TiO_2 for various applications wherein a larger specific surface area is a necessity (Bae et al., 2008; Chang et al., 2010; Lee et al., 2010). Vertically aligned but electrically interconnected TiO_2 nanotube arrays were fabricated using atomic layer deposition combined with an AAO template suitable for H_2 gas sensing (Lee et al., 2011c). The use of porous AAO membrane is an established strategy for the synthesis of one-dimensional nanotubular forms of metals (Lahav et al., 2003), semiconductors (Cai et al., 2004), and polymers (Steinhart et al., 2002). Besides transition metal oxides, spinel AB_2O_4-type nanotubes are also found to have improved reactivity than the corresponding single oxides. MCo_2O_4 (M = Ni, Cu, Zn) nanotubes have displayed excellent selectivity and high sensitivity to various gases such as ethanol and SO_2 (Zhang et al., 2006). Esman et al. reported the fabrication of functional polypyrrole (PPy) nanotubes by compromising between effectiveness and mildness of template dissolution conditions (Esman & Lellouche, 2010).

The AAO membrane mask has also been used along with the PLD technique for nanopatterning well-ordered nanodot arrays of magnetic $CoFe_2O_4$ for a wide range of applications such as sensors, drug delivery, and data storage (Gao et al., 2009). For Au deposition over ZnO nanorod arrays, Chik et al. have used AAO membranes as a shadow mask. But the stiffness and hydrophilicity of AAO membranes limited the transfer to a much smaller scale (approximately in the area size range of mm^2) with the inevitable occurrence of large voids in the pattern (Chik et al., 2004).

4.2.3 Layer-by-layer assembly on templated nanostructures

The technique of developing application-oriented nanostructures gained more success after the advent of the sequential LBL transfer of ultrathin films onto solid substrates via self-assembly, with a limited single-layer thickness at around the 1–10 nm range. In the LBL assembly method the exfoliation of solids is done to produce colloids of sheets having a lateral thickness in the nano range (~10 nm). In this process the charged species is adsorbed onto a substrate of opposite charge, which reverses the substrate surface charge. The subsequent layers are then deposited by the alternate adsorption of oppositely charged species onto the substrate. The layering continues until the desired film thickness is achieved. Following a conceptual proposal on the LBL assembly of charged colloidal particles (Iler, 1966), Decher et al. demonstrated LBL assembly by the consecutive

adsorption of anionic and cationic bipolar amphiphiles and polyelectrolytes in 1991 (Decher & Hong, 1991). In 1996 Kotov et al. developed ultrathin graphite oxide/polyelectrolyte (GO/P) composites using the self-assembly technique (Kotov et al., 1996). They could benefit from properties such as controllable conductivity, magnetoresistance with proper adhesion to different surfaces, flexibility, and inherent self-assembly. The lateral conductivities and the ease of transition between the nonconductive GO to the conductive graphite made them qualified as components of advanced optical and electronic devices. Kovtyukhova et al. have also reported the preparation of GO/polycation films grown on planar Si and Al_2O_3/Al supports following electrostatic self-assembly (Kovtyukhova et al., 1999). The references for active research progress on the LBL assembling technique, especially in the early 1990s, had been listed by Cassagneau et al. in 2000, indicating the use of this technique for ultrathin electronic, electrooptical, charge storage devices and sensors (Cassagneau et al., 2000).

LBL proved to be an efficient technique for assembling supramolecular structures and was also used for creating LBL thin films of CNTs with polyelectrolytes similar to the graphene/polyelectrolyte combinations (Shen et al., 2008; Zhang et al., 2004). A review published in 2008 by Wang et al. focuses on the two main classes of templates, namely, planar and colloidal templates, to prepare nanostructured materials (Wang et al., 2008b). These porous planar and colloidal substrates, when used in LBL, offer immense opportunities to develop materials with advanced structuring. Colloidal templates of different compositions (such as polymer, inorganic, liquid droplets, gas bubbles) and geometries (such as spheres, rods, fibers) could create nanostructures in different forms such as films, capsules, nanotubes, nanoporous particles, and macroporous and biomimetic structures, fit for potential applications such as adsorption, immobilization, catalysis, drug delivery, sensing, separations, and synthesis. In 2009 again, a review was published centering on the physicochemical parameters, such as ionic strength, layer number, and pH, affecting the permeability of multilayer shells (Mansouri et al., 2009). The authors also discussed the synergic effect on the loading and release of biologically active molecules from LBL multilayers. LBL has also been employed in developing composite films composed of graphene and noble metal nanoparticles (such as gold and platinum) through vacuum filtration or ionic liquid linking (Kong et al., 2009; Zhu et al., 2010). Also, the LBL technique could realize RGO sheets with the multilayer film thickness in the subnanometer scale by simply varying the number of stacking layers, fit for OLED device applications (Lee et al., 2011a). In 2011 Azzaroni et al., in their review, provided a diverse range of LBL nanotube devices demonstrating the versatility of the nanotemplated LBL toolbox for generating functional soft nanotechnology

(Azzaroni & Lau, 2011). LBL is already in the limelight, especially due to its application in cell-surface engineering, cell-based bioscience, and biomedical technologies. In a recent review published in 2019 Ariga et al. unraveled the prospects of realizing LBL assemblies to layered nanoarchitectonics (Ariga et al., 2019). However, we need to see an evolution in this process in terms of the development of cheap mass-production processes for LBL materials.

In 2007 for the first time, Du et al developed porous and polycrystalline In_2O_3 nanotubes with diameters of ~20–60 nm using LBL assembly on CNT templates with subsequent calcination. The as-prepared In_2O_3 nanotubes exhibited a greater sensitivity and short response/recovery times to NH_3 at room temperature due to their ultrahigh surface-to-volume ratio and porous surface morphology (Du et al., 2007). The sensing of gaseous forms of aromatic hydrocarbons such as hexane, cyclohexane, ethanol, acetone, benzene, pyridine, and toluene was also demonstrated using layered graphene/ionic liquid (G–IL) composites on quartz crystal microbalances (QCM), wherein the layered structures are formed by the *in situ* reduction of GO layers in the presence of nonvolatile ionic liquids and subsequent electrostatic LBL assembly (Ji et al., 2010).

Ethanol sensing devices working at room temperature were developed using multiwalled CNT/polymer film–based sensors on the printed circuit board substrate using LBL self-assembly technology. The performance of multiwalled CNT/polymer film sensors fabricated by LBL self-assembly was compared with that of sensors made by other means such as drop-casting and thermal evaporation technique, which highlighted a faster response and sensitive resistance change when exposed to ethanol gas, showing its prospects in terms of both performance and cost (Zhang et al., 2014). Recently, catalyst-decorated hollow WO_3 nanotubes were successfully synthesized through the LBL self-assembly of inorganic precursors on sacrificial polymeric (here, polymethylmethacrylate) nanofiber templates followed by subsequent calcination (Koo et al., 2016). The sensing performances were evaluated toward various analytic gases such nitrous oxide and toluene in a highly humid atmosphere using pristine WO_3, Pt loaded-WO_3, and Pd loaded-WO_3 nanotubes. The LBL synthesis approach for producing hollow metal oxide nanotubes functionalized with various catalysts was found to be promising in exhaled breath analysis for the detection of nitrous oxide and toluene, which are biomarker gases for asthma and lung cancer diagnosis, respectively.

In 2014 an exclusive review on emerging strategies and applications of LBL self-assembly gave a whole list of various substrates utilized in the LBL self-assembly technique and their applications, including those for gas sensing (Rawtani & Agrawal, 2014). Naisiri et al, in 2019, in their review focusing on the nanodimensional

design of current state-of-the-art gas sensors, superlative in selectivity, specificity, and sensitivity, considered human breath sensors as a promising candidate for rapid and noninvasive disease diagnosis (Nasiri & Clarke, 2019). They have also indicated the LBL technique as an effective method to yield low-cost composite nanodimensional materials.

4.3 Prospects of biocages as templates in nanotechnology

Enormous research has been garnered by biological systems such as capsids of viruses, protein complexes like ferritins and heat shock, lipid vesicles and artificial cells with well-defined interior cavities and chemically amenable features, modifying them into nanoreactors for interesting applications such as immunosensing, gas sensing, drug delivery, and electrocatalysis in fuel cells (Du et al., 2011; Gálvez et al., 2005, 2008; Liu et al., 2006; Yan et al., 2016b). The most familiar technique of synthesizing metal nanoparticles for nanobiotechnological applications is the use of a chemically and spatially confined organic molecular matrix for nanoparticle encapsulation.

In the early 1990s itself Mann, Douglas, and others started employing horse spleen apoferritin cavity in the preparation of size-restricted metal oxides and oxyhydroxides (Douglas & Stark, 2000; Douglas & Young, 1998; Liu et al., 2006). Apoferritin is the protein shell of ferritin, which can accommodate around 7000 iron atoms. The removal of iron from ferritin through a complex chemical process yields apoferritin, a biocompatible nanocage. Apoferritin consists of 24 polypeptide subunits with a hollow sphere structure with inner and outer diameters of 8 and 12 nm, respectively (Wong et al., 1998). The channels between the polypeptide subunits allow the transport of metal ions in and out of the cavity. Ferritins have been suitably modified for various protein-inorganic hybrids, such as Pt, Pd, Au, Ag, FeS, CdS, CeSe, and ZnSe cores with ferritin shells (Fan et al., 2011; Uchida et al., 2007; Ueno et al., 2004). These nanoparticle-encapsulated apoferritins give rise to superior dispersion in polar solvents due to the repulsion forces between surface-charged apoferritins. The high-precision size control and monodispersity of these nanoparticle-encapsulated apoferritins make them efficient catalysts or carriers in applications such as catalysis, sensing, drug delivery, magnetic resonance imaging (MRI), and fuel cells (Qiu et al., 2013). A recent review on ferritin family proteins describes their structural properties, organization, and the ability to sequester metal within their cavities that channelize their functions as containers for drug delivery and scaffolds for the production of vaccines (Fig. 4.3) (He & Marles-Wright, 2015).

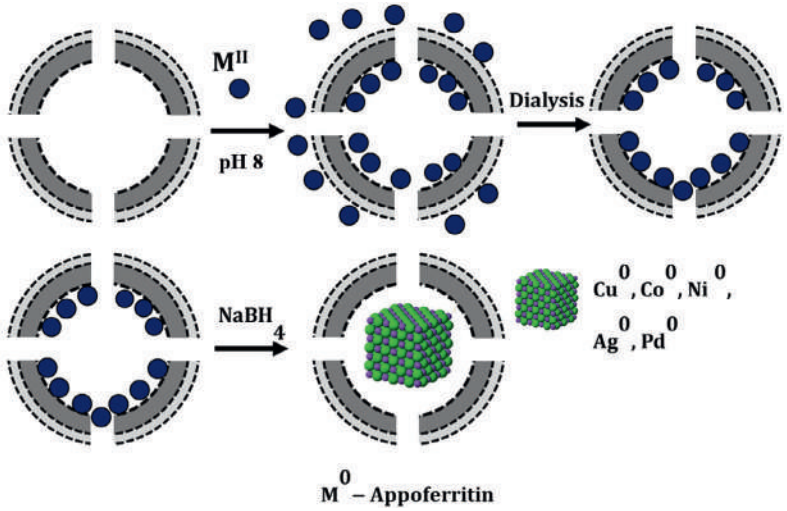

Figure 4.3. Schematic representation of the preparation of metallic nanoparticles.

As discussed above, the protein cage templates were primarily used on a large scale as nanoparticle containers or capsules, especially in bionanotechnology. Our present lifestyle makes us increasingly prone to different hazards due to toxic chemicals and gases, which we should be alerted of whenever beyond a tolerance level. Many organophosphates are being used as pesticides for agriculture and a few of them have been zoned as chemical warfare agents or nerve agents (Casida & Quistad, 2004; Guo et al., 2006; Noort et al., 2002). These organophosphates bind with the hydroxyl group of serine in the active site of cholinergic enzymes such as acetylcholinesterase and butyrylcholinesterase and inhibit their function (Fennouh et al., 1997; Pardío et al., 2001). This inhibition results in the accumulation of neurotransmitter acetylcholine, which in turn interferes with muscular responses and can even cause death (Quinn, 1987; Shi et al., 2006; Young et al., 2004). Thus the development of facile and reliable diagnostic tools for the rapid monitoring of organophosphates is of immense priority. Initial efforts toward such an immunosensor employed zirconia nanoparticles as a selective sorbent for quantifying immune-recognition events through the recognition of the phosphorylation moiety with phosphomoieties and quantum dots as tags (Fang et al., 1997; Liu et al., 2008; Liu & Lin, 2005). However, this technique suffered the drawback of using a strong acid to dissolve nanoparticle tags before electrochemical detection (Du et al., 2008; Hansen et al., 2006; Wang et al., 2008a). In 2011 Du et al. developed a ZrO_2 nanoparticle–based disposable immunosensor taking advantage of the protein cage apoferritin to prepare encoded metallic tags instead of quantum dot–based labels (Du et al., 2011). Apoferritin has six hydrophobic

channels and eight hydrophilic channels, wherein the hydrophilic channels facilitate the passage of metal ions and small molecules into the cavity of the protein. The central cavity, the characteristics for dissociation and reconstruction at different pH environments, a multichannel structure, and the chemical properties of apoferritin make it a perfect choice for a core–shell composite or encoded nanoparticle tag. The apoferritin-templated metallic phosphate nanoparticle tag and ZrO_2 nanoparticle–based electrode as a sandwich-like immunosensor was the first reported combination avoiding the usage of horseradish peroxidase or quantum dot labels for the detection of organophosphates. The ultrasensitive detection of this immunosensor was due to the efficiency of apoferritin to encode a large number of metal ions. The technique also stood out in terms of selectivity, simplicity, portability, and expense, and additionally, it did not demand organophosphate-specific antibodies.

Apart from the toxicity due to chemicals, toxic gases emanating from mines, explosives, or any other environmental hazards can now be detected using nanostructured metal oxide–based chemiresistive sensors. The growing demand for improving the quality of life and life expectancy has attracted immense interest in exhaled breath analysis as a powerful candidate for future human health diagnostics, which proves itself as an easy tool for the diagnosis of diseases using noninvasive, affordable, fast, and facile technology. Exhaled breath contains volatile organic compounds (VOCs) and volatile sulfuric compounds (VSCs) such as acetone (CH_3COCH_3), toluene ($C_6H_5CH_3$), and hydrogen sulfide (H_2S), which are known as biomarkers for the diagnosis of diabetes, lung cancer, and halitosis, respectively (Dong et al., 2006; Khalid et al., 2013; Peng et al., 2009). Several breath analysis methods such as gas chromatography (GC), GC coupled with mass spectrometry (GC-MS), and selected ion flow tube mass spectrometry (SIFT-MS) have been implemented (Deng et al., 2004; Mark et al., 1994; Sousa et al., 2006). Among the various approaches, chemiresistive-type breath sensors with semiconductor metal oxides as the sensing layer seem to be promising due to the high potential for low-cost fabrication and portable application (Liu et al., 2012). Numerous researches have progressed in metal oxide–based exhaled breath analyzers using SnO_2 (Kolmakov et al., 2003; Xu et al., 1991), WO_3 (Li et al., 2004; Solis et al., 2001), In_2O_3 (Yamaura et al., 1996), TiO_2 (Wang et al., 2017), and ZnO (Wan et al., 2004; Wang et al., 2006) as the sensor materials. However, the low sensitivity and selectivity of sensors to detect trace biomarker gases in breath still remain a challenge in developing high-performance breath sensors. Enhancing the exposed surface area as well as catalytic sensitization are the only possibilities to overcome the challenge since gas reaction occurs on the surface of the oxide material and can be effectively activated by catalytic sensitization. Breath

analyzers have extraordinary requirements such as remarkable sensitivity as well as selectivity toward low concentrations (sub-ppm level) of specific biomarker molecules in an uncontrolled environment (exhaled breath) with high humidity and many other interfering gases, imposing extraordinary challenges in terms of sensitivity and selectivity to the target biomarkers. To conquer these challenges, the gas sensing properties of metal oxide–based gas sensors can be enhanced by tailoring their microstructure to achieve high sensitivity and sensitizing their response to the target gas species by using catalysts. One-dimensional (1D) nanotubes are a preferable nanomorphology due to their high surface area that provides a maximum ratio of reactive surface sites, both at the inner and outer surfaces of the tube as compared to the unexposed bulk area in case of other structures. 1D nanotubular morphology for metal oxide–based (Fe_2O_3, SnO_2, WO_3, In_2O_3) gas sensors has been widely reported to be prepared by thin film deposition on sacrificial templates followed by template decomposition gas sensors (Chen et al., 2005; Choi et al., 2013; Du et al., 2007; Kim et al., 2010). For improved sensitivity and selectivity to specific biomarker molecules, nanocatalyst-functionalized (Pt, Ag, Pd) metal oxide–based 1D nanotubes such as Pt–WO_3, Ag_2O–SnO_2, Pd–V_2O_5, Pt–NiO, and Ag–SnO_2 were also reported (Chen et al., 2011; Cho et al., 2011; Fu et al., 2013; Jin et al., 2014; Miao et al., 2013).

The role of bioinspired (i.e., protein cages or shells) nanocatalysts in the synthesis of functionalized 1D metal oxide–based nanotubes is noteworthy, especially for their contribution as breath sensors. Pt (~2 nm) and Au (~2.7 nm) catalysts were encapsulated by apoferritin, a protein nanocage, via the templating route, wherein Pt–apoferritin and Au–apoferritin directly functionalized on the interior and exterior walls of electrospun SnO_2 nanotubes during controlled single-nozzle electrospinning. The tubular morphology and uniform distribution of catalysts synergistically enhanced the gas sensing performances. Pt-loaded SnO_2 and Au-loaded SnO_2 nanotubes could sense acetone and H_2S with a maximum response (R_{air}/R_{gas}) of 92 and 34, respectively, at 5 ppm. The detection limit was improved even up to 100 ppb in a highly humid environment (90% RH) with a noticeable response of 2.7 and 2 for acetone and H_2S, respectively. The gas sensing performances of the Pt- or Au-loaded SnO_2 NTs were remarkably better than those of dense SnO_2 nanofibers, confirming the significance of effective nanocatalyst loading and morphology evolution (Jang et al., 2015).

The high dispersion property due to repulsive force between protein shells in apoferritin has also been effectively used to functionalize well-distributed catalytic nanoparticles onto 1D metal oxide nanofibers. Cho et al. decorated catalytic nanoparticles homogeneously on ZnO nanofibers (Cho et al., 2017). Both precious catalysts such as Pt and

nonprecious catalysts such as La and Cu were successfully apoferritin encapsulated in the nanoscale (i.e., 3–5 nm). Catalytic Pt and Cu nanoparticle–functionalized ZnO nanofibers exhibited approximately sixfold and threefold acetone response, respectively, compared to pure ZnO nanofibers. Also, La-functionalized ZnO nanofibers showed around a ninefold response to nitrogen monoxide. The authors also introduced the principal component analysis (PCA) method for distinguishing simulated breath components such as acetone, toluene, nitrogen monoxide, carbon monoxide (CO), and ammonia (NH_3) using the catalyst ZnO nanofibers. The potential of using nonprecious catalysts to establish diverse sensing material libraries applicable to breath pattern recognition for the diagnosis of diseases was also well demonstrated. Another precious metal, ruthenium (Ru), has also been used for functionalizing metal oxides (Kruefu et al., 2015; Lee et al., 2011b; Niranjan et al., 2002). Recently, nanoparticles of RuO_2 were loaded into WO_3 nanofibers through the electrospinning method using apoferritin as the catalyst carrier (Kim et al., 2017). The hollow nature of apoferritin helps in realizing RuO_2 nanoparticles with average diameters of 1.8 ± 0.9 nm and RuO_2-functionalized WO_3 nanofibers show significantly enhanced acetone sensing response at a highly humid atmosphere (95% RH), proving their potential for diagnosing diabetes from exhaled breath. These nanofibers also showed outstanding selectivity toward acetone gas against hydrogen sulfide, toluene, ethanol, pentane, ammonia, hydrogen, and water vapor. The observed results seem to be encouraging for the precise detection of acetone in exhaled breath, resulting in the easy diagnosis of diabetes.

In addition to the synthesis of metal nanocatalysts for metal oxide breath sensors, apoferritin has also been a carrier of metal catalysts for hydrogen sensing (Choi et al., 2016). Coaxial electrospinning combined with sacrificial templating and apoferritin-encapsulated functionalization was employed to load a Pd nanocatalyst into macroporous WO_3 nanotubes. Pd-functionalized nanotubes exhibited a very high H_2 response of 17.6 (R_{air}/R_{gas}) at 500 ppm, and furthermore, the sensor was highly selective to H_2 against CO, NH_3, and methane (CH_4). Recently, quantum dots of cadmium telluride were also synthesized within the hollow cavity of apoferritin. It was interesting to note that the control of the reaction conditions and pH of the precursor solution with varying the molar ratio of Cd and Te could yield CdTe quantum dots of different diameters (Peng et al., 2017).

Apoferritin used for research purposes is extracted from the equine and horse spleen. However, chemical companies do supply apoferritin but at very high prices of around $1900 for 1 g of 0.2-m filtered apoferritin from the equine spleen. The process of eliminating iron atoms from ferritin to obtain the empty protein or organic shell is the first

tedious step to convert ferritin into apoferritin as a nanoreactor for different nanotechnological applications. Most of the available protocols for apoferritin synthesis are time consuming, tedious, and difficult to reproduce. This intricate and long process flow makes apoferritin expensive. Nevertheless, Moglia et al. proposed a method for the efficient generation of iron-devoid ferritin in a single-day timeframe, using biocompatible nondenaturing reagents (Moglia et al., 2018). They tested several protocols and characterized the apoferritin products using size exclusion chromatography, UV-Vis spectroscopy, inductively coupled plasma optical emission spectrometry, and dynamic light scattering. They could finally remove more than 99% of the iron from the loaded holoferritin and recover 70%–80% of the original protein as monomeric apoferritin nanocages by managing the pH conditions of the reduction step and the nature of chelating agents used for iron removal. It was found that the spectrophotometric measure for protein determination in ferritin–iron complexes is not viable due to the absorbance of 280 nm by iron in ferritin. However, the best process protocol was standardizable, scalable, and applicable to be used for yielding iron-free apoferritin nanocages based on lower ferritin iron content and higher protein recovery; applicable for nanotechnological and biotechnological uses.

Besides ferritin-based biocages, viruses have also been exploited as a constrained template to direct nanoparticle synthesis. Virus-based templates offer confined cages, high symmetry, robust functional protein capsids, unique structural architectures, unique protein surface topology (such as polarity, residue charge, and surface relief), and repeating motifs and are amenable to molecular biology manipulations (Douglas et al., 2002; Douglas & Young, 1998). Viruses are used as scaffolds or templates to fabricate metalized nanoparticles and nanotube structures using mineralization techniques (Shenton et al., 1999). Extensive research on these techniques has helped in the development of mineralized nanotubes and NWs for applications such as batteries and data storage devices (Lee et al., 2009; Nam et al., 2006, 2008). Commonly used viral templates include tobacco mosaic virus (TMV) and cowpea chlorotic mottle virus (CCMV) (Douglas et al., 2002; Douglas & Young, 1998; Dujardin et al., 2003; Knez et al., 2004; Liu et al., 2016; Shenton et al., 1999; Wang et al., 2002). Slocik et al. described two viral-mediated pathways for the synthesis of gold nanoparticles directed by the surface chemistry of the virus capsid and the selection of a metal precursor. They endorse the opportunity lying in the reductive capacity of tyrosine for gold by introducing tyrosine residues into peptide-binding domains within the viral cage or cavities of protein templates. However, other metal precursor substrates of Ag^{+}, Pt^{4+}, Pd^{4+}, and an insoluble Au(I) complex were not found to be reduced to zero-valent nanoclusters by the virus.

Viral capsids can be icosahedral or rod shaped. Icosahedral particles range in size from 18 to 500 nm, whereas rod-shaped or filamentous viral nanoparticles can reach up to 2 μm in length. CCMV is an icosahedral protein capsid that is 28 nm in diameter. A review on the art of engineering viral nanoparticles by Pokorski and Steinmetz details their varied kinds and applications in drug delivery, imaging, and other nanobiomedical applications (Pokorski & Steinmetz, 2011). The surface chemistry of the outer surface of the virus is adequate for the site-selective covalent binding of gold nanoparticles with size <5 nm (Blum et al., 2004; Radloff et al., 2005; Slocik et al., 2005). However, larger single gold nanoparticles (with size >8 nm) can be encapsulated within the cavity of the viruses through self-assembly from protein subunits (Aniagyei et al., 2009; Chen et al., 2006; Loo et al., 2006; Wang et al., 2011). At neutral pH, the RNA cargo of the virus can be disassembled into coat protein (CP) dimers under high Ca^{2+} concentrations (Jeffrey et al., 1995). Upon adjusting the pH to 5 at high ionic strength, the native cage-like structures of the viruses can be regained through self-assembly.

Yan et al. used M13 bacteriophage as a viral template to fabricate 1D gold/PPy nanopeapods (Yan et al., 2016b). The filamentous virus was genetically modified for the selective attachment of gold nanoparticles along its length, following which PPy shell was electropolymerized on the Au nanoparticle chains, forming nanopeapod structures. The networks of the hybrid Au/PPy nanostructures were excellent chemiresistive NH_3 sensors. The sensing performance of the nanostructures was evaluated from 5 to 50 ppmv at room temperature. The lowest detection limit was calculated to be as low as 0.005 ppmv.

4.4 Summary

Nanomaterials in their wide range of morphologies and geometries are being effectively used as biosensors, chemical sensors, optical sensors, gas sensors, and so on. In this chapter we have attempted to focus only on the gravity of research that has been done on developing nanostructures through templating. We could observe that templating through different means using sacrificial templates, AAO, and LBL assembly helped to modulate the structure, size, and composition of hybrid particles in a controllable way to tailor their optical, electrical, thermal, mechanical, electrooptical, magnetic, and catalytic properties. The emphasis on the much trickier use of protein-based biocages for catalyst encapsulation, enzyme immobilization, and breath analysis could also highlight the current relevance of templating nanobiotechnology.

References

Aniagyei, S.E., Kennedy, C.J., Stein, B., Willits, D.A., Douglas, T., Young, M.J., De, M., Rotello, V.M., Srisathiyanarayanan, D., Kao, C.C., Dragnea, B., 2009. Synergistic effects of mutations and nanoparticle templating in the self-assembly of cowpea chlorotic mottle virus capsids. Nano Lett. 9 (1), 393–398. https://doi.org/10.1021/nl8032476.

Ariga, K., Ahn, E., Park, M., Kim, B.-S., 2019. Layer-by-layer assembly: Recent progress from layered assemblies to layered nanoarchitectonics. Chemistry—An Asian Journal, 14 (15), 2553–2566. https://doi.org/10.1002/asia.201900627.

Azzaroni, O., Lau, K.H.A., 2011. Layer-by-layer assemblies in nanoporous templates: Nano-organized design and applications of soft nanotechnology. Soft Matter 7 (19), 8709–8724. https://doi.org/10.1039/C1SM05561E.

Bae, C., Yoo, H., Kim, S., Lee, K., Kim, J., Sung, M.M., Shin, H., 2008. Template-directed synthesis of oxide nanotubes: Fabrication, characterization, and applications. Chem. Mater. 20 (3), 756–767. https://doi.org/10.1021/cm702138c.

Blum, A.S., Soto, C.M., Wilson, C.D., Cole, J.D., Kim, M., Gnade, B., Chatterji, A., Ochoa, W.F., Lin, T., Johnson, J.E., Ratna, B.R., 2004. Cowpea mosaic virus as a scaffold for 3-D patterning of gold nanoparticles. Nano Lett. 4 (5), 867–870. https://doi.org/10.1021/nl0497474.

Breen, M.L., Dinsmore, A.D., Pink, R.H., Qadri, S.B., Ratna, B.R., 2001. Sonochemically produced ZnS-coated polystyrene core−shell particles for use in photonic crystals. Langmuir 17 (3), 903–907. https://doi.org/10.1021/la0011578.

Cai, F.-S., Zhang, G.-Y., Chen, J., Gou, X.-L., Liu, H.-K., Dou, S.-X., 2004. $Ni(OH)_2$ tubes with mesoscale dimensions as positive-electrode materials of alkaline rechargeable batteries. Angew. Chem. Int. Ed. 43 (32), 4212–4216. https://doi.org/10.1002/anie.200460053.

Caruso, F., Caruso, R.A., Möhwald, H., 1998. Nanoengineering of inorganic and hybrid hollow spheres by colloidal templating. Science 282 (5391), 1111. https://doi.org/10.1126/science.282.5391.1111.

Caruso, F., Spasova, M., Susha, A., Giersig, M., Caruso, R.A., 2001. Magnetic nanocomposite particles and hollow spheres constructed by a sequential layering approach. Chem. Mater. 13 (1), 109–116. https://doi.org/10.1021/cm001164h.

Casida, J.E., Quistad, G.B., 2004. Organophosphate toxicology: Safety aspects of nonacetylcholinesterase secondary targets. Chem. Res. Toxicol. 17 (8), 983–998. https://doi.org/10.1021/tx0499259.

Cassagneau, T., Guérin, F., Fendler, J.H., 2000. Preparation and characterization of ultrathin films layer-by-layer self-assembled from graphite oxide nanoplatelets and polymers. Langmuir 16 (18), 7318–7324. https://doi.org/10.1021/la000442o.

Chang, Y.-H., Liu, C.-M., Tseng, Y.-C., Chen, C., Chen, C.-C., Cheng, H.-E., 2010. Direct probe of heterojunction effects upon photoconductive properties of TiO_2 nanotubes fabricated by atomic layer deposition. Nanotechnology 21 (22), 225602. https://doi.org/10.1088/0957-4484/21/22/225602.

Chen, C., Daniel, M.-C., Quinkert, Z.T., De, M., Stein, B., Bowman, V.D., Chipman, P.R., Rotello, V.M., Kao, C.C., Dragnea, B., 2006. Nanoparticle-templated assembly of viral protein cages. Nano Lett. 6 (4), 611–615. https://doi.org/10.1021/nl0600878.

Chen, X., Guo, Z., Xu, W.-H., Yao, H.-B., Li, M.-Q., Liu, J.-H., Huang, X.-J., Yu, S.-H., 2011. Templating synthesis of SnO_2 nanotubes loaded with Ag_2O nanoparticles and their enhanced gas sensing properties. Adv. Funct. Mater. 21 (11), 2049–2056. https://doi.org/10.1002/adfm.201002701.

Chen, D., Shen, G., Tang, K., Liang, Z., Zheng, H., 2004. AOT-microemulsions-based formation and evolution of $PbWO_4$ crystals. J. Phys. Chem. B 108 (31), 11280–11284. https://doi.org/10.1021/jp0377681.

Chen, J., Xu, L., Li, W., Gou, X., 2005. α-Fe_2O_3 nanotubes in gas sensor and lithium-ion battery applications. Adv. Mater. 17 (5), 582–586. https://doi.org/10.1002/adma.200401101.

Cheng, B., Samulski, E.T., 2001. Fabrication and characterization of nanotubular semiconductor oxides In_2O_3 and Ga_2O_3. J. Mater. Chem. 11 (12), 2901–2902. https://doi.org/10.1039/B108167E.

Chik, H., Liang, J., Cloutier, S.G., Kouklin, N., Xu, J.M., 2004. Periodic array of uniform ZnO nanorods by second-order self-assembly. Appl. Phys. Lett. 84 (17), 3376–3378. https://doi.org/10.1063/1.1728298.

Cho, H.-J., Kim, S.-J., Choi, S.-J., Jang, J.-S., Kim, I.-D., 2017. Facile synthetic method of catalyst-loaded ZnO nanofibers composite sensor arrays using bio-inspired protein cages for pattern recognition of exhaled breath. Sens. Actuators B 243, 166–175. https://doi.org/10.1016/j.snb.2016.11.137.

Cho, N.G., Woo, H.-S., Lee, J.-H., Kim, I.-D., 2011. Thin-walled NiO tubes functionalized with catalytic Pt for highly selective C_2H_5OH sensors using electrospun fibers as a sacrificial template. Chem. Commun. 47 (40), 11300–11302. https://doi.org/10.1039/C1CC13876F.

Choi, S.-H., Ankonina, G., Youn, D.-Y., Oh, S.-G., Hong, J.-M., Rothschild, A., Kim, I.-D., 2009. Hollow ZnO nanofibers fabricated using electrospun polymer templates and their electronic transport properties. ACS Nano 3 (9), 2623–2631. https://doi.org/10.1021/nn900126k.

Choi, S.-J., Chattopadhyay, S., Kim, J.J., Kim, S.-J., Tuller, H.L., Rutledge, G.C., Kim, I.-D., 2016. Coaxial electrospinning of WO_3 nanotubes functionalized with bio-inspired Pd catalysts and their superior hydrogen sensing performance. Nanoscale 8 (17), 9159–9166. https://doi.org/10.1039/C5NR06611E.

Choi, S.-J., Lee, I., Jang, B.-H., Youn, D.-Y., Ryu, W.-H., Park, C.O., Kim, I.-D., 2013. Selective diagnosis of diabetes using Pt-functionalized WO_3 hemitube networks as a sensing layer of acetone in exhaled breath. Anal. Chem. 85 (3), 1792–1796. https://doi.org/10.1021/ac303148a.

Correa-Duarte, M.A., Giersig, M., Liz-Marzán, L.M., 1998. Stabilization of CdS semiconductor nanoparticles against photodegradation by a silica coating procedure. Chem. Phys. Lett. 286 (5), 497–501. https://doi.org/10.1016/S0009-2614(98)00012-8.

Dai, Z., Dähne, L., Möhwald, H., Tiersch, B., 2002. Novel capsules with high stability and controlled permeability by hierarchic templating. Angew. Chem. Int. Ed. 41 (21), 4019–4022. https://doi.org/10.1002/1521-3773(20021104)41:21<4019::AID-ANIE4019>3.0.CO;2-Z.

Decher, G., 1997. Fuzzy nanoassemblies: Toward layered polymeric multicomposites. Science 277 (5330), 1232. https://doi.org/10.1126/science.277.5330.1232.

Decher, G., Hong, J.-D., 1991. Buildup of ultrathin multilayer films by a self-assembly process, 1 consecutive adsorption of anionic and cationic bipolar amphiphiles on charged surfaces. Makromolekulare Chemie. Macromol. Symp. 46 (1), 321–327. https://doi.org/10.1002/masy.19910460145.

Deng, C., Zhang, J., Yu, X., Zhang, W., Zhang, X., 2004. Determination of acetone in human breath by gas chromatography–mass spectrometry and solid-phase microextraction with on-fiber derivatization. J. Chromatogr. B 810 (2), 269–275. https://doi.org/10.1016/j.jchromb.2004.08.013.

Ding, S.-J., Zhang, C.-L., Yang, M., Qu, X.-Z., Lu, Y.-F., Yang, Z.-Z., 2006. Template synthesis of composite hollow spheres using sulfonated polystyrene hollow spheres. Polymer 47 (25), 8360–8366. https://doi.org/10.1016/j.polymer.2006.10.001.

Dong, L., Shen, X., Deng, C., 2006. Development of gas chromatography–mass spectrometry following headspace single-drop microextraction and simultaneous derivatization for fast determination of the diabetes biomarker, acetone in human

blood samples. Anal. Chim. Acta 569 (1), 91–96. https://doi.org/10.1016/j.aca.2006.03.095.

Dong, A., Tang, R., Buhro, W.E., 2007. Solution-based growth and structural characterization of homo- and heterobranched semiconductor nanowires. J. Am. Chem. Soc. 129 (40), 12254–12262. https://doi.org/10.1021/ja0737772.

Douglas, T., Stark, V.T., 2000. Nanophase Cobalt oxyhydroxide mineral synthesized within the protein cage of ferritin. Inorg. Chem. 39 (8), 1828–1830. https://doi.org/10.1021/ic991269q.

Douglas, T., Strable, E., Willits, D., Aitouchen, A., Libera, M., Young, M., 2002. Protein engineering of a viral cage for constrained nanomaterials synthesis. Adv. Mater. 14 (6), 415–418. https://doi.org/10.1002/1521-4095(20020318)14:6<415::AID-ADMA415>3.0.CO;2-W.

Douglas, T., Young, M., 1998. Host–guest encapsulation of materials by assembled virus protein cages. Nature 393 (6681), 152–155. https://doi.org/10.1038/30211.

Du, D., Chen, A., Xie, Y., Zhang, A., Lin, Y., 2011. Nanoparticle-based immunosensor with apoferritin templated metallic phosphate label for quantification of phosphorylated acetylcholinesterase. Biosens. Bioelectron. 26 (9), 3857–3863. https://doi.org/10.1016/j.bios.2011.02.047.

Du, D., Ding, J., Tao, Y., Li, H., Chen, X., 2008. CdTe nanocrystal-based electrochemical biosensor for the recognition of neutravidin by anodic stripping voltammetry at electrodeposited bismuth film. Biosens. Bioelectron. 24 (4), 863–868. https://doi.org/10.1016/j.bios.2008.07.020.

Du, H., Wang, J., Su, M., Yao, P., Zheng, Y., Yu, N., 2012. Formaldehyde gas sensor based on SnO_2/In_2O_3 hetero-nanofibers by a modified double jets electrospinning process. Sens. Actuators B 166–167, 746–752. https://doi.org/10.1016/j.snb.2012.03.055.

Du, N., Zhang, H., Chen, B.D., Ma, X.Y., Liu, Z.H., Wu, J.B., Yang, D.R., 2007. Porous indium oxide nanotubes: Layer-by-layer assembly on carbon-nanotube templates and application for room-temperature NH_3 gas sensors. Adv. Mater. 19 (12), 1641–1645. https://doi.org/10.1002/adma.200602128.

Dujardin, E., Peet, C., Stubbs, G., Culver, J.N., Mann, S., 2003. Organization of metallic nanoparticles using tobacco mosaic virus templates. Nano Lett. 3 (3), 413–417. https://doi.org/10.1021/nl034004o.

Esman, N., Lellouche, J.-P., 2010. Fabrication of functional polypyrrole (PolyPyr)-nanotubes using anodized aluminium oxide (AAO) template membranes. Compromising between effectiveness and mildness of template dissolution conditions for a safe release of PolyPyr-nanotubes. Polym. Chem. 1 (2), 158–160. https://doi.org/10.1039/B9PY00206E.

Fan, J., Yin, J.-J., Ning, B., Wu, X., Hu, Y., Ferrari, M., Anderson, G.J., Wei, J., Zhao, Y., Nie, G., 2011. Direct evidence for catalase and peroxidase activities of ferritin–platinum nanoparticles. Biomaterials 32 (6), 1611–1618. https://doi.org/10.1016/j.biomaterials.2010.11.004.

Fang, M., Kaschak, D.M., Sutorik, A.C., Mallouk, T.E., 1997. A "mix and match" ionic−covalent strategy for self-assembly of inorganic multilayer films. J. Am. Chem. Soc. 119 (50), 12184–12191. https://doi.org/10.1021/ja972569e.

Feng, C., Li, W., Li, C., Zhu, L., Zhang, H., Zhang, Y., Ruan, S., Chen, W., Yu, L., 2012. Highly efficient rapid ethanol sensing based on $In_2-xNixO_3$ nanofibers. Sens. Actuators B 166–167, 83–88. https://doi.org/10.1016/j.snb.2011.12.083.

Feng, C., Li, X., Ma, J., Sun, Y., Wang, C., Sun, P., Zheng, J., Lu, G., 2015a. Facile synthesis and gas sensing properties of In_2O_3–WO_3 heterojunction nanofibers. Sens. Actuators B 209, 622–629. https://doi.org/10.1016/j.snb.2014.12.019.

Feng, C., Wang, C., Cheng, P., Li, X., Wang, B., Guan, Y., Ma, J., Zhang, H., Sun, Y., Sun, P., Zheng, J., Lu, G., 2015b. Facile synthesis and gas sensing properties of La_2O_3–WO_3

nanofibers. Sens. Actuators B 221, 434–442. https://doi.org/10.1016/j.snb.2015.06.114.

Fennouh, S., Casimiri, V., Burstein, C., 1997. Increased paraoxon detection with solvents using acetylcholinesterase inactivation measured with a choline oxidase biosensor. Biosens. Bioelectron. 12 (2), 97–104. https://doi.org/10.1016/S0956-5663(97)87055-8.

Fu, J., Zhao, C., Zhang, J., Peng, Y., Xie, E., 2013. Enhanced gas sensing performance of electrospun Pt-functionalized NiO nanotubes with chemical and electronic sensitization. ACS Appl. Mater. Interfaces 5 (15), 7410–7416. https://doi.org/10.1021/am4017347.

Gálvez, N., Fernandez, B., Valero, E., Sánchez, P., Cuesta, R., & Domínguez-Vera, J. M. (2008). Apoferritin as a nanoreactor for preparing metallic nanoparticles. Magnétisme Moléculaire: Nouvelles Tendances, 11(10), 1207–1212. https://doi.org/10.1016/j.crci.2008.09.003

Gálvez, N., Sánchez, P., Domínguez-Vera, J.M., 2005. Preparation of Cu and CuFe Prussian Blue derivative nanoparticles using the apoferritin cavity as nanoreactor. Dalton Trans. 15, 2492–2494. https://doi.org/10.1039/B506290J.

Gao, X., Liu, L., Birajdar, B., Ziese, M., Lee, W., Alexe, M., Hesse, D., 2009. High-density periodically ordered magnetic cobalt ferrite nanodot arrays by template-assisted pulsed laser deposition. Adv. Funct. Mater. 19 (21), 3450–3455. https://doi.org/10.1002/adfm.200900422.

Garg, A., Matijević, E., 1988. Preparation and properties of uniform coated inorganic colloidal particles: III. Zirconium hydrous oxide on hematite. J. Colloid Interface Sci. 126 (1), 243–250. https://doi.org/10.1016/0021-9797(88)90118-X.

Guo, J., Zhang, J., Zhu, M., Ju, D., Xu, H., Cao, B., 2014. High-performance gas sensor based on ZnO nanowires functionalized by Au nanoparticles. Sens. Actuators B 199, 339–345. https://doi.org/10.1016/j.snb.2014.04.010.

Guo, J.-X., Wu, J.J.-Q., Wright, J.B., Lushington, G.H., 2006. Mechanistic insight into acetylcholinesterase inhibition and acute toxicity of organophosphorus compounds: A molecular modeling study. Chem. Res. Toxicol. 19 (2), 209–216. https://doi.org/10.1021/tx050090r.

Guo, X.-C., Dong, P., 1999. Multistep coating of thick titania layers on monodisperse silica nanospheres. Langmuir 15 (17), 5535–5540. https://doi.org/10.1021/la990220u.

Gyger, F., Hübner, M., Feldmann, C., Barsan, N., Weimar, U., 2010. Nanoscale SnO_2 hollow spheres and their application as a gas-sensing material. Chem. Mater. 22 (16), 4821–4827. https://doi.org/10.1021/cm1011235.

Han, W.-Q., Zettl, A., 2003. Coating single-walled carbon nanotubes with tin oxide. Nano Lett. 3 (5), 681–683. https://doi.org/10.1021/nl034142d.

Hansen, J.A., Wang, J., Kawde, A.-N., Xiang, Y., Gothelf, K.V., Collins, G., 2006. Quantum-dot/aptamer-based ultrasensitive multi-analyte electrochemical biosensor. J. Am. Chem. Soc. 128 (7), 2228–2229. https://doi.org/10.1021/ja060005h.

He, D., Marles-Wright, J., 2015. Ferritin family proteins and their use in bionanotechnology. European Congress of Biotechnology—ECB 16 32 (6), 651–657. https://doi.org/10.1016/j.nbt.2014.12.006.

Mark, K., Anita, P., Richard, S., 1994. High-speed GC analysis of VOCs: Sample collection and inlet systems. Environ. Sci. Technol. 28 (8), 369A–376A. https://doi.org/10.1021/es00057a716.

Iler, R.K., 1966. Multilayers of colloidal particles. J. Colloid Interface Sci. 21 (6), 569–594. https://doi.org/10.1016/0095-8522(66)90018-3.

Imai, H., Takei, Y., Shimizu, K., Matsuda, M., Hirashima, H., 1999. Direct preparation of anatase TiO_2 nanotubes in porous alumina membranes. J. Mater. Chem. 9 (12), 2971–2972. https://doi.org/10.1039/A906005G.

Jang, J.-S., Kim, S.-J., Choi, S.-J., Kim, N.-H., Hakim, M., Rothschild, A., Kim, I.-D., 2015. Thin-walled SnO_2 nanotubes functionalized with Pt and Au catalysts via the protein templating route and their selective detection of acetone and hydrogen sulfide molecules. Nanoscale 7 (39), 16417–16426. https://doi.org/10.1039/C5NR04487A.

Jani, M. M., A., Losic, D., Voelcker, N.H, 2013. Nanoporous anodic aluminium oxide: Advances in surface engineering and emerging applications. Prog. Mater Sci. 58 (5), 636–704. https://doi.org/10.1016/j.pmatsci.2013.01.002.

Jeffrey, a, Speir, S., Munshi, G., Wang, T.S., Baker, J.E., Johnson, 1995. Structure 3, 135–136. https://doi.org/10.1016/s0969-2126(01)00135-6.

Jessensky, O., Müller, F., Gösele, U., 1998. Self-organized formation of hexagonal pore arrays in anodic alumina. Appl. Phys. Lett. 72 (10), 1173–1175. https://doi.org/10.1063/1.121004.

Ji, Q., Honma, I., Paek, S.-M., Akada, M., Hill, J.P., Vinu, A., Ariga, K., 2010. Layer-by-layer films of graphene and ionic liquids for highly selective gas sensing. Angew. Chem. Int. Ed. 49 (50), 9737–9739. https://doi.org/10.1002/anie.201004929.

Jin, W., Yan, S., Chen, W., Yang, S., Zhao, C., Dai, Y., 2014. Enhanced ethanol sensing characteristics by decorating dispersed Pd nanoparticles on vanadium oxide nanotubes. Mater. Lett. 128, 362–365. https://doi.org/10.1016/j.matlet.2014.04.159.

Ju, D., Xu, H., Qiu, Z., Guo, J., Zhang, J., Cao, B., 2014. Highly sensitive and selective triethylamine-sensing properties of nanosheets directly grown on ceramic tube by forming NiO/ZnO PN heterojunction. Sens. Actuators B 200, 288–296. https://doi.org/10.1016/j.snb.2014.04.029.

Ju, D., Xu, H., Xu, Q., Gong, H., Qiu, Z., Guo, J., Zhang, J., Cao, B., 2015. High triethylamine-sensing properties of NiO/SnO_2 hollow sphere P–N heterojunction sensors. Sens. Actuators B 215, 39–44. https://doi.org/10.1016/j.snb.2015.03.015.

Jung, Y., Ko, D.-K., Agarwal, R., 2007. Synthesis and structural characterization of single-crystalline branched nanowire heterostructures. Nano Lett. 7 (2), 264–268. https://doi.org/10.1021/nl0621847.

Kalantar-Zadeh, K., Katoch, A., Kim, J.-H., Kim, S.S., 2015. Significance of the nanograin size on the H_2S-sensing ability of CuO-SnO_2 composite nanofibers. Journal of Sensors 2015, 387641. https://doi.org/10.1155/2015/387641.

Kaneti, Y.V., Moriceau, J., Liu, M., Yuan, Y., Zakaria, Q., Jiang, X., Yu, A., 2015. Hydrothermal synthesis of ternary α-Fe_2O_3–ZnO–Au nanocomposites with high gas-sensing performance. Sens. Actuators B 209, 889–897. https://doi.org/10.1016/j.snb.2014.12.065.

Katoch, A., Choi, S.-W., Sun, G.-J., Kim, H.W., Kim, S.S., 2014a. Mechanism and prominent enhancement of sensing ability to reducing gases in p/n core–shell nanofiber. Nanotechnology 25 (17), 175501. https://doi.org/10.1088/0957-4484/25/17/175501.

Katoch, A., Kim, J.-H., Kim, S.S., 2014b. TiO_2/ZnO inner/outer double-layer hollow fibers for improved detection of reducing gases. ACS Appl. Mater. Interfaces 6 (23), 21494–21499. https://doi.org/10.1021/am506499e.

Khalid, T.Y., Saad, S., Greenman, J., de Lacy Costello, B., Probert, C.S.J., Ratcliffe, N.M., 2013. Volatiles from oral anaerobes confounding breath biomarker discovery. J. Breath Res. 7 (1), 017114. https://doi.org/10.1088/1752-7155/7/1/017114.

Kim, K.-H., Kim, S.-J., Cho, H.-J., Kim, N.-H., Jang, J.-S., Choi, S.-J., Kim, I.-D., 2017. WO_3 nanofibers functionalized by protein-templated RuO_2 nanoparticles as highly sensitive exhaled breath gas sensing layers. Sens. Actuators B 241, 1276–1282. https://doi.org/10.1016/j.snb.2016.09.192.

Kim, W.-S., Lee, B.-S., Kim, D.-H., Kim, H.-C., Yu, W.-R., Hong, S.-H., 2010. SnO_2 nanotubes fabricated using electrospinning and atomic layer deposition and their gas sensing performance. Nanotechnology 21 (24), 245605. https://doi.org/10.1088/0957-4484/21/24/245605.

Kim, S., Park, S., Park, S., Lee, C., 2015. Acetone sensing of Au and Pd-decorated WO_3 nanorod sensors. Sens. Actuators B 209, 180–185. https://doi.org/10.1016/j.snb.2014.11.106.

Knez, M., Sumser, M., Bittner, A.M., Wege, C., Jeske, H., Martin, T.P., Kern, K., 2004. Spatially selective nucleation of metal clusters on the tobacco mosaic virus. Adv. Funct. Mater. 14 (2), 116–124. https://doi.org/10.1002/adfm.200304376.

Kolmakov, A., Zhang, Y., Cheng, G., Moskovits, M., 2003. Detection of CO and O_2 using tin oxide nanowire sensors. Adv. Mater. 15 (12), 997–1000. https://doi.org/10.1002/adma.200304889.

Kong, B.-S., Geng, J., Jung, H.-T., 2009. Layer-by-layer assembly of graphene and gold nanoparticles by vacuum filtration and spontaneous reduction of gold ions. Chemical Communication 16, 2174–2176. https://doi.org/10.1039/B821920F.

Koo, W.-T., Choi, S.-J., Kim, N.-H., Jang, J.-S., Kim, I.-D., 2016. Catalyst-decorated hollow WO_3 nanotubes using layer-by-layer self-assembly on polymeric nanofiber templates and their application in exhaled breath sensor. Sens. Actuators B 223, 301–310. https://doi.org/10.1016/j.snb.2015.09.095.

Koo, W.-T., Jang, J.-S., Choi, S.-J., Cho, H.-J., Kim, I.-D., 2017. Metal–organic framework templated catalysts: Dual sensitization of PdO–ZnO composite on hollow SnO_2 nanotubes for selective acetone sensors. ACS Appl. Mater. Interfaces 9 (21), 18069–18077. https://doi.org/10.1021/acsami.7b04657.

Kotov, N.A., Dékány, I., Fendler, J.H., 1996. Ultrathin graphite oxide–polyelectrolyte composites prepared by self-assembly: Transition between conductive and non-conductive states. Adv. Mater. 8 (8), 637–641. https://doi.org/10.1002/adma.19960080806.

Kovtyukhova, N.I., Ollivier, P.J., Martin, B.R., Mallouk, T.E., Chizhik, S.A., Buzaneva, E.V., Gorchinskiy, A.D., 1999. Layer-by-layer assembly of ultrathin composite films from micron-sized graphite oxide sheets and polycations. Chem. Mater. 11 (3), 771–778. https://doi.org/10.1021/cm981085u.

Kruefu, V., Wisitsoraat, A., Tuantranont, A., Phanichphant, S., 2015. Ultra-sensitive H_2S sensors based on hydrothermal/impregnation-made Ru-functionalized WO_3 nanorods. Sens. Actuators B 215, 630–636. https://doi.org/10.1016/j.snb.2015.03.037.

Kuno, M., Ahmad, O., Protasenko, V., Bacinello, D., Kosel, T.H., 2006. Solution-based straight and branched CdTe nanowires. Chem. Mater. 18 (24), 5722–5732. https://doi.org/10.1021/cm061559m.

Lahav, M., Sehayek, T., Vaskevich, A., Rubinstein, I., 2003. Nanoparticle nanotubes. Angew. Chem. Int. Ed. 42 (45), 5576–5579. https://doi.org/10.1002/anie.200352216.

Lee, C.-S., Kim, I.-D., Lee, J.-H., 2013. Selective and sensitive detection of trimethylamine using ZnO–In_2O_3 composite nanofibers. Sens. Actuators B 181, 463–470. https://doi.org/10.1016/j.snb.2013.02.008.

Lee, D.W., Hong, T.-K., Kang, D., Lee, J., Heo, M., Kim, J.Y., Kim, B.-S., Shin, H.S., 2011a. Highly controllable transparent and conducting thin films using layer-by-layer assembly of oppositely charged reduced graphene oxides. J. Mater. Chem. 21 (10), 3438–3442. https://doi.org/10.1039/C0JM02270E.

Lee, H., Yoon, J., Kim, B., Jang, H., Kim, J., 2011b. Gas sensing characteristics of Ru doped-WO_3 micro gas sensors. Taehan-Kŭmsok-Hakhoe-Chi—Journal of the Korean Institute of Metals and Materials 49, 395–399. https://doi.org/10.3365/KJMM.2011.49.5.395.

Lee, J.-H., 2009. Gas sensors using hierarchical and hollow oxide nanostructures: Overview. Sens. Actuators B 140 (1), 319–336. https://doi.org/10.1016/j.snb.2009.04.026.

Lee, J., Kim, D.H., Hong, S.-H., Jho, J.Y., 2011c. A hydrogen gas sensor employing vertically aligned TiO_2 nanotube arrays prepared by template-assisted method. Sens. Actuators B 160 (1), 1494–1498. https://doi.org/10.1016/j.snb.2011.08.001.

Lee, J., Ju, H., Lee, J.K., Kim, H.S., Lee, J., 2010. Atomic layer deposition of TiO_2 nanotubes and its improved electrostatic capacitance. Electrochem. Commun. 12 (2), 210–212. https://doi.org/10.1016/j.elecom.2009.11.026.

Lee, W., Ji, R., Gösele, U., Nielsch, K., 2006. Fast fabrication of long-range ordered porous alumina membranes by hard anodization. Nat. Mater. 5 (9), 741–747. https://doi.org/10.1038/nmat1717.

Lee, W., Park, S.-J., 2014. Porous anodic aluminum oxide: Anodization and templated synthesis of functional nanostructures. Chem. Rev. 114 (15), 7487–7556. https://doi.org/10.1021/cr500002z.

Lee, Y.J., Yi, H., Kim, W.-J., Kang, K., Yun, D.S., Strano, M.S., Ceder, G., Belcher, A.M., 2009. Fabricating genetically engineered high-power lithium-ion batteries using multiple virus genes. Science 324 (5930), 1051. https://doi.org/10.1126/science.1171541.

Li, A.P., Müller, F., Birner, A., Nielsch, K., Gösele, U., 1998. Hexagonal pore arrays with a 50–420 nm interpore distance formed by self-organization in anodic alumina. J. Appl. Phys. 84 (11), 6023–6026. https://doi.org/10.1063/1.368911.

Li, W.-Z., Qin, C.-G., Xiao, W.-M., Chen, J.-S., 2005. Preparation of hollow layered MoO_3 microspheres through a resin template approach. J. Solid State Chem. 178 (1), 390–394. https://doi.org/10.1016/j.jssc.2004.09.037.

Li, X.-L., Lou, T.-J., Sun, X.-M., Li, Y.-D., 2004. Highly sensitive WO_3 hollow-sphere gas sensors. Inorg. Chem. 43 (17), 5442–5449. https://doi.org/10.1021/ic049522w.

Liu, A., Traulsen, C.H.-H., Cornelissen, J.J.L.M., 2016. Nitroarene reduction by a virus protein cage based nanoreactor. ACS Catalysis 6 (5), 3084–3091. https://doi.org/10.1021/acscatal.6b00106.

Liu, G., Lin, Y., 2005. Electrochemical sensor for organophosphate pesticides and nerve agents using zirconia nanoparticles as selective sorbents. Anal. Chem. 77 (18), 5894–5901. https://doi.org/10.1021/ac050791t.

Liu, G., Wang, J., Barry, R., Petersen, C., Timchalk, C., Gassman, P.L., Lin, Y., 2008. Nanoparticle-based electrochemical immunosensor for the detection of phosphorylated acetylcholinesterase: An exposure biomarker of organophosphate pesticides and nerve agents. Chemistry—A European Journal, 14 (32), 9951–9959. https://doi.org/10.1002/chem.200800412.

Liu, G., Wu, H., Wang, J., Lin, Y., 2006. Apoferritin-templated synthesis of metal phosphate nanoparticle labels for electrochemical immunoassay. Small 2 (10), 1139–1143. https://doi.org/10.1002/smll.200600206.

Liu, X., Cheng, S., Liu, H., Hu, S., Zhang, D., Ning, H., 2012. A survey on gas sensing technology. Sensors, 12 (7). https://doi.org/10.3390/s120709635.

Liz-Marzán, L.M., Giersig, M., Mulvaney, P., 1996. Synthesis of nanosized gold—silica core—shell particles. Langmuir 12 (18), 4329–4335. https://doi.org/10.1021/la9601871.

Loo, L., Guenther, R.H., Basnayake, V.R., Lommel, S.A., Franzen, S., 2006. Controlled encapsidation of gold nanoparticles by a viral protein shell. J. Am. Chem. Soc. 128 (14), 4502–4503. https://doi.org/10.1021/ja057332u.

Ma, X., Song, H., Guan, C., 2013. Interfacial oxidation–dehydration induced formation of porous SnO_2 hollow nanospheres and their gas sensing properties. Sens. Actuators B 177, 196–204. https://doi.org/10.1016/j.snb.2012.10.127.

Mansouri, S., Winnik, F.M., Tabrizian, M., 2009. Modulating the release kinetics through the control of the permeability of the layer-by-layer assembly: A review. Null 6 (6), 585–597. https://doi.org/10.1517/17425240902967599.

Martin, C.R., 1994. Nanomaterials: A membrane-based synthetic approach. Science 266 (5193), 1961. https://doi.org/10.1126/science.266.5193.1961.

Masuda, H., Fukuda, K., 1995. Ordered metal nanohole arrays made by a two-step replication of honeycomb structures of anodic alumina. Science 268 (5216), 1466. https://doi.org/10.1126/science.268.5216.1466.

Meng, G., Jung, Y.J., Cao, A., Vajtai, R., Ajayan, P.M., 2005. Controlled fabrication of hierarchically branched nanopores, nanotubes, and nanowires. Proc. Nat. Acad. Sci. U.S.A. 102 (20), 7074. https://doi.org/10.1073/pnas.0502098102.

Merkle, V., Zeng, L., Teng, W., Slepian, M., Wu, X., 2013. Gelatin shells strengthen polyvinyl alcohol core–shell nanofibers. Polymer 54 (21), 6003–6007. https://doi.org/10.1016/j.polymer.2013.08.056.

Miao, Y.-E., He, S., Zhong, Y., Yang, Z., Tjiu, W.W., Liu, T., 2013. A novel hydrogen peroxide sensor based on Ag/SnO_2 composite nanotubes by electrospinning. Electrochim. Acta 99, 117–123. https://doi.org/10.1016/j.electacta.2013.03.063.

Milchev, A. (2002). Electrocrystallization: Fundamentals of Nucleation and Growth. ISBN: 978-0-306-47552-8. Springer. https://link.springer.com/book/10.1007/b113784.

Milchev, A., Stoyanov, S., Kaischev, R., 1974. Atomistic theory of electrolytic nucleation: I. Thin. Solid. Films 22 (3), 255–265. https://doi.org/10.1016/0040-6090(74)90296-X.

Miller, D.R., Akbar, S.A., Morris, P.A., 2014. Nanoscale metal oxide-based heterojunctions for gas sensing: A review. Sens. Actuators B 204, 250–272. https://doi.org/10.1016/j.snb.2014.07.074.

Moglia, I., Santiago, M., Olivera-Nappa, Á., Soler, M., 2018. An optimized low-cost protocol for standardized production of iron-free apoferritin nanocages with high protein recovery and suitable conformation for nanotechnological applications. J. Inorg. Biochem. 183, 184–190. https://doi.org/10.1016/j.jinorgbio.2017.11.019.

Nam, K.T., Kim, D.-W., Yoo, P.J., Chiang, C.-Y., Meethong, N., Hammond, P.T., Chiang, Y.-M., Belcher, A.M., 2006. Virus-enabled synthesis and assembly of nanowires for lithium ion battery electrodes. Science 312 (5775), 885. https://doi.org/10.1126/science.1122716.

Nam, K.T., Wartena, R., Yoo, P.J., Liau, F.W., Lee, Y.J., Chiang, Y.-M., Hammond, P.T., Belcher, A.M., 2008. Stamped microbattery electrodes based on self-assembled M13 viruses. Proceedings of the National Academy of Sciences of the United States of America, 105 (45), 17227. https://doi.org/10.1073/pnas.0711620105.

Nasiri, N., Clarke, C., 2019. Nanostructured gas sensors for medical and health applications: Low to high dimensional materials. Biosensors, 9 (1). https://doi.org/10.3390/bios9010043.

Niranjan, R.S., Sainkar, S.R., Vijayamohanan, K., Mulla, I.S., 2002. Ruthenium: Tin oxide thin film as a highly selective hydrocarbon sensor. Sens. Actuators B 82 (1), 82–88. https://doi.org/10.1016/S0925-4005(01)00994-7.

Noort, D., Benschop, H.P., Black, R.M., 2002. Biomonitoring of exposure to chemical warfare agents: A review. Toxicol. Appl. Pharmacol. 184 (2), 116–126. https://doi.org/10.1006/taap.2002.9449.

Ohnishi, M., Kozuka, Y., Ye, Q.-L., Yoshikawa, H., Awaga, K., Matsuno, R., Kobayashi, M., Takahara, A., Yokoyama, T., Bandow, S., Iijima, S., 2006. Phase selective preparations and surface modifications of spherical hollow nanomagnets. J. Mater. Chem. 16 (31), 3215–3220. https://doi.org/10.1039/B605472B.

Papadopoulos, C., Rakitin, A., Li, J., Vedeneev, A.S., Xu, J.M., 2000. Electronic transport in Y-junction carbon nanotubes. Phys. Rev. Lett. 85 (16), 3476–3479. https://doi.org/10.1103/PhysRevLett.85.3476.

Pardío, V.T., Ibarra, N., Rodríguez, M.A., Waliszewski, K.N., 2001. Use of cholinesterase activity in monitoring organophosphate pesticide exposure of cattle produced in tropical areas. J. Agric. Food Chem. 49 (12), 6057–6062. https://doi.org/10.1021/jf010431g.

Park, J.Y., Choi, S.-W., Lee, J.-W., Lee, C., Kim, S.S., 2009. Synthesis and gas sensing properties of TiO_2–ZnO core-shell nanofibers. J. Am. Ceram. Soc. 92 (11), 2551–2554. https://doi.org/10.1111/j.1551-2916.2009.03270.x.

Peng, G., Tisch, U., Adams, O., Hakim, M., Shehada, N., Broza, Y.Y., Billan, S., Abdah-Bortnyak, R., Kuten, A., Haick, H., 2009. Diagnosing lung cancer in exhaled

breath using gold nanoparticles. Nat. Nanotechnol. 4 (10), 669–673. https://doi.org/10.1038/nnano.2009.235.
Peng, S., Kim, J.H., Park, S.J., 2017. Size controlled preparation of CdTe nanoparticles by apoferritin, 468, pp. 79–83. https://doi.org/10.1016/j.jcrysgro.2016.12.042.
Pokorski, J.K., Steinmetz, N.F., 2011. The art of engineering viral nanoparticles. Mol. Pharmaceutics 8 (1), 29–43. https://doi.org/10.1021/mp100225y.
Qi, L., Li, J., Ma, J., 2002. Biomimetic morphogenesis of calcium carbonate in mixed solutions of surfactants and double-hydrophilic block copolymers. Adv. Mater. 14 (4), 300–303. https://doi.org/10.1002/1521-4095(20020219)14:4<300::AID-ADMA300>3.0.CO;2-P.
Qin, W., Xu, L., Song, J., Xing, R., Song, H., 2013. Highly enhanced gas sensing properties of porous SnO_2–CeO_2 composite nanofibers prepared by electrospinning. Sens. Actuators B 185, 231–237. https://doi.org/10.1016/j.snb.2013.05.001.
Qiu, H., Dong, X., Sana, B., Peng, T., Paramelle, D., Chen, P., Lim, S., 2013. Ferritin-templated synthesis and self-assembly of Pt nanoparticles on a monolithic porous graphene network for electrocatalysis in fuel cells. ACS Appl. Mater. Interfaces 5 (3), 782–787. https://doi.org/10.1021/am3022366.
Quinn, D.M., 1987. Acetylcholinesterase: Enzyme structure, reaction dynamics, and virtual transition states. Chemical Review 87 (5), 955–979. https://doi.org/10.1021/cr00081a005.
Radloff, C., Vaia, R.A., Brunton, J., Bouwer, G.T., Ward, V.K., 2005. Metal nanoshell assembly on a virus bioscaffold. Nano Lett. 5 (6), 1187–1191. https://doi.org/10.1021/nl050658g.
Rawtani, D., Agrawal, Y.K., 2014. Emerging strategies and applications of layer-by-layer self-assembly. Nanobiomedicine 1, 8. https://doi.org/10.5772/60009.
Satishkumar, B.C., Govindaraj, A., Vogl, E.M., Basumallick, L., Rao, C.N.R., 1997. Oxide nanotubes prepared using carbon nanotubes as templates. J. Mater. Res. 12 (3), 604–606 https://doi.org/DOI.10.1557/JMR.1997.0089.
Shen, J., Hu, Y., Qin, C., Ye, M., 2008. Layer-by-layer self-assembly of multiwalled carbon nanotube polyelectrolytes prepared by in situ radical polymerization. Langmuir 24 (8), 3993–3997. https://doi.org/10.1021/la703957t.
Shenton, W., Douglas, T., Young, M., Stubbs, G., Mann, S., 1999. Inorganic–organic nanotube composites from template mineralization of tobacco mosaic virus. Adv. Mater. 11 (3), 253–256. https://doi.org/10.1002/(SICI)1521-4095(199903)11:3<253::AID-ADMA253>3.0.CO;2-7.
Shi, M., Xu, J., Zhang, S., Liu, B., Kong, J., 2006. A mediator-free screen-printed amperometric biosensor for screening of organophosphorus pesticides with flow-injection analysis (FIA) system. Talanta 68 (4), 1089–1095. https://doi.org/10.1016/j.talanta.2005.07.007.
Shiho, H., Kawahashi, N., 2000. Iron compounds as coatings on polystyrene latex and as hollow spheres. J. Colloid Interface Sci. 226 (1), 91–97. https://doi.org/10.1006/jcis.2000.6789.
Slocik, J.M., Naik, R.R., Stone, M.O., Wright, D.W., 2005. Viral templates for gold nanoparticle synthesis. J. Mater. Chem. 15 (7), 749–753. https://doi.org/10.1039/B413074J.
Solis, J.L., Saukko, S., Kish, L., Granqvist, C.G., Lantto, V., 2001. Semiconductor gas sensors based on nanostructured tungsten oxide. Proceedings of the 2nd International Seminar on Semiconductor Gas Sensors 391 (2), 255–260. https://doi.org/10.1016/S0040-6090(01)00991-9.
Song, P., Wang, Q., Yang, Z., 2012. Preparation, characterization and acetone sensing properties of Ce-doped SnO_2 hollow spheres. Sens. Actuators B 173, 839–846. https://doi.org/10.1016/j.snb.2012.07.115.
Sousa, E.T., de M. Rodrigues, F., Martins, C.C., de Oliveira, F.S., de P. Pereira, P.A., de Andrade, J.B., 2006. Multivariate optimization and HS-SPME/GC-MS analysis of

VOCs in red, yellow and purple varieties of *Capsicum chinense* sp. peppers. Selected Papers Presented at the 13th National Analytical Chemistry Meeting and the 1st Ibero-American Analytical Chemistry Congress 82 (2), 142–149. https://doi.org/10.1016/j.microc.2006.01.017.

Steinhart, M., Wendorff, J.H., Greiner, A., Wehrspohn, R.B., Nielsch, K., Schilling, J., Choi, J., Gösele, U., 2002. Polymer nanotubes by wetting of ordered porous templates. Science 296 (5575), 1997. https://doi.org/10.1126/science.1071210.

Sun, Z., Yuan, H., Liu, Z., Han, B., Zhang, X., 2005. A highly efficient chemical sensor material for H_2S: α-Fe_2O_3 nanotubes fabricated using carbon nanotube templates. Adv. Mater. 17 (24), 2993–2997. https://doi.org/10.1002/adma.200501562.

Suryanarayana, C., 2002. The structure and properties of nanocrystalline materials: Issues and concerns. JOM 54 (9), 24. https://doi.org/10.1007/BF02709088.

Tian, Y., Meng, G., Biswas, S.K., Ajayan, P.M., Sun, S., Zhang, L., 2004. Y-branched Bi nanowires with metal–semiconductor junction behavior. Appl. Phys. Lett. 85 (6), 967–969. https://doi.org/10.1063/1.1779956.

Uchida, M., Klem, M.T., Allen, M., Suci, P., Flenniken, M., Gillitzer, E., Varpness, Z., Liepold, L.O., Young, M., Douglas, T., 2007. Biological containers: Protein cages as multifunctional nanoplatforms. Adv. Mater. 19 (8), 1025–1042. https://doi.org/10.1002/adma.200601168.

Ueno, T., Suzuki, M., Goto, T., Matsumoto, T., Nagayama, K., Watanabe, Y., 2004. Size-selective olefin hydrogenation by a Pd nanocluster provided in an apo-ferritin cage. Angew. Chem. Int. Ed. 43 (19), 2527–2530. https://doi.org/10.1002/anie.200353436.

Vallejos, S., Stoycheva, T., Umek, P., Navio, C., Snyders, R., Bittencourt, C., Llobet, E., Blackman, C., Moniz, S., Correig, X., 2011. Au nanoparticle-functionalised WO_3 nanoneedles and their application in high sensitivity gas sensor devices. Chemical Communication 47 (1), 565–567. https://doi.org/10.1039/C0CC02398A.

Walsh, D., Mann, S., 1995. Fabrication of hollow porous shells of calcium carbonate from self-organizing media. Nature 377 (6547), 320–323. https://doi.org/10.1038/377320a0.

Wan, Q., Huang, J., Xie, Z., Wang, T., Dattoli, E.N., Lu, W, 2008. Branched SnO_2 nanowires on metallic nanowire backbones for ethanol sensors application. Appl. Phys. Lett. 92 (10), 102101. https://doi.org/10.1063/1.2890735.

Wan, Q., Li, Q.H., Chen, Y.J., Wang, T.H., He, X.L., Li, J.P., Lin, C.L., 2004. Fabrication and ethanol sensing characteristics of ZnO nanowire gas sensors. Appl. Phys. Lett. 84 (18), 3654–3656. https://doi.org/10.1063/1.1738932.

Wang, H., Wang, J., Timchalk, C., Lin, Y., 2008a. Magnetic electrochemical immunoassays with quantum dot labels for detection of phosphorylated acetylcholinesterase in plasma. Anal. Chem. 80 (22), 8477–8484. https://doi.org/10.1021/ac801211s.

Wang, Y., Angelatos, A.S., Caruso, F., 2008b. Template synthesis of nanostructured materials via layer-by-layer assembly. Chem. Mater. 20 (3), 848–858. https://doi.org/10.1021/cm7024813.

Wang, J.X., Sun, X.W., Yang, Y., Huang, H., Lee, Y.C., Tan, O.K., Vayssieres, L., 2006. Hydrothermally grown oriented ZnO nanorod arrays for gas sensing applications. Nanotechnology 17 (19), 4995–4998. https://doi.org/10.1088/0957-4484/17/19/037.

Wang, Q., Lin, T., Tang, L., Johnson, J.E., Finn, M.G., 2002. Icosahedral virus particles as addressable nanoscale building blocks. Angewandte Chemie International Edition, 41 (3), 459–462. https://doi.org/10.1002/1521-3773(20020201)41:3<459::AID-ANIE459>3.0.CO;2-O.

Wang, T., Zhang, Z., Gao, D., Li, F., Wei, H., Liang, X., Cui, Z., Zhang, X.-E., 2011. Encapsulation of gold nanoparticles by simian virus 40 capsids. Nanoscale 3 (10), 4275–4282. https://doi.org/10.1039/C1NR10568J.

Wang, Y., Wu, T., Zhou, Y., Meng, C., Zhu, W., Liu, L., 2017. TiO_2-based nanoheterostructures for promoting gas sensitivity performance: Designs, developments, and prospects. Sensors, 17 (9). https://doi.org/10.3390/s17091971.

Wang, Z.L., Kong, X.Y., Zuo, J.M., 2003. Induced growth of asymmetric nanocantilever arrays on polar surfaces. Phys. Rev. Lett. 91 (18), 185502. https://doi.org/10.1103/PhysRevLett.91.185502.

Wang, Z., Li, Z., Sun, J., Zhang, H., Wang, W., Zheng, W., Wang, C., 2010. Improved hydrogen monitoring properties based on p-NiO/n-SnO_2 heterojunction composite nanofibers. J. Phys. Chem. C 114 (13), 6100–6105. https://doi.org/10.1021/jp9100202.

Wong, K.K.W., Douglas, T., Gider, S., Awschalom, D.D., Mann, S., 1998. Biomimetic synthesis and characterization of magnetic proteins (magnetoferritin). Chem. Mater. 10 (1), 279–285. https://doi.org/10.1021/cm970421o.

Xiong, Y., Xie, Y., Yang, J., Zhang, R., Wu, C., Du, G., 2002. In situ micelle–template–interface reaction route to CdS nanotubes and nanowires. J. Mater. Chem. 12 (12), 3712–3716. https://doi.org/10.1039/B206377H.

Xu, C., Tamaki, J., Miura, N., Yamazoe, N., 1991. Grain size effects on gas sensitivity of porous SnO_2-based elements. Sens. Actuators B 3 (2), 147–155. https://doi.org/10.1016/0925-4005(91)80207-Z.

Xu, Q., Meng, G., Han, F., Zhao, X., Kong, M., Zhu, X., 2009. Controlled fabrication of gold and polypyrrole nanowires with straight and branched morphologies via porous alumina template-assisted approach. Mater. Lett. 63 (16), 1431–1434. https://doi.org/10.1016/j.matlet.2009.03.026.

Yamaura, H., Jinkawa, T., Tamaki, J., Moriya, K., Miura, N., Yamazoe, N., 1996. Indium oxide-based gas sensor for selective detection of CO. Proceedings of the Sixth International Meeting on Chemical Sensors 36 (1), 325–332. https://doi.org/10.1016/S0925-4005(97)80090-1.

Yan, H., Song, P., Zhang, S., Zhang, J., Yang, Z., Wang, Q., 2016a. Au nanoparticles modified MoO_3 nanosheets with their enhanced properties for gas sensing. Sens. Actuators B 236, 201–207. https://doi.org/10.1016/j.snb.2016.05.139.

Yan, Y., Zhang, M., Moon, C.H., Su, H.-C., Myung, N.V., Haberer, E.D., 2016b. Viral-templated gold/polypyrrole nanopeapods for an ammonia gas sensor. Nanotechnology 27 (32), 325502. https://doi.org/10.1088/0957-4484/27/32/325502.

Yang, H.G., Zeng, H.C., 2004. Creation of intestine-like interior space for metal-oxide nanostructures with a quasi-reverse emulsion. Angew. Chem. Int. Ed. 43 (39), 5206–5209. https://doi.org/10.1002/anie.200460767.

Yang, H.X., Qian, J.F., Chen, Z.X., Ai, X.P., Cao, Y.L., 2007. Multilayered nanocrystalline SnO_2 hollow microspheres synthesized by chemically induced self-assembly in the hydrothermal environment. J. Phys. Chem. C 111 (38), 14067–14071. https://doi.org/10.1021/jp074159a.

Yang, Z., Niu, Z., Lu, Y., Hu, Z., Han, C.C., 2003. Templated synthesis of inorganic hollow spheres with a tunable cavity size onto core–shell gel particles. Angew. Chem. Int. Ed. 42 (17), 1943–1945. https://doi.org/10.1002/anie.200250443.

Yogeswaran, U., Chen, S.-M., 2008. A review on the electrochemical sensors and biosensors composed of nanowires as sensing material. Sensors 8 (1). https://doi.org/10.3390/s8010290.

Young, S., Balluz, L., Malilay, J., 2004. Natural and technologic hazardous material releases during and after natural disasters: A review. Sci. Total Environ. 322 (1), 3–20. https://doi.org/10.1016/S0048-9697(03)00446-7.

Yu, X., Li, Y., Kalantar-zadeh, K., 2009. Synthesis and electrochemical properties of template-based polyaniline nanowires and template-free nanofibril arrays: Two potential nanostructures for gas sensors. Sens. Actuators B 136 (1), 1–7. https://doi.org/10.1016/j.snb.2008.10.068.

Yun, S.H., Wu, J.Z., Dibos, A., Zou, X., Karlsson, U.O., 2006. Self-assembled boron nanowire Y-junctions. Nano Lett. 6 (3), 385–389. https://doi.org/10.1021/nl052138r.

Zhang, D., Qi, L., Ma, J., Cheng, H., 2002. Synthesis of submicrometer-sized hollow silver spheres in mixed polymer–surfactant solutions. Adv. Mater. 14 (20), 1499–1502. https://doi.org/10.1002/1521-4095(20021016)14:20<1499::AID-ADMA1499>3.0.CO;2-5.

Zhang, D., Wang, K., Tong, J., Xia, B., 2014. Characterization of layer-by-layer nano self-assembled carbon nanotube/polymer film sensor for ethanol gas sensing properties. Microsystem Technologies 20 (3), 379–385. https://doi.org/10.1007/s00542-013-1943-4.

Zhang, G.-Y., Guo, B., Chen, J., 2006. MCo_2O_4 (M = Ni, Cu, Zn) nanotubes: Template synthesis and application in gas sensors. Sens. Actuators B 114 (1), 402–409. https://doi.org/10.1016/j.snb.2005.06.010.

Zhang, M., Yan, Y., Gong, K., Mao, L., Guo, Z., Chen, Y., 2004. Electrostatic layer-by-layer assembled carbon nanotube multilayer film and its electrocatalytic activity for O_2 reduction. Langmuir 20 (20), 8781–8785. https://doi.org/10.1021/la048923l.

Zhang, X.-J., Qiao, G.-J., 2012. High performance ethanol sensing films fabricated from ZnO and In_2O_3 nanofibers with a double-layer structure. Appl. Surf. Sci. 258 (17), 6643–6647. https://doi.org/10.1016/j.apsusc.2012.03.098.

Zhang, Y., Liu, J., He, R., Zhang, Q., Zhang, X., Zhu, J., 2002. Synthesis of alumina nanotubes using carbon nanotubes as templates. Chem. Phys. Lett. 360 (5), 579–584. https://doi.org/10.1016/S0009-2614(02)00874-6.

Zhao, H., Liu, L., Lei, Y., 2018. A mini review: Functional nanostructuring with perfectly-ordered anodic aluminum oxide template for energy conversion and storage. Frontiers of Chemical Science and Engineering 12 (3), 481–493. https://doi.org/10.1007/s11705-018-1707-x.

Zhao, Q., Gao, Y., Bai, X., Wu, C., Xie, Y., 2006. Facile synthesis of SnO_2 hollow nanospheres and applications in gas sensors and electrocatalysts. Eur. J. Inorg. Chem. 2006 (8), 1643–1648. https://doi.org/10.1002/ejic.200500975.

Zhong, Z., Yin, Y., Gates, B., Xia, Y., 2000. Preparation of mesoscale hollow spheres of TiO_2 and SnO_2 by templating against crystalline arrays of polystyrene beads. Adv. Mater. 12 (3), 206–209. https://doi.org/10.1002/(SICI)1521-4095(200002)12:3<206::AID-ADMA206>3.0.CO;2-5.

Zhu, C., Guo, S., Zhai, Y., Dong, S., 2010. Layer-by-layer self-assembly for constructing a graphene/platinum nanoparticle three-dimensional hybrid nanostructure using ionic liquid as a linker. Langmuir 26 (10), 7614–7618. https://doi.org/10.1021/la904201j.

5

An introduction to biosensors

Shibi Thomas[a], **K.J. Saji**[b,c] **and M.K. Jayaraj**[d,e]

[a]*Department of Physics, Bharata Mata College, Thrikkakara, Kochi, India.* [b]*Centre of Excellence in Advanced Materials, Cochin University of Science and Technology, Kochi, India.* [c]*International School of Photonics, Cochin University of Science and Technology, Kochi, India.* [d]*University of Calicut, Malappuram, India.* [e]*Cochin University of Science and Technology, Kochi, India*

5.1 Introduction

A biosensor is an analytical device that transforms biochemical reactions into a measurable signal proportional to analyte concentration (Arora, 2013). Biosensors constitute promising tools that are applicable in wide areas such as the fields of biomedical, environmental monitoring, food processing, and other fields where fast and authentic analyses are needed (Rastislav et al., 2012). In addition to these day-to-day applications, biosensors can also serve as low-cost sense contaminating bioagents in the atmosphere. A widely accepted definition for biosensors is: "a biosensor is a chemical sensing device in which a biologically derived recognition entity is coupled to a transducer, to allow the quantitative development of some complex biochemical parameter." One of the major applications of biosensors so far is in blood glucose sensing because of its abundant market potential. In spite of its potential, nowadays, commercial adoption has been slowed down due to various technical problems like environmental contamination due to the presence of biomolecules (S.P. & E., 2006). Researchers from different fields such as physics, chemistry, biology, engineering, and medicine are interested in evolving and manufacturing efficient and reliable sensing devices to get rapid and reliable information (Sagadevan & Periasamy, 2014).

Nanotechnology has an important role in the development of biosensors. The detection limit, reliability, and sensitivity of biosensors can be enhanced using nanomaterials. Nanomaterials possess unique physical and chemical features due to various effects such as the quantum size effect, various surface effects, and quantum tunnel effect. It has been demonstrated that the physical and chemical properties of nanomaterials have a strong influence on the performance of

Nanomaterials for Sensing and Optoelectronic Applications. DOI: https://doi.org/10.1016/B978-0-12-824008-3.00013-8

biosensors (Bin et al., 2010; Lei & Ju, 2012). Nanosensors, nanoprobes, and other nanosystems are revolutionizing the fields of chemical and biological sensors to enable the rapid analysis of multiple substances due to their submicron size. Different types of nanomaterials, like gold nanoparticles, carbon nanotubes (CNTs), magnetic nanoparticles, and quantum dots, are being applied to biosensors because of their distinctive physical, chemical, optical, mechanical, and magnetic properties, along with enhanced reliability and sensitivity of detection (Ali et al., 2017; Sagadevan & Periasamy, 2014). The latest development in nanomaterial-based biosensors is the use of two-dimensional (2D) materials for developing ultrafast and ultrasensitive sensors. Numerous biosensors have been reported with graphene (Bitounis et al., 2013; He et al., 2010; Liu et al., 2013), the first 2D material, and many other 2D materials like transition metal dichalcogenides (TMDCs) and transition metal oxides (Subbaiah et al., 2016). With a single or few layers of atoms, 2D materials typically offer the advantage of the largest surface area for analyte detection and the possibility to explore biosensors based on new detection principles, owing to the extreme charge confinement effects in such materials (Oh et al., 2021).

5.2 Fundamentals of biosensors

A biosensor is a device that amalgamates a biological recognition element with a transducer, i.e., a biosensor is a probe that integrates a biorecognition element with an electronic component to yield a measurable signal. A biosensor consists of three essential components: a biological recognition element, a transducer, and a signal processing unit. The bioelement can be any organic body that detects any particular analyte from the medium of interest. The sensing element consists of a transducer, which can be magnetic, optical, electrical, electrochemical, etc. A biosensor should possess rapid sensitivity, reliability, portability, productivity, and long-lasting stability. Some important parameters that play a very crucial role in the manufacturing of biosensors are immobilization/fabrication of biorecognition element, high accessibility of the reception sites to the species of interest, successful adsorption of the analyte, etc. All these demands should be actively addressed while designing biosensors (Ali et al., 2017).

A typical biosensor has five different levels of functions, as shown in Fig. 5.1: (1) a bioreceptor or bioelement (bacterium, antibodies, nucleic acids, enzymes, etc.) that accepts the specific analyte from the sample; (2) an electrical interface in which biological processes occur; (3) a transducer that converts the biochemical reaction into an electronic signal; (4) the signal processor, which converts the electronic signal into a physical parameter; and finally, (5) an interface to display the results (Sagadevan & Periasamy, 2014). The

bioreceptor/bioelement shall not recognize any other analyte and is very specific to the analyte to which it is sensitive. The analytes of interest may be not only biological in nature (such as DNA, protein, cell, exosome, etc.) but also ions, dissolved gases, drugs, and toxins. When a bioreceptor element recognizes a specific analyte and eventually binds it, the transducer element provides quantitative or semiquantitative information about the target by converting the physico-chemical signal generated during the biorecognition event into a measurable electrical signal (Chen & Shamsi, 2017). The fundamental idea of the biosensor was first pointed out by Leland C. Clark Jr., the father of the biosensor concept. His fabulous idea of the Clark oxygen electrode became the basis for a wide range of bioanalytical instruments. One of the classic examples is immobilized glucose oxidase (GOx), which transforms a simple platinum electrode into an efficient scientific instrument for the detection of glucose levels in human samples (Turner, 2013).

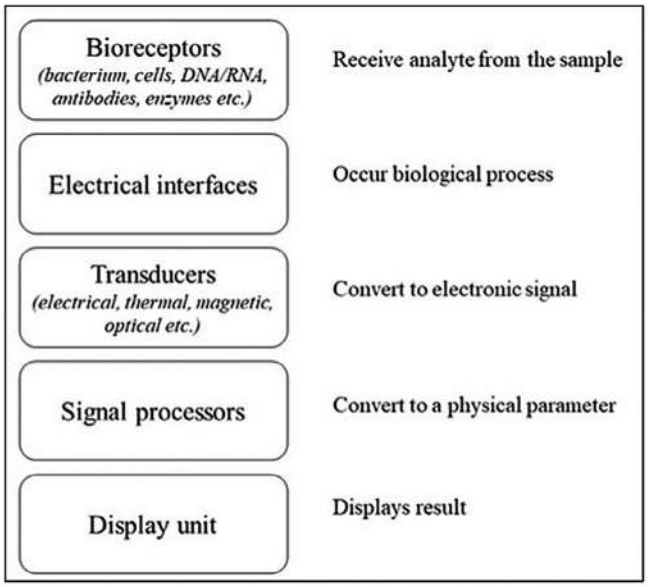

Figure 5.1. Schematic representation of components and functionalities of a typical biosensor.

5.3 Classification of biosensors

Biosensors can be classified based on the order of their discovery into first-, second-, and third-generation biosensors. First-generation biosensors involve the direct detection of either an increase of an enzymatically generated product or a decrease of a substrate of redox enzymes using a natural mediator for electron transfer, for example, a glucose biosensor (Arora, 2013). Second-generation biosensors use artificial redox mediators like ferrocene, ferricyanide, and quinones for electron transfer, which increases their reproducibility and sensitivity. A typical example is self-monitoring amperometric glucose sensors. In third-generation biosensors the redox enzymes are immobilized on the electrode surface in such a manner that direct electron transfer is possible between the enzyme and transducer.

Biosensors can also be classified based on their transduction principle into categories such as electrochemical (including amperometric, potentiometric, and conductometric), electrical (including field-effect transistor [FET]–based), optical (including fluorescence and surface plasmon resonance [SPR]–based), piezoelectric (including quartz

crystal microbalance [QCM] biosensors), and calorimetric (thermometric) or based on their recognition element, such as immunosensors, aptasensors, genosensors, and enzymatic biosensors, when antibodies, aptamers, nucleic acids, and enzymes are used (Justino et al., 2017; S.P. & E., 2006).

5.3.1 Classification by transduction mechanism

5.3.1.1 Electrochemical biosensors

An electrochemical biosensor transforms the interaction between the target and the biomolecule into an electric current or potential. Among the various available biorecognition elements, enzymes are the most used biorecognition element owing to their specific binding ability as well as biocatalytic activity (Rastislav et al., 2012). Electrochemical biosensors are categorized according to the signal property, which allows the quantification based on biological fluctuations into amperometric, potentiometric, and conductometric biosensors.

Amperometric

Amperometric biosensors are the most commonly used biosensors. Most biochemicals can be detected and quantified amperometrically by using their enzyme-catalyzed electrooxidation or electroreduction process. The working electrode is normally a noble metal or screen-printed layer covered by the bioelement. The modern option is to use CNTs. At the applied working potential, the conversion of electroactive species generated in the enzyme layer occurs at the electrode and the resulting current (typically in the nA to μA range) is measured.

Potentiometric

The potentiometric transducer calculates the difference in potential that is generated across an ion-selective membrane separating two solutions at virtually zero current flow. Potentiometric sensors such as glass electrodes, metal oxide–based sensors, and ion-selective electrodes are usually available (Rastislav et al., 2012). Moreover, they can be easily mass fabricated in miniature form using advanced thin-film technologies.

Conductometric (Impedimetric)

The conductivity or resistivity of a solution changes when ions or electrons are produced during the biochemical reaction. The parameter measured using this type of transducer is the electrical

conductance/resistance of the solution (Rastislav et al., 2012). Conductance measurements have comparatively low sensitivity.

5.3.1.2 FET-based electronic transducer

An electronic transducer directly converts the reaction between the biological detector element and the analyte to an electrical signal (Jeho et al., 2014). In field-effect transistors (FETs) the charges on the analyte create a modulation of the electrical conductivity of a channel by the externally induced electric field. The external field, however, penetrates only a short distance into the material and this distance is very limited even in semiconductors that have a lower density of electrons or holes. FET-based electrical transducers have the potential to be used to make very sensitive, label-free, and real-time biosensors.

5.3.1.3 Optical transducers

Optical transduction recognizes changes in the optical properties in the form of absorption, emission, transmittance, scattering, reflection, refraction, etc., of the transducer surface induced by the biorecognition event (Chen & Shamsi, 2017). In optical biosensors the transducer signal output is quantified as light. The interaction between the target and receptors, immobilized on the transducer surface, leads to a variation in refractive index, which is subsequently detected and quantified based on transducer illuminations. Various optical biosensing approaches are categorized into absorption spectroscopy, fluorescence and SPR and so on.

5.3.1.4 Piezoelectric (mass-sensitive)

Biosensors based on mechanical transduction are mass-sensitive label-free transducers, and examples include surface acoustic wave (SAW) sensors and QCM. An SAW sensor detects variations in the velocity of an SAW using interdigitated transducers (IDTs) on a ceramic resonator or quartz crystal–based piezoelectric substrate (Chen & Shamsi, 2017). QCM detects a change in the resonating frequency of a piezoelectric quartz crystal transducer. An applied external electrical potential to a piezoelectric material produces internal mechanical stress and it oscillates quartz crystal at its resonance frequency.

5.3.1.5 Calorimetric (Thermometric)

This type of biosensor is manufactured via the immobilization of biomolecules onto temperature sensors (Rastislav et al., 2012). When the analyte comes in contact with the biorecognition element, heat is generated as a result of a chemical reaction, which is proportional

to the analyte concentration. The total amount of heat produced or absorbed in a reaction is proportional to the molar enthalpy and to the total number of molecules in the reaction. The enzyme thermistors measure the temperature of such a system.

5.3.2 Classification by biorecognition layer

5.3.2.1 Enzymes

Enzymes are widely used as biorecognition elements for the development of biosensors. These biosensors utilize enzymes that are specific to the desired molecules and catalyze biochemical reactions, which are then directly determined using transducers (Rastislav et al., 2012). Glucose biosensors are the most successful and commercially available biosensors that use enzymes like GOx or glucose dehydrogenase. Many factors like enzyme loading, the use of a suitable pH, and temperature have an influence on the performance of enzyme-based biosensors.

5.3.2.2 Antibodies

An antibody is a network of biomolecules that is made up of hundreds of individual amino acids arranged in a specific ordered sequence. An antigen-specific antibody matches its unique antigen in a distinct way. This particular property of antibodies is crucial to their usefulness in immunosensors, where only the specific analyte of interest, the antigen, fits into the antibody binding site.

5.3.2.3 Nucleic acids

Biosensors based on DNA, RNA, and peptide nucleic acid gain their high reactivity and selectivity from the very strong base-pair affinity between complementary sections of lined-up nucleotide strands (Chen & Shamsi, 2017; Rastislav et al., 2012). Nucleic acid (NA)–based biosensors integrate an NA (natural and biomimetic forms of oligo- and polynucleotides) as the biological recognition element. Synthetic oligodeoxyribonucleotides (ODNs) are used as probes in the DNA hybridization sensors. End-labels, such as thiols, disulfides, amines, or biotin, are integrated to immobilize ODNs to transducer surfaces.

5.3.2.4 Cells

In a cell-based system the biorecognition is done by an entire cell/microorganism or a specific cellular element capable of specific binding to definite species. The main advantage of using this type of bioreceptor is that the detection limits can be very low because of signal amplification. Cell-based biosensors can execute real-time bioassays

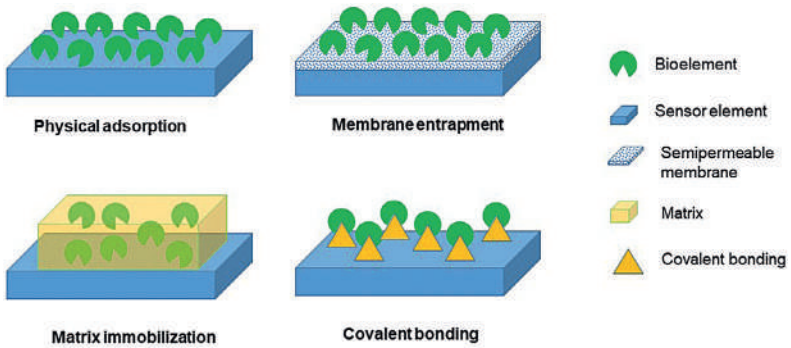

Figure 5.2. Various kinds of biomaterial–sensor coupling mechanisms.

very rapidly and have wide applications varying from biomedicine to environmental monitoring (Rastislav et al., 2012).

5.4 Coupling/Immobilization methods

One of the most crucial parts of biosensor fabrication is the immobilization of the biomolecule on the sensor head. Various factors that affect the performance of biosensors with immobilized molecules are the chemical and physical conditions (pH, temperature, and contaminants), thickness, and stability of the materials (Rastislav et al., 2012). The most commonly used immobilization techniques for the construction of biosensors are membrane entrapment/immobilization, physical adsorption, matrix entrapment, and covalent bonding, as demonstrated in Fig. 5.2.

In the physical adsorption method the coupling of different types of forces like van der Waals forces, hydrophobic forces, hydrogen bonds, and ionic forces is held together to attach the biomaterial to the surface of the sensor. In the membrane entrapment technique a semipermeable membrane separates the analyte and the bioelement, and the sensor is attached to the bioelement. Here the organic element is embedded into the particular semipermeable membrane that is directly placed over the sensor element. In this type the membrane acts as a separating phase between the organic element and the analyte (Chen & Shamsi, 2017; S.P. & E., 2006). If any porous material, like sol or gel matrices, is used as the restricting medium for the biological element and this matrix encapsulation forms a direct link with the sensor element, it is called matrix immobilization (Chen & Shamsi, 2017). For the covalent bonding method, the sensor surface is treated as a reactive group to which the biological materials can bind, and hence in the covalent coupling the bioelement and the sensor element are directly attached by covalent interactions (S.P. & E., 2006).

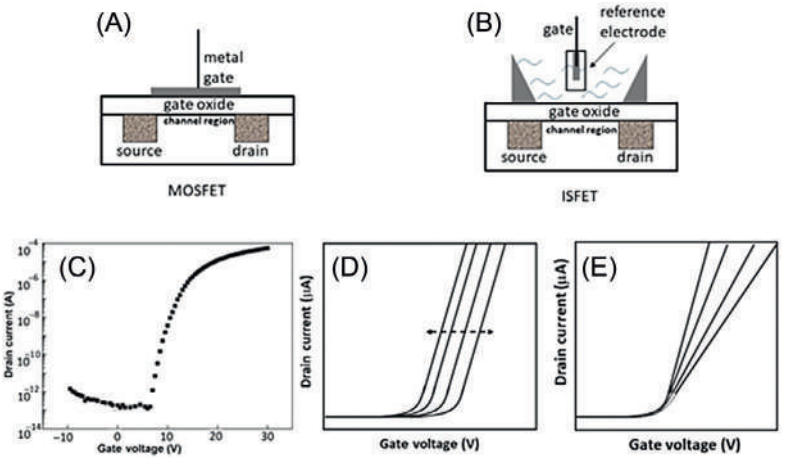

Figure 5.3. Schematic diagram of (A) MOSFET and (B) ISFET. (C) Transfer curve of an n-channel MOSFET, (D) typical threshold voltage shift when the dielectric layer is exposed to an analyte, and (E) change in transconductance when the channel layer is exposed to an analyte.

5.5 Field-effect transistor biosensors

Nowadays, increasing interest has been garnered by the FET-based biosensor, which is the most attractive electrical biosensor due to its outstanding benefits like greater signal-to-noise ratio (SNR), fast measurement capabilities with small amounts of sample requirement, compact or portable instrumentation, low cost with mass-production capability, and high-speed and efficient integration with other electronic components (Jeho et al., 2014). FET-based devices have innumerable biological applications comprising the recognition of several biological elements like small molecules, proteins, DNA, peptides, and cells. A number of FET-based biosensors have been developed to study biomolecular interactions, which are the key drivers of biological responses in in vitro or in vivo systems. FET-based biosensors have been considered better candidates for next-generation point-of-care testing (POCT) (Syu et al., 2018).

The metal–oxide–semiconductor FET (MOSFET) is the commonly used FET device. In its simple configuration a MOSFET consists of source and drain contacts on either side of a semiconducting channel layer. The electrical conductance of this channel layer or, in other words, the flow of charge carriers between the source and drain terminals, is modulated by an electric field generated by applying a suitable voltage to a third electrode called a gate, which is physically separated from the channel layer by an oxide dielectric, as shown in Fig. 5.3A. Depending on the type of charge carrier induced in the channel by the action of the gate field, the FET can be either n-channel (electrons) or p-channel (holes). The typical transfer characteristics of an n-channel FET, obtained by scanning the voltage between the gate and source terminals for a fixed small voltage applied between the source and

drain terminals, are shown in Fig. 5.3C. The shape of this characteristic curve strongly depends on the nature of the gate insulator and the conditions prevailing at the gate region and channel layer (Mohanty et al., 2012). When used for sensing applications, either the dielectric layer or the channel layer can be exposed to the analyte. In the former case adsorbed analytes cause a change in the capacitance, which in turn causes a change in the charge carrier density in the channel, leading to a change in the drain current (I_{DS}). This is manifested as a change in the threshold voltage of the FET, as shown in Fig. 5.3D. When the channel layer is exposed, the adsorbed analytes directly influence the conductance of the channel layer. This is manifested as a change in the transconductance or mobility of the charge carrier (Fig. 5.3E).

In biological sensing FETs (BioFETs) the conventional physical gate is removed and the dielectric layer is functionalized with specific receptors to selectively absorb the target biomolecule. This biomolecule (which is usually charged) absorption on the gate electrostatically modulates the conductance of the channel region, which is reflected in the performance metrics (threshold voltage, field-effect mobility, on/off ratio, subthreshold swing, etc.) of the transistor (Jeho et al., 2014). This gating effect is also possible by using other methods like covering the sensing channel region with polymers/lipids, which enables functionalization for specific biomolecule absorption, or by the direct functionalization of the channel layer material with specific receptors. In another approach the channel layer can be directly functionalized with antibodies without an intermediate dielectric layer. Biomolecule reception in such cases induces disorders in the channel potential and hence affects the on-state transconductance of the transistor. Biomolecule detection is usually quantified in terms of variations in the FET performance metrics. There are many advantages to using a FET biosensor in biological sensing. MOSFET-based biosensors are very useful for detecting the DNA-binding activity of proteins (Han et al., 2010). However, the shorter Debye screening length is a fundamental issue for FET devices. The Debye length specifies the spatial extent of the sensed bound charge on the sensor or how far its electrostatic effects persist. Several attempts have been made to explore a better FET architecture with advanced performance and to conquer the physical limitations of the FET technology in recent years (Jeho et al., 2014).

FET-based sensors can be devised either using a gate electrode (conventional FET) or without a conventional gate electrode (ion-selective FET [ISFET]). The metal gate electrode in an ISFET is replaced with an ion-selective electrode, an electrolyte solution, and a reference electrode (Fig. 5.3B). The magnitude of the current of an ISFET device depends on the charge density of the analyte molecules on the gate surface. Park et al. were the first to describe the application of an ISFET-based biosensor to measure conformational changes in proteins

(Park et al., 2009; Syu et al., 2018). For the accurate detection of biomolecules, the reference electrode in ISFET needs to provide a constant stable potential during the operation. Finding a compact, stable reference electrode is a challenge in this field (Kaisti, 2017).

Antibodies are the most widely used capture agents for identifying, isolating, and quantifying analytes of interest due to their specificity to the binding antigen. When antigen–antibody binding occurs (Fig. 5.3), a change in the gate potential arises, which varies the charge density on the surface and it is an important factor when measuring the interaction patterns of biomolecules using FET-based biosensors. Park et al. reported the ISFET-based detection of a CRP (C-reactive protein) antigen and its concentration as a useful indicator of inflammation in the early stages of an infection (Park et al., 2009). FETs can also be used to investigate enzyme-catalyzed reactions quantitatively and qualitatively. These enzymatic reactions allow the accumulation of charge carriers at the gate surface in proportion to the analyte concentration. The concentration of the charge carriers accumulated onto the gate electrode increases in accordance with the enzyme–substrate reaction until the substrate molecules are depleted. This enzymatic reaction can cause a measurable change in the electrical signal between the source (S) and the drain (D). A common example of an enzyme FET is the glucose-sensitive FET sensor, which has a glucose oxidase membrane-modified gate surface and is used to determine the level of glucose in the blood (Jeho et al., 2014).

FET-based biosensors can be used for specific interactions of biomolecules, such as enzymatic reactions, DNA hybridization, and antibody–antigen reactions (Sang et al., 2016). Depending on the type of biomolecules, there are different types of biosensors like enzyme-based FETs (ENFETs), cell-based FETs, and immune detection–based FETs (ImmunoFETs). ENFETs are a combined form of ISFETs with enzymes, are based on biocatalytic reactions affecting the charge at the gate surface, and produce an electronic signal dependent on the enzyme–substrate concentration. The various kinds of enzymes studied by ENFETs include glucose oxidase, urease, and penicillinase. Cell-based FETs are exploited for the detection of cell metabolism and analysis of the interaction of drugs and cells. They can also record electric potentials inside cells. The nanotube can penetrate the cell membrane, bringing the cell cytosol in contact with the FET, and hence is able to record the intracellular transmembrane potential. ImmunoFETs are the most frequently used biosensors. They detect the charged antigens related to serious diseases using immobilized antibody-modified FETs (Sang et al., 2016). Sarangadharan et al. (2018) reported the study of high field gated FET biosensors engineered to directly detect target analytes in a physiological salt environment. A few biomedical applications using high field gated FET biosensors have been demonstrated,

such as direct protein detection in serum/whole blood and DNA/RNA detection in 1X phosphate buffered saline (PBS).

The major challenge for FET-based biological sensing is the selection of appropriate channel materials that provide fast detection in low concentration regimes. Many types of nanomaterials have been widely used as promising candidates for FET biosensors. One-dimensional (1D) semiconducting nanomaterials configured with FETs offer opportunities for real-time and label-free sensing applications, such as silicon nanowires (SW) and CNTs. Persnova et al. developed a FET biosensor using silicon nanowires for the detection of prostate-specific antigen (PSA) in human serum (Presnova et al., 2017). These 1D structures suffer from fundamental constraints in terms of both sensitivity and detection limits.

2D semiconducting nanomaterials, like graphene, have attracted great attention as they can be used for developing biosensors with high selectivity and sensitivity because of their excellent electrostatics due to their atomically thin structure (Sang et al., 2016). It also is of a planar nature, which enables large-scale integrated device processing and fabrication. However, sensitivity is limited in graphene-based FETs due to a lack of bandgap. Unlike this, TMDCs have a sizable bandgap and have unique physical properties. TMDCs like MoS_2 have 2D stacked layers of covalently bonded transition metals and dichalcogenide atoms kept together in a hexagonal lattice with weak interlayer van der Walls forces. MoS_2 based FET have wide application in biosensors devices (Tong et al., 2015). Unlike graphene-based FETs, 2D MoS_2 FETs help suppress direct source-to-drain tunneling leakage currents and hence ensure better switching. Most oxide dielectrics are hydrophilic and hence have relatively low affinity to biomolecule adsorption. Therefore in order to monitor the binding events the oxide surface needs to be treated with additional chemicals if an ISFET geometry is used. However, MoS_2 deposited on oxide surface has hydrophobic nature and hence it shows a higher affinity to biomolecule binding. Therefore MoS_2 can be used either as a surface-adsorption layer on gate oxide or as a sensing channel layer. Hydrophobic MoS_2 surface allows the physical adsorption of biomolecules onto the sensor surface.

Sarkar et al. have reported a MoS_2-based FET biosensor in an aqueous environment and operating in the subthreshold region for the ultrasensitive and specific detection of biomolecule (Sarkar et al., 2014). They showed that this biosensor achieves excellent sensitivity in pH sensing and in biomolecule detection (Fig. 5.4). Here micromechanical exfoliation techniques were used for the preparation of MoS_2 flakes and the device was fabricated on a 270-nm SiO_2/Si substrate. A fluidic channel for transferring the electrolyte is fabricated using an acrylic sheet. It is important that the devices operate in a wet environment

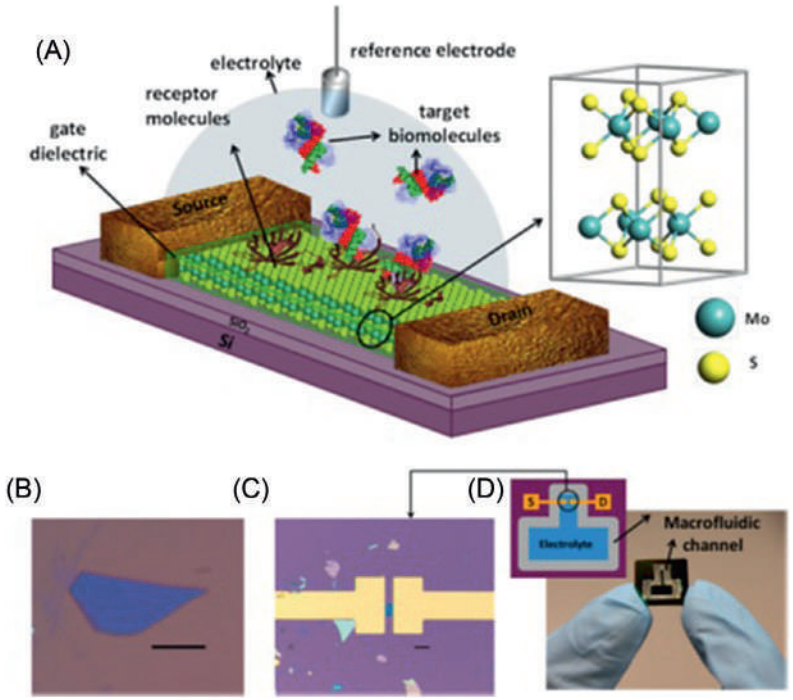

Figure 5.4. MoS_2-based FET biosensor device. (A) Schematic diagram of a MoS_2-based FET biosensor. For biosensing, the dielectric layer covering the MoS_2 channel is functionalized with receptors for specifically capturing the target biomolecules. The charged biomolecules, after being captured, induce a gating effect, modulating the device current. An electrolyte gate in the form of a Ag/AgCl reference electrode is used for applying bias to the electrolyte. The source and drain contacts are also covered with a dielectric layer to protect them from the electrolyte (not shown in this figure). (B) Optical image of a MoS_2 flake on 270-nm SiO_2 grown on degenerately doped Si substrate. Scale bar, 10 μm. (C) Optical image of the MoS_2 FET biosensor device showing the extended electrodes made of Ti/Au. Scale bar, 10 μm. (D) Image and schematic diagram (inset figure) of the chip with the biosensor device and macrofluidic channel for containing the electrolyte. Reprinted with permission from Sarkar, D., Liu, W., Xie, X., Anselmo, A. C., Mitragotri, S., & Banerjee, K. (2014). MoS_2 field-effect transistor for next-generation label-free biosensors. ACS Nano, 8(4), 3992–4003. © 2014 American Chemical Society.

for the biosensing application. Hence the devices were measured in a wet environment by transferring the electrolyte solution to the fluidic channel (Sarkar et al., 2014).

The MoS_2 biosensor detects the pH changes in the electrolyte solution (Fig. 5.4). The pH sensing was done by the protonation/deprotonation of the OH groups on the gate dielectric depending on the pH value of the electrolyte, which produces a change in the dielectric surface charge. This pH-dependent surface charge, together with the electrolyte gate voltage applied through the reference electrode, determines the effective surface potential of the dielectric. A significant increase in current was obtained at a particular applied bias with a decrease in pH value, leading to the successful demonstration of the MoS_2 pH sensor (Sarkar et al., 2014). Thus a MoS_2-based pH sensor with ultrahigh sensitivity (713 for a pH change of 1 unit) as well as a wide operation range (pH of 3 to 9) was demonstrated. Also, specific sensing of biomolecules using the MoS_2 biosensor was investigated through the well-known biotin–streptavidin interaction where the biotin and streptavidin act as models for receptor and target molecules, respectively.

Liu et al. (2014) developed chemical sensors using Schottky-contacted CVD-grown monolayer MoS_2 FET. Some of the optical and

electronic properties of MoS_2 FET devices are unique and superior to usual semiconductor FET devices, hence rendering them suitable for novel electronic and optoelectronic applications. This label-free, ultrasensitive, highly flexible sensor is very cheap and its low power consumption provides great opportunities in healthcare and security applications.

Recently, COVID-19 has locked people across the world and brought our global economic growth to a halt. FET biosensors were proven to be an accurate and efficient method to detect this virus. Recently Sadighbayan et al. (2020) proposed the use of FET biosensors for the detection of viruses such as COVID-19. They developed FET biosensors for identifying SARS-CoV-2 in biological fluids. This device was fabricated by modifying sheets of graphene as the sensing material with a monoclonal antibody specific to the SARS-CoV-2 spike protein. It was a successful approach and their work also involves the detection of many other viruses too. The FET technology is found to be very effective for detecting a variety of such infectious diseases (Panahi et al., 2021).

5.6 Applications of biosensor

Biosensors have been utilized in many areas like medical and health care (for monitoring glucose, lactose levels in the body, analytical measurement of folic acid, biotin, vitamin B_{12}, etc.), pharmaceutical (estimation of drug residues in food, such as antibiotics and growth promoters), environmental (detection of pesticides and river water contaminants), defense (remote sensing of airborne bacteria, e.g., in counter-bioterrorist activities), and food technology (microbial biosensor, pathogen detection). Biosensors play a significant role in tissue engineering as well (Chen & Shamsi, 2017).

In order to avoid hazards to human health and to the surroundings a mechanism to understand, detect, and remove contaminants from the surroundings, like water, soil, and air within affordable costs, quite quickly, and with enhanced precision has to be adopted today and this can be achieved using the biosensing techniques. Different types of biosensors based on enzymatic inhibition and those based on DNA with high specificity to certain DNA, RNA, or proteins that they can encounter have been used for the removal of contaminants like pesticides, other toxins, and heavy metals from the soil, air, and water, including many other versatile types of biosensors (Ali et al., 2017).

Several types of biosensors have provided great success in the detection and monitoring of the toxic levels of heavy metals that would lead to injurious health conditions. Bacteria-based cell biosensors require the use of genes that resist certain types of heavy metals like

copper, mercury, tin, and cobalt. In order to ensure the safety of processed foodstuffs specific methods have been adopted by food industries to sort out problems leading to food spoilage and the detection and destruction of such chemicals or biological agents that are responsible for the spread of some serious health-related problems. Biosensors, being target specific, are highly sensitive, and quickly responsive, would be helpful in that regard to enable us to determine the cause of chemical activities that lead to food spoilage, not only that of canned and industrial food products but also food crops. There are many known types of biosensors, but in the food industry mainly enzyme-based biosensors and immunosensors are commonly employed.

5.7 Summary

This chapter describes and characterizes different classes of biosensors according to the utilized types of bioelements, transducers, and methods of entrapment. Working principles, constructions, advantages, and applications of many biosensors are presented. Biosensors represent promising analytical tools applicable in areas such as clinical diagnosis, food industry, environmental monitoring, and all fields where rapid and reliable analyses are needed. FETs are label-free, sensitive, and selective electronic biosensors. Due to the advantages of sensitivity, selectivity, miniaturization, lightweight, low power consumption, and seamless fitting in electronic read-out systems, FET-based biosensors have become competitive candidates for future POCT applications in contrast to bulky optical-based instruments. In summary, FET-based biosensors are most suitable for POCT and would initiate a diagnostic revolution for next-generation development. Within a few years, FET biosensors will find their way from the laboratory to the market, especially for the early detection of various infectious diseases.

References

Ali, J., Najeeb, J., Asim Ali, M., Farhan Aslam, M., Raza, A. (2017). Biosensors: Their fundamentals, designs, types and most recent impactful applications: A review. Journal of Biosensors and Bioelectronics, 08(01), 1–9. https://doi.org/10.4172/2155-6210.1000235

Arora, N., 2013. Recent Advances in Biosensors Technology: A Review. Octa. J. Biosci. 1, 147–150.

Bin, X., Sargent, E.H., Kelley, S.O., 2010. Nanostructuring of sensors determines the efficiency of biomolecular capture. Anal. Chem. 82 (14), 5928–5931. https://doi.org/10.1021/ac101164n.

Bitounis, D., Ali-Boucetta, H., Hong, B.H., Min, D.H., Kostarelos, K., 2013. Prospects and challenges of graphene in biomedical applications. Adv. Mater. 25 (16), 2258–2268. https://doi.org/10.1002/adma.201203700.

Chen, S., Shamsi, M.H., 2017. Biosensors-on-chip: A topical review. J. Micromech. Microeng. 27 (8). https://doi.org/10.1088/1361-6439/aa7117.
Han, S.H., Kim, S.K., Park, K., Yi, S.Y., Park, H.J., Lyu, H.K., Kim, M., Chung, B.H., 2010. Detection of mutant p53 using field-effect transistor biosensor. Analytica Chimica Acta 665 (1), 79–83. https://doi.org/10.1016/j.aca.2010.03.006.
He, S., Song, B., Li, D., Zhu, C., Qi, W., Wen, Y., Wang, L., Song, S., Fang, H., Fan, C., 2010. A craphene nanoprobe for rapid, sensitive, and multicolor fluorescent DNA analysis. Adv. Funct. Mater. 20 (3), 453–459. https://doi.org/10.1002/adfm.200901639.
Jeho, P., Hiep, N.H., Abdela, W., Moonil, K., 2014. Applications of field-effect transistor (FET)-type biosensors. Applied Science and Convergence Technology 61–71. https://doi.org/10.5757/ASCT.2014.23.2.61.
Justino, C.I.L., Duarte, A.C., Rocha-Santos, T.A.P., 2017. Recent progress in biosensors for environmental monitoring: A review. Sensors (Switzerland) 17 (12). https://doi.org/10.3390/s17122918.
Kaisti, M., 2017. Detection principles of biological and chemical FET sensors. Biosens. Bioelectron. 98, 437–448. https://doi.org/10.1016/j.bios.2017.07.010.
Lei, J., Ju, H., 2012. Signal amplification using functional nanomaterials for biosensing. Chem. Soc. Rev. 41 (6), 2122–2134. https://doi.org/10.1039/c1cs15274b.
Liu, B., Chen, L., Liu, G., Abbas, A.N., Fathi, M., Zhou, C., 2014. High-performance chemical sensing using Schottky-contacted chemical vapor deposition grown monolayer MoS_2 transistors. ACS Nano 8 (5), 5304–5314. https://doi.org/10.1021/nn5015215.
Liu, J., Wang, C., Jiang, Y., Hu, Y., Li, J., Yang, S., Li, Y., Yang, R., Tan, W., Huang, C.Z., 2013. Graphene signal amplification for sensitive and real-time fluorescence anisotropy detection of small molecules. Anal. Chem. 85 (3), 1424–1430. https://doi.org/10.1021/ac3023982.
Mohanty, P., Chen, Y., Wang, X., Hong, M.K., Rosenberg, C.L., Weaver, D.T., Erramillia, S, 2012. Field effect transistor nanosensor for breast cancer diagnostics. In: Herold, K.H., Rasooly, A. (Eds.), Invited Review in Biosensors and Molecular Technologies for Cancer Diagnostics. CRC Press. https://doi.org/10.48550/arXiv.1401.1168.
Oh, S.H., Altug, H., Jin, X., Low, T., Koester, S.J., Ivanov, A.P., Edel, J.B., Avouris, P., Strano, M.S., 2021. Nanophotonic biosensors harnessing van der Waals materials. Nat. Commun. 12 (1). https://doi.org/10.1038/s41467-021-23564-4.
Panahi, A., Sadighbayan, D., Forouhi, S., Ghafar-Zadeh, E., 2021. Recent advances of field-effect transistor technology for infectious diseases. Biosensors 11 (4), 103. https://doi.org/10.3390/bios11040103.
Park, H.J., Kim, S.K., Park, K., Lyu, H., Lee, C., Chung, S.J., Yun, W.S., Kim, M., Chung, B.H., 2009. An ISFET biosensor for the monitoring of maltose-induced conformational changes in MBP. FEBS Lett. 583 (1), 157–162. https://doi.org/10.1016/j.febslet.2008.11.039.
Presnova, G., Presnov, D., Krupenin, V., Grigorenko, V., Trifonov, A., Andreeva, I., Ignatenko, O., Egorov, A., Rubtsova, M., 2017. Biosensor based on a silicon nanowire field-effect transistor functionalized by gold nanoparticles for the highly sensitive determination of prostate specific antigen. Biosens. Bioelectron. 88, 283–289. https://doi.org/10.1016/j.bios.2016.08.054.
Rastislav, M., Miroslav, S., Ernest, Š., 2012. Biosensors—classification, characterization and new trends. Acta Chimica Slovaca 109–120. https://doi.org/10.2478/v10188-012-0017-z.
Sadighbayan, D., Hasanzadeh, M., Ghafar-Zadeh, E., 2020. Biosensing based on field-effect transistors (FET): Recent progress and challenges. TrAC Trends Anal. Chem. 133, 116067. https://doi.org/10.1016/j.trac.2020.116067.

Sagadevan, S., Periasamy, M., 2014. Recent trends in nanobiosensors and their applications—A review. Reviews on Advanced Materials Science 36 (1), 62–69. http://www.ipme.ru/e-journals/RAMS/no_13614/06_13614_suresh.pdf.

Sang, S., Wang, Y., Feng, Q., Wei, Y., Ji, J., Zhang, W., 2016. Progress of new label-free techniques for biosensors: A review. Crit. Rev. Biotechnol. 36 (3), 465–481. https://doi.org/10.3109/07388551.2014.991270.

Sarangadharan, I., Pulikkathodi, A.K., Chu, C.H., Chen, Y.W., Regmi, A., Chen, P.C., Hsu, C.P., Wang, Y.L., 2018. Review-high field modulated FET biosensors for biomedical applications. ECS Journal of Solid State Science and Technology 7 (7), Q3032–Q3042. https://doi.org/10.1149/2.0061807jss.

Sarkar, D., Liu, W., Xie, X., Anselmo, A.C., Mitragotri, S., Banerjee, K., 2014. MoS_2 field-effect transistor for next-generation label-free biosensors. ACS Nano 8 (4), 3992–4003. https://doi.org/10.1021/nn5009148.

S.P., M., E., K, 2006. Biosensors: A tutorial review. IEEE Potentials 35–40. https://doi.org/10.1109/MP.2006.1649009.

Subbaiah, Y.P.V., Saji, K.J., Tiwari, A., 2016. Atomically thin MoS_2: A versatile nongraphene 2D material. Adv. Funct. Mater. 26 (13), 2046–2069. https://doi.org/10.1002/adfm.201504202.

Syu, Y.C., Hsu, W.E., Lin, C.T., 2018. Review-field-effect transistor biosensing: Devices and clinical applications. ECS Journal of Solid State Science and Technology 7 (7), Q3196–Q3207. https://doi.org/10.1149/2.0291807jss.

Tong, X., Ashalley, E., Lin, F., Li, H., Wang, Z.M., 2015. Advances in MoS_2-based field effect transistors (FETs). Nano-Micro Letters, 7 (3), 203–218. https://doi.org/10.1007/s40820-015-0034-8.

Turner, A.P.F., 2013. Biosensors: Sense and sensibility. Chem. Soc. Rev. 42 (8), 3184–3196. https://doi.org/10.1039/c3cs35528d.

6

Luminescent nanoparticles for bio-imaging application

T.K. Krishnapriya [a], M.K. Jayaraj [a,b] and A.S. Asha [a,c]

[a] Cochin University of Science and Technology, Kochi, India. [b] University of Calicut, Malappuram, India. [c] Centre of Excellence in Advanced Materials, Cochin University of Science and Technology, Kochi, India

6.1 Introduction

Even though the medical world is showing phenomenal progress, the chances of curing disease are directly dependent on the early detection of the disease and proper treatment methods. In the present scenario one of the major health risks faced globally is cancer. The problems associated with the detection and treatment of cancer are mainly due to the difficulty of identifying diseased tissues from healthy tissues (Hanahan & Weinberg, 2000, 2011). The common detection methods for cancer cells include mammography, computed tomography, endoscopy, ultrasound, and magnetic resonance imaging (MRI). These imaging techniques suffer from low sensitivity and limited ability to differentiate between malignant and benign tissues. Morphological analysis techniques such as cytology and histopathology are not efficient for the early detection of the disease (Choi et al., 2010; Xing et al., 2010).

A better imaging technique having the ability to detect cancer cells at their early stage is necessary. The development of luminescent nanoparticles as a probe for the early detection of cancer is therefore an important topic of research. Optical imaging is an important noninvasive imaging technique based on the interaction of light with tissues. Parameters such as wavelength, intensity, polarization, lifetime, interference, coherence, and nonlinear effects are varied to create tissue contrast. Fluorescence microscopy has developed as a significant technique among the various optical imaging techniques (Sharma et al., 2006). The specific types of nanoparticles used for cancer diagnosis include gold nanoparticles (Giljohann et al., 2010; Huang et al., 2007), semiconductor quantum dots (QDs) (Smith et al., 2008), upconversion

Nanomaterials for Sensing and Optoelectronic Applications. DOI: https://doi.org/10.1016/B978-0-12-824008-3.00006-0

nanoparticles (UCNPs) (Chatterjee et al., 2008), polymeric nanoparticles (Perumal et al., 2019), polymer dots (Jeong et al., 2020), and silica nanoparticles (Cheng et al., 2013; Chinen et al., 2015).

6.2 Luminescence

Luminescence is the spontaneous emission of photons from electronically or vibrationally excited species that are not in thermal equilibrium with their surroundings. It is considered a cold light originating due to a mechanism other than rising temperature. Light emission by bodies solely because of their temperature is called incandescence. The term luminescence was introduced by E. Wiedemann, in which lumen means light in Latin (Valeur & Berberan-Santos, 2011). Later Vavilov made the definition more specific to luminescence by adding the criterion of duration. Luminescence can be classified based on the mode of excitation of electrons; for example, chemiluminescence is caused as a result of chemical reaction, bioluminescence by biochemical reactions in living organisms, photoluminescence by interaction with photons, etc.

Photoluminescence (PL) is one of the many forms of luminescence, which is initiated by photoexcitation, hence the prefix "photo." It is the light emission from any form of matter after the absorption of photons. The three elementary processes involved here are excitation, nonradiative transitions, and emission. Emission from a luminescent center is a process of returning to the ground state radiatively from an excited state. The emission from pure materials is called intrinsic photoluminescence and the emission because of the intentionally incorporated impurities or defects is called extrinsic luminescence (Kitai, 2008). The phenomenon of PL can be pictorially represented using either a Jablonski diagram or a configurational coordinate diagram.

Jablonski diagrams (Fig. 6.1) are named after the Polish physicist Aleksander Jablonski. The electronic states of a molecule are arranged vertically on the basis of energy, in which thicker lines are vibrational ground states and thinner lines are higher vibrational states. The transitions between them are portrayed using arrows. Straight arrows are used to symbolize radiative transitions and squiggly arrows are used for nonradiative transitions. The states are clustered horizontally by spin multiplicity.

The theoretical basis for the mechanism of absorption and emission was reported by George G. Stokes in 1852. When a molecule or atom absorbs a photon, it gets excited to a higher energy state by gaining energy. Since the excited state lifetime is very small (of the order of 10^{-8} s), the system returns to its ground state after losing a small amount of energy through vibrational relaxation, and this return can be radiative or nonradiative. The Franck–Condon principle states that the

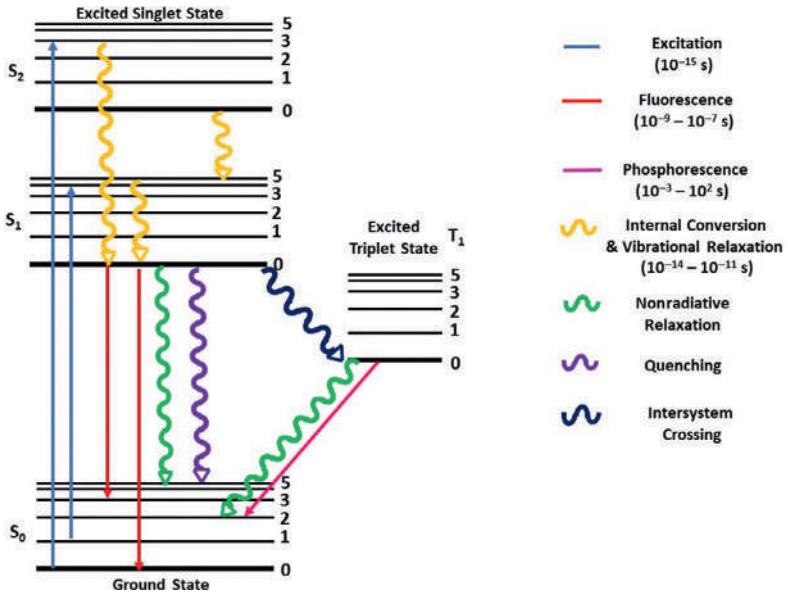

Figure 6.1. Jablonski diagram showing the various relaxation processes of excited electrons.

separation between the nuclei does not change during the transition. The nuclei remain at rest during the optical excitation from the ground state to the excited state, leading to an absorption energy of E_{abs}. After the absorption, the nuclei do not occupy the equilibrium position of the excited state, and the system moves gradually to the minimum of the excited band, with the emission of phonons (Fig. 6.2). This is due to the small lifetime of the excited state. Thus the luminescence center is in general transparent, or nearly so, with respect to their own emission bands (Marfunin & Spectroscopy, 1979).

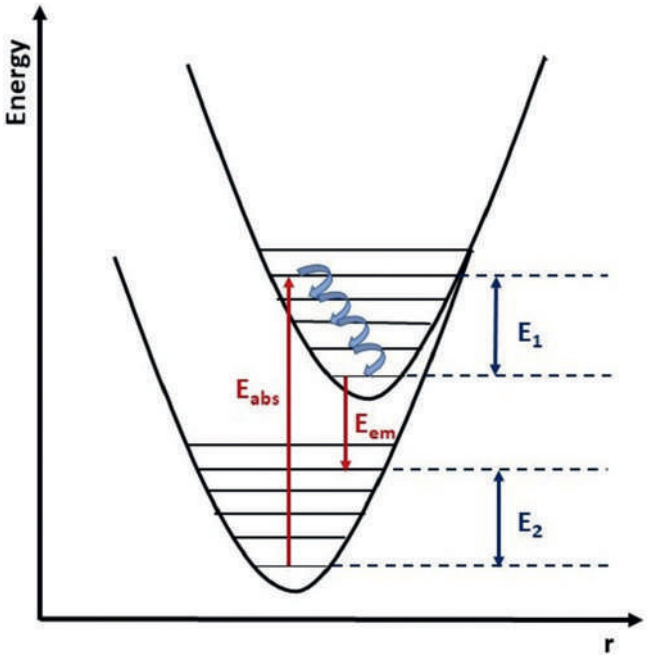

Figure 6.2. Configurational coordinate diagram showing Stokes shift.

Following excitation, various relaxation processes can occur, one of which is nonradiative relaxation, which includes intersystem crossing, internal conversion, vibrational relaxation, etc., as shown in Fig. 6.1. The energy absorbed by the luminescent materials that are not emitted as radiation is dissipated to the crystal lattice as heat. Based on the energy of the emitted photon with respect to the excitation photon, the PL

Table 6.1 Differences between fluorescence and phosphorescence.

Fluorescence	Phosphorescence
Excitation and emission are almost instantaneous	Excitation and emission are not instantaneous
Lifetime 10^{-8} to 10^{-5} s	Lifetime longer than 10^{-5} s
Temperature independent	Temperature dependent
No change in spin direction of electron	Electron spin direction changes
Fluorescence involves emission from states having the same spin	Phosphorescence comes from "spin forbidden" transitions
Stops instantly when the excitation is turned off	Glow for several seconds up to a couple of days after the excitation has been turned off
E.g.: fluorescent lights and neon signs	E.g.: glow-in-the-dark toys, stickers, paint etc.

process can be classified as Stokes and anti-Stokes. Emissions in which the excitation energy is higher come under Stokes luminescence, for example, fluorescence and phosphorescence. If the emission energy is more than the excitation energy, it is called anti-Stokes luminescence, for example, upconversion, single harmonic generation, and two-photon absorption. Allowed electrostatic dipole transitions are between electronic states of different parity based on spin and Laporte selection rules (Mini Krishna & Jayaraj, 2020).

Two important parameters that describe luminescence based on the nature of fluorophore are quantum efficiency and lifetime. The luminescence quantum efficiency/quantum yield (QY) is defined as the number of photons emitted divided by the number of photons absorbed (Kitai, 2008). Luminescence lifetime is the time required for luminescence intensity to decrease to 1/e of its maximum intensity. Both QY and lifetime are independent of the amount of fluorophore and hence are better parameters to deal with when compared to luminescence intensity (Lakowicz, 1999).

6.2.1 Stokes luminescence

Luminescence in which the energy of the excitation photon is higher compared to the emission photon is called Stokes luminescence and the difference in the energy between the two is Stokes shift. Phosphors are luminescent materials that are designed to provide visible color emission. This can be either fluorescence or phosphorescence, depending on whether the emission is fast or slow. Major differences between fluorescence and phosphorescence are shown in Table 6.1.

6.2.2 Anti-Stokes luminescence

Luminescence in which the emitted photon has a higher energy than the exciting photon is called anti-Stokes luminescence and the shift in energy is called anti-Stokes shift. Optical excitations absorb phonons in order to attain thermal equilibrium with the lattice. These excitations rejoin to emit radiation of higher energy, thereby cooling the crystal in the process (Patterson et al., 2008). Such an exchange of energy radiation (absorption or emission) is unique to a molecular structure. Albert Einstein was the first one who explained this in a satisfactory manner. This can occur basically in three ways: simultaneous two-photon absorption (STPA), second-harmonic generation (SHG), and upconversion (Zhang, 2015).

STPA is the process in which two low-energy photons (which can be either identical or of different frequencies) are absorbed simultaneously by a molecule to excite to a higher energy state. Under coherent radiation, this could happen with highly hyperpolarizable materials (a nonlinear optical property that is described as the second-order electric susceptibility per unit volume), in which the emitted photon has twice the frequency and half the wavelength of the incident light. SHG is similar to STPA in considering the energy of excited photons and the emitted photons but differs from it due to the presence of virtual excited energy levels. SHG was first discovered by Franken et al. (1961), who observed second-harmonic light with half the wavelength when ruby laser light was sent through a quartz crystal in 1961.

Like STPA and SHG, upconversion is also an anti-Stokes process. It refers to nonlinear optical processes that convert two or more low-energy pump photons to a higher-energy output photon (Xing et al., 2010). Electrons are getting excited to an intermediate energy level by absorbing the first photon. The second photon raises the electron to an excited state and emission occurs from that level. Materials that show this effect are known as upconverters. They can be made to respond to IR energy using diode lasers and can be made to emit a range of photon energies at visible wavelengths (Cheng et al., 2013; Sharma et al., 2006; Smith et al., 2008). But it is more efficient when it requires no coherent or high-intensity radiation. In a typical upconversion process there are several metastable energy states. This upconversion process exhibits a higher efficiency, than STPA and SHG, since real energy levels are used for accommodating the absorbed photons (Zhang, 2015). The basic energy level diagram for STPA, SHG, and UC is shown in Fig. 6.3.

Real energy levels make the upconversion process more feasible and it proceeds by different mechanisms, as shown in Fig. 6.4. Excited-state absorption (ESA), energy transfer upconversion (ETU), cooperative sensitization upconversion (CSU), cross-relaxation (CR), and photon avalanche (PA) are the possible mechanisms (Zhang, 2015).

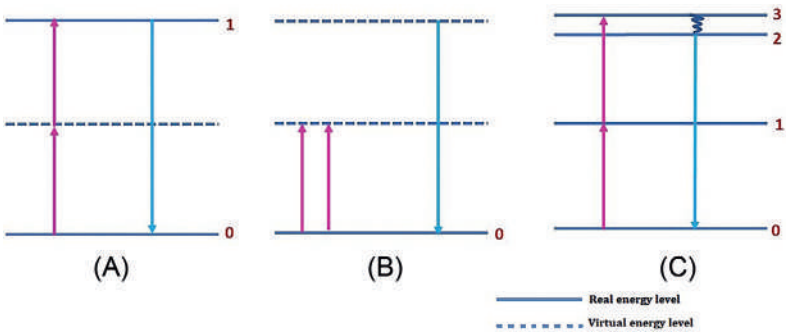

Figure 6.3. (A) Simultaneous two-photon absorption, (B) second-harmonic generation, and (C) upconversion.

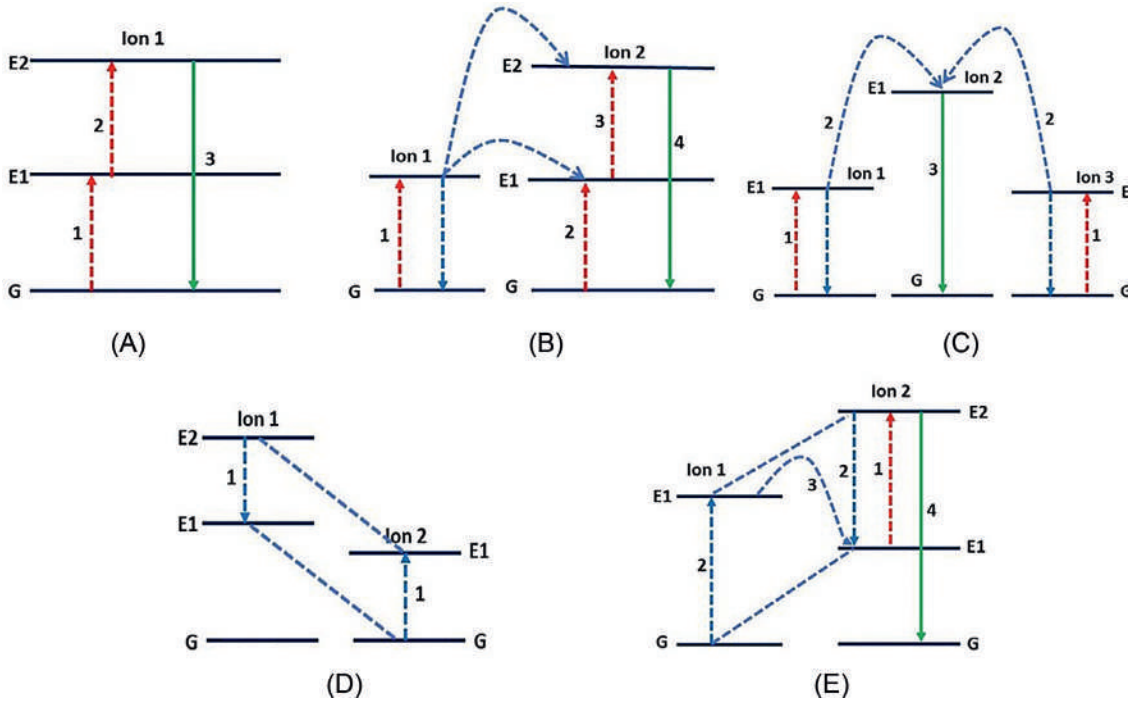

Figure 6.4. Different mechanisms of upconversion: (A) Excited-state absorption, (B) energy transfer upconversion, (C) cooperative sensitization upconversion, (D) cross-relaxation, and (E) photon avalanche.

Only one type of ion is involved in ESA, whereas two and three types of ions are involved in ETU and CSU, respectively. Lanthanide ions, such as Er^{3+}, Ho^{3+}, Tm^{3+}, and Nd^{3+}, which have a ladder-like energy level structure, are required to achieve highly efficient ESA and these are the most common emitters (activators) in ESA-based upconversion phosphors. The upconversion efficiency of an ETU process is strongly dependent on the dopant concentration, which determines the average distance between the neighboring dopant ions. The efficiency for CSU is very less compared to ESA and ETU (Patterson et al., 2008). The QY differs considerably among these mechanisms. Theoretically,

ESA < ETU < PA, but PA always needs high excitation energy and suffers from a slow response to excitation. The QY of ETU is two orders of magnitude higher than that of ESA, making it suitable for many applications (Wang & Zhang, 2016).

6.3 Bioimaging

The first X-ray image captured by Wilhelm Roentgen in 1896 was a great start of imaging in the medical field (Sharma et al., 2006). Digital image processing, which started in the early 1960s for space applications, has undergone dramatic progress within a short span of time due to the improvements in hardware and software industries, extending the applications of image processing to various fields such as remote sensing, medical field, astronomy, food and agriculture and many more. Imaging includes various types of techniques covering a wide range of the electromagnetic spectrum, from simple imaging in the visible spectrum to X-ray, thermal, MRI, and hyperspectral imaging.

The term *bioimaging* refers to the imaging of biological materials, which are the basis of the food and agriculture, aquaculture, health, forestry, and environmental industries. It is a technique using a variety of imaging equipment and processing. It can be defined as a visualization method in which a biological process can be recognized noninvasively and it interferes as little as possible with life processes. A 3D structure of the observed specimen can be made using bioimaging without any physical interference (Vadivambal & Jayas, 2015).

Biological imaging is a computer vision technology that uses artificial vision to observe, capture, process, and present an object of interest. Acquired images of biological materials are processed using different imaging softwares to get useful information and knowledge. Subcellular structures, cells, tissues, and even multicellular organisms can be observed using bioimaging. The evaluation of cellular processes or the ion metabolite levels is also possible using this technique (Ghamsari, 2018). A bioimaging system makes use of equipment that has the basic components, like any other imaging system. Fig. 6.5 shows the basic requirements for an imaging system.

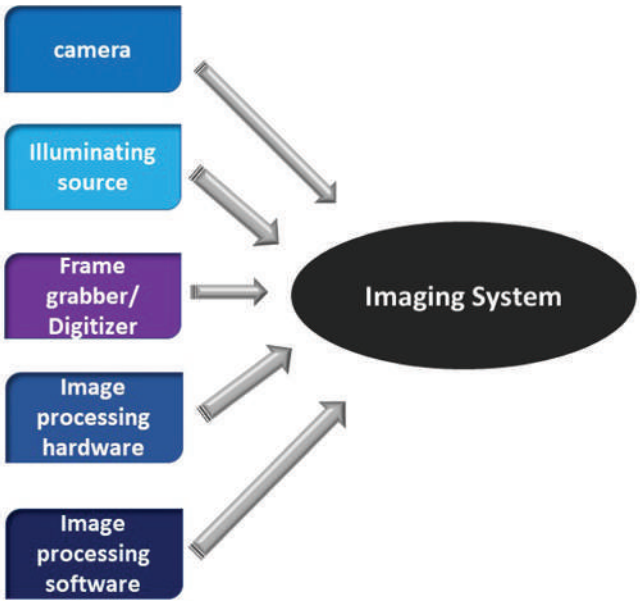

Figure 6.5. Basic components of an imaging system.

A good-quality camera is the primary component of a bioimaging system. A wide variety of sensors, including a charge-coupled device (CCD) camera, X-ray, X-ray CT, ultrasound, and MRI, are used. Among these, a CCD camera is the most commonly used one to evaluate external characteristics such as shape, size, surface structure, and color. X-ray, X-ray CT, MRI, and ultrasound are used to evaluate internal quality characteristics. Proper illuminating light sources are needed to observe a better-clarity image of the biological system. A frame grabber or digitizer is used to convert the pictorial images captured by the camera into a digital signal. This conversion of analog signals to digital signals is called digitization. After digitization, the image must be processed properly by image processing hardware and software to create the necessary output. Image processing hardware is used to perform arithmetic and logical operations, and software is used to write codes to analyze the captured images. The different steps involved in image processing are image acquisition, preprocessing, enhancement, segmentation, representation, and description (Vadivambal & Jayas, 2015).

MRI, one of the leading noninvasive imaging techniques specifically for soft tissues, works on the principle of nuclear magnetic resonance (NMR). NMR signals from all the hydrogen nuclei in an organism are collected to generate the tissue contrast. Contrast agents such as iron particles or gadolinium chelates are used to selectively distinguish tumors from normal tissues (Smith et al., 2008). But optical imaging is better than MRI in comparing the sensitivity. Recently developed techniques in bioimaging include super-resolution microscopy (Wang et al., 2019), two-photon fluorescence excitation microscopy (Liu et al., 2017), fluorescence recovery/redistribution after photobleaching (FRAP) (Sprague et al., 2004), and fluorescence resonance energy transfer (FRET) (Chinen et al., 2015). Each of these techniques has advantages and disadvantages. The low resolution of the image, which is a major limitation faced by bioimaging, can be circumvented by the use of super-resolution microscopy (Wang et al., 2019). But the high cost of hardware and software makes it difficult for common use.

The fluorescence microscopic imaging technique is normally based on Stokes shift. For cancer diagnosis, a high-energy excitation radiation is absorbed by the fluorescent probe near the tumor site and low-energy radiation is emitted, which can be detected using a detector. The autofluorescence of cells and light scattering can decrease the quality of the image in this case.

Nanotechnology can be used here as a tool to increase the resolution of current techniques, thereby raising medical imaging to the next level. Nanomaterials have immense potential in the biological and medical imaging field, especially for targeted imaging, as they

improve the contrast of the image (Ghamsari, 2018). From the conventional organic dye to cadmium-free QDs such as InP, $CuInS_2$, and $CuInSe_2$, which are called new generation QDs, there is a huge variety of imaging probes (Wang & Zhang, 2016).

6.4 Luminescent nanoparticles used for bioimaging

The optical properties of nanomaterials depend on parameters such as size, shape, surface characteristics, and other variables, including doping and interaction with the surrounding environment and other nanostructures. For example, the blue shift in absorption edge shown by semiconductor nanoparticles on decreasing size is a remarkable effect of its change in the bandgap. Likewise, the shape can have a dramatic influence on the optical properties of metal nanostructures. The optical, electronic, and magnetic properties of nanomaterials can be effectively altered by doping. It can be varied by controlling the chemical nature of the dopants, the level of doping, and the ratio of codopants. These tunable properties of nanomaterials make it an ideal candidate for imaging applications.

Different synthesis techniques (both top-down and bottom-up methods) for particles in the nanometer scale have led to considerable development in the field of optical imaging. To make the synthesized nanoparticles biocompatible with good water dispersibility and physiologic stability, surface modifications are done. Ligand exchange, ligand attraction, ligand oxidation, and layer-by-layer assembly are some methods to convert hydrophobic NPs to hydrophilic NPs. Usually, this is done by using carboxylic acid (–COOH) and amine ($–NH_2$) functional groups (Yang, 2014).

A schematic diagram showing the method for the targeted imaging of the tumor site using luminescent nanoparticles is shown below (Fig. 6.6). Surface-modified luminescent nanoparticles applied in the tissue get attached specifically to the tumor site. On applying an excitation light of a particular wavelength, a visible emission can be observed using the detector. The early detection of diseased cells is possible using this method. Different types of nanoparticles used for imaging are described in detail in this section.

6.4.1 Organic dyes

Organic dyes are the traditional fluorescent labels. Based on the origin of emission, they can be classified into resonant dyes and charge transfer dyes (CT dyes). A comparison between these two is given in Table 6.2.

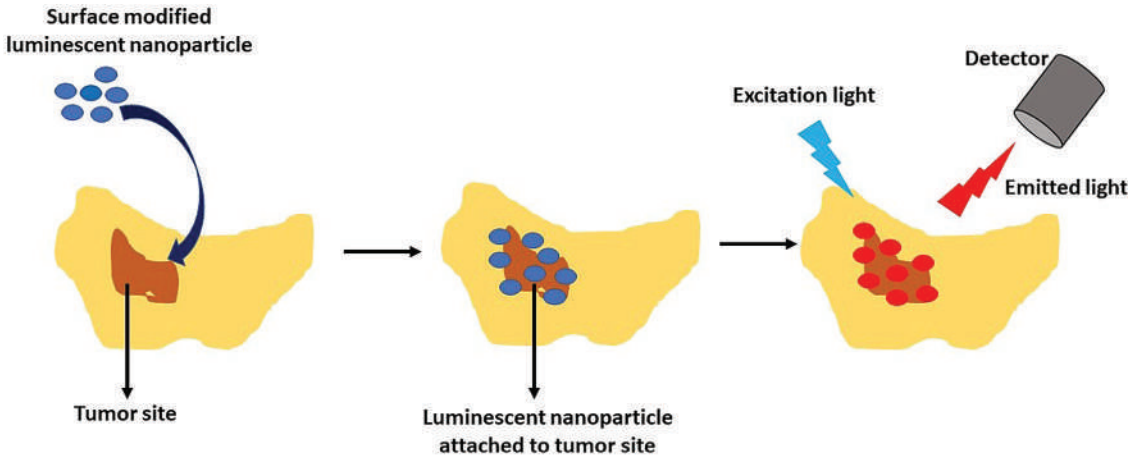

Figure 6.6. Schematic diagram showing the method of targeted imaging of tumor site using luminescent nanoparticles.

Table 6.2 Comparison between resonant dyes and CT dyes.

Resonant dyes	CT dyes
Emission originates from optical transitions delocalized over the whole chromophore	Emission originates from intramolecular charge transfer transitions.
Slightly structured, narrow emission and absorption bands that mirror each other	Well-separated, broader and structureless absorption and emission bands (in polar solvents)
Small Stokes shift (insensitive to solvent polarity)	Large Stokes shift (depends on solvent/matrix polarity)
High molar absorption coefficient	Small molar absorption coefficient
Moderate to high fluorescence quantum yield	Small fluorescence quantum yield

Organic dyes have a high fluorescence QY in the visible light range and a moderate value in the near-infrared (NIR) range. The majority of them have a fluorescence lifetime of about 5 ns in visible light and 1 ns in the NIR wavelength. Limited photostability makes it less efficient for the temporal discrimination of short-lived fluorescence interference from the scattered excitation light. The advantages of organic dyes include the availability of functionalized dyes with proper labeling protocols and with information on the site-specificity of the labeling procedure. Also, the small size of organic dye labels

helps minimize steric hindrance and allows the attachment of several fluorophores to a single biomolecule, enhancing the fluorescence signal. But high label density can result in fluorescence quenching and may interfere with the biomolecule function. In the case of toxicity, organic dyes do not pose a major problem except for DNA intercalators (Resch-Genger et al., 2008).

Commonly used dyes include DAPI, TRITC, FITC, and cyanine dyes (Cy2, Cy3, and Cy5), among which DAPI is used to stain the nucleus of cells. Moses et al. (2010) studied the effect of exposure to ionizing radiation and X-ray on human lymphocytes, and Fig. 6.7 shows the fluorescence microscope images of lymphocytes stained with DAPI, FITC, and TRITC. Chromosomes 18 and 19 in the undamaged nuclei were labeled separately using FITC (green) and TRITC (red) (Fig. 6.7C and D). Blue signal from DAPI indicates the whole genome DNA. Fig. 6.7A represents the merged image of Fig. 6.7B, C, and D.

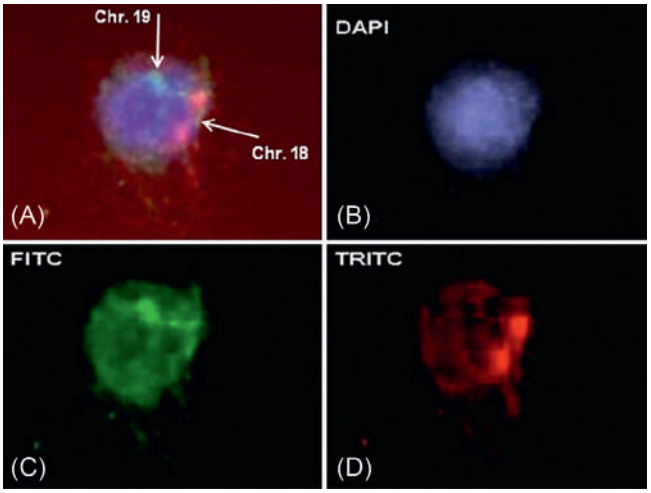

Figure 6.7. (A) Agarose-embedded untreated G0 human lymphocyte stained by fluorescence in situ hybridization (FISH) using DNA probes specific to human chromosomes 18 and 19. Image acquisition was performed with a fluorescence microscope equipped with single bandpass filters for DAPI, FITC, and TRITC. (B–D) Fluorescent images of the same cell generated with single bandpass filters for DAPI, FITC, and TRITC, respectively. A: Merge of images B–D (Mosesso et al., 2010). Reproduced with permission from (Mosesso et al., 2010), Copyright (2010), Elsevier.

da Silva Viana et al. (2019) reported the production of six new luminescent nanoprobes based on the combination of europium-doped sodium yttrium fluoride ($NaYF_4$:5%Eu) nanoparticles and the organic compounds *p*-coumaric acid, tyrosine (Tyr3), boradiazaindacene (BODIPY), and zinc phthalocyanine (ZnPc) using a surface modification strategy. The samples showed good phase purity on powder XRD analysis. FTIR and TEM analysis revealed the formation of conjugated particles with a size less than 50 nm. The optical properties of $NaYF_4$:5%Eu–coumaric acid and $NaYF_4$:5%Eu–Tyr3 showed only the f–f transitions of the $4f^6$ configuration of the Eu^{3+} ion for excitation and emission spectra. But the compounds $NaYF_4$:5%Eu–BODIPY COOH, $NaYF_4$:5%Eu–BODIPY NCS, $NaYF_4$:5%Eu–BODIPY NCS/Tyr3, and $NaYF_4$:5%Eu–ZnPc presented wide bands in the excitation and emission spectra, which were related to the conjugated organic chromophores on the surface of the particles. The evaluation of luminescent nanoprobes as targeting colon cancer cells was performed. The compounds showed cellular internalization with no morphological damage to the human colorectal adenocarcinoma cell line, HT-29, after 24 h, making it a potential candidate for cancer diagnosis.

A novel redshifted polymethine dye with emission wavelengths ranging from 680 to 1045 nm for shortwave infrared (SWIR) in vivo

imaging was developed by Cosco et al. (Cosco et al., 2017). 1- and 3-methine dyes exhibited improved photostability and 5- and 7-methine dyes exhibited exceptional brightness upon photophysical characterizations. SWIR imaging in mice was done with the 7-methine dye because of its micelle formulation capacity. Imaging in the SWIR region is really promising because of low autofluorescence and greater penetration depth in tissues.

6.4.2 Quantum dots

The most commonly used QDs for life science applications are the group II–VI compounds, such as CdSe and CdTe, which contain cytotoxic cadmium ion surrounded by a less toxic shell material such as ZnS. This coating improves the QY by passivating the nonradiative recombination sites on the surface. The coating acts as a barrier, protecting CdSe from direct contact with the surrounding solvent. The optical properties of QDs depend on the type of the constituent material, its particle size and size distribution, surface chemistry, and the number of dangling bonds favoring the nonradiative deactivation. QDs have an emission band of symmetric shape and the width of the emission peak is determined by the size distribution. The quantum size effect determines the spectral position of absorption and emission. They have a large molar absorption coefficient and QY compared to organic dyes. Biofunctionalization is needed to attach this to biomolecules. QDs are made water dispersible and are bound to the cell via electrostatic linking, through covalent cross-linking, or by binding to polyhistidine tags (Chen et al., 2012; Wang et al., 2013; Yong et al., 2009).

Su et al. made a comparison of the cytotoxicity of CdTe QD with that of CdTe/CdS/ZnS core–shell–shell (CSS) QD and free cadmium ion in $CdCl_2$ solution and found that CdTe QDs are more cytotoxic than the other two. Fig. 6.8A shows the cytotoxicity studies and Fig. 6.8B shows the change in the morphology of HEK293 cells upon the addition of these QDs. From the results obtained, the conclusion was that the cytotoxicity of QDs is based on not only the release of Cd^{2+} ions but also the concentration of total QDs ingested by cells (Su et al., 2010).

One major drawback that severely limits the clinical translation of QDs is the toxicity concern of II–VI semiconductor QDs in biomedical applications. These are easily disintegrated in biological systems if their surface is not modified with shell coating (Yong et al., 2009). Therefore the emphasis has shifted toward the fabrication of noncadmium-based QDs in recent years.

QDs made up of III–V semiconductors (such as InP) are extremely promising as they are not only cadmium free but also more robust structurally, owing to the presence of covalent bonds in their matrix (Resch-Genger et al., 2008). Yong et al. (2009) effectively used InP/ZnS QDs, functionalized with mercaptosuccinic acid and bioconjugated

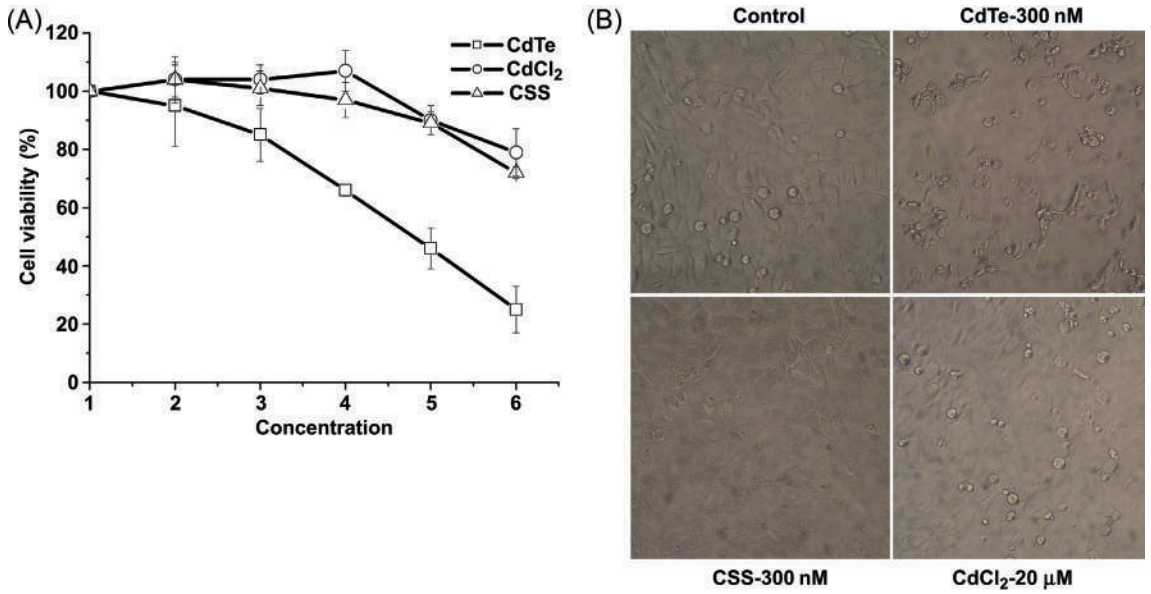

Figure 6.8. Cytotoxicity of different concentrations of CdTe, CSS-QDs and $CdCl_2$ exposed to HEK293 cells for 24 h (For CdTe and CSS-QDs, 1–6 in the X axis of Fig. A were 0, 18.75, 37.5, 75, 150, and 300 nm, respectively. For $CdCl_2$, they were 0, 1.25, 2.5, 5, 10, and 20 μm, respectively). (A) Viability of HEK293 cells after treatment with CdTe, CSS-QDs, and $CdCl_2$. The cell viability was calculated as a percentage from the viability of the control (untreated) cells. The viability of the control cells was considered 100%. The results are expressed as means ± SD from three or four independent experiments. (B) Morphology of HEK293 cells after incubation with 300-nm CdTe, 300-nm CSS-QDs, and 20-μm $CdCl_2$ for 24 h, with the untreated cells as control (Su et al., 2010). Reproduced with permission from (Su et al., 2010), Copyright (2010), Elsevier.

with pancreatic cancer–specific monoclonal antibodies, such as anti-claudin-4 and anti–prostate stem cell antigen (anti-PSCA), for specific in vitro targeting of pancreatic cancer cell lines. Surface functionalization was done to make them highly dispersible in aqueous media. The optical properties of the core–shell structures were strongly dependent on the nature of the shell around InP. The emission wavelength can be tuned by simply changing the shell material. For example, ZnS coating gives an emission wavelength of~520 nm, whereas a ZnSe shell allows it to be tuned to ~ 590 nm. ZnS-coated InP QDs have a greater QY (up to 40%) compared to bare QDs. Folic acid–InP QD bioconjugates were successively used for the confocal and two-photon imaging of KB cancer cells. The major difficulty with this type of QDs is their lengthy and complicated synthesis procedure (Fan et al., 2014).

Another type of QD that has many easy synthesis techniques is the carbon dot (CD). It was discovered accidentally in 2004 using the top-down arc discharge method and possesses the advantages of low cost, chemical inertness, photostability, low cytotoxicity, and biocompatibility. Emission wavelength can be tuned by varying the size of QDs. The different types of synthesis techniques for CDs include

laser ablation, hydrothermal treatment, microwave approach, thermal decomposition, ultrasonic treatment, and electrochemical oxidation (Chu et al., 2019).

De Yro et al. (2019) successfully prepared CDs from biowaste using the hydrothermal treatment of calamansi (*Citrofortunella microcarpa*) and pineapple (*Ananas comosus*) waste as a carbon source. The synthesized CDs showed coagulation in an aqueous solution and a strong blue fluorescence under UV light (λ= 365 nm). TEPA (tetraethylenepentamine) was added for the surface passivation of QDs to increase the QY. Fluorescence was also observed in *Escherichia coli* bacterial culture after the addition of CDs due to the attachment of positively charged, surface-passivated (with–OH and –NH functional groups) CDs with a negatively charged *E. coli* bacterial cell.

Two main points related to CDs that are not well understood are the mechanism by which they emit light and their core structure. The PL mechanism of CDs can be explained by using different theories, including surface state, quantum confinement, and molecular state (Mintz et al., 2019). Wang et al. (2015) tried different combinations of nitrogen sources such as EDA (ethylenediamine), DETA (diethylenetriamine), and TEPA for surface passivation. Citric acid (CA) was used as the carbon source. Using hydrothermal synthesis at 200°C for 6 h, surface-passivated photoluminescent QDs were formed. The CA–EDA combination gave highly luminescent QDs (having high QY) but the photostability was poor. Whereas for the CA–TEPA combination, the QDs showed high photostability but at the cost of QY. In vitro and in vivo studies were conducted with these. In vitro imaging was done using cancerous HeLa cells. A bright green fluorescence was observed for CD–EDA and CD–DETA samples compared to CD–TEPA in the cytoplasmic region of HeLa cells. In vivo studies were conducted in mice and the CD–EDA sample showed better signal intensity.

6.4.3 Lanthanide-based inorganic materials

Inorganic nanoparticle–based bioimaging probes have been extensively studied because of their better imaging performance, stimuli response, and targeted imaging. But far more research is needed for their effective use in clinical applications due to safety issues and less optimized efficiency. Lanthanide-doped calcium phosphate nanoparticles attract attention compared to QDs and luminescent silica nanoparticles mainly because of their low cytotoxicity (Kim et al., 2018).

The property of splitting of electonic energy levels in the pescence of an electric field produced by the crystalline environment of a dielectric crystal makes lanthanides spectroscopically active materials (Chen et al., 2014). The 4f orbitals are shielded by the 6s, 5p, and 5d orbitals, making the emission insensitive to the environment.

Emission and absorption in the NIR, visible (Vis), and ultraviolet (UV) spectral range are possible due to this electronic arrangement. Spectra arising from f–f transitions are narrow, unlike transition metal d–d transition spectra. Triply ionized lanthanide ions have lower emission line widths, with an FWHM value of ~10–20 nm. Fig. 6.9 shows the increase in the FWHM of the emission bands of different nanoparticles used in imaging. Lanthanide emissions are highly resistant to photobleaching since they involve only atomic transitions. Compared to organic dyes, lanthanides show a larger Stokes shift. The shift between excitation and emission bands can be hundreds of nanometers due to the energy level structure of these ions. Both downconversion and upconversion luminescence are possible with the doping of lanthanide ions (Anjana et al., 2020; Krishnapriya et al., 2021).

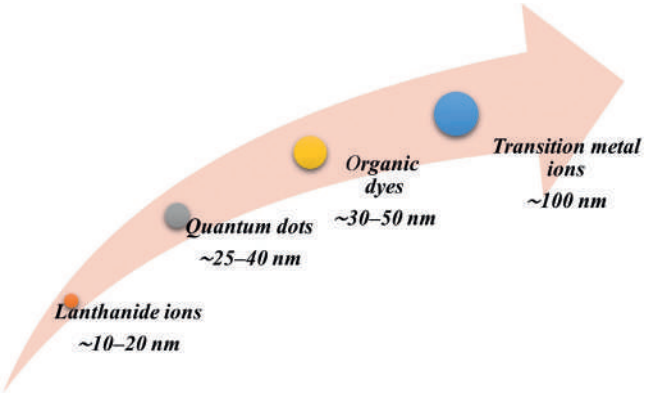

Figure 6.9. Increase in the FWHM of the emission bands of different nanoparticles used in imaging.

A variety of solids like ceramics, crystals, or fibers can be used as the host material. They are also ideal for spectral conversion because of the large possibility of absorption and emission wavelengths, independence on host materials, and low vibration energy losses. So these have been widely used in lasers, sensors, solar cells, photodynamic therapy, and optical imaging (Wang & Zhang, 2016).

6.4.4 Upconversion nanoparticles

The drawbacks of conventional imaging probes led to the development of a new class of fluorophores called upconversion nanoparticles (UCNPs). Although organic dyes, QDs, or metal complexes have high QY, the UV or visible excitation can cause autofluorescence from tissues, DNA damage, and cell death. Low signal-to-noise ratio, low sensitivity, low photostability, and unsuitability for multiplex labeling due to the broad emission spectra are some disadvantages of these nanoprobes. For QDs, toxicity is the main problem. As already discussed, the main advantage of UCNPs is their emission in the visible or near-infrared (NIR) range under NIR irradiation. Since excitation is through low-energy IR radiation, there is no cell damage and autofluorescence from living tissues. High detection sensitivity and high light penetration depth are added advantages. These UCNPs also show high photostability, tunable emission, low toxicity, sharp emission bandwidth, and long lifetime.

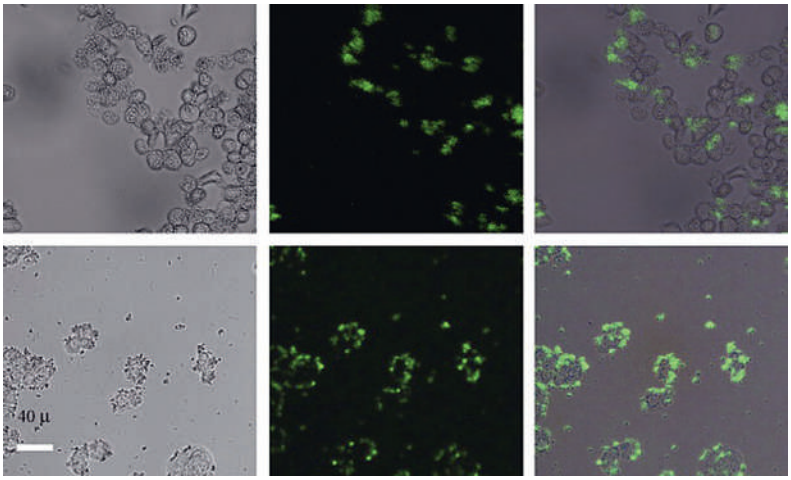

Figure 6.10. Bright field, confocal, and superimposed images of live human ovarian carcinoma cells (OVCAR-3, top row) and human colonic adenocarcinoma cells (HT-29, bottom row), with PEI/$NaYF_4$ nanoparticles attached. The nanoparticles were surface modified with folic acid (Chatterjee et al., 2008). Reproduced with permission from (Chatterjee et al., 2008), Copyright (2008), Elsevier.

UCNPs can be excited by a normal continuous wave laser, which makes them easier to use. The sol–gel method, coprecipitation method, thermal decomposition, and hydro-/solvothermal method are the major synthesis techniques for UCNPs.

Cao et al. (2019) designed and prepared $NaYF_4$:Yb and Tm@ $LiLuF_4$:Nd core–shell nanoparticles, which had the special property of emission at approximately 800 nm under 980-nm excitation and at approximately 1060 nm under 808-nm excitation. Therefore these particles show upconversion and downshifting mechanisms for NIR emission. The surface of the particles was modified with sodium citrate to make them soluble. Upconversion was originated from Yb^{3+}–Tm^{3+} ions and downshifting from Nd^{3+} ions. By analyzing various optical signals, the authors confirmed that these two luminescent imaging modes showed similar performance.

The application of the UCNP, $NaYF_4$ doped with Er^{3+} and Yb^{3+}, for cytoplasm-selective cellular imaging was proposed by Nampi et al. (2019). Hydrothermally synthesized particles were surface-functionalized with PEI for better long-term stability in water. A biocompatible sample was used for multiphoton imaging. Imaging of liver tissue proved its property of tissue imaging without tissue autofluorescence.

The first report on *in vivo* imaging of small mammals using UCNPs was by Chatterjee et al. (2008). *In vitro* and *in vivo* imaging of human cells and Wizar rats using $NaYF_4$:Er/Tm, Yb UCNPs surface modified with PEI is shown in Figs. 6.10 and 6.11, respectively. In vitro studies were done with a folic acid modification on the surface of nanoparticles for attachment to the cancer cells used.

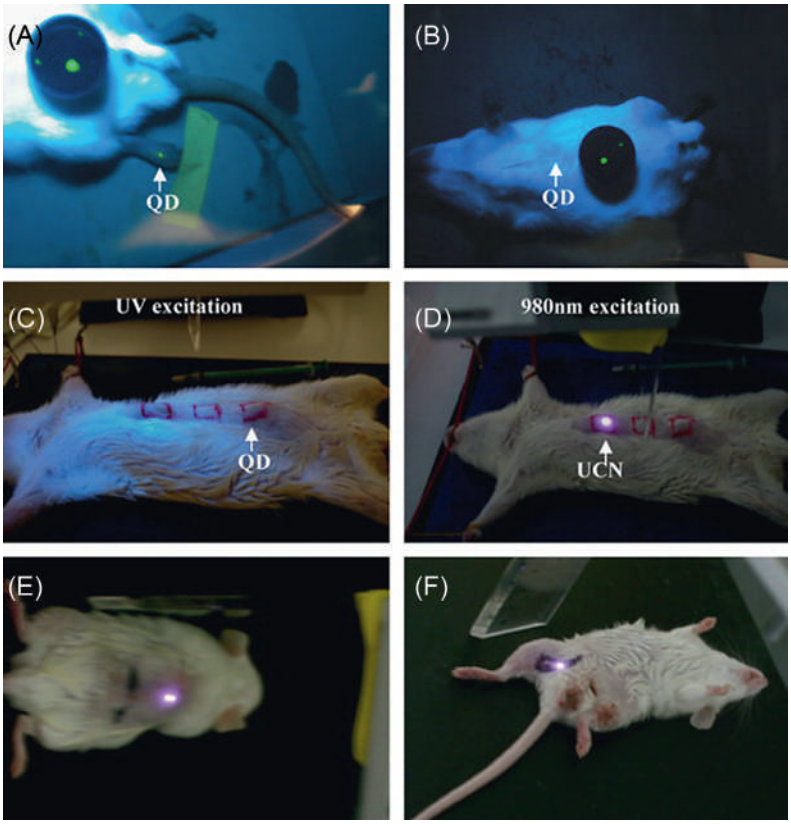

Figure 6.11. *In vivo* imaging of rat: quantum dots (QDs) injected into translucent skin of (A) the foot show fluorescence, but not through thicker skin of the (B) back or (C) abdomen; PEI/$NaYF_4$:Yb,Er nanoparticles injected below (D) abdominal skin, (E) thigh muscles, or (F) the skin of the back show luminescence. QDs on a black disk in (A, B) are used as the control (Chatterjee et al., 2008). Reproduced with permission from (Chatterjee et al., 2008), Copyright (2008), Elsevier.

In vivo studies were done on Wizar rats and it was found that, compared to QD luminescence, upconversion luminescence was more intense and was visible through thicker body muscles, as shown in Fig. 6.11.

The QY of UCNPs is usually between 0.005% and 0.3%, which is very low compared to usual luminescent imaging probes. Although studies have proved good cell viability for UCNPs, their long-term effect on living beings is yet to be studied. The shape, size, surface charge, and surface coating have significant effects on the behavior of UCNPs in biological systems (Yang, 2014). Research is fast progressing in this field to develop high-QY, multifunctional UCNPs for imaging, drug delivery, photothermal therapy, etc.

6.5 Summary

In this chapter the fundamentals of luminescence (Stokes and anti-Stokes), basics of bioimaging, and different nanoparticles used for

bioimaging were discussed. Surface-modified luminescent nanoparticles get attached to specific cells of interest and help in the identification of the same. High QY, photostability, low toxicity, and high biocompatibility are the essential qualities of a fluorescent nanoparticle for its use as an imaging probe. The traditional fluorescent labels, organic dyes, have a comparatively high QY but low photostability. QDs, on the other hand, have a large molar absorption coefficient and QY compared to organic dyes. III–V QDs are preferred over II–VI QDs because of their low toxicity. Similarly, lanthanide-doped inorganic materials have low toxicity issues and give emission insensitive to the surrounding environment but more research is needed for their effective clinical use. UCNP based imaging is proposed as a better alternative, because of the visible or near-infrared (NIR) range emission under NIR excitation. NIR radiation causes no cell damage and autofluorescence from living tissues compared to UV light. High detection sensitivity, high light penetration depth, high photostability, tunable emission, low toxicity, sharp emission bandwidth, and long lifetime make UCNPs ideal candidates for bioimaging.

References

Anjana, R., Krishnapriya, T.K., Jayaraj, M.K., 2020. Clean synthesis of Er, Yb doped fluorapatite upconversion luminescent nanoparticles through liquid phase pulsed laser ablation. Opt. Laser Technol. 131, 106452. doi:10.1016/j.optlastec.2020.106452.

Cao, C., Liu, Q., Shi, M., Feng, W., Li, F., 2019. Lanthanide-doped nanoparticles with upconversion and downshifting near-infrared luminescence for bioimaging. Inorg. Chem. 58 (14), 9351–9357. https://doi.org/10.1021/acs.inorgchem.9b01071.

Chatterjee, D.K., Rufaihah, A.J., Zhang, Y., 2008. Upconversion fluorescence imaging of cells and small animals using lanthanide doped nanocrystals. Biomaterials 29 (7), 937–943. https://doi.org/10.1016/j.biomaterials.2007.10.051.

Chen, N., He, Y., Su, Y., Li, X., Huang, Q., Wang, H., Zhang, X., Tai, R., Fan, C., 2012. The cytotoxicity of cadmium-based quantum dots. Biomaterials 33 (5), 1238–1244. https://doi.org/10.1016/j.biomaterials.2011.10.070.

Chen, X., Liu, Y., Tu, D., 2014. A general introduction to Lanthanide ions. Nanomedicine and Nanotoxicology. Springer, pp. 1–15.

Cheng, L., Wang, C., Liu, Z., 2013. Upconversion nanoparticles and their composite nanostructures for biomedical imaging and cancer therapy. Nanoscale 5 (1), 23–37. https://doi.org/10.1039/c2nr32311g.

Chinen, A.B., Guan, C.M., Ferrer, J.R., Barnaby, S.N., Merkel, T.J., Mirkin, C.A., 2015. Nanoparticle probes for the detection of cancer biomarkers, cells, and tissues by fluorescence. Chem. Rev. 115 (19), 10530–10574. https://doi.org/10.1021/acs.chemrev.5b00321.

Choi, Y.E., Kwak, J.W., Park, J.W., 2010. Nanotechnology for early cancer detection. Sensors 10 (1), 428–455. https://doi.org/10.3390/s100100428.

Chu, K.W., Lee, S.L., Chang, C.J., Liu, L., 2019. Recent progress of carbon dot precursors and photocatalysis applications. Polymers 11 (4). https://doi.org/10.3390/polym11040689.

Cosco, E.D., Caram, J.R., Bruns, O.T., Franke, D., Day, R.A., Farr, E.P., Bawendi, M.G., Sletten, E.M., 2017. Flavylium polymethine fluorophores for near- and shortwave infrared imaging. Anngew Chemie 129, 13306–13309. doi:10.1002/ange.201706974.

da Silva Viana, R., de Mascena Costa, L.A., Leal, A.N.R., Williams, T.M., Luan, L., Zhang, G., Wang, M., Harmon, A.C., dos Anjos, J.V., Cueto, R., Filho, M.A.G., Falcão, E.H.L., Vicente, M.G.H., Junior, S.A., Mathis, J.M., 2019. Surface modification strategy based on the conjugation of NaYF 4 :5%Eu luminescent nanoprobe with organic aromatic compounds for application in bioimaging assays. J Nanoparticle Res 21 (21), 23. doi:10.1007/s11051-018-4422-0.

De Yro, P.A.N., Quaichon, G.M.O., Cruz, R.A.T., Emolaga, C.S., Que, M.C.O., Magdaluyo, E.J.R., Basilia, B.A., 2019. Hydrothermal synthesis of carbon quantum dots from biowaste for bio-imaging. In: AIP Conference Proceedings. American Institute of Physics Inc. (Vol. 2083).

Fan, G., Wang, C., Fang, J., 2014. Solution-based synthesis of III-V quantum dots and their applications in gas sensing and bio-imaging. Nano Today 9 (1), 69–84. https://doi.org/10.1016/j.nantod.2014.02.007.

Franken, P.A., Hill, A.E., Peters, C.W., Weinreich, G., 1961. Generation of optical harmonics. Phys. Rev. Lett. 7 (4), 118–119. https://doi.org/10.1103/PhysRevLett.7.118.

Ghamsari, M.S., 2018. Introductory Chapter: Nano-bioimaging—Past, Present, and Future. In: State of the Art in Nanobioimaging. IntechOpen, pp. 1–9. doi:10.5772/intechopen.74959.

Giljohann, D.A., Seferos, D.S., Daniel, W.L., Massich, M.D., Patel, P.C., Mirkin, C.A., 2010. Gold nanoparticles for biology and medicine. Angewandte Chemie—International Edition 49 (19), 3280–3294. https://doi.org/10.1002/anie.200904359.

Hanahan, D., Weinberg, R.A., 2000. The hallmarks of cancer review. Cell 100, 81683–81689. https://doi.org/10.1016/S0092-8674(00.

Hanahan, D., Weinberg, R.A., 2011. Hallmarks of cancer: The next generation. Cell 144 (5), 646–674. https://doi.org/10.1016/j.cell.2011.02.013.

Huang, X., Jain, P.K., El-Sayed, I.H., El-Sayed, M.A., 2007. Gold nanoparticles: Interesting optical properties and recent applications in cancer diagnostics and therapy. Nanomedicine 2 (5), 681–693. https://doi.org/10.2217/17435889.2.5.681.

Jeong, J.E., Uddin, M.A., Ryu, H.S., Kim, H.C., Kang, M., Joung, J.F., Park, S., Shim, S.H., Woo, H.Y., 2020. Green-, red-, and near-infrared-emitting polymer dot probes for simultaneous multicolor cell imaging with a single excitation wavelength. Chem. Mater. 32 (15), 6685–6696. https://doi.org/10.1021/acs.chemmater.0c02172.

Kim, D., Kim, J., Park, Y.I., Lee, N., Hyeon, T., 2018. Recent development of inorganic nanoparticles for biomedical imaging. ACS Central Science 4 (3), 324–336. https://doi.org/10.1021/acscentsci.7b00574.

Kitai, A., 2008. Luminescent materials and applications. Luminescent Materials and Applications. Wiley Blackwell, pp. 1–278.

Krishnapriya, T.K., Deepti, A., Baby Chakrapani, P.S., Asha, A.S., Jayaraj, M.K., 2021. Eggshell derived europium doped hydroxyapatite nanoparticles for cell imaging application. J. Fluoresc. 31, 1927–1936. https://doi.org/10.1007/s10895-021-02814-0.

Lakowicz, J.R., 1999. Introduction to fluorescence. Principles of Fluorescence Spectroscopy. Kluwer Academic/Plenum Publishers, pp. 10–12.

Liu, H.W., Liu, Y., Wang, P., Zhang, X.B., 2017. Molecular engineering of two-photon fluorescent probes for bioimaging applications. Methods and Applications in Fluorescence 5 (1). https://doi.org/10.1088/2050-6120/aa61b0.

Marfunin, A. S. (1979). Spectroscopy, Luminescence and Radiation Centers in Minerals. Springer. https://doi.org/10.1007/978-3-642-67112-8.

Mini Krishna, K., Jayaraj, M.K., 2020. Oxide luminescent materials. In: M.K. Jayaraj (Ed.), Nanostructured Met Oxides Devices. Springer, pp. 1–46. doi:10.1007/978-981-15-3314-3_1.

Mintz, K.J., Zhou, Y., Leblanc, R.M., 2019. Recent development of carbon quantum dots regarding their optical properties, photoluminescence mechanism, and core structure. Nanoscale 11 (11), 4634–4652. https://doi.org/10.1039/c8nr10059d.

Mosesso, P., Palitti, F., Pepe, G., Piñero, J., Bellacima, R., Ahnstrom, G., Natarajan, A.T., 2010. Relationship between chromatin structure, DNA damage and repair following X-irradiation of human lymphocytes. Mutation Research—Genetic Toxicology and Environmental Mutagenesis 701 (1), 86–91. https://doi.org/10.1016/j.mrgentox.2010.03.005.

Nampi, P.P., Vakurov, A., Mackenzie, L.E., Scrutton, N.S., Millner, P.A., Jose, G., Saha, S., 2019. Selective cellular imaging with lanthanide-based upconversion nanoparticles. J. Biophotonics 12 (4). https://doi.org/10.1002/jbio.201800256.

Patterson, W., Bigotta, S., Sheik-Bahae, M., Parisi, D., Tonelli, M., Epstein, R., 2008. Anti-stokes luminescence cooling of Tm^{3+} doped BaY_2F_8. Opt. Express 16 (3), 1704–1710. https://doi.org/10.1364/OE.16.001704.

Perumal, V., Sivakumar, P.M., Zarrabi, A., Muthupandian, S., Vijayaraghavalu, S., Sahoo, K., Das, A., Das, S., Payyappilly, S.S., Das, S., 2019. Near infra-red polymeric nanoparticle based optical imaging in cancer diagnosis. J. Photochem. Photobiol. B 199. https://doi.org/10.1016/j.jphotobiol.2019.111630.

Resch-Genger, U., Grabolle, M., Cavaliere-Jaricot, S., Nitschke, R., Nann, T., 2008. Quantum dots versus organic dyes as fluorescent labels. Nat. Methods 5 (9), 763–775. https://doi.org/10.1038/nmeth.1248.

Sharma, P., Brown, S., Walter, G., Santra, S., Moudgil, B., 2006. Nanoparticles for bioimaging. Adv. Colloid Interface Sci. 123–126, 471–485. https://doi.org/10.1016/j.cis.2006.05.026.

Smith, A.M., Duan, H., Mohs, A.M., Nie, S., 2008. Bioconjugated quantum dots for in vivo molecular and cellular imaging. Adv. Drug. Deliv. Rev. 60 (11), 1226–1240. https://doi.org/10.1016/j.addr.2008.03.015.

Sprague, B.L., Pego, R.L., Stavreva, D.A., McNally, J.G., 2004. Analysis of binding reactions by fluorescence recovery after photobleaching. Biophys. J. 86 (6), 3473–3495. https://doi.org/10.1529/biophysj.103.026765.

Su, Y., Hu, M., Fan, C., He, Y., Li, Q., Li, W., Wang, L.h., Shen, P., Huang, Q., 2010. The cytotoxicity of CdTe quantum dots and the relative contributions from released cadmium ions and nanoparticle properties. Biomaterials 31 (18), 4829–4834. https://doi.org/10.1016/j.biomaterials.2010.02.074.

Vadivambal, R., Jayas, D.S., 2015. Bio-imaging: Principles, techniques, and applications. Bio-Imaging: Principles, Techniques, and Applications 1–361. https://doi.org/10.1201/b18840.

Valeur, B., Berberan-Santos, M.N., 2011. A brief history of fluorescence and phosphorescence before the emergence of quantum theory. J. Chem. Educ. 88 (6), 731–738. https://doi.org/10.1021/ed100182h.

Wang, L., Frei, M.S., Salim, A., Johnsson, K., 2019. Small-molecule fluorescent probes for live-cell super-resolution microscopy. J. Am. Chem. Soc. 141 (7), 2770–2781. https://doi.org/10.1021/jacs.8b11134.

Wang, Y., Hu, R., Lin, G., Roy, I., Yong, K.T., 2013. Functionalized quantum dots for biosensing and bioimaging and concerns on toxicity. ACS Appl. Mater. Interfaces 5 (8), 2786–2799. https://doi.org/10.1021/am302030a.

Wang, R., Zhang, F., 2016. Lanthanide-based near infrared nanomaterials for bioimaging. RSC Nanoscience and Nanotechnology. Royal Society of Chemistry, pp. 1–39 Vols. 2016, Issue 40.

Wang, J., Zhang, P., Huang, C., Liu, G., Leung, K.C.F., Wáng, Y.X.J., 2015. High performance photoluminescent carbon dots for in vitro and in vivo bioimaging: Effect of nitrogen doping ratios. Langmuir 31 (29), 8063–8073. https://doi.org/10.1021/acs.langmuir.5b01875.

Xing, L., Todd, N.W., Yu, L., Fang, H., Jiang, F., 2010. Early detection of squamous cell lung cancer in sputum by a panel of microRNA markers. Mod. Pathol. 23 (8), 1157–1164. https://doi.org/10.1038/modpathol.2010.111.

Yang, Y., 2014. Upconversion nanophosphors for use in bioimaging, therapy, drug delivery and bioassays. Microchim. Acta 181 (3–4), 263–294. https://doi.org/10.1007/s00604-013-1139-8.

Yong, K.T., Ding, H., Roy, I., Law, W.C., Bergey, E.J., Maitra, A., Prasad, P.N., 2009. Imaging pancreatic cancer using bioconjugated inp quantum dots. ACS Nano 3 (3), 502–510. https://doi.org/10.1021/nn8008933.

Zhang, F., 2015. General Introduction to Upconversion Luminescence Materials. Photon Upconversion Nanomaterials. Springer, pp. 1–17. doi:10.1007/978-3-662-45597-5_1.

7

Nanophotonic biosensors for disease diagnosis

R. Anjana [a,c] **and M.K. Jayaraj** [a,b]

[a] *Cochin University of Science and Technology, Kochi, India.* [b] *University of Calicut, Malappuram, India.* [c] *Department of Physics, St. Albert's College (Autonomous), Ernakulam, India*

7.1 Introduction

Nanotechnology can contribute immensely to the early-stage detection of communicable and noncommunicable diseases. Nanophotonics refers to the study of light with matter on the nanometric scale (Mishra & Shandilya, 2020). Nanophotonics has created extensive opportunities and enabled new technologies. The most exciting fact is that nanophotonics deals with the interaction of light with matter having a size less than the wavelength of light in many cases. Nanoconfinement can be achieved in three ways: confining light in the nanoscale dimension, limiting matter size to the nano regime, or confining the photo process in the nanoscale (Prasad, n.d.). By designing metallic or dielectric two-dimensional or three-dimensional (3D) nanostructures, light can be scattered, confined, refracted, and processed in new ways that are almost impossible using conventional materials. The main aim of nanophotonics is to overcome Abbe's diffraction limit, the classical limit of diffraction of light, and study the effect of light in a region smaller than its wavelength. When light shrinks to such a volume that it can eventually be compared to atomic unit cells, the classical models for describing optical interactions fail, and nanoscale quantum effects dominate (Koenderink et al., 2015).

Different nanophotonic phenomena can be utilized to implement sensing. Whatever the technique used, these devices have some unique advantages like better sensitivity, good portability, and the possibility of multiplexing (Mishra & Shandilya, 2020).

Nucleic acid amplification, antigen detection, and antibody detection (serological assays) are the commonly used techniques for the diagnosis of communicable diseases. The most successful biosensors are based on real-time polymerase chain reaction (RT-PCR). PCR improves the sensitivity of the sensor through gene amplification.

Nanomaterials for Sensing and Optoelectronic Applications. DOI: https://doi.org/10.1016/B978-0-12-824008-3.00001-1

Issues include sophisticated equipment and trained personnel required for sample preparation and analysis and high response time. Compared to PCR sensors, using the conventional enzyme-linked immunosorbent assay (ELISA) for antibody detection is simple. However, the sensitivity is poor and the time required and costs are high. Antigen and antibody detection is possible using immunochromatographic (IC) lateral flow assays (LFAs) qualitatively. Existing antigen and antibody detection have limited sensitivity for detecting acute infections. Demand exists for a susceptible, specific, fast, and convenient detection method, for which optical biosensors are the most promising solution. Generally, a biosensor has three main elements: target, recognition element, and transducer. The analyte molecule is the target that is detected by the recognition element through some analyte-specific interactions. The selective binding with the target molecule causes some changes in the physical or chemical property of the recognition element. The changes are translated to a signal using the transducer. These changes can be in conductivity, refractive index, pH value, emission, etc. (Klar, 2007; Lee et al., 2020; Shrivastav et al., 2021).

Optical biosensors evaluate variations in the optical properties of the propagated light during the interaction of the target analyte and the receptor. The optical property can be wavelength, absorption, polarization, dispersion, intensity, or refractive index (Soler et al., 2020). The ultimate level of disease diagnosis is molecular recognition, which occurs at the molecular level, which falls in the nanometer range. For example, single-stranded DNA can be recognized using complementary DNA, or antibodies can identify proteins. The question of how efficiently these molecules can be recognized using different nanophotonic phenomena and the information can obtain as signals remain exciting. The process is more challenging when the analyte concentration is less (Klar, 2007).

Efforts have been made to create electrical and electrochemical biosensors as well. Even though these methods promise a high detection limit, they lack repeatability and are highly sensitive to pH change. Many efforts on the development of optical biosensors to overcome these limitations are ongoing, among which many of them utilize light–matter interaction in nanoscale materials. We discuss the possibilities of such sensors in detail further in this chapter (Suthanthiraraj & Sen, 2019).

7.2 Plasmonic biosensors

Plasmonic biosensing can be used for the fast, real-time, and label-free detection of biomolecules with a short response time. Mainly, they

are of two types: those that use metallic thin films and those with inorganic plasmonic nanostructures (Mejía-Salazar & Oliveira, 2018; Shrivastav et al., 2021). Surface charge waves produced due to the confinement and propagation of electromagnetic waves at the dielectric–metal interface are surface plasmons (Hill, 2015). These waves exhibit an electromagnetic field that evanescently penetrates the dielectric up to a few hundreds of nanometers (10−300 nm) and is extremely sensitive to the changes induced due to biomolecular interactions. When specific biomolecules' recognition elements (e.g., antibodies or DNA strands) are immobilized on the gold surface, the specific binding between the target and analyte molecule induces a change in the refractive index or in the light properties, which can be monitored as signal and quantitative detection is possible by monitoring the changes (Soler et al., 2020).

A diverse spectrum of types of sensing is possible using plasmonic nanostructures (Hill, 2015). The key benefit of plasmonic biosensors is label-free detection, and the main limitation is the requirement of a pure sample to avoid nonspecific interactions (Mejía-Salazar & Oliveira, 2018). Different plasmonic sensors are discussed in detail as follows.

7.2.1 Propagating surface plasmons–based sensors

Traditional plasmon sensors are based on propagating plasmon waves through a metal–dielectric interface known as surface plasmon polaritons. If the external excitation used is in resonance with plasmon oscillation, surface plasmon resonance (SPR) can be achieved. Gold thin films are frequently used for sensing because of the SPR in visible wavelength and the ease of surface functionalization using gold–thiol interaction. A coupling medium is required to match the momentum of the excitation photon with that of the plasmon wave. The wave vector of the traveling plasmon wave and the excitation photon must match. Conventionally, this is achieved by using a prism, where the light falling on a metal–dielectric interface passes through the prism and facilitates total internal reflection at the metal–prism interface, as shown in Fig. 7.1. The method is known as the Kretschmann configuration. Propagating surface plasmons–based sensors with Kretschmann geometry are now a mature technology, and these sensors are commercially available. The coupling can also be achieved by using grating, waveguide, and optical fiber (Hill, 2015; Shrivastav et al., 2021; Svedendahl et al., 2009). The sensor can be developed either in an angle-resolved configuration or a wavelength-resolved configuration. In the angle-resolved configuration the excitation angle at which SPR

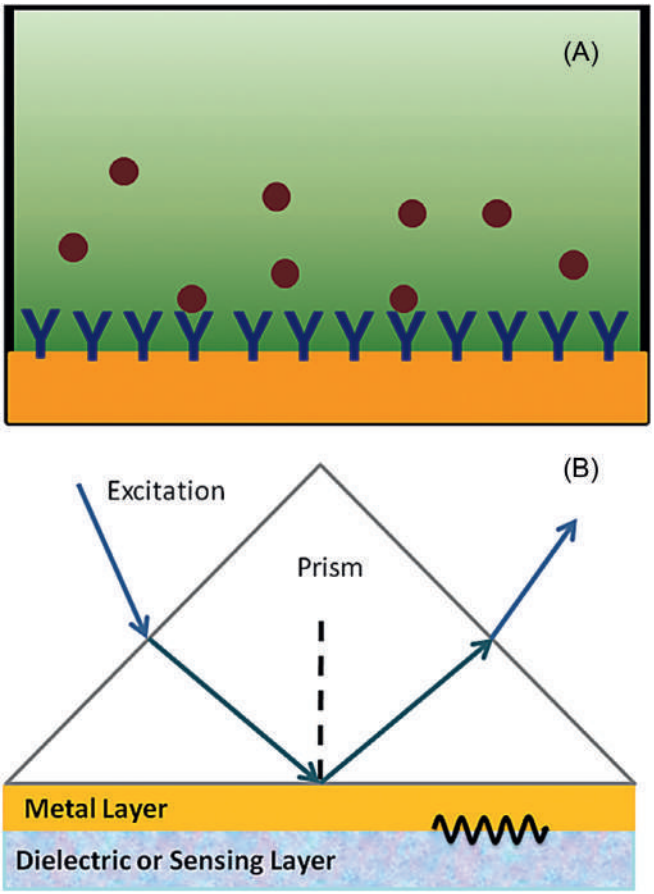

Figure 7.1. (A) Metal thin-film plasmonic biosensor to detect biomolecules through biomolecular interactions; (B) prism-based coupling used in the sensor.

occurs is found for single wavelength excitation. In wavelength resolved configuration the wavelength at which SPR occurs is scanned. In both cases SPR is highly sensitive to the refractive index of the dielectric medium, which in biosensors is an aqueous solution containing the analyte. The specific biomolecular interactions change the refractive index, and hence a change in the SPR angle or wavelength can be tackled. It can detect the refractive index change at the surface. Proper surface chemistry has to be used to immobilize an analyte-specific target at the metal thin-film surface. Thin film–based sensors are the most used because of the established technology and availability of instruments (Hill, 2015).

Companies like Biacore produce chip-based sensors using thin metal (~50 nm)–coated glass substrate. Even though label-free, fast detection is possible, these sensors have disadvantages like limitations of mass transportation and the risk of data misinterpretation. The equipment is massive due to the optics required to couple excitation light into the metal film and the need for temperature control to stabilize the SPR signal. Also, the propagation length of the SPR laterally on the film surface sets a lower limit on the size of the sensor surface (Hill, 2015).

The sensitivity in wavelength-resolved configuration can be defined as

$$S = \Delta\lambda/\Delta n \tag{7.1}$$

where $\Delta\lambda$ is the wavelength shift of the response spectrum when the refractive index of the test medium changes by Δn [12]. The figure of merit of the sensor can be calculated as

$$\text{FoM} = \frac{S}{\text{fwhm}} \tag{7.2}$$

where fwhm is the full width at half the maximum of the SPR peak (Svedendahl et al., 2009).

The limit of detection (LOD) of a sensor is the lowest concentration that can be reliably detected using the sensor. The LOD depends on the sensitivity of the sensor and the noise in the detection (Molina-Fernández et al., 2019).

Since this method is well established, many sensors have been reported so far. Here we attempt to review only the recent efforts. Omar et al. reported the sensitive detection of dengue virus using an SPR thin-film sensor. They used self-assembled monolayers of reduced graphene oxide–polyamidoamine dendrimer thin film. DENV-2 E proteins induced by the virus were detected using antibodies as a receptor. The authors claim early-stage detection of viral infection using the sensor with a detection limit of 0.08 pM (Omar et al., 2020).

The Kretschmann coupling method has been studied well and even commercialized, but the equipment needed for it is bulky. Here comes the importance of grating-based compact and portable sensors that can be integrated with other plasmonic structures (Nejat & Nozhat, 2020).

Shi et al. reported precise and label-free testing of clinical biomarkers by using an Au nanohole array–based sandwiched plasmon ruler. They could detect C-reactive protein and procalcitonin in patient serum samples without using a prism coupler, which proposes a miniature and more sensitive sensor. They measured the thickness change caused by the adsorption of biomolecules through molecular-specific binding using optical methods (Nan et al., 2020).

Prism-based coupling is not needed in a nanohole array platform as the periodic array acts as two-dimensional grating. The grating momentum wavevector can fulfill the energy and momentum conservation between excitation photons and surface plasmons. Incident photons couple through the periodic nanohole array and convert to plasmons that couple with the film and reradiate as photons through the opposite side. Since this radiation process occurs after excitations and propagation through the metal–dielectric interface, it is sensitive to refractive index changes in dielectric and hence can sense biomolecular interactions. Fig. 7.2 shows the experimental setup used for sensing. The local refractive index change can be obtained by analyzing the CCD image by integrating the transmission intensity over each spot area corresponding to holes (Lesuffleur et al., 2008).

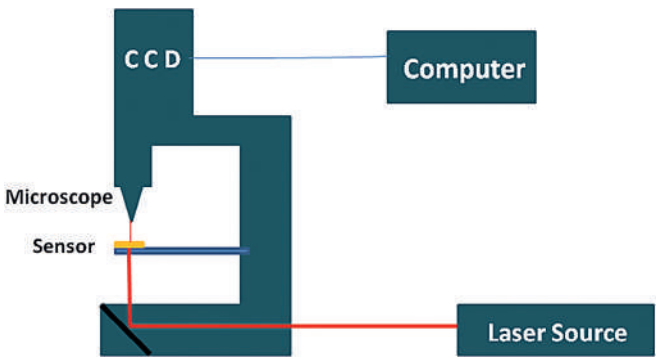

Figure 7.2. Experimental setup used for sensing using nanohole array.

A biosensor consisting of graphene–gold ellipse grating with SPR in the midinfrared region has been proposed by Sadeghi et al. They have used the geometrical features of the ellipse

grating to increase the strength of the biomolecules–ligand interaction, and the sensor has increased sensitivity and quality factor (Sadeghi & Shirkani, 2020).

Wu et al. used a graphene-protected Cu SPR sensor chip for biosensing. The analyte solution usually causes the corrosion of metals, which reduces the quality factor and sensitivity of the sensor. Also, surface functionalization of the plasmonic thin film itself might reduce the quality of the surface, which also causes lower sensitivity. The usage of graphene as a passivation layer can increase the sensitivity by three to four orders of magnitude. The graphene layer also preserves the plasmonic resonances under biofunctionalization (Wu et al., 2019). Xu et al. reported a MoS_2–aluminum-based sensor with high sensitivity and accuracy. The sensor exhibited better performance than graphene-based plasmonic sensors (Xu et al., 2014).

7.2.2 Localized SPR biosensor

The plasmon oscillations of metal nanoparticles are slightly different from those of thin films. It is known as localized surface plasmon resonance (LSPR), since the electromagnetic field is confined to metal nanostructure, as shown in Fig. 7.3 (Klar, 2007).

The size of the nanoparticles is so small that light can penetrate into the whole nanoparticle and oscillate the entire free electrons. The sea of free electrons is displaced from the positively charged ions and oscillates like a harmonic oscillator driven by the excitation light wave. There will be damping due to losses like ohmic loss and scattering loss. The scattering or radiative loss may lead to the reemission of a photon. Since LSPR does not travel, no coupling is required for excitation, which is the most significant advantage of nanoparticle-based sensors over thin-film sensors. The direction of excitation is not important; only the wavelength of excitation is important (Klar, 2007).

Similar to propagating SPR sensors, LSPR sensors are also susceptible to changes in the refractive index of the surrounding medium. However, LSPRs extend only a few nanometers into the analyte medium, hence the information is more localised. On the other hand, for thin films, the plasmon oscillation extends to hundreds of nanometers. The reduced sensing volume can lead to the extension of the detection limit to a single-molecule level. In consequence, extreme care must be taken when developing such a sensor to ensure that the binding of the target molecule occurs within the sensing volume (Hill, 2015).

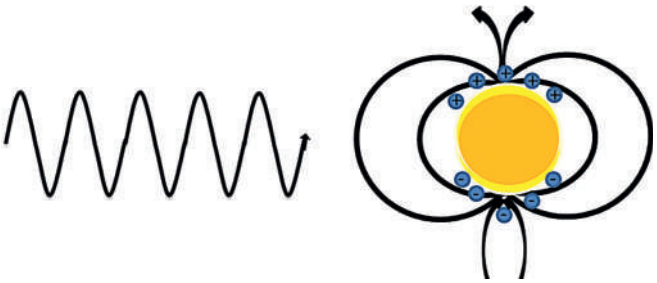

Figure 7.3. Plasmon resonance in metal nanoparticles.

Consider a metallic nanosphere with radius R, metallic dielectric constant ϵ_m and with a dielectric material of index ϵ_d around. According to Mie theory, the total extinction coefficient for an excitation ω:

$$\sigma_{ext} = 12\left(\frac{\omega}{c}\right)\pi\ \epsilon_d^{3/2}\ R^3 \frac{\mathrm{Im}\ (\epsilon_m)}{[\mathrm{Re}(\epsilon_m) + 2\epsilon_d]^2 + [\mathrm{Im}\ (\epsilon_m)]^2} \tag{7.3}$$

The equation has to be modified with the shape of the particle. Resonance occurs when the denominator is minimum, and hence the extinction coefficient is maximum. So the resonance condition can be written as:

$$\mathrm{Re}(\epsilon_m) + 2\ \epsilon_d = 0 \tag{7.4}$$

Eq. 7.4 is known as the Fröhlich condition to achieve LSPR. A strong absorption peak is observed at resonance due to the localization of a strong electromagnetic field around the nanoparticle. The resonance wavelength is highly sensitive to the nanoparticle's shape, size, and material and the medium around it (Shrivastav et al., 2021).

The shift in LSPR peak due to the adsorption of a molecular monolayer producing a change in refractive index Δn due to adsorption later can be found using

$$\Delta\lambda = \eta_b.\Delta n\left(1 - e^{-2d/I_d}\right) \tag{7.5}$$

where d is the effective thickness of the adsorption layer, I_d is the electromagnetic field decay length around the metal nanoparticle, and η_b is the bulk sensitivity of the sensor. Bulk sensitivity can be written as

$$\eta_b = \frac{\Delta\lambda_{LSPR}}{\Delta n_d} \tag{7.6}$$

$\Delta\lambda_{LSPR}$ — the wavelength shift in LSPR

Δn_d — the change in the refractive index of the surrounding medium

Sensing performance can be measured by exploring the figure of merit given by Eq. 7.2 (Csáki et al., 2018; Farooq & de Araujo, 2018). The sensitivity varies with the shape of the metal nanoparticles. Nanoparticles with a high aspect ratio have higher sensitivity. Compared to single nanoparticles, core–shell nanoparticles can be used to produce more sensitive sensors (Csáki et al., 2018).

LSPR-based sensors can be low cost, easy to use, and integrated with lateral flow-based ones where the color variation can be detected as the signal. When a metal nanoparticle colloidal solution experiences a refractive index change due to some molecular interaction, the color of the solution changes. The color change is due to a shift in resonance wavelength. The sensors can be called colorimetric sensors. The color can be enhanced by using fluorescent labels (Shrivastav et al., 2021).

Alafeef et al. reported a nanoamplified, RNA extraction–free colorimetric rapid test for COVID-19. The diagnosis can be made using the naked eye with a response time of less than 1 h. They detected the amplified nucleic acid from COVID-19 by using gold nanoparticles capped with antisense oligonucleotides as the colorimetric reporter. It is a low-cost, rapid sensor with minimal instrumentation. But the sensor demands a suitably clean environment as contaminations may lead to false signals, and the color perception cannot be trusted entirely (Alafeef et al., 2021).

Thermally annealed silver nanostructures were used to detect NS1 antigen, a dengue nonstructural protein, by Prashanth et al. For selective antigen detection, antibodies were immobilized on thermally annealed Ag thin film. The NS1 antigen was detected from blood plasma with a detection limit of 0.06 μg ml^{-1}. The sensor inlet was provided with a polyethersulfone membrane that can separate blood cells from plasma (Suthanthiraraj & Sen, 2019).

A fiber-optic biosensor based on Au nanoparticles–decorated ZnO nanowires was reported by Kim et al. Here, the LSPR of 3D nanostructures is used for sensing. The 3D nanostructure is composed of ZnO nanowires grown on the cross-section of optical fibers using the hydrothermal method and Au nanoparticles are immobilized on the nanowires. The sensor had a linear response to refractive index changes due to biomolecular interaction. Prostate cancer was detected by sensing prostate-specific antigen with an LOD of 0.51 pg mL^{-1}. In structures in which nanowires and nanoparticles are combined the surface area of the sensor is high, which traps more incident light to the sensing region due to its forest-like structure. As a result of the enhanced interaction of incident light, the sensor will have improved sensitivity (Kim et al., 2019).

Optical fiber coupling is important for dealing with LSPR sensors. Tuning the SPR frequency to the NIR regime will be highly beneficial since the attenuation coefficient at NIR is low. Ultrasensitive and long-range sensors can be deployed with NIR excitations. The SPR of Au nanostructures can be tuned to the NIR range if the aspect ratio is of the order of 10. The resonance band of transparent conducting oxide (TCO) nanomaterials can be shifted to the NIR range. That is, we should not be restricted to the use of typical metals for SPR sensors. Heavily doped degenerate semiconductors like Sn-doped In_2O_3 (ITO), Al-doped ZnO (AZO), In-doped CdO (ICO), and Ga-doped ZnO (GZO) have plasmonic resonance at the longer wavelengths. Superstructures, in which smaller nanoparticles are coupled to larger nanoparticles, forming core/satellite structures, can also have SPR in the NIR region (Dos Santos et al., 2021). F- and In-doped CdO nanoparticles with SPR between 1500 and 3300 nm were reported as excellent candidates for LSPR sensing applications (Ye et al., 2014).

The reproducibility of the sensing platform is one of the main challenges in the development of the LSPR sensor (Prabowo et al., 2018). Highly controllable and efficient fabrication of nanostructures is possible by adapting nanolithography techniques. The developments in cost-effective lithographic techniques have boosted the growth of chip-based LSPR. These are miniaturized and have high sensitivity and repeatability (Shrivastav et al., 2021).

El barghouti et al. reported an LSPR sensor based on Ag nanoparticles coated with graphene. They found that the graphene thickness can affect the sensitivity of the device, and a sensor with a 9-nm-thick graphene layer shows a 300% increase in sensitivity compared to a sensor without graphene. Also, graphene can protect Ag nanoparticles from oxidation (El barghouti et al., 2020).

The main advantages of LSPR sensors are a high surface area for the immobilization of sensing elements, the possibility of miniaturization of the device, and an increased likelihood for multiplexed detection. But on the other hand, LSPR sensors have lower refractive index sensitivity than thin-film SPR sensors, but the increased surface area provides more accommodation to biomolecules at sensing, resulting in the high sensitivity for biomolecule detection (Shrivastav et al., 2021).

SPR-based sensors were introduced three decades ago and have even been commercialized (LAuRA Digital Diagnostic Platform). SPR-based sensors have great potential to improve clinical detection accuracy and do not need a well-equipped laboratory and well-trained personnel, which is the main challenge in situations like pandemics (Soler et al., 2020; Bhalla et al., 2020). But the main challenge is the high cost of the equipment and components. For commercial implementation, low-cost sensors have to be developed (Prabowo et al., 2018).

7.3 Evanescent field waveguide biosensors

Evanescent field biosensors constructed using optical waveguides have high sensitivity. So these will be helpful in detecting biomolecules for which amplification is not possible. Ta_2O_5, Si, Si_3N_4, SiON, or SiO_2 waveguides have been widely studied in this regard. The fundamental discovery behind the development of evanescent field sensing was by Lukosz and colleagues in the 1980s. The light-guiding characteristics of high refractive index waveguides change due to a change in their environment. The group velocity of the guided mode in the waveguide changes in two ways: either due to a change in the refractive index of the surrounding liquid or gaseous medium or due to the adsorption of molecules from the medium onto the waveguide surface,

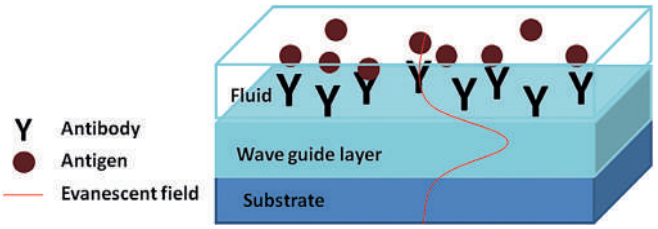

Figure 7.4. Schematic diagram showing the theory of evanescent field biosensing.

forming an adlayer. The evanescent field produced by the light traveling through the waveguide extends 30–100 nm into the surrounding cover layer, and the presence of the analyte in the cover layer can be detected through molecular-specific bonding. The schematic of the working of the evanescent field biosensor is shown in Fig. 7.4.

The group velocity of the guided mode:

$$V_p = \frac{c}{n_{eff}} \tag{7.7}$$

c—Speed of light in vacuum

n_{eff}—Refractive index of the waveguide

n_{eff} depends on the wavelength of light, the refractive index of the substrate, the refractive index of the waveguide, the refractive index of the cover, the thickness of the waveguide, the refractive index of the adlayer, and the thickness of the adlayer.

If the material of the waveguide has a high refractive index, then the adsorption of the molecule on the surface will lead to a significant change in n_{eff}. Such a waveguide, together with a grating coupler setup, can be used for the label-free detection of immune affinity reactions. If one of the binding partners is immobilized onto the surface of the waveguide, the presence of the other partner in the surrounding liquid medium can be selectively found (Schmitt, 2006; Schmitt et al., 2008).

These waveguides can be made compact and patterned in complex forms allowing the construction of a sensor array in a photonic chip. The waveguide sensor chip can be used for multiplexed analysis. Si photonic structures can be fabricated using etching and lithography. These methods also offer excellent reproducibility and precision (Huertas et al., 2019). With the help of lithographic methods, the sensor can be made on a chip of dimension in the micro- or nanoscale. For optical signal communication, the chip has to be integrated with optical fiber. Micron and nanochips maintain a small and elliptical mode field, whereas optical fiber has a relatively large (9–10 m) and single, circular mode field. This mismatch demands a grating coupler (Chen & Wang, 2020).

Instead of measuring the refractive index change, sensing is possible through evanescent fluorescence detection as well. Fluorescence-labeled sensors have been reported to have higher sensitivity and a higher possibility for multiplexing (Duveneck et al., 2002). The waveguide surface can be surface modified using emitting molecules. The target biomolecules are marked with a fluorescent tag and immobilized

on the receptor surface of the waveguide. The reduction in luminescent intensity in the presence of analyte due to fluorescent resonance energy transfer (FRET) can be used for detection (Aparicio et al., 2014).

The evanescent field can excite the fluorescence through the waveguide. Fluorescence-based optical waveguide sensors have better sensitivity and specificity, as well as ease of labeling. Since the detection is based on an evanescent field, the autofluorescence from complex analyte solutions can be avoided. The disadvantage of fluorescence detection is the rapid photobleaching of fluorescent organic dye markers (Mukundan et al., 2009a). This can be overcome by using quantum dots as fluorescent labels. Also, multiplex detection is possible by using quantum dots that emit at different wavelengths (Luchansky et al., 2010).

Mukundan et al. used a sensitive waveguide-based optical biosensor for cancer detection. They developed a sandwich immunoassay by functionalizing the surface of single-mode planar optical waveguides using a fluorescently labeled detector antibody. Fluorescent molecules are excited only when they are within the evanescent field of the waveguide (within a 0–250 nm distance from the surface). This spatial filtering can be used to identify the presence of an analyte through selective binding. It also minimizes the background fluorescence because of biomolecules in complex biological samples like blood and sputum (Luchansky et al., 2010; Mukundan et al., 2009b).

Waveguide-based biosensors are already commercialized, for example, OWLSTM 210 by MicroVacuum Ltd. It is a highly sensitive, label-free biosensor system. It offers real-time quantitative measurements. The main application of the sensor is in drug determination (Aparicio et al., 2014).

Makela et al. used Si_3N_4 nanoslot fluidic waveguides to detect coronavirus DNA (cDNA) sequences. A strong evanescent field can be created by a nanoslot arrangement that makes strong confinement of light within the slot region. The slot also serves as a fluidic channel for the analyte solution. cDNA was synthesized using a standard reverse transcription protocol on viral RNA. The excitation light was collimated through a single-mode silica fiber that was butt-coupled with the waveguide through its front facet. The green light guided through the waveguide excites fluorescence from the labeled DNA, and the emission is collected using a multimode silica fiber connected to a CCD spectrometer (Makela & Lin, 2021).

Instead of the waveguide, light through a resonator can also be used for sensing. When light travels through a ring shaped micro-waveguide, the evanescent field forms whispering gallery modes (WGMs). These WGMs are extremely sensitive to the refractive index outside the resonator.

These Si-based direct-detection biosensors have a high potential as low-cost, high-yield, and portable sensors for point-of-care diagnosis (Gauglitz, 2020).

7.4 Förster resonance energy transfer sensors

Förster resonance energy transfer, or FRET, is a sensitive and selective analytical technique employed for fluorescence chemical sensing. It is a distance-dependent nonradioactive process between two fluorophores in which resonance energy transfer occurs between a fluorophore (donor) and another fluorophore or quencher nanoparticle (acceptor), as shown in Fig. 7.5. The method can be used to measure the nanoscale distance between two molecules. FRET is one of the best methods aimed at biosensing, bioimaging, and drug delivery. Integrating nanomaterials in FRET sensing will improve its sensitivity and specificity. Luminescent nanoparticles as donors can overcome the demerits of conventional dyes like poor photobleaching resistance, short fluorescence lifetime, and low chemical stability. Fluorescent proteins can also be used as a donor, permitting sensing within living cells to detect dynamic intracellular interactions. Noble metal nanoparticles and graphene oxide (GO) are the commonly used acceptors in FRET sensors. FRET sensors are widely studied for detecting biomolecules like glucose, antibodies, nucleic acids, etc. This method has unique advantages like high sensitivity and reproducibility. In this method the concentration of the analyte can also be measured with good accuracy. Accurate detection of biomolecules like glucose both in vivo and in vitro has attracted much attention. FRET allows the monitoring of the concentration of an analyte in sensitive samples with minimal disturbance (Choi et al., 2021; Shi et al., 2015a).

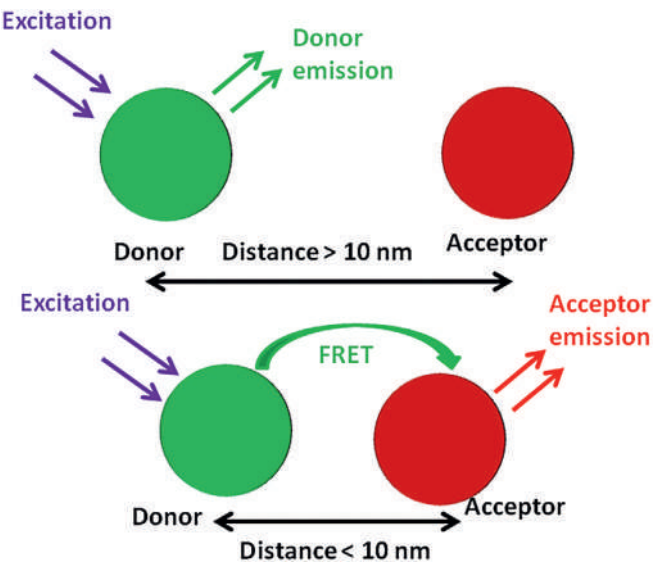

Figure 7.5. The mechanism of FRET. FRET occurs when the donor and acceptor distance is <10 nm.

A Coulombic interaction between the excited donor molecules and the acceptor molecules can be electric dipole–dipole approximately. Suppose there is a spectral overlap between the emission and absorption of donor and acceptor molecules. In that case if the donor's fluorescence quantum yield and the acceptor's absorption coefficient are high

enough, the excitation energy will transfer nonradiatively from the donor to the acceptor when the two dipoles are close enough (with a separation smaller than 10 nm). The process is nonradiative, which means that the transition occurs without the emission or absorption of a photon.

The efficiency (E) of FRET can be defined as the number of energy transfer events per donor excitation.

$$E = \frac{k_{ET}}{k_f + k_{ET} + \sum_i k_i} \tag{7.8}$$

where

k_{ET}—the rate of energy transfer

k_f—the radiative decay rate

ki—the rate of other deexcitation pathways

The rate of energy transfer is inversely proportional to the fluorescence lifetime of the donor molecule in the absence of the acceptor molecule.

$$E = \frac{\tau_D - \tau_{DA}}{\tau_D} \tag{7.9}$$

τ_D—Donor lifetime in the absence of the acceptor

τ_{DA}—Fluorescence lifetime of the donor in the presence of the acceptor

The efficiency of FRET depends on:

- Spectral overlap between the donor and acceptor
- Excited-state lifetime of the donor and acceptor
- The relative orientation of donor and acceptor dipoles
- Donor–acceptor distance

The relation between efficiency and donor–acceptor distance can be written as:

$$E = \frac{1}{1 + \left(\frac{r_{DA}}{R_0}\right)^6} \tag{7.10}$$

where

r_{DA}—the donor–acceptor distance

R_0—the distance at which the transfer efficiency is 50% (Förster distance) (Clegg, 2009).

The energy transfer efficiency is inversely proportional to the sixth power of the donor–acceptor distance, making it highly sensitive to the distance between donor and acceptor. Hence it is a sharp tool for molecular-level information tackling. FRET need not always be associated with fluorescence. It is only one way to measure the energy transfer between the donor and acceptor (Clegg, 2009; Shi et al., 2015b).

Shi et al. reported a graphene quantum dot (donor)–gold nanoparticles (acceptor) FRET biosensor to detect the *mecA* gene sequence

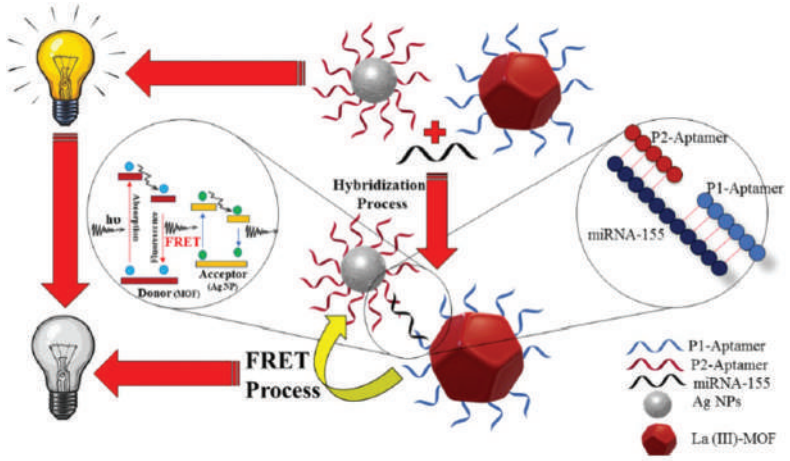

Figure 7.6. Schematic diagram for the FRET sensing of miRNA-155 using La(III)-MOF and Ag nanoparticles. Reprinted (adapted) with permission from Afzalinia & Mirzaee (2020). Copyright 2020 American Chemical Society.

of *Staphylococcus aureus*. This borne bacterium can produce heat-resistant toxins in food. The LOD of their biosensor was around 1 nM (Shi et al., 2015a).

An upconversion (Anjana et al., 2018) FRET sensor was developed by Xu et al. to detect lead ions in human serum. The NIR excitation in upconversion luminescent donors helps overcome self-luminescence from the serum. The LOD of their biosensor was 80 nM (Xu et al., 2014).

Afzalinia et al. developed an ultrasensitive FRET sensor for early-stage cancer diagnosis, as shown in Fig. 7.6. The rapid and selective detection of MicroRNA-155 (miRNA-155), a cancer biomarker, was demonstrated. There have been reports about the presence of miRNA-155 unusually in biological fluid samples of breast or lung cancer patients. So the detection of this biomarker with high sensitivity can lead to an early-stage diagnosis. A modified La(III) metal–organic framework (MOF) is used as the donor and an Ag nanoparticle as acceptor. The LOD of the sensor is 0.0386 ppb (Afzalinia & Mirzaee, 2020).

Specific, sensitive, fast, and quantitative detection of SARS-CoV-2 was demonstrated using a FRET assay by Alhadrami et al. The extracellular protease is used as the virus biomarker. The LOD of the method was 9.7 ± 3 pfu mL^{-1}. They propose a short time and low-cost diagnosis. Fluorogenic dipeptide with a fluorophore and a quencher on both ends was used as a substrate, and the SARS-CoV-2 protease analyte was identified and quantized by the increase in fluorescence (Alhadrami et al., 2021).

Fu et al. achieved the specific and rapid detection of the intracellular pathogen using a FRET nanoprobe. Aptamer-modified quantum dots were used as the donor and Teicoplanin antibiotic functionalized-gold nanoparticles as the acceptor (Fu et al., 2020).

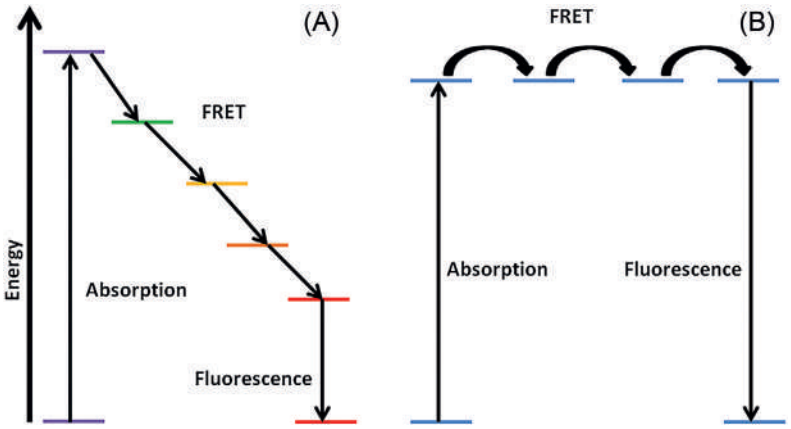

Figure 7.7. Schematic diagram showing energy level transitions of multistep (A) hetero-FRET and (B) homo-FRET.

Geldert et al. proposed an aptamer- and MoS_2 nanosheet paper–based FRET sensor for detecting plasmodium lactate dehydrogenase (pLDH), a malarial biomarker. Developing a paper-based FRET sensor that is simple and cost-effective will encourage the commercialization of FRET sensors that already have advantages like high sensitivity and accuracy in quantitative analysis (Geldert et al., 2017).

In some cases a single FRET transfer is not sufficient. The distance between the two molecules can be too large, or in some cases more accurate positioning may be required. In such situations the FRET can be expanded to include more than one donor and acceptor, as shown in Fig. 7.7.

Snell et al. developed a homotransfer FRET (homo-FRET) double-fluorophore biosensor. Homotransfer sensors have advantages over heterotransfer (hetero-FRET) biosensors, including increased measurement precision, flexibility for multiplexing, and improved data analysis methods (Snell et al., 2018). A six-color FRET multiplexed biosensor was developed by Geißler et al. for detecting five different binding events simultaneously. Five different organic dyes can be used for measurement in a filter-based time-resolved detection format. All five markers have a detection limit in the picomolar range. The sensor can distinguish between small-cell and non-small-cell lung carcinoma from human serum. The sensor will be helpful in early-stage screening and therapy monitoring, which can replace lung biopsies (Geißler et al., 2013).

7.5 Multimodal sensors

Different nanophotonic sensing platforms can be used in combination to develop a more reliable sensor. Many multimodal sensors

have been reported so far. Surface-enhanced Raman spectroscopy (SERS) is a commonly used sensing platform with unique advantages like excellent detection limit and specificity. Fluorescence–SERS dual nanotag is commonly used for multimodal sensing. Wang et al. developed organic−metal−QD hybrid nanoparticles as a fluorescent–SERS dual tag for immunoassay (Wang et al., 2012). Cui et al. used Au@organosilica multifunctional nanoparticles for fluorescent–SERS dual-sensing. The Au core acts as a SERS substrate and silica as a fluorophore (Cui et al., 2011). Niu et al. developed upconversion SERS dual-mode tags for in vivo imaging (Niu et al., 2014). All these reports suggest that dual-modal sensing can increase the reliability of the device as the fluorescence serves as a fast indicator and the SERS signal is more target specific.

Sensitive and accurate FRET–SERS dual sensors can also be developed. The disadvantage of FRET sensors is that they are not very specific to the analyte. This can be overcome by combining a SERS-based sensor and FRET sensor in the form of a dual sensor. Some reports exist about dual-channel FRET sensors that combine FRET with pH change (Cui et al., 2011; Niu et al., 2014).

Qiu et al. reported dual-functional plasmonic photothermal biosensors for coronavirus 2 detection. They have combined the photothermal effect and plasmonic sensing for nucleic acid detection with improved sensitivity and detection limit (0.22 pM) (Qiu et al., 2020). SARS-CoV-2 DNA sequences were identified using nucleic acid hybridization. The authors used LSPR in nanoparticles along with plasmonic photothermal (PPT) effect. The *in situ* hybridization temperature was elevated using thermoplasmonic heat to discriminate between two similar gene sequences (Bhalla et al., 2020).

7.6 Summary

Nanophotonic biosensors are very promising for disease diagnosis. Many of the methods have been well studied and they have been reported to have many advantages compared to conventional sensor kits. All these are excellent platforms for molecular recognition. Even though there are commercially available sensors, the large-scale application is not possible due to the production cost and advanced detection setup requirement. These sensors have to be cost effective and have to be implemented without costly equipment requirements. Paper-based FRET sensors and fluorescence-based waveguide chip sensors are promising in this aspect. The majority of the methods offer multiplexed detection, which is crucial for diagnosing newly found or mutating pathogens. Multimodal detection offers highly desirable sensors by combining the advantages of multiple methods. For example,

FRET–SERS sensors can provide the specificity of SERS sensors and accuracy in quantitative detection provided by FRET sensing.

References

Afzalinia, A., Mirzaee, M., 2020. Ultrasensitive fluorescent miRNA biosensor based on a "sandwich" oligonucleotide hybridization and fluorescence resonance energy transfer process using an Ln(III)-MOF and Ag nanoparticles for early cancer diagnosis: Application of central composite design. ACS Appl. Mater. Interfaces 12 (14), 16076–16087. https://doi.org/10.1021/acsami.0c00891.

Alafeef, M., Moitra, P., Dighe, K., Pan, D., 2021. RNA-extraction-free nano-amplified colorimetric test for point-of-care clinical diagnosis of COVID-19. Nat. Protoc. 16 (6), 3141–3162. https://doi.org/10.1038/s41596-021-00546-w.

Alhadrami, H.A., Hassan, A.M., Chinnappan, R., Al-Hadrami, H., Abdulaal, W.H., Azhar, E.I., Zourob, M., 2021. Peptide substrate screening for the diagnosis of SARS-CoV-2 using fluorescence resonance energy transfer (FRET) assay. Microchim. Acta 188 (4). https://doi.org/10.1007/s00604-021-04766-5.

Anjana, R., Jayaraj, M.K., Yadav, A.K., Jha, S.N., Bhattacharyya, D., 2018. Investigating the evolution of local structure around Er and Yb in ZnO:Er and ZnO:Er, Yb on annealing using X-ray absorption spectroscopy. J. Appl. Phys. 123 (15), 153102. https://doi.org/10.1063/1.5022638.

Aparicio, F.J., Froner, E., Rigo, E., Gandolfi, D., Scarpa, M., Han, B., Ghulinyan, M., Pucker, G., Pavesi, L., 2014. Silicon oxynitride waveguides as evanescent-field-based fluorescent biosensors. J. Phys. D Appl. Phys. 47 (40). https://doi.org/10.1088/0022-3727/47/40/405401.

Bhalla, N., Pan, Y., Yang, Z., Payam, A.F., 2020. Opportunities and challenges for biosensors and nanoscale analytical tools for pandemics: COVID-19. ACS Nano 14 (7), 7783–7807. https://doi.org/10.1021/acsnano.0c04421.

Chen, C., Wang, J., 2020. Optical biosensors: An exhaustive and comprehensive review. Analyst 145 (5), 1605–1628. https://doi.org/10.1039/c9an01998g.

Choi, J.H., Ha, T., Shin, M., Lee, S.N., Choi, J.W., 2021. Nanomaterial-based fluorescence resonance energy transfer (Fret) and metal-enhanced fluorescence (mef) to detect nucleic acid in cancer diagnosis. Biomedicines 9 (8). https://doi.org/10.3390/biomedicines9080928.

Clegg, R.M., 2009. Förster resonance energy transfer-FRET what is it, why do it, and how it's done. Lab. Tech. Biochem. Mol. Biol., Elesvier B.V 1–5. https://doi.org/10.1016/S0075-7535(08.

Csáki, A., Stranik, O., Fritzsche, W., 2018. Localized surface plasmon resonance based biosensing. Expert Rev. Mol. Diagn. 18 (3), 279–296. https://doi.org/10.1080/14737159.2018.1440208.

Cui, Y., Zheng, X.S., Ren, B., Wang, R., Zhang, J., Xia, N.S., Tian, Z.Q., 2011. Au@organosilica multifunctional nanoparticles for the multimodal imaging. Chem. Sci. 2 (8), 1463–1469. https://doi.org/10.1039/c1sc00242b.

Dos Santos, P.S.S., de Almeida, J.M.M.M., Pastoriza-santos, I., Coelho, L.C.C, 2021. Advances in plasmonic sensing at the NIR—A review. Sensors 21 (6), 1–48. https://doi.org/10.3390/s21062111.

Duveneck, G.L., Abel, A.P., Bopp, M.A., Kresbach, G.M., Ehrat, M., 2002. Planar waveguides for ultra-high sensitivity of the analysis of nucleic acids. Anal. Chim. Acta 469 (1), 49–61. https://doi.org/10.1016/S0003-2670(01)01593-8.

El barghouti, M., Akjouj, A., Mir, A., 2020. Design of silver nanoparticles with graphene coatings layers used for LSPR biosensor applications. Vacuum 180. https://doi.org/10.1016/j.vacuum.2020.109497.

Farooq, S., de Araujo, R.E., 2018. Engineering a localized surface plasmon resonance platform for molecular biosensing. Open Journal of Applied Sciences 126–139. https://doi.org/10.4236/ojapps.2018.83010.

Fu, F., Zhang, Y., Li, L., Wang, H., Li, Q., Tao, X., Song, Y., Song, E., 2020. Intracellular pathogen detection based on dual-recognition units constructed fluorescence resonance energy transfer nanoprobe. Anal. Chem. 92 (16), 11462–11468. https://doi.org/10.1021/acs.analchem.0c02695.

Gauglitz, G., 2020. Critical assessment of relevant methods in the field of biosensors with direct optical detection based on fibers and waveguides using plasmonic, resonance, and interference effects. Anal. Bioanal.Chem. 412 (14), 3317–3349. https://doi.org/10.1007/s00216-020-02581-0.

Geißler, D., Stufler, S., Löhmannsröben, H.G., Hildebrandt, N., 2013. Six-color time-resolved Förster resonance energy transfer for ultrasensitive multiplexed biosensing. J. Am. Chem. Soc. 135 (3), 1102–1109. https://doi.org/10.1021/ja310317n.

Geldert, A., Kenry, Lim, C.T, 2017. Paper-based MoS_2 nanosheet-mediated FRET aptasensor for rapid malaria diagnosis. Sci. Rep. 7 (1). https://doi.org/10.1038/s41598-017-17616-3.

Hill, R.T., 2015. Plasmonic biosensors. WIREs Nanomedicine and Nanobiotechnology 7 (2), 152–168. https://doi.org/10.1002/wnan.1314.

Huertas, C.S., Calvo-Lozano, O., Mitchell, A., Lechuga, L.M., 2019. Advanced evanescent-wave optical biosensors for the detection of nucleic acids: An analytic perspective. Frontiers in Chemistry 7. https://doi.org/10.3389/fchem.2019.00724.

Kim, H.M., Park, J.H., Lee, S.K., 2019. Fiber optic sensor based on ZnO nanowires decorated by Au nanoparticles for improved plasmonic biosensor. Sci. Rep. 9 (1). https://doi.org/10.1038/s41598-019-52056-1.

Klar, T.A., 2007. Biosensing with plasmonic nanoparticles. Nanophotonics With Surface Plasmons. Elsevier, pp. 219–270.

Koenderink, A.F., Alù, A., Polman, A., 2015. Nanophotonics: Shrinking light-based technology. Science 348 (6234), 516–521. https://doi.org/10.1126/science.1261243.

Lee, W., Straube, S., Sincic, R., Noble, J. A., Montoy, J. C., Kornblith, A. E., Prakash, A., Wang, R., Bainton, R. J., & Kurien, P. A. (2020). Clinical evaluation of a COVID-19 antibody lateral flow assay using point of care samples. medRxiv. https://doi.org/10.1101/2020.12.02.20242750

Lesuffleur, A., Im, H., Lindquist, N.C., Lim, K.S., Oh, S.H., 2008. Laser-illuminated nanohole arrays for multiplex plasmonic microarray sensing. Opt. Express 16 (1), 219–224. https://doi.org/10.1364/OE.16.000219.

Luchansky, M.S., Washburn, A.L., Martin, T.A., Iqbal, M., Gunn, L.C., Bailey, R.C., 2010. Characterization of the evanescent field profile and bound mass sensitivity of a label-free silicon photonic microring resonator biosensing platform. Biosens. Bioelectron. 26 (4), 1283–1291. https://doi.org/10.1016/j.bios.2010.07.010.

Makela, M., Lin, P.T., 2021. Detection of SARS-CoV-2 DNA targets using femtoliter optofluidic waveguides. Anal. Chem. 93 (9), 4154–4159. https://doi.org/10.1021/acs.analchem.0c02971.

Mejía-Salazar, J.R., Oliveira, O.N., 2018. Plasmonic biosensing. Chem. Rev. 118 (20), 10617–10625. https://doi.org/10.1021/acs.chemrev.8b00359.

Mishra, P.K., Shandilya, R., 2020. Nanophotonic biosensors as point-of-care tools for preventive health interventions. Nanomedicine 15 (16), 1541–1544. https://doi.org/10.2217/nnm-2020-0162.

Molina-Fernández, Í., Leuermann, J., Ortega-Moñux, A., Wangüemert-Pérez, J.G., Halir, R., 2019. Fundamental limit of detection of photonic biosensors with coherent phase read-out. Opt. Express 27 (9), 12616–12629. https://doi.org/10.1364/OE.27.012616.

Mukundan, H., Anderson, A.S., Grace, W.K., Grace, K.M., Hartman, N., Martinez, J.S., Swanson, B.I., 2009a. Waveguide-based biosensors for pathogen detection. Sensors 9 (7), 5783–5809. https://doi.org/10.3390/s90705783.

Mukundan, H., Xie, H., Anderson, A.S., Grace, W.K., Shively, J.E., Swanson, B.I., 2009b. Optimizing a waveguide-based sandwich immunoassay for tumor biomarkers: Evaluating fluorescent labels and functional surfaces. Bioconjugate Chem. 20 (2), 222–230. https://doi.org/10.1021/bc800283e.

Nan, J., Zhu, S., Ye, S., Sun, W., Yue, Y., Tang, X., Shi, J., Xu, X., Zhang, J., Yang, B., 2020. Ultrahigh-sensitivity sandwiched plasmon ruler for label-free clinical diagnosis. Adv. Mater. 32 (2). https://doi.org/10.1002/adma.201905927.

Nejat, M., Nozhat, N., 2020. Multi-band MIM refractive index biosensor based on Ag-air grating with equivalent circuit and T-matrix methods in near-infrared region. Sci. Rep. 10 (1). https://doi.org/10.1038/s41598-020-63459-w.

Niu, X., Chen, H., Wang, Y., Wang, W., Sun, X., Chen, L., 2014. Upconversion fluorescence-SERS dual-mode tags for cellular and in vivo imaging. ACS Appl. Mater. Interfaces 6 (7), 5152–5160. https://doi.org/10.1021/am500411m.

Omar, N.A.S., Fen, Y.W., Abdullah, J., Mustapha Kamil, Y., Daniyal, W.M.E.M.M., Sadrolhosseini, A.R., Mahdi, M.A., 2020. Sensitive detection of dengue virus type 2 E-proteins signals using self-assembled monolayers/reduced graphene oxide-PAMAM dendrimer thin film-SPR optical sensor. Sci. Rep. 10 (1). https://doi.org/10.1038/s41598-020-59388-3.

Prabowo, B.A., Purwidyantri, A., Liu, K.C., 2018. Surface plasmon resonance optical sensor: A review on light source technology. Biosensors 8 (3). https://doi.org/10.3390/bios8030080.

Prasad, P. N. (n.d.). Introduction. In: Nanophotonics (Vol. 2, Issue 1, pp. 1–8). Wiley. https://doi.org/10.1002/0471670251.ch1.

Qiu, G. Gai, Z., Tao, Y., Schmitt, J., Kullak-Ublick, G.A., Wang, J., Dual-Functional Plasmonic Photothermal Biosensors for Highly Accurate Severe Acute Respiratory Syndrome Coronavirus 2 Detection, ACS Nano. 14 (2020) 5268–5277. doi:10.1021/acsnano.0c02439.

Sadeghi, Z., Shirkani, H., 2020. Highly sensitive mid-infrared SPR biosensor for a wide range of biomolecules and biological cells based on graphene-gold grating. Physica E 119. https://doi.org/10.1016/j.physe.2020.114005.

Schmitt, K. (2006). A new waveguide interferometer for the label free detection of biomolecules. (PhD thesis), Louis Pasteur University of Strasbourg.

Schmitt, K., Oehse, K., Sulz, G., Hoffmann, C., 2008. Evanescent field sensors based on tantalum pentoxide waveguides—A review. Sensors 8 (2), 711–738. https://doi.org/10.3390/s8020711.

Shi, J., Chan, C., Pang, Y., Ye, W., Tian, F., Lyu, J., Zhang, Y., Yang, M., 2015a. A fluorescence resonance energy transfer (FRET) biosensor based on graphene quantum dots (GQDs) and gold nanoparticles (AuNPs) for the detection of mecA gene sequence of *Staphylococcus aureus*. Biosens. Bioelectron. 67, 595–600. https://doi.org/10.1016/j.bios.2014.09.059.

Shi, J., Tian, F., Lyu, J., Yang, M., 2015b. Nanoparticle based fluorescence resonance energy transfer (FRET) for biosensing applications. Journal of Materials Chemistry B 3 (35), 6989–7005. https://doi.org/10.1039/c5tb00885a.

Shrivastav, A.M., Cvelbar, U., Abdulhalim, I., 2021. A comprehensive review on plasmonic-based biosensors used in viral diagnostics. Communications Biology 4 (1). https://doi.org/10.1038/s42003-020-01615-8.

Snell, N.E., Rao, V.P., Seckinger, K.M., Liang, J., Leser, J., Mancini, A.E., Rizzo, M.A., 2018. Homotransfer FRET reporters for live cell imaging. Biosensors 8 (4). https://doi.org/10.3390/bios8040089.

Soler, M., Estevez, M.C., Cardenosa-Rubio, M., Astua, A., Lechuga, L.M., 2020. How nanophotonic label-free biosensors can contribute to rapid and massive

diagnostics of respiratory virus infections: COVID-19 case. ACS Sensors 5 (9), 2663–2678. https://doi.org/10.1021/acssensors.0c01180.

Suthanthiraraj, P. A., P., Sen, A.K, 2019. Localized surface plasmon resonance (LSPR) biosensor based on thermally annealed silver nanostructures with on-chip blood-plasma separation for the detection of dengue non-structural protein NS1 antigen. Biosens. Bioelectron. 132, 38–46. https://doi.org/10.1016/j.bios.2019.02.036.

Svedendahl, M., Chen, S., Dmitriev, A., Käll, M., 2009. Refractometric sensing using propagating versus localized surface plasmons: A direct comparison. Nano Lett. 9 (12), 4428–4433. https://doi.org/10.1021/nl902721z.

Wang, Z., Zong, S., Li, W., Wang, C., Xu, S., Chen, H., Cui, Y., 2012. SERS-fluorescence joint spectral encoding using organic-metal-QD hybrid nanoparticles with a huge encoding capacity for high-throughput biodetection: Putting theory into practice. J. Am. Chem. Soc. 134 (6), 2993–3000. https://doi.org/10.1021/ja208154m.

Wu, F., Thomas, P.A., Kravets, V.G., Arola, H.O., Soikkeli, M., Iljin, K., Kim, G., Kim, M., Shin, H.S., Andreeva, D.V., Neumann, C., Küllmer, M., Turchanin, A., De Fazio, D., Balci, O., Babenko, V., Luo, B., Goykhman, I., Hofmann, S., … Grigorenko, A.N., 2019. Layered material platform for surface plasmon resonance biosensing. Sci. Rep. 9 (1). https://doi.org/10.1038/s41598-019-56105-7.

Xu, S., Xu, S., Zhu, Y., Xu, W., Zhou, P., Zhou, C., Dong, B., Song, H., 2014. A novel upconversion, fluorescence resonance energy transfer biosensor (FRET) for sensitive detection of lead ions in human serum. Nanoscale 6 (21), 12573–12579. https://doi.org/10.1039/c4nr03092c.

Ye, X., Fei, J., Diroll, B.T., Paik, T., Murray, C.B., 2014. Expanding the spectral tunability of plasmonic resonances in doped metal-oxide nanocrystals through cooperative cation-anion codoping. J. Am. Chem. Soc. 136 (33), 11680–11686. https://doi.org/10.1021/ja5039903.

8

Precision nanoclusters: promising materials for sensing, optoelectronics, and biology

J.V. Rival[a], **P. Mymoona**[b,c] **and E.S. Shibu**[a]

[a]*Smart Materials Lab, Department of Nanoscience and Technology, University of Calicut, Kerala, India.* [b]*Electroplating and Metal Finishing Division (EMFD), Council of Scientific and Industrial Research (CSIR)-Central Electrochemical Research Institute (CECRI), Karaikudi, India.* [c]*Academy of Scientific and Innovative Research (AcSIR)-CSIR, Ghaziabad, India*

8.1 Introduction

Precision nanoclusters-based sensors have grown exponentially over the last few decades. During this time, the size-focused synthetic strategies and surface functionalization of nanoclusters have been significantly improved. Nanoclusters with photoluminescence properties have been proven to be extremely useful in the qualitative and quantitative detection of analytes due to their ultrasmall size, low toxicity, aqueous solubility, large Stokes shift, and high photoluminescence quantum yield. The photoluminescence enhancement or quenching could be used as a visual detection method for different analytes, including metal cations, anions, gases, and biomolecules due to the different possible interactions between nanoclusters and analytes. In this section we summarize the sensing applications of precision noble metal nanoclusters.

8.1.1 Cation sensing

The metal pollutants present in the environment harm both the ecosystem and the metabolic pathways of living organisms. As a result, the metal pollutants must be monitored and controlled. Metal pollutants have been detected conventionally using spectroscopic or chromatographic techniques. However, this process requires a more prolonged duration since it needs sophisticated instrumentation techniques or experienced personnel. Many advanced nanomaterials have

Nanomaterials for Sensing and Optoelectronic Applications. DOI: https://doi.org/10.1016/B978-0-128-24008-3.00009-6

been used for the fast and reliable sensing of metal ions in the recent past, emphasizing the importance of portable and low-cost sensors. Precision noble metal nanoclusters, possessing inherent photoluminescence, were found to have good metal ion sensing ability. Therefore analytes can be detected in situ by exploiting the strong interactions with nanoclusters' metallic core or their surface ligands. For example, some analytes have a strong affinity to the closed electronic configuration of the metal core. In other cases the analytes interact with surface ligands through electrostatic interaction, resulting in metal chelation. These specific interactions cause changes in the photoluminescence of nanoclusters, making the analytes detectable. The changes in the photoluminescence intensity of nanoclusters could also be directly correlated with the concentration of analytes. The specific sensing of various metal ions is described below.

8.1.1.1 Mercury (Hg^{2+}) sensing

Mercury is one of the potentially toxic heavy metals that harm living organisms (Holmes et al., 2009). It can trigger neurological, cardiovascular, and renal disorders even in trace amounts. As a result, the selective detection of mercury in the environment is critical for preventing health problems. Luminescent noble metal nanoclusters were found to be excellent probes for detecting mercury ions. The metallic core of nanoclusters has a higher percentage of M(I) (M = Au or Ag) content compared to plasmonic nanoparticles. Au(I) or Ag(I) metal cores with a closed-shell electronic configuration or d^{10} structure have a greater binding affinity toward Hg(II) ions. Since Hg(II) ions also hold a d^{10} electronic configuration, an efficient metallophilic bond formation is possible between the nanocluster core and Hg(II) ions. Such an Au(I)–Hg(II) interaction helps alter the electronic structures of gold nanoclusters. As a result, even a trace amount of Hg(II) ions in the solution can quench the photoluminescence of nanoclusters. Based on this molecular recognition chemistry, several nanocluster-based fluorescent probes have been developed to detect Hg(II) ions. For example, bovine serum albumin–protected luminescent gold nanoclusters (Au@BSA) were found to be an effective Hg(II) sensor (Fig. 8.1A–C) as they could selectively quench their photoluminescence in the presence of Hg(II) ions (Xie et al., 2010). Different surface-modified nanoclusters, including Au@BSA nanoclusters–entrapped sol–gel sensory films (Hofmann et al., 2014), α-chymotrypsin-protected gold nanoclusters blotted in the cellulose membrane (Liu et al., 2014), and Au@BSA nanoclusters–coated polymeric electrospun nanofibers (Senthamizhan et al., 2015), have also been used for selective Hg(II) ion detection. In contrast to Hg(II) ions, another toxic species of mercury,

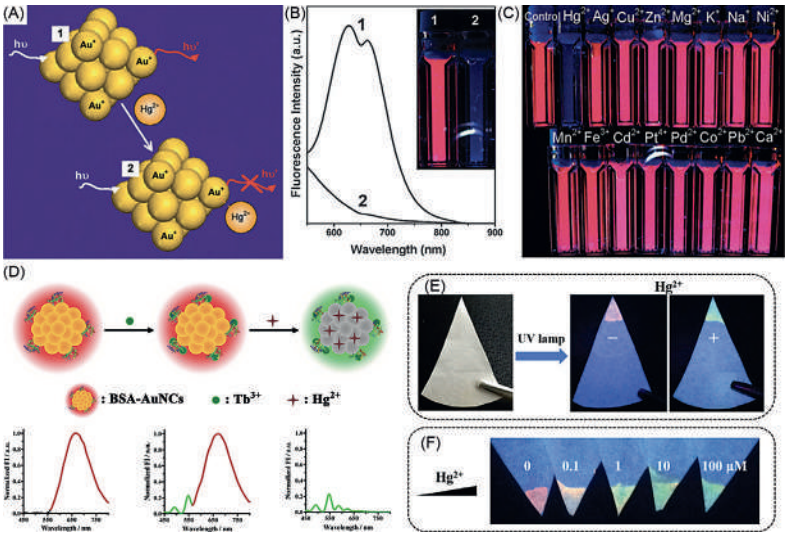

Figure 8.1. (A) Schematic representation of Hg(II) sensing based on the fluorescence quenching of Au@BSA nanoclusters. (B) Photoemission spectra and photographs of Au@BSA nanoclusters under UV light in the (1) absence and (2) presence of Hg(II) ions (50 μM). (C) Photographs of an aqueous solution of nanoclusters (20 mM) under UV light in the presence of 50 μM concentration of various metal ions. (D) Schematic illustration of Hg(II) sensing using Tb^{3+}/Au@BSA nanoclusters. (E) Fluorescent probe digital photographs of Tb^{3+}/Au@BSA nanocluster–derived paper-based visual sensor. (F) Fluorescence color image of the visual sensor at different concentrations of Hg(II) solution under 254-nm UV light (Fig. 8.1A–C from Xie et al. [2010] and Fig. 8.1D–F from (Qi et al., 2015)).

viz., $CH_3Hg(I)$ (methyl mercury), could also be detected in seawater using lysozyme-protected gold nanoclusters (Lin & Tseng, 2010). Later, a cellulose paper-based visual sensor for the ratiometric sensing of Hg(II) ions was developed by dropping the Tb^{3+}/Au@BSA nanocluster composite over the paper and drying it (Fig. 8.1D–F). To better understand the practical application capability, internal organ samples collected from the rats artificially infected with Hg(II) ions were studied using the nanocomposite mentioned above. The nanocomposite-based Hg(II) ions sensing results were in good agreement with results from traditional atomic absorption spectrometer (AAS)–based detection. This ensured that Hg(II) ion detection using the Tb^{3+}/Au@BSA nanocluster composite has excellent practical potential (Qi et al., 2015). Similar metallophilic interactions (d^{10}–d^{10}) have also been used to display the silver nanoclusters–based sensors. For example, Adhikari and Banerjee achieved the selective detection of Hg(II) ions at subnanomolar levels using lipoic acid–protected silver nanoclusters (Adhikari & Banerjee, 2010). Later, lysozyme- and oligonucleotide-stabilized silver nanoclusters were used for the selective detection of Hg(II) with a limit of detection of 0.6 mM and 5 nM, respectively (Guo et al., 2009; Zhou et al., 2012). In another study Guo and Irudayaraj developed denatured BSA (denatured using guanidine and tris(2-carboxyethyl)phosphine hydrochloride [TCEP.HCl])–protected silver nanoclusters for the selective detection of Hg(II) ions with a limit of detection of 10 nM (Guo & Irudayaraj, 2011). Glutathione-protected silver nanoclusters holding a higher percentage of Ag(I) content that have a better quantum yield (15%) showed remarkable selectivity and sensitivity for Hg(II) ion sensing (Yuan et al., 2012).

Several studies have shown that metallophilic interactions between Hg(II) ions and nanoclusters could quench photoluminescence. Still, a comprehensive understanding of such fundamental interactions and mechanical aspects has not yet been identified. To better understand the hypothesis mentioned above, Yu et al. studied a variety of nanoclusters using steady-state fluorescence and time-resolved transient absorption measurements (Fig. 8.2A and B) (Yu et al., 2013b). When the interactions of three nanoclusters, namely, Au_8@BSA, Au_{10}@histidine, and Au_{25}@BSA, with Hg(II) ions were compared, the former two nanoclusters preserved their photoluminescence due to the absence of Au(I) species on the metal core. On the other hand, the Au_{25}@BSA nanocluster showed luminescence quenching, confirming the presence of the Au(I) center. These Au(I) semirings on the Au_{25}@BSA nanocluster could effectively bind with Hg(II) ions, which demonstrates the existence of Au(I)–Hg(II) interactions. Lifetime measurement showed a steady decrease in the decay profile as the concertation of Hg(II) ions increased. Similar experiments were conducted with silver nanoclusters also. Interestingly, the lifetime values of excited-state silver nanoclusters were comparable to those of gold nanoclusters in the presence of varying concentrations of Hg(II) ions (Guo et al., 2009). The studies revealed that the photoluminescence quenching of nanoclusters with mercury ions contact was triggered by a static quenching process. The formation of a nonluminescent static complex between Hg(II) ions and silver nanoclusters resulted in their photoluminescence quenching.

In some cases the presence of negatively charged functional moieties on the nanocluster surface could directly interact with positively charged metal ions. Such attractive electrostatic interaction could result in the aggregation of nanoclusters. The luminescence intensity of nanoclusters changes during the aggregation. This process results in two photophysical phenomena, viz., aggregation-induced emission and aggregation-induced quenching. Here the former increases the luminescence intensity, whereas the latter diminishes it. Both aggregation-induced emission and aggregation-induced quenching could be exploited for analyte detection. For example, Huang et al. proposed an aggregation-induced quenching mechanism for the detection of Hg(II) ions using 11-mercaptoundecanoic acid (11-MUA)–tethered gold nanoclusters (Huang et al., 2007). However, the detection trials showed photoluminescence quenching when interacting with different metals ions such as Hg(II), Pb(II), and Cd(II). To overcome such selectivity issues, a masking reagent, viz., 2,6-pyridine dicarboxylic acid, was introduced into the detection medium. The capability of Pb(II) and Cd(II) ions to form complexes with 2,6-pyridine dicarboxylic acids could deactivate them from the screening process. This masking technique helped create a highly selective Hg(II) ions

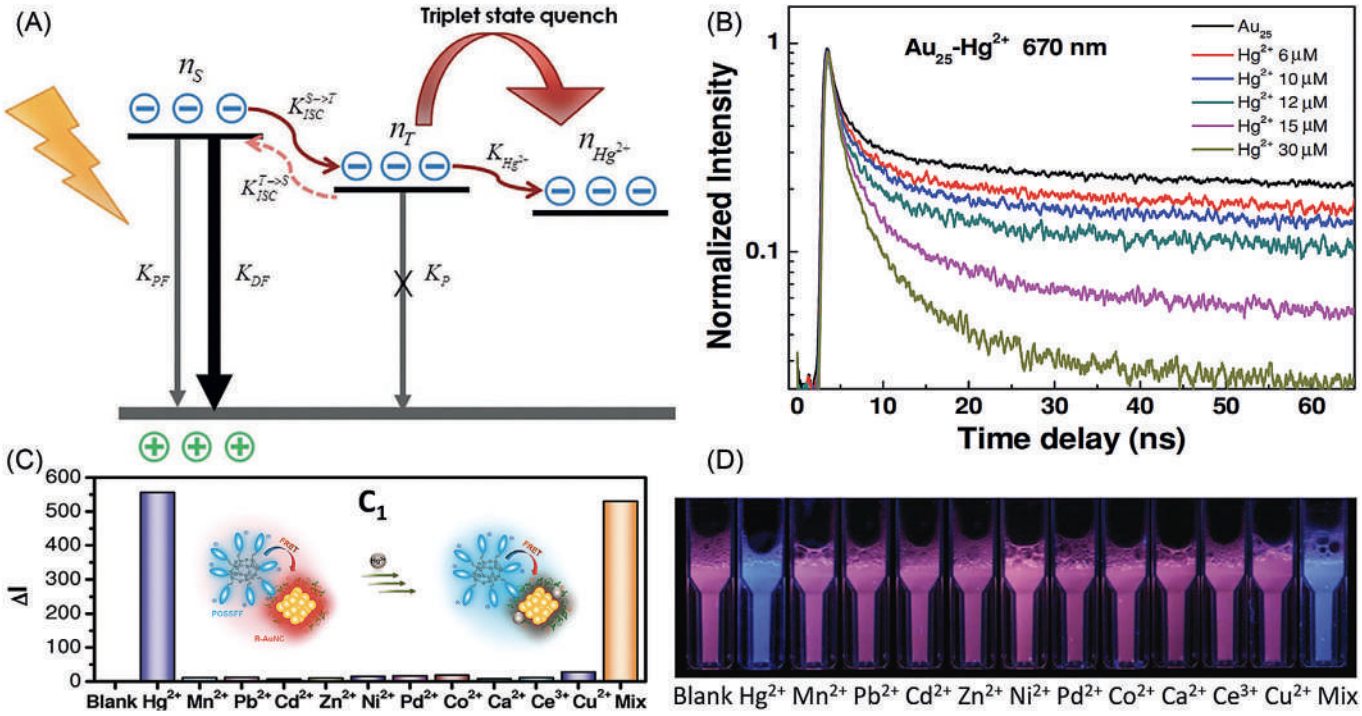

Figure 8.2. (A) The proposed mechanism for the triplet electron transfer from Au_{25}@BSA nanoclusters to Hg(II) ions (LUMO). (B) Fluorescence decay profile (at 467 nm excitation) of Au_{25}@BSA nanoclusters recorded at 670 nm with the increasing concentration of Hg(II) ion. (C) Relative fluorescence intensity (ΔI) and (D) photographs of blue-emitting POSS and red-emitting gold nanoclusters in the presence of various metal ions (2.4 μM). Inset C_1 shows a schematic illustration of FRET-based visual detection of mercury ions (Fig. 8.2A and B from (Yu et al., 2013b) and Fig. 8.2C and D from Pu et al. [2011]).

sensor with a limit of detection of 5 nM. Later, Deng et al. fabricated hybridized DNA duplexes–tethered silver nanoclusters for the "turn-on" detection of Hg(II) ions (Deng et al., 2011). Initially, the cytosine loops containing DNA strands and complementary DNA strands were hybridized to generate the DNA duplex scaffolds. To fabricate luminescent silver nanoclusters, the above-prepared DNA duplex scaffolds and silver salt were chemically reduced using an aqueous $NaBH_4$ solution. Since silver nanocluster formation is highly sequence dependent, the introduction of several thymine–thymine (T–T) mismatches on the DNA duplex restricted the formation of such luminescent nanoclusters. But, the introduction of Hg(II) ions to such mismatched DNA duplexes on the nanocluster surface was strengthened by the T–Hg(II)–T base pair formation, resuming the production of highly luminescent silver nanoclusters. Such a synthetic protocol could be exploited for the sensitive detection of Hg(II) ions with a limit of detection of 10 nM. The fluorescence resonance energy transfer (FRET) mechanism was also employed to detect Hg(II) ions using two fluorophores. For example, Pu et al. used blue-emitting conjugated oligomer-substituted polyhedral oligomeric silsesquioxane (POSS) and red-emitting gold nanoclusters for the selective detection of Hg(II) ions (Fig. 8.2C and D) (Pu et al., 2011). When the dual emissive nanocomposites were excited, an efficient spectral overlap occurred with the donor (blue-emitting POSS) and acceptor (red-emitting gold nanoclusters). This resulted in the generation of pink fluorescence due to the energy transfer from POSS to nanoclusters. However, the addition of Hg(II) ions induced a shift in luminescence from pink to blue due to the quenching of red-emitting nanoclusters. The strong Au(I)–Hg(II) interaction plays a critical role in the quenching mechanism, allowing Hg(II) ion detection with a limit of detection of $\sim$ 0.1 nM.

8.1.1.2 Copper (Cu^{2+}) sensing

Although copper is a necessary trace element in biological systems, excessive consumption causes copper accumulation in the body. A variety of luminescent gold nanoclusters–based sensors have been employed for the selective detection of copper. For example, glutathione-protected gold nanoclusters (Au@SG) were used to detect copper ion (Cu(II)) with a limit of detection of 86 nM (Zhang et al., 2013a). The effective chelation between the carboxyl group of glutathione and Cu(II) results in nanocluster aggregation. However, the detection selectivity is extremely poor since the chelation is also possible with other metal ions such as Hg(II) and Pb(II). Later, a mixture of two separate ligand-protected gold nanoclusters (Au@BSA and Au@lysine) was employed to detect Cu(II) ions with a limit of detection of 0.8 pM (Yang et al., 2013). Cu(II) could coordinate with the –COOH and

–NH_2 groups of each of these nanoclusters. Hence the efficient coordination helped form the anisotropic aggregates accompanied by luminescence quenching. This selective quenching resulted in the detection of Cu(II) ions. Meanwhile, Muhammed et al. fabricated an Au_{38}@BSA nanoclusters–based Cu(II) ion sensor by adopting a similar quenching mechanism (Muhammed et al., 2010). Durgadas et al. employed Au@BSA nanoclusters for the Cu(II) ions sensing in living cells (Durgadas et al., 2011). Later, Shang et al. developed a reversible luminescent copper sensor using poly(methacrylic acid) (PMAA)–stabilized silver nanoclusters (Shang and Dong, 2008). The detection mechanism of Cu(II) ions was purely based on luminescence quenching. In this case nanoclusters showed reversible photoluminescence in the presence of disodium ethylenediaminetetraacetate (EDTA). When EDTA was added to a mixture of nanocluster and Cu(II) ions, the preferential coordination between EDTA and Cu(II) ions released the nanoclusters. This resulted in the restoration of the original photoluminescence of nanoclusters. Later, Lan et al. developed a water-soluble DNA-stabilized silver nanocluster for the specific sensing of Cu(II) ion (Lan et al., 2010). This approach was attractive because of its practical usefulness in the detection of Cu(II) in pond water and soil.

8.1.1.3 Iron (Fe^{2+}/Fe^{3+}) sensing

Iron is an essential metal that is needed in biological processes. Being the metal center of the heme group, iron is critical in the transfer and storage of oxygen. Iron deficiency causes anemia, and excess iron in the body causes iron poisoning. As a result, it is vital to monitor the iron selectively and sensitively. For example, Ho et al. used a solvent-free (green synthesis) one-pot synthesis approach to creating L-DOPA (L-3,4-dihydroxyphenylalanine)–protected luminescent gold nanoclusters (Ho et al., 2012). The presence of Fe(III) ions was able to be detected based on the aggregation-induced fluorescence quenching of nanoclusters. The nanocluster is highly attractive for the sensing of Fe(III) ions because of its liner concentration range of 5 to 1280 μM and strong selectivity toward Fe(III) ions with a limit of detection of 3.5 μM. Su et al. developed L-histidine-protected blue-green emitting gold nanoclusters using a similar green synthesis technique, which has been used to detect Fe(III) ions in plants. Later, Yu et al. developed antibiotic vancomycin-protected luminescent gold nanoclusters for Fe(III) ion detection (Yu et al., 2017). The interaction between vancomycin and Fe(III) ions could selectively quench the photoluminescence of nanocluster, enabling the detection of Fe(III) ions with a limit of detection of 1.4 μM. The addition of EDTA into the above mixture could restore the photoluminescence of nanoclusters due to the stronger coordination between Fe(III) ions and EDTA. In

another study an alloy metal nanocluster containing Au, Ag, Cu, and Pt metal atoms was used to detect Fe(III) ions (Zhou et al., 2017b). The photoluminescence quenching of nanoclusters in Fe(III) ions and the visual change in color of the nanocluster solution in Fe(III) ions could be used to detect the ions. George et al. fabricated surfactant-free Pt nanoclusters for the "turn-off" detection of Fe(III) ions (George et al., 2017). The better stability of the nanoclusters with static quenching capabilities enabled the detection of Fe(III) ions in human blood samples at room temperature. Later, Yang et al. used a ligand exchange followed by the chemical reduction approach to create aqueous-soluble, red luminescent $[Au_7(DHLA)_2Cl_2]$ nanoclusters for the detection of ferrous Fe(II) ions (Yang et al., 2017). The photoluminescence resulting from the aggregation-induced emission of outer Au(I)-thiolates around Au(0) core of the nanocluster has been efficiently used to detect Fe(II) ions with a limit of detection of 3.8 μM.

8.1.2 Anion sensing

Some anions are poisonous and classified as hazardous environmental pollutants. The detection of such anions is possible when they interact with the metallic core of nanoclusters. Anions such as cyanides, sulfides, and nitrites could etch the metallic core, leading to the decomposition or aggregation of nanoclusters. This process could be monitored by recording and analyzing the photoluminescence intensities of nanoclusters.

8.1.2.1 Cyanide (CN^-) sensing

Monitoring cyanide (CN^-) anions is critical because they are incredibly toxic and adversely influence bioactivities. The core etching of the nanocluster in the presence of CN^- ions could result in the formation of an $[Au(CN)_2]^-$ complex. As a result, the photoluminescence intensity of nanoclusters quenches simultaneously. Such interactions between the nanoclusters and cyanide ions have been used to detect CN^- ions very efficiently. For example, Liu et al. developed a cyanide sensor using Au@BSA nanoclusters (Fig. 8.3A) (Liu et al., 2010). The red emission of nanoclusters was selectively quenched within 20 min due to the strong interaction between cyanide ions and gold atoms. This method exhibited superior cyanide specificity over many other anions present in the environment. It also showed better cyanide sensitivity, with a limit of detection of 200 nM, which is 14 times lower than the optimum standard level of cyanide in drinking water (2.7 μM). Similarly, Lu et al. fabricated lysosome-tethered gold nanoclusters for the selective detection of CN^- ions (Lu et al., 2014). The color of nanocluster solution under visible light and UV light (photoemission)

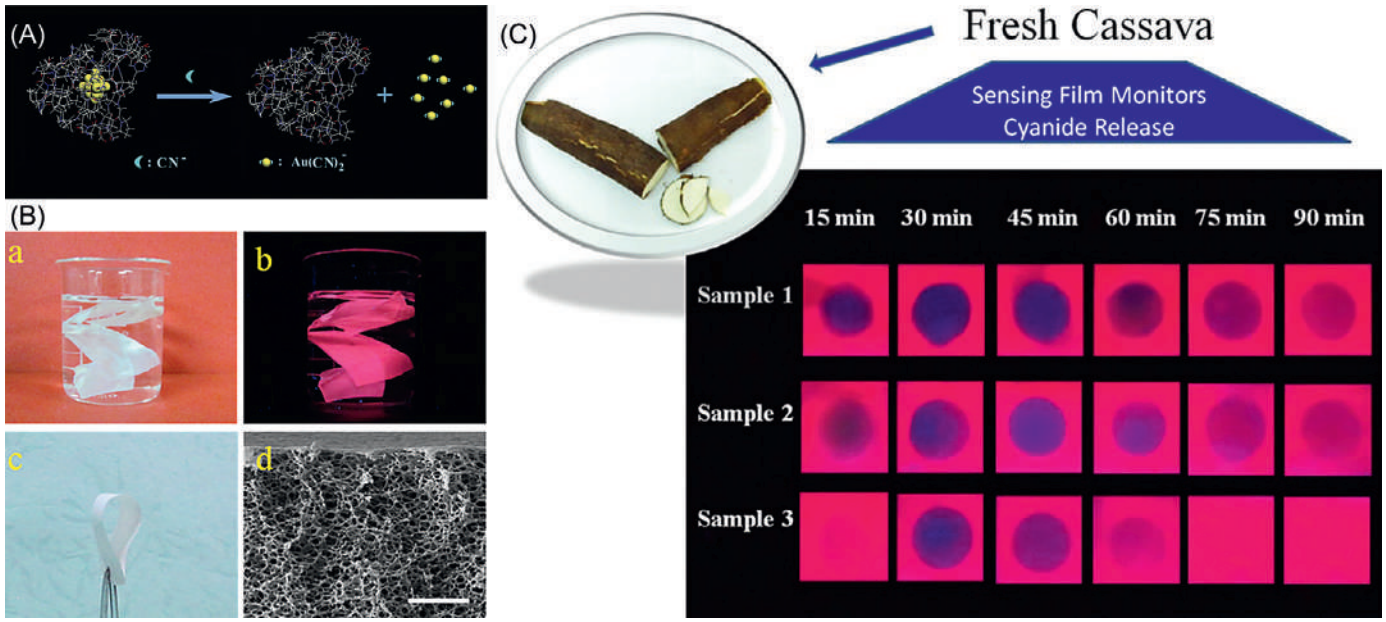

Figure 8.3. (A) Schematic representation of a nanocluster-based sensor for the selective detection of CN^- ions. (B) Photographs of porous films in water under (*a*) visible and (*b*) UV light. The photographs of the porous film (*c*) after drying and (*d*) the corresponding SEM image (the scale bar is 5 μm) are also shown. (C) Comparison of cyanide release during heating in three cassava samples that were subjected to different pretreatment strategies (Fig. 8.3A from (Liu et al., 2010) and Fig. 8.3B and C from Zong et al. [2014]).

changed when they interacted with CN^- ions, thus resulting in a selective CN^- ion sensor with a limit of detection of 190 nM. Later, Zong et al. developed $(Au(I)MTA)_3$ (MTA = 3-mercapto-1,2,4-triazole) and poly(acrylonitrile) nanocluster–based nanocomposite polymer films for the selective detection of CN^- ions (Zong et al., 2014). The photoluminescence intensity of the fabricated film was quenched due to the gold–cyanide interactions. The macroporous structure of the polymer film greatly enhanced CN^- ions' diffusion by improving Au(I) interaction sites, resulting in rapid and sensitive detection. Also, these macropores amplified the signals by instantly capturing and concentrating the volatile CN^- ions. The practical applications of these films were further evaluated for the selective detection of CN^- ions in red wine, juice, and coffee and the real-time detection of CN^- ions release during the cassava processing (Fig. 8.3B and C).

8.1.2.2 Sulfide (S_2^-) sensing

Sulfide (S_2^-) ion is another toxic pollutant anion present in the environment, despite being an essential gaseous signal transmitter in the neuron. They could prevent cellular respiratory actions by forming complexes with iron present in the mitochondrial cytochrome enzymes. The rapid and sensitive detection of S_2^- with a limit of detection of 29 nM was achieved using Au@BSA nanoclusters (Cui et al., 2013). The interaction of S_2^- ions with the gold metallic core leads to the degradation of nanoclusters via the formation of an Au_2S precipitate. This degradation resulted in luminescence quenching, which can be directly correlated with S_2^- concentration. The Cui et al. were able to detect S_2^- present in river water, which demonstrated the practical application of the sensor. Yuan et al. used a gold nanocluster costabilized by (10-mercaptodecyl)-5-methyl pyrimidine-2,4-dione (TSH) and 11-MUA to develop a "turn-on" fluorescence detection of S_2^- ions (Yuan et al., 2013a). A ligand exchange procedure was used to introduce TSH. However, due to their poor solubility, it induced nanocluster aggregation, which resulted in decreased fluorescence. On the other hand, sulfide ions could efficiently be adsorbed on metallic surfaces. As a result, an increased surface charge and static repulsion were created on the nanocluster surface. This led to the disaggregation and luminescence restoration of nanoclusters. Such a sulfide ion–nanocluster interaction was used to develop an ecofriendly nanocluster-based detector with a limit of detection of 0.5 M.

8.1.2.3 Nitrite (NO_2^-) sensing

Nitrite (NO_2^-) ion is a necessary nutrient for plant growth, and it is also used as an antimicrobial preservative in meat. However, excessive nitrite ion consumption in human beings could result in serious health

problems such as gastric cancer and methemoglobinemia. Nitrites can produce highly carcinogenic nitrosamine compounds by interacting with proteins in the body. As a result, it is critical to monitor the concentration of nitrites in food and water samples. Various metal nanoclusters have been used to detect nitrite ions. For example, Liu et al. used sonochemically prepared Au@BSA nanoclusters for the detection of NO_2^- ions in the drinking water (Liu et al., 2013b). Although nitrite ions could be detected using the photoluminescence quenching mechanism, the selectivity was questioned due to the interactions of Au@BSA nanoclusters with other metal ions and anions. To avoid this issue, Unnikrishnan et al. thoroughly investigated the sensing ability of Au@BSA nanoclusters and the mechanistic aspects of photoluminescence quenching (Unnikrishnan et al., 2014). From XPS (X-ray photoelectron spectroscopy) data, they found that the binding energy values of gold increased only in the presence of nitrite ions. This result shows that a higher oxidation state is created for gold in the presence of nitrite ions. The authors further scrutinized various factors influencing nitrite quantification. For example, the detection of nitrite ions was highly feasible without any interference under an acidic environment (pH ~3). Furthermore, the addition of masking agents such as EDTA has been shown to improve selectivity. Finally, the authors could develop an Au@BSA nanocluster–modified nanocellulose membrane to detect nitrite ions in water and urine samples. Later, Chen et al. fabricated gold nanoclusters cotethered with a series of amphiphilic ligands and 11-mercaptoundecanol (Chen et al., 2014). Among them, tetradecanoic acid and 11-mercaptoundecanol–costabilized gold nanoclusters showed better photoluminescence quantum yield and dispersibility. They have been used for the selective detection of nitrite ions with a limit of detection of 40 nM. It is also possible to detect nitrite ions electrochemically using nanoclusters. For example, Dhanya et al. fabricated silver nanoclusters–modified electrodes to detect nitrite ions using square wave voltammetry (Dhanya et al., 2013). The fabricated electrode showed the limit of detection of 1.5 fM and a broad response range of 100 pM to 100 nM. Similarly, Xu et al. fabricated a nanocomposite using the graphene oxide–supported gold nanoclusters to quantitatively analyze nitrite ions (Xu et al., 2015). Later, Chen et al. utilized hyperbranched polyethyleneimine-protected silver nanoclusters (Ag@hPEI) for the detection of nitrite ions by two-step processes (Chen et al., 2016). Under acidic settings, nitrite and externally introduced hydrogen peroxide combined to generate peroxynitrous acid. The interaction of in situ–formed peroxynitrous acid and nanocluster could result in aggregation-induced luminescence quenching. This process was utilized for the detection of nitrite ions with a limit of detection of 100 nM. Later, copper nanoclusters were also used for the detection of nitrite ions. For example, both stabilizer-free (Zheng et al., 2016)

and glutathione-protected (Zhou et al., 2017a) copper nanoclusters (Cu@SG) have been efficiently used for the selective detection of nitrite ions.

8.1.3 Biosensing

This section discusses in detail the sensing of different biomolecules using precision nanoclusters.

8.1.3.1 Glucose sensing

Glucose is a significant carbohydrate that most living beings use as a source of energy. The glucose levels in the human blood influence both metabolic activity and health conditions. An abnormal glucose level in the blood or urine may be an indication of underlying health problems, which can sometimes progress to diabetes. So it is essential to fabricate selective and sensitive sensors to monitor the glucose level in blood or urine. There are many approaches available to detect the glucose level in human body fluids. However, in nanocluster-based sensing the sensitive interaction between luminescent nanoclusters and H_2O_2 is predominantly used. H_2O_2 is produced as a byproduct of the enzymatic oxidation of glucose in the presence of oxygen. The generated H_2O_2 can be detected by monitoring the change in photoluminescence intensity of nanoclusters. Thus the indirect detection of glucose is possible based on the amount of H_2O_2 produced. Many nanocluster-based sensors have been developed using the mechanism described above. For example, Shiang et al. fabricated luminescent 11-MUA-tethered gold nanoclusters for the selective detection of H_2O_2 and glucose (Shiang et al., 2009). The surface Au–S bonds get oxidized in the presence of H_2O_2 to form disulfides, which eventually leads to photoluminescence quenching. The glucose detection is carried out in a two-step process, in which the glucose oxidase enzyme (GOx) was initially allowed to react with glucose in the presence of sodium phosphate buffer. Subsequently, the produced H_2O_2 further interacted with gold nanoclusters. The overall process was monitored by recording and analyzing the time-dependent photoluminescence spectra. Based on the amount of H_2O_2 generated, glucose could be detected with a limit of detection of 1 μM (Fig. 8.4A and B). Notably, the sensitivity of this method was in good agreement and comparable with that of methods that use the electrochemical biosensors reported earlier. Likewise, glutathione- (Wu et al., 2019b), L-cysteine- (Hussain et al., 2011), and BSA-stabilized gold nanoclusters (Jin et al., 2011) have been demonstrated for the selective detection of glucose using a similar mechanism. Among them, the L-cystine-stabilized gold nanoclusters

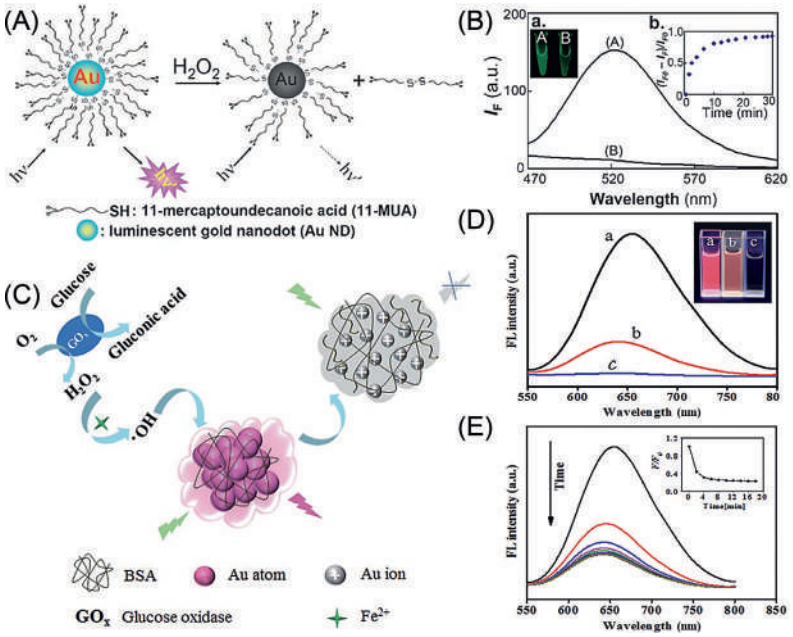

Figure 8.4. (A) Schematic representation of H_2O_2 nanosensor; (B) the photoluminescence spectra were recorded from 11-MUA–gold nanoclusters in the (*a*) absence and (*b*) presence of H_2O_2. The corresponding photographs captured under UV light are shown in the inset. (C) The Fenton reaction–mediated H_2O_2 and glucose sensing. (D) Fluorescence response and corresponding photographs of gold nanoclusters in the (*a*) absence and presence of (*b*) 10-mM H_2O_2 and (*c*) 20-mM H_2O_2, respectively. (E) The time-dependent fluorescence response of gold nanoclusters was recorded after adding 10-mM H_2O_2 (F_0 and F are the fluorescence intensity of the nanocluster at 660 nm in the absence and presence of H_2O_2, respectively) (Fig. 8.4A and B from Shiang et al. [2009] and Fig. 8.4C–E from Zong et al. [2017]).

showed a wider range of detection sensitively due to their better photoluminescence intensity. The Au@BSA nanoclusters showed a detection range of 100 mM to 0.5 mM with a limit of detection of 5 μM. Later, Xia et al. fabricated GOx-tethered gold nanoclusters by conjugating the enzyme with the surface-bound lipoic acid (Xia et al., 2013). The as-synthesized enzyme-conjugated nanoclusters could be directly used for the in situ detection of glucose. The oligonucleotide-protected silver nanoclusters (Schroeder et al., 2019) and glucose oxidase/copper nanocluster hybrid structures (Su & Liu, 2017) were also similarly used to detect glucose. Later, Zong et al. proposed a different approach for detecting H_2O_2 and glucose by blending the Fenton reaction on the nanocluster surface (Zong et al., 2017). In the Fenton reaction H_2O_2 gets oxidized in the presence of a Fenton reagent (Fe(II)) to form hydroxyl radicals (˙OH). Since ˙OH are more reactive and aggressive oxidizing agents than H_2O_2, improved oxidation of nanoclusters with a higher sensitivity is ensured. Similarly, H_2O_2 produced by the catalytic oxidation of glucose could be detected much more efficiently by converting it into hydroxyl radicals (OH) using the Fenton reaction (Fig. 8.4C–E). In contrast to this method, Chen et al. demonstrated the formation of silver nanoclusters and the subsequent detection of glucose via the Fenton reaction (Chen et al., 2017c). Here, the free radicals produced by the Fenton reaction were used to initiate the polymerization of methacrylic acid (MAA). The polymerized product

(PMMA) could act as a comfortable template to stabilize the luminescent silver nanoclusters. Based on the photoluminescence intensity of the silver nanoclusters generated, the accurate detection of glucose was feasible. Later, Naaz et al. carefully created the preferential affinity between the cis diol groups of glucose and phenylboronic acid for the direct detection of glucose (Naaz et al., 2018). To fabricate the glucose sensor, dihydrolipoic acid–stabilized silver nanoclusters (Ag@DHLA) were initially conjugated with 3-aminophenyl boronic acid (APBA) via a hydrogen bond–mediated interaction. The molecular interaction led to the aggregation of nanoclusters with enhanced photoluminescence. The addition of glucose into the assembled nanoclusters quenched their luminescent intensity due to the disaggregation.

8.1.3.2 Biothiol sensing

Biothiols (primarily cysteine, homocysteine, and glutathione) are essential constituents of the majority of peptides. These biothiols have critical physiological roles, including maintaining redox balance, stimulating gene expression, and preventing damage from free radicals and toxins. However, unusual quantities of biothiols in the human body have been connected to various diseases, including cancer, Alzheimer's disease, Parkinson's disease, and AIDS. As a result, developing tools for detecting biothiol concentrations in living cells is critical for learning more about biothiol-related pathophysiological processes. Several reports on biothiol detection based on nanocluster are available. For example, Han and Wang fabricated single-stranded DNA–stabilized silver nanoclusters to detect biothiols (cysteine, homocysteine, and glutathione) in human plasma samples (Han & Wang, 2011). For this, silver nanoclusters were initially synthesized by reducing silver salts in the presence of thiolated single-stranded DNA using an aqueous $NaBH_4$ solution. The purified nanoclusters were stored in the dark for 3 hours before usage. The addition of biothiols into the nanocluster sample creates a coordination complex between sulfur and silver atoms. The vacant d orbitals of silver atoms are filled by the electron pair from sulfur atoms, forming a metal–ligand bond. The XPS binding energies validated the formation of such Ag–S bonds. UV-Vis spectroscopy and lifetime measurements suggested a static quenching mechanism. Later, Huang et al. investigated various DNA-stabilized silver nanoclusters and found that the nanocluster's properties are highly dependent on DNA templates (Huang et al., 2011). Some DNA-templated nanoclusters preserved their photoluminescence when interacting with thiol molecules. However, a group of other nanoclusters quenched their photoluminescence by forming ground state complexes. The third possibility is the enhancement of photoluminescence in the presence of biothiols. For example, the interaction

of biothiols with polycytosine DNA-protected silver nanoclusters boosted their photoluminescence. Based on their understanding, a turn-on detection of biothiols has been achieved. Later, Chen and Tseng used lysozyme type VI–stabilized blue-emitting Au_8 nanoclusters with a high quantum yield to detect glutathione in a single drop of blood (Chen & Tseng, 2012). Here, the photoluminescence intensity of about 455 nm gradually decreased with the increasing glutathione concentration with a limit of detection of 20 nM. However, cysteine could also quench the photoluminescence of nanoclusters, which breaks the selectivity. Hence, fluorosurfactant-capped gold nanoparticles were used to improve the selectivity by masking cysteine. The greater thiol–mercury affinity has also been used to detect biothiols. For example, the interaction of MUA-protected gold nanoclusters with Hg(II) ions could form a stable complex via coordination with the carboxylic acid group, resulting in photoluminescence quenching (Chang et al., 2014). However, introducing a thiol moiety restores the original photoluminescence due to the better affinity of Hg(II) ions to thiol groups compared to carboxylic acid groups. This method has been further extended to detect biothiols in real biological samples. Similarly, water-soluble DNA-protected silver nanoclusters complexed with Hg(II) ions were used for biothiol detection (glutathione and cysteine) (Yan et al., 2018). Later, Shang and Dong used PMAA–stabilized aqueous luminescent silver nanocluster to detect cysteine (Shang & Dong, 2009). Glutathione-protected silver nanoclusters (Ag@SG) were also used to detect cysteine selectively and sensitively (Yuan et al., 2013b). The specific silver–thiol interaction and steric hindrance resulted in cysteine sensing with a limit of detection of <3 nM (Fig. 8.5A–C).

8.1.3.3 Adenosine triphosphate sensing

Adenosine triphosphate (ATP) is a compound that transports energy to cells and regulates their metabolic activities. Abnormal ATP levels signify various pathogeneses, emphasizing the importance of ATP monitoring in human beings. Precision noble metal nanoclusters are useful probes to monitor ATP levels in the human body. For example, Zhou et al. demonstrated ATP detection using DNA-stabilized silver nanoclusters (Zhou et al., 2011a). For this, silver nanoclusters were initially synthesized via the chemical reduction of silver ions in the presence of thiolated DNA. Since there were only a few base pairs in the DNA sample without the ATP (ATP aptamer *ATPS1*/*ATPS2* was in a free state), injection of an aqueous solution of $NaBH_4$ into a mixture of silver ions and DNA resulted in the formation of less luminescent nanoclusters. However, the addition of ATP into the above-prepared nanocluster solution results in bright photoluminescence. As a result, the method mentioned above is helpful in detecting ATP levels.

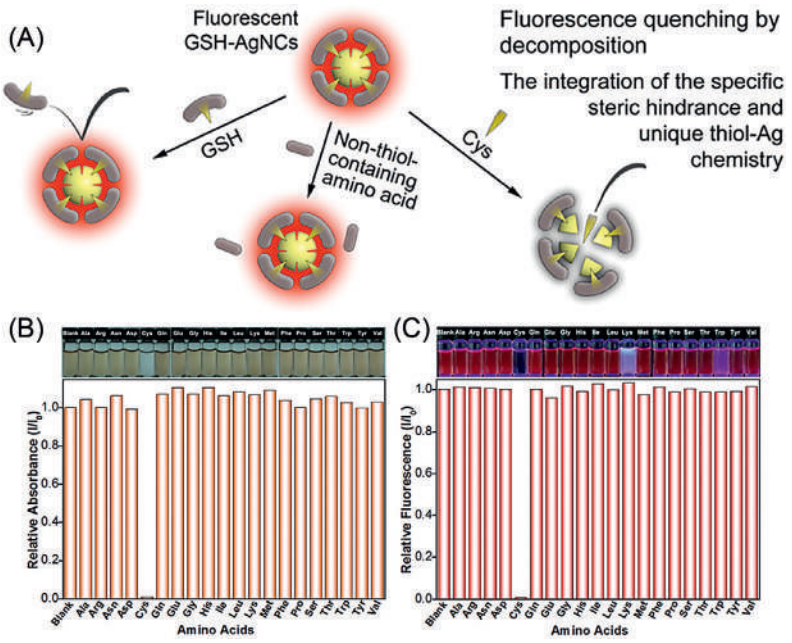

Figure 8.5. (A) Schematic representation for the selective sensing of cysteine by Ag@SG nanoclusters. (B, C) Top panel: digital photos under (B) visible light and (C) UV light, and bottom panel: (B) relative optical intensity (I/I_0) of absorption at 489 nm and (C) relative fluorescence intensity (I/I_0) at 647 nm of aqueous Ag@SG nanocluster solutions (10 μM) in the presence of 50 μM concertation of different amino acids (Yuan et al., 2013b).

The selectivity of this technique was comparable to that of existing methods with a limit of detection of 0.2 μM. Further, the authors extended this work using luminescent double-stranded DNA (dsDNA)–stabilized copper nanoclusters (Zhou et al., 2011b). In this case the addition of ascorbic acid into an aqueous solution of copper ions in the presence of dsDNA resulted in the formation of highly luminescent dsDNA-stabilized copper nanoclusters. However, the addition of ATP into the mixture of DNA and copper ions before the ascorbic acid reduction results in the formation of an ATP–aptamer complex, which prevents the formation of dsDNA and nanoclusters. Consequently, a low photoluminescence intensity was observed. This investigation has been efficiently utilized to detect ATP in human serum and human adenocarcinoma HeLa cells due to its simplicity and high sensitivity (limit of detection 28 nM). Later, Liu et al. demonstrated a nanohybrid system made up of nucleic acid–stabilized nanoclusters and graphene oxide for the turn-on detection of ATP (Liu et al., 2013a). The interaction between graphene oxide nanosheets and nanoclusters quenched the photoluminescence intensity of nanoclusters. However, the addition of ATP into the above sample could restore their photoluminescence intensity due to the preferential interaction between ATP and nanoclusters. This method allows the selective detection of ATP (Fig. 8.6A–C). Li et al. introduced a new nanohybrid system com-

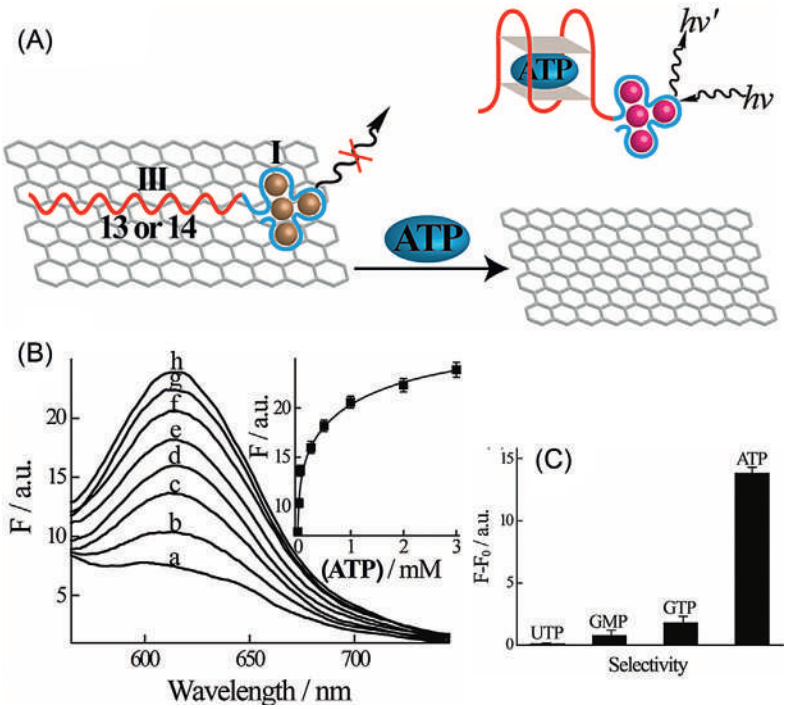

Figure 8.6. (A) ATP assay using DNA-protected aptamer–silver nanocluster/graphene oxide system. (B) Fluorescence spectra of red-emitting silver nanoclusters upon analyzing different concentrations of ATP by the silver nanocluster/graphene oxide system: (a) 0 mM, (b) 0.025 mM, (c) 0.05 mM, (d) 0.25 mM, (e) 0.5 mM, (f) 1 mM, (g) 2 mM, and (h) 3 mM. Inset: calibration curve corresponding to the luminescence signal at $\lambda = 616$ nm. (C) Selectivity of the ATP sensor by using 1 mM of uridine-5′-triphosphate (UTP), guanosine-5′-triphosphate (GTP), guanosine-5′-monophosphate (GMP), and ATP (Liu et al., 2013a).

posed of glutathione-stabilized nanoclusters and Fe^{3+} ions (Li et al., 2012b). The photoluminescence intensity of glutathione stabilized nanoclusters is quenched when they interact with Fe^{3+} ions. However, the addition of phosphate-containing molecules restores their original photoluminescence, which aids in detecting ATP.

8.1.3.4 Protein sensing

The selective detection of proteins can be carried out by connecting the respective protein receptors on the nanocluster surface and subsequently monitoring the photoluminescence changes during the protein interactions. For example, Huang et al. developed a sensor for the selective detection of breast cancer marker protein (platelet-derived growth factor AA [PDGF AA]) using the gold nanocluster–gold nanoparticle hybrid donor and acceptor system (Huang et al., 2008). For this, 11-MUA-protected nanoclusters were conjugated with PDGF AA, and the gold nanoparticles were conjugated with PDGF binding aptamer separately. When these nanosystems were mixed, the unique relationship between PDGF AA and PDGF binding aptamer led to the FRET that resulted in the photoluminescence quenching of PDGF AA–conjugated nanoclusters. However, the addition of excess PDGF AA

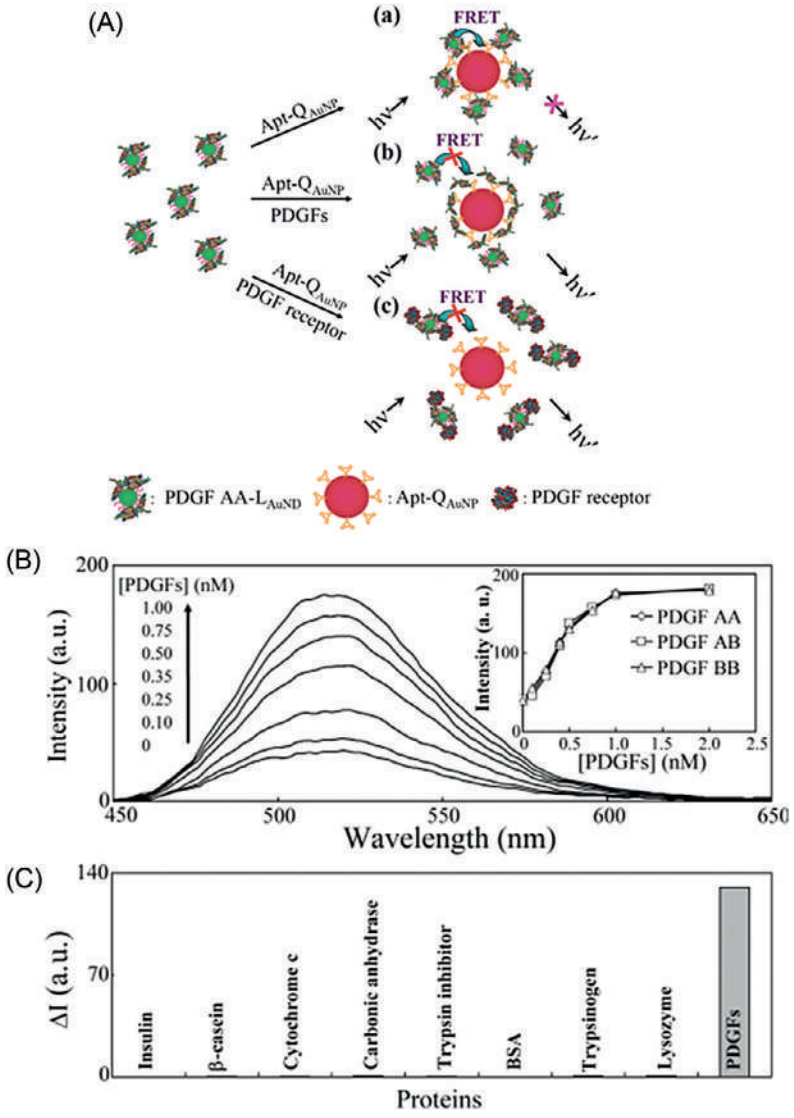

Figure 8.7. (A) Schematic representations of PDGF and PDGF receptor nanosensors based on the modulation of the photoluminescence quenching between PDGF AA–gold nanocluster and PDGF binding aptamer–gold nanoparticle probe. (B) Competitive binding assay for PDGF AA–gold nanocluster and PDGF binding aptamer–gold nanoparticle probe. (C) Photoluminescence changes of PDGF AA–gold nanocluster and PDGF binding aptamer–gold nanoparticle probe toward PDGFs and other proteins (Huang et al., 2008).

restores the photoluminescence of nanoclusters due to the specific binding between PDGF protein and PDGF receptors (Fig. 8.7A–C).

Later, the authors chose mannose-tethered luminescent nanoclusters for the selective detection of Concanavalin A (ConA) and *Escherichia coli* (Huang et al., 2009). When these nanoclusters were coupled with ConA, aggregation-induced quenching occurred, which was efficiently used to detect Con A with high selectivity and a limit of detection of 75 pM. On the other hand, when these nanoclusters were

incubated with *E. coli* bacteria, the photoluminescence of nanoclusters was significantly enhanced due to the specific binding of nanoclusters on the bacteria surfaces. The calculated limit of detection was about 7.2×10^5 cells mL^{-1} based on the linear connection between the photoluminescence of gold nanoclusters and the concentration of *E. coli*. Later, Triulzi et al. reported the selective detection of human immunoglobulin G (IgG) antigen using PAMAM (poly[amidoamine])–stabilized gold nanoclusters (Triulzi et al., 2006). Here, the nanoclusters were initially conjugated with goat-derived polyclonal antihuman IgG. The subsequent addition of human IgG to the bioconjugated nanoclusters resulted in photoluminescence quenching. This mechanism has been successfully used for the selective detection of human IgG antigen. Similarly, Shiang et al. demonstrated the detection of human IgG in plasma using protein A–modified gold nanoclusters (Shiang et al., 2011). Hu et al. employed Au@BSA nanoclusters to detect trypsin. In this case the ability of trypsin to enzymatically hydrolyze BSA leads to the decomposition of nanoclusters and enables fluorescence quenching–based detection (Hu et al., 2012). Further, Sharma et al. showed the detection of thrombin using antithrombin aptamer sequence–conjugated silver nanoclusters (Sharma et al., 2011). Similarly, Li et al. demonstrated the detection of human α-thrombin using luminescent guanine-rich DNA sequence–stabilized silver nanoclusters (Li et al., 2012a). Here, two different aptamers, viz., Apt15 and Apt29, were linked to the nanocluster surface, and the complementary sequence was linked to G-rich overhang, respectively. The interactions of both aptamers with target proteins could push G-rich overhang very near to silver nanoclusters, resulting in enhanced photoluminescence from nanoclusters.

8.1.3.5 Nucleic acid sensing

The selective detection of nucleic acids (DNA/RNA) proved vital for biomedical research and genetic disease diagnosis. As an optical probe for the selective detection of nucleic acid, precision nanoclusters offer many potentials. The research group of Prof. Wang has been working on nanocluster-based nucleic acid sensing for a long time. For example, cytosine loops containing DNA strands were hybridized together to build DNA duplex scaffolds and employed as a stabilizing agent for preparing silver nanoclusters (Guo et al., 2010). Interestingly, these nanoclusters could detect single nucleotide mutations such as sickle cell anemia mutations due to the significant sequence-dependent formation of nanoclusters. Subsequently, the authors developed a nanocluster-based molecular beacon for DNA and ATP detection by utilizing the photon-induced energy transfer between DNA-protected silver nanoclusters and G-quadruplex/hemin complexes (Fig. 8.8A–C)

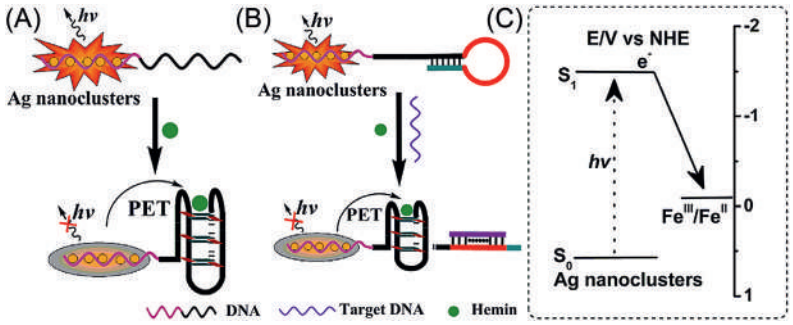

Figure 8.8. (A) Schematic Illustration of photon-induced energy transfer between DNA/silver nanoclusters and the G-quadruplex/hemin complex. (B) Schematic illustrations of the analysis of DNA using DNA/silver nanocluster–G-quadruplex/hemin conjugate. (C) Comparison of the redox state of the G-quadruplex/hemin complex and the energy levels of DNA/silver nanoclusters (Zhang et al., 2013b).

(Zhang et al., 2013b). Such a nanocluster-based molecular beacon allowed for the "turn-off" detection of analytes. Later, they devised another molecular beacon that provides for the "turn-on" detection of DNA (Zhang et al., 2013c). In this case the strand displacement reaction was used to detect DNA and thrombin, with the G-rich overhang strand acting as a photoluminescence enhancer. Yeh et al. created yet another "turn-on" model for detecting DNA targets (Yeh et al., 2010). Initially, they discovered that when DNA-stabilized silver nanoclusters were placed near guanine-rich DNA sequences, the photoluminescence of nanoclusters was enhanced up to 500 times. Based on these findings, they fabricated a nanocluster beacon that brightens up with target binding. Single nucleotide polymorphisms or point mutations cause a variety of genetic diseases, so it is critical to investigate them. A chameleon nanocluster beacon was utilized to detect such single nucleotide polymorphisms (Yeh et al., 2012). The chameleon nanocluster beacon is a novel form of luminescent probe that emits at multiple wavelengths when bound to single nucleotide polymorphisms, and the luminescence of the same beacons was enhanced when placed near specific DNA sequences. Based on the emissive color and luminescence amplification of the silver nanocluster, the authors were able to distinguish up to six disease-related single nucleotide polymorphisms. Later, Jia et al. used a copper nanocluster to detect single nucleotide polymorphs by exploiting the delicate interaction between the base types in the main grooves (Jia et al., 2012). The single mismatch and its mismatch type could be instantly and precisely identified in the DNA sequence at room temperature. Similarly, Lan et al. fabricated oligonucleotide-stabilized silver nanoclusters for the selective detection of single nucleotide polymorphisms (Lan et al., 2011). Later, Liu et al. fabricated DNA-stabilized silver nanocluster dimers to locate the single nucleotide polymorphisms (Liu et al., 2017b). The photoluminescence intensities of the nanocluster dimer were reduced linearly when the single mismatched base moved from the center point to the end of the target DNA. The changes in the photoluminescence

intensities of nanoclusters could help to locate the single mismatched base pairs.

8.1.3.6 Microenvironment sensing

The microenvironment (e.g., temperature and pH) of nanoclusters has a significant impact on their photoluminescence. Therefore the correlation between the microenvironment and the photoluminescent intensity of nanoclusters is helpful during the fabrication of sensors. With this idea, nanoclusters or their nanocomposites have been used to measure intracellular temperature based on the changes in their photoluminescence intensity. For example, the temperature change in living cells was detected using red-emissive lipoic acid–protected gold nanoclusters (Au@LA) (Shang et al., 2013). For this, gold nanoclusters were synthesized through the chemical reduction of gold precursor ($HAuCl_4$) in the presence of lipoic acid, followed by microwave irradiation and purification via triple centrifugation. The quenching of photoluminescence with increasing the temperature has been utilized for temperature sensing. Experiments with gold nanoclusters and HeLa cells could detect the intracellular temperature ranging from 14 to 43°C with a resolution of 0.3 to 0.5°C. These nanocluster-based optical sensors were found to be more reliable and sensitive than molecule-based sensors. Later, a dual-emissive carbon dot/gold nanocluster nanocomposite was used to develop the intracellular thermometer (Wang et al., 2016a). Here, the amino-functional group–terminated carbon dots and glutathione-protected gold nanoclusters were used to fabricate the nanohybrid system via the coupling reaction. This nanohybrid has been further used for temperature sensing at cellular levels. Such nanohybrids will be highly useful to resolve the problems like probe concentration, excitation efficiency, and other local environmental parameters of the conventional techniques (Fig. 8.9A–C). Later, Jia et al. developed a self-assembled nanocomposite using luminescent carbon dots and gold nanoclusters for intracellular temperature sensing (Jia et al., 2019). The communication between the positively charged carbon dots and negatively charged gold nanoclusters resulted in electrostatic interaction–induced assembly. This dual emissive nanohybrid system has been further used to detect temperatures ranging from 20 to 80°C. Later, the gold nanoclusters embedded in peptide nanofibers have also been used to develop a biocompatible thermometer to measure the temperature of living cells (Zhang et al., 2017). The pH is a crucial parameter for many biological processes, and hence it can act as an essential indicator to monitor disease progression in living organisms. As the luminescent intensity of nanoclusters is highly dependent on the pH, nanocluster-based sensors could be efficiently used to monitor the pH in a constrained biological environment. For example, Deng

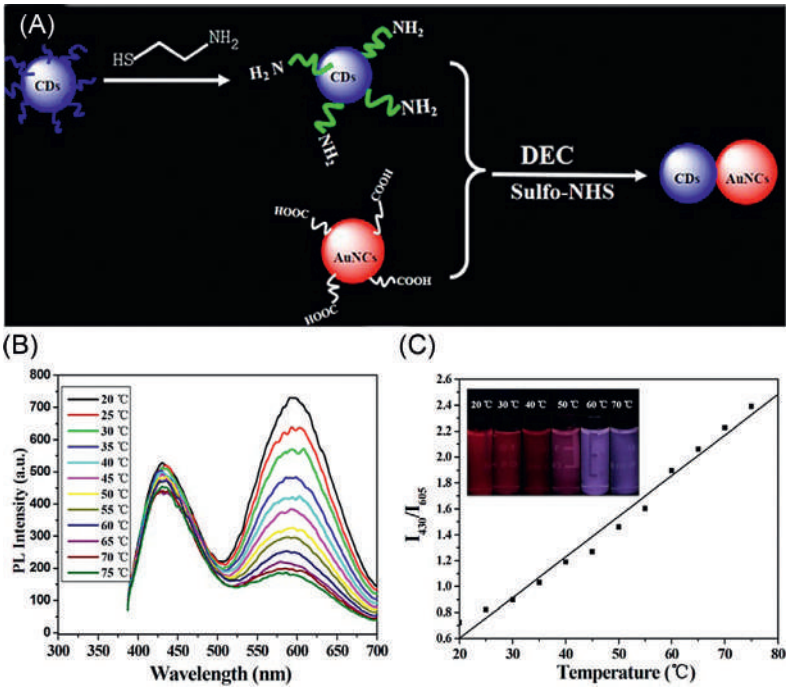

Figure 8.9. (A) Schematic illustration of the synthesis of carbon dot and Au@SG nanocluster nanohybrid system. (B) Fluorescence spectra (excitation 367 nm) of the nanohybrid system with an increase of temperature from 20 to 75°C (top to bottom). (C) The ratios of the emission intensities at 430 and 605 nm (I_{430}/I_{605}) versus temperature. Inset: photographs of the nanohybrid solution at various temperatures under UV light (Wang et al., 2016a).

et al. fabricated gold nanoclusters using N-acetyl-L-cysteine (NAC) as a reducing and stabilizing agent (Deng et al., 2015). Interestingly, the photoluminescence intensity of the fabricated nanoclusters had shown ultrasensitivity in the pH range of 6.05 to 6.40. The smaller core size and easy synthesis protocol of the nanocluster were found to make them superior to the other known pH sensors. The lifetime measurements revealed that photoluminescence quenching follows a static quenching mechanism. At the same time, the XPS study avoided the possibility of potential Au(I) ion reduction–based photoluminescence quenching. Hence, the luminescence quenching could be attributed to the pH-induced aggregation of gold nanoclusters. In addition, the abovementioned nanoclusters have also been used to detect urea, urease, and urease inhibitors by correlating with the acidity or basicity of the environment. For example, the ammonia molecule obtained from urease-catalyzed urea hydrolysis could alter the pH of the gold nanocluster. In another study Cuaran-Acosta et al. fabricated biocompatible and ratiometric pH nanosensors using nicotinamide adenosine dinucleotide (NAD)–tethered gold nanoclusters holding two acidic phosphoric groups with a detection range of 3 to 11 (Cuaran-Acosta et al., 2019). Here, the degree of chelation of bidentate ligands with gold atoms varies with the pH values. As a result, different emissions from gold nanoclusters could be available for ratiometric pH sensing.

8.2 LED fabrication

Precision noble metal nanoclusters have recently emerged as an attractive phosphor for fabricating light-emitting diodes (LEDs) due to their easy preparation routes, high stability, low toxicity, and better photoluminescence quantum yield. Nanoclusters or their composites have been used in LED fabrication as color conversion layers. For example, Wang et al. combined two copper nanoclusters that emit in the orange and blue regions to develop a rare-earth-free, low-cost, white light–emitting diode (WLED) (Wang et al., 2016b). The fabrication of the orange-emitting copper nanoclusters was carried out using glutathione as both the reducing and stabilizing agent. Subsequently, the photoluminescence quantum yield of orange-emitting nanoclusters was enhanced via a solvent-assisted aggregation-induced method. As a result, the quantum yield was improved up to 24% and 43% in solution and solid state, respectively. At the same time, blue-emitting copper nanoclusters were synthesized by reducing Cu(II) ions using ascorbic acid as the reducing agent and polyvinylpyrrolidone as the stabilizing agent. Postsynthetic surface treatment of blue-emitting nanoclusters using sodium citrate helped improve their stability and quantum yield up to 14%. The above-synthesized blue- and orange-emitting copper nanocluster powders have been further used to fabricate monochrome LEDs and WLEDs by integrating them as color conversion layers on a commercially available GaN LED chip with 370 nm excitation. To fabricate white light–emitting devices, the authors further extended their work by preparing thermally and mechanically stable luminescent copper nanocluster–polymer nanocomposite films (Wang et al., 2016d). The amine acid condensation reaction between the glutathione-protected copper nanoclusters and carboxylated polyurethane helped fabricate the dual-emissive (blue and orange) nanocomposite films. Here, the condensation and aging led to the aggregation of copper nanoclusters, resulting in an enhanced emission with a quantum yield of up to 18%. This flexible film was further used as the color conversion layer on the ultraviolet LED chip. Later, poly(vinylpyrrolidone)-supported copper nanoclusters were examined with various electron-rich ligands to find out a better photoluminescence quantum yield. For example, the treatment of poly(vinylpyrrolidone)-supported copper nanoclusters with glutathione resulted in an enhanced blue emission with a quantum yield of up to 27% (Wang et al., 2016c). The combination of the powder form of such a nanocomposite and commercially available red and green phosphors has been further used to fabricate WLEDs with an excellent color rendering index. Later, Wu et al. developed LEDs by integrating the self-assembled superstructures fabricated

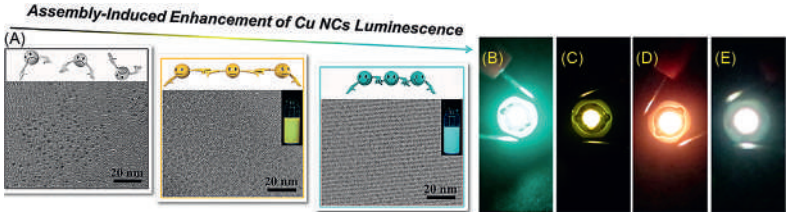

Figure 8.10. (A) TEM images of the$[Cu_{14}(DT)_{10}]$ nanocluster and its polymorphic assembly. (B–D) The fluorescent images of LEDs fabricated from different nanocluster assemblies; (B) copper nanocluster ribbons, (C) copper nanocluster sheets, and (D) gold nanocluster sheets. (E) Fluorescent image of the WLED from a mixture of assembled copper nanocluster ribbons, copper nanocluster sheets, and gold nanocluster sheets (Wu et al., 2015).

from $[Cu_{14}(DT)_{10}]$ (DT = dodecanethiol) nanoclusters as a color conversion layer and a 365-nm GaN LED chip as a light source (Wu et al., 2015). The $[Cu_{14}(DT)_{10}]$ nanoclusters were first synthesized by dissolving copper precursor ($CuCl_2$•$2H_2O$) in benzyl ether and employing DT as a stabilizing and reducing agent. These nanoclusters were self-assembled into two forms of polymorphic assemblies: ribbons (blue-green emitting) and sheets (yellow emitting), upon thermal treatment at elevated temperatures of 128°C and 140°C, respectively. Such self-assembled superstructures were formed due to efficient van der Waals attractions between the DT ligands. Based on the nature of ligand and internanocluster Cu(I)–Cu(I) interactions, they exhibited mechanochromic and thermochromic photoluminescence properties. The blue-green-emitting self-assembled $[Cu_{14}(DT)_{10}]$ ribbons and yellow-emitting self-assembled $[Cu_{14}(DT)_{10}]$ sheets were used to create LEDs of the respective colors. Furthermore, the authors used a combination of $[Cu_{14}(DT)_{10}]$ ribbon, $[Cu_{14}(DT)_{10}]$ sheet, and gold nanocluster sheet (red-emitting) assemblies to develop WLEDs (Fig. 8.10A–E). They expanded their research activities by modulating the internanocluster distances in the nanocluster assembly by controlling the experimental variables such as solvents, ligands, duration of assembly, and temperature (Ai et al., 2017b). The different photoluminescence colors produced by the various assemblies were further used to fabricate LEDs and WLEDs. Later, the authors used aromatic thiols holding different substituents for tuning the photoluminescence of red-emissive copper assemblies in the 548- to 698-nm region (Ai et al., 2017a). The difference in the emission wavelength of assemblies achieved is attributed to the electron-donating nature of the substituents on the aromatic ligand. The authors could enhance the quantum yield of copper nanoclusters by up to 23.5% by doping the nanoclusters with Au(I) centers. Based on the percentage of metal doping, the photoluminescence quantum yield of the nanocluster was changed (Liu et al., 2017c). Here, copper nanoclusters were prepared by reducing the copper precursor ($CuCl_2$•$2H_2O$) in the presence of dodecanethiol. To introduce varied percentages of Au(I) centers, different amounts of gold precursors ($HAuCl_4$) were mixed with copper precursors before the reduction. Powders of gold-doped copper nanoclusters with 0%, 0.3%, and 80% gold content were mixed with

polydimethylsiloxane (PDMS) precursors to generate the color conversion layer for WLEDs. Later, the electrophoretic deposition of blue-green-emitting copper and red-emitting gold nanocluster sheets deposited on ITO (indium tin oxide) plates has been used as a color conversion layer in the creation of WLEDs (Liu et al., 2016a). Similarly, Huang et al. fabricated WLEDs using the solid-state-emitting Zn-coordinated gold nanocluster assemblies (Huang et al., 2019). For this, glutathione-protected gold nanoclusters were initially synthesized using a gold precursor ($HAuCl_4$) and glutathione via the microwave-assisted method. The efficient metal coordination of Zn ions with the carboxylate group of the glutathione-tethered nanocluster surface helps create a yellow-orange-emitting Zn-coordinated gold nanocluster assembly via electrostatic interactions. Here, a combination of green-emitting carbon nanodots and yellow-orange-emitting Zn-coordinated gold nanocluster assemblies have been paired with blue-emissive LEDs to fabricate the WLED quickly. Later, Bhandari et al. developed a biofriendly WLED nanocomposite using red-emitting gold nanoclusters and green-emitting ZnS quantum dots (which consist of ZnQ_2; HQ = hydroxyquinoline) (Bhandari et al., 2016). In the presence of sodium sulfide Au@BSA nanocluster reacted with zinc precursors to produce Au@BSA nanoclusters–ZnS quantum dot, which then reacted with hydroxyquinoline to form the required Au@BSA nanocluster–ZnS quantum dot complex. The combined emission from the gold nanocluster–ZnS quantum dot complex produced nearly white light emission (in both liquid and solid). Further, the self-assembled orange-red-emitting $(NH_4)_9[Ag_9(o\text{-}MBA)_9]$ or $(NH_4)_9[Ag_9(p\text{-}MBA)_9]$ nanoclusters were used to produce WLEDs (Sun et al., 2020; Xie et al., 2020). Each nanocluster was prepared via the ultrasonication method in the presence of respective ortho- (o-) or para- (p-)mercaptobenzoic acid (MBA). Here, the $(NH4)_9[Ag_9(o\text{-}MBA)_9]$ nanoclusters produce self-assembled nanofibers by interacting with succinic acid, while the pH-guided assembly of the $(NH_4)_9[Ag_9(p\text{-}MBA)_9]$ nanocluster results in self-assembled nanorods. By combining commercially available phosphors, these nanocluster assemblies have been effectively used to produce the color conversion layers in LEDs.

8.3 Solar energy harvesting

Precision noble metal nanoclusters have recently been identified as a promising photosensitizing candidate for light energy conversion devices. The attractive photosensitizing properties of the nanoclusters have mainly been attributed to their broad absorption spectrum, excited-state lifetimes, light extinction coefficients, high stability in the visible and infrared regimes, and energy-level positions for charge

injection and regeneration. For the first time, Sakai and Tatsuma investigated the photovoltaic response of precision nanoclusters using a series of magic number glutathione-protected gold nanoclusters [Au_n (n = 15, 18, 22, 25, 29, 33, 39)] (Sakai & Tatsuma, 2010). These gold nanoclusters were used as the photosensitizer material by integrating with nanoporous TiO_2 films via electrostatic interaction, in which the negatively charged carboxyl groups of glutathione ligands were anchored on positively charged TiO_2 films. Among all the nanoclusters tested, the [$Au_{25}SG_{18}$] nanocluster showed the maximum photoelectric conversion efficiency (~0.26%). Also, the Au_{25}-modified TiO_2 electrode achieved a short-circuit current density (J_{SC}) of 290 μA cm^{-2} and an open-circuit voltage (V_{OC}) of 460 mV when exposed to light. Though the figures mentioned above were less significant compared to current advancements, the results provided a solid foundation for future developments in metal nanocluster-sensitized solar cells. The authors further extended their research activities by correlating the electronic structure of gold nanoclusters with the photocurrent responses of gold nanocluster–modified TiO_2 electrodes (Kogo et al., 2012). The photocurrent influence on irradiation wavelength and the standard electrode potentials of electron donors were used to estimate the highest occupied molecular orbital-lowest unoccupied molecular orbital (HOMO–LUMO) levels. The estimated values are extremely useful in devising metal nanocluster–sensitized solar cells by choosing the proper nanocluster and redox couple combination. As a result, the conduction band of the semiconductor material and the redox potential value of the electrolytes were discovered to be critical to constructing a metal nanocluster–sensitive solar cell. Later, Chen et al. made a breakthrough by developing a metal nanocluster–sensitized solar cell through the appropriate selection of nanocluster and redox couple (Chen et al., 2013). Using Au(0)@Au(I)–thiolate nanocluster-modified mesoscopic TiO_2 films and a redox couple of $Co(bpy)_3(PF_6)_2/Co(bpy)_3(PF_6)_3$ (bpy = bipyridine), they were able to achieve a much higher power conversion efficiency (2.3%). While the previous methods could only generate microampere currents, the latest method could generate a J_{SC} of 3.96 mA cm^{-2} and a V_{OC} of 832 mV, comparable to the widely known CdS quantum dot–based solar cells (Fig. 8.11A). The absorbance of these Au(0)@Au(I)–thiolate nanoclusters was limited by less than 525 nm, suggesting that there is still room for improvement. Later, Abbas et al. constructed photosensitizers based on four different gold nanoclusters, viz, [$Au_{10-12}(SR)_{10-12}$], [$Au_{15}(SR)_{13}$], [$Au_{18}(SR)_{14}$], and [$Au_{25}(SR)_{18}$] using the I^-/I_3^- redox couple (Abbas et al., 2016). They initially investigated the size effect of gold nanoclusters and redox couple selection on the efficiency of metal nanocluster–based solar cells. The I^-/I_3^- electrolyte displayed

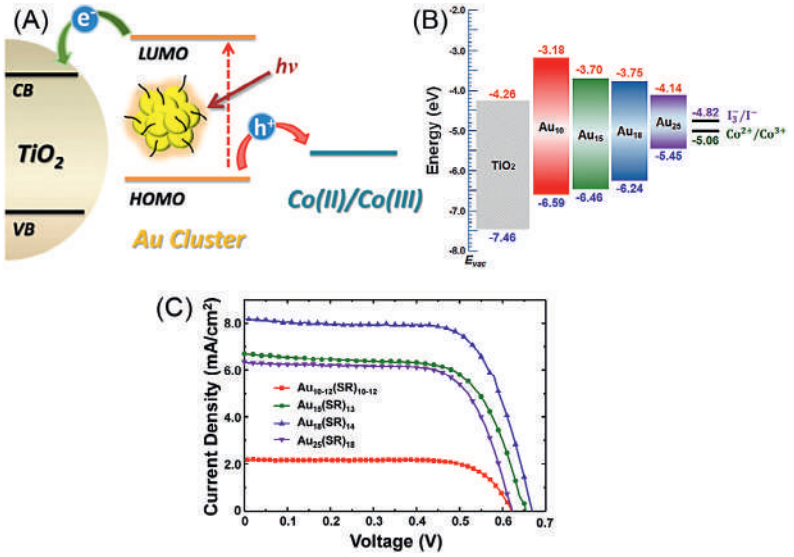

Figure 8.11. (A) Schematic illustration of the working principle of a nanocluster-sensitized solar cell. (B) Energy band diagram and (C) J—V characteristics of $[Au_{10\text{-}12}(SR)_{10\text{-}12}]$, $[Au_{15}(SR)_{13}]$, $[Au_{18}(SR)_{14}]$, and $[Au_{25}(SR)_{18}]$ nanocluster-sensitized solar cells (Fig. 8.11A from Chen et al. [2013] and Fig. 8.11B and C from Abbas et al. [2016]).

a good photosensitizing efficiency due to its appropriate redox potential for the regeneration of oxidized gold nanoclusters. Furthermore, the relatively rapid diffusivity of the I^-/I_3^- electrolyte reduced the mass transport restrictions associated with Co^{2+}/Co^{3+} redox couples. Later, they used electrochemical impedance spectroscopy and other characterization techniques to look into the performance-limiting issues. Among the four nanoclusters, the Au_{18} nanocluster produced the best photoelectric conversion efficiency (3.8%) with a J_{SC} of 8.18 mA cm^{-2} and a V_{OC} of 672 mV due to the balance in their optical absorption and charge recombination rate. (Fig. 8.11B and C). Even though the electrochemical impedance spectroscopy analysis showed that the Au_{15} nanocluster had the highest charge recombination rate, the comparatively narrow absorption spectrum was their drawback. On the other hand, the Au_{25} nanocluster showed better optical absorption but was limited by the charge recombination rate. As a result, increasing the size or number of gold atoms or even having broad optical absorption spectra for nanoclusters does not assure improved performance. Later, silver nanoclusters were also introduced to evaluate their performance as a photosensitizer in the solar energy device (Sakai et al., 2013). The stability and efficiency of silver nanocluster–based solar cells were found to be significantly lower than those with gold nanoclusters when exposed to light for an extended period of time. However, problems such as chemical stability and short excited-state lifetimes of silver nanoclusters have been solved by introducing Ag(0)@Ag(I)–thiolate nanoclusters as the photosensitizer (Abbas et al., 2019). Here, the pH-induced aggregation strategy was employed

to introduce oxidation resistive Ag(I)–thiolate complexes around the Ag(0) core. Such nanoclusters performed well compared to all other silver nanocluster–based sensitizers. Still, the performance was not as good as gold nanocluster–sensitized solar cells. Hence Naveen et al. introduced a doping method to improve the efficiency. They doped silver atoms on a $[Au_{18}(SR)_{14}]$ nanocluster via the chemical method and subsequently evaluated their photosensitizing performance. These silver-doped gold nanoclusters demonstrated an intriguing rise in extinction coefficient and HOMO–LUMO gap. Single silver atom–doped $[Au_{17}Ag_1(SR)_{14}]$ nanoclusters showed a record photoelectric conversion efficiency of 4.22% with a photovoltage of 832 mV. Doping such nanoclusters with up to three silver atoms did not affect their stability. However, higher doping resulted in rapid photocurrent degradation. It has been suggested that doped silver atoms ($\leq$3) are confined within the gold metallic core, preventing rapid degradation. Similarly, copper, platinum, palladium, and bimetallic (silver–gold and silver–copper) nanoclusters were also employed for solar cell applications (Li & Chen, 2015; Sakai et al., 2011; Shahzad et al., 2015). Among these, silver–copper bimetallic nanoclusters showed a photoelectric conversion efficiency of 1.1%, the best photoelectric conversion efficiency reported from a nongold sensitizer (Shahzad et al., 2015). It has recently been discovered that nanoclusters function both nontraditionally and uniquely throughout the optical energy conversion process compared to dye-sensitized solar cells and quantum dot–sensitized solar cells (Khan et al., 2021). For example, nanoclusters were found to show anomalous J—V hysteresis behavior, and their dependency on the hysteresis response suggested that it was not inherent to any particular structure or size. However, the less purified or nanoclusters-containing impurities could reduce the hysteresis and enhance photoelectric conversion efficiency, showing that these beneficial impurities were the source of hysteresis and decreased photoelectric conversion efficiency. Abbas et al. demonstrated that an alkali metal ion (Na^+) must be present among all possible contaminants to enable higher adsorption of $[Au_{22}SG_{18}]$ nanoclusters, hence eliminating hysteresis and improving photoelectric conversion efficiency. Here, the increased interaction of gold nanoclusters with TiO_2 in the presence of Na^+ ions boosted the charge transfer and recombination kinetics dramatically. Furthermore, these nanocluster-sensitized electrodes improved photovoltaic performance while retaining significant photostability. Later, they found a strange hole transfer mechanism while studying three different nanoclusters, viz., $[Au_{15}(SG)_{13}]$, $[Au_{18}(SG)_{14}]$, and $[Au_{25}(SG)_{18}]$, using photoelectrochemical impedance spectroscopy (PEIS) (Abbas & Bang, 2020). In the smaller-sized $[Au_{15}(SG)_{13}]$ and $[Au_{18}(SG)_{14}]$ nanoclusters the hole transfer process occurred from the HOMO levels to the electrolyte. However, in the $[Au_{25}(SG)_{18}]$–TiO_2 electrode the hole

transfer took place through the deep trap states in TiO_2. This suggests that depending on the size of the nanoclusters, the hole transfer in TiO_2–nanocluster photoelectrodes could occur indirectly via interfacial surface trap states, even in the presence of an effective hole scavenger electrolyte.

8.4 Photocatalysis

The singlet oxygen ($^1O_2$) production efficiency of precision nanoclusters has been efficiently used to catalyze organic reactions. For example, Kawasaki et al. employed $[Au_{25}PET_{18}]^-$ (PET = 2-phenylethanethiol) nanoclusters to generate $^1O_2$ by using visible/NIR irradiation followed by the oxidation of sulfide to sulfoxide with a higher selectivity (Kawasaki et al., 2014). Chen et al. developed an Au_{25} nanocluster–TiO_2 photocatalyst for the selective oxidation of amine to an imine (Chen et al., 2017a). The oxidation reaction was carried out at mild temperatures under the visible light irradiation of $Au_{25}(PPh_3)_{10}Cl_2(SC_3H_6SiO_3)_5/TiO_2$ in the presence of molecular oxygen ($^3O_2$). Among the different nanoclusters investigated, the rod-shaped Au_{25} showed 98% conversion and 99% selectivity for the oxidation of 4-methylbenzylamine, with a turnover frequency of 1522 h^{-1}. Photoexcited $Au_{25}(PPh_3)_{10}Cl_2(SC_3H_6SiO_3)_5/TiO_2$ nanoclusters showed an effective electron–hole separation due to their long lifetime. Thus these photogenerated electrons are transferred to the conduction band of TiO_2 and then to $^3O_2$ to produce active oxygen ($O_2^{\bullet -}$) species. At the same time, benzylamine consumes the holes to generate a benzylamine radical cation. Finally, the benzylamines oxidized to yield the imine product via intermediates such as Au-H species and carbocation (Fig. 8.12A). Later, Li et al. reported $[Au_{38}S_2(SAdm)_{20}]$ (HSAdm = adamantanethiol) nanoclusters with a high $^1O_2$ generation capacity (Li et al., 2017). These nanoclusters have been used to catalyze the oxidation of methyl phenyl sulfide to sulfoxide and amine to an imine. The photocatalyst $[Au_{38}S_2(SAdm)_{20}]$ nanocluster accomplished a 57% conversion efficiency and 100% selectivity during the oxidation of methyl phenyl sulfide to methyl phenyl sulfoxide. In this case the excited nanoclusters transferred their energy to $^3O_2$ to generate $^1O_2$, the key active species in this process. Furthermore, the same nanocluster could attain 99% selectivity and conversion efficiency for amine to imine oxidation. Hanbao et al. recently achieved 100% conversion efficiency and selectivity for the amine to imine oxidation of benzylamine by using bimetallic $[Au_{25-x}Ag_xSR_{18}]$ nanoclusters (Hanbao et al., 2018). The photocatalytic effect of nanoclusters has been further employed for the decomposition of pollutants. For example, Yu et al. demonstrated the photocatalytic impact of $[Au_{25}PET_{18}]$ nanoclusters

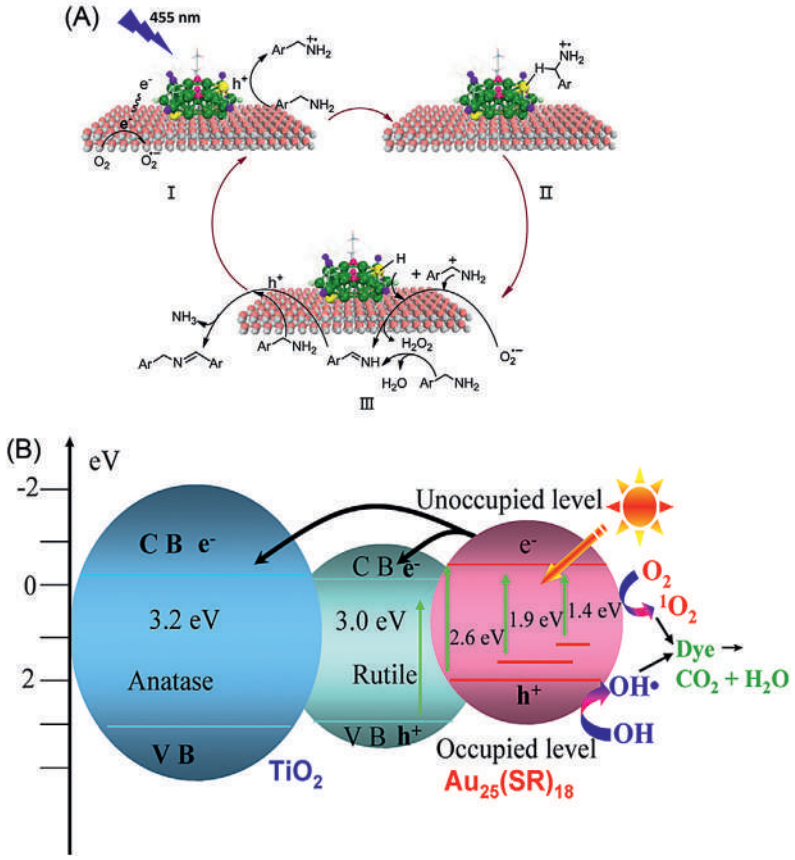

Figure 8.12. Proposed mechanisms under visible light irradiation for (A) the photo-oxidation of benzylamine by $[Au_{25}(PPh_3)_{10}C_{l2}(SC_3H_6SiO_3)_5]/TiO_2$. (B) Photocatalytic dye degradation by $[Au_{25}(PET)_{18}]/TiO_2$ (Fig. 8.12A from (Chen et al., 2017a) and Fig. 12B from (Yu et al. 2013a).

combined with TiO_2 nanocrystals on the degradation of methyl orange stable $Au_{25}(SR)_{18}/TiO_2$ composite nanostructure with enhanced visible light (Yu et al., 2013a). Compared to pure TiO_2 nanocrystals, this nanocomposite exhibits 1.6 times the catalytic activity when exposed to visible light. Under visible light irradiation, the HOMO–LUMO bandgap (~1.3 eV) of nanoclusters showed an efficient separation of electrons–holes by transporting electrons to the conduction band of TiO_2 nanocrystal. The holes formed on the nanocluster were subsequently transformed into hydroxyl radicals, which are crucial in degrading dyes (Fig. 8.12B). Liu et al. developed a one-pot method to fabricate the SAdm-capped bimetallic silver-doped gold nanoclusters (Liu et al., 2019a). The resulting nanocluster showed more excellent photocatalytic degradation capability for rhodamine B and phenol. Compared to the homometallic nanocluster, the bimetallic nanocluster dramatically improved its catalytic activity due to the excellent separation of electrons and holes. For example, the relative 0.5-wt%

Au_{23}/TiO_2 composite took ~30 min to decompose rhodamine B completely, but 0.5-wt% $Au_{23-x}Ag_x/TiO_2$ took only 19 min to achieve complete degradation. Later, Deng et al. developed a thiol-modified covalent organic framework to synthesize metal nanocluster inside its pores (Deng et al., 2020). The nanocluster produced within such framework has improved photostability and photocatalytic activity and was used in the degradation of rhodamine B.

8.5 Bioimaging

Optical bioimaging techniques help monitor biological components and their activities in real-time. Compared to traditional imaging methods, fluorescence-based bioimaging provides advantages such as noninvasiveness, high spatial and temporal resolution, and a better signal-to-noise ratio. Luminescent nanomaterials such as quantum dots, carbon dots, upconversion nanoparticles, and atomically precise nanoclusters have been used for bioimaging applications for many years. Among them, luminescent nanoclusters are very attractive due to their easy synthetic routes, different possible surface functionalization, low toxicity, photostability, and biocompatibility. For example, Wu et al. used luminescent Au@BSA nanoclusters to image MDA-MB-45 and HeLa cells owing to their high tumor uptake (Wu et al., 2010). Furthermore, the enhanced permeability and retention (EPR) effect resulted in a higher contrast difference, which was beneficial in obtaining good images. Later, Wang et al. successfully fabricated luminescent nanoclusters inside cancer cells by introducing the biocompatible micromolar solution of chloroauric acid into cells (Wang et al., 2013a). In this case the overexpressed glutathione present in cancer cells could react with Au(III) species in situ to form gold nanoclusters. Glutathione-protected silver nanoclusters (Ag@SG) synthesized similarly inside cancer cells have also been used for bioimaging applications (Gao et al., 2014). Later, the researchers attempted to conjugate a tumor-targeting molecule on the nanocluster surface for targeted imaging and delivery. Simple coupling reactions have been used to connect the target molecules on the nanocluster surface. For example, Retnakumari et al. used an EDC (1-ethyl-3-(3-dimethylaminopropyl)carbodiimide) coupling reaction to link folic acid with the Au@BSA nanocluster through an amide bond formation (Retnakumari et al., 2010). The NIR photoluminescence of nanoclusters (700–800 nm) has been successfully used to image the oral cancer cells. Similarly, folic acid conjugated thiolated polyethyleneimine–stabilized silver nanoclusters were also used for in vitro and in vivo bioimaging (Wang et al., 2014b). Wang et al. connected a humanized monoclonal antibody (Herceptin)

on the Au@BSA nanocluster surface via bioconjugate chemistry (Wang et al., 2011). The Herceptin-conjugated nanoclusters found better target selectivity for imaging and had the potential to reach the cell nucleus, causing nuclear damage of the malignant cells. Furthermore, the nanoclusters were fabricated using specific biomolecules that can continue their biological functions even when bound to nanoclusters. For example, transferrin (Tf) is a protein that is essential for iron homeostasis and cell growth regulation. The overexpression of Tf receptors in the cancer cell is 100 times more than in normal cells. Wang et al. synthesized gold–transferrin (Au–Tf) nanoclusters in which Tf acts as both a stabilizing and reducing agent during the synthesis (Wang et al., 2013b). The ability of Tf to bind with Tf receptors had been preserved even though it stabilized nanoclusters. The authors developed an NIR-emitting nanocomposite probe for in vitro and in vivo fluorescence bioimaging using Au–Tf nanoclusters and graphene oxide. The addition of graphene oxide quenched the fluorescence of Tf-stabilized nanoclusters. However, when this composite was in contact with Tf receptor overexpressed cells, the fluorescence was restored due to the specific interaction between Tf and its receptors, which promptly removed the graphene oxide (Fig. 8.13A and B). Using an ultrafast synthetic method, Yin et al. fabricated gold nanoclusters stabilized with cyclic arginine–glycine–aspartic acid (RGD) peptides (Yin et al., 2015). Here, the specific interaction of the cyclic peptide with melanoma A375 cells has been utilized for luminescence-based bioimaging. Zhu et al. used NIR light–assisted reduction to fabricate gold nanoclusters stabilized with antimicrobial peptides (AMPs) (Zhu et al., 2020). Such Au@AMP nanoclusters could diagnose and treat cancer cells and simultaneously fight against bacterial infections. Later, cancer cells overexpressed by nucleolin (nucleolar phosphoprotein) and mucin were imaged using silver nanoclusters stabilized by G-quadruplex AS1411 and MUC1 targeting aptamers, respectively (Feng et al., 2020; Zhu et al., 2015). Lyu et al. introduced cationic polyelectrolyte (poly(diallyldimethylammonium chloride) [PDDA]) into DNA-tethered silver nanoclusters to improve their stability against nuclease digestion. Such a highly stable PDDA–DNA@Ag nanoclusters nanosystem has been further employed for cellular imaging (Lyu et al., 2019). Several metal-doped nanoclusters have also been used for bioimaging applications due to their improved photoluminescence quantum yield and stability. For example, Ag_xAu_{25-x} nanoclusters holding 200-fold high quantum yield have been used for cancer cell bioimaging (Wang et al., 2014a). All of the abovementioned bioimaging techniques have been used in the visible–NIR (Vis-NIR) regime (400–900 nm). Later, near-infrared second (NIR-II) or short-wave infrared (SWIR) window (1000–1700 nm) fluorescence imaging emerged to address

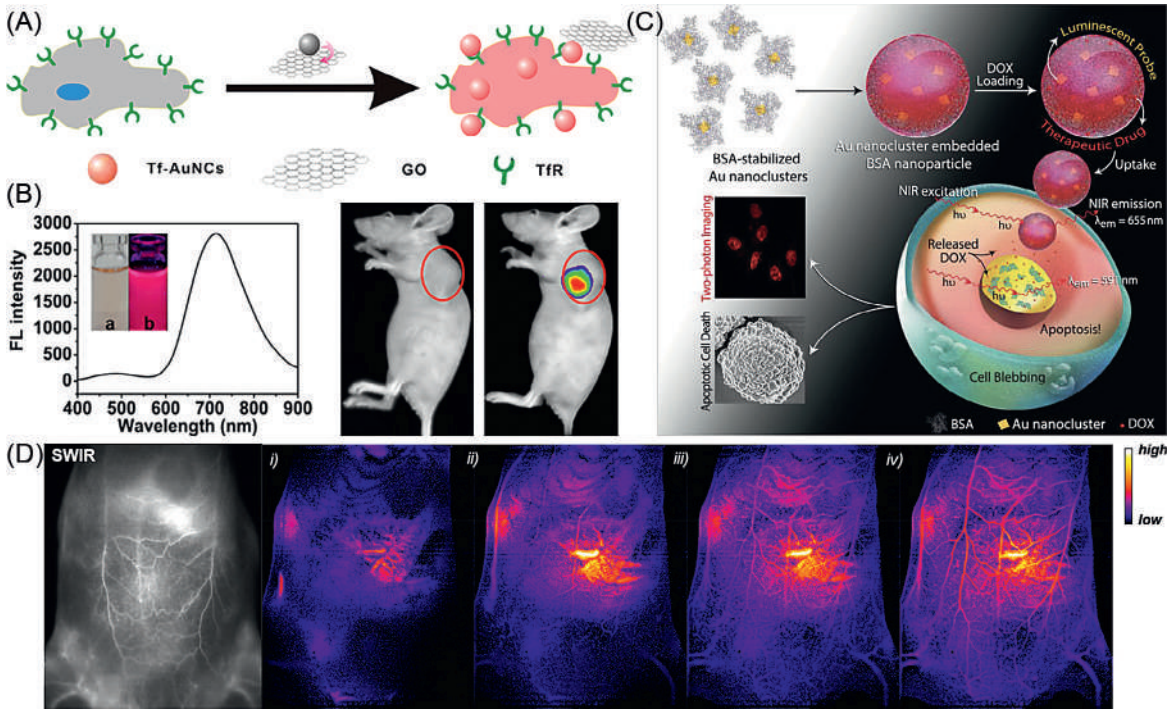

Figure 8.13. (A) Schematic illustration Tf–Au nanoclusters/graphene oxide composite as a turn-on NIR fluorescent probe for bioimaging TfR overexpressed cancer cells. (B) Fluorescence spectra and photographs of as-prepared Tf–Au nanoclusters and fluorescence imaging of HeLa tumor–bearing mice and normal nude mice after injecting the Tf–Au nanoclusters/graphene oxide composite. (C) Schematic illustration of the formation of DOX-loaded gold nanocluster–embedded BSA nanoparticles, followed by the uptake and release of DOX inside the HeLa cells, leading to apoptotic cell death, in addition to two-photon imaging. (D) SWIR image of blood vasculature in mice after intravenous injection of AuMHA/TDT and MCR+ HP filter–treated SWIR images (false colors): (i) 1.5 s, (ii) 5 s, (iii) 25 s, and (iv) 65 s after AuMHA/TDT bolu.s intravenous injection (Fig. 8.13A and B from Wang et al. 2013b; Fig. 8.13C from Khandelia et al. [2015]; and Fig. 8.13D from Yu et al. [2020]).

the issues associated with the Vis-NIR regime. The use of SWIR fluorescence imaging could enhance deep tissue penetration, reduce photodamage to biological samples, and lower the background interference. For example, Chen et al. synthesized a gold nanocluster stabilized with zwitterionic ligands (lipoic acid sulfobetaine) that emit in the SWIR region (~1000 nm) (Chen et al., 2017b). A mixture of the as-prepared gold nanocluster and excess lipoic acid–sulfobetaine was directly injected into a mouse tail vein before in vivo imaging. Interestingly, the mouse blood vessel images were more detailed when the SWIR (808 nm) laser was used to excite the nanoclusters. Later, Yu et al. developed a mercaptohexanoic acid (MHA) and tetra(ethylene glycol) dithiol (TDT)–costabilized luminescent (quantum yield of 8%) gold nanoclusters (Yu et al., 2020). The SWIR images of the mouse vascular network system using such nanoclusters showed an increased spatial resolution and contrast (Fig. 8.13D). Liu et al. used NIR-II (1100–1350 nm) light-emitting glutathione-protected gold nanoclusters $[Au_{25}(SG)_{18}]$ to image mice brain arteries and monitor tumor metastasis in vivo (Liu et al., 2019b). In another work a protein corona structure–stabilized gold nanocluster having emission at 1050 nm with a quantum yield of 1.9% was prepared. The excellent acid stability of this nanocluster made it ideal for NIR-II-imaging the gastrointestinal tract (Wang et al., 2020).

Two-photon fluorescence imaging is another advanced technique that has been used to analyze biological specimens. In this case the fluorophore or nanocluster is excited by simultaneously absorbing two photons. This method has shown to be a powerful tool in biomedical applications due to its better tissue-penetrating capabilities, improved three-dimensional spatial resolution, superior signal-to-noise ratio, and ability to limit interference due to autofluorescence. Patel et al. were the first to show that DNA-stabilized silver nanoclusters have a good two-photon absorption cross-section (10^{-50} cm^4 photon s^{-1}) (Patel et al., 2008). Later, Oh et al. fabricated a series of polyethylene glycol (PEG) dithiolane–protected gold nanoclusters with better photoluminescence quantum yield (4%–8%). Such nanoclusters have further been used to visualize cellular uptake processes via two-photon emission (Oh et al., 2013). Later, Khandelia et al. developed a nanotheranostic system for two-photon imaging and cancer treatment using BSA-stabilized gold nanoclusters preloaded with the anticancer drug doxorubicin (DOX) ((Fig. 8.13C) (Khandelia et al., 2015). Jiang et al. prepared mixed ligand-stabilized gold nanoclusters using zwitterionic ligands and 11-MUA (Jiang et al., 2019). The higher absorption cross-section (~10^5 GM) of such gold nanoclusters has successfully been employed for one-photon, two-photon, and fluorescence lifetime imaging. Multimodal imaging techniques combine two or more imaging modalities in a single probe in the nanometer regime. All of

the previous imaging techniques discussed were fluorescence based. However, there are alternative imaging approaches such as X-ray computed tomography (CT), magnetic resonance imaging (MRI), photoacoustic (PA) imaging, positron emission tomography (PET), Raman imaging, and ultrasound (US) imaging. Each of these imaging methods has its own set of benefits and drawbacks. Hence, introducing multimodalities in a single probe improves the challenges associated with single modal imaging techniques and combines the help of two imaging techniques by enhancing imaging resolution and sensitivity. Gold can be utilized for multimodal imaging due to its high X-ray attenuation coefficient, making it ideal for PL/CT/PA imaging. For example, PL/CT multimodal imaging was successfully demonstrated using two independent gold nanoclusters protected with glutathione and lysosome ligands (Liu et al., 2016b; Zhang et al., 2013a). It has been further used for targeted imaging of malignant cells by coupling with folic acid. Later, Wu et al. loaded a NIR fluorescent dye (indocyanine green [ICG]) on the surface of pea protein isolates–protected gold nanoclusters (Wu et al., 2019a). Such a nanohybrid system was then used for PL/CT dual-modal imaging and therapy in A549 cells. Shen et al. fabricated thioctic zwitterion–protected gold nanoclusters for multimodal in vivo imaging using their NIR photoluminescence and PA signals (Shen et al., 2017). Later, the PL/MRI multimodal imaging approach was used by developing nanohybrid probes comprised of nanoclusters and magnetic nanomaterials such as Gd-based compounds and Fe_3O_4 nanoparticles. For example, Liang et al. used cyclodecapeptides as a protective ligand to fabricate gold nanoclusters. Subsequently, the coordinating capacity of the protective ligand with Gd^{3+} was used to integrate the magnetic ions, resulting in the formation of a nanohybrid system capable of PL/MRI imaging (Liang et al., 2013). Likewise, Gd^{3+} coordinating ligands (diethylenetriaminepentaacetic acid dianhydride and diethylenetriaminepentaacetic acid) were conjugated on the surface of gold nanoclusters to use for PL/MRI contrast imaging applications (Wu et al., 2020). Furthermore, the considerably higher proton relaxivity of Gd_2O_3 nanoparticles compared to Gd^{3+} chelates was exploited for PL/MRI imaging by incorporating with Au@BSA nanoclusters and aptamer-coated silver nanoclusters (Sun et al., 2013). Apart from lanthanide chelates/nanoparticles, the nanohybrid system composed of Fe_3O_4 nanoparticles and metal nanoclusters has also been used for PL/MRI imaging (Zhao et al., 2016). Furthermore, the PET technique, along with the photoluminescence of nanoclusters, was used for PET/PL imaging. The ^{64}Cu-doped luminescent gold nanoclusters were used for such dual-modal imaging based on Cerenkov resonance energy transfer (Hu et al., 2014). The ^{64}Cu dopant is a β^+ radioisotope used as an energy donor for gold nanoclusters excitation and as a positron-emitting radionuclide for PET

imaging. Similar to dual-modal imaging, triple-modal imaging has also been developed to increase the accuracy of bioimaging. For example, nanocomposites such as Gd_2O_3-gold nanoclusters-ICG and Gd^{3+}-assembled gold nanoclusters were separately employed to perform PL/CT/MRI triple-modal imaging (Han et al., 2017; Wu et al., 2014). Similarly, the incorporation of gold nanoclusters with mesoporous silica shells has been demonstrated to perform PL/PA/MRI triple-modal imaging (Hembury et al., 2015).

8.6 Photodynamic and photothermal therapies

Photodynamic therapy is a noninvasive treatment method that uses light to activate the photosensitizer, which transfers the incident photon energy to the surrounding oxygen species. As a result, cytotoxic reactive oxygen species (ROS) such as $^1O_2$, superoxide, hydrogen peroxide, and hydroxyl radicals are generated, causing severe damage to malignant cells. Since the conventional photosensitizers faced poor selectivity, solubility, and targeting capability, their transport to malignant cells is very complicated. To overcome such issues, the nanoclusters have started to be used as an efficient probe to transport the photosensitizer by conjugating both of them covalently before the delivery. For example, Nair et al. fabricated very efficient singlet oxygen-producing multifunctional nanoclusters via conjugate chemistry. The targeting (folic acid) and photosensitizer (protoporphyrin IX) molecules were initially conjugated on a nanocluster surface via an EDC coupling reaction (Nair et al., 2015). Such multifunctional nanoclusters were used to generate singlet oxygen in tumor cells by laser irradiation. Even a low photosensitizer loading on a nanocluster surface resulted in an enhanced $^1O_2$ efficiency (80%) compared to protoporphyrin IX alone (63%). Furthermore, the NIR photoluminescence from the nanoclusters was used to monitor the progress of the photodynamic therapy in real time. Similarly, the NIR-emitting DNA-stabilized silver nanocluster coupled with protoporphyrin IX was employed for photodynamic therapy and attained ~80% cell mortality rate (Ai et al., 2016). The enhanced mortality rate is attributed to the synergic effect of the photodynamic efficiency of protoporphyrin IX and the photothermal efficiency of the NIR luminescent nanoprobes. Later, Zhang et al. loaded another photosensitizer (chlorin e6 [Ce6]) on the nanocluster surface for the targeted photodynamic therapy (Zhang et al., 2015). Here, folic acid–capped PEG was covalently bonded with glutathione-capped gold nanoclusters. Subsequently, the photosensitizer Ce6 was adsorbed on the nanocluster surface via the hydrophobic interactions with PEG chains, and the Ce6 carboxyl group interaction with the metallic core.

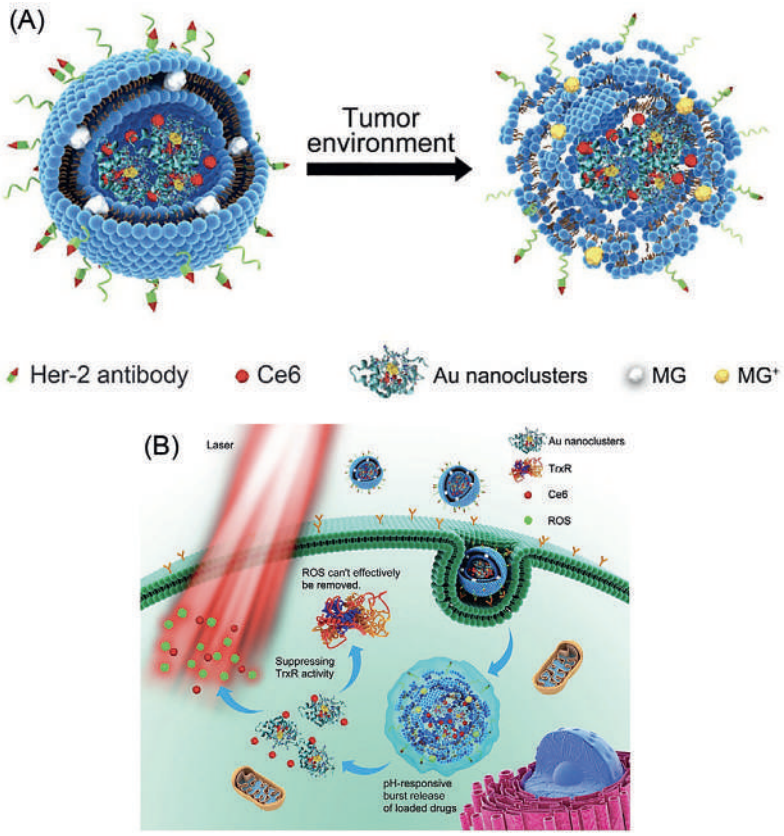

Figure 8.14. Schematic illustration of gold nanoclusters and photosensitizer Ce6 dual-loaded spatiotemporal controllable liposomal nanocomposites to enhance tumor photodynamic therapy effect by inhibiting thioredoxin reductase (TrxR) (Gao et al., 2017).

This multifunctional nanocluster was used for targeted photodynamic therapy with improved tumor penetration and long-time retention. The same photosensitizer (Ce6) was coloaded with gold nanoclusters using a pH-sensitive liposome, resulting in a nanocomposite that inhibits the antioxidant defense activity of thioredoxin reductase and stimulates $^1O_2$ generation to cause mitochondrial damage (Gao et al., 2017) (Fig. 8.14A and B). On the other hand, Huang et al. used Ce6 covalently linked silica-coated gold nanoclusters for photodynamic therapy (Huang et al., 2013). Similarly, Dutta et al. combined photodynamic treatment and bioimaging by loading methylene blue on gold nanocluster embedded mucin nanoparticles (Dutta et al., 2019). Later, Cheng et al. fabricated a nanocomposite consisting of TiO_2 nanoparticles, gold nanoclusters, and graphene (TAG) to boost the light energy conversion efficiency of photodynamic therapy (Cheng et al., 2017d). When TAG was exposed to sunlight, the excited electrons from the gold nanocluster were transferred to the conduction band of TiO_2 nanoparticles and then to graphene, resulting in free electrons that combine

with O_2 to produce superoxide radicals. Due to staggered energy levels, the holes were accumulated on the HOMO level of gold nanoclusters that generate hydroxyl radicals from H_2O. As a result, when exposed to sunlight, the TAG nanocomposite generates an abundant supply of ROS that kill melanoma cancer cells. The intrinsic catalytic activities of PAMAM-dendrimer-protected gold nanoclusters have been used to convert H_2O_2 into O_2 (Liu et al., 2017a). When such nanoclusters were conjugated with protoporphyrin IX, the efficiency of photodynamic therapy in the treatment of hypoxic cancer was significantly improved. Later, the intrinsic photosensitizing ability of metal nanoclusters was probed for photodynamic therapy without the photosensitizers. For example, Yu et al. used red-luminescent BSA-protected Ag_{13} nanoclusters to demonstrate photodynamic treatment in breast cancer cells (Yu et al., 2016). From the ultrafast laser spectroscopic studies, it was found that the photoexcited Ag_{13}BSA nanoclusters have a high predominance of triply excited states capable of producing singlet oxygen with high efficiency. Similarly, the nucleus-targeting TAT peptide–protected gold nanoclusters with intrinsic photosensitizing activity were used to destroy cancer cells (Vankayala et al., 2015). Recently, Han et al. developed in vivo two-photon-induced photodynamic therapy using dihydrolipoic acid–protected gold (Au@LA) nanoclusters (Han et al., 2020). In this case the photochemical electron transfer mechanism (type I) worked preferentially over the conventional singlet oxygen mechanism (type II). As a result, the superoxide anion was generated instead of $^1O_2$. Nanoclusters have recently been discovered to be good probes for photothermal treatment. The light energy collected by the nanocluster is converted to vibrational energy, which generates local heat and eventually eliminates the malignant cell lines with superior spatiotemporal resolution. For example, Katla et al. used the $Au_{25}SG_{18}$ nanocluster for the photothermal treatment of MDA-MB-231 breast cancer cells using an 808-nm laser (Katla et al., 2018). They performed the phototherapy using various laser powers and achieved 100% cancer cell death with 10 W cm^{-2} for 5 min of irradiation. Later Jiang et al. conjugated ICG NIR dye with the [$Au_{25}SG_{18}$] nanocluster for the photothermal therapy (Jiang et al., 2020). When compared to the ICG solution alone (~10°C), the ICG_4–GS–Au_{25} nanocomposite produced ~20°C temperature gain with negligible decay when irradiated with 0.5 W cm^{-2} NIR laser. As a result, the combined effect of ICG and nanocluster could be obtained by using a lower power density than that used in the abovementioned work. (Katla et al., 2018) Furthermore, these systems showed better renal clearance, low toxicity, and excellent biocompatibility. Recently, the Au_4Cu_4/Au_{25}@Lip nanohybrid system was utilized for combined photodynamic and photothermal therapy (Liu et al., 2021). Organic-soluble Au_4Cu_4 bimetallic nanoclusters

and aqueous-soluble Au_{25} nanoclusters self-assemble into the spherical Au_4Cu_4/Au_{25}@Lip nanohybrid system. The photothermal and fluorescence activity of the Au_{25} nanocluster was probed here for imaging and therapy.

8.7 Summary

This chapter outlines the applications of precision nanoclusters in different aspects of chemistry, physics, and biology. The bright photoluminescence of metal nanoclusters has been successfully used to detect hazardous metal ions and biologically relevant compounds with great effectiveness. The functionalized nanoclusters have also been used for (1) LED fabrication as color conversion layers, (2) green energy harvesting, (3) photocatalysis, (4) bioimaging, and (5) therapeutics due to their simple and well-established synthetic routes, broad absorption spectrum, improved photostability in the Vis-NIR regimes, lower toxicity, and increased photoluminescence quantum yield. The improved photophysical properties of nanoclusters resulting from metal doping, aggregation-induced emission, supramolecular self-assembly, and other methods will aid in the development of next-generation technologies and biology.

References

Abbas, M.A., Bang, J.H., 2020. Anomalous transition of hole transfer pathways in gold nanocluster-sensitized TiO_2 photoelectrodes. ACS Energy Letters 5 (12), 3718–3724. https://doi.org/10.1021/acsenergylett.0c02180.

Abbas, M.A., Kim, T.Y., Lee, S.U., Kang, Y.S., Bang, J.H., 2016. Exploring interfacial events in gold-nanocluster-sensitized solar cells: insights into the effects of the cluster size and electrolyte on solar cell performance. J. Am. Chem. Soc. 138 (1), 390–401. https://doi.org/10.1021/jacs.5b11174.

Abbas, M.A., Yoon, S.J., Kim, H., Lee, J., Kamat, P.V., Bang, J.H., 2019. Ag(I)-thiolate-protected silver nanoclusters for solar cells: electrochemical and spectroscopic look into the photoelectrode/electrolyte interface. ACS Appl. Mater. Interfaces 11 (13), 12492–12503. https://doi.org/10.1021/acsami.9b00049.

Adhikari, B., Banerjee, A., 2010. Facile synthesis of water-soluble fluorescent silver nanoclusters and Hg^{II} sensing. Chem. Mater. 22 (15), 4364–4371. https://doi.org/10.1021/cm1001253.

Ai, L., Jiang, W., Liu, Z., Liu, J., Gao, Y., Zou, H., Wu, Z., Wang, Z., Liu, Y., Zhang, H., Yang, B., 2017a. Engineering a red emission of copper nanocluster self-assembly architectures by employing aromatic thiols as capping ligands. Nanoscale 9 (34), 12618–12627. https://doi.org/10.1039/c7nr03985a.

Ai, J., Li, J., Ga, L., Yun, G., Xu, L., Wang, E., 2016. Multifunctional near-infrared fluorescent nanoclusters for simultaneous targeted cancer imaging and photodynamic therapy. Sens. Actuators B 222, 918–922. https://doi.org/10.1016/j.snb.2015.09.026.

Ai, L., Liu, Z., Zhou, D., Liu, J., Zou, H., Wu, Z., Liu, Y., Zhang, H., Yang, B., 2017b. Copper inter-nanoclusters distance-modulated chromism of self-assembly induced emission. Nanoscale 9 (47), 18845–18854. https://doi.org/10.1039/c7nr06918a.

Bhandari, S., Pramanik, S., Khandelia, R., Chattopadhyay, A., 2016. Gold nanocluster and quantum dot complex in protein for biofriendly white-light-emitting material. ACS Appl. Mater. Interfaces 8 (3), 1600–1605. https://doi.org/10.1021/acsami.6b00039.

Chang, H.C., Chang, Y.F., Fan, N.C., Ho, J.A.A., 2014. Facile preparation of high-quantum-yield gold nanoclusters: application to probing mercuric ions and biothiols. ACS Appl. Mater. Interfaces 6 (21), 18824–18831. https://doi.org/10.1021/am504546f.

Chen, C., Yuan, Z., Chang, H.T., Lu, F., Li, Z., Lu, C., 2016. Silver nanoclusters as fluorescent nanosensors for selective and sensitive nitrite detection. Anal. Methods 8 (12), 2628–2633. https://doi.org/10.1039/c6ay00214e.

Chen, Y., Sun, Y., Song, R., Song, S., Zhao, Y., Yang, X., Yu, C., Lin, Q., 2017c. Fluorometric "turn-on" glucose sensing through the in situ generation of silver nanoclusters. RSC Adv 7 (3), 1396–1400. https://doi.org/10.1039/c6ra26303h.

Chen, T.H., Tseng, W.L., 2012. Lysozyme type VI)-stabilized Au_8 clusters: synthesis mechanism and application for sensing of glutathione in a single drop of blood. Small 8 (12), 1912–1919. https://doi.org/10.1002/smll.201102741.

Chen, W.Y., Huang, C.C., Chen, L.Y., Chang, H.T., 2014. Self-assembly of hybridized ligands on gold nanodots: tunable photoluminescence and sensing of nitrite. Nanoscale 6 (19), 11078–11083. https://doi.org/10.1039/c4nr02817a.

Chen, Y.S., Choi, H., Kamat, P.V., 2013. Metal-cluster-sensitized solar cells. a new class of thiolated gold sensitizers delivering efficiency greater than 2%. J. Am. Chem. Soc. 135 (24), 8822–8825. https://doi.org/10.1021/ja403807f.

Chen, H., Liu, C., Wang, M., Zhang, C., Luo, N., Wang, Y., Abroshan, H., Li, G., Wang, F., 2017a. Visible light gold nanocluster photocatalyst: selective aerobic oxidation of amines to imines. ACS Catalysis 7 (5), 3632–3638. https://doi.org/10.1021/acscatal.6b03509.

Chen, Y., Montana, D.M., Wei, H., Cordero, J.M., Schneider, M., Le Guével, X., Chen, O., Bruns, O.T., Bawendi, M.G., 2017b. Shortwave infrared in vivo imaging with gold nanoclusters. Nano Lett 17 (10), 6330–6334. https://doi.org/10.1021/acs.nanolett.7b03070.

Cheng, Y., Chang, Y., Feng, Y., Liu, N., Sun, X., Feng, Y., Li, X., Zhang, H., 2017d. Simulated sunlight-mediated photodynamic therapy for melanoma skin cancer by titanium-dioxide-nanoparticle-gold-nanocluster-graphene heterogeneous nanocomposites. Small 13 (20), 1603935. https://doi.org/10.1002/smll.201603935.

Cuaran-Acosta, D., Londoño-Larrea, P., Zaballos-García, E., Pérez-Prieto, J., 2019. Reversible pH-induced fluorescence colour change of gold nanoclusters based on pH-regulated surface interactions. Chem. Commun. 55 (11), 1604–1606. https://doi.org/10.1039/c8cc06664g.

Cui, M.L., Liu, J.M., Wang, X.X., Lin, L.P., Jiao, L., Zheng, Z.Y., Zhang, L.H., Jiang, S.L., 2013. A promising gold nanocluster fluorescent sensor for the highly sensitive and selective detection of S^{2-}. Sens. Actuators B 188, 53–58. https://doi.org/10.1016/j.snb.2013.05.098.

Deng, H.H., Wu, G.W., Zou, Z.Q., Peng, H.P., Liu, A.L., Lin, X.H., Xia, X.H., Chen, W., 2015. pH-Sensitive gold nanoclusters: preparation and analytical applications for urea, urease, and urease inhibitor detection. Chem. Commun. 51 (37), 7847–7850. https://doi.org/10.1039/c5cc00702j.

Deng, L., Zhou, Z., Li, J., Li, T., Dong, S., 2011. Fluorescent silver nanoclusters in hybridized dna duplexes for the turn-on detection of Hg^{2+} ions. Chem. Commun. 47 (39), 11065–11067. https://doi.org/10.1039/c1cc14012d.

Deng, Y., Zhang, Z., Du, P., Ning, X., Wang, Y., Zhang, D., Liu, J., Zhang, S., Lu, X., 2020. Embedding ultrasmall au clusters into the pores of a covalent organic framework

for enhanced photostability and photocatalytic performance. Angew. Chem. Int. Ed. 59 (15), 6082–6089. https://doi.org/10.1002/anie.201916154.
Dhanya, S., Saumya, V., Rao, T.P., 2013. Synthesis of silver nanoclusters, characterization and application to trace level sensing of nitrate in aqueous media. Electrochim. Acta 102, 299–305. https://doi.org/10.1016/j.electacta.2013.04.017.
Durgadas, C.V., Sharma, C.P., Sreenivasan, K., 2011. Fluorescent gold clusters as nanosensors for copper ions in live cells. Analyst 136 (5), 933–940. https://doi.org/10.1039/c0an00424c.
Dutta, D., Sailapu, S.K., Simon, A.T., Ghosh, S.S., Chattopadhyay, A., 2019. Gold-nanocluster-embedded mucin nanoparticles for photodynamic therapy and bioimaging. Langmuir 35 (32), 10475–10483. https://doi.org/10.1021/acs.langmuir.9b00998.
Feng, B., Xing, Y., Lan, J., Su, Z., Wang, F., 2020. Synthesis of MUC1 aptamer-stabilized gold nanoclusters for cell-specific imaging. Talanta 212. https://doi.org/10.1016/j.talanta.2020.120796.
Gao, F., Zheng, W., Gao, L., Cai, P., Liu, R., Wang, Y., Yuan, Q., Zhao, Y., Gao, X., 2017. Au nanoclusters and photosensitizer dual loaded spatiotemporal controllable liposomal nanocomposites enhance tumor photodynamic therapy effect by inhibiting thioredoxin reductase. Adv. Healthc. Mater. 6 (7), 1601453. https://doi.org/10.1002/adhm.201601453.
Gao, S., Chen, D., Li, Q., Ye, J., Jiang, H., Amatore, C., Wang, X., 2014. Near-infrared fluorescence imaging of cancer cells and tumors through specific biosynthesis of silver nanoclusters. Sci. Rep. 4. https://doi.org/10.1038/srep04384.
George, A., Gopalakrishnan, H., Mandal, S., 2017. Surfactant free platinum nanocluster as fluorescent probe for the selective detection of Fe (III) ions in aqueous medium. Sens. Actuators B 243, 332–337. https://doi.org/10.1016/j.snb.2016.11.138.
Guo, C., Irudayaraj, J., 2011. Fluorescent Ag clusters via a protein-directed approach as a Hg(II) ion sensor. Anal. Chem. 83 (8), 2883–2889. https://doi.org/10.1021/ac1032403.
Guo, W., Yuan, J., Dong, Q., Wang, E., 2010. Highly sequence-dependent formation of fluorescent silver nanoclusters in hybridized DNA duplexes for single nucleotide mutation identification. J. Am. Chem. Soc. 132 (3), 932–934. https://doi.org/10.1021/ja907075s.
Guo, W., Yuan, J., Wang, E., 2009. Oligonucleotide-stabilized Ag nanoclusters as novel fluorescence probes for the highly selective and sensitive detection of the Hg^{2+} ion. Chem. Commun. 23, 3395–3397. https://doi.org/10.1039/b821518a.
Han, B., Wang, E., 2011. Oligonucleotide-stabilized fluorescent silver nanoclusters for sensitive detection of biothiols in biological fluids. Biosens. Bioelectron. 26 (5), 2585–2589. https://doi.org/10.1016/j.bios.2010.11.011.
Han, L., Xia, J.M., Hai, X., Shu, Y., Chen, X.W., Wang, J.H., 2017. Protein-stabilized gadolinium oxide-gold nanoclusters hybrid for multimodal imaging and drug delivery. ACS Appl. Mater. Interfaces 9 (8), 6941–6949. https://doi.org/10.1021/acsami.7b00246.
Han, R., Zhao, M., Wang, Z., Liu, H., Zhu, S., Huang, L., Wang, Y., Wang, L., Hong, Y., Sha, Y., Jiang, Y., 2020. Super-efficient in vivo two-photon photodynamic therapy with a gold nanocluster as a type I photosensitizer. ACS Nano 14 (8), 9532–9544. https://doi.org/10.1021/acsnano.9b05169.
Hanbao, C., Guiqi, G., Jinsong, C., Sha, Y., Bo, R., Guang, L., Manzhou, Z., 2018. Photoinduced oxidation catalysis by $Au_{25-x}Ag_x(SR)_{18}$ nanoclusters. ChemNanoMat 4 (5), 482–486. https://doi.org/10.1002/cnma.201700336.
Hembury, M., Chiappini, C., Bertazzo, S., Kalber, T.L., Drisko, G.L., Ogunlade, O., Walker-Samuel, S., Krishna, K.S., Jumeaux, C., Beard, P., Kumar, C.S.S.R., Porter, A.E., Lythgoe, M.F., Boissière, C., Sanchez, C., Stevens, M.M., Langer, R.,

2015. Gold-silica quantum rattles for multimodal imaging and therapy. Proc. Nat. Acad. Sci. U.S.A. 112 (7), 1959–1964. https://doi.org/10.1073/pnas.1419622112.

Ho, A.J.A., Chang, H.C., Su, W.T., 2012. DOPA-mediated reduction allows the facile synthesis of fluorescent gold nanoclusters for use as sensing probes for ferric ions. Anal. Chem. 84 (7), 3246–3253. https://doi.org/10.1021/ac203362g.

Hofmann, C.M., Essner, J.B., Baker, G.A., Baker, S.N., 2014. Protein-templated gold nanoclusters sequestered within sol-gel thin films for the selective and ratiometric luminescence recognition of Hg^{2+}. Nanoscale 6 (10), 5425–5431. https://doi.org/10.1039/c4nr00610k.

Holmes, P., James, K.A.F., Levy, L.S., 2009. Is low-level environmental mercury exposure of concern to human health? Sci. Total Environ. 408 (2), 171–182. https://doi.org/10.1016/j.scitotenv.2009.09.043.

Hu, H., Huang, P., Weiss, O.J., Yan, X., Yue, X., Zhang, M.G., Tang, Y., Nie, L., Ma, Y., Niu, G., Wu, K., Chen, X., 2014. PET and NIR optical imaging using self-illuminating ^{64}Cu-doped chelator-free gold nanoclusters. Biomaterials 35 (37), 9868–9876. https://doi.org/10.1016/j.biomaterials.2014.08.038.

Hu, L., Han, S., Parveen, S., Yuan, Y., Zhang, L., Xu, G., 2012. Highly sensitive fluorescent detection of trypsin based on BSA-stabilized gold nanoclusters. Biosens. Bioelectron. 32 (1), 297–299. https://doi.org/10.1016/j.bios.2011.12.007.

Huang, C.C., Chen, C.T., Shiang, Y.C., Lin, Z.H., Chang, H.T., 2009. Synthesis of fluorescent carbohydrate-protected Au nanodots for detection of concanavalin a and *escherichia coli*. Anal. Chem. 81 (3), 875–882. https://doi.org/10.1021/ac8010654.

Huang, C.C., Chiang, C.K., Lin, Z.H., Lee, K.H., Chang, H.T., 2008. Bioconjugated gold nanodots and nanoparticles for protein assays based on photoluminescence quenching. Anal. Chem. 80 (5), 1497–1504. https://doi.org/10.1021/ac701998f.

Huang, C.C., Yang, Z., Lee, K.H., Chang, H.T., 2007. Synthesis of highly fluorescent gold nanoparticles for sensing mercury(II). Angew. Chem. Int. Ed. 46 (36), 6824–6828. https://doi.org/10.1002/anie.200700803.

Huang, H.Y., Cai, K.B., Talite, M.J., Chou, W.C., Chen, P.W., Yuan, C.T., 2019. Coordination-induced emission enhancement in gold-nanoclusters with solid-state quantum yields up to 40% for eco-friendly, low-reabsorption nano-phosphors. Sci. Rep. 9 (1). https://doi.org/10.1038/s41598-019-40706-3.

Huang, P., Lin, J., Wang, S., Zhou, Z., Li, Z., Wang, Z., Zhang, C., Yue, X., Niu, G., Yang, M., Cui, D., Chen, X., 2013. Photosensitizer-conjugated silica-coated gold nanoclusters for fluorescence imaging-guided photodynamic therapy. Biomaterials 34 (19), 4643–4654. https://doi.org/10.1016/j.biomaterials.2013.02.063.

Huang, Z., Pu, F., Lin, Y., Ren, J., Qu, X., 2011. Modulating DNA-templated silver nanoclusters for fluorescence turn-on detection of thiol compounds. Chem. Commun. 47 (12), 3487–3489. https://doi.org/10.1039/c0cc05651k.

Hussain, A.M.P., Sarangi, S.N., Kesarwani, J.A., Sahu, S.N., 2011. Au-nanocluster emission based glucose sensing. Biosens. Bioelectron. 29 (1), 60–65. https://doi.org/10.1016/j.bios.2011.07.066.

Jia, X., Li, J., Han, L., Ren, J., Yang, X., Wang, E., 2012. DNA-hosted copper nanoclusters for fluorescent identification of single nucleotide polymorphisms. ACS Nano 6 (4), 3311–3317. https://doi.org/10.1021/nn3002455.

Jia, Y., Zhang, X., Yin, C., Zhang, X., Zhang, J., Wang, X., Xin, J., 2019. An electrostatic self-assembly route to prepare C-dots/gold nanoclusters for dual-emission ratiometric optical thermometry in living cells. Anal. Methods 11 (31), 3974–3980. https://doi.org/10.1039/c9ay01115c.

Jiang, X., Du, B., Huang, Y., Yu, M., Zheng, J., 2020. Cancer photothermal therapy with ICG-conjugated gold nanoclusters. Bioconjugate Chem 31 (5), 1522–1528. https://doi.org/10.1021/acs.bioconjchem.0c00172.

Jiang, X., Wang, X., Yao, C., Zhu, S., Liu, L., Liu, R., Li, L., 2019. Surface-engineered gold nanoclusters with biological assembly-amplified emission for multimode imaging. J. Phys. Chem. Lett. 10 (17), 5237–5243. https://doi.org/10.1021/acs.jpclett.9b02046.

Jin, L., Shang, L., Guo, S., Fang, Y., Wen, D., Wang, L., Yin, J., Dong, S., 2011. Biomolecule-stabilized Au nanoclusters as a fluorescence probe for sensitive detection of glucose. Biosens. Bioelectron. 26 (5), 1965–1969. https://doi.org/10.1016/j.bios.2010.08.019.

Katla, S.K., Zhang, J., Castro, E., Bernal, R.A., Li, X., 2018. Atomically precise $Au_{25}(SG)_{18}$ nanoclusters: rapid single-step synthesis and application in photothermal therapy. ACS Appl. Mater. Interfaces 10 (1), 75–82. https://doi.org/10.1021/acsami.7b12614.

Kawasaki, H., Kumar, S., Li, G., Zeng, C., Kauffman, D.R., Yoshimoto, J., Iwasaki, Y., Jin, R., 2014. Generation of singlet oxygen by photoexcited $Au_{25}(SR)_{18}$ clusters. Chem. Mater. 26 (9), 2777–2788. https://doi.org/10.1021/cm500260z.

Khan, R., Naveen, M.H., Bang, J.H., 2021. Similar looks, different photoelectrochemical behavior: unique aspects of metal-nanocluster-sensitized electrodes. ACS Energy Letters 6 (8), 2713–2725. https://doi.org/10.1021/acsenergylett.1c01095.

Khandelia, R., Bhandari, S., Pan, U.N., Ghosh, S.S., Chattopadhyay, A., 2015. Gold nanocluster embedded albumin nanoparticles for two-photon imaging of cancer cells accompanying drug delivery. Small 11 (33), 4075–4081. https://doi.org/10.1002/smll.201500216.

Kogo, A., Sakai, N., Tatsuma, T., 2012. Photoelectrochemical analysis of size-dependent electronic structures of gold clusters supported on TiO_2. Nanoscale 4 (14), 4217–4221. https://doi.org/10.1039/c2nr30480e.

Lan, G.Y., Chen, W.Y., Chang, H.T., 2011. One-pot synthesis of fluorescent oligonucleotide Ag nanoclusters for specific and sensitive detection of DNA. Biosens. Bioelectron. 26 (5), 2431–2435. https://doi.org/10.1016/j.bios.2010.10.026.

Lan, G.Y., Huang, C.C., Chang, H.T., 2010. Silver nanoclusters as fluorescent probes for selective and sensitive detection of copper ions. Chem. Commun. 46 (8), 1257–1259. https://doi.org/10.1039/b920783j.

Li, W., Chen, F., 2015. Alloying effect on performances of bimetallic Ag-Au cluster sensitized solar cells. J. Alloys Compd. 632, 845–848. https://doi.org/10.1016/j.jallcom.2015.01.306.

Li, P.H., Lin, J.Y., Chen, C.T., Ciou, W.R., Chan, P.H., Luo, L., Hsu, H.Y., Diau, E.W.G., Chen, Y.C., 2012b. Using gold nanoclusters as selective luminescent probes for phosphate-containing metabolites. Anal. Chem. 84 (13), 5484–5488. https://doi.org/10.1021/ac300332t.

Li, Z., Liu, C., Abroshan, H., Kauffman, D.R., Li, G., 2017. $Au_{38}S_2(SAdm)_{20}$ photocatalyst for one-step selective aerobic oxidations. ACS Catalysis 7 (5), 3368–3374. https://doi.org/10.1021/acscatal.7b00239.

Li, J., Zhong, X., Zhang, H., Le, X.C., Zhu, J.J., 2012a. Binding-induced fluorescence turn-on assay using aptamer-functionalized silver nanocluster DNA probes. Anal. Chem. 84 (12), 5170–5174. https://doi.org/10.1021/ac3006268.

Liang, G., Ye, D., Zhang, X., Dong, F., Chen, H., Zhang, S., Li, J., Shen, X., Kong, J., 2013. One-pot synthesis of Gd^{3+}-functionalized gold nanoclusters for dual model (fluorescence/magnetic resonance) imaging. J. Mater. Chem. B 1 (29), 3545–3552. https://doi.org/10.1039/c3tb20440e.

Lin, Y.H., Tseng, W.L., 2010. Ultrasensitive sensing of Hg^{2+} and CH_3Hg^+ based on the fluorescence quenching of lysozyme type VI-stabilized gold nanoclusters. Anal. Chem. 82 (22), 9194–9200. https://doi.org/10.1021/ac101427y.

Liu, Y., Tian, G.F., He, X.W., Li, W.Y., Zhang, Y.K., 2016b. Microwave-assisted one-step rapid synthesis of near-infrared gold nanoclusters for NIRF/CT dual-modal bioimaging. J. Mater. Chem. B 4 (7), 1276–1283. https://doi.org/10.1039/c5tb02322j.

Liu, X., Wang, F., Aizen, R., Yehezkeli, O., Willner, I., 2013a. Graphene oxide/nucleic-acid-stabilized silver nanoclusters: functional hybrid materials for optical aptamer sensing and multiplexed analysis of pathogenic DNAs. J. Am. Chem. Soc. 135 (32), 11832–11839. https://doi.org/10.1021/ja403485r.

Liu, J., Wu, Z., Li, T., Zhou, D., Zhang, K., Sheng, Y., Cui, J., Zhang, H., Yang, B., 2016a. Electrophoretic deposition of fluorescent Cu and Au sheets for light-emitting diodes. Nanoscale 8 (1), 395–402. https://doi.org/10.1039/c5nr06599b.

Liu, C.P., Wu, T.H., Liu, C.Y., Chen, K.C., Chen, Y.X., Chen, G.S., Lin, S.Y., 2017a. Self-supplying O_2 through the catalase-like activity of gold nanoclusters for photodynamic therapy against hypoxic cancer cells. Small 13 (26). https://doi.org/10.1002/smll.201700278.

Liu, J., Lu, Y., Feng, L., Wang, S., Zhang, S., Zhu, X., Sheng, L., Zhang, S., Zhang, X., 2017b. Pinpoint the positions of single nucleotide polymorphisms by a nanocluster dimer. Anal. Chem. 89 (4), 2622–2627. https://doi.org/10.1021/acs.analchem.6b04981.

Liu, C., Ren, X., Lin, F., Fu, X., Lin, X., Li, T., Sun, K., Huang, J., 2019a. Structure of the $Au_{23-x}Ag_x(S\text{-}Adm)_{15}$ nanocluster and its application for photocatalytic degradation of organic pollutants. Angewandte Chemie—International Edition 58 (33), 11335–11339. https://doi.org/10.1002/anie.201904612.

Liu, H., Hong, G., Luo, Z., Chen, J., Chang, J., Gong, M., He, H., Yang, J., Yuan, X., Li, L., Mu, X., Wang, J., Mi, W., Luo, J., Xie, J., Zhang, X., 2019b. Atomic-precision gold clusters for NIR-II imaging. Adv. Mater. 31 (46), 1901015. https://doi.org/10.1002/adma.201901015.

Liu, P., Shang, L., Li, H., Cui, Y., Qin, Y., Wu, Y., Hiltunen, J.K., Chen, Z., Shen, J., 2014. Synthesis of fluorescent α-chymotrypsin A-functionalized gold nanoclusters and their application to blot-based technology for Hg^{2+} detection. RSC Adv 4 (60), 31536–31543. https://doi.org/10.1039/c4ra05686h.

Liu, J., Wu, Z., Tian, Y., Li, Y., Ai, L., Li, T., Zou, H., Liu, Y., Zhang, X., Zhang, H., Yang, B., 2017c. Engineering the self-assembly induced emission of Cu nanoclusters by Au(I) doping. ACS Appl. Mater. Interfaces 9 (29), 24899–24907. https://doi.org/10.1021/acsami.7b06371.

Liu, H., Yang, G., Abdel-Halim, E.S., Zhu, J.J., 2013b. Highly selective and ultrasensitive detection of nitrite based on fluorescent gold nanoclusters. Talanta 104, 135–139. https://doi.org/10.1016/j.talanta.2012.11.020.

Liu, X., Yang, Y., Wang, X., Liu, X., Cheng, H., Wang, P., Shen, Y., Xie, A., Zhu, M., 2021. Self-assembled Au_4Cu_4/Au_{25} NCs@liposome tumor nanotheranostics with PT/fluorescence imaging-guided synergetic PTT/PDT. J. Mater. Chem. B 9 (32), 6396–6405. https://doi.org/10.1039/d1tb01092a.

Liu, Y., Ai, K., Cheng, X., Huo, L., Lu, L., 2010. Gold-nanocluster-based fluorescent sensors for highly sensitive and selective detection of cyanide in water. Adv. Funct. Mater. 20 (6), 951–956. https://doi.org/10.1002/adfm.200902062.

Lu, D., Liu, L., Li, F., Shuang, S., Li, Y., Choi, M.M.F., Dong, C., 2014. Lysozyme-stabilized gold nanoclusters as a novel fluorescence probe for cyanide recognition. Spectrochimica Acta Part A: Molecular and Biomolecular Spectroscopy 121, 77–80. https://doi.org/10.1016/j.saa.2013.10.009.

Lyu, D., Li, J., Wang, X., Guo, W., Wang, E., 2019. Cationic-polyelectrolyte-modified fluorescent DNA–silver nanoclusters with enhanced emission and higher stability for rapid bioimaging. Anal. Chem. 91 (3), 2050–2057. https://doi.org/10.1021/acs.analchem.8b04493.

Muhammed, M.A.H., Verma, P.K., Pal, S.K., Retnakumari, A., Koyakutty, M., Nair, S., Pradeep, T., 2010. Luminescent quantum clusters of gold in bulk by albumin-induced core etching of nanoparticles: metal ion sensing, metal-enhanced luminescence, and biolabeling. Chem. Eur. J. 16 (33), 10103–10112. https://doi.org/10.1002/chem.201000841.

Naaz, S., Poddar, S., Bayen, S.P., Mondal, M.K., Roy, D., Mondal, S.K., Chowdhury, P., Saha, S.K., 2018. Tenfold enhancement of fluorescence quantum yield of water soluble silver nanoclusters for nano-molar level glucose sensing and precise determination of blood glucose level. Sens. Actuators B 255, 332–340. https://doi.org/10.1016/j.snb.2017.07.143.

Nair, L.V., Nazeer, S.S., Jayasree, R.S., Ajayaghosh, A., 2015. Fluorescence imaging assisted photodynamic therapy using photosensitizer-linked gold quantum clusters. ACS Nano 9 (6), 5825–5832. https://doi.org/10.1021/acsnano.5b00406.

Oh, E., Fatemi, F.K., Currie, M., Delehanty, J.B., Pons, T., Fragola, A., Lévêque-Fort, S., Goswami, R., Susumu, K., Huston, A.L., Medintz, I.L., 2013. PEGylated luminescent gold nanoclusters: synthesis, characterization, bioconjugation, and application to one- and two-photon cellular imaging. Part. Part. Syst. Char. 30 (5), 453–466. https://doi.org/10.1002/ppsc.201200140.

Patel, S.A., Richards, C.I., Hsiang, J.C., Dickson, R.M., 2008. Water-soluble Ag nanoclusters exhibit strong two-photon-induced fluorescence. J. Am. Chem. Soc. 130 (35), 11602–11603. https://doi.org/10.1021/ja804710r.

Pu, K.Y., Luo, Z., Li, K., Xie, J., Liu, B., 2011. Energy transfer between conjugated-oligoelectrolyte-substituted POSS and gold nanocluster for multicolor intracellular detection of mercury ion. J. Phys. Chem. C 115 (26), 13069–13075. https://doi.org/10.1021/jp203133t.

Qi, Y.X., Zhang, M., Zhu, A., Shi, G., 2015. Terbium(III)/gold nanocluster conjugates: the development of a novel ratiometric fluorescent probe for mercury(II) and a paper-based visual sensor. Analyst 140 (16), 5656–5661. https://doi.org/10.1039/c5an00802f.

Retnakumari, A., Setua, S., Menon, D., Ravindran, P., Muhammed, H., Pradeep, T., Nair, S., Koyakutty, M., 2010. Molecular-receptor-specific, non-toxic, near-infrared-emitting Au cluster-protein nanoconjugates for targeted cancer imaging. Nanotechnology 21 (5), 055103. https://doi.org/10.1088/0957-4484/21/5/055103.

Sakai, N., Ikeda, T., Teranishi, T., Tatsuma, T., 2011. Sensitization of TiO_2 with Pt, Pd, and Au clusters protected by mercapto-and dimercaptosuccinic acid. ChemPhysChem 12 (13), 2415–2418. https://doi.org/10.1002/cphc.201100223.

Sakai, N., Nakamura, S., Tatsuma, T., 2013. Photovoltaic properties of TiO_2 loaded with glutathione-protected silver clusters. Dalton Trans 42 (45), 16162–16165. https://doi.org/10.1039/c3dt51648b.

Sakai, N., Tatsuma, T., 2010. Photovoltaic properties of glutathione-protected gold clusters adsorbed on TiO_2 electrodes. Adv. Mater. 22 (29), 3185–3188. https://doi.org/10.1002/adma.200904317.

Schroeder, K.L., Goreham, R.V., Nann, T., 2019. Glucose sensor using redox active oligonucleotide-templated silver nanoclusters. Nanomaterials 9 (8). https://doi.org/10.3390/nano9081065.

Senthamizhan, A., Celebioglu, A., Uyar, T., 2015. Real-time selective visual monitoring of Hg^{2+} detection at ppt level: an approach to lighting electrospun nanofibers using gold nanoclusters. Sci. Rep. 5. https://doi.org/10.1038/srep10403.

Shahzad, N., Chen, F., He, L., Li, W., Wang, H., 2015. Silver-copper nanoalloys-an efficient sensitizer for metal-cluster-sensitized solar cells delivering stable current and high open circuit voltage. J. Power Sources 294, 609–619. https://doi.org/10.1016/j.jpowsour.2015.06.124.

Shang, L., Dong, S., 2008. Silver nanocluster-based fluorescent sensors for sensitive detection of Cu(II). J. Mater. Chem. 18, 4636–4640. https://doi.org/10.1039/b810409c.

Shang, L., Dong, S., 2009. Sensitive detection of cysteine based on fluorescent silver clusters. Biosens. Bioelectron. 24 (6), 1569–1573. https://doi.org/10.1016/j.bios.2008.08.006.

Shang, L., Stockmar, F., Azadfar, N., Nienhaus, G.U., 2013. Intracellular thermometry by using fluorescent gold nanoclusters. Angew. Chem. Int. Ed. 52 (42), 11154–11157. https://doi.org/10.1002/anie.201306366.

Sharma, J., Yeh, H.C., Yoo, H., Werner, J.H., Martinez, J.S., 2011. Silver nanocluster aptamers: in situ generation of intrinsically fluorescent recognition ligands for protein detection. Chem. Commun. 47 (8), 2294–2296. https://doi.org/10.1039/c0cc03711g.

Shen, D., Henry, M., Trouillet, V., Comby-Zerbino, C., Bertorelle, F., Sancey, L., Antoine, R., Coll, J.L., Josserand, V., Le Guével, X., 2017. Zwitterion functionalized gold nanoclusters for multimodal near infrared fluorescence and photoacoustic imaging. APL Materials 5 (5). https://doi.org/10.1063/1.4977203.

Shiang, Y.C., Huang, C.C., Chang, H.T., 2009. Gold nanodot-based luminescent sensor for the detection of hydrogen peroxide and glucose. Chem. Commun. 23, 3437–3439. https://doi.org/10.1039/b901916b.

Shiang, Y.C., Lin, C.A., Huang, C.C., Chang, H.T., 2011. Protein A-conjugated luminescent gold nanodots as a label-free assay for immunoglobulin G in plasma. Analyst 136 (6), 1177–1182. https://doi.org/10.1039/c0an00889c.

Su, X., Liu, J., 2017. pH-guided self-assembly of copper nanoclusters with aggregation-induced emission. ACS Appl. Mater. Interfaces 9 (4), 3902–3910. https://doi.org/10.1021/acsami.6b13914.

Sun, S.K., Dong, L.X., Cao, Y., Sun, H.R., Yan, X.P., 2013. Fabrication of multifunctional Gd_2O_3/Au hybrid nanoprobe via a one-step approach for near-infrared fluorescence and magnetic resonance multimodal imaging in vivo. Anal. Chem. 85 (17), 8436–8441. https://doi.org/10.1021/ac401879y.

Sun, P., Wang, Z., Sun, D., Bai, H., Zhu, Z., Bi, Y., Zhao, T., Xin, X., 2020. pH-guided self-assembly of silver nanoclusters with aggregation-induced emission for rewritable fluorescent platform and white light emitting diode application. J. Colloid Interface Sci. 567, 235–242. https://doi.org/10.1016/j.jcis.2020.02.016.

Triulzi, R.C., Micic, M., Giordani, S., Serry, M., Chiou, W.-A., Leblanc, R.M., 2006. Immunoasssay based on the antibody-conjugated PAMAM-dendrimer–gold quantum dot complex. Chem. Commun. 48, 5068–5070. https://doi.org/10.1039/b611278a.

Unnikrishnan, B., Wei, S.C., Chiu, W.J., Cang, J., Hsu, P.H., Huang, C.C., 2014. Nitrite ion-induced fluorescence quenching of luminescent BSA-Au_{25} nanoclusters: mechanism and application. Analyst 139 (9), 2221–2228. https://doi.org/10.1039/c3an02291a.

Vankayala, R., Kuo, C.L., Nuthalapati, K., Chiang, C.S., Hwang, K.C., 2015. Nucleus-targeting gold nanoclusters for simultaneous in vivo fluorescence imaging, gene delivery, and NIR-light activated photodynamic therapy. Adv. Funct. Mater. 25 (37), 5934–5945. https://doi.org/10.1002/adfm.201502650.

Wang, C., Lin, H., Xu, Z., Huang, Y., Humphrey, M.G., Zhang, C., 2016a. Tunable carbon-dot-based dual-emission fluorescent nanohybrids for ratiometric optical thermometry in living cells. ACS Appl. Mater. Interfaces 8 (10), 6621–6628. https://doi.org/10.1021/acsami.5b11317.

Wang, J., Zhang, G., Li, Q., Jiang, H., Liu, C., Amatore, C., Wang, X., 2013a. In vivo self-bio-imaging of tumors through in situ biosynthesized fluorescent gold nanoclusters. Sci. Rep. 3, 1157. https://doi.org/10.1038/srep01157.

Wang, Y., Chen, J.T., Yan, X.P., 2013b. Fabrication of transferrin functionalized gold nanoclusters/graphene oxide nanocomposite for turn-on near-infrared fluorescent bioimaging of cancer cells and small animals. Anal. Chem. 85 (4), 2529–2535. https://doi.org/10.1021/ac303747t.

Wang, Z., Chen, B., Zhu, M., Kershaw, S.V., Zhi, C., Zhong, H., Rogach, A.L., 2016d. Stretchable and thermally stable dual emission composite films of on-purpose

aggregated copper nanoclusters in carboxylated polyurethane for remote white light-emitting devices. ACS Appl. Mater. Interfaces 8 (49), 33993–33998. https://doi.org/10.1021/acsami.6b10828.

Wang, Y., Dai, C., Yan, X.-P., 2014b. Fabrication of folate bioconjugated near-infrared fluorescent silver nanoclusters for targeted in vitro and in vivo bioimaging. Chem. Commun. 50 (92), 14341–14344. https://doi.org/10.1039/C4CC06329E.

Wang, W., Kong, Y., Jiang, J., Xie, Q., Huang, Y., Li, G., Wu, D., Zheng, H., Gao, M., Xu, S., Pan, Y., Li, W., Ma, R., Wu, M.X., Li, X., Zuilhof, H., Cai, X., Li, R., 2020. Engineering the protein corona structure on gold nanoclusters enables red-shifted emissions in the second near-infrared window for gastrointestinal imaging. Angew. Chem. Int. Ed. 59 (50), 22431–22435. https://doi.org/10.1002/anie.202010089.

Wang, Z., Chen, B., Susha, A.S., Wang, W., Reckmeier, C.J., Chen, R., Zhong, H., Rogach, A.L., 2016b. All-copper nanocluster based down-conversion white light-emitting devices. Adv. Sci. 3 (11). https://doi.org/10.1002/advs.201600182.

Wang, Y., Chen, J., Irudayaraj, J., 2011. Nuclear targeting dynamics of gold nanoclusters for enhanced therapy of HER^{2+} breast cancer. ACS Nano 5 (12), 9718–9725. https://doi.org/10.1021/nn2032177.

Wu, M., Zhang, Y., Zhuo, N., Wu, M., Ye, Z., Zhang, X., 2020. DTPAA-Gd functionalized ultrasmall Au_{15} NCs nanohybrids for multimodal imaging. Int. J. Nanomed. 15, 227–238. https://doi.org/10.2147/IJN.S227169.

Wu, Y., Gao, Y., Du, J., 2019b. Bifunctional gold nanoclusters enable ratiometric fluorescence nanosensing of hydrogen peroxide and glucose. Talanta 197, 599–604. https://doi.org/10.1016/j.talanta.2019.01.087.

Wu, X., He, X., Wang, K., Xie, C., Zhou, B., Qing, Z., 2010. Ultrasmall near-infrared gold nanoclusters for tumor fluorescence imaging in vivo. Nanoscale 2 (10), 2244–2249. https://doi.org/10.1039/c0nr00359j.

Wu, X., Li, C., Liao, S., Li, L., Wang, T., Su, Z., Wang, C., Zhao, J., Sui, C., Lin, J., 2014. Silica-encapsulated Gd^{3+}-aggregated gold nanoclusters for in vitro and in vivo multimodal cancer imaging. Chem. Eur. J. 20 (29), 8876–8882. https://doi.org/10.1002/chem.201403202.

Wang, S., Meng, X., Das, A., Li, T., Song, Y., Cao, T., Zhu, X., Zhu, M., Jin, R., 2014a. A 200-fold quantum yield boost in the photoluminescence of silver-doped Ag_xAu_{25-x} nanoclusters: the 13 th silver atom matters. Angew. Chem. Int. Ed. 53 (9), 2376–2380. https://doi.org/10.1002/anie.201307480.

Wang, Z., Susha, A.S., Chen, B., Reckmeier, C., Tomanec, O., Zboril, R., Zhong, H., Rogach, A.L., 2016c. Poly(vinylpyrrolidone) supported copper nanoclusters: glutathione enhanced blue photoluminescence for application in phosphor converted light emitting devices. Nanoscale 8 (13), 7197–7202. https://doi.org/10.1039/c6nr00806b.

Wu, M., Li, Z., Yao, J., Shao, Z., Chen, X., 2019a. Pea protein/gold nanocluster/indocyanine green ternary hybrid for near-infrared fluorescence/computed tomography dual-modal imaging and synergistic photodynamic/photothermal therapy. ACS Biomater. Sci. Eng. 5 (9), 4799–4807. https://doi.org/10.1021/acsbiomaterials.9b00794.

Wu, Z., Liu, J., Gao, Y., Liu, H., Li, T., Zou, H., Wang, Z., Zhang, K., Wang, Y., Zhang, H., Yang, B., 2015. Assembly-induced enhancement of Cu nanoclusters luminescence with mechanochromic property. J. Am. Chem. Soc. 137 (40), 12906–12913. https://doi.org/10.1021/jacs.5b06550.

Xia, X., Long, Y., Wang, J., 2013. Glucose oxidase-functionalized fluorescent gold nanoclusters as probes for glucose. Anal. Chim. Acta 772, 81–86. https://doi.org/10.1016/j.aca.2013.02.025.

Xie, J., Zheng, Y., Ying, J.Y., 2010. Highly selective and ultrasensitive detection of Hg^{2+} based on fluorescence quenching of Au nanoclusters by Hg^{2+}-Au^{+} interactions. Chem. Commun. 46 (6), 961–963. https://doi.org/10.1039/b920748a.

Xu, H., Zhu, H., Sun, M., Yu, H., Li, H., Ma, F., Wang, S., 2015. Graphene oxide supported gold nanoclusters for the sensitive and selective detection of nitrite ions. Analyst 140 (5), 1678–1685. https://doi.org/10.1039/c4an02181a.

Xie, Z., Sun, P., Wang, Z., Li, H., Yu, L., Sun, D., Chen, M., Bi, Y., Xin, X., Hao, J., 2020. Metal–organic gels from silver nanoclusters with aggregation-induced emission and fluorescence-to-phosphorescence switching. Angew. Chem. Int. Ed. 59, 9922–9927. https://doi.org/10.1002/anie.201912201.

Yan, Z., Tian, C., Sun, X., Wu, Y., Li, D., Ye, B., 2018. Ratiometric detection of biothiols by using the DNA-templated silver nanoclusters-Hg^{2+} system. Anal. Methods 10 (7), 706–712. https://doi.org/10.1039/c7ay02564e.

Yang, L., Chen, J., Huang, T., Huang, L., Sun, Z., Jiang, Y., Yao, T., Wei, S., 2017. Red-emitting Au_7 nanoclusters with fluorescence sensitivity to Fe^{2+} ions. J. Mater. Chem. C 5 (18), 4448–4454. https://doi.org/10.1039/c7tc00724h.

Yang, X., Yang, L., Dou, Y., Zhu, S., 2013. Synthesis of highly fluorescent lysine-stabilized Au nanoclusters for sensitive and selective detection of Cu^{2+} ion. J. Mater. Chem. C 1 (41), 6748–6751. https://doi.org/10.1039/c3tc31398k.

Yeh, H.C., Sharma, J., Han, J.J., Martinez, J.S., Werner, J.H., 2010. A DNA-silver nanocluster probe that fluoresces upon hybridization. Nano Lett 10 (8), 3106–3110. https://doi.org/10.1021/nl101773c.

Yeh, H.C., Sharma, J., Shih, I.M., Vu, D.M., Martinez, J.S., Werner, J.H., 2012. A fluorescence light-up Ag nanocluster probe that discriminates single-nucleotide variants by emission color. J. Am. Chem. Soc. 134 (28), 11550–11558. https://doi.org/10.1021/ja3024737.

Yin, H.Q., Bi, F.L., Gan, F., 2015. Rapid synthesis of cyclic RGD conjugated gold nanoclusters for targeting and fluorescence imaging of melanoma A375 cells. Bioconjugate Chem 26 (2), 243–249. https://doi.org/10.1021/bc500505c.

Yu, P., Wen, X., Toh, Y.R., Huang, J., Tang, J., 2013b. Metallophilic bond-induced quenching of delayed fluorescence in Au_{25}@BSA nanoclusters. Part. Part. Syst. Char. 30 (5), 467–472. https://doi.org/10.1002/ppsc.201200111.

Yu, M., Zhu, Z., Wang, H., Li, L., Fu, F., Song, Y., Song, E., 2017. Antibiotics mediated facile one-pot synthesis of gold nanoclusters as fluorescent sensor for ferric ions. Biosens. Bioelectron. 91, 143–148. https://doi.org/10.1016/j.bios.2016.11.052.

Yu, Y., Geng, J., Ong, E.Y.X., Chellappan, V., Tan, Y.N., 2016. Bovine serum albumin protein-templated silver nanocluster (BSA-Ag_{13}): an effective singlet oxygen generator for photodynamic cancer therapy. Adv. Healthc. Mater. 5 (19), 2528–2535. https://doi.org/10.1002/adhm.201600312.

Yu, C., Li, G., Kumar, S., Kawasaki, H., Jin, R., 2013a. Stable $Au_{25}(SR)_{18}/TiO_2$ composite nanostructure with enhanced visible light photocatalytic activity. J. Phys. Chem. Lett. 4 (17), 2847–2852. https://doi.org/10.1021/jz401447w.

Yu, Z., Musnier, B., Wegner, K.D., Henry, M., Chovelon, B., Desroches-Castan, A., Fertin, A., Resch-Genger, U., Bailly, S., Coll, J.L., Usson, Y., Josserand, V., Le Guével, X., 2020. High-resolution shortwave infrared imaging of vascular disorders using gold nanoclusters. ACS Nano 14 (4), 4973–4981. https://doi.org/10.1021/acsnano.0c01174.

Yuan, Z., Peng, M., Shi, L., Du, Y, Cai, N, He, Y., Chang, H.-T., Yeung, E.S., 2013a. Disassembly mediated fluorescence recovery of gold nanodots for selective sulfide sensing. Nanoscale 5, 4683–4686. https://doi.org/10.1039/c2nr33202g.

Yuan, X., Tay, Y., Dou, X., Luo, Z., Leong, D.T., Xie, J., 2013b. Glutathione-protected silver nanoclusters as cysteine-selective fluorometric and colorimetric probe. Anal. Chem. 85 (3), 1913–1919. https://doi.org/10.1021/ac3033678.

Yuan, X., Yeow, T.J., Zhang, Q., Lee, J.Y., Xie, J., 2012. Highly luminescent Ag^+ nanoclusters for Hg^{2+} ion detection. Nanoscale 4 (6), 1968–1971. https://doi.org/10.1039/c2nr11999d.

Zhang, C., Li, C., Liu, Y., Zhang, J., Bao, C., Liang, S., Wang, Q., Yang, Y., Fu, H., Wang, K., Cui, D., 2015. Gold nanoclusters-based nanoprobes for simultaneous fluorescence imaging and targeted photodynamic therapy with superior penetration and retention behavior in tumors. Adv. Funct. Mater. 25 (8), 1314–1325. https://doi.org/10.1002/adfm.201403095.

Zhang, C., Zhou, Z., Qian, Q., Gao, G., Li, C., Feng, L., Wang, Q., Cui, D., 2013a. Glutathione-capped fluorescent gold nanoclusters for dual-modal fluorescence/X-ray computed tomography imaging. J. Mater Chem. B 1 (38), 5045–5053. https://doi.org/10.1039/c3tb20784f.

Zhang, L., Zhu, J., Guo, S., Li, T., Li, J., Wang, E., 2013b. Photoinduced electron transfer of DNA/Ag nanoclusters modulated by G-quadruplex/hemin complex for the construction of versatile biosensors. J. Am. Chem. Soc. 135 (7), 2403–2406. https://doi.org/10.1021/ja3089857.

Zhang, W., Lin, D., Wang, H., Li, J., Nienhaus, G.U., Su, Z., Wei, G., Shang, L., 2017. Supramolecular self-assembly bioinspired synthesis of luminescent gold nanocluster-embedded peptide nanofibers for temperature sensing and cellular imaging. Bioconjugate Chem 28 (9), 2224–2229. https://doi.org/10.1021/acs.bioconjchem.7b00312.

Zhang, L., Zhu, J., Zhou, Z., Guo, S., Li, J., Dong, S., Wang, E., 2013c. A new approach to light up DNA/Ag nanocluster-based beacons for bioanalysis. Chem. Sci. 4 (10), 4004–4010. https://doi.org/10.1039/c3sc51303c.

Zhao, C., Du, T., Rehman, F.u., Lai, L., Liu, X., Jiang, X., Li, X., Chen, Y., Zhang, H., Sun, Y., Luo, S., Jiang, H., Selke, M., Wang, X., 2016. Biosynthesized gold nanoclusters and iron complexes as scaffolds for multimodal cancer bioimaging. Small 12 (45), 6255–6265. https://doi.org/10.1002/smll.201602526.

Zheng, X.J., Liang, R.P., Li, Z.J., Zhang, L., Qiu, J.D., 2016. One-step, stabilizer-free and green synthesis of Cu nanoclusters as fluorescent probes for sensitive and selective detection of nitrite ions. Sens. Actuators B 230, 314–319. https://doi.org/10.1016/j.snb.2016.02.063.

Zhou, D.L., Huang, H., Wang, Y., 2017a. Sensitive and selective detection of nitrite ions with highly fluorescent glutathione-stabilized copper nanoclusters. Anal. Methods 9 (38), 5668–5673. https://doi.org/10.1039/c7ay02035j.

Zhou, T., Huang, Y., Li, W., Cai, Z., Luo, F., Yang, C.J., Chen, X., 2012. Facile synthesis of red-emitting lysozyme-stabilized Ag nanoclusters. Nanoscale 4 (17), 5312–5315. https://doi.org/10.1039/c2nr31449e.

Zhou, Z., Du, Y., Dong, S., 2011b. Double-strand DNA-templated formation of copper nanoparticles as fluorescent probe for label-free aptamer sensor. Anal. Chem. 83 (13), 5122–5127. https://doi.org/10.1021/ac200120g.

Zhou, Z., Du, Y., Dong, S., 2011a. DNA-Ag nanoclusters as fluorescence probe for turn-on aptamer sensor of small molecules. Biosens. Bioelectron. 28 (1), 33–37. https://doi.org/10.1016/j.bios.2011.06.028.

Zhu, J., Zhang, L., Teng, Y., Lou, B., Jia, X., Gu, X., Wang, E., 2015. G-quadruplex enhanced fluorescence of DNA-silver nanoclusters and their application in bioimaging. Nanoscale 7 (31), 13224–13229. https://doi.org/10.1039/c5nr03092g.

Zhou, S., Zhang, M., Yang, F., Wang, F., Wang, C., 2017b. Facile synthesis of water soluble fluorescent metal (Pt, Au, Ag and Cu) quantum clusters for the selective detection of Fe^{3+} ions as both fluorescent and colorimetric probes. J. Mater. Chem. C 2466–2473. https://doi.org/10.1039/C6TC05253C.

Zhu, S., Wang, X., Li, S., Liu, L., Li, L., 2020. Near-infrared-light-assisted in situ reduction of antimicrobial peptide-protected gold nanoclusters for stepwise killing of bacteria and cancer cells. ACS Appl. Mater. Interfaces 12 (9), 11063–11071. https://doi.org/10.1021/acsami.0c00310.

Zong, C., Wang, M., Li, B., Liu, X., Zhao, W., Zhang, Q., Liang, A., Yu, Y., 2017. Sensing of hydrogen peroxide and glucose in human serum: via quenching fluorescence of biomolecule-stabilized Au nanoclusters assisted by the fenton reaction. RSC Adv 7 (43), 26559–26565. https://doi.org/10.1039/c7ra01498h.

Zong, C., Zheng, L.R., He, W., Ren, X., Jiang, C., Lu, L., 2014. In situ formation of phosphorescent molecular gold(I) cluster in a macroporous polymer film to achieve colorimetric cyanide sensing. Anal. Chem. 86 (3), 1687–1692. https://doi.org/10.1021/ac403480q.

9

Recent trends in core–shell nanostructures–based SERS substrates

K.S. Anju[a], **K.K. Rajeev**[b,c] **and M.K. Jayaraj**[a,d]

[a]Cochin University of Science and Technology, Kochi, India. [b]Department of Instrumentation, Cochin University of Science and Technology, Kochi, India. [c]Centre of Excellence in Advanced Materials, Cochin University of Science and Technology, Kochi, India. [d]University of Calicut, Malappuram, India

9.1 Introduction

Nanomaterial research has progressed as a new realm due to its unique properties compared to the properties of bulk materials and their applications in different fields such as optics, biomedicine, electronics, and environmental science. The inherent human nature of thirst for knowledge, curiosity, and interest in the exploration of new materials has led to tremendous advancements in these fields. Technological advancements in characterization techniques such as scanning electron microscopy, transmission electron microscopy, and atomic force microscopy have helped researchers to explore new nanomaterials and probe into their properties and, moreover, to gain insight into the infinite possibilities where the fascinating materials are applicable.

Among the various applications of nanoparticles (NPs), surface-enhanced Raman spectroscopy (SERS) is a technique for detecting molecules, even at the single molecular level. It is a comparatively new yet fast-evolving technique, owing to its efficiency in molecular detection. This technique finds applications in various fields such as biosensing, forensics, and food adulterant detection.

9.2 Surface-enhanced Raman spectroscopy

An enhancement in Raman signals of pyridine molecules adsorbed on the roughened silver electrode was first observed by Fleischmann et al. in 1974 (Fleischmann et al., 1974). Their explanation for this phenomenon was the increase in the number of pyridine molecules

Nanomaterials for Sensing and Optoelectronic Applications. DOI: https://doi.org/10.1016/B978-0-12-824008-3.00014-X

adsorbed on the surface of the silver electrode due to the increased surface area of the silver electrode. Later, Van Duyne recognized that there is an enhancement in Raman signal in the order of 10^6 and it may not be attributed to the increased surface area but may be due to the increased Raman scattering cross-section. Jeanmaire et al. and Albrecht et al. proposed that Raman signal enhancement is due to the increase in the electric field near the adsorbed molecules, which arises from the localized surface plasmon resonance (LSPR) on the metal surface (Jeanmaire & Van Duyne, 1977).

To explain the 10^6-fold enhancement in intensity, two mechanisms are proposed in general.

- Electromagnetic enhancement mechanism
- Chemical enhancement mechanism

These two mechanisms are taken into account since, according to the classical theory of Raman scattering, the Raman scattering intensity is directly proportional to the square of the induced dipole moment, μ_{ind}. Induced dipole moment is a product of Raman polarizability, α, and the magnitude of the incident electromagnetic field, E. Due to the presence of plasmons on the surface of the metal, a LSPR (Petryayeva & Krull, 2011) arises, which enhances the local electromagnetic field and produces an enhancement of the order of 10^4. The chemical enhancement factor (EF) of 10^2 may be attributed to the metal-to-adsorbate charge-transfer resonances, which in turn induce a change in polarizability and cause an enhancement in the Raman signal (Hasna & Jayaraj, 2020).

9.2.1 Electromagnetic enhancement mechanism of SERS

When electromagnetic radiation falls on the metal surface, conduction electrons in metal get resonantly excited with the electromagnetic field as a driving force, exactly like a driven harmonic oscillatory system. The resonant frequency of oscillations (plasmons) ω_{max} is a function of the dielectric constant of the metal $\varepsilon_{\text{metal}}$ (ω) and the surrounding medium ε_{m} (ω). For metals like silver and gold, plasmon peaks are in the visible region and visible light can be used to excite these colloidal particles. This system can be resonantly excited by laser radiation with angular frequency ω_{inc} and amplitude E_0, which leads to charge separation in a metal nanoparticle (LSPR), and hence a local dipole is developed and the induced dipole moment is a function of the polarizability of the metallic NP α_{metal} and the strength of the incident field:

$$\mu_{ind} = \alpha_{metal} E_0 (\omega_{inc}) \tag{9.1}$$

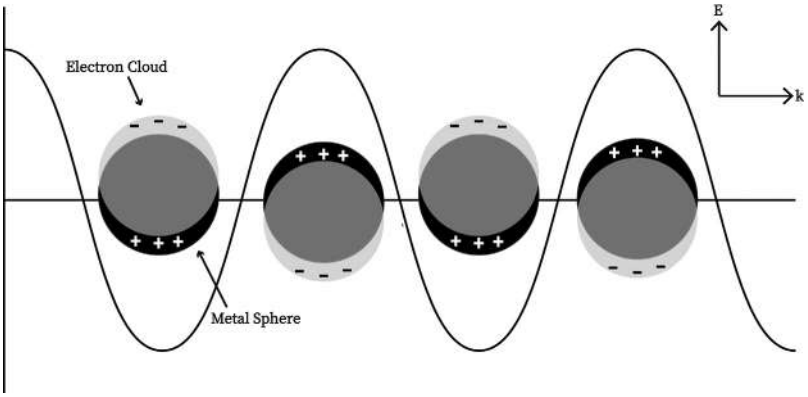

Figure 9.1. Localized surface plasmons on the surface of a metal nanoparticle.

This charge separation coupled with the incident field leads to an increased local field near the vicinity of the metal NP $E_{loc}(\omega_{inc})$, which can be felt by a molecule in the vicinity of the metal NP (Cialla et al., 2012). This phenomenon is shown in Fig. 9.1.

In 1908 Mie proposed that extinction cross-section (C_{ext}) for metal NPs depends on the real and imaginary parts of the complex dielectric function (Mie, 1908). For metal NPs with radius R dispersed in a material with dielectric constant ε_m extinction cross-section C_{ext} is:

$$C_{ext} = \frac{24\pi^2 R^3 \varepsilon_m^{3/2}}{\lambda} \frac{\varepsilon''}{(\varepsilon^1 + 2\varepsilon_m)^2 + \varepsilon''^2} \tag{9.2}$$

where ε' and ε'' represent the real and imaginary components of the complex dielectric function, respectively, and this equation indicates the dependence of plasmon resonance on the size of the NPs and the medium surrounding the NP.

The second term has a maximum value for

$$\varepsilon\prime = -2\varepsilon_m$$

which is the the surface plasmon resonance condition. In the optical absorption spectra of Au and Ag hydrosols this is observed as strong absorption bands and explains the strong colors observed in these colloids.

From the works of Nie et al. and Kneipp et al. on single-molecular SERS, it is evident that isolated single particles could not achieve high EFs (Kneipp et al., 1997; Nie & Emory, 1997). Regions of intense field enhancement are observed in the junction between particles due to the plasmonic coupling. This effect is known as hot spot formation and leads to even higher enhancement of Raman signal. This effect is known as hot spot enhancement. Intense field enhancement are also observed in particles of sharp edges and tips and this effect is known as lightning rod effect. as shown in Fig. 9.2.

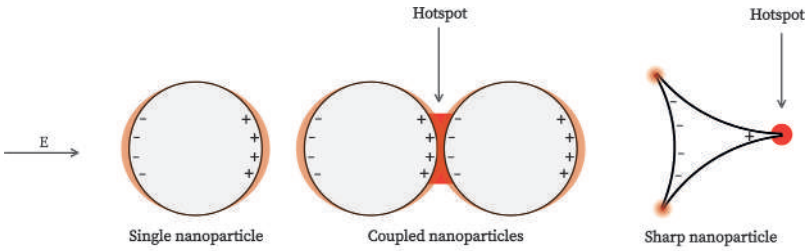

Figure 9.2. Electric field enhancement in the vicinity of (A) single metallic nanoparticles, (B) coupled metallic nanoparticles, and (C) sharp metallic nanoparticles.

9.2.2 Enhancement factor

Raman signal enhancement is qualitatively stated in terms of EF, which is the ratio of the intensity of the enhanced Raman signal to the normal Raman signal. Since the intensities of the Raman signal depend on the number of molecules giving the Raman signal, both intensities must be normalized by dividing the intensities by the number of molecules giving the Raman signal. An equation of the form of Eq. (9.3) is used normally to calculate EFs.

$$EF = \frac{I_{SERS}}{I_{RS}} \times \frac{N_{RS}}{N_{SERS}} \tag{9.3}$$

where I_{SERS} and I_{RS} are the intensities of enhanced Raman signal and normal Raman signal, respectively, and N_{RS} and N_{SERS} denote the number of molecules contributing to the Raman signal in SERS and non-SERS cases, respectively.

For calculating analytical EFs, mostly in the case of colloidal SERS substrates, Eq. (9.4) can be used.

$$EF = \frac{I_{SERS}}{I_{RS}} \times \frac{C_{RS}}{C_{SERS}} \tag{9.4}$$

Here, C_{RS} is the concentration of an analyte in bulk and C_{SERS} denotes the concentration of the analyte solution adsorbed onto the metal surface under given experimental conditions.

The SERS EF depends on the wavelength and polarizations of lasers used for excitation, SERS substrate, the intrinsic Raman cross-section of the analyte molecule, and the extent to which the analyte molecule can adsorb onto the surface of the metal (Le Ru and Etchegoin, 2009).

Single-molecular identification by using SERS has led to the increase in the popularity of this unique molecular identification technique. SERS finds wide applications in chemical and biological sensing. Researchers in this field are in search of suitable SERS substrates that can provide high EFs and enable the in vivo and in vitro detection of molecules, selective detection of molecules, the study of change in the properties of molecules in varying environments, etc.

The power of SERS has not been explored fully until now. New SERS substrates must be developed to exploit the advantages of SERS in sensing and detecting molecules even at low concentrations. Also, efforts must be made to fabricate SERS substrates with stability, reproducibility, and a high EF. Although significant improvements have been possible in the synthesis of complex and highly efficient plasmonic SERS NPs with controllable sizes and shapes, challenges in the preparation of stable, well-defined nanoassemblies with consistent hotspots exist, implying an opportunity for further research.

9.2.3 SERS substrates

SERS substrates are usually structures made of metals that can support surface plasmons. Metal-coated rough surfaces were used in the beginning (Fleischmann et al., 1974). The synthesis of metal NPs in different shapes and sizes enables one to control surface plasmon resonances. Arrays of metallic NPs supported on other planar surfaces are a recent development in fabricating SERS substrates. These arrays are made by using self-assembly methods or lithographic techniques.

9.3 SERS substrates: an overview

Since its discovery in 1977, SERS has invited the attention of researchers due to its high sensitivity and efficiency in molecular identification. Progress in the development of SERS substrates is tremendous considering the short time span over which it has evolved. Over the past few decades, researchers all over the world have tried to develop novel and effective methods for the development of SERS substrates owing to the huge applications of this technique. Some of those works are listed below.

9.3.1 Metal electrodes

The first reported work in SERS was in 1974 by Fleischmann et al., who observed enhanced Raman signals of pyridine molecules adsorbed on a roughened silver electrode. The main advantage of this method is the increased surface area. Recent advancements have been in depositing the roughened metal layer into indium tin oxide (Zhu et al., 2011), anodic aluminum oxide (Chen et al., 2015)(), etc. Oxidized forms of metal electrodes have also been used as SERS substrates (Taranenko et al., 1996).

9.3.2 Ordered metallic nanostructures

Ordered metallic nanostructures that can give high enhancement are also used as SERS substrates. They are made directly on

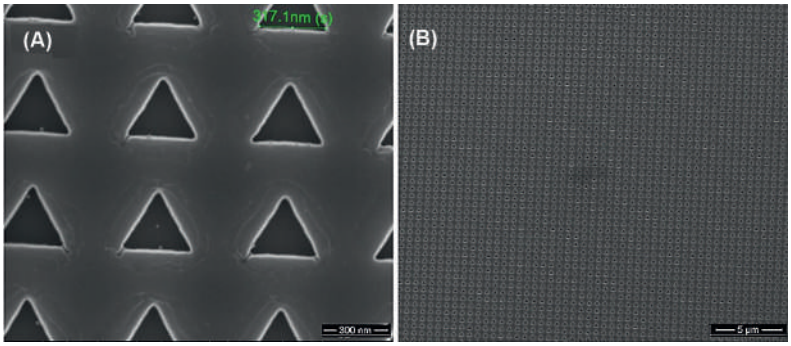

Figure 9.3. (A) Sample FESEM images of silicon master with triangular pits with an average edge length of 300 nm and (B) large area view.

a solid platform. The methods for developing such substrates include electron beam lithography, electron migration, electrochemical metal growth, and nanosphere lithography (; Petti et al., 2016; Amin et al., 2021; Zhao et al., 2017). In electron beam lithography nanostructured features are obtained on solid surfaces by selective area etching using the electron beam, as shown in Fig. 9.3. A layer of metallic film is coated on these solid platforms using sputtering techniques. Following this technique, Hasna et al. fabricated arrays of nanotriangular pillars on silicon (Hasna et al., 2016). These patterns of arrays of nanotriangular pillars on silicon were replicated on poly(methyl methacrylate) (PMMA) by means of the nanoimprinting technique. A silver film is made on this pattern using the thermal evaporation technique. This technique enables the fast and inexpensive production of highly uniform and reproducible SERS substrate on a large scale. In nanosphere lithography metallic particles are deposited on the surface of nanospheres and the nanospheres are removed by dissolving in suitable solvents, leading to ordered nanostructures (Haynes & Van Duyne, 2002).

9.3.3 Colloidal metal nanoparticles

NPs of metals such as gold, silver, copper, and palladium have been widely used in their colloidal form as SERS substrates and they provide high sensitivity. The development of new physical and chemical synthesis routes has enabled good control over particle size distribution, shape, and particle arrangement, which control the SERS efficiency of substrates (Schlücker, 2014).

9.4 Core–shell nanostructures

Core–shell nanostructures are mainly composed of a material that is usually referred to as the core, which has a thin or thick coating of another material, referred to as the shell, as shown in Fig. 9.4.

Core–shell nanostructures have invited great interest recently due to their high tunability and optical properties. Coating, if chosen properly, provides good stability for these core–shell structures. Proper binding should be ensured between the core and the shell. For that, some surface functionalization is used in general, depending on the chemical properties of the core and shell. The tunability of substrates is achieved by varying parameters such as core radius, shell thickness, material, surface morphology, and suitable surface modification to fit into specific applications (Chaudhuri & Paria, 2012). Various morphologies of core-shell anoparticles as shown in Fig. 9.5

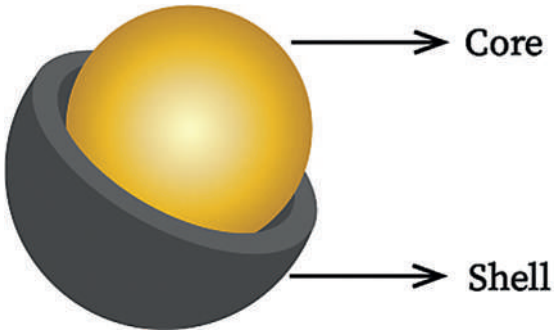

Figure 9.4. Core–shell nanoparticle general morphology.

9.4.1 Bimetallic core–shell nanostructures

In bimetallic core–shell nanostructures the core and shell are fabricated using metals, which enable high SERS activity by tuning the size and shape of the structure. Bimetallic core–shell nanostructures play a vital role in the category of core–shell nanostructures–based SERS substrates owing to the fact that both the core and shell are plasmonic nanostructures and this leads to very high EFs. Extensive works have been done on bimetallic core–shell nanostructures, especially using silver and gold. The reason for the popularity of bimetallic core–shell nanostructures is that the surface plasmon resonance of both the core and shell can be easily tuned to match specific applications since both core and shell exhibit plasmonic properties. The SPR of the bimetallic nanostructures varies to a great extent from that of its single counterparts. Chemical synthesis routes are preferred for the fabrication of core–shell nanostructures in general. Core–shell nanostructures of gold and silver are used mainly. Other noble metals like Cu, Al, and Pt are also used for fabrication depending on the application involved. The fabricated substrates can be used for environmental monitoring, food adulterant detection, and immunoassay analysis.

The optimization of core radius and shell thickness plays a major role in the EF. In a work by Khlebtsov et al. 1,4-aminothiophenol (4-ATP) molecules were embedded between Au core and Ag shells of thickness 1 to 25 nm and their detection was studied using SERS. Further, the substrates were used to demonstrate the effective detection of thiram fungicide in solutions with concentrations as low as 10^{-9} M (Khlebtsov et al., 2016)

In a work by Khurana et al. Au shell was coated over an Ag shell with varying thickness to fabricate Ag@Au bimetallic nanocomposite based SERS substrate. Fig. 9.6 demonstrates the variation in surface plasmon resonance peak upon adding an increased amount of gold NPs. This

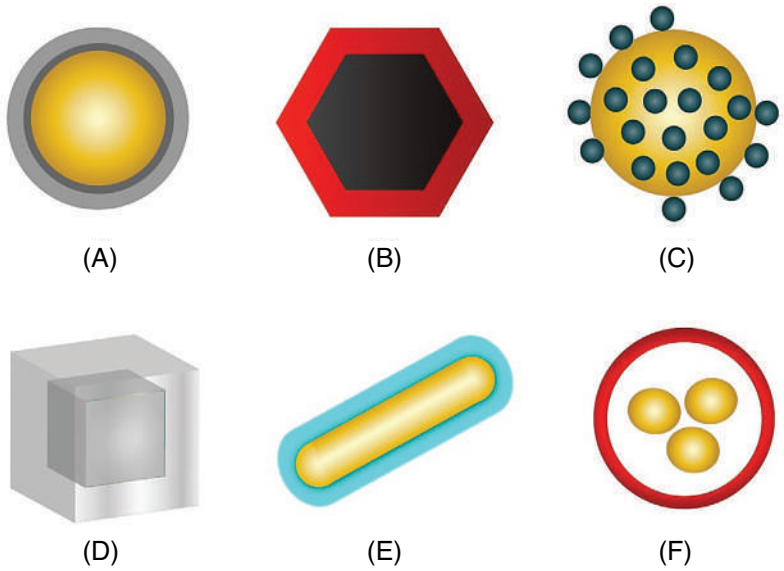

Figure 9.5. Various core–shell nanoparticle morphologies: (A) spherical core–shell nanoparticles, (B) hexagonal core–shell nanoparticles, (C) core decorated by small nanoparticles, (D) cubical core–shell nanoparticles, (E) cylindrical core–shell nanoparticles, and (F) movable core nanoparticles within the hollow shell material.

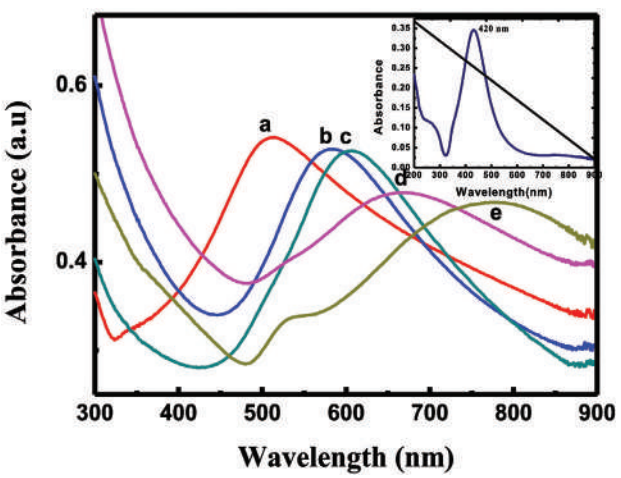

Figure 9.6. UV-Vis spectra of synthesized Ag@Au nanocomposite having an Au shell thickness of (A) 5, (B) 8, (C) 13, (D) 17, and (E) 21 nm; inset shows the spectrum of Ag NPs Reprinted with permission from (Khurana et al., 2016) Copyright 2015 Elsevier.

indicates a redshift in surface plasmon resonance wavelength on increasing the shell thickness. Correspondingly, the enhancement in the Raman signal of 10^{-4} M crystal violet (CV) molecule is found to be varying, as shown in Fig. 9.7. The shell thickness is optimized to be 30 nm for the core and 8 nm for the shell to get a maximum enhancement of 10^{13} in detecting CV dye (Khurana et al., 2016). A SERS substrate based on AuNPs modified with 4-nitrothiophenol (4-NTP) and coated with Ag shell of controlled thickness at 6.6 nm was developed by Wang et al. to detect staphylococcal enterotoxin B (SEB) on a microplate. The efficiency of the developed SERS substrate was used to analyze SEB-spiked milk samples. The SERS-based immunosensor had a limit of detection of 1.3 pg mL^{-1} (Wang et al., 2016)

Bimetallic structures of diverse morphology have also been investigated. The morphology plays a significant role in the enhancement of the Raman signal due to the lightning rod effect. The amplified field enhancement on the corners and tips of NPs enables the detection of ultralow concentration. Joseph et al. fabricated cubic hollow nanostructures of AuAg@Ag SERS substrates following simple chemical methods. First, the AuAg hollow cubic nanostructures

were synthesized as the core, and an Ag shell was arranged from $AgNO_3$ in the presence of ascorbic acid under an alkaline environment. The feed ratio of the Ag ion is increased to get increased shell thickness and the nanostructures are named AuAg@Ag2 and AuAg@Ag5, respectively, for feed concentrations of (Au:Ag):Ag of (5:1):1 and (5:1):4. The increase in Ag ion concentration leads to a blueshift in the LSPR compared to that of AuAg NPs, as shown in Fig. 9.8A. For AuAg alloy, the plasmon peak is observed to be at 785 nm and for AuAg@Ag2 and AuAg@Ag5 samples, the same is observed to be at 666 nm and 558 nm, respectively, which shows the tunability of plasmon frequency by changing the shell thickness. Transmission electron microscopy (TEM) images of these samples (Fig. 9.8B–D) reveal the thin Ag coating in the AuAg@Ag2 sample and a thick Ag coating in the AuAg@Ag5 sample. The result of the SERS performance evaluation of the AuAg, AuAg@Ag2, and AuAg@Ag5 samples (Fig. 9.9) reveals that both AuAg@Ag2 and AuAg@Ag5 show enhanced SERS performance compared to the AuAg sample. The study indicates that the SERS efficiency increases due to the presence of an Ag shell on AuAg nanostructure and further increases with an increase in shell thickness. This increase in the SERS performance of AuAg@Ag2 and AuAg@Ag5 over the AuAg nanostructure may be attributed to the shift in plasmon resonance from the NIR to the visible range. Further, an increase in the intensity in SERS performance for AuAg@Ag5 compared to AuAg@Ag2 can be attributed to the favorable hotspot formation by Ag NPs on the AuAg nanostructure. 4-Mercaptothiophenol (4-MPh) was used as the probe molecule to conduct a concentration-dependent SERS analysis and the detection limit was found to be of the order of 10^{-18} M (Joseph et al., 2019).

Khlebtsov et al. reported a synthesis method for the preparation of Au@Ag core–shell cuboids and dumbbells and further studied their SERS efficiency in detecting 1,4-aminothiophenol. The SERS EF of the colloidal dumbbells was determined to be of the order of 10^6, which is more than that of cuboids (Khlebtsov et al., 2015).

Bimetallic core–shell nanostructures of copper or platinum coupled with gold or silver NPs are also used as SERS substrates widely. Efficient SERS substrates using water-dispersed Cu@Ag core–shell nanoparticles (NPs) with a 15-nm-diameter Cu core and a 5-nm-thick Ag shell have been synthesized by Jin et al. for detecting CV with an enhancement of 1.0×10^4 by one-step chemical reduction (Jin et al., 2016).

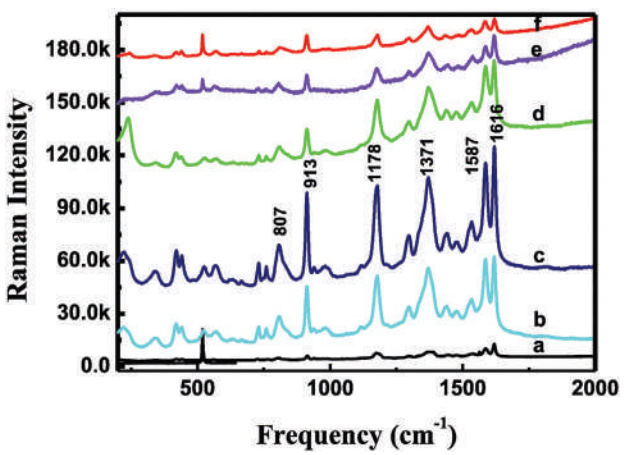

Figure 9.7. SERS spectra of (A) CV (10^{-4} M) molecule and CV (10^{-4} M) molecule using Ag@Au nanocomposites with increased Au shell thicknesses of (B) 5, (C) 8, (D) 13, (E) 17, and (F) 21 nm Reprinted with permission from (Khurana et al., 2016). Copyright 2015 Elsevier.

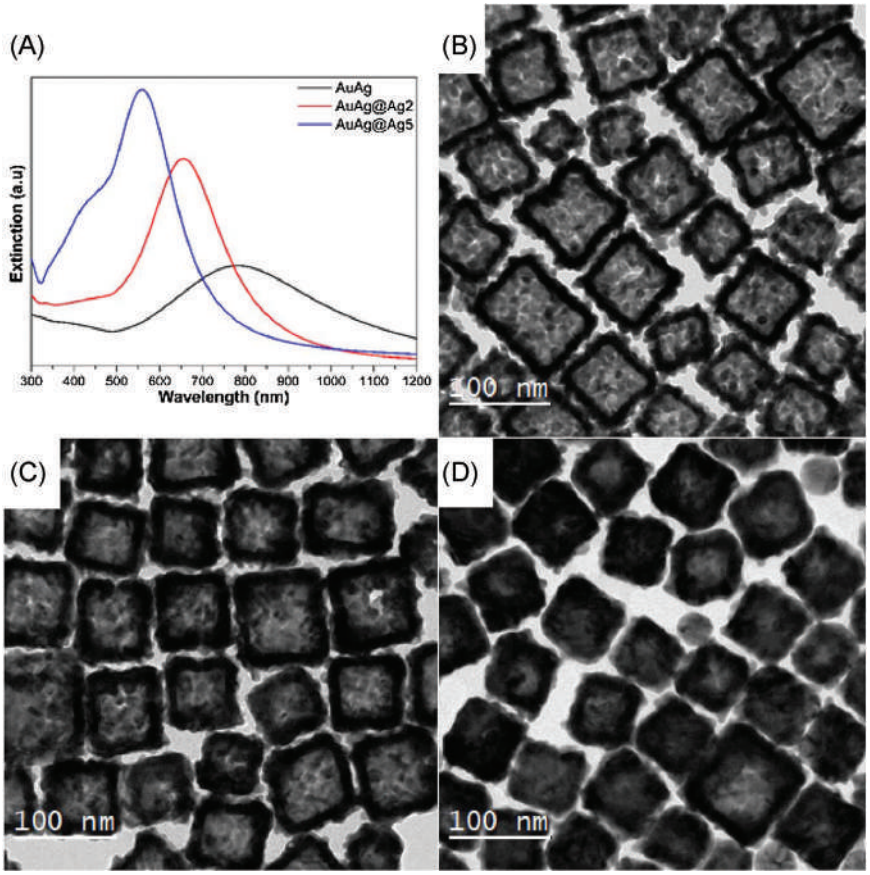

Figure 9.8. (A) UV-Vis-NIR extinction spectra of AuAg core and AuAg@Ag core@shell cubic nanostructures and their corresponding TEM images: (B) AuAg, (C) AuAg@Ag2, and (D) AuAg@Ag5. Reprinted with permission from (Joseph et al., 2019) Copyright 2018 Elsevier

Sharma et al. reported their work on the SERS activity of platinum-coated gold nanorods with tunable shell thickness. The developed SERS substrates were used for the detection of methylene blue dye with an enhancement of 10^4 (Sharma et al., 2016).

Metal core–shell NPs are widely used as chemical sensors. In a work by Song et al. Au@Ag core-shell NPs were synthesized by using the chemical method for the detection of arsenic pollution in water with a detection limit of 0.1 ppb. CV was used as a probe molecule to test the SERS activity (Song et al., 2016). Luo et al. fabricated silver-coated gold bimetallic NPs–based SERS substrates for the detection of triphenylmethane drugs in fish muscle (Luo et al., 2014).

Bimetallic nanostructures have the disadvantages of low stability and low reproducibility, and a new type of hybrid nanostructures is being synthesized.

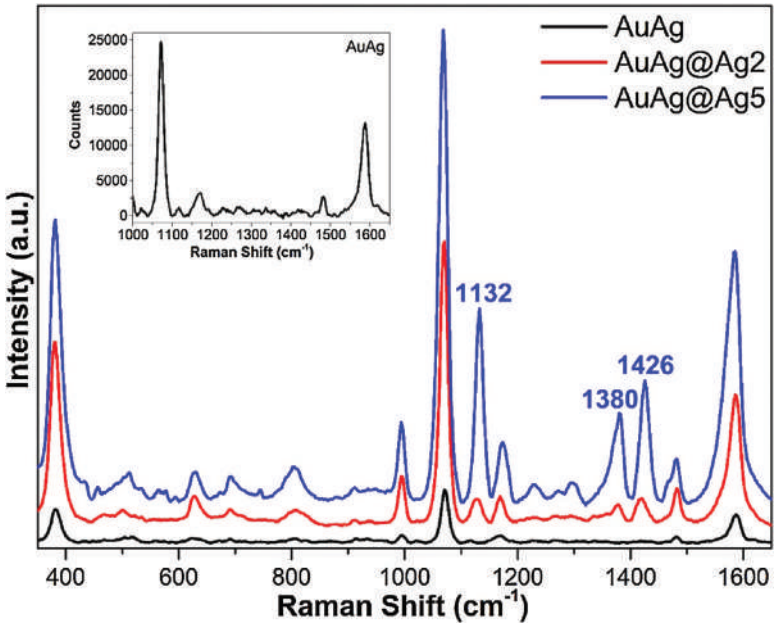

Figure 9.9. Characteristic SERS spectra of 4-ATP on AuAg core and AuAg@Ag core@shell cubic nanostructures. Inset is the enlarged SERS spectrum of AuAg. Reprinted with permission from (Joseph et al., 2019) Copyright 2018 Elsevier.

9.4.2 Dielectric–metal core–shell nanostructures

Dielectric–metal core–shell nanostructures are widely used nowadays as SERS substrates, either to provide high stability to the nanostructure or to provide environmental modification of the NP, thereby increasing the enhancement. The highly tunable properties of dielectric–metal core–shell NPs make them a suitable candidate as a SERS substrate.

Li et al. reported an efficient way to selectively detect rhodamine 6G from water by the surface modification of silica silver core–shell nanostructures and the detection limit was found to be 10^{-14} M (Li et al., 2017).

Higher-order enhancements can be obtained by properly tuning the dimensions of core–shell structures. For example, the authors of this chapter has fabricated silica silver core–shell nanostructures following a simple chemical route (Anju et al., 2019). Firstly, the core radius is increased and the shell thickness is fixed at constant to study the effect of varying core radius on the SERS performance. The core radius is varied from 37 nm to 126 nm. For a very small core radius, a complete shell of silver NPs is formed. But as the core radius increases, the Ag NPs get distributed apart, leaving the possibility for the formation of a hotspot, as shown in Fig. 9.10. This increase in hotspots is reflected in the SERS performance, as shown in Fig. 9.11. The limit of detection in the optimized case was found to be 10^{-18} M.

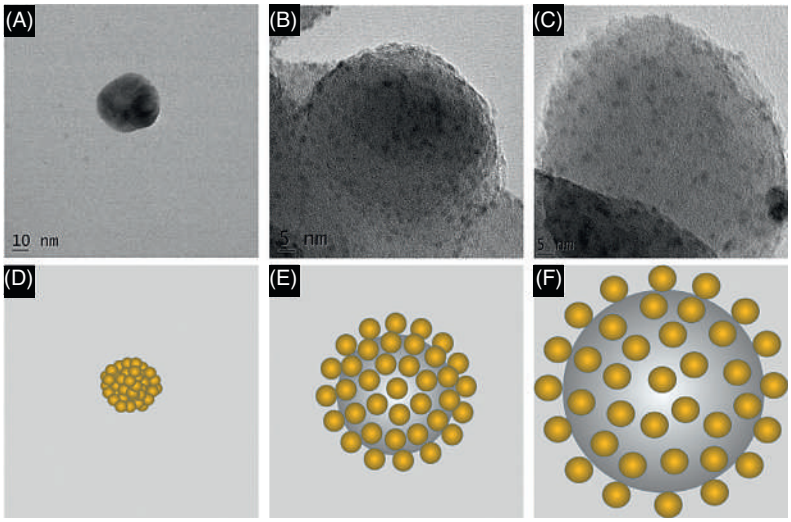

Figure 9.10. TEM images of Ag–SiO_2 nanospheres prepared using silica spheres with varying sizes of (A) 37 nm, (B) 61 nm, and (C) 89 nm with a fixed $AgNO_3$ concentration (1 mM). (D–F) Schematic representation of the possible distribution of silica nanospheres on silver nanoparticles with increasing silica size. Reprinted with permission from (Anju et al., 2019) Copyright (2019) Elsevier.

The same effect is observed while increasing the shell thickness also (Anju et al., 2019). Shell thickness is increased by increasing the concentration of the silver precursor ($AgNO_3$) in the order of 1 mM, 5 mM, and 10 mM. As the shell thickness increases, the SERS efficiency is found to be decreasing, as shown in Fig. 9.12

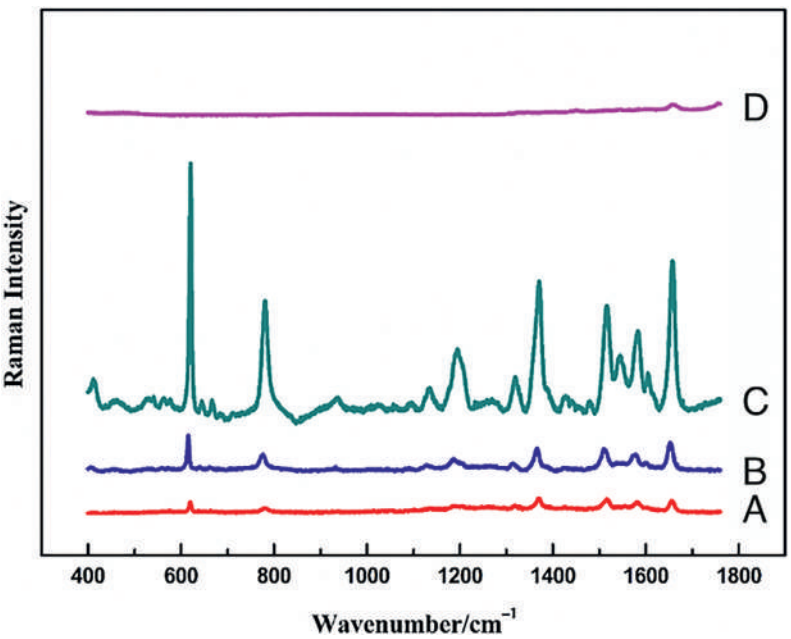

Figure 9.11. Comparison of the SERS spectra of 10^{-14} M solution of rhodamine 6G on Ag–SiO_2 substrates with varying silica sizes of (A) 37 nm, (B) 61 nm, (C) 89 nm, and (D)126 nm and a fixed $AgNO_3$ concentration Reprinted with permission from (Anju et al., 2019) Copyright 2019 Elsevier

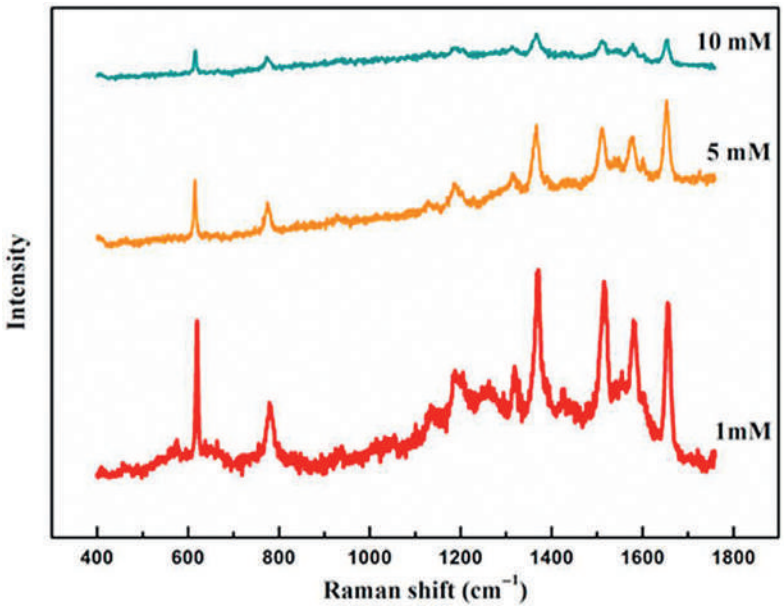

Figure 9.12. SERS of rhodamine 6G measured using prepared Ag–SiO_2 colloidal substrates with varying shell thicknesses prepared using 1 mM, 5 mM, and 10 mM of $AgNO_3$ Reprinted with permission from (Anju et al., 2019) Copyright 2019 Elsevier.

9.4.3 Polymer–metal core–shell nanostructures

Polymer–metal NPs are usually fabricated by arranging metal NPs on polymers such as polystyrene (PS) beads and polyaniline (PANI). The main advantage of PS is that it is commonly available and very economical compared to bimetallic substrates. The PS beads are readily available in highly monodisperse spherical form and these beads are stable, which makes it easier for the further attachment of metallic shell. Further, the self-assembling property of these spheres ensures the formation of uniform and reproducible SERS substrates. This property was used by Yamaguchi et al. for developing AuNPs-decorated PS beads–based SERS substrate on a lab-on-a-chip scenario. The aggregation of AuNPs-decorated PS beads was controlled by an AC electric field. The AuNPs-decorated PS beads were prepared by varying the coverage of Au NPs on the PS beads for optimization as SERS activity depends on the coverage. Advanced technologies such as integrated medical machines can be developed using this method (Yamaguchi et al., 2019).

9.4.4 Magnetic–metal core–shell nanostructures

In magnetic–metal core–shell nanostructures, either the core or the shell is fabricated using magnetic NPs. Plasmonic nanostructures are incorporated either as the core or as the shell to invoke surface

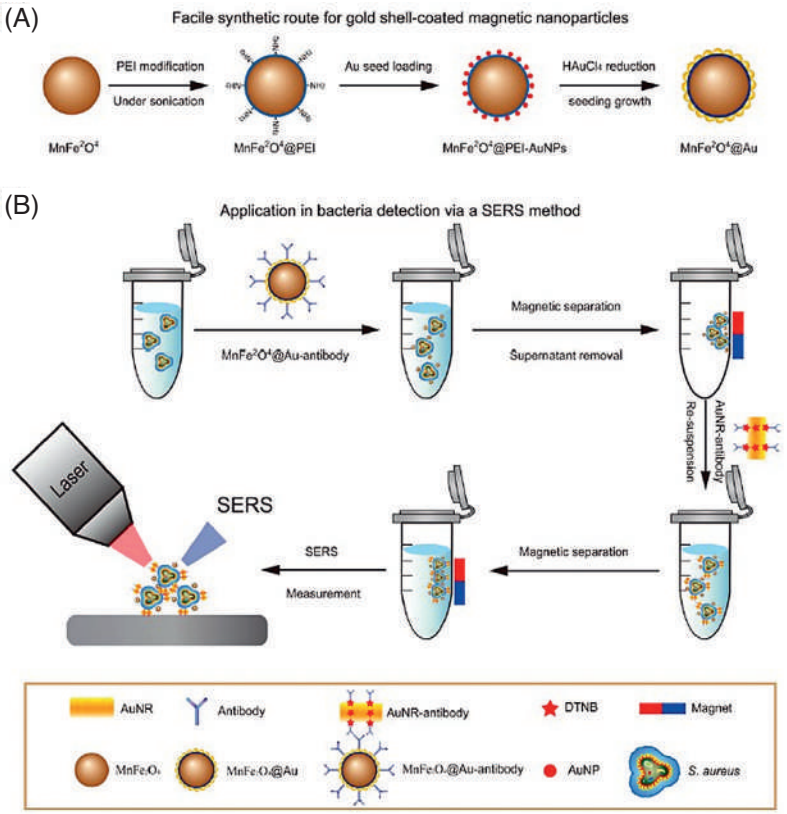

Figure 9.13. (A) Synthetic route for gold shell–coated magnetic nanoparticles and (B) schematic illustration of the operating procedures for bacteria detection via a SERS method. Reprinted with permission from (Wang et al., 2016a) Copyright 2016 American Chemical Society

plasmon resonance. The main aspect of involving magnetic NPs is to enable SERS detection along with magnetic separation. As an example, Au-coated $MnFe_2O_4$ magnetic NPs (AuMNPs) have been used as the SERS substrate by Wang et al. to detect p-aminothiophenol (PATP) with a detection limit of 10^{-9} M. The magnetic core is found to be of high magnetic responsivity and it enables the magnetic separation of *Staphylococcus aureus* as shown in Fig. 9.13. Also, the presence of magnetic NPs enables the formation of a sandwich-like structure for high hotspot formation. Further, the synthesized AuMNPs were conjugated with *S. aureus* antibody for bacteria detection with a detection limit of 10 cells mL^{-1} (Wang et al., 2016a).

The magnetic–metal core–shell NPs find wide application in biological detection. Lin et al. developed a rapid and simple method to detect carcinoembryonic antigen (CEA) using antibody-modified Au and γ-Fe_2O_3@Au NPs (Lin et al., 2016).

9.5 Core–shell nanostructures for biological applications

SERS is a versatile technique that can provide molecular vibrational information, which leads to the detection of molecules at very low concentrations. The negligible interference from the Raman signal of water molecules makes this technique highly suitable for use in biological systems. SERS is widely used for the analysis of biological molecules and for bioimaging, disease diagnosis, and cancer cell detection. The basic application of SERS in bioscenarios comes from the detection of molecules in living cells. Colloidal core–shell nanostructures find extensive possibilities in biological application because of their excellent properties. The main advantage of colloidal core–shell NPs is that they can be used in the native environment of biosamples without any interference in the form of Raman signals from water molecules. Another prospect is the possibility of the modification of the surface of NPs for specific applications. For example, hydrogen peroxide is generated in living organisms as a normal product of oxidative mechanisms. Nevertheless, severe human diseases are related to the dysregulation of hydrogen peroxide. AuAg alloy NPs possess high chemical stability, excellent plasmonic property, and low cytotoxicity, and coating with porous SiO_2 makes them more stable. The surface is further modified using 4-mercaptophenylboronic acid (MPBA) and an internal standard Raman molecule of 4-mercaptophenylacetylene (MPAE). A bridging molecule (dopamine) is then introduced, followed by the addition of 3-(4-(phenylethynyl)benzylthio) propanoic acid (PEB) as a Raman signaling molecule, as shown in Fig. 9.14. In the presence of H_2O_2 the Raman peak intensity of the peak at 2214 cm^{-1} of PEB is decreased due to the chemical modification in the structure compared to the intensity at normal circumstances. But the peak of MPAE at 1986 cm^{-1} is independent of the presence or absence of H_2O_2. By comparing the intensity of both these peaks, a quantitative analysis of the amount of H_2O_2 can be realized. The developed nanosensor is used successfully for the detection of H_2O_2 both exogenously and endogenously in living cells (Si et al., 2019).

SERS substrates are widely used as pH sensors owing to the structural change associated with molecules changing the pH of the environment. This result may be used for the detection and Raman imaging of cancer tissues since the pH value of cancerous tissue is lower than that of normal cells. PANI is a polymer is present as emeraldine salt in an acidic environment while it is converted to an emeraldine base in an alkaline environment. Upon increasing the pH, the peak at 1164 cm^{-1} shows a decayed intensity. This property is exploited by fabricating a

Table 9.1 Major applications of core–shell SERS substrates in the biological scenario.

Sl. No.	SERS substrate	Application	Reference
1	Double-strand DNA functionalized Au@Ag NPs	17β-estradiol	Pu et al. (2019)
2	Nanogapped Au (core)@AuAg (shell)	Ochratoxin A	Shao et al. (2018)
3	Au–SiO_2@Ag wire	Thiocyanate in urine and human serum	Ankudze et al. (2019)
4.	Spherical gold satellites on the surface of Au@Ag@SiO_2	Ultrasensitive SERS immunoassay of α-fetoprotein	Yang et al. (2019))
5	Magnetic Ni@C nanospheres	Hypersensitive C–reactive protein detection	Wang et al. (2018)
6	Gold nanostar@Raman reporter@nanoshell structures	Exosomes	Tian et al. (2018)
7	AuNS@Ag@SiO_2	α-Fetoprotein	Zhao et al. (2019)
8	Au@Ag core–shell nanocuboid	Detection of protein single-point mutations	Tu et al. (2018)
9	Ag/ZnO/Au	DNA detection	Pal et al. (2019))
10	AgNPs@RGO	DNA detection	Han et al. (2018)
11	Ag@Au core–shell porous nanocages	SERS immunoassay	Huang et al. (2019)
12	rGO@CD@Au	Trace detection for doxorubicin	Wei et al. (2019)
13	Aptamer-conjugated Au nanocage/SiO_2 core—shell bifunctional nanoprobes	Cellular SERS imaging	Wen et al. (2019)
14	SiO_2@Ag immune probes	SERS-based multiplex immunoassay of tumor markers	Wang et al. (2018)
15	Vertical flow assays based on core–shell SERS nanotags	Multiplex prostate cancer biomarker detection	Chen et al. (2019)
16	Enzyme-induced Au@Ag core–shell nanostructure	Immunoassay of cancer biomarkers	Yang et al. (2017)
17	Monodisperse Au@Ag core–shell nanoprobes	Raman imaging of living cancer cells	Chang et al. (2019)
18	Au@Bi_2Se_3	Synergetic therapy by SERS-traceable antagomiR delivery and photothermal treatment	Mohammadniaei et al. (2018)
19	Polypyrrole/iron oxide core/gold shell	Multimodal imaging and photothermal cancer therapy	Han et al. (2017)
20	Fe_3O_4@Cu_2O	Imaging-guided NIR photothermal therapy	Wang et al. (2018)

No Permission Required

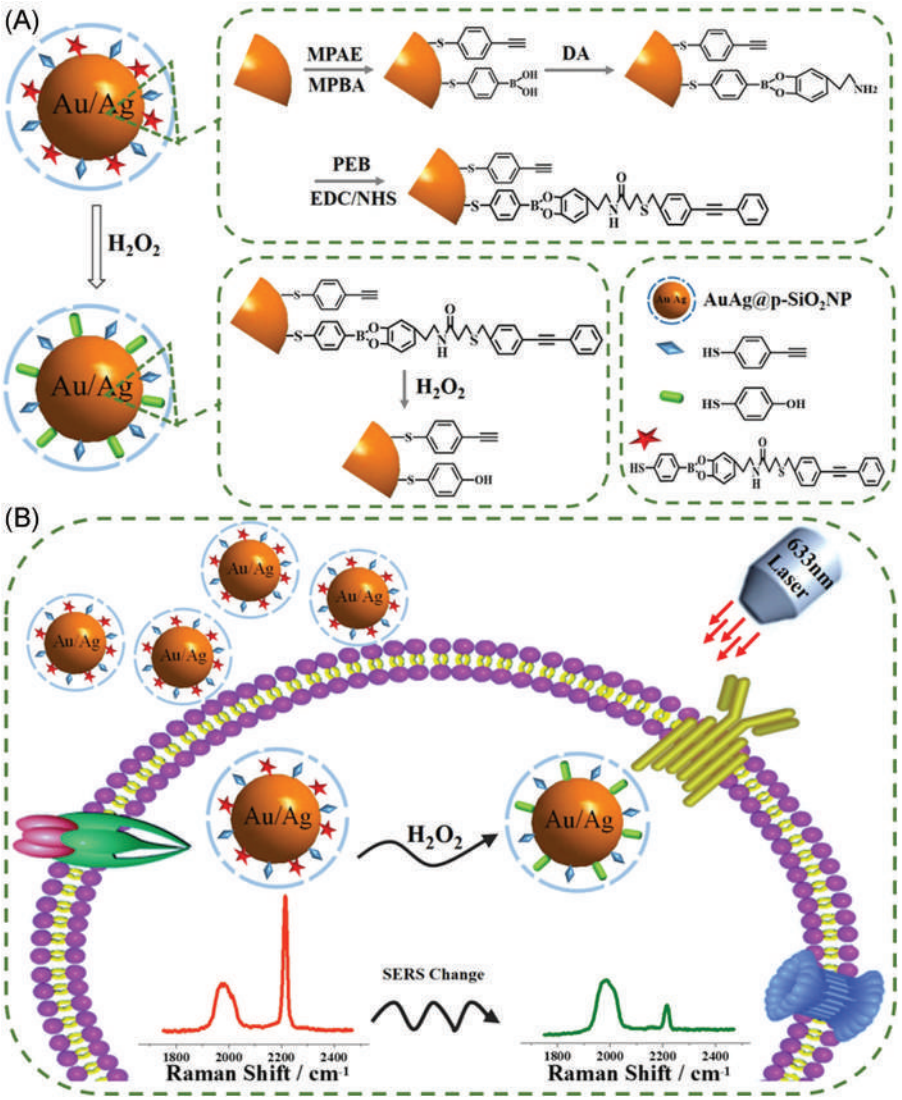

Figure 9.14. (A) Preparation mechanism of an AuAg@p-SiO_2NPs-based nanosensor. (B) Detection of H_2O_2 in living cells. Reprinted with permission from (Si et al., 2019) Copyright 2019 Elsevier.

core–shell nanostructure with PANI as the core and gold NPs as the shell (PANI@AuNPs). These NPs were introduced into HeLa cancer cells for Raman imaging.

Numerous applications of core–shell SERS substrates in biological scenarios are summarized in Table 9.1.

Summary

This chapter offers a general idea about the basic theory and advances in exploration in the field of development of SERS substrates based on core–shell nanostructures. Development strategies adopted for formulating SERS substrates based on some general architectures such as bimetallic, dielectric–metal, polymer–metal, and magnetic–metal are also discussed. It has also been shown that the morphology and size of both the core and shell play an important role in tuning the SERS efficiency of core–shell NP-based SERS substrates. The ways in which research is being broadened into biological scenarios are also emphasized in detail. With these developments, a wide range of quantitative and qualitative applications are enabled for SERS in the biomedical field for the evaluation and trace detection of molecules.

References

Amin, M.U., Zhang, L., Hao, R., Zhang, D., You, H., Fang, J., 2021. Electrochemical growth of dendritic silver nanostructures as facile SERS substrates. CrystEngComm 23 (3), 694–699. https://doi.org/10.1039/D0CE01258K.

Anju, K.S., Gayathri, R., Subha, P.P., Kumar, K.R., Jayaraj, M.K., 2019. Optimally distributed Ag over SiO_2 nanoparticles as colloidal SERS substrate. Microchem. J. 147, 349–355. https://doi.org/10.1016/j.microc.2019.03.027.

Ankudze, B., Philip, A., Pakkanen, T.T., 2019. Ultrasensitive and recyclable superstructure of $AuSiO_2$@Ag wire for surface-enhanced Raman scattering detection of thiocyanate in urine and human serum. Anal. Chim. Acta 1049, 179–187. https://doi.org/10.1016/j.aca.2018.10.040.

Chang, J., Zhang, A., Huang, Z., Chen, Y., Zhang, Q., Cui, D., 2019. Monodisperse au@ag core-shell nanoprobes with ultrasensitive SERS-activity for rapid identification and Raman imaging of living cancer cells. Talanta 198, 45–54. https://doi.org/10.1016/j.talanta.2019.01.085.

Chaudhuri, R.G., Paria, S., 2012. Core/shell nanoparticles: classes, properties, synthesis mechanisms, characterization, and applications. Chem. Rev. 112 (4), 2373–2433. https://doi.org/10.1021/cr100449n.

Chen, J, Feng, S, Gao, F, Grant, E, Xu, J, Wang, S, Huang, Q, Lu, X, 2015. Fabrication of SERS-active substrates using silver nanofilm-coated porous anodic aluminum oxide for detection of antibiotics. J Food Sci 80 (4), N834–40. doi:10.1111/1750-3841.12825.

Chen, R., Liu, B., Ni, H., Chang, N., Luan, C., Ge, Q., Dong, J., Zhao, X., 2019. Vertical flow assays based on core–shell SERS nanotags for multiplex prostate cancer biomarker detection. Analyst 144 (13), 4051–4059. https://doi.org/10.1039/C9AN00733D.

Cialla, D., März, A., Böhme, R., Theil, F., Weber, K., Schmitt, M., Popp, J., 2012. Surface-enhanced Raman spectroscopy (SERS): progress and trends. Anal. Bioanal.Chem. 403 (1), 27–54. https://doi.org/10.1007/s00216-011-5631-x.

Fleischmann, M., Hendra, P.J., McQuillan, A.J., 1974. Raman spectra of pyridine adsorbed at a silver electrode. Chem. Phys. Lett. 26 (2), 163–166. https://doi.org/10.1016/0009-2614(74)85388-1.

Han, B., Zhang, Y.-L., Zhu, L., Chen, X.-H., Ma, Z.-C., Zhang, X.-L., Wang, J.-N., Wang, W., Liu, Y.-Q., Chen, Q.-D., Sun, H.-B., 2018. Direct laser scribing of

AgNPs@RGO biochip as a reusable SERS sensor for DNA detection. Sens. Actuators B 270, 500–507. https://doi.org/10.1016/j.snb.2018.05.043.

Han, L., Zhang, Y., Zhang, Y., Shu, Y., Chen, X.-W., Wang, J.-H., 2017. A magnetic polypyrrole/iron oxide core/gold shell nanocomposite for multimodal imaging and photothermal cancer therapy. Talanta 171, 32–38. https://doi.org/10.1016/j.talanta.2017.04.056.

Hasna, K., Antony, A., Puigdollers, J., Kumar, K.R., Jayaraj, M.K., 2016. Fabrication of cost-effective, highly reproducible large area arrays of nanotriangular pillars for surface enhanced Raman scattering substrates. Nano Res. 9 (10), 3075–3083. https://doi.org/10.1007/s12274-016-1190-y.

Hasna, K., Jayaraj, M.K., 2020. Metal Oxides-Based SERS Substrates. In: Jayaraj, M.K. (Ed.), Nanostructured Metal Oxides and Devices. Materials Horizons: From Nature to Nanomaterials. Springer, Singapore, pp. 155–175.

Haynes, C.L., Van Duyne, R.P., 2002. Plasmon scanned surface-enhanced Raman scattering excitation profiles. MRS Proceedings 728, 1–6.

Huang, Y., Lin, D., Li, M., Yin, D., Wang, S., Wang, J., 2019. Ag@Au core–shell porous nanocages with outstanding SERS activity for highly sensitive SERS immunoassay. Sensors (Basel, Switzerland), 19 (7). https://doi.org/10.3390/s19071554.

Jeanmaire, D.L., Van Duyne, R.P., 1977. Surface Raman spectroelectrochemistry: part I. heterocyclic, aromatic, and aliphatic amines adsorbed on the anodized silver electrode. J. Electroanal. Chem. Interfacial Electrochem. 84 (1), 1–20. https://doi.org/10.1016/S0022-0728(77)80224-6.

Jin, X., Mao, A., Ding, M., Ding, P., 2016. A simple route to synthesize Cu@Ag core–shell bimetallic nanoparticles and their surface-enhanced Raman scattering properties. Appl. Spectrosc. 70 (10), 1692–1699.

Joseph, D., Kwak, C.H., Huh, Y.S., Han, Y.-K., 2019. Synthesis of AuAg@Ag core@shell hollow cubic nanostructures as SERS substrates for attomolar chemical sensing. Sens. Actuators B 281, 471–477. https://doi.org/10.1016/j.snb.2018.10.092.

Khlebtsov, B.N., Liu, Z., Ye, J., Khlebtsov, N.G., 2015. Au@Ag core/shell cuboids and dumbbells: optical properties and SERS response. J. Quant. Spectrosc. Radiat. Transfer 167, 64–75. https://doi.org/10.1016/j.jqsrt.2015.07.024.

Khlebtsov, B., Khanadeev, V., Khlebtsov, N., 2016. Surface-enhanced Raman scattering inside Au@Ag core/shell nanorods. Nano Res. 9 (8), 2303–2318. https://doi.org/10.1007/s12274-016-1117-7.

Khurana, P., Thatai, S., Prasad, S., Soni, S., Kumar, D., 2016. Agcore–Aushell bimetallic nanocomposites: gold shell thickness dependent study for SERS enhancement. Microchem. J. 124, 819–823. https://doi.org/10.1016/j.microc.2015.10.009.

Kneipp, K., Wang, Y., Kneipp, H., Perelman, L.T., Itzkan, I., Dasari, R.R., Feld, M.S., 1997. Single molecule detection using surface-enhanced Raman scattering (SERS). Phys. Rev. Lett. 78 (9), 1667–1670. https://doi.org/10.1103/PhysRevLett.78.1667.

Le Ru, E.C., Etchegoin, P.G., 2009. Calculations of electromagnetic enhancements. In: Le Ru, E.C., Etchegoin, P.G. (Eds.), Principles of Surface-Enhanced Raman Spectroscopy. Elsevier, Amsterdam, pp. 265–297. doi:10.1016/B978-0-444-52779-0.00011-8.

Li, H., Jiang, J., Wang, Z., Wang, X., Liu, X., Yan, Y., Li, C., 2017. A high performance and highly-controllable core-shell imprinted sensor based on the surface-enhanced Raman scattering for detection of R6G in water. J. Colloid Interface Sci. 501, 86–93. https://doi.org/10.1016/j.jcis.2017.04.010.

Lin, Y., Xu, G., Wei, F., Zhang, A., Yang, J., Hu, Q., 2016. Detection of CEA in human serum using surface-enhanced Raman spectroscopy coupled with antibody-modified Au and γ-Fe_2O_3@Au nanoparticles. J. Pharm. Biomed. Anal. 121, 135–140. https://doi.org/10.1016/j.jpba.2016.01.027.

Luo, Y., Pei, L., Huang, Y., Li, C., Zhang, Y., Rasco, B.A., Lai, K., 2014. Detection of triphenylmethane drugs in fish muscle by surface-enhanced Raman spectroscopy coupled with Au-Ag core-shell nanoparticles. Journal of Nanomaterials 2014, 730915. https://doi.org/10.1155/2014/730915.

Mie, G., 1908. Contributions to the Optics of Turbid Media, Particularly of Colloidal Metal solutions. Annalen der Physik 25, 377–445. doi:10.1002/andp.19083300302.

Mohammadniaei, M., Lee, T., Bharate, B.G., Yoon, J., Choi, H.K., Park, S., Kim, J., Kim, J., Choi, J.-W., 2018. Bifunctional Au@Bi_2Se_3 core–shell nanoparticle for synergetic therapy by SERS-traceable antagomiR delivery and photothermal treatment. Small 14 (38), 1802934. https://doi.org/10.1002/smll.201802934.

Nie, Emory, 1997. Probing single molecules and single nanoparticles by surface-enhanced Raman scattering. Science (New York) 275 (5303), 1102–1106.

Pal, A.K., Pagal, S., Prashanth, K., Chandra, G.K., Umapathy, S., D., B.M, 2019. Ag/ZnO/Au 3D hybrid structured reusable SERS substrate as highly sensitive platform for DNA detection. Sens. Actuators B 279, 157–169. https://doi.org/10.1016/j.snb.2018.09.085.

Petryayeva, E., Krull, U.J., 2011. Localized surface plasmon resonance: nanostructures, bioassays and biosensing—A review. Anal. Chim. Acta 706 (1), 8–24. https://doi.org/10.1016/j.aca.2011.08.020.

Petti, L., Capasso, R., Rippa, M., Pannico, M., La Manna, P., Peluso, G., Calarco, A., Bobeico, E., Musto, P., 2016. A plasmonic nanostructure fabricated by electron beam lithography as a sensitive and highly homogeneous SERS substrate for bio-sensing applications. Vib. Spectrosc. 82, 22–30. https://doi.org/10.1016/j.vibspec.2015.11.007.

Pu, H., Xie, X., Sun, D.-W., Wei, Q., Jiang, Y., 2019. Double strand DNA functionalized Au@Ag nps for ultrasensitive detection of 17β-estradiol using surface-enhanced Raman spectroscopy. Talanta 195, 419–425. https://doi.org/10.1016/j.talanta.2018.10.021.

Schlücker, S., 2014. Surface-enhanced Raman spectroscopy: concepts and chemical applications. Angew. Chem. Int. Ed. 53 (19), 4756–4795. https://doi.org/10.1002/anie.201205748.

Shao, B., Ma, X., Zhao, S., Lv, Y., Hun, X., Wang, H., Wang, Z., 2018. Nanogapped $Au_{(core)}$ @ $Au\text{-}Ag_{(shell)}$ structures coupled with Fe_3O_4 magnetic nanoparticles for the detection of ochratoxin A. Anal. Chim. Acta 1033, 165–172. https://doi.org/10.1016/j.aca.2018.05.058.

Sharma, V., Sinha, N., Dutt, S., Chawla, M., Siril, P.F., 2016. Tuning the surface enhanced Raman scattering and catalytic activities of gold nanorods by controlled coating of platinum. J. Colloid Interface Sci. 463, 180–187. https://doi.org/10.1016/j.jcis.2015.10.036.

Si, Y., Li, L., Qin, X., Bai, Y., Li, J., Yin, Y., 2019. Porous SiO_2-coated Au-Ag alloy nanoparticles for the alkyne-mediated ratiometric Raman imaging analysis of hydrogen peroxide in live cells. Anal. Chim. Acta 1057, 1–10. https://doi.org/10.1016/j.aca.2018.12.061.

Song, L., Mao, K., Zhou, X., Hu, J., 2016. A novel biosensor based on Au@Ag core–shell nanoparticles for SERS detection of arsenic (III). Talanta 146, 285–290. https://doi.org/10.1016/j.talanta.2015.08.052.

Taranenko, N., Alarie, J.-P., Stokes, D.L., Vo-Dinh, T., 1996. Surface-enhanced Raman detection of nerve agent simulant (DMMP and DIMP) vapor on electrochemically prepared silver oxide substrates. J. Raman Spectrosc. 27 (5), 379–384. https://doi.org/10.1002/(SICI)1097-4555(199605)27:5<379::AID-JRS925>3.0.CO;2-G.

Tian, Y.-F., Ning, C.-F., He, F., Yin, B.-C., Ye, B.-C., 2018. Highly sensitive detection of exosomes by SERS using gold nanostar@Raman reporter@nanoshell structures modified with a bivalent cholesterol-labeled DNA anchor. Analyst 143 (20), 4915–4922. https://doi.org/10.1039/c8an01041b.

Tu, G., Deogratias, N., Xu, M., Li, X., Liu, J., Jiang, L., Yang, Y., Zhang, J., 2018. Sharp-featured Au@Ag core/shell nanocuboid synthesis and the label-free ultrasensitive SERS detection of protein single-point mutations. Mater. Chem. Front. 2 (9), 1720–1724. https://doi.org/10.1039/C8QM00185E.

Wang, J., Wu, X., Wang, C., Rong, Z., Ding, H., Li, H., Li, S., Shao, N., Dong, P., Xiao, R., Wang, S., 2016a. Facile synthesis of Au-coated magnetic nanoparticles and their application in bacteria detection via a SERS method. ACS Appl. Mater. Interfaces 8 (31), 19958–19967. https://doi.org/10.1021/acsami.6b07528.

Wang, S., Luo, J., He, Y., Chai, Y., Yuan, R., Yang, X., 2018a. Combining porous magnetic Ni@C nanospheres and $CaCO_3$ microcapsule as surface-enhanced Raman spectroscopy sensing platform for hypersensitive C-reactive protein detection. ACS Appl. Mater. Interfaces 10 (39), 33707–33712. https://doi.org/10.1021/acsami.8b13061.

Wang, W., Wang, W., Liu, L., Xu, L., Kuang, H., Zhu, J., Xu, C., 2016b. Nanoshell-enhanced Raman spectroscopy on a microplate for staphylococcal enterotoxin b sensing. ACS Appl. Mater. Interfaces 8 (24), 15591–15597. https://doi.org/10.1021/acsami.6b02905.

Wang, Z., Yang, H., Wang, M., Petti, L., Jiang, T., Jia, Z., Xie, S., Zhou, J, 2018b. SERS-based multiplex immunoassay of tumor markers using double SiO_2@Ag immune probes and gold-film hemisphere array immune substrate. Colloids Surf. A 546, 48–58. https://doi.org/10.1016/j.colsurfa.2018.02.069.

Wang, Z., Zhang, J., Wang, H., Hai, J., Wang, B., 2018c. Se atom-induced synthesis of concave spherical Fe_3O_4@Cu_2O nanocrystals for highly efficient MRI-SERS imaging-guided NIR photothermal therapy. Particle & Particle Systems Characterization 35 (11), 1800197. https://doi.org/10.1002/ppsc.201800197.

Wei, W., Wang, L., Huang, Q., Li, T., 2019. Controlled synthesis of biocompatible rGO@CD@Au nanocomposites for trace detection for doxorubicin by Raman imaging spectroscopy. J. Alloys Compd. 783, 37–43. https://doi.org/10.1016/j.jallcom.2018.12.285.

Wen, S., Miao, X., Fan, G.-C., Xu, T., Jiang, L.-P., Wu, P., Cai, C., Zhu, J.-J., 2019. Aptamer-conjugated Au nanocage/SiO_2 core–shell bifunctional nanoprobes with high stability and biocompatibility for cellular SERS imaging and near-infrared photothermal therapy. ACS Sens. 4 (2), 301–308. https://doi.org/10.1021/acssensors.8b00682.

Yamaguchi, A., Utsumi, Y., Fukuoka, T., 2019. Aggregation and dispersion of Au-nanoparticle-decorated polystyrene beads with SERS-activity using ac electric field and brownian movement. Appl. Surf. Sci. 465, 405–412. https://doi.org/10.1016/j.apsusc.2018.09.206.

Yang, L., Gao, M.X., Zhan, L., Gong, M., Zhen, S.J., Huang, C.Z., 2017. An enzyme-induced Au@Ag core–shell nanoStructure used for an ultrasensitive surface-enhanced Raman scattering immunoassay of cancer biomarkers. Nanoscale 9 (7), 2640–2645. https://doi.org/10.1039/C6NR07979B.

Yang, Y., Zhu, J., Zhao, J., Weng, G.-J., Li, J.-J., Zhao, J.-W., 2019. Growth of spherical gold satellites on the surface of Au@Ag@SiO_2 core-shell nanostructures used for an ultrasensitive SERS immunoassay of alpha-fetoprotein. ACS Appl. Mater. Interfaces 11 (3), 3617–3626. https://doi.org/10.1021/acsami.8b21238.

Zhao, J., Wu, C., Zhai, L., Shi, X., Li, X., Weng, G., Zhu, J., Li, J., Zhao, J.-W., 2019. A SERS-based immunoassay for the detection of α-fetoprotein using AuNSs@Ag@SiO_2 core–shell nanostars. J. Mater. Chem. C 7 (27), 8432–8441. https://doi.org/10.1039/C9TC01890E.

Zhao, X., Wen, J., Zhang, M., Wang, D., Wang, Y., Chen, L., Zhang, Y., Yang, J., Du, Y., 2017. Design of hybrid nanostructural arrays to manipulate SERS-active substrates by nanosphere lithography. ACS Appl. Mater. Interfaces 9 (8), 7710–7716. https://doi.org/10.1021/acsami.6b14008.

Zhu, C., Meng, G., Huang, Q., Zhang, Z., Xu, Q., Liu, G., Huang, Z., Chu, Z., 2011. Ag nanosheet-assembled micro-hemispheres as effective SERS substrates. Chem. Commun. 47 (9), 2709–2711. https://doi.org/10.1039/C0CC04482B.

10

Noninvasive biomarker sensors using surface-enhanced Raman spectroscopy

Navami Sunil and Biji Pullithadathil
Nanosensor Laboratory, PSG Institute of Advanced Studies, Coimbatore, India.

10.1 Introduction

Wearable sensors have become extremely useful in providing accurate information about an individual's activities and behaviors and thus have become inevitable in many applications such as medical, environmental, and commercial fields. The wearables that possess sensors to monitor how the body is functioning may provide a better understanding of our health conditions (Mukhopadhyay, 2015). Advancements in sensing technologies and their miniaturization to the lab-on-a-chip model have made it possible to monitor the activities of human beings continuously.

In general, biosensors have three major operations: sample collection, assay chemistry, and detection and recording of a quantifiable signal. In recent times, there has been a huge increase in the use of wearable sensors in the biomedical field. Some of these include monitoring a patient's body temperature, heart rate, pressure, and oxygen saturation and even the detection of analytes such as alcohol content, glucose level, urea, and other metabolites (Bandodkar & Wang, 2014). This has led to a tremendous improvement in the field of biomedical science as it involves faster analysis and response time. Recent advances have focused more on the electrochemical monitoring of various biomarkers in biological fluids. The wearable sensors that noninvasively analyze body fluids such as saliva, sweat, and tears are of greater importance these days because of their ability to assess the health status by continuously monitoring the changes in the metabolic process (Heikenfeld, 2016). Both finger pricking and venous puncture are invasive and causes pain and stress during the blood collection. Thus a simple and non-invasive method is necessary for diagnostic applications which is possible through biological fluids such as saliva, sweat and tears.

Nanomaterials for Sensing and Optoelectronic Applications. DOI: https://doi.org/10.1016/B978-0-12-824008-3.00002-3

Sweat is an alternative biological matrix that can be used to detect drug intake and abuse. It is produced by eccrine and apocrine glands that begin in the dermis of the skin and end in secretory canals that flow into the skin surface and hair follicles. Sweat consists of 99% water, with sodium chloride being the most concentrated solute. Sweating rates are highly dependent on environmental temperatures, and rates as high as 3 L min^{-1} have been recorded for short periods of time (Chawarski et al., 2007). Sweat and sebaceous glands are housed in the dermis and are disproportionally distributed throughout the body. The hands have the highest concentration of sweat glands, while the forehead has the densest population of sebaceous glands (Cone et al., 1994). Sweat is particularly attractive due to the ease of collection and the presence of different biomarkers, contains rich information about the health status, and provides detailed information regarding a wide spectrum of the biomarkers, metabolites, etc. Many years have passed since it was demonstrated that endogenous and exogenous chemicals are secreted in this biological sample, necessitating its collection and analysis. Despite of its non-invasive and easy collection advantages, quantitative sweat analysis faces practical challenges in the direct sampling and detection of multiple biomarkers without evaporation. Traditional sweat research and analysis relied on absorbent pads or fabric substrates that adhere to the skin to collect sweat and require professional handling to retrieve the deployed patch for precision measurements (De Giovanni & Fucci, 2013).

Saliva is another extracellular fluid produced and secreted by salivary glands, containing 98% water and 2% other compounds such as electrolytes (sodium, potassium, calcium, chloride, magnesium, bicarbonate, and phosphate), glucose, nitrogenous products, and various biocompounds (enzymes, immunoglobulin, mucosal glycoproteins, albumin, polypeptides, oligopeptides, antimicrobial factors, etc.). All these biocomponents are vital to the oral cavity's wellbeing and are responsible for a variety of functions attributed to saliva. Human salivary glands produce about 0.5 L to 1.0 L of saliva per day via three distinct major salivary gland pairs, namely, parotid, submandibular, and sublingual glands, as well as numerous minor salivary glands, such as oral palatal and buccal glands and those in the labial mucosa (Rathnayake et al., 2013). Saliva is a complex fluid that contains a huge library of hormones, proteins, enzymes, antibodies, antimicrobial constituents, and cytokines. Saliva has been considered extremely important in screening and diagnosis because it is a readily available specimen that can be collected using non-invasive procedures and contains many hormones, drugs, and antibodies. Additionally, saliva has good correlation with the blood concentrations of numerous analytes such as glucose, lactate, phosphate, uric acid hormones, and antibodies and also contains an array of analytes (proteins, mRNA, and DNA) that can be used as biomarkers for translation and clinical

applications. Saliva has much potential as a diagnostic fluid, and it has an advantage over serum and other biological fluids in terms of being a cheap and non-invasive way to monitor systemic health and disease progression. The numerous components in this fluid can be used as biomarkers to diagnose a variety of systemic and local diseases (Lee & Wong, 2009).

The term "tears" refers to the fluid found in the precorneal film and the conjunctival sac. The volume of tear fluid is approximately 5 to 10 μL. The lacrimal gland produces the majority of it (95% or more); goblet cells and the accessory lacrimal gland of the conjunctiva produce lesser amounts. The total mass of the fluid produced by the latter is approximately one-tenth that of the main lacrimal gland (Van Haeringen, 1981). Tears contain proteins, electrolytes, metabolites, and mucins. Tears have been proposed as a diagnostic tool for drug monitoring, confirming dry eye syndrome (Schirmer test), detecting lysosomal storage diseases (e.g., Morbus Gaucher), and detecting hyperglycemia (Haeckel & Hänecke, 1993). Biomarker molecules in tears diffuse directly from the blood, and their concentrations in the blood are more closely correlated with concentrations in tears compared to other biofluids, which makes tears superior to other biological fluids such as sweat. Tears also contain a wide range of components like proteins, peptides, lipids, metabolites, and electrolytes and possess unique merits in diagnosing specific ocular diseases.

Biological fluids such as sweat, saliva, and tears have a long history of use in clinical diagnostics because of the ease of collecting their samples and the presence of a wide range of both host and associated biomarkers due to infection (Corrie et al., 2015). Wearable electrochemical sensors and biosensors have been developed for noninvasive real-time monitoring of electrolytes and metabolites in sweat, tears, or saliva as indicators of the wearer's health status. Such noninvasive sensors and biosensors are expected to open up new and exciting avenues in the field with continued innovation and attention to key challenges and their significant use in a variety of personal health care monitoring applications, as well as in sports and military applications (Bandodkar & Wang, 2014). Many methods have been employed for the detection of biomarkers in the fields of the aforementioned biological fluids, including immunological procedures, isolation processes, and, more recently, electrochemical methods, optical methods, and surface-enhanced Raman spectroscopy (SERS) using biosensors, which have all been used to identify biomarkers and metabolites from sweat, saliva, and tears. Over the conventional techniques, SERS biosensors have many advantages such as lower detection limits, low cost, simple design, ease of manipulation, low consumption of costly and/or toxic reagents, and, more importantly, improved sensitivity even at trace concentration levels, allowing the measurement event with tiny amounts of samples.

SERS is essentially a combination of two techniques: Raman spectroscopy and nanotechnology. SERS, like normal Raman spectroscopy, is an emission technique that involves the inelastic scattering of incident laser energy resulting in spectral peaks that are frequency-shifted from the incident energy due to the vibrational modes of the molecule. The adsorption of analyte molecules onto the SERS substrate is required for the SERS technique. The Raman signal of the analyte is enhanced upon adsorption onto the SERS surface, and the resulting signal intensity is comparable to that obtained by fluorescence (Mosier-Boss, 2017). The speed with which samples can be analyzed is one of the main advantages of using SERS over traditional analytical techniques. Other benefits, such as exceptional spectral selectivity, ease of sample manipulation, speed of analysis, *in situ* analyte identification, and the availability of commercially available, robust, portable Raman spectrometers, have made SERS an appealing technique for detecting a wide range of chemical species. Also, the high resolution of the SERS spectra makes simultaneous multicomponent analysis possible. To obtain a SERS, the protocol can be as simple and quick as dropping a microliter sample onto a SERS substrate followed by a split-second laser integration time, thereby analyzing the signal and comparing it to a reference spectrum Fig. 10.1. Another important advantage of the SERS method involves sensitivity, reproducibility, selectivity, and portability, which makes it suitable for the detection of trace amounts of analyte (Pang et al., 2016). Typical SERS substrates are roughened silver/copper/gold surfaces. Noble metal nanostructures such as silver, gold, and copper use electromagnetic and chemical enhancement mechanisms to amplify the Raman signals of molecules in close proximity to the surface.

This book chapter focuses on the advances in the field of SERS-based biological fluid sensors and their promising impact on the non-invasive and continuous health monitoring aspects. Here, the recent advancements of the sensors for the detection of different biomarkers and metabolites are explored in detail. The content includes a summary of the analysis of each biomarker, its fabrication method, and its practical application for biochemical sensing. The concluding section discusses the challenges and future scope of these types of wearable biosensors.

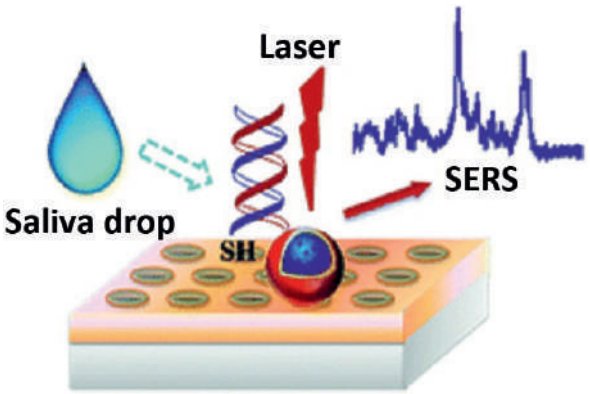

Figure 10.1. Schematic illustration of a gold nanohole array–based surface-enhanced Raman scattering biosensor for the detection of silver(I) and mercury(II) in human saliva (Zheng, 2015).

10.2 Non-invasive biological fluids

10.2.1 Sweat

Sweat, an important biological fluid that can be retrieved conveniently and non-invasively, contains a wealth of information about one's health status, and sweat-based biosensors provide detailed information on a wide range of biomarkers, metabolites, and other electrolytes during physical activities. This slightly acidic biofluid (pH range 4.0–6.8) is primarily composed of water (99%), which contains electrolytes (e.g., sodium, chloride, and potassium), urea, pyruvate, and lactate proteins, peptides, amines, amino acids, and metal ions, as well as inhibitors, antigens, antibodies, and a variety of xenobiotics such as drugs, cosmetics, and ethanol. These substances are stored in sweat glands, secreted into the sweat, and finally transported to the epidermis surface with partial selective reabsorption of sodium and chloride during transportation, resulting in the hypotonicity of the secreted sweat in healthy individuals (Sato et al., 1989). Among various biological fluids, sweat is particularly attractive due to the ease of collection and the presence of biomarkers related to various health conditions such as dehydration, mental stress, and other diseases (Jadoon et al., 2015).

For sweat analysis, common analytical equipment for high-resolution separation (GC, liquid chromatographs [LC], and capillary electrophoresis [CE] equipment) is most often coupled to mass spectrometers (MSs) of varying complexity, primarily for the analysis of drug or complex metabolites (Jurado-Gámez et al., 2014). Fluorescent sensing, colorimetric sensing, and electrochemical sensing are some of the other detection methods used for sweat analysis. Despite the fact that these sweat sensing principles are widely used and that many wearable sweat biosensors have been developed, there are still several complicated issues to be considered: (1) sweat detection necessitates sensors with high selectivity and sensitivity, so costs will inevitably rise; (2) the reagents in continuous sweat detection must be replaced on a regular basis, or measurement accuracy will be affected; and (3) changes in the environment (humidity, pressure, and temperature) can cause significant changes in the signal, affecting the sensor reading (Yu & Sun, 2020).

Among different types of detection methods used for sweat analysis, surface-enhanced Raman spectroscopy (SERS) has a high potential in clinical diagnosis due to its low susceptibility to environmental variables; miniature/portable instruments for *in situ* detection, and ability to provide highly sensitive, timely, accurate, and non-destructive information. SERS is a nondestructive, ultrasensitive, and fast analytical technique that can provide rich and distinguishable vibrational

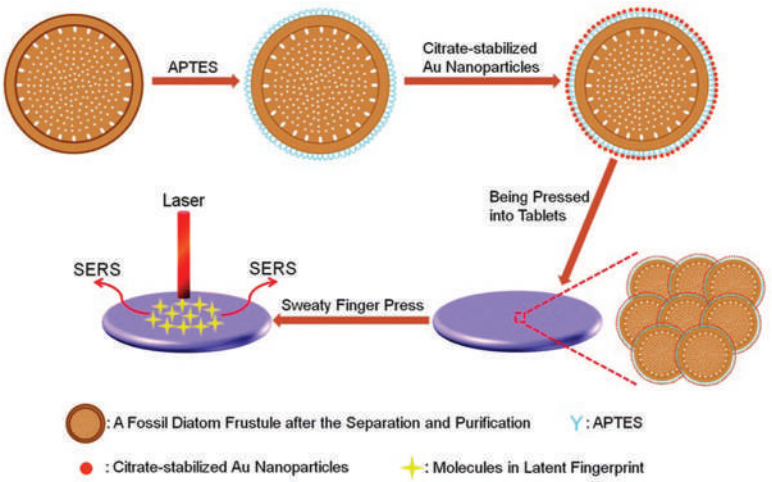

Figure 10.2. Schematic diagram showing the fabricated button-like portable tablet for SERS detection of the chemical composition of eccrine sweat in latent fingerprints, developed by Chen et al. (2015).

information used for molecule identification and can perform trace detection or even single-molecule detection. Furthermore, SERS requires little to no sample preparation, which makes it an ideal spectroscopy technique for analyzing the chemical composition of sweat and for diagnostic purposes (Kleinman et al., 2011).

A button-like substrate made of periodically ordered diatomaceous earth and Au nanoparticles for the SERS analysis of the chemical composition of eccrine sweat in latent fingerprints was proposed by Chen et al (2015). It may reveal an individual's medical condition by analyzing the obtained SERS spectra, implying that the SERS-based methodology has a potentially wide range of applications in fields that require trace detection, such as medical diagnostics and forensic investigations, due to its high sensitivity Fig. 10.2.

With the help of a mussel-inspired surface-imprinted capillary SERS sensor, a novel ultrasensitive and universal Raman indicator sensing strategy for protein detection was proposed by Arabi et al. (2021). The proposed method offers ultra-low LOD, down to 4.1×10^{-3} μg L^{-1} for trypsin in complex biological fluid samples without any pretreatment because of the advantages of the indicator sensing mechanism and the excellent specificity of the capillary sensor. The SERS substrate of Au nanoparticles–dotted magnetic nanocomposites (AMNs) modified with inositol hexakisphosphate (IP6) used to quickly monitor trace drug–related biomarkers in saliva and to screen a trace drug biomarker in fingerprints on-site was developed by Yang et al. (2015). The detection limit for a drug biomarker in a fingerprint was 100 nM and hence this methodology could be used to accurately differentiate between smokers and drug addicts on-site in the near future.

10.2.2 Saliva

Saliva is an extracellular fluid produced and secreted by the salivary glands. It comprises 98% water, but it also contains many important substances such as electrolytes, mucus, antibacterial compounds, and various enzymes. Human salivary glands produce about 0.5 L to 1 L of saliva per day via three distinct major salivary gland pairs, namely, parotid, submandibular, and sublingual glands, as well as numerous minor salivary glands, such as oral palatal and buccal and those in the labial mucosa. Additionally, saliva has good correlation with the blood concentrations of numerous analytes such as glucose, lactate, phosphate, uric acid hormones, and antibodies. Saliva contains a variety of analytes (including protein, mRNA, and DNA) that can be used as biomarkers in translation and clinical applications. The report of saliva as a diagnostic tool for oral cancer detection was reviewed by Devaraj et al. in 2013 where he had explored the diagnostic purposes of saliva for the detection of a variety of diseases including cancer detection (Devaraj, 2013). Another important biomarker in saliva is glucose, as studies have shown that in diabetes patients salivary glucose concentration is significantly higher than in healthy subjects (Malon et al., 2014). In addition, the entire human saliva normally contains many normal and pathogenic microorganisms (e.g., bacteria, fungi, or viruses) and their metabolites, as well as several types of cells that are excreted, secreted, or migrated from the oral mucosa or between the gums. Therefore saliva provides a large number of analytes that are comparable to blood for disease diagnosis and monitoring and hence can be used as a powerful tool for disease diagnosis and monitoring (Yeh et al., 2010).

Molecules found in blood, such as DNA, RNA, proteins, metabolites, and microbiota, are also found in saliva, and therefore changes in their concentrations can be used as biomarkers to detect early-stage cancer or to monitor response to therapeutic management (Lee et al., 2009). A review done by Wang et al explored in detail the potential mechanisms by which distal tumors mediate changes in salivary biomarker profiles, as well as a description of the recent advances in salivary biomarkers used for systemic cancer detection (Wang et al., 2017). Saliva has been used as a powerful tool for the detection of various types of cancers, including oral cancer (Cheng et al , 2014), breast cancer (Zhang et al., 2010), pancreatic cancer (Wong et al., 2009), lung Cancer (Wong et al., 2017), and ovarian cancer (Lee et al., 2012).

Salivaomics research is critical for identifying disease biomarkers and potential drug targets (Zhang et al., 2016). Salivaomics has the potential to detect diseases in their early stages as well. However, saliva research and its applications for disease diagnosis are still in their early stage, and progress in these studies is hampered by a lack of efficient and useful methods and technology. Based on the SERS spectra

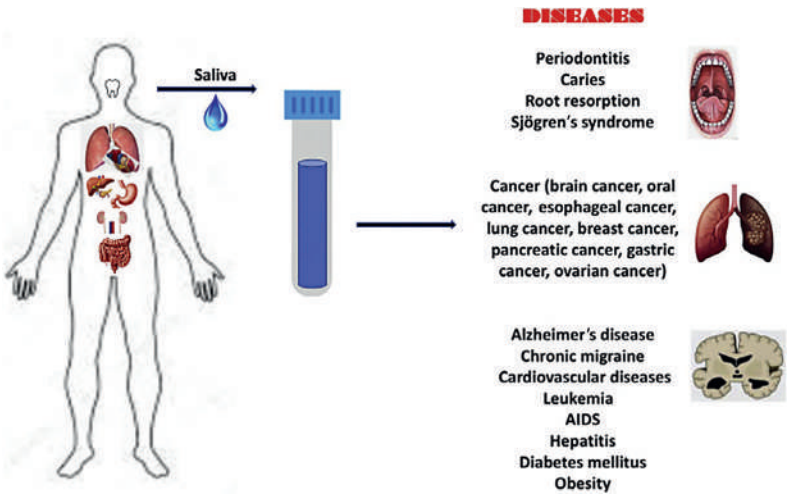

Figure 10.3. Clinical utilities of saliva for the diagnosis of local and systemic diseases (Kaczor et al., 2019).

of saliva, a number of diseases like diabetes mellitus, cardiovascular disease, renal disease, genetic disorders, periodontal diseases were successfully identified and analyzed Fig. 10.3.

Many attempts have been made in order to correlate blood glucose level and salivary glucose level (Panchbhai, 2012). The typical molar concentration levels of glucose in urine range from 0 to 0.8 mM, and higher glucose levels in blood result in higher glucose levels in urine. The glucose levels in saliva are much lower, in the range of 50 to 500 **μM**, but are measurable due to the sensitivity of the SERS technique. According to studies, diabetic patients have significantly higher salivary glucose concentrations than healthy subjects (Ben-Aryeh et al., 1988). As a result, saliva was developed as a diagnostic tool for diabetes. Botta et al. developed a sensor for the noninvasive detection of glucose in diabetic patients using saliva samples (Botta et al., 2016). SERS-active substrates were created using an inert gas-phase condensation technique. They used 2-thienylboronic acid as a linker or bridge molecule that was attached to the silver surface on one side and to the glucose molecule on the other side to quantify the glucose concentration in the molar concentration range of 1 M–500 M. A work done by Ceja's group demonstrated the use of gold nanoparticles (AuNPs), multibranched gold nanoparticles (MBGNs), and silica-coated MBGNs (MBGNs-silica) for the detection of rhodamine B (RB) and α-glucose detection at low concentrations. The SERS signals of RB and α-glucose using MBGNs-silica were improved in comparison to AuNPs and MBGNs, which is attributed to MBGN aggregation and a stronger interaction and the functionalization process improves the interaction and allows measurements at low concentrations with

detection limits of 50 pM for rhodamine B and 5 mM for α-glucose respectively (Ceja-Fdez et al., 2014). A similar work was done by Hu et al. using the composite of Au nanoparticles and porphyrin-based metal–organic framework for the SERS detection of glucose in saliva samples (Hu et al., 2020). The quantitative detection of glucose was then achieved by monitoring the SERS intensity of the Raman-active MG, and the detection concentration was as low as 0.16 mmol L^{-1}. The developed sensor offered a good sensitivity and selectivity, showing good recovery from 96.9 to 100.8%, thereby paving a new way to design a nanozyme-based SERS protocol for biomolecule analysis. Al-Ogaidi's group developed an SERS biosensor for label-free glucose detection using gold nanostar@silica core–shell nanoparticles conjugated with glucose oxidase (GOx) enzyme molecules (Al-Ogaidi et al., 2014). The surface-immobilized GOx enzyme catalyzes the oxidation of glucose, resulting in the formation of hydrogen peroxide, which produces a strong SERS signal upon excitation by a laser that is used to determine the concentration of glucose ranging from 25 M to 25 mM in the aqueous solution with a limit of detection of 16 M. A versatile SERS-based platform for the quantitative detection of monosaccharides (glucose, fructose, and galactose) in a single test via a displace-and-trap mechanism was developed by Lin's group (Lin et al., 2021). The detection range of the developed platform was found to be 0.125 to 7 mg dL^{-1}, which is perfectly covered by the use of multiple optical interference-free (1800–2200 cm^{-1}) signal-independent Raman probes, thereby providing a better platform for the noninvasive and high-efficiency screening of clinical diabetes and other carbohydrate-related diseases.

Many works have been carried out to study the potential biomarkers in saliva for cardiovascular, renal, and neurodegenerative diseases using SERS. SERS is a powerful tool for identifying and quantifying cardiovascular biomarkers such as uric acid (Lu et al., 2018) and linoleic acid (Farvid et al., 2014).

Rapid and sensitive detection of TNF-α, a biomarker for the early diagnosis of cardiovascular disease, using a magnetic bead pull-down assay in combination with SERS was demonstrated by Lai's group (Lai et al., 2018). Silica-encapsulated small gold nanoclusters served as highly sensitive SERS labels, were applied for detection, which can achieve a sensitive detection for TNF-α down to ca. 1 pg mL^{-1}, thus indicating the great potential of the developed SERS labels as promising and sensitive reporters in multiplexed bioanalytical applications such as immunoassays. A Rapid and reproducible analysis of thiocyanate in real human serum and saliva was developed by Wu et al. using a droplet (Wu et al., 2014) microfluidic device using the SERS technique for the detection of thiocyanate in real human serum and saliva, which is a biomarker for both cardiovascular and periodontal disease. Their method utilized the rapid detection of SCN in real human saliva such that it can be

used to distinguish smokers from nonsmokers, thereby demonstrating a quick, dependable, and simple method for SCN detection with high reproducibility. The first approach using nanotechnology to identify biomarkers involved in the development and progression of different endotypes and stages of asthma in saliva was demonstrated by Zamora-Mendoza et al. (2019). Their research revealed that IL-8, IL10, and sCD163 are potential biomarkers of bronchial inflammation, and the bands in the Raman spectra 760, 1127, 1231, 1326, 1456, and 1750 cm^{-1} provide high sensitivity for the potential diagnosis of asthma, making SERS a useful tool for the identification of the inflammatory endotype in asthma. Severe acute respiratory syndrome coronavirus 2 (SARS-CoV-2) is a novel severe acute respiratory syndrome coronavirus that is continuously spreading and that has become a worldwide emergency. The recommended specimens for diagnostic tests are nasopharyngeal and oropharyngeal swabs, with real-time reverse transcription-polymerase chain reaction (rRT-PCR) on respiratory specimens representing the gold-standard method for detecting SARS-CoV-2 infection (Sofi et al., 2020). The analytical protocol required for SARS-CoV-2 detection via RT-PCR faces many drawbacks like time, specialized laboratories, expensive reagents, and adequate personnel in a process that is highly susceptible to operator error affecting the final sensitivity. Carlomagno's group published the first report on the Raman-based approach for saliva analysis to significantly differentiate the signal of patients currently infected with COVID-19 from healthy subjects and subjects with a previous infection (Carlomagno et al., 2021). The Raman-based classification model was able to discriminate the signal collected from COVID-19 patients with more than 95% accuracy, precision, sensitivity, and specificity in the range of 89% to 92%, confirming this technique as a diagnostic tool that uses saliva as a minimally invasive and highly informative biofluid and demonstrating the technique's efficacy. In 2021 Liu et al. reported an SERS–based lateral flow immunoassay (SERS-LFIA) for the simultaneous detection of anti-SARS-CoV-2 IgM/IgG with high sensitivity using SiO_2@Ag (Liu et al., 2021). The detection sensitivity of the proposed method for virus-specific IgM and IgG was 800 times higher than that of the standard Au-based LFIA method. The SERS–clinical LFIA's application potential was further validated using 68 clinical serum samples, including 19 positive serum samples that gave 100% accuracy and specificity with SERS-LFIA for the combined analysis of IgM and IgG.

Carlomagno et al. developed a method for the diagnosis of amyotrophic lateral sclerosis (ALS) through saliva, a neurodegenerative disease leading to progressive and irreversible muscle atrophy, using the SERS technique. SERS was used to analyze saliva collected from 19 late-stage patients with ALS (pALS) and compared to data obtained from saliva collected from 10 healthy controls (CTRL), 10 Parkinson's

disease (PD) patients, and 10 Alzheimer's disease (AD) and mild cognitive impairment patients. Their results showed promising accuracy in ALS onset discrimination, thereby introducing a quick and sensitive procedure to improve the diagnosis as well as the monitoring of therapeutic and rehabilitative processes in ALS (Carlomagno et al., 2020). A noninvasive method based on the SERS of tears as a tool for diagnosing neurodegenerative pathologies such as AD and other forms of dementia (AD) was proposed by Cennamo and coworkers (Cennamo et al., 2020). They were able to differentiate the spectra acquired from tears collected from AD subjects, healthy subjects and subjects with ascertained mild cognitive impairment symptoms.

There are numerous organisms that live in and on our bodies causing respiratory infections, spreading through respiratory secretions, and shedding in nasal secretions and saliva samples. As a result, nasal fluid and saliva have become useful clinical samples for diagnosing infectious diseases and have been explored by many researchers. A method for the detection of nonstructural protein 1 (NS1) from the SERS spectra of adulterated saliva using the artificial neural network (ANN) was developed by Othman et al. (2018). The ANN was used to distinguish the SERS spectra of saliva and saliva adulterated with NS1 by illuminating it with a 785-nm laser source. A total of 128 spectra were analyzed, with each spectrum containing 1801 Raman shifts. Later, the same group aimed to explore the effect of the number of hidden nodes in the ANN topology and the PCA termination criterion on the performance of the PCA-SCG-ANN classifier for detecting NS1 from the SERS spectra of the saliva of subjects (Othman et al., 2017). They evaluated the performance of 42 classifier models and found out that the EOC criteria paired with the ANN topology of 13 hidden nodes outperformed the other models, with 91% accuracy, 94% precision, 94% sensitivity, and 96% specificity. Later, in 2019 they investigated the various ELM-RBF classifier models in combination with the PCA termination criteria for classifying the NS1 salivary SERS spectra. The performance of the ELM-RBF classifier models is found to be dependent on the number of principal components and kernel parameters, with the conclusion that the CPV- and EOC-ELM-RBF classifier models outperform the Scree-ELM-RBF classifier models (Othman et al., 2019).

Another work in the field of detection of pyocyanin (PYO), a metabolite specific for *Pseudomonas aeruginosa*, which is currently considered a biomarker for life-threatening *Pseudomonas* infections, in saliva done by employing SERS combined with a microfluidic platform was also reported (Žukovskaja et al., 2017). Saliva collected from three individuals with pneumonia was used to successfully detect PYO down to a concentration of 10 M for two of the tested samples and 25 M for the third, indicating the possibility of detection of PYO directly from complex matrices. In 2019 a SERS-based diagnostic method

for oseltamivir-resistant pH1N1/H275Y mutant virus found in human nasal and saliva samples was developed by Eom et al. Au NPs with OHT functionalization bound to the mutant virus, and strong SERS signals were obtained only in the presence of the mutant virus, and detection at a low concentration of 1 PFU was obtained using the developed method, hence proving its use for the practical diagnosis of pH1N1/H275Y mutant virus infection (Eom et al., 2019).

Saliva plays a very important role when considering forensic applications. Saliva evidence is not as common as blood or semen, but it can still be useful in cases involving sexual assault, bite marks, and even envelopes since DNA can be extracted from saliva (Dziegelewski et al., 2002). The ability of SERS to identify and quantify drugs and their metabolites in saliva has recently been investigated. The extreme sensitivity of SERS, the ability to measure very small samples, and the ability to identify molecular structures of drugs using the rich vibrational information provided by Raman spectroscopy, all contributed to the expected success of this approach and hence proved its application in forensics (Farquharson et al., 2008).

Yang et al. presented a magnetically optimized SERS protocol for rapidly detecting trace drug–related biomarkers in saliva and fingerprints (Yang et al., 2015). The SERS substrate in this study were AuNPs-dotted magnetic nanocomposites stabilized and bound with IP6. The main observation in their work is that the SERS detection of CV in aqueous solution is reduced to 5 pM while that of nicotine in aqueous solution is reduced to 5 nM via a magnetic field-inducing effect. The LOD values for benzoylecgonine and cotinine in saliva were 29 ppb and 8.8 ppb, respectively, whereas the LOD reached 100 nM (17.6 ng mL^{-1}) for cotinine in fingerprints using the magnetically optimized SERS assay. A microfluidic flow-focusing device was presented by Andreou's group (Andreou et al., 2013) in which the transport and aggregation of SERS active silver nanoparticles could be explicitly controlled, allowing for the rapid detection of methamphetamine in saliva. The presence of methamphetamine in the sample was determined at concentrations as low as 10 nM, and the results obtained in their work provide evidence for a reproducible and rapid detection method that could be realized in the form of a cartridge-based microfluidic system that can detect and identify narcotics in biological fluids in a matter of minutes.

10.2.3 Tears

Tears are a clear liquid secreted by the lacrimal glands found in the eyes of all land mammals, which helps in lubricating the eyes, removing irritants, and aiding the immune system. Biomarker molecules in tears diffuse directly from the blood, and their concentrations in the

blood are more closely correlated with concentrations in tears compared to other biofluids, which makes tears superior to other biological fluids such as sweat (Pankratov et al., 2016). Tears contain a wide range of components like proteins, peptides, lipids, metabolites, and electrolytes and possess unique merits in diagnosing specific ocular diseases such as dry eye syndrome, trachoma, glaucoma, keratoconus, and thyroid-associated orbitopathy and systematic disorders such as diabetes mellitus, cancer, systemic or multiple sclerosis, cystic fibrosis, Parkinson's disease, and sclerosis. Wearable sensing systems based on tear biofluid have been reported for a variety of analytes, including glucose and lactate, with the primary focus being on the incorporation of electrochemical sensors into contact lens–based platforms with integrated electronic components for direct measurements in basal tears (Yu et al., 2019). A number of tear-based sensors for continuous analyte monitoring have been developed. This includes:

1. Strip-based sensors, the first tear-based wearable devices, were developed by placing electrochemical sensors on flexible or stretchable strips (Kudo et al., 2006).
2. Contact lens–based sensors (Tseng et al., 2018) are an appealing platform for fabricating tear-based sensors because of their comfort, consistent yield of tear fluid, excellent oxygen permeability, and ability to provide accurate continuous monitoring.
3. The spring-like electrochemical sensor coated with a protective polysaccharide-based hydrogel material is another type of tear-based sensor (Kownacka et al., 2018).
4. Recently, eyeglasses-based tear biosensing systems (Sempionatto et al., 2019) were developed in which a microfluidic electrochemical detector was integrated into the nose bridge pad of the eyeglasses to monitor tear biomarkers noninvasively.

Over the last few decades, a large number of studies have been conducted to analyze the tear composition using conventional biochemical methods such as high-performance liquid chromatography, enzyme-linked immunosorbent assays, or ferric-reducing antioxidant power, allowing for a thorough characterization of this fluid (Fullard & Snyder, 1990). These traditional techniques have largely been replaced by optical spectroscopy methods, such as those based on Raman scattering, which offer many advantages like being less time consuming, not requiring specific sample preparation, and having high sensitivity and specificity. Raman spectroscopy and SERS have been used to study human tears, primarily in the diagnosis of eye diseases. Raman and SERS can be used to assess the global changes in tear composition caused by the pathological state in addition to the direct detection of biomarkers (Willcox, 2019).

The use of a plasmonic SERS Schirmer strip has been reported by Park et al. (2017) for rapid, label-free, and on-demand bioassays of

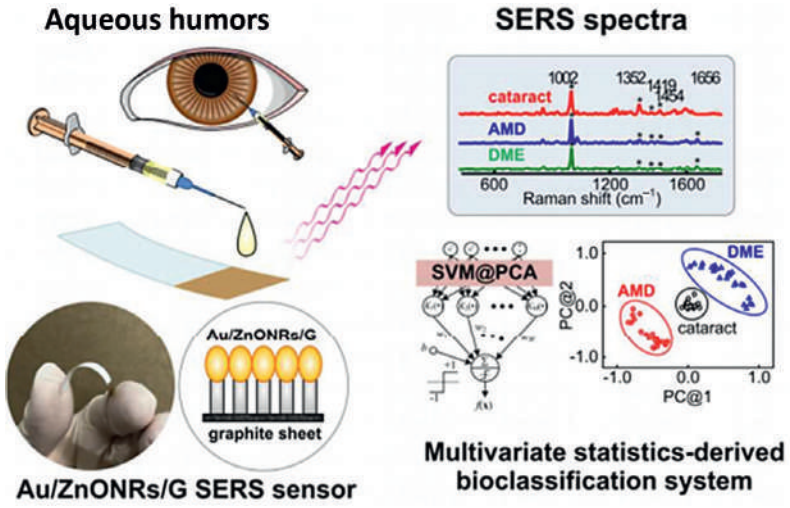

Figure 10.4. SERS sensor developed by Kim et al for identifying oxidative stress-induced age-related macular degeneration (AMD) and diabetic macular edema (DME) (Kim et al., 2017).

tear molecules. The diagnostic strip contains gold nanoislands that are directly and evenly formed on the top surface of cellulose fibers, allowing for efficient tear collection and also providing a plasmonic enhancement in SERS signals for tear molecule identification. Uric acid in human tears has been quantitatively detected at physiological levels using SERS (25–150 μM). In a work done by Leordean et al. they showed how SERS could be used to directly and reliably identify urea metabolic by-products in tears and fingerprints, using gold colloidal particulate films as active plasmonic substrates (Leordean et al., 2012). By combining the specificity and sensitivity, low cost and ease of use of the SERS method, the SERS substrate in the presence of alternative body fluids is a viable alternative for the development of advanced biosensors for the early detection of various kidney diseases.

Kim and coworkers (2017) presented a highly reproducible and practical SERS sensor for the detection of trace amounts of biofluids based on Au-decorated ZnO NR arrays grown on a graphite sheet (Au/ZnONRs/G). This was built in two stages: hydrothermal synthesis-induced growth of ZnO NRs on graphite sheets for nanostructure fabrication, followed by gold metallization on ZnONRs/G via e-beam evaporator for SERS functionalization. The performance of this Au/ZnONRs/G sensor was evaluated using human aqueous humors with cataract as well as two oxidative stress-induced eye diseases-age-related macular degeneration, and diabetic macular edema. The results showed that this sensor, which is supported by a multivariate statistics–derived bioclassification method, has great potential in POCT applications for identifying eye diseases (Fig. 10.4).

Later, the same group presented the fabrication of a monometallic SERS-functionalized paper platform using a screen-printing technique

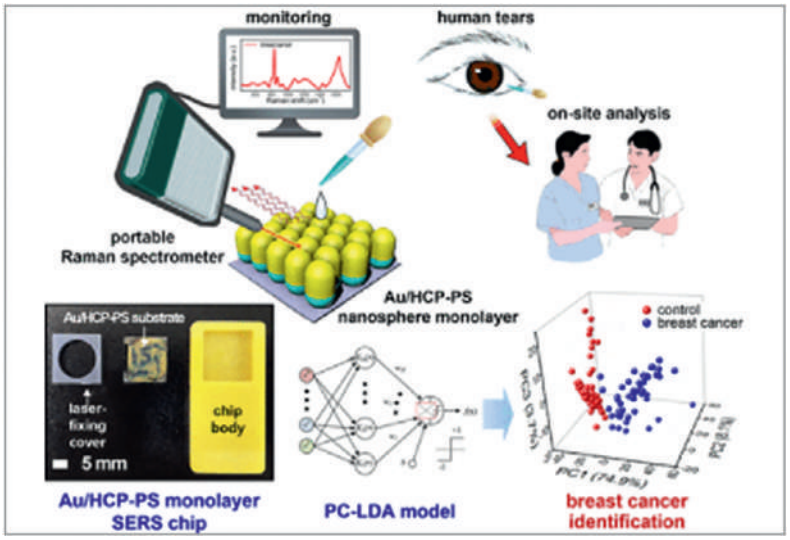

Figure 10.5. Schematic representation of the label-free SERS biosensor developed by Kim et al. for on-site breast cancer detection using human tears (Kim et al., 2020).

and a mixture of AuNPs and viscous ink. The SERS effect was optimized by varying the amount of AuNPs synthesized, and its reproducibility was confirmed by varying the viscosity of CMC-AuNP screen printing inks (Kim et al., 2016). The in vivo application of two representative ocular infectious diseases (conjunctivitis) revealed clear Raman peaks and SERS effects to aid in the rapid POC diagnosis of biofluids in clinics. In their previous studies, they have analyzed human tears and aqueous humors for various ocular diseases using different SERS substrates. However, although these SERS substrates showed both high SERS-EF and reproducibility, most SERS substrates showed low uniformity. Hence, to overcome these, they presented a novel strategy and progress in the highly sensitive detection and quantification of tear fluids, as well as their potential application for breast cancer detection (Kim et al., 2020). The high discriminatory power of a portable Raman spectrometer device with a well-aligned Au/HCP-PS monolayer SERS biosensor supported by a multivariate statistics–based identification method suggested that asymptomatic breast cancer could be detected or predicted from human tear fluids, indicating that this noninvasive, real-time, label-free screening technology can be used immediately for the early detection of asymptomatic tumors, thereby decreasing the likelihood of tumor recurrence (Fig. 10.5).

In a study conducted by Hu et al they systematically compared two Raman techniques with improved sensitivity for detecting microliter quantities of whole human tears: drop-coating deposition Raman spectroscopy (DCDRS) and SERS. The results show that DCDRS is useful for detecting some highly abundant components in whole tears,

while SERS is useful for detecting some less abundant components (Hu et al., 2014). A combination of both techniques can be used to extract multiparameter information for a systematic analysis of clinical tears, the use of which can be extended to other body fluids according to their findings.

Cennamado's group investigated SERS's potential in the study of human tears. In total, 26 tear samples were analyzed using an AuNP–based substrate, and the SERS enhancement factor was calculated using rhodamine 6G water solutions. When the SERS signal was compared to the one obtained by using conventional Raman spectroscopy, a SERS enhancement factor of about 4×10^3 was calculated. A direct comparison of SERS and Raman response of human tears has also been reported, clearly indicating an increase in signal intensity in the case of SERS when compared to conventional Raman spectroscopy (Camerlingo et al., 2019). In 2020 the same group proposed a noninvasive method based on the SERS of tears as a tool for diagnosing neurodegenerative pathologies such as Alzheimer Disease (AD) and other forms of dementia. Even if specific biomarkers of AD could not be distinguished, the global SERS response reflects small but intriguing changes in tear composition that can be attributed to altered levels of specific pathological and disease-stimulated substances. Their findings were very encouraging, with intriguing implications for medical applications such as clinical diagnosis support and discrimination of AD from other forms of dementia (Cennamo et al., 2020).

The study conducted by Chois' group aimed to evaluate the potential of optical DCD-SERS detection as a diagnostic tool for adenoviral conjunctivitis using human tear fluids. Their findings revealed that the DCD-SERS Raman technique provides high chemical structure sensitivity without the need for additional tagging or chemical modification. Because of this benefit, DCD-SERS Raman technology is an excellent tool for the early detection of adenoviral conjunctivitis (Choi et al., 2014). In another work, Narasimhan et al created a cost-effective, scalable, and flexible plasmonic metasurface-based platform for label-free SERS using a simple biomimetic fabrication process (Narasimhan et al., 2020). The flexible metasurface (flex-MS) is a modular system consisting of a dense array of tightly coupled Au nanodisks in which Au nanoholes are separated by sub-10-nm SiO_2 nanogaps in a MIM configuration on flexible PDMS thin films. Finally, they demonstrated the label-free detection of UA in both artificial tear buffer and whole human tear samples using flex-MS as a broadband diagnostic platform and also compared the flex-MS's performance with that of a commercial UA measurement assay and found that they are in good agreement.

10.3 Challenges and future perspectives

In recent times there has been a huge increase in the use of wearable sensors in the biomedical field, which include monitoring the patient's body temperature, heart rate, pressure, and oxygen saturation and even the detection of biomarkers and metabolites. Saliva, sweat, and tear-based wearable sensors are of particular importance because of the presence of important biomarkers that can be used to assess health status by continuously monitoring the changes in the metabolic process. Some of the significant challenges faced by the biological fluid–based wearable sensors are material biocompatibility, efficient energy usage, acceptable performance, comfort, and practical usage model. The concentration of many important biomarkers present in the sweat, saliva, and tears is much lower as compared to that in the blood, thereby requiring a highly sensitive sensor for accurate monitoring, which is another important task in the case of the biological fluid base wearable sensors. Biological fluids consist of a rich matrix of constituents that can easily be contaminated by means of external factors and the presence of a high concentration of proteins in these, especially saliva, can lead to rapid biofouling of the oral cavity along with the food debris through nonspecific adsorption at the transducer surface. On the other hand, wearable sensors placed in close contact with the body are easily accessible and do not suffer to the same extent from biofouling. More importantly, they are subjected to short-term use (hours or days rather than many years for implants). Despite these challenges, it is clear that the wearable biological fluid–based sensors play a prominent part in providing the patients and clinicians with abundant information regarding health conditions and making it possible for a home-based therapeutic strategy and health care, causing a significant improvement in the quality of life and life expectancy of the people. This also overcomes the limitations of the conventional system of finger pricking.

SERS is a powerful spectral characterization technique, offering numerous advantages, including high sensitivity, specificity, efficiency, and noninvasiveness, and has been widely used in trace and rapid investigations of body fluids. SERS analysis of biological fluids like sweat, saliva, and tears, in particular, provides noninvasive, sensitive, and reliable recognition of various cancers, diseases, and illicit drugs, allowing for a more convenient and painless diagnosis approach. In addition to this, there are still a few scientific issues to be stated. SERS methodologies are expected to be more expensive for a possible routine clinical application. Similarly, drying the sample prior to analysis results in a loss of salivary component quality. The major challenges with SERS substrate include the need for intimate contact

between the enhancing surface and the analyte; degradation of the substrate over time, resulting in a decrease in signal; limited reusability of the substrates; and problems with homogeneity and reproducibility of the SERS signal within a substrate. In order to overcome these challenges SERS substrate optimization is required, particularly to improve substrate stability, reproducibility, and specificity, which are critical for quantitative detections. With perseverance, SERS, when combined with advancements in nanotechnology, optical technology, biochemical methodology, and data processing strategy, will have a better chance of being used in noninvasive clinical diagnosis, human health promotion, and disease prevention, demonstrating its superior capabilities in the next generation.

10.4 Summary

Biosensors that noninvasively analyze body fluids such as saliva, sweat, and tears are of greater importance recently because of their ability to assess the health status by continuously monitoring the changes in metabolic processes. Among various types of biosensor platforms, SERS-based biosensors have many advantages over conventional techniques, including lower detection limits, lower cost, simple design, ease of manipulation, low consumption of costly and/or toxic reagents, and, most importantly, improved sensitivity even at trace concentration levels, allowing measurement even with tiny amounts of samples. The SERS analysis of biological fluids such as sweat, saliva, and tears, in particular, provides noninvasive, sensitive, and reliable identification of various cancers, diseases, and illicit drugs, allowing for a more convenient and painless diagnosis approach. Recent advances in the field of SERS-based biological fluid sensors and their promising impact on noninvasive and continuous health monitoring aspects are focused on in this chapter. The most recent sensor advancements for detecting various biomarkers, an analysis of each biomarker, the fabrication method for the sensors, and the practical applications of the developed sensors for biochemical sensing and metabolites are thoroughly reviewed.

Acknowledgment

Authors wish to acknowledge DST-INSPIRE fellowship and DST-WTI (Ref No: DST/TMD-EWO/ WTI/2K19/EWFH/2019/273(G) dated 20-08-2020), Government of India, and also PSG Sons and Charities, Coimbatore for the support.

References

Al-Ogaidi, I., Gou, H., Al-kazaz, A.K.A., Aguilar, Z.P., Melconian, A.K., Zheng, P., Wu, N., 2014. A gold@silica core-shell nanoparticle-based surface-enhanced Raman scattering biosensor for label-free glucose detection. Anal. Chim. Acta 811, 76–80. https://doi.org/10.1016/j.aca.2013.12.009.

Andreou, C., Hoonejani, M.R., Barmi, M.R., Moskovits, M., Meinhart, C.D., 2013. Rapid detection of drugs of abuse in saliva using surface enhanced Raman spectroscopy and microfluidics. ACS Nano 7 (8), 7157–7164. https://doi.org/10.1021/nn402563f.

Arabi, M., Ostovan, A., Zhang, Z., Wang, Y., Mei, R., Fu, L., Wang, X., Ma, J., Chen, L., 2021. Label-free SERS detection of Raman-Inactive protein biomarkers by Raman reporter indicator: Toward ultrasensitivity and universality. Biosens. Bioelectron. 174, 112825. https://doi.org/10.1016/j.bios.2020.112825.

Bandodkar, A.J., Wang, J., 2014. Non-invasive wearable electrochemical sensors: A review. Trends Biotechnol. 32 (7), 363–371. https://doi.org/10.1016/j.tibtech.2014.04.005.

Ben-Aryeh, H., Cohen, M., Kanter, Y., Szargel, R., Laufer, D., 1988. Salivary composition in diabetic patients. J. Diabet. Complications 2 (2), 96–99. https://doi.org/10.1016/0891-6632(88)90011-6.

Botta, R., Rajanikanth, A., Bansal, C., 2016. Silver nanocluster films for glucose sensing by surface enhanced Raman scattering (SERS). Sensing and Bio-Sensing Research 9, 13–16. https://doi.org/10.1016/j.sbsr.2016.05.001.

Camerlingo, C., Lisitskiy, M., Lepore, M., Portaccio, M., Montorio, D., Prete, S., Cennamo, G., 2019. Characterization of human tear fluid by means of surface-enhanced Raman spectroscopy. Sensors 19 (5), 1177. https://doi.org/10.3390/s19051177.

Carlomagno, C., Banfi, P.I., Gualerzi, A., Picciolini, S., Volpato, E., Meloni, M., Lax, A., Colombo, E., Ticozzi, N., Verde, F., Silani, V., Bedoni, M., 2020. Human salivary Raman fingerprint as biomarker for the diagnosis of amyotrophic lateral sclerosis. Sci. Rep. 10 (1). https://doi.org/10.1038/s41598-020-67138-8.

Carlomagno, C., Bertazioli, D., Gualerzi, A., Picciolini, S., Banfi, P.I., Lax, A., Messina, E., Navarro, J., Bianchi, L., Caronni, A., Marenco, F., Monteleone, S., Arienti, C., Bedoni, M., 2021. COVID-19 salivary Raman fingerprint: Innovative approach for the detection of current and past SARS-CoV-2 infections. Sci. Rep. 11 (1). https://doi.org/10.1038/s41598-021-84565-3.

Ceja-Fdez, A., López-Luke, T., Torres-Castro, A., Wheeler, D.A., Zhang, J.Z., De La Rosa, E, 2014. Glucose detection using SERS with multi-branched gold nanostructures in aqueous medium. RSC Adv. 4 (103), 59233–59241. https://doi.org/10.1039/c4ra11055b.

Cennamo, G., Montorio, D., Morra, V.B., Criscuolo, C., Lanzillo, R., Salvatore, E., Camerlingo, C., Lisitskiy, M., Delfino, I., Portaccio, M., Lepore, M., 2020. Surface-enhanced Raman spectroscopy of tears: Toward a diagnostic tool for neurodegenerative disease identification. J. Biomed. Opt. 25 (8). http://www.spie.org/x866.xml.

Chawarski, M.C., Fiellin, D.A., O'Connor, P.G., Bernard, M., Schottenfeld, R.S, 2007. Utility of sweat patch testing for drug use monitoring in outpatient treatment for opiate dependence. J. Subst. Abuse Treat. 33 (4), 411–415. https://doi.org/10.1016/j.jsat.2007.03.004.

Chen, J., Qin, G., Chen, Q., Yu, J., Li, S., Cao, F., Yang, B., Ren, Y., 2015. A synergistic combination of diatomaceous earth with Au nanoparticles as a periodically ordered, button-like substrate for SERS analysis of the chemical composition of eccrine sweat in latent fingerprints. J. Mater. Chem. C 3 (19), 4933–4944. https://doi.org/10.1039/c5tc00717h.

Cheng,, Y.-S.L., Rees, T., Wright, J, 2014. A review of research on salivary biomarkers for oral cancer detection. Clin. Transl. Med. 3 (1). https://doi.org/10.1186/2001-1326-3-3.

Choi, S., Moon, S.W., Shin, J.H., Park, H.K., Jin, K.H., 2014. Label-free biochemical analytic method for the early detection of adenoviral conjunctivitis using human tear biofluids. Anal. Chem. 86 (22), 11093–11099. https://doi.org/10.1021/ac5025478.

Cone, E.J., Hillsgrove, M.J., Jenkins, A.J., Keenan, R.M., Darwin, W.D., 1994. Sweat testing for heroin, cocaine, and metabolites. J. Anal. Toxicol. 18 (6), 298–305. https://doi.org/10.1093/jat/18.6.298.

Corrie, S.R., Coffey, J.W., Islam, J., Markey, K.A., Kendall, M.A.F., 2015. Blood, sweat, and tears: Developing clinically relevant protein biosensors for integrated body fluid analysis. Analyst 140 (13), 4350–4364. https://doi.org/10.1039/c5an00464k.

De Giovanni, N., Fucci, N., 2013. The current status of sweat testing for drugs of abuse: A review. Curr. Med. Chem. 20 (4), 545–561. https://doi.org/10.2174/092986713804910139.

Devaraj, S.D., 2013. Salivary biomarkers-a review. J. Pharm. Sci. Res. 5 (10), 210–212.

Dziegelewski, M., Simich, J.P., Rittenhouse-Olson, K., 2002. Use of a Y chromosome probe as an aid in the forensic proof of sexual assault. J. Forensic Sci. 47 (3), 601–604.

Eom, G., Hwang, A., Kim, H., Yang, S., Lee, D.K., Song, S., Ha, K., Jeong, J., Jung, J., Lim, E.K., Kang, T., 2019. Diagnosis of Tamiflu-resistant influenza virus in human nasal fluid and saliva using surface-enhanced Raman scattering. ACS Sensors 4 (9), 2282–2287. https://doi.org/10.1021/acssensors.9b00697.

Farquharson, S., Gift, A., Shende, C., Inscore, F., Ordway, B., Farquharson, C., Murren, J., 2008. Surface-enhanced Raman spectral measurements of 5-fluorouracil in saliva. Molecules 13 (10), 2608–2627. https://doi.org/10.3390/molecules13102608.

Farvid, M.S., Ding, M., Pan, A., Sun, Q., Chiuve, S.E., Steffen, L.M., Willett, W.C., Hu, F.B., 2014. Dietary linoleic acid and risk of coronary heart disease: A systematic review and meta-analysis of prospective cohort studies. Circulation 130 (18), 1568–1578. https://doi.org/10.1161/CIRCULATIONAHA.114.010236.

Fullard, R.J., Snyder, C., 1990. Protein levels in nonstimulated and stimulated tears of normal human subjects. Invest. Ophthalmol. Vis. Sci. 31 (6), 1119–1126.

Haeckel, R., Hänecke, 1993. The application of saliva, sweat and tear fluid for diagnostic purposes, 51. Annales de biologie clinique, pp. 903–910.

Heikenfeld, J., 2016. Non-invasive analyte access and sensing through eccrine sweat: Challenges and outlook circa 2016. Electroanalysis 28 (6), 1242–1249. https://doi.org/10.1002/elan.201600018.

Hu, S., Jiang, Y., Wu, Y., Guo, X., Ying, Y., Wen, Y., Yang, H., 2020. Enzyme-free tandem reaction strategy for surface-enhanced Raman scattering detection of glucose by using the composite of Au nanoparticles and porphyrin-based metal-organic framework. ACS Appl. Mater. Interfaces 12 (49), 55324–55330. https://doi.org/10.1021/acsami.0c12988.

Hu, P., Zheng, X.S., Zong, C., Li, M.H., Zhang, L.Y., Li, W., Ren, B., 2014. Drop-coating deposition and surface-enhanced Raman spectroscopies (DCDRS and SERS) provide complementary information of whole human tears. Journal of Raman Spectroscopy,, 45, pp. 565–573.

Jadoon, S., Karim, S., Akram, M.R., Kalsoom,, K.A., Zia, M.A., Siddiqi, A.R., Murtaza, G., 2015. Recent developments in sweat analysis and its applications. International Journal of Analytical Chemistry 2015. https://doi.org/10.1155/2015/164974.

Jurado-Gámez, V.B., Santiago, M., Priego-Capote, F., Castro, M.D., 2014. Method of classification, diagnosis and monitoring of individuals at risk of lung cancer, TRUCO Newsletter. No. 13.

Kim, S., Kim, T.G., Lee, S.H., Kim, W., Bang, A., Moon, S.W., Song, J., Shin, J.H., Yu, J.S., Choi, S., 2020. Label-free surface-enhanced Raman spectroscopy biosensor for on-site breast cancer detection using human tears. ACS Appl. Mater. Interfaces 12 (7), 7897–7904. https://doi.org/10.1021/acsami.9b19421.

Kim, W., Lee, S.H., Kim, S.H., Lee, J.C., Moon, S.W., Yu, J.S., Choi, S., 2017. Highly reproducible Au-decorated ZnO nanorod array on a graphite sensor for classification of human aqueous humors. ACS Appl. Mater. Interfaces 9 (7), 5891–5899. https://doi.org/10.1021/acsami.6b16130.

Kim, W.S., Shin, J.H., Park, H.K., Choi, S., 2016. A low-cost, monometallic, surface-enhanced Raman scattering-functionalized paper platform for spot-on bioassays. Sens. Actuators B 222, 1112–1118. https://doi.org/10.1016/j.snb.2015.08.030.

Kleinman, S.L., Ringe, E., Valley, N., Wustholz, K.L., Phillips, E., Scheidt, K.A., Schatz, G.C., Van Duyne, R.P., 2011. Single-molecule surface-enhanced Raman spectroscopy of crystal violet isotopologues: Theory and experiment. J. Am. Chem. Soc. 133 (11), 4115–4122. https://doi.org/10.1021/ja110964d.

Kownacka, A.E., Vegelyte, D., Joosse, M., Anton, N., Toebes, B.J., Lauko, J., Buzzacchera, I., Lipinska, K., Wilson, D.A., Geelhoed-Duijvestijn, N., Wilson, C.J., 2018. Clinical evidence for use of a noninvasive biosensor for tear glucose as an alternative to painful finger-prick for diabetes management utilizing a biopolymer coating. Biomacromolecules 19 (11), 4504–4511. https://doi.org/10.1021/acs.biomac.8b01429.

Kudo, H., Sawada, T., Kazawa, E., Yoshida, H., Iwasaki, Y., Mitsubayashi, K., 2006. A flexible and wearable glucose sensor based on functional polymers with Soft-MEMS techniques. Biosens. Bioelectron. 22 (4), 558–562. https://doi.org/10.1016/j.bios.2006.05.006.

Lai, Y., Schlücker, S., Wang, Y., 2018. Rapid and sensitive SERS detection of the cytokine tumor necrosis factor alpha (tnf-α) in a magnetic bead pull-down assay with purified and highly Raman-active gold nanoparticle clusters. Anal. Bioanal.Chem. 410 (23), 5993–6000. https://doi.org/10.1007/s00216-018-1218-0.

Lee, J.M., Garon, E., Wong, D.T., 2009. Salivary diagnostics. Orthodontics and Craniofacial Research 12 (3), 206–211. https://doi.org/10.1111/j.1601-6343.2009.01454.x.

Lee, Y.H., Kim, J.H., Zhou, H., Kim, B.W., Wong, D.T., 2012. Salivary transcriptomic biomarkers for detection of ovarian cancer: For serous papillary adenocarcinoma. J. Mol. Med. 90 (4), 427–434. https://doi.org/10.1007/s00109-011-0829-0.

Lee, Y.H., Wong, D.T., 2009. Saliva: An emerging biofluid for early detection of diseases. Am. J. Dent. 22 (4), 241–248.

Leordean, C., Canpean, V., Astilean, S., 2012. Surface-enhanced Raman scattering (SERS) analysis of urea trace in urine, fingerprint, and tear samples. Spectrosc. Lett. 45 (8), 550–555. https://doi.org/10.1080/00387010.2011.649439.

Lin, D., Yang, S.W., Hsieh, C.L., Hsu, K.J., Gong, T., Wu, Q., Qiu, S., Feng, S., Kong, K.V., 2021. Tandem quantification of multiple carbohydrates in saliva using surface-enhanced Raman spectroscopy. ACS Sensors 6 (3), 1240–1247. https://doi.org/10.1021/acssensors.0c02533.

Liu, H., Dai, E., Xiao, R., Zhou, Z., Zhang, M., Bai, Z., Shao, Y., Qi, K., Tu, J., Wang, C., Wang, S., 2021. Development of a SERS-based lateral flow immunoassay for rapid and ultra-sensitive detection of anti-SARS-CoV-2 IgM/IgG in clinical samples. Sens. Actuators B 329, 129196. https://doi.org/10.1016/j.snb.2020.129196.

Lu, Y., Wu, C., You, R., Wu, Y., Shen, H., Zhu, L., Feng, S., 2018. Superhydrophobic silver film as a SERS substrate for the detection of uric acid and creatinine. Biomedical Optics Express 9 (10), 4988. https://doi.org/10.1364/BOE.9.004988.

Malon, R.S.P., Sadir, S., Balakrishnan, M., Córcoles, E.P., 2014. Saliva-based biosensors: Noninvasive monitoring tool for clinical diagnostics. Biomed. Res. Int. 2014. https://doi.org/10.1155/2014/962903.

Mosier-Boss, P.A., 2017. Review of SERS substrates for chemical sensing. Nanomaterials 7 (6). https://doi.org/10.3390/nano7060142.

Mukhopadhyay, S.C., 2015. Wearable sensors for human activity monitoring: A review. IEEE Sensors J. 15 (3), 1321–1330. https://doi.org/10.1109/JSEN.2014.2370945.

Narasimhan, V., Siddique, R.H., Siddique, R.H., Park, H., Choo, H., Choo, H., 2020. Bioinspired disordered flexible metasurfaces for human tear analysis using broadband surface-enhanced Raman scattering. ACS Omega 5 (22), 12915–12922. https://doi.org/10.1021/acsomega.0c00677.

Othman, N.H., Khuan, L.Y., Radzol, A.R.M., Mansor, W, 2018. Detection of NS1 from SERS spectra of adulterated saliva using ANN. Adv. Sci. Lett. 1138–1142. https://doi.org/10.1166/asl.2018.10703.

Othman, N.H., Lee, K.Y., Radzol, A.R.M., Mansor, W., 2017. PCA-SCG-ANN for detection of non-structural protein 1 from SERS salivary spectra. In Lecture Notes in Computer Science (including subseries Lecture Notes in Artificial Intelligence and Lecture Notes in Bioinformatics), 10192. Springer Verlag, pp. 424–433.

Othman, N.H., Lee, K.Y., Radzol, A.R.M., Mansor, W., 2019. Optimal ELM-RBF model and SERS analysis of saliva for classification of NS1. In: Proceedings of the Annual International Conference of the IEEE Engineering in Medicine and Biology Society, EMBS. Institute of Electrical and Electronics Engineers Inc, pp. 3551–3554.

Panchbhai, A.S., 2012. Correlation of salivary glucose level with blood glucose level in diabetes mellitus. Journal of Oral and Maxillofacial Research. https://doi.org/10.5037/jomr.2012.3303.

Pang, S., Yang, T., He, L., 2016. Review of surface enhanced Raman spectroscopic (SERS) detection of synthetic chemical pesticides. TrAC—Trends in Analytical Chemistry 85, 73–82. https://doi.org/10.1016/j.trac.2016.06.017.

Pankratov, D., González-Arribas, E., Blum, Z., Shleev, S., 2016. Tear based bioelectronics. Electroanalysis 28 (6), 1250–1266. https://doi.org/10.1002/elan.201501116.

Park, M., Jung, H., Jeong, Y., Jeong, K.H., 2017. Plasmonic Schirmer strip for human tear-based gouty arthritis diagnosis using surface-enhanced Raman scattering. ACS Nano 11 (1), 438–443. https://doi.org/10.1021/acsnano.6b06196.

Rathnayake, N., Åkerman, S., Klinge, B., Lundegren, N., Jansson, H., Tryselius, Y., Sorsa, T., Gustafsson, A., Goletti, D., 2013. Salivary biomarkers for detection of systemic diseases. PLoS One 8 (4), e61356. https://doi.org/10.1371/journal.pone.0061356.

Sato, K., Kang, W.H., Saga, K., Sato, K.T., 1989. Biology of sweat glands and their disorders. I. Normal sweat gland function. J. Am. Acad. Dermatol. 20 (4), 537–563. https://doi.org/10.1016/S0190-9622(89)70063-3.

Sempionatto, J.R., Brazaca, L.C., García-Carmona, L., Bolat, G., Campbell, A.S., Martin, A., Tang, G., Shah, R., Mishra, R.K., Kim, J., Zucolotto, V., Escarpa, A., Wang, J., 2019. Eyeglasses-based tear biosensing system: Non-invasive detection of alcohol, vitamins and glucose. Biosens. Bioelectron. 137, 161–170. https://doi.org/10.1016/j.bios.2019.04.058.

Sofi, M.S., Hamid, A., Bhat, S.U., 2020. SARS-CoV-2: A critical review of its history, pathogenesis, transmission, diagnosis and treatment. Biosafety and health, 2(4), 217–225. https://doi.org/10.1016/j.bsheal.2020.11.002.

Tseng, R., Chen, C.-C., Hsu, S.-M., Chuang, H.-S., 2018. Contact-lens biosensors. Sensors 18 (8), 2651. https://doi.org/10.3390/s18082651.

Van Haeringen, N.J., 1981. Clinical biochemistry of tears. Surv. Ophthalmol. 26 (2), 84–96. https://doi.org/10.1016/0039-6257(81)90145-4.

Wang, X., Kaczor-Urbanowicz, K.E., Wong, D.T.W., 2017. Salivary biomarkers in cancer detection. Med. Oncol. 49 (352). https://doi.org/10.1007/s12032-016-0863-4.

Willcox, M.D.P., 2019. Tear film, contact lenses and tear biomarkers. Clinical and Experimental Optometry 102 (4), 350–363. https://doi.org/10.1111/cxo.12918.

Wong, D.T., Zhang, L., Farrell, J., Zhou, H., Elashoff, D., Gao, K., Paster, B., 2009. Salivary biomarkers for pancreatic cancer detection. J. Clin. Oncol. 4630. –4630 https://doi.org/10.1200/jco.2009.27.15_suppl.4630.

Wong, D.T, Zhang, L, Xiao, H, Zhou, H., 2017. U.S. Patent No. 9,689,039. DC: U.S. Patent and Trademark Office. U.S. Patent, Washington.

Wu, L., Wang, Z., Zong, S., Cui, Y., 2014. Rapid and reproducible analysis of thiocyanate in real human serum and saliva using a droplet SERS-microfluidic chip. Biosens. Bioelectron. 62, 13–18. https://doi.org/10.1016/j.bios.2014.06.026.

Yang, T., Guo, X., Wang, H., Fu, S., wen, Y., Yang, H., 2015. Magnetically optimized SERS assay for rapid detection of trace drug-related biomarkers in saliva and fingerprints. Biosens. Bioelectron. 68, 350–357. https://doi.org/10.1016/j.bios.2015.01.021.

Yeh, C.K., Christodoulides, N.J., Floriano, P.N., Miller, C.S., Ebersole, J.L., Weigum, S.E., McDevitt, J., Redding, S.W., 2010. Current development of saliva/oral fluid-based diagnostics. Tex. Dent. J. 127 (7), 651–661.

Yu, H., Sun, J., 2020. Sweat detection theory and fluid driven methods: A review. Nanotechnology and Precision Engineering 3 (3), 126–140. https://doi.org/10.1016/j.npe.2020.08.003.

Yu, L., Yang, Z., An, M., 2019. Lab on the eye: A review of tear-based wearable devices for medical use and health management. BioScience Trends 13 (4), 308–313. https://doi.org/10.5582/bst.2019.01178.

Zamora-Mendoza, B.N., Espinosa-Tanguma, R., Ramírez-Elías, M.G., Cabrera-Alonso, R., Montero-Moran, G., Portales-Pérez, D., Rosales-Romo, J.A., Gonzalez, J.F., Gonzalez, C., 2019. Surface-enhanced Raman spectroscopy: A non invasive alternative procedure for early detection in childhood asthma biomarkers in saliva. Photodiagn. Photodyn. Ther. 27, 85–91. https://doi.org/10.1016/j.pdpdt.2019.05.009.

Zhang, C.Z., Cheng, X.Q., Li, J.Y., Zhang, P., Yi, P., Xu, X., Zhou, X.D., 2016. Saliva in the diagnosis of diseases. International Journal of Oral Science 8 (3), 133–137. https://doi.org/10.1038/ijos.2016.38.

Zhang, L., Xiao, H., Karlan, S., Zhou, H., Feng, Z., Elashoff, D., Wong T.D., 2010. Salivary biomarkers for breast cancer detection. 2726–2726. https://doi.org/10.1158/1538-7445.AM10-2726.

Zheng P., Li, M., Jurevic, R., Cushing, S.K., Liu, Y., Wu, N., 2015. A gold nanohole array based surface-enhanced Raman scattering biosensor for detection of silver (I) and mercury (II) in human saliva. Nanoscale 7(25), 11005-11012. https://doi.org/10.1039/C5NR02142A.

Žukovskaja, O., Jahn, I.J., Weber, K., Cialla-May, D., Popp, J., 2017. Detection of *Pseudomonas aeruginosa* metabolite pyocyanin in water and saliva by employing the SERS technique. Sensors (Switzerland) 17 (8). https://doi.org/10.3390/s17081704.

11

Nanomaterials-based flexible electrochemical sensors for health care monitoring

A.M.V. Mohan [a] **and A.M. Starvin** [b]

[a] *Electrodics & Electrocatalysis Division, CSIR-Central Electrochemical Research Institute (CECRI), Karaikudi, India.* [b] *Department of Chemistry, Christian College, Kattakada, Thiruvananthapuram, India*

11.1 Introduction

The existing health care management processes necessitate patients to reach hospitals, and the clinical diagnosis is mainly associated with blood analysis (Bandodkar & Wang, 2014). Invasive, repetitive blood sampling is painful and cumbersome for infants and elderly people (Bandodkar et al., 2016b). Also, blood analysis often suffers from delayed diagnosis and treatment that adversely causes serious health problems. Hence conducting point-of-care testing (POCT) at or near the patient site is crucial for improving the therapeutic turnaround time and the efficiency of treatment and therapy (Nambiar & Mohan, 2021). POCT devices are portable or handheld meters capable of providing rapid, real-time information directly by using biofluids without depending on pretreatment or sophisticated instruments (Heikenfeld et al., 2018). POCT analysis can be carried out by untrained personnel in the home, hospital, field, ambulance, or critical care unit. The recent advancements in flexible electronics provide continuous point-of-care analysis noninvasively using other biofluids like interstitial fluid (ISF), sweat, saliva, and tear fluid (Bocchetta et al., 2020; Mohan et al., 2020). These wearable devices can replace invasive blood analysis and provide real-time data on the health and fitness level of individuals (Ray et al., 2019).

The majority of the existing health care–monitoring wearable devices are focused on monitoring physical parameters such as body temperature, blood pressure, blood oxygenation, heart rate, pulse rate, electrocardiogram, and electroencephalogram signals. The tracking of the physiological parameters alone is insufficient to comprehend the detailed health conditions of the human body (Gubala et al., 2012).

Nanomaterials for Sensing and Optoelectronic Applications. DOI: https://doi.org/10.1016/B978-0-12-824008-3.00010-2

The estimation of chemical constituents from body fluids delivers vital information about the underlying diseases of individuals, and these chemical species are called biomarkers. Biofluids consist of several metabolites, electrolytes, amino acids, proteins, enzymes, and other nutrients. Colorimetric sensors provide rapid detection of multiple analytes in a single platform, including gases and vapors. But such devices suffer from a deprived limit of detection, poor reproducibility, and complicated data collection and analytics. Electrochemical sensors provide rapid, sensitive, and selective detection of biomarkers with minimal power consumption and can be easily miniaturized for various applications. Recently, electrochemical sensors have been used for the analysis of health care biomarkers (Aswini et al., 2014; Li et al., 2019), metabolites (Mohan et al., 2013), environmental pollutants (Mohan et al., 2014b), toxic heavy metals, pesticides (Mohan, 2020), nerve agents (Goud et al., 2020), drugs (Aswini et al., 2016; Mishra et al., 2020), and proteins (Mohan et al., 2015).

Nanostructured materials have received significant attention for use in developing highly sensitive electrochemical sensors owing to their ability to enhance electron transfer in electrode–electrolyte interfaces. Carbon nanomaterials like multiwalled and single-walled carbon nanotubes, graphene, and fullerenes have been extensively utilized due to their unique shape- and size-dependent chemical, physical, and electrochemical characteristics. The high surface area and surface-to-volume ratio of nanomaterials augment the sensitivity and increase the lowest limit of detection (Mohanan et al., 2018). Metal nanoparticles and metal nanowires also have shown tremendous electrochemical sensing abilities due to their ease of synthesis, functionalization, electrical conductivity, and electron transfer rates. Noble metal nanoparticles such as platinum (Pt), gold (Au), and silver (Ag) are highly stable during electrochemical reactions and show intact catalytic properties even under repetitive usage or high potential cycling (Mohan et al., 2014a). Parameters like stoichiometric compositions, crystal structure, crystallographic axis orientation, and surface properties collectively contribute to the catalytic, electrocatalytic, and electron transport kinetics of nanomaterials (Allibai Mohanan et al., 2016). The present chapter addresses the recent developments in flexible electrodes, electrode materials, and the role of nanostructured materials for improving the sensing capabilities of skin-based wearable biosensors, particularly for monitoring biofluids such as sweat, saliva, ISF, and tear fluid.

11.2 Wearable electrochemical sensors for sweat monitoring

Perspiration is a physiological process primarily correlated with the thermoregulation of the human body. Sweat production is associated

with the physical or emotional burden that stimulates the production of a neurotransmitter called acetylcholine (Kim et al., 2019). The neurotransmitter activates the sweat glands and causes the secretion of water-rich sweat fluid. Sweat consists of numerous biologically important biomarkers that provide imperative information about the underlying health and physiological status of the human body (Bandodkar & Wang, 2014b). The correlation of biomarkers' levels in blood and sweat is greatly related to various sweat-stimulating mechanisms. Intense physical activities enhance the body temperature and upset metabolic processes, which subsequently causes changes in sweat composition. Hence, continuous tracking of the dynamic variation in sweat is necessary for the precise analysis of the real-time health condition of the human body (Kim et al., 2018a).

11.2.1 Flexible sensors for electrolytes monitoring

During perspiration, metabolites, biomolecules, proteins, amino acids, hormones, peptides, and ions are excreted from the body. The partition mechanisms associated with sweat, after its secretion from endocrine glands, play a vital role in the sweat components and compositions (Baker, 2019). Sweat is carried to an epithelial surface by means of a dermal duct and the sodium–potassium pump effectively transports Na^+ and Cl^- ions between blood serum and the secretory coil. As a result, an osmotic pressure gradient (hypotonic to the serum) develops that drags fluid into the eccrine glands (Bariya et al., 2018). When sweat is transported via the sweat ducts, the reabsorption of Na^+ and Cl^- happens, and when the sweat rate increases, the rate of Na^+ secretion enhances than the reabsorption. Sodium is one of the major components in sweat; the assessment of its concentration provides critical information about electrolyte loss during ultraendurance activities. An abnormal Na^+ level in sweat indicates low blood plasma sodium concentration (hyponatremia) and dehydration. In addition, an unbalanced level of sweat sodium is clinically relevant, especially for diagnosing cystic fibrosis, a progressive genetic disorder rooted in the mutation of the transmembrane conductance regulator channel that predominantly affects lungs and other internal organs. Determining the specific concentration of Na^+ or Cl^- is typically utilized for its successful diagnosis. The failure of Cl^- reabsorption at the eccrine glands is leads to the devastation of the lungs and thus enhances the Cl^- concentration in sweat (Bear et al., 1992). Iontophoresis-based sweat sensing enables rapid screening and precise diagnosis of cystic fibrosis, particularly for newborn babies.

Developing epidermal sensors for biomarker monitoring requires specific wearable substrates and fabrication methods due to the distinctive mechanophysiology of the human skin. Intense research is

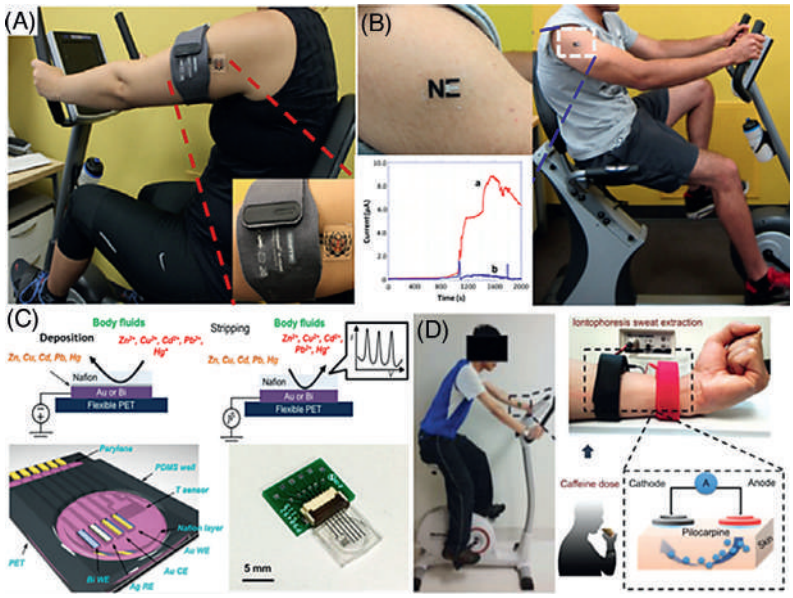

Figure 11.1. (A) Photograph showing real-time sweat sodium measurement during exercise activities (inset represents the zoomed image of a Na-ISE tattoo). (B) An "NE" lactate biosensor attached to a male volunteer's deltoid; response of the LOx- (*a*) and enzyme-free (*b*) tattoo biosensors during exercise activities. (C) Schematic representation of the concept of deposition and stripping on microelectrodes and the composition of the microsensor array for heavy metal analysis; optical image of a flexible sensor array integrated with a printed circuit board. (D) Image of a subject having an s-band drug sensing platform in a cycling exercise; schematic of iontophoresis-based sweat extraction (Fig. 11.1A from Bandodkar et al. [2014]; Fig. 11.1B from Jia et al. [2013)]; Fig. 11.1C from Gao et al. [2016a]; and Fig. 11.1D from Tai et al. [2018]).

being focused on developing skin-worn epidermal electronics that are in close contact with the wearer's epidermis and mimic the properties of the skin. One of the new methods explores the direct printing of electrochemical devices onto temporary tattoo substrates (Windmiller et al., 2012). The tattoo platform facilitates people to wear the sensors effortlessly without affecting their regular daily activities. The tattoo platform allows a unique opportunity to develop body-compliant electrochemical sensors that are continuously in contact with the human skin (Bandodkar et al., 2015a). Bandodkar et al. developed a tattoo-based epidermal patch for the continuous noninvasive assessment of sweat Na^+ levels directly from the human skin (Bandodkar et al., 2014). The excreted sodium during perspiration is a reliable marker for detecting electrolyte imbalance and provides vital information about physical and mental well-being. A solid-state ion-selective electrode (ISE) has been designed on a temporary transfer tattoo substrate, and the device was realized by merging several advanced technologies such as laser printing, thick film, solid-state potentiometry, microfluidics, and wireless communication (Fig. 11.1A). Such a smart device could alert the wearer about their electrolyte loss and thus help avoid dehydration-related complications.

Ammonium ions accumulate in blood as a result of protein metabolism. Therefore monitoring ammonium ions from blood plasma provides vital physiological information related to the metabolic state and dietary conditions of individuals. During exercise or intense hard work, metabolism changes from an aerobic to an

anaerobic state, and also diets with a deficit of carbohydrates often lead to temporary abnormal levels of ammonium ions in blood plasma. Moreover, the liver converts ammonium ions to urea prior to its excretion, and any hepatic disorder like hepatitis or cirrhosis leads to increased ammonium ions in plasma, which is often reflected as ammonia smell in sweat. Ammonium ions are excreted through sweat via nonionic diffusion from plasma and studies have reported that ammonium concentration in sweat correlates very well with its level in plasma. Wang et al reported a temporary transfer tattoo–based screen-printed solid-state potentiometric sensor for monitoring ammonium ions from sweat. The sensor showed good stability, Nernstian responses, and a wide working range of 10^{-4} to 10^{-1} M, and its analytical performances are not affected by mechanical deformations such as stretching or bending (Guinovart et al., 2013).

The pH value of a healthy individual varies in the range of 4.5 to 6.5, but abnormal pH levels indicate disorders such as kidney stones, diabetes, or cystic fibrosis. Persons suffering from cystic fibrosis have alkaline sweat (pH 9) due to the deficiency in the bicarbonate-reabsorption (H^+-secretion) process. As the pH value reflects the metabolism and homeostasis level, monitoring hydrogen ion concentration in body fluids provides vital physiological information about the human body. Potentiometric ISEs are widely utilized for pH monitoring owing to their simplicity, wide detection range, stability, and repeatability. Tattoo-based flexible pH sensors have been developed for monitoring sweat pH during intense exercise activities (Bandodkar et al., 2013). Polyaniline was deposited onto printed carbon electrodes via electropolymerization and the tattoo sensor showed rapid and sensitive responses toward pH changes with negligible carryover effects. The elasticity of the tattoo substrate provides conformal attachment onto the skin surface, and the incorporation of carbon fiber within the ink offers adequate tensile strength to withstand mechanical deformations (Windmiller et al., 2012).

Wounds cause a significant burden and unique health care concerns for patients, particularly when wounds are chronic and not healing in time. The wound healing process is very complex and influenced by several environmental factors. Adhesive bandages are usually used to protect wounds from moisture, dust, and debris and to provide an unperturbed environment for facilitating rapid healing processes. Microbial growth is a major concern that adversely affects the wound status and delays the healing processes. Monitoring the pH of the wound fluid can provide vital information about the wound site. The presence of different types of bacteria and enzymes increases the pH to neutral or slightly alkaline. Hence the wound healing status is highly correlated with the pH of the wound fluid. Wang et al. reported a bandage-based pH sensing patch that can provide real-time information on hydrogen

ion variations in a wound (Guinovart et al., 2014). By integrating with a printed circuit board having low-energy radiofrequency identification or Bluetooth communication abilities, the bandage-based sensors can be exploited for wearable wound monitoring devices.

11.2.2 Flexible sensors for metabolites tracking

Among the various biomarkers in body fluids, the measurement of glucose level is garnering great attention due to its direct relevance to diabetes. Studies have shown that sweat glucose levels hold a good correlation with blood glucose levels and thus perspiration-based wearable glucose sensors can avoid the painful process of finger pricking. One-dimensional (1D) nanomaterials showed significant advantages for improving the sensing performances and designing stretchable electrodes with good electrical conductivity. Vertically aligned gold nanowires possess advantages like a broad electrochemical window, good biocompatibility, electrical conductivity, chemical inertness, and surface modification moieties. Compared to the percolated networks of gold nanowires, three-dimensional (3D) upright nanowires provide a very high surface area and enormous electron transfer rate. Cheng et al. explored such 1D nanomaterials for electrochemical glucose sensing along with Prussian blue nanoparticles and glucose oxidase enzyme (Zhai et al., 2019). The electrode showed a sensitivity of 4.55 $\mu A\ mM^{-1}\ cm^{-2}$ even when exposed to 30% strain.

Sweat sampling is usually carried out by sweat stimulation methods such as intense exercise, heat, or iontophoresis. Understanding the mechanism behind the partitioning of glucose from the blood to sweat is vital for the precise self-testing of glucose. Sweat sampling needs to be simpler and faster for user-friendly personalized health care analysis. The fingertip possesses a high density of sweat glands of around 400 glands cm^{-2}, which produces sweat at high rates ranging from 50 to 500 $nL\ cm^{-2}\ min^{-1}$. Wang et al. developed a touch-based sweat collection method directly from the fingertip and electrochemical detection of glucose (Sempionatto et al., 2021b). Sweat was collected by simply touching the fingertip on the electrochemical transducer which is functionalized with a sweat-absorbing polyvinyl alcohol–based porous hydrogel that draws sweat by capillary action. Such a rapid sweat accessing touch-based blood-free glucose assay offers promising patient compliance and improved diabetes management.

Lactate is one of the most significant biomarkers for evaluating the physical performances for various military-, sports-, and health care–related applications. Lactate is primarily an indicator of tissue oxygenation, and monitoring its level in perspiration can avoid invasive blood sampling methods. During endurance-based activities like

cycling or triathlon, the normal aerobic metabolism is not sufficient to meet the energy demands of the human body. Hence, in such occasions the anaerobic process is induced and energy is produced from the stored glycogen at the muscle cells. This process is associated with the production of lactate and is called glycolysis or lactate acidosis. As the eccrine gland's energy metabolism also follows the anaerobic pathway during abnormal physical activities, sweat lactate can serve as a precise marker for tissue oxygenation. Sweat lactate can also provide a warning for pressure ischemia, which reflects insufficient oxidative metabolism, and tissue viability. Wang et al. demonstrated an epidermal electrochemical biosensor based on temporary tattoo electrodes functionalized with lactate oxidase (Fig. 11.1B) that provides data on real-time sweat lactate levels during exercise (Jia et al., 2013).

11.2.3 Flexible sensors for heavy metal monitoring

Human body fluids contain a variety of heavy metals such Zn, Cu, Cd, Pb, and Hg, which are closely related to human physiological conditions. Cu and Zn are essential trace metals, and their deficiency or their presence in abnormal levels can have detrimental effects on individuals. Excessive copper accumulation causes Wilson's disease, liver damage, heart and kidney failure, and brain disorders, whereas low concentrations of copper lead to anemia and osteoporosis. Poor zinc levels lead to a lethal form of pneumonia and diarrhea, but its presence in abnormal levels can be toxic and cause liver diseases, cardiac disorders, and low pancreatic enzyme counts. A high level of Cd causes toxic effects on the human body, including liver, respiratory tract, and kidney problems. Lead poisoning causes developmental delay, irritability, violent behavior, fatigue, and loss of appetite. Mercury poisoning leads to several serious diseases such as Minamata disease, Hunter–Russell syndrome, and acrodynia. Hence monitoring the levels of heavy metals in the body is vital for health care development and detoxification. Sweat examination assists in gaining insight into a person's heavy metal levels and can alert exposure to toxic metals. Wang et al. developed a wearable electrochemical sensor for the noninvasive assessment of trace metals in human perspiration (Kim et al., 2015a). The tattoo-based stripping oltametric sensor exploits bismuth/Nafion film–modified screen-printed electrode for the real-time monitoring of zinc from sweat during physical activity. The noninvasive stripping oltametric analysis can be readily expanded for the on-body measurements of other significant heavy metals. Javey et al. developed a flexible microsensor array for the simultaneous determination of heavy metals

from human body fluids (Gao et al., 2016a). Au and Bi microelectrodes were utilized for square wave anodic stripping voltammetry–based analysis (Fig. 11.1C).

11.2.4 Flexible sensors for drug monitoring

Drug analysis is the chemical examination of human biological samples to determine the individual's drug level. It has importance in several fields such as doping control, drug abuse detection, clinical therapeutics, forensic investigation, and digital health monitoring. Blood analysis provides precise information about the drug history, but its invasive nature makes it cumbersome for sample collection. Recently, wearable sensors have been used for the *in situ* real-time tracking of drug usage noninvasively from sweat samples owing to its nature of secretion and accessibility. Javey et al. demonstrated the monitoring of caffeine, a methyl xanthine drug, from sweat sample (Tai et al., 2018). Caffeine is usually a safe drug administered via coffee, tea, and other related products. But, its prolonged overdose causes serious health problems such as hypertension, coronary syndromes, and depression. Herein, carbon nanotubes–modified printed flexible electrode was utilized for the differential pulse voltammetric (DPV) detection of caffeine at around 1.4 V (Fig. 11.1D).

The facile sweat tracking process can be utilized to monitor the level of drugs in an individual's bloodstream, which has attracted attention for use in applications such as drug abuse detection, therapy management, drug–drug interaction assessment, drug compliance analysis, and personalized dosing. The drug level in sweat is usually very low when compared to that in the blood; hence highly sensitive sensors are required for its precise determination. The use of ultramicroelectrodes and the surface functionalization of electrodes with nanostructured materials can enhance the limit of detection of the transducers. Emaminejad et al. used the DPV technique for the detection of three model drugs, namely, dipyridamole, acetaminophen, and caffeine, using a boron-doped diamond electrode (Lin et al., 2020). Pulse voltammetric techniques like DPV and square wave voltammetry can suppress nonfaradaic background current and thus enable sensitive detection. The wireless readout system in this sensing patch provided real-time electroactive drug levels in a sample-to-answer manner. Nicotine exposure can also be detected from sweat samples with a flexible electrode array interfaced to a compact printed circuit board (Tai et al., 2020). A gold working electrode was deposited on a flexible plastic film, and then gold nanodendrites were directly grown and further modified with a nicotine-oxidizing enzyme. The results suggested confirmable and elevated levels of nicotine in sweat for individuals inhaling cigarette smoke.

11.2.5 Flexible sensors for nutrition tracking

Nutrition is a significant factor that regulates our physiological functions, and an improper nutritional level can affect fetal, infant, and maternal health. In children nutritional balance is vital for normal growth, physical and mental development, and maintaining a healthy body weight. For elderly patients and institutionalized people, malnutrition causes enhanced morbidity and delay in the recovery of diseases. Hence periodic monitoring of nutrition levels in the body is important for overall health and well-being. In general, nutrition levels are examined by using anthropometric assessments and serum biomarkers. Javey et al. developed a wearable sensor for monitoring vitamin C from biofluids such as sweat, urine, and blood (Zhao et al., 2021). The sensor is developed by growing Au nanodendrites on flexible poly(ethylene terephthalate) substrates having gold electrode, and further modified with an electroactive conducting polymer, poly(3,4-ethylenedioxythiophene). The top protective membrane of Nafion prevents the leaching of the enzyme from the working electrode. Sweat and urine analysis are promising modes to regularly monitor nutritional levels and dietary interventions.

Sweat generated during exercise or high endurance activities is ideal for fitness monitoring applications. But a different sweat-producing mechanism is required for sweat-based clinical health care monitoring. Iontophoresis is a method widely used to improve the transdermal delivery of compounds (drug) through the skin via the application of a small electric current. Iontophoresis functions based on the principle of electroosmosis and electromigration, which augments the permeation of charged and neutral materials and enables programmed or target responsive drug delivery (Priya et al., 2006). Iontophoresis could be used for artificially stimulating sweat by transdermal delivering a sweat-stimulating drug called pilocarpine with the help of iontophoretic electrodes. Wang et al. monitored vitamin C profiles from induced sweat after consuming vitamin C pills or vitamin C–rich beverages (Sempionatto et al., 2020). A flexible epidermal tattoo was developed with iontophoretic sweat-stimulating electrodes, and amperometric transducers for monitoring oxygen that formed during the enzymatic reaction. Wang et al. developed an amperometric sensor for the noninvasive monitoring of alcohol from induced sweat (Kim et al., 2016). The wearable sensor was constructed on a tattoo platform by integrating an iontophoretic-enzyme electrode along with flexible wireless electronics. The skin-worn biosensor realizes the controlled delivery of pilocarpine and the wireless transmission of real-time signals to any smart device.

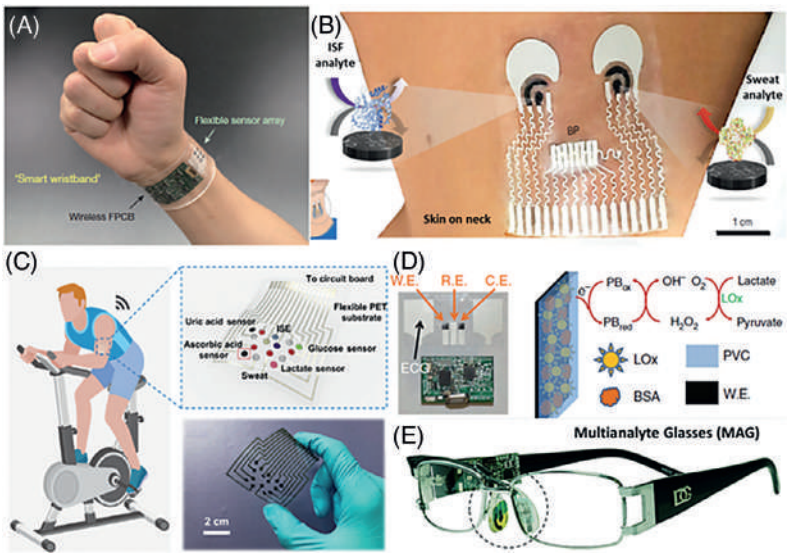

Figure 11.2. (A) Photograph of a wearable multiplexed sweat sensor integrated with a wireless circuit board. (B) Stretchable integrated blood pressure–chemical sensing patch on the neck, and the enzymatic chemical sensing from ISF and sweat. (C) Wearable sweat analysis based on silk fabric–derived intrinsically nitrogen (N)–doped carbon textile; photograph of the multiplex electrochemical sensor array. (D) Image of a Chem–Phys patch for electrocardiogram and lactate signals monitoring; schematic representing the mechanism behind lactate biosensor. (E) Photograph of the eyeglasses-integrated biosensor system for lactate and potassium monitoring (Fig. 11.2A from Gao et al. [2016b]; Fig. 11.2B from Sempionatto et al., [2017]; Fig. 11.2C from He et al., [2019]; Fig. 11.2D from Imani et al. [2016]; and Fig. 11.2E from Sempionatto et al., [2017]).

11.2.6 Flexible sensors for multiplexed biomarker analysis

The efficacy of sweat-based noninvasive biosensors can be improved by monitoring multiple analytes simultaneously. The incorporation of on-site signal processing circuitry and advanced sensor calibration mechanisms provide the precise quantification of the physiological state. The technological gap exists in many aspects such as signal transduction, conditioning, processing, signal crosstalk between the sensors, and wireless transmission. The development of a flexible circuit board and its integration with flexible sensors and the maintenance of robust electrical contact with the transducers are also crucial for the productive commercialization of wearable sensors. Javey et al. developed a multiplexed biosensing system to track sweat biomarkers (Gao et al., 2016b). The fully integrated mechanically flexible platform allows the in situ monitoring of sweat metabolites like lactate and glucose, electrolytes such as Na^+ and K^+, and the skin temperature for calibrating the sensor responses (Fig. 11.2A). The sensors are fabricated on mechanically flexible thin sheets of poly(ethylene terephthalate), which enables conformal sensor–skin contact. Also, the use of a flexible printed circuit board allows stable integration into 3D skin surfaces.

Cardiovascular parameters such as heart rate and blood pressure directly reflect the physiological status of the body. These parameters are influenced by body movements, stress, food intake, drug consumption, and variations in biomarker concentrations. Parallel monitoring of these physiological parameters along with that of chemical markers

can provide comprehensive health information, particularly for the elderly or individuals suffering from obesity, diabetes, and other cardiovascular disorders. Integrating multiple sensors in the same patch reduces the discomfort of using multiple devices for tracking these parameters, and such biomedical devices can prevent harmful cardiac events and save lives. Wang et al. recently developed a stretchable sensing patch that can seamlessly be attached to the epidermis and monitor the levels of biomarkers like glucose, lactate, alcohol, and caffeine, along with blood pressure and heart rate (Sempionatto et al., 2021a). The flexible device possesses sufficient mechanical resiliency to adapt to the irregular skin surfaces and ensures the precise sensing of glucose in subdermal fluid and other metabolites from induced sweat without affecting any crosstalk between the sensors (Fig. 11.2B).

Textile substrates are another class of ideal wearable substrates because of their maximum epidermal contact and conformity (Rajendran et al., 2019). Silk is a natural fiber generally used for constructing flexible and breathable fabrics. In comparison with animal fibers like wool, silk fibers show significant advantages such as high mechanical strength, good uniformity, and large length, up to 1.5 km. The textile substrates need to be transformed into a conductive form for various electrochemical sensing or energy storage applications. Silk-derived carbon textiles possess intrinsic conductivity and a hierarchical porous mesh-woven configuration that enables them to be used as transducers for sensing applications. Recently, Zhang et al. developed nitrogen-doped carbon textile for multiplexed sweat analysis (Fig. 11.2C). The wearable patch could simultaneously monitor various biomarkers such as lactate, glucose, ascorbic acid, uric acid, Na^+, and K^+ with good selectivity, high sensitivity, and long-term stability (He et al., 2019).

The epidermal sensors that monitor either chemical or physiological parameters alone do not provide the complete health care state of individuals. The majority of the existing wearable sensors are focused on monitoring physiological signals like body temperature, pressure, heart rate, pulse rate, electrocardiogram signals, respiration rate, and tissue oxygenation levels. The fruitful amalgamation of both chemical and physiological sensors is necessary for improving the efficacy of the point-of-care analysis and personalized health care monitoring. Cross-signal transfer is a critical obstacle when harvesting such skin-based electrochemical signals (e.g., amperometric) and physical sensor responses parallelly from individuals. Imani et al. addressed this issue and developed a wearable epidermal sensing patch that can monitor lactate, a biomarker for oxygenation levels, and electrocardiogram signals simultaneously to assess an individual's exertion and endurance level (Imani et al., 2016). The presence of a vertically oriented hydrophobic coating adjacent to the amperometric lactate

sensor geometrically detaches the sensors and avoids the possibility of signal interference and shunting effects (Fig. 11.2D).

Most wearable devices for sweat-based biomarker analysis have relied on flexible substrates like thin plastic films, wristbands, headbands, or temporary tattoo–like devices. As part of advances in wearable technologies, there is tremendous demand for wearable fashion accessories to integrate chemical sensors without disturbing body movements or routine activities. Smart bandages are used for understanding the status of wound healing by monitoring the pH of the wound fluid (Kassal et al., 2015; McLister et al., 2016). Contact lenses are another class of wearable platforms, initially introduced for tear analysis, particularly for continuous glucose monitoring (Yao et al., 2011, 2012). Wang et al integrated an amperometric lactate biosensor and a potentiometric K^+ ISE into both the nose-bridge pads of eyeglasses (Sempionatto et al., 2017). The sensors are interfaced with a printed circuit board placed on the glasses' arms, capable of performing electrochemical measurements and wireless data transmission (Fig. 11.2E).

11.3 Flexible microfluidic sensors for sweat analysis

Though skin-worn wearable electrochemical sensors offer reliable, real-time tracking of vital signals selectively from complex biofluids, sweat analysis still involves some challenges. The major bottlenecks include uneven sweat generation and capturing rates, dilution of sweat due to the mixing up of sweat secreted at various intervals of time, the carryover of sweat biomarkers, irregular movement of sweat over the transducer surface, unsymmetrical sweat volumes, and inconvenient sample evaporation (Vinoth et al., 2021). The burgeoning microfluidics technology offers the development of miniaturized devices for various applications like cell/particle trapping (Kobel et al., 2010), size-based sorting/exclusion of particles (Chirica et al., 2006), droplet formation (Liu & Zhang, 2011), nanomaterials synthesis (Song et al., 2008), and drug delivery (Sanjay et al., 2018). Paper-based microfluidic devices are widely used for various applications such as POCT, food quality assessment, and environmental analysis. Paper substrate is made up of porous cellulose fibers that facilitate liquid to flow through capillary force of action and allow sample filtering, mixing, and transport. Paper-based analytical devices are ideal for point-of-care diagnosis due to their simplicity, cost-efficiency, biodegradability, and biocompatibility. Zhong-Yang et al developed a paper-based flexible microfluidic system that can selectively and parallelly measure metabolites like lactate and electrolytes such as sodium and pH (Anastasova et al., 2017). Also, the fully integrated on-body patch possesses a temperature

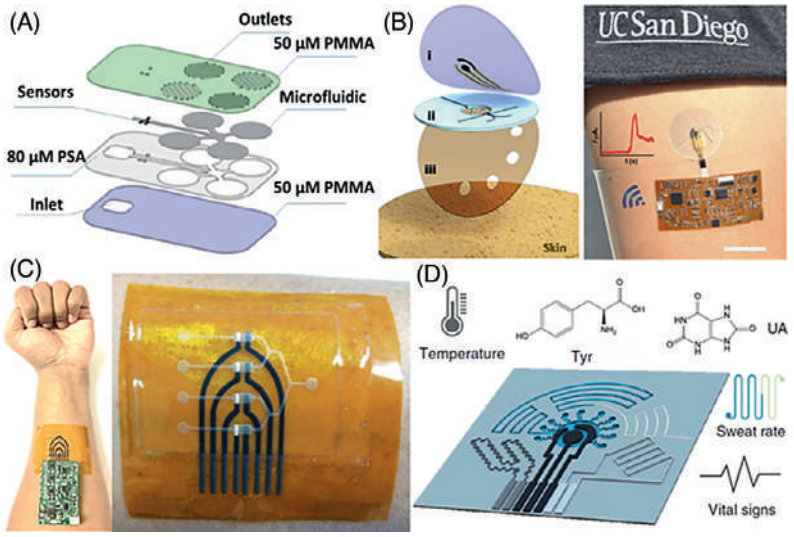

Figure 11.3. (A) Schematic representation of the paper-based microfluidic chip for simultaneously measuring lactate and electrolytes. (B) A soft epidermal microchip device for the electrochemical sensing of sweat metabolites; photograph of patch integrated with wireless conformal electronics on the skin. (C) Photograph showing fully integrated, skin-interfaced microfluidic sensor and the close-up part of a multiarray electrode used for lactate and electrolyte monitoring. (D) Schematics show a laser-engraved wearable microfluidic sensor for the sensitive detection of uric acid and tyrosine in sweat (Fig. 11.3A from Anastasova et al. [2017]; Fig. 11.3B from Martín et al. [2017]; Fig. 11.3C from Vinoth et al. [2021]; and Fig. 11.3D from Yang et al. [2020]).

sensor for internal calibration, and the patch is capable of real-time data collection from human subjects during treadmill running and cycle ergometry (Fig. 11.3A).

Although paper-based sensors possess several advantages, such devices are not appropriate for the continuous tracking of health care markers. The incessant exposure of biofluids to the paper substrate often causes memory effects and adversely affects the precise monitoring of biomarkers. Recently, soft microfluidic channels have been exploited for sweat collection, sampling, and analysis (Martín et al., 2017; Zhang et al., 2019). Photolithographic techniques are usually employed for developing high-resolution masters, which are expensive and time consuming and require clean-room facilities. An epidermal sweat monitoring patch was developed by merging soft lithographic and screen-printing techniques (Martín et al., 2017). The electrochemical system possessed intrinsic sweat sampling and continuous flow of sweat through the sensing electrodes and hence obviates the requirement for complicated electrokinetic or hydrodynamic platforms (Fig. 11.3B).

Screen-printing is a cost-effective technique widely used for realizing planar electrodes for sensing applications. The printing technique replaces the use of conventional rod/disc-type electrodes for electrochemical analysis. The planar electrodes printed on an inexpensive paper or plastic substrate are ideal for cost-effective practical applications. The ideal three-electrode system is typically realized by printing carbon- and silver-based inks to function as the working/counter and reference electrode, respectively. And the top layer of the dielectric ink defines the active area of the sensing electrodes, which is

crucial for all electrochemical measurements. Recently, the printing technique has been exploited for constructing low-cost microfluidic channels (Vinoth et al., 2021). The soft microfluidic sensors possessed *in situ* sweat harvesting and multiplexed in situ detection abilities and have been used for the continuous monitoring of lactate, Na^+, K^+, and pH simultaneously from sweat samples during intense physical activities. The sweat sampling efficiency was enhanced by the surface functionalization of soft microfluidic channels, and the patch could monitor regional variation in sweat compositions (Fig. 11.3C). Many of the wearable microfluidic systems are related to silicone elastomers that require advanced microfabrication facilities. Although the screen-printing technique allows the large-scale production of uniform patterns and the repetitive use of the same master for channel preparation, the printing dimension is relatively poor when compared to lithographic techniques.

Laser engraving is a promising fabrication technology for the rapid realization of high-resolution fluidic channels directly on wearable plastic substrates. The CO_2 laser technology requires minimal personnel training and process optimization and allows the scalable production of precise microfluidic channels at ambient conditions. The laser technology has recently been exploited for realizing reduced graphene oxide for a wide variety of applications (Strong et al., 2012). Keegan et al. demonstrated the ability of laser-scribed graphene for electrochemical sensing applications. The method enables the direct patterning of electrochemically active graphene layers on the flexible substrate (polyimide) and facilitates the roll-to-roll production of large-scale disposable sensors. Graphene offers a 2D environment for electron transport and realizes rapid heterogeneous electron transfer at their edge planes. Gao et al. exploited this technique for the multimodal sensing of molecular analytes more comprehensively by including both chemical and physical signatures (Yang et al., 2020). The system allows the wireless monitoring of uric acid and tyrosine by means of laser-engraved graphene sensors and the tracking of real-time temperature and respiration rate using a laser-engraved multiinlet microfluidic module (Fig. 11.3D). The laser-engraved multimodal platform allows efficient microfluidic sweat sampling, sensitive biomarker sensing, and multiplexed analysis. The graphene-based chemical sensors possess rapid electron mobility, ultralarge surface area, high current density, and high sensitivity.

11.4 Flexible sensors for saliva monitoring

Saliva is a biofluid that is extremely attractive for the noninvasive monitoring of biomarkers owing to its continuous and convenient

availability. Saliva possesses a good correlation with blood levels of various analytes due to the permeation of multiple analytes from the blood via the paracellular or transcellular path. Hence sialochemistry, the chemical analysis of saliva, has been recognized as a proficient tool for the noninvasive monitoring (alternative to blood analysis) of the hormonal, stress, and metabolic states of individuals. Saliva is an exocrine secretion containing several electrolytes such as sodium-potassium; chloride; magnesium; calcium; phosphate and bicarbonate; and proteins, immunoglobulins, mucosal glycoproteins, polypeptides, and albumins. Metabolites like glucose and lactate and nitrogenous compounds like ammonia and urea are also excreted through saliva fluid (Humphrey & Williamson, 2001). The unstimulated basal secretion moisturizes and lubricates the oral tissues, whereas exogenous or pharmacologically stimulated saliva contributes to the majority of the daily salivary production.

Monitoring pH from saliva would be highly beneficial for understanding oral health conditions like the disintegration of tooth enamels and diagnosing gastroesophageal reflux disease. Diamond et al developed a potentiometric testing strip using a planar screen-printed electrode for monitoring pH from saliva samples. The pH strip contains an H^+ ion-selective membrane electrode and a solid-state ionogel reference electrode. The pH values of the collected real saliva samples were measured and validated by using standard glass electrode–based pH analysis (Zuliani et al., 2014). For COVID-19 diagnostic testing, naso- and oropharyngeal swabs are widely used; however, saliva testing is also recently suggested. Recently, monitoring RNA from saliva samples was approved by the US Food and Drug Administration, which supports the concept of saliva tracking for the detection of the coronavirus and antibodies produced against it (Ceron et al., 2020).

Denture-based sensors are reported for estimating biomarkers from saliva fluid. Coltro et al. developed a paper-based microfluidic device and integrated it into a 3D-printed mouthguard for the colorimetric detection of glucose and nitrite (de Castro et al., 2019). Mouthguards are generally used by athletes to prevent sports-related injuries. These polymeric devices attach firmly over the teeth and can be easily worn and removed without depending on specialized assistance. The mouthguard can easily access real-time saliva secretion and enables the facile integration of transducer and related microcontrollers. Electrochemical sensors can also be merged with the denture platform for the noninvasive monitoring of salivary metabolites. Wang et al. developed an amperometric sensor for lactate using Prussian blue–based screen-printed electrodes, functionalized with poly-(o-phenylenediamine)-lactate oxidase enzyme layer. The system allows highly sensitive and selective lactate detection in undiluted saliva samples owing to its low-potential signal measurement and elimination

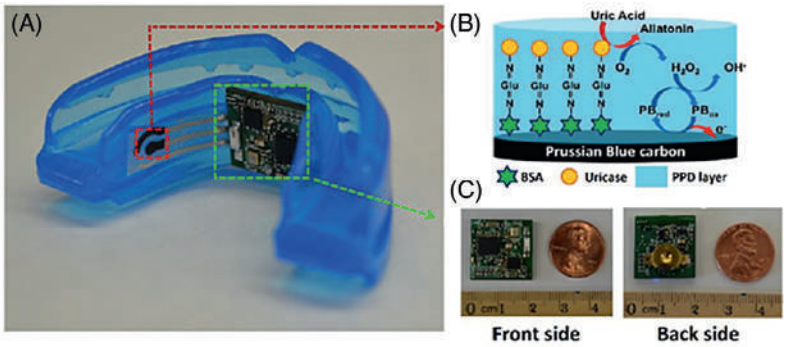

Figure 11.4. (A) Photograph showing the mouthguard biosensor interfaced with an amperometric circuit board. (B) Mechanism behind the Prussian blue–based uric acid biosensor. (C) Photographs showing the front and back side of the wireless circuit board (Kim et al., 2015).

of coexisting electroactive and bulky protein constituents (Kim et al., 2014).

Uric acid is another biomarker that could be detectable from saliva, which is the end product of purine metabolism. The abnormal uric acid levels in the human body indicate several diseases, including hyperuricemia, renal syndrome, Lesch–Nyhan syndrome, and gout. Uric acid can function as a marker for reactive oxygen species induced by physical stress, which acts as a free radical scavenger. Also, an abnormal uric acid concentration increases the risk of type 2 diabetes and the associated complications. The salivary uric acid measurement can replace invasive blood testing and the real-time analysis can be conducted in a continuous manner. Wang et al developed a mouthguard biosensor for uric acid based on screen-printed electrodes on a flexible plastic substrate. The Prussian blue electrode was chemically functionalized by crosslinking uricase enzyme during the electropolymerization of o-phenylenediamine (Fig. 11.4). The sensor signals could be wirelessly shared with any smart devices like smartphones, tablets, laptops, or smartwatches (Kim et al., 2015b).

The noninvasive monitoring of glucose is highly needed to avoid the pain and discomfort related to invasive blood analysis. Saliva is a good biofluid for noninvasive glucose analysis, wherein the saliva glucose levels significantly correlate with the blood glucose concentrations. However, saliva contains a very low level of glucose, usually less than 100 μM, which is much lower than that detected using blood glucose sensors (3.6–7.5 mM). Therefore it is important to augment the sensitivity of the sensors for detecting low levels of glucose. Modification of electrode surfaces with nanostructured materials allows for a high surface area and energy compared with the traditional bulk materials. Carbon-based nanomaterials are conductive, easy to functionalize, and biocompatible and possess a large surface area and low overpotential for electrochemical reactions. 3D carbon nanotubes, 2D graphene, and 1D nanofibers have been well explored for electrochemical

sensing. The combination of these materials often causes a synergistic effect and leads to better electrochemical performances. Kong et al. developed a nonenzymatic sensor for glucose based on CuO nanoneedle/graphene/carbon nanofiber–modified electrode (Ye et al., 2013). The sensor showed high electrocatalytic ability for glucose oxidation with a low limit of detection of 0.1 μM, and it can be utilized for monitoring glucose levels from saliva samples. Bouchikhi et al. reported a molecularly imprinted sensor for the selective detection of salivary glucose. The imprinted sensor was constructed on a screen-printed gold electrode by electropolymerizing acrylamide/bis-acrylamide in the presence of glucose as template molecules. The sensor could effectively avoid structurally similar coexisting interferents such as sucrose and lactose and showed a lowest detection limit of 0.59 μg mL^{-1} (Diouf et al., 2019).

11.5 Flexible sensors for interstitial fluid analysis

ISF has shown the greatest potential to substitute existing blood-based clinical diagnostics. ISF is the transcapillary fluid from the blood that surrounds the cells and tissue and functioning for transporting nutrients and waste materials. In addition, ISF is responsible for immune regulation and signaling molecules between cells. The biomarker composition in ISF closely correlates with that in the blood, which allows precise diagnosis. ISF contains a negligible amount of coagulating elements and is thus free from clotting problems and useful for continuous monitoring of biomarkers. ISF can be sampled minimally or noninvasively with minimal personal inconveniences and provides local information about tissues without the requirement for biopsies. Such benefits have attracted researchers to harvest vital information from ISF for reliable on-body analysis (Teymourian et al., 2021).

Microneedle arrays are promising devices for directly accessing ISF under the skin. Microneedles are sharp, vertically oriented structures, hardly visible but able to puncture the uppermost layer of the skin. Microneedles access ISF from a lower depth and the penetration does not reach the capillary bed or nerve endings in the underlying dermis. Microneedles offer a painless, blood-free, and minimally invasive tool for accessing the ISF biomarkers. Microneedle arrays provide the advantages of integrating multiple sensors on a single platform, ease of miniaturization, and the ability to collect multiplexed molecular information (Mishra et al., 2017).

Lactate monitoring is used for assessing the maximum performance of athletes and clinical care. The normal blood lactate level for healthy individuals ranges from 0.5 to 2 mM and increases to 15

mM during exercise activities. Several pathological conditions also influence lactate levels, including pulmonary embolism, cardiac disease, liver disorder, and endotoxic shock. Recently, lactate has been found to play a key role in cancer diagnosis as it causes acidification around the cancer tissues (Hirschhaeuser et al., 2011). Amperometric biosensors are ideal for the accurate and cost-effective detection of lactate with improved selectivity and sensitivity. Antiochia et al. developed a microneedle-based mediated biosensor for monitoring lactate levels from ISF. Gold microneedles were electrodeposited with Au-multiwalled carbon nanotubes and further modified with poly(methylene blue) prior to enzyme immobilization by drop-casting. The microneedle array could detect lactate in human serum and in artificial ISF (Bollella et al., 2019).

Currently, continuous glucose-monitoring devices are attracting tremendous interest as they can record real-time glucose signals for several days. The direct contact of transducers with the ISF is ideal for precise sensing, as opposed to extracting the fluid with other methods. Anderson et al. developed a microneedle-based amperometric sensor for glucose that uses the needle itself as a functional constituent. The elegant microneedle sensor is capable of the painless continuous analysis of glucose for diabetic patients (Invernale et al., 2014). Self-powered devices are appropriate for personal health care monitoring as they can continuously harvest signals even in the absence of external powering sources. Biofuel cells convert the biochemical energy from the transdermal fluid of the wearer into measurable responses proportional to the analyte concentration (Bandodkar et al., 2017; Mohan, 2021). Wang et al. reported a microneedle-based self-powered biosensor for monitoring glucose from the subdermal fluid (Valdés-Ramírez et al., 2014). The biofuel cell consists of GOx–tetrathiafulvalene-modified carbon paste as the bioanode and carbon paste/Pt black cathode in a hollow microneedle array (Fig. 11.5A).

Unhealthy alcohol consumption represents a critical health hazard due to severe accident-involved traffic fatalities. Alcoholism leads to potential health risks, including a variety of disorders, diseases, and injuries. Breathalyzers (functioning based on Henry's law) are commonly utilized for measuring breath alcohol levels. However, the performance of these devices can be affected by local humidity, temperature, and other environmental fumes. Hence there is significant demand for easy-to-use, accurate alcohol monitoring devices that provide reliable and real-time information about alcohol consumption and misuse. Wang et al. developed a transdermal microneedle-based biosensing system for the continuous real-time tracking of alcohol from ISF (Mohan et al., 2017b). The array of microneedle systems consists of Pt and Ag wires integrated within the aperture of hollow microneedles to function as an ideal three-electrode system (Fig. 11.5B). The Pt wire–based working electrode was functionalized with alcohol

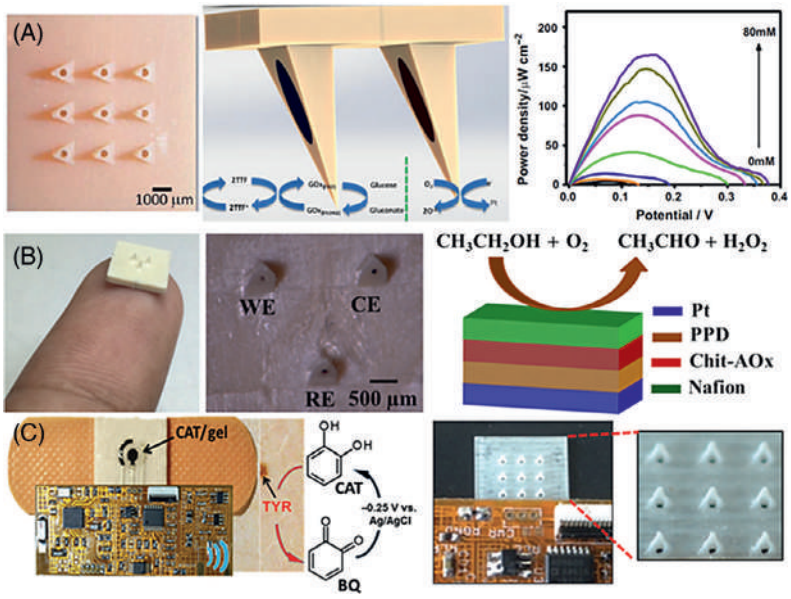

Figure 11.5. (A) Optical image of a microneedle array; schematic representation of microneedle-based carbon paste bioanode and cathode electrodes, and the mechanism behind self-powered glucose sensor. (B) Photograph of a microneedle array mounted on the fingertip and the optical micrograph of the microneedles integrated with Pt and Ag wires; schematic demonstration of the construction of an alcohol biosensor. (C) Images showing a bandage-based electrochemical sensor for tyrosinase and a microneedle sensor integrated into soft flexible electronics (Fig. 11.5A from Valdés-Ramírez et al. [2014]; Fig. 11.5B from Mohan et al. [2017b]; and Fig. 11.5C from Ciui et al. [2018]).

oxidase enzyme, along with a perm-selective poly(phenylenediamine) membrane. The sensor possessed good sensitivity and stability and was successfully used for measuring alcohol levels from the artificial ISF.

The simultaneous analysis of ISF and sweat from the epidermis using a single wearable bioelectronics platform is highly desired for expanding the scope of biofluid monitoring and improving clinical accuracy. The common sweat generation methods such as exercise and thermal heating cause uncontrolled sweat generation and extensive intersample mixing. These challenges can be resolved by employing iontophoresis and reverse iontophoresis processes for the controlled and localized sampling of sweat and ISF, respectively. The electrically induced migration of ions or molecules across the skin can be explored for both delivering and extracting compounds. Administering the drug pilocarpine induces sweat production, but the same iontophoresis can be used for drawing molecules toward the skin surface from the ISF, called reverse iontophoresis. Wang et al. developed such an innovative wearable biosensing device for the simultaneous and independent sampling of both the epidermal biofluids (Kim et al., 2018b). These biosensors could electrochemically measure glucose from the ISF (at the cathode) and alcohol from sweat (at the anode). Such dual sampling and parallel sensing modalities hold considerable potential for improving the capabilities and scope of noninvasive health care monitoring.

Melanoma is an aggressive skin disease, the early diagnosis of which is crucial for timely treatment and reducing mortality. At

present, time-consuming, complex methods are used for detecting melanoma biomarkers, such as melanocytic lineage indicators. The synthesis of melanin involves a polyphenol oxidase enzyme called tyrosinase. The overexpression of tyrosinase and its accumulation in skin cells causes the skin cancer. Hence monitoring tyrosinase levels is a faster and simpler technique for the rapid detection of skin melanoma. Wang et al. developed a fully integrated wearable bandage and microneedle-based electrochemical sensing systems for detecting tyrosinase from the skin surface and under the skin, respectively (Ciui et al., 2018). The bandage sensor contains a biocompatible hydrogel having catechol, the enzyme substrate. In presence of tyrosinase enzyme, the immobilized catechol is oxidized to benzoquinone, which can be reduced and measured using amperometric technique (Fig. 11.5C).

11.6 Flexible sensors for tear fluid analysis

Human tear fluid or lachrymal liquid is one of the most complex biological fluids that contains 98% water, and the remaining 2% is made up of low- and high-molecular-weight constituents such as electrolytes, metabolites, enzymes, proteins, and small organic molecules. The majority of these molecules possess diagnostic potential and can be used for the noninvasive evaluation of the health care status of individuals. Tear fluid is covered as a thin film on the surface of the eye bulb, with a thickness of about 9 to 10 μm. Also, the lachrymal secretion protects the exposed area of the eye capped with a lipid membrane that prevents the evaporation of the tear liquid. The physiological pH and temperature of the tear fluid are about pH 7.5 and 35°C, respectively, and its total volume is nearly 6.2 ± 2.0 μL (Pankratov et al., 2016).

Continuous biomarker monitoring directly from human blood is complex and practically difficult. Subcutaneous fluid–based glucose monitoring has been well studied and shows a very good correlation with blood glucose levels. The relationship between the levels of bioindicators in the tear fluid and personal physical conditions has recently been well studied. Mitsubayashi et al. developed a promising wearable amperometric biosensor for the continuous monitoring of glucose from the tear liquid (Iguchi et al., 2007). A soft microelectromechanical system–based technique was utilized for preparing flexible electrodes and functionalized with a gas-permeable membrane and glucose oxidase enzyme. The sensor could continuously detect glucose concentrations from tear fluid on a rabbit's eye.

The levels of several metabolites in tears have been shown to have a good correlation with the blood levels, suggesting tears as a promising biofluid for personalized health care monitoring. These platforms have

primarily focused on contact lens–based sensors for direct analysis in basal tears. Integrating microcontrollers, wireless data transmitters, and power sources with a contact lens is challenging and efforts for improving such wearable modalities are progressing. Wang et al developed a noninvasive flexible device integrated into eyeglasses for the real-time monitoring of multiple target molecules such as glucose, alcohol, and vitamins in tears (Sempionatto et al., 2019). An online microfluidic channel is mounted onto the eyeglasses' nose-bridge pad to facilitate the direct sampling of stimulated tears. The effect of alcohol consumption over the tear alcohol level was evaluated in human subjects over multiple drinking courses, which displayed a notable correlation to parallel breath alcohol content measurements.

11.7 Challenges and future perspectives

Wearable chemical sensors are witnessing significant progress and are expected to grow rapidly over the following decade. However, there are some bottlenecks that still exist that need to be addressed to fill the technological gap between the existing prototypes and commercialized promising health care devices. The mechanical properties of these devices should be considered while maintaining electrochemical performances and stability. Developing electrochemical transducers having stretchability (Mohan et al., 2017a) and self-healing abilities can maintain stable performances when subjected to repeated mechanical deformations (Bandodkar et al., 2015b, 2016a). The mechanical properties of the controlled electronics and the power sources are also crucial as their conformal attachment is mandatory for facile integration with flexible sensors. As the continuous sensing and wireless data collection processes necessitate an abundant source of energy for a prolonged period of time, the development of soft, lightweight, miniature energy sources like batteries (Mohan et al., 2014b) and supercapacitors with a high energy density is required (Rajendran et al., 2019). The wearable sensors must possess good repeatability and reproducibility; hence the large-scale fabrication of uniform electrodes and accurate surface functionalization procedures are a matter of major concern. There are irregularities in biofluid secretion with respect to gender, age, and ethnicity; thus advanced smart calibration methods need to be utilized for error correction and precise monitoring. The level of biomarkers in various biofluids is extremely lower than the detection limit of the existing sensors. Hence attention must be paid to the development and use of suitable nanostructured materials so as to further improve the sensitivity of the existing transducers.

11.8 Summary

Advances in wearable point-of care-devices for the real-time tracking of the health and fitness state of individuals are discussed. Information-rich biofluids like sweat, saliva, ISF, and tear fluid could be efficiently utilized as an alternative for painful, tedious blood analysis. The seamless integration of these sensors into the irregular or curved surfaces of the human body necessitates significant flexibility, stretchability, and mechanical strength so as to withstand the mechanical strain. Information about the composition of biofluids, the underlying partition mechanisms, and their correlation with blood biomarkers' levels is vital for the design and development of epidermal biosensors. Nanostructured materials play a crucial role in detecting low levels of these chemical indicators from various body fluids. Real-time biofluid capture and analysis is important to avoid dilution or carryover-related problems, and the microfluidic technology offers superior fluid extraction, sampling, preconditioning, and transport. Conducting large population studies including different age groups, continents, genders, and ethnicities can improve the efficacy of these personalized diagnostic systems and facilitate the commercialization pathways.

References

Anastasova, S., Crewther, B., Bembnowicz, P., Curto, V., Ip, H.M., Rosa, B., Yang, G.Z., 2017. A wearable multisensing patch for continuous sweat monitoring. Biosensors and Bioelectronics 93, 139–145. https://doi.org/10.1016/j.bios.2016.09.038.

Aswini, K.K., Mohan, A.M.V., Biju, V.M., 2014. Molecularly imprinted polymer based electrochemical detection of L-cysteine at carbon paste electrode. Materials Science and Engineering C 37 (1), 321–326. https://doi.org/10.1016/j.msec.2014.01.020.

Aswini, K.K., Mohan, A.M.V., Biju, V.M., 2016. Molecularly imprinted poly(4-amino-5-hydroxy-2,7-naphthalenedisulfonic acid) modified glassy carbon electrode as an electrochemical theophylline sensor. Materials Science and Engineering C 65, 116–125. https://doi.org/10.1016/j.msec.2016.03.098.

Baker, L.B., 2019. Physiology of sweat gland function: The roles of sweating and sweat composition in human health. Temperature 6 (3), 211–259. https://doi.org/10.1080/23328940.2019.1632145.

Bandodkar, A.J., Hung, V.W.S., Jia, W., Valdés-Ramírez, G., Windmiller, J.R., Martinez, A.G., Ramírez, J., Chan, G., Kerman, K., Wang, J., 2013. Tattoo-based potentiometric ion-selective sensors for epidermal pH monitoring. Analyst 138 (1), 123–128. https://doi.org/10.1039/c2an36422k.

Bandodkar, A.J., Jia, W., Wang, J., 2015a. Tattoo-based wearable electrochemical devices: A review. Electroanalysis 27 (3), 562–572. https://doi.org/10.1002/elan.201400537.

Bandodkar, A.J., Mohan, V., López, C.S., Ramírez, J., Wang, J., 2015b. Self-healing inks for autonomous repair of printable electrochemical devices. Advanced Electronic Materials 1 (12), 1500289. https://doi.org/10.1002/aelm.201500289.

Bandodkar, A.J., López, C.S., Mohan, A.M.V., Yin, L., Kumar, R., Wang, J., 2016a. All-printed magnetically self-healing electrochemical devices. Science Advances 2 (11). https://doi.org/10.1126/sciadv.1601465.

Bandodkar, A.J., Jeerapan, I., Wang, J., 2016b. Wearable chemical sensors: Present challenges and future prospects. ACS Sensors 1 (5), 464–482. https://doi.org/10.1021/acssensors.6b00250.

Bandodkar, A.J., Molinnus, D., Mirza, O., Guinovart, T., Windmiller, J.R., Valdés-Ramírez, G., Andrade, F.J., Schöning, M.J., Wang, J., 2014. Epidermal tattoo potentiometric sodium sensors with wireless signal transduction for continuous non-invasive sweat monitoring. Biosensors and Bioelectronics 54, 603–609. https://doi.org/10.1016/j.bios.2013.11.039.

Bandodkar, A.J., Wang, J., 2014. Non-invasive wearable electrochemical sensors: A review. Trends in Biotechnology 32 (7), 363–371. https://doi.org/10.1016/j.tibtech.2014.04.005.

Bandodkar, A.J., You, J.M., Kim, N.H., Gu, Y., Kumar, R., Mohan, A.M.V., Kurniawan, J., Imani, S., Nakagawa, T., Parish, B., Parthasarathy, M., Mercier, P.P., Xu, S., Wang, J., 2017. Soft, stretchable, high power density electronic skin-based biofuel cells for scavenging energy from human sweat. Energy and Environmental Science 10 (7), 1581–1589. https://doi.org/10.1039/c7ee00865a.

Bariya, M., Nyein, H.Y.Y., Javey, A., 2018. Wearable sweat sensors. Nature Electronics 1 (3), 160–171. https://doi.org/10.1038/s41928-018-0043-y.

Bear, C.E., Li, C., Kartner, N., Bridges, R.J., Jensen, T.J., Ramjeesingh, M., Riordan, J.R., 1992. Purification and functional reconstitution of the cystic fibrosis transmembrane conductance regulator (CFTR). Cell 68 (4), 809–818. https://doi.org/10.1016/0092-8674(92)90155-6.

Bocchetta, P., Frattini, D., Ghosh, S., Mohan, A.M.V., Kumar, Y., Kwon, Y., 2020. Soft materials for wearable/flexible electrochemical energy conversion, storage, and biosensor devices. Materials 13 (12). https://doi.org/10.3390/ma13122733.

Bollella, P., Sharma, S., Cass, A.E.G., Antiochia, R., 2019. Microneedle-based biosensor for minimally-invasive lactate detection. Biosensors and Bioelectronics 123, 152–159. https://doi.org/10.1016/j.bios.2018.08.010.

Ceron, J.J., Lamy, E., Martinez-Subiela, S., Lopez-Jornet, P., Silva, F.C.E., Eckersall, P.D., Tvarijonaviciute, A., 2020. Use of saliva for diagnosis and monitoring the SARS-CoV-2: A general perspective. Journal of Clinical Medicine 9 (5). https://doi.org/10.3390/jcm9051491.

Chirica, G., Lachmann, J., Chan, J., 2006. Size exclusion chromatography of microliter volumes for on-line use in low-pressure microfluidic systems. Analytical Chemistry 78 (15), 5362–5368. https://doi.org/10.1021/ac060258t.

Ciui, B., Martin, A., Mishra, R.K., Brunetti, B., Nakagawa, T., Dawkins, T.J., Lyu, M., Cristea, C., Sandulescu, R., Wang, J., 2018. Wearable wireless tyrosinase bandage and microneedle sensors: Toward melanoma screening. Advanced Healthcare Materials 7 (7). https://doi.org/10.1002/adhm.201701264.

de Castro, L.F., de Freitas, S.V., Duarte, L.C., de Souza, J.A.C., Paixão, T.R.L.C., Coltro, W.K.T., 2019. Salivary diagnostics on paper microfluidic devices and their use as wearable sensors for glucose monitoring. Analytical and Bioanalytical Chemistry 411 (19), 4919–4928. https://doi.org/10.1007/s00216-019-01788-0.

Diouf, A., Bouchikhi, B., El Bari, N., 2019. A nonenzymatic electrochemical glucose sensor based on molecularly imprinted polymer and its application in measuring saliva glucose. Materials Science and Engineering C 98, 1196–1209. https://doi.org/10.1016/j.msec.2019.01.001.

Gao, W., Nyein, H.Y.Y., Shahpar, Z., Fahad, H.M., Chen, K., Emaminejad, S., Gao, Y., Tai, L.C., Ota, H., Wu, E., Bullock, J., Zeng, Y., Lien, D.H., Javey, A., 2016a. Wearable microsensor array for multiplexed heavy metal monitoring of body fluids. ACS Sensors 1 (7), 866–874. https://doi.org/10.1021/acssensors.6b00287.

Gao, W., Emaminejad, S., Nyein, H.Y.Y., Challa, S., Chen, K., Peck, A., Fahad, H.M., Ota, H., Shiraki, H., Kiriya, D., Lien, D.-H., Brooks, G.A., Davis, R.W., Javey, A.,

2016b. Fully integrated wearable sensor arrays for multiplexed in situ perspiration analysis. Nature 529 (7587), 509–514. https://doi.org/10.1038/nature16521.

Goud, K.Y., Teymourian, H., Sandhu, S.S., Tostado, N., Mishra, R.K., Moore, L.C., Harvey, S.P., Wang, J., 2020. OPAA/fluoride biosensor chip towards field detection of G-type nerve agents. Sensors and Actuators, B: Chemical 320. https://doi.org/10.1016/j.snb.2020.128344.

Gubala, V., Harris, L.F., Ricco, A.J., Tan, M.X., Williams, D.E., 2012. Point of care diagnostics: Status and future. Analytical Chemistry 84 (2), 487–515. https://doi.org/10.1021/ac2030199.

Guinovart, T., Bandodkar, A.J., Windmiller, J.R., Andrade, F.J., Wang, J., 2013. A potentiometric tattoo sensor for monitoring ammonium in sweat. Analyst 138 (22), 7031–7038. https://doi.org/10.1039/c3an01672b.

Guinovart, T., Valdés-Ramírez, G., Windmiller, J.R., Andrade, F.J., Wang, J., 2014. Bandage-based wearable potentiometric sensor for monitoring wound pH. Electroanalysis 26 (6), 1345–1353. https://doi.org/10.1002/elan.201300558.

He, W., Wang, C., Wang, H., Jian, M., Lu, W., Liang, X., Zhang, X., Yang, F., Zhang, Y., 2019. Integrated textile sensor patch for real-time and multiplex sweat analysis. Science Advances 5 (11). https://doi.org/10.1126/sciadv.aax0649.

Heikenfeld, J., Jajack, A., Rogers, J., Gutruf, P., Tian, L., Pan, T., Li, R., Khine, M., Kim, J., Wang, J., Kim, J., 2018. Wearable sensors: Modalities, challenges, and prospects. Lab on a Chip 18 (2), 217–248. https://doi.org/10.1039/c7lc00914c.

Hirschhaeuser, F., Sattler, U.G.A., Mueller-Klieser, W., 2011. Lactate: A metabolic key player in cancer. Cancer Research 71 (22), 6921–6925. https://doi.org/10.1158/0008-5472.CAN-11-1457.

Humphrey, S.P., Williamson, R.T., 2001. A review of saliva: Normal composition, flow, and function. Journal of Prosthetic Dentistry 85 (2), 162–169. https://doi.org/10.1067/mpr.2001.113778.

Iguchi, S., Kudo, H., Saito, T., Ogawa, M., Saito, H., Otsuka, K., Funakubo, A., Mitsubayashi, K., 2007. A flexible and wearable biosensor for tear glucose measurement. Biomedical Microdevices 9 (4), 603–609. https://doi.org/10.1007/s10544-007-9073-3.

Imani, S., Bandodkar, A.J., Mohan, A.M.V., Kumar, R., Yu, S., Wang, J., Mercier, P.P., 2016. A wearable chemical-electrophysiological hybrid biosensing system for real-time health and fitness monitoring. Nature Communications 7. https://doi.org/10.1038/ncomms11650.

Invernale, M.A., Tang, B.C., York, R.L., Le, L., Hou, D.Y., Anderson, D.G., 2014. Microneedle electrodes toward an amperometric glucose-sensing smart patch. Advanced Healthcare Materials 3 (3), 338–342. https://doi.org/10.1002/adhm.201300142.

Jia, W., Bandodkar, A.J., Valdés-Ramírez, G., Windmiller, J.R., Yang, Z., Ramírez, J., Chan, G., Wang, J., 2013. Electrochemical tattoo biosensors for real-time noninvasive lactate monitoring in human perspiration. Analytical Chemistry 85 (14), 6553–6560. https://doi.org/10.1021/ac401573r.

Kassal, P., Kim, J., Kumar, R., De Araujo, W.R., Steinberg, I.M., Steinberg, M.D., Wang, J., 2015. Smart bandage with wireless connectivity for uric acid biosensing as an indicator of wound status. Electrochemistry Communications 56, 6–10. https://doi.org/10.1016/j.elecom.2015.03.018.

Kim, J., Campbell, A.S., de Ávila, B.E.F., Wang, J., 2019. Wearable biosensors for healthcare monitoring. Nature Biotechnology 37 (4), 389–406. https://doi.org/10.1038/s41587-019-0045-y.

Kim, J., De Araujo, W.R., Samek, I.A., Bandodkar, A.J., Jia, W., Brunetti, B., Paixão, T.R.L.C., Wang, J., 2015a. Wearable temporary tattoo sensor for real-time trace metal monitoring in human sweat. Electrochemistry Communications 51, 41–45. https://doi.org/10.1016/j.elecom.2014.11.024.

Kim, J., Imani, S., de Araujo, W.R., Warchall, J., Valdés-Ramírez, G., Paixão, T.R.L.C., Mercier, P.P., Wang, J., 2015b. Wearable salivary uric acid mouthguard biosensor with integrated wireless electronics. Biosensors and Bioelectronics 74, 1061–1068. https://doi.org/10.1016/j.bios.2015.07.039.

Kim, J., Jeerapan, I., Imani, S., Cho, T.N., Bandodkar, A., Cinti, S., Mercier, P.P., Wang, J., 2016. Noninvasive alcohol monitoring using a wearable tattoo-based iontophoretic-biosensing system. ACS Sensors 1 (8), 1011–1019. https://doi.org/10.1021/acssensors.6b00356.

Kim, J., Jeerapan, I., Sempionatto, J.R., Barfidokht, A., Mishra, R.K., Campbell, A.S., Hubble, L.J., Wang, J., 2018a. Wearable bioelectronics: Enzyme-based body-worn electronic devices. Accounts of Chemical Research 51 (11), 2820–2828. https://doi.org/10.1021/acs.accounts.8b00451.

Kim, J., Sempionatto, J.R., Imani, S., Hartel, M.C., Barfidokht, A., Tang, G., Campbell, A.S., Mercier, P.P., Wang, J., 2018b. Simultaneous monitoring of sweat and interstitial fluid using a single wearable biosensor platform. Advanced Science 5 (10), 1800880. https://doi.org/10.1002/advs.201800880.

Kim, J., Valdés-Ramírez, G., Bandodkar, A.J., Jia, W., Martinez, A.G., Ramírez, J., Mercier, P., Wang, J., 2014. Non-invasive mouthguard biosensor for continuous salivary monitoring of metabolites. The Analyst 139 (7), 1632–1636. https://doi.org/10.1039/C3AN02359A.

Kobel, S., Valero, A., Latt, J., Renaud, P., Lutolf, M., 2010. Optimization of microfluidic single cell trapping for long-term on-chip culture. Lab on a Chip 10 (7), 857–863. https://doi.org/10.1039/b918055a.

Li, Z., Mohamed, M.A., Mohan, A.M.V., Zhu, Z., Sharma, V., Mishra, G.K., Mishra, R.K., 2019. Application of electrochemical aptasensors toward clinical diagnostics, food, and environmental monitoring: Review. Sensors (Switzerland) 19 (24). https://doi.org/10.3390/s19245435.

Lin, S., Wang, B., Yu, W., Castillo, K., Hoffman, C., Cheng, X., Zhao, Y., Gao, Y., Wang, Z., Lin, H., Hojaiji, H., Tan, J., Emaminejad, S., 2020. Design framework and sensing system for noninvasive wearable electroactive drug monitoring. ACS Sensors 5 (1), 265–273. https://doi.org/10.1021/acssensors.9b02233.

Liu, H., Zhang, Y., 2011. Droplet formation in microfluidic cross-junctions. Physics of Fluids 23 (8). https://doi.org/10.1063/1.3615643.

Martín, A., Kim, J., Kurniawan, J.F., Sempionatto, J.R., Moreto, J.R., Tang, G., Campbell, A.S., Shin, A., Lee, M.Y., Liu, X., Wang, J., 2017. Epidermal microfluidic electrochemical detection system: Enhanced sweat sampling and metabolite detection. ACS Sensors 2 (12), 1860–1868. https://doi.org/10.1021/acssensors.7b00729.

McLister, A., McHugh, J., Cundell, J., Davis, J., 2016. New developments in smart bandage technologies for wound diagnostics. Advanced Materials 28 (27), 5732–5737. https://doi.org/10.1002/adma.201504829.

Mishra, R.K., Mohan, A.M.V., Soto, F., Chrostowski, R., Wang, J., 2017. A microneedle biosensor for minimally-invasive transdermal detection of nerve agents. Analyst 142 (6), 918–924. https://doi.org/10.1039/c6an02625g.

Mishra, R.K., Sempionatto, J.R., Li, Z., Brown, C., Galdino, N.M., Shah, R., Liu, S., Hubble, L.J., Bagot, K., Tapert, S., Wang, J., 2020. Simultaneous detection of salivary Δ9-tetrahydrocannabinol and alcohol using a wearable electrochemical ring sensor. Talanta 211. https://doi.org/10.1016/j.talanta.2020.120757.

Mohan, A.M.V., 2020. Screen-printed electrochemical sensors for environmental contaminants. Nanotechnology in the Life Sciences. Springer Science and Business Media B.V, pp. 85–108. https://doi.org/10.1007/978-3-030-45116-5_5.

Mohan, A.M.V., (2021). Wearable energy storage devices. https://doi.org/10.1515/9781501521287.

Mohan, A.M.V., Aswini, K.K., Biju, V.M., 2014a. Electrochemical codeposition of gold particle-poly(2-(2-pyridyl) benzimidazole) hybrid film on glassy carbon electrode for the electrocatalytic oxidation of nitric oxide. Sensors and Actuators, B: Chemical 196, 406–412. https://doi.org/10.1016/j.snb.2014.02.030.

Mohan, A.M.V., Rambabu, G., Aswini, K.K., Biju, V.M., 2014b. Electrocatalytic behaviour of hybrid cobalt-manganese hexacyanoferrate film on glassy carbon electrode. Thin Solid Films 565, 207–214. https://doi.org/10.1016/j.tsf.2014.06.018.

Mohan, A.M.V., Aswini, K.K., Starvin, A.M., Biju, V.M., 2013. Amperometric detection of glucose using Prussian blue-graphene oxide modified platinum electrode. Analytical Methods 5 (7), 1764–1770. https://doi.org/10.1039/c3ay26310j.

Mohan, A.M.V., Brunetti, B., Bulbarello, A., Wang, J., 2015. Electrochemical signatures of multivitamin mixtures. Analyst 140 (22), 7522–7526. https://doi.org/10.1039/c5an01964h.

Mohan, A.M.V., Kim, N., Gu, Y., Bandodkar, A.J., You, J., Kumar, R., Kurniawan, J.F., Xu, S., Wang, J, 2017a. Merging of thin- and thick-film fabrication technologies: Toward soft stretchable "island–bridge" devices. Advanced Materials Technologies 2 (4), 1600284. https://doi.org/10.1002/admt.201600284.

Mohan, A.M.V., Windmiller, J.R., Mishra, R.K., Wang, J., 2017b. Continuous minimally-invasive alcohol monitoring using microneedle sensor arrays. Biosensors and Bioelectronics 91, 574–579. https://doi.org/10.1016/j.bios.2017.01.016.

Mohan, A.M.V., Rajendran, V., Mishra, R.K., Jayaraman, M., 2020. Recent advances and perspectives in sweat based wearable electrochemical sensors. TrAC Trends in Analytical Chemistry 131, 116024. https://doi.org/10.1016/j.trac.2020.116024.

Mohanan, A.V.M., Kunnummal, A.K., Biju, V.M.N., 2016. Electrochemical sensing of hydroxylamine using a wax impregnated graphite electrode modified with a nanocomposite consisting of ferric oxide and copper hexacyanoferrate. Microchimica Acta 183 (6), 2013–2021. https://doi.org/10.1007/s00604-016-1839-y.

Mohanan, V.M.A., Kunnummal, A.K., Biju, V.M.N., 2018. Selective electrochemical detection of dopamine based on molecularly imprinted poly(5-amino 8-hydroxy quinoline) immobilized reduced graphene oxide. Journal of Materials Science 53 (15), 10627–10639. https://doi.org/10.1007/s10853-018-2355-8.

Nambiar, S.R., Mohan, A.M.V., 2021. Metal nanoparticles-based disposable sensors. RSC Detection Science, (Vol. 2021. Royal Society of Chemistry, pp. 170–203. https://doi.org/10.1039/9781839163364-00170.

Pankratov, D., González-Arribas, E., Blum, Z., Shleev, S., 2016. Tear based bioelectronics. Electroanalysis 28 (6), 1250–1266. https://doi.org/10.1002/elan.201501116.

Priya, B., Rashmi, T., Bozena, M., 2006. Transdermal iontophoresis. Expert Opinion on Drug Delivery 3 (1), 127–138. https://doi.org/10.1517/17425247.3.1.127.

Rajendran, V., Mohan, A.M.V., Jayaraman, M., Nakagawa, T., 2019. All-printed, interdigitated, freestanding serpentine interconnects based flexible solid state supercapacitor for self powered wearable electronics. Nano Energy 65, 104055. https://doi.org/10.1016/j.nanoen.2019.104055.

Ray, T.R., Choi, J., Bandodkar, A.J., Krishnan, S., Gutruf, P., Tian, L., Ghaffari, R., Rogers, J.A., 2019. Bio-integrated wearable systems: A comprehensive review. Chemical Reviews 119 (8), 5461–5533. https://doi.org/10.1021/acs.chemrev.8b00573.

Sanjay, S.T., Zhou, W., Dou, M., Tavakoli, H., Ma, L., Xu, F., Li, X.J., 2018. Recent advances of controlled drug delivery using microfluidic platforms. Advanced Drug Delivery Reviews 128, 3–28. https://doi.org/10.1016/j.addr.2017.09.013.

Sempionatto, J.R., Brazaca, L.C., García-Carmona, L., Bolat, G., Campbell, A.S., Martin, A., Tang, G., Shah, R., Mishra, R.K., Kim, J., Zucolotto, V., Escarpa, A., Wang, J., 2019. Eyeglasses-based tear biosensing system: Non-invasive detection of alcohol, vitamins and glucose. Biosensors and Bioelectronics 137, 161–170. https://doi.org/10.1016/j.bios.2019.04.058.

Sempionatto, J.R., Khorshed, A.A., Ahmed, A., De Loyola E Silva, A.N., Barfidokht, A., Yin, L., Goud, K.Y., Mohamed, M.A., Bailey, E., May, J., Aebischer, C., Chatelle, C., Wang, J, 2020. Epidermal enzymatic biosensors for sweat vitamin C: Toward personalized nutrition. ACS Sensors 5 (6), 1804–1813. https://doi.org/10.1021/acssensors.0c00604.

Sempionatto, J.R., Lin, M., Yin, L., De la paz, E., Pei, K., Sonsa-ard, T., de Loyola Silva, A.N., Khorshed, A.A., Zhang, F., Tostado, N., Xu, S., Wang, J., 2021a. An epidermal patch for the simultaneous monitoring of haemodynamic and metabolic biomarkers. Nature Biomedical Engineering 5 (7), 737–748. https://doi.org/10.1038/s41551-021-00685-1.

Sempionatto, J.R., Moon, J.M., Wang, J., 2021b. Touch-based fingertip blood-free reliable glucose monitoring: Personalized data processing for predicting blood glucose concentrations. ACS Sensors 6 (5), 1875–1883. https://doi.org/10.1021/acssensors.1c00139.

Sempionatto, J.R., Nakagawa, T., Pavinatto, A., Mensah, S.T., Imani, S., Mercier, P., Wang, J., 2017. Eyeglasses based wireless electrolyte and metabolite sensor platform. Lab on a Chip 17 (10), 1834–1842. https://doi.org/10.1039/c7lc00192d.

Song, Y., Hormes, J., Kumar, C.S.S.R., 2008. Microfluidic synthesis of nanomaterials. Small 4 (6), 698–711. https://doi.org/10.1002/smll.200701029.

Strong, V., Dubin, S., El-Kady, M.F., Lech, A., Wang, Y., Weiller, B.H., Kaner, R.B., 2012. Patterning and electronic tuning of laser scribed graphene for flexible all-carbon devices. ACS Nano 6 (2), 1395–1403. https://doi.org/10.1021/nn204200w.

Tai, L.C., Ahn, C.H., Nyein, H.Y.Y., Ji, W., Bariya, M., Lin, Y., Li, L., Javey, A., 2020. Nicotine monitoring with a wearable sweat band. ACS Sensors 5 (6), 1831–1837. https://doi.org/10.1021/acssensors.0c00791.

Tai, L., Gao, W., Chao, M., Bariya, M., Ngo, Q.P., Shahpar, Z., Nyein, H.Y.Y., Park, H., Sun, J., Jung, Y., Wu, E., Fahad, H.M., Lien, D., Ota, H., Cho, G., Javey, A., 2018. Methylxanthine drug monitoring with wearable sweat sensors. Advanced Materials 30 (23), 1707442. https://doi.org/10.1002/adma.201707442.

Teymourian, H., Tehrani, F., Mahato, K., Wang, J., 2021. Lab under the skin: Microneedle based wearable devices. Advanced Healthcare Materials 10 (17), 2002255. https://doi.org/10.1002/adhm.202002255.

Valdés-Ramírez, G., Li, Y.C., Kim, J., Jia, W., Bandodkar, A.J., Nuñez-Flores, R., Miller, P.R., Wu, S.Y., Narayan, R., Windmiller, J.R., Polsky, R., Wang, J., 2014. Microneedle-based self-powered glucose sensor. Electrochemistry Communications 47, 58–62. https://doi.org/10.1016/j.elecom.2014.07.014.

Vinoth, R., Nakagawa, T., Mathiyarasu, J., Mohan, A.M.V., 2021. Fully printed wearable microfluidic devices for high-throughput sweat sampling and multiplexed electrochemical analysis. ACS Sensors 6 (3), 1174–1186. https://doi.org/10.1021/acssensors.0c02446.

Windmiller, J.R., Bandodkar, A.J., Valdés-Ramirez, G., Parkhomovsky, S., Martinez, A.G., Wang, J., 2012. Electrochemical sensing based on printable temporary transfer tattoos. Chemical Communications 48 (54), 6794–6796. https://doi.org/10.1039/c2cc32839a.

Yang, Y., Song, Y., Bo, X., Min, J., Pak, O.S., Zhu, L., Wang, M., Tu, J., Kogan, A., Zhang, H., Hsiai, T.K., Li, Z., Gao, W., 2020. A laser-engraved wearable sensor for sensitive detection of uric acid and tyrosine in sweat. Nature Biotechnology 38 (2), 217–224. https://doi.org/10.1038/s41587-019-0321-x.

Yao, H., Liao, Y., Lingley, A.R., Afanasiev, A., Lähdesmäki, I., Otis, B.P., Parviz, B.A., 2012. A contact lens with integrated telecommunication circuit and sensors for wireless and continuous tear glucose monitoring. Journal of Micromechanics and Microengineering 22 (7), 075007. https://doi.org/10.1088/0960-1317/22/7/075007.

Yao, H., Shum, A.J., Cowan, M., Lähdesmäki, I., Parviz, B.A., 2011. A contact lens with embedded sensor for monitoring tear glucose level. Biosensors and Bioelectronics 26 (7), 3290–3296. https://doi.org/10.1016/j.bios.2010.12.042.

Ye, D., Liang, G., Li, H., Luo, J., Zhang, S., Chen, H., Kong, J., 2013. A novel nonenzymatic sensor based on CuO nanoneedle/graphene/carbon nanofiber modified electrode for probing glucose in saliva. Talanta 116, 223–230. https://doi.org/10.1016/j.talanta.2013.04.008.

Zhai, Q., Gong, S., Wang, Y., Lyu, Q., Liu, Y., Ling, Y., Wang, J., Simon, G.P., Cheng, W., 2019. Enokitake mushroom-like standing gold nanowires toward wearable noninvasive bimodal glucose and strain sensing. ACS Applied Materials and Interfaces 11 (10), 9724–9729. https://doi.org/10.1021/acsami.8b19383.

Zhang, Y., Guo, H., Kim, S.B., Wu, Y., Ostojich, D., Park, S.H., Wang, X., Weng, Z., Li, R., Bandodkar, A.J., Sekine, Y., Choi, J., Xu, S., Quaggin, S., Ghaffari, R., Rogers, J.A., 2019. Passive sweat collection and colorimetric analysis of biomarkers relevant to kidney disorders using a soft microfluidic system. Lab on a Chip 19 (9), 1545–1555. https://doi.org/10.1039/c9lc00103d.

Zhao, J., Nyein, H.Y.Y., Hou, L., Lin, Y., Bariya, M., Ahn, C.H., Ji, W., Fan, Z., Javey, A., 2021. A wearable nutrition tracker. Advanced Materials 33 (1), 2006444. https://doi.org/10.1002/adma.202006444.

Zuliani, C., Matzeu, G., Diamond, D., 2014. A potentiometric disposable sensor strip for measuring pH in saliva. Electrochimica Acta 132, 292–296. https://doi.org/10.1016/j.electacta.2014.03.140.

12

Resistive switching in metal oxides for various applications

P.S. Subin [a], **K.J. Saji** [a,b] **and M.K. Jayaraj** [c,d]

[a] *Centre of Excellence in Advanced Materials, Cochin University of Science and Technology, Kochi, India.* [b] *International School of Photonics, Cochin University of Science and Technology, Kochi, India.* [c] *University of Calicut, Malappuram, India.* [d] *Cochin University of Science and Technology, Kochi, India*

12.1 Introduction

Resistive switching (RS) is referred to as the phenomena of changing resistance/conductance of materials under the action of a current or strong electric field. It was first observed in metal oxides (MOs) back in the 1960s by Hickmott (1962). He observed a sudden drop in resistance while applying a bias voltage to an aluminum oxide–sandwiched structure. The as-prepared aluminum oxide film was an excellent insulator, and it showed an exponential I–V relationship at low voltages (Lee et al., 2015). The resistance suddenly switched from high resistance state (HRS) to low resistance state (LRS) as an increased bias voltage was applied; the resulting resistance state was nonvolatile and reversible. This effect is commonly observed in MOs (Sawa, 2008), nitrides (Zhang et al., 2015), chalcogenides (Bogoslovskiy & Tsendin, 2012), semiconductors (Mehonic et al., 2012), and organic materials (Scott & Bozano, 2007). However, the RS property has been investigated most thoroughly in transition metal oxides (TMOs). TMOs such as CuO (Kim et al., 2009), TiO_2 (Yoshida et al., 2007), HfO_2 (Yu et al., 2011), and NiO (Seo et al., 2004) (Y. & Y.-H., 2008) show excellent RS property.

As shown in Fig. 12.1, a typical RS device has a capacitor-like structure in which a TMO is sandwiched between two electrodes. The electrodes may be Ag, Pt, Al, Au, ITO, etc., and not all combinations of electrode–TMO work. There are also a large variety of materials that do not belong to TMO still showing RS property including graphene oxide (GO) (He et al., 2009) and ternary perovskites such as $SrTiO_3$ (Wang et al., 2013) and $SrZrO_3$ (Meng-Han et al., 2010). The RS phenomenon is used in the fabrication of devices for different applications such as novel high-density resistive random access memory (RRAM - also called memristor) and synaptic memory. An RS device is capable

Nanomaterials for Sensing and Optoelectronic Applications. DOI: https://doi.org/10.1016/B978-0-12-824008-3.00007-2

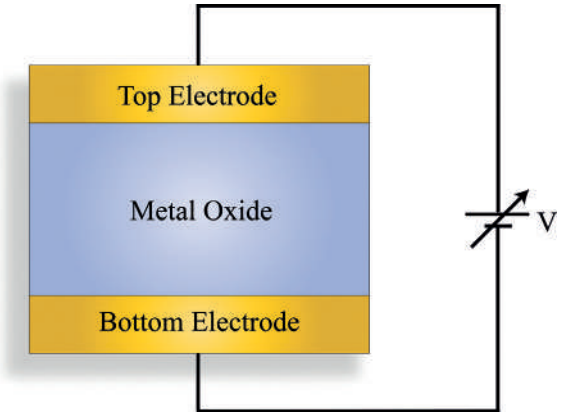

Figure 12.1. Schematic representation of the RS device.

of switching from HRS to LRS or vice versa several times depending upon the applied voltage/current. The critical parameters for memory device characterizations are operating power, speed, retention, and endurance. RS devices usually require low power and possess high-speed switching (~20–50 ns) (Cheng et al., 2010). An RRAM device exhibits a high retention time (time for which the device can withstand data) of approximately more than 10 years (Cabout et al., 2014; Lee et al., 2008). Endurance is defined as the number of cycles of operation that can be withstood by a device. An RRAM device usually has a very high endurance (cycle) of about 10^9 cycles (Kent & Worledge, 2015; Niu et al., 2016).

12.2 Types of resistive switching

A typical RS device is a two-terminal device (capacitor-like structure) with an oxide layer of thickness below 100 nm. That is, an MO thin film is sandwiched in between two electrodes. This two-terminal configuration is relatively easy to fabricate, which enables the RS device to be a highly scalable and economically feasible memory device. Because of the high bandgap (typically 1–4 eV), the as-prepared oxide thin films have very high resistance (HRS), which can be switched to an LRS by applying a sufficient external voltage. This initial process is called the forming process: the voltage at which tremendous resistance change takes place during the forming process is termed the forming voltage. Current passing through the oxide material is very high during formation, which might lead to a complete dielectric breakdown (irreversible breakdown) of the oxide materials. Therefore it is necessary to limit the current to an optimum value, and this current limit is usually called "current compliance" (CC). Once the conducting filament is formed, the device will continue to be in LRS for a longer time without any external power supply, thus nonvolatile. To change the resistance state of the device, another voltage pulse either of the same or opposite polarity must be applied. The process of changing the resistance state of the system from LRS to HRS is called the RESET process, and the voltage at which the RESET takes place is termed the RESET voltage (V_{reset}). Once again, to change the resistance state from HRS to LRS, a voltage pulse that is less than that of the forming voltage must be applied. This process is called the SET process, and the voltage at which the SET process takes place is termed the SET voltage (V_{set}). Thus the state of the device can be switched back and forth between LRS and HRS by controlling the voltage of the applied pulse. Based on

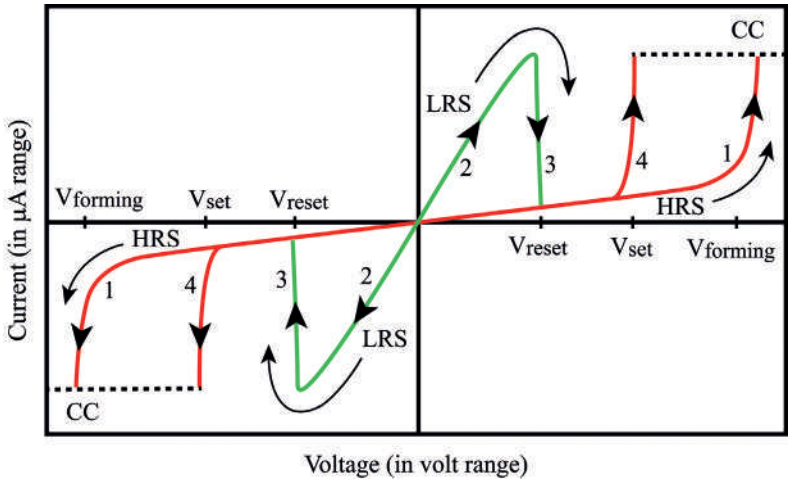

Figure 12.2. I–V characteristics of a unipolar RS device.

current–voltage (I–V) characteristics of the RS device, the RS phenomenon is roughly classified into two types: unipolar and bipolar RS.

12.2.1 Unipolar resistive switching

In unipolar RS the resistance state of the device can be switched back and forth by applying different voltages of consistent polarity. Unipolar RS action does not depend upon the polarity of the applied voltage, i.e., SET and RESET occur under the same polarity. Unipolar switching is usually exhibited by simple binary oxide structures like NiO (Y. & Y.-H., 2008), CuO (K. C. Kim et al., 2009), CoO (Wang et al., 2010), Fe_2O_3 (Jin-Yong et al., 2013), HfO (Wang et al., 2010a), and Nb_2O_5 (Mähne et al., 2012). Fig. 12.2 represents the I–V characteristics of unipolar RS. As-prepared MO-based devices will be in HRS (also represented by OFF state). A relatively high positive voltage applied to the device brings its resistance to LRS (forming process) at a particular voltage called forming voltage. The curve "1" in Fig. 12.2 represents the forming process of a unipolar device. After the forming process, the current becomes very high, and this current must be limited by CC. This is a nonvolatile state, and hence the device will remain in LRS even if we remove the applied voltage. A positive voltage sweep (from 0 up to V_{reset}) applied to the device after forming is represented by curve "2" in Fig. 12.2, which is an LRS (also represented by ON state). When the applied voltage reaches V_{reset}, the resistance changes from LRS to HRS (represented by curve "3" in Fig. 12.2); this is called the RESET process. During this process, CC is not mandatory since HRS restricts the

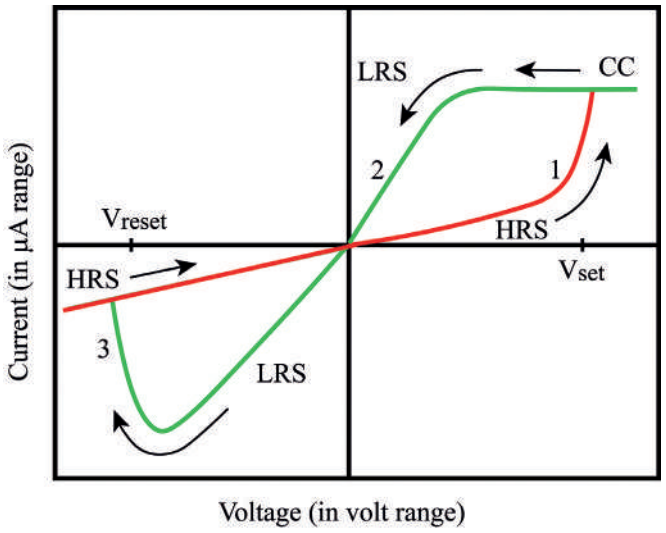

Figure 12.3. I–V characteristics of a bipolar RS device.

current overshoot through the device. In order to change the state of the device again from HRS to LRS a voltage that is greater than that of V_{reset} has to be applied. This process is called the SET process (represented by curve "4" in Fig. 12.2). From the I–V characteristics, it can be observed that the device behavior is the same for both polarities of the applied voltage. Hence all these processes can be observed by applying negative voltage also (positive voltage is not needed this time). So unipolar RS is advantageous from a schematic point of view because no polarity change in the voltage is needed (Nardi et al., 2011).

12.2.2 Bipolar resistive switching

Bipolar RS is sensitive to the polarity of the applied voltage, i.e., SET and RESET occur under opposite polarities. Bipolar RS has been observed in numerous oxides such as TiO_2 (Yoshida et al., 2007), MnO_2 (Yang et al., 2009), $BiFeO_3$ (Shuai et al., 2011), and ternary oxides with a perovskite structure such as $SrTiO_3$ (STO) (Szot et al., 2007) and $SrZrO_3$ (Lin et al., 2007). Fig. 12.3 represents the I–V characteristics of a bipolar RS device. Here curve "1" represents the SET process under the application of a positive voltage, which brings the device from HRS to LRS, whereas a negative voltage is required for the RESET process, which brings the device from the LRS to the HRS (curve "3" represents the RESET process). In unipolar RS, the forming process is mandatory; however, the requirement for a forming process in bipolar RS varies depending on the type of oxide materials. In the case of bipolar RS the choice of top and bottom electrodes is very important because the work functions of electrodes play a crucial role in bipolar RS. The difference in work function leads to the formation of a Schottky-like barrier at the interface. Studies show that an ohmic contact of Au/$Pr_{0.7}Ca_{0.3}MnO_3$ (PCMO), $SrRuO_3$ (SRO)/PCMO, and Ti/$SrTi_{0.99}Nb_{0.01}O_3$ (Nb:STO) interfaces shows no RS. However, the I–V curves for Ti/PCMO, Au/Nb:STO, and SRO/Nb:STO interfaces exhibit hysteretic behavior indicating RS in addition to the rectification (Sawa, 2008). In light of these results, it can be concluded that the Schottky barrier plays an essential role in bipolar RS.

12.3 Mechanism of resistive switching

The mechanism behind the RS effect has been explained with the help of a variety of processes including ohmic conduction (Chen & Wu, 2010), Schottky emission (Xin, 2012), fuse–antifuse mechanism (Kwon et al., 2010), Poole–Frenkel (PF) conduction, trapping/detrapping of charge carriers (Jeong et al., 2011; Shang et al., 2010), and oxygen vacancy migration (Choi et al., 2009; Strachan et al., 2010; Chen et al., 2013). The mechanisms behind unipolar and bipolar switching are separately explained and discussed as follows.

12.3.1 Mechanism of unipolar resistive switching

In unipolar RS the mechanism is explained by the formation and rupture of the filamentary conducting path in an insulating matrix. Fig. 12.4 shows a possible driving mechanism for filament-type RS that shows unipolar behavior. The as-prepared device possesses high resistance (HRS); it does not contain any conducting channel between the electrodes (Fig. 12.4A). The forming process occurs when a sufficient voltage is applied across the electrode, where filamentary conducting paths form as a soft breakdown in the dielectric material (Fig. 12.4B). Due to the filamentary conducting path formation, the resistance of the RS device becomes very low as compared to the as-prepared device. This state of the device continues unless another voltage is applied. Again, when a voltage with the same polarity is applied, the rupturing of filaments takes place (RESET process) due to the Joule heating effect (Fig. 12.4C). These ruptured filaments can be reformed to convert from HRS to LRS (SET process) again by applying a voltage with the same polarity (Fig. 12.4D). The temperature dependence of resistance in the low-resistance state of the Pt/CuO/Pt structure suggests the presence of a copper metal filament network embedded within the CuO_x bridge (Fujiwara et al., 2008). The formation and rupturing of filaments are widely considered the mechanism behind unipolar RS. The mechanism of unipolar switching is simple, with no negative voltage needed for the entire operation. But thermal instabilities are observed in many unipolar RS devices due to thermal breakage of the filaments.

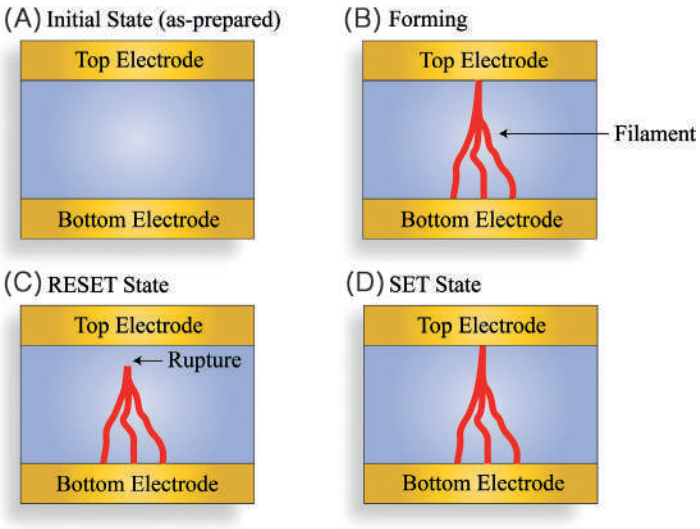

Figure 12.4. Schematic representation of the (A) initial state (as-prepared), (B) filament formation, (C) RESET state, (D) SET state.

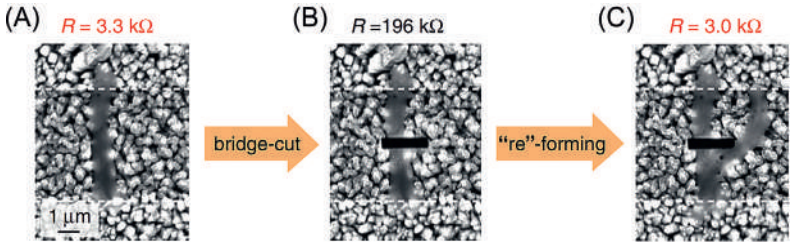

Figure 12.5. (A) SEM image of the Ni/CuO/Ni RS device after the forming operation; the conducting filament can be clearly seen, and the resistance is 3 kΩ, indicating that the device is in LRS. The channel length of this device was 5.2 μm, and the width was 80 μm. (B) The conducting filament physically cut by creating a narrow slit using FIB. After filament cutting, resistance recovers to its as-prepared value of ~200 kΩ. (C) Reformation of the conducting filament after cutting the initially formed filament. The device recovered an LRS value of 3 kΩ (Fujiwara et al., 2008).

12.3.2 Evidence for metallic conducting filament

Fujiwara et al. have reported the direct observation of structural changes in a CuO device having a planar geometry and electrodes a few microns apart (Fujiwara et al., 2008). They investigated to obtain evidence of filament formation by using the scanning electron microscope (SEM) imaging technique. Fig. 12.5 shows the SEM image, from which the formation of conducting filament/conducting bridge (CB) after forming operation can be seen (Fig. 12.5A). After filament formation, resistance becomes very low, and a transition from HRS ~200 kΩ to LRS ~3.3 kΩ occurs. Then, the filament is physically cut by creating a narrow slit using the focused ion beam (FIB) method (Fig. 12.5B). The device switches to its initial state (as-prepared) after cutting the conducting filament (HRS ~196 kΩ). When trying to reform (set) the device, branching of the filament occurs, and resistance goes to ~3 kΩ (Fig. 12.5C). They observed the temperature dependence of resistance similar to metals in the LRS, strongly suggesting the presence of a Cu metal filament network embedded within the CuO_x bridge. They also proposed that SET and RESET processes are respectively associated with the reduction and oxidation of a narrow segment of the Cu metal path promoted by an electric field or current (Fujiwara et al., 2008).

For a better understanding of the physical properties of formed filament, the channel resistance of both LRS and HRS has been measured as a function of temperature. Fig. 12.6 shows the temperature dependence of both HRS and the LRS of the Pt/CuO/Pt device, which exhibits unipolar RS. Here the resistance of LRS increases as the temperature increases, indicating that LRS possesses a typical metallic behavior (positive temperature coefficient of resistance). In contrast, this implies the presence of a Cu metal path inside the bridge (Fujiwara et al., 2008). HRS possesses semiconductor behavior with a negative temperature coefficient of resistance. In the case of the Pt/NiO/Pt unipolar RS device (Lee et al., 2008), HRS behaves like a semiconductor (i.e., resistance decreases as temperature increases), whereas LRS behaves like a metallic conductor with a positive temperature coefficient of resistance. These results strongly indicate the formation of metal filaments inside the NiO matrix (Lee et al., 2008).

12.3.3 Mechanism of bipolar resistive switching

Based on experimental results, the mechanism of a bipolar system is usually regarded as a redox reaction and electrochemical migration of oxygen vacancies. Hence the mechanism depends on the polarity of the operating voltage. When a voltage is applied across the electrodes, an intense electric field ($\sim 10^8$ V m^{-1} for a typical 100-nm-thick device with 10 V applied across it) is generated inside the active materials (say, TMO). This electric field induces the electrochemical migration of oxygen vacancies inside the active material. Fig. 12.7 illustrates the conduction filament formation and rupturing upon the application of positive and negative voltages at the top electrode. A positive voltage applied at the top electrode attracts negatively charged oxygen ions in the MO toward that electrode (Fig. 12.7A) (Wei et al., 2008; Yang et al., 2008). Oxygen vacancies are also created and migrated along with oxygen ions toward the top electrode. These oxygen vacancies that migrate toward the top electrode form conducting channels between the two electrodes. After forming a conduction channel between the electrodes, the resistance becomes low (LRS) as compared with the initial value (Fig. 12.7B). This state is nonvolatile and reversible to the initial state. A negative voltage at the top electrode repels the oxygen toward the bottom electrode resulting in high resistance by breaking the conducting channel (Fig. 12.7C) (Yang et al., 2008). RESET is thus not the result of the rupture of a conducting filament by Joule heating (even though the process may be heat-assisted). Again, a positive voltage at the top electrode switches the device back to LRS (Fig. 12.7D). In fact, LRS and HRS occur at the rectifying Schottky (top) junction, not at the ohmic junction. So it is better if one of the junctions is Schottky for the device to exhibit bipolar switching. The applied voltage bias can also create oxygen vacancies/oxygen ions at the ohmic junction, but small variations in the concentration of oxygen vacancies/oxygen ions will not alter the band structure of the ohmic junction (Yang et al., 2008).

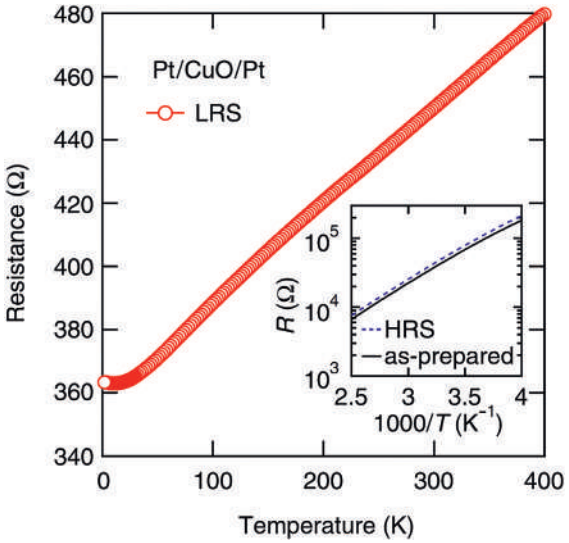

Figure 12.6. The resistance change of HRS and LRS as a function temperature. Temperature dependence of the filament resistance R(T) of a Pt/CuO/Pt - RS device with a channel length of 1.8 μm and a width of 95 μm was measured at each stage of resistance switching. The main panel shows R(T) in the LRS, indicating that conduction is dominated by a good metal, probably Cu. The inset shows R(T) in the as-prepared state and in the HRS. The activation energy of ~0.19 eV was established from the temperature dependence (Fujiwara et al., 2008).

12.3.4 Evidence for oxygen vacancy conducting filament

As mentioned earlier, bipolar RS in MOs is regarded as the creation and electromigration of oxygen vacancies, which changes the carrier density and valence states of cations in the dielectric matrix

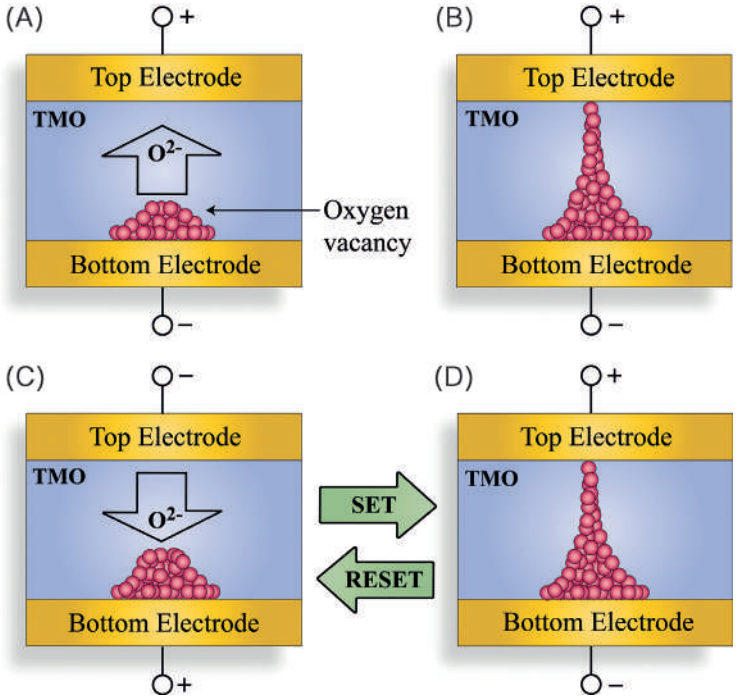

Figure 12.7. Illustration of the RS mechanism in bipolar devices. In each case voltage is applied at the electrodes, and the corresponding oxygen vacancy configuration is shown. (A) During the forming process, (B) during the SET process, (C) in the RESET state, and (D) in the SET state.

(Kwon et al., 2010). Selective area electron diffraction (SAED) patterns and fast Fourier transform (FFT) micrographs of the HRTEM images of TiO_2 planar structure reveal the change in crystallographic structure and oxidation state after the forming step. Fig. 12.8 shows the HRTEM images of such nanofilaments. During the forming step, nanofilament formation starts at the cathode; many filaments will grow from the cathode to anode. In fact, once one of the nanofilament connects between the cathode and anode (Fig. 12.8A and C), a large current flows through the device. When this current reaches the compliance limit, the potential drop across the electrodes reduces and prevents the growth of other nanofilaments. Such filaments are called partial filaments (Fig. 12.8B and D). These results support the filament growth model for the TiO_2-based devices (Kim et al., 2007; Kim and Hwang, 2009; Subin et al., 2021). TEM analysis reveals that the formed filament's diameter ranges from 5 to 10 nm (Figs. 12.8C and D).

Iron oxide (which exhibits several crystal phases such as Fe_3O_4, γ-Fe_2O_3, and α-Fe_2O_3 in its different oxidation states)-based devices show bipolar RS (Muraoka et al., 2007). When an Fe_3O_4-based device is electroformed to a conducting state, a change in the crystal phase of Fe_3O_4 to γ-Fe_2O_3 is observed. Fig. 12.9 shows the schematic representation of the device and testing configuration specially designed for Raman studies. The Raman spectrum of Fe_3O_4 was investigated before and after the forming step. A prominent peak is observed at 668 cm^{-1} before forming, which corresponds to the A_{1g} mode of Fe_3O_4 (magnetite). After forming, an additional peak at 718 cm^{-1} corresponding to γ-Fe_2O_3 is observed, thus confirming the oxidation state change during nanofilament formation.

12.4 Chalcogenides-based RRAM

Chalcogenides-based memory relies on the mechanism of phase-change memory (PCM). PCMs are capable of switching their structural

phase under the application of voltage pulses (Ciocchini et al., 2016). Most chalcogenide materials exist in at least two distinct solid phases: one amorphous and one (or more) crystalline phase (Raoux et al., 2010). The amorphous and crystalline phases of chalcogenide exhibit different optical and electrical properties. This difference in the electrical and optical properties for distinct phases can be used as memory if the phases can be switched back and forth a number of times. These different phases have different resistivity and band structures so that the phase can be differentiated by measuring the electrical current. This effect is utilized for the realization of high-density nonvolatile PCM. Many chalcogenides such as $Ge_2Sb_2Te_5$ (GST) (Maimon et al., 2004; Pradel et al., 2011), CdS (Ju et al., 2012), GeTe (Yu et al., 2008), and MoS_2 (Bertolazzi et al., 2013) are good candidates for PCM, conducting bridge resistive random access memory (CBRAM), and RRAM.

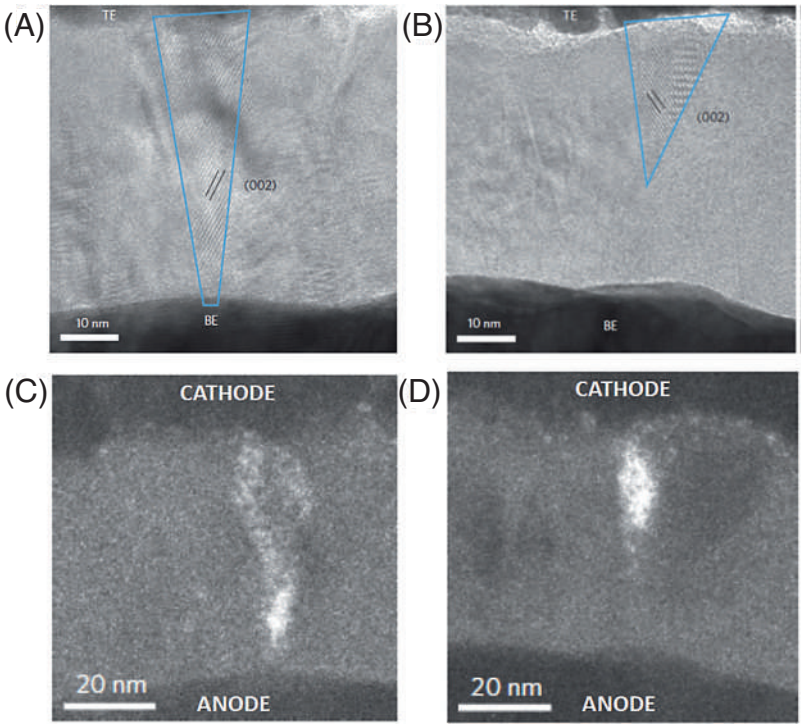

Figure 12.8. Magnéli structures after the forming step. (A) and (B): High-resolution TEM image of a Ti_4O_7 nanofilament. (C) and (D): a fast Fourier transform micrograph of the high-resolution image of Ti_4O_7 (Kwon et al., 2010).

In PCM the amorphous phase exhibits structural relaxation (SR) due to thermally accelerated atomic rearrangement in the disordered networks (Boniardi & Ielmini, 2011), which can be commonly observed in amorphous semiconductors (Koughia et al., 2005; Roorda et al., 1991) and metallic glasses (Miracle et al., 2007). The mechanism behind GST-based RRAM seems to be a high local enhancement of ionic diffusivity due to Joule heating and ion migration and the subsequent formation/collapse of a depleted layer at the bottom electrode due to the large electric field (Ciocchini et al., 2016). In the case of GST a positive sweep causes crystallization and a consequent decrease of resistance (1 GΩ to 30 MΩ), called the SET process. On the other hand, a negative sweep causes an increase in resistance (30 MΩ to 1 GΩ), called the RESET process. One of the main limitations of PCM is the SR of the amorphous phase and crystallization even at low temperatures (Ciocchini et al., 2016).

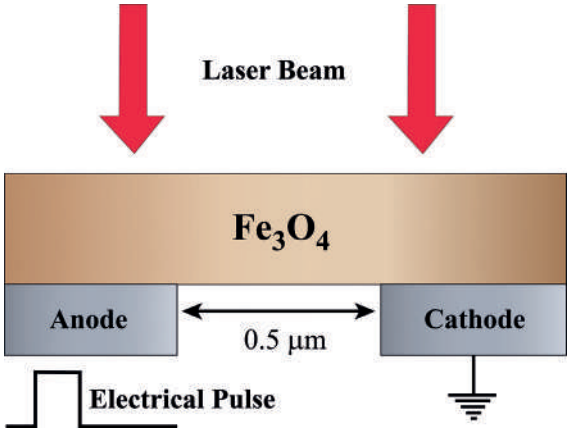

Figure 12.9. Schematic cross-section of the lateral device with two bottom electrodes to investigate the oxidation state change during switching using Raman spectroscopy.

12.5 Carbon-based RRAM

The RS property can be seen in a wide variety of materials, including carbon compounds, which could be utilized for RRAM applications. Carbon-based materials have attracted both industrial and academic interests for future RRAM applications because of their simple chemical composition, high stability, low cost, and compatibility with complementary metal-oxide-semiconductor (CMOS) processes (Kent & Worledge, 2015). Graphene, GO (He et al., 2009), thin films of graphitic sheets, amorphous carbon, and hydrogenated amorphous carbon show excellent RS properties. Reliable and reproducible switching phenomena were observed in the metal/a-C : H/Pt structures (Zhuge et al., 2010). The RS mechanism investigated in the metal/GO/Pt device reveals the diffusion of metal atoms through the GO matrix (Zhuge et al., 2011). In an Al/GO/ITO device a combined mechanism of diffusion and oxygen migration is proposed (Hong et al., 2011). The oxygen depth profile in the GO layer obtained by X-ray photoelectron spectroscopy (XPS) analysis shows a remarkable change in the oxygen functional group density for the two distinct resistance states (HRS and LRS). In the case of HRS the C–OH bonding peak decreases with depth, whereas in the case of LRS the C=O bonding peak increases with depth. The oxygen functional group density distribution in GO-based RRAM shows a remarkable difference for the two resistance states. This clearly indicates the oxygen migration through the GO layer during the formation process. More clearly, the oxygen migration and diffusion of the metal electrode are the main mechanisms behind the switching phenomena in GO-RRAM.

Figure 12.10. Hypothetical diagram of the current paths: (A) ON process; (B, C, D) OFF process.

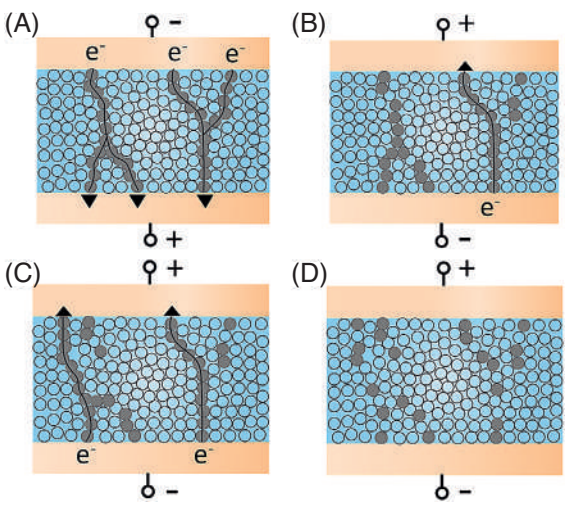

12.6 Perovskite-based RRAM

Organic and inorganic perovskite materials have recently attracted significant interest for applications in RS memory. Perovskite materials like $BaTiO_3$ (Chu et al., 2014; Pan et al., 2012), $SrZrO_3$ (Lin et al., 2008; Panda & Tseng, 2014), $SrTiO_3$ (Muenstermann et al., 2010; Song et al., 2012), $CsPbBr_3$ (Liu et al., 2017), $Pr_{1-x}Ca_xMnO_3$ (PCMO) (Chen et al., 2010; Kumbhare et al., 2017), $CH_3NH_3PbBr_3$

perovskite quantum dots (QDs) (Vijila et al., 2019; Yang et al., 2017), $CsPbBr_3$ QDs (Wang et al., 2018), and $CH_3NH_3PbI_{3-x}Cl_x$ (Yoo et al., 2015) are good candidates for RRAM application. The RS properties of perovskite materials strongly depend on the crystal structures and oxygen concentration of the films (Lin et al., 2008; Panda & Tseng, 2014). The commonly observed RS type in perovskite-based RRAM is bipolar RS. The RS mechanism behind the perovskite-based RRAM includes ohmic conduction (Lin et al., 2006; Yan & Liu, 2015), hopping conduction (Cheng et al., 2018), Schottky emission (Cai et al., 2018), PF conduction (Chen & Wu, 2010), trap-controlled space-charge-limited conduction (SCLC), and charge carrier trapping or detrapping (Liu et al., 2016; Yang et al., 2017). In the case of the $BaTiO_3$ perovskite RS device, the RS mechanism originates from the formation and the rupture of conductive filaments by electrical migration and thermal diffusion of oxygen vacancies, respectively (Yan et al., 2011). Fig. 12.10 shows the proposed conduction mechanism of vanadium-doped $SrZrO_3$ (V:SZO) perovskite RS memory. In the forming process, a conducting path is formed through possible point defects such as oxygen vacancy, ionic and electronic defects associated with zirconium replaced by vanadium (Lin et al., 2006). Due to this conduction path, the overall resistance of the device gets reduced (ON state). Fig. 12.10A shows the hypothetical diagram of conduction path formation in the ON state. The mechanism behind the RESET process (OFF state) is regarded as the rupturing of the conduction paths. When a positive voltage is applied at the top electrode, electrons would be trapped randomly in the defects of V:SZO. A part of the current paths is ruptured due to the trapping of electrons at the conducting path, as shown in Fig. 12.10B. This process does not bring the device to a stable HRS (OFF state) because current could flow through other unruptured or newly formed conducting paths, as shown in Fig. 12.10C. But, when more current passes through the transition region (say, 13 V), electrons get trapped in the defects of the V:SZO film to some degree; therefore the path is considered to be ruptured, as shown in Fig. 12.10D (Lin et al., 2006). Such a RESET process (OFF state) consumes more power than the SET process (ON state).

12.7 Multilayer RRAM

The RS property has also been reported in many bilayer structures (Chen et al., 2014; Varandani et al., 2010). Fig. 12.11 shows the schematic representation of a bilayer device. Although most of the reported literature on RRAM devices is centered on single-layered

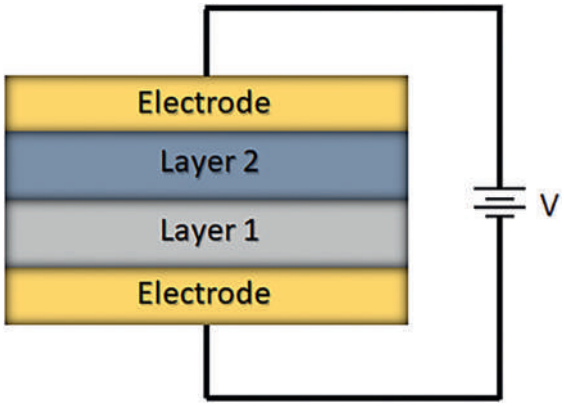

Figure 12.11. Schematic of the multilayer RRAM.

RS devices, improved memory characteristics are observed in many bilayered devices such as $Pt/Al_2O_3/TiO_2/Ru$ (Kim et al., 2006), Cu-doped MoO_x/GdO_x (Yoon et al., 2009), CuO-$CuInO_2$ (Varandani et al., 2010), ZrO_x/HfO_x (Lee et al., 2010), TaO_x/WO_x (Prakash et al., 2012), and WO_x/NbO_x (Sadaf et al., 2012). The self-formed WO_x/NbO_x bilayer structure exhibits significantly improved memory performance and can address the sneak path issue in the crossbar array (high-density memory) (Liu et al., 2011). This WO_x/NbO_x device exhibits low SET and RESET voltages, excellent switching uniformity, high HRS-to-LRS ratio, high-speed switching, and excellent retention even at 85°C (Sadaf et al., 2012). Hu et al. showed stable bipolar RS characteristics with a high resistance ratio ($\sim 10^5$) in $Ag/MnO/CeO_2/Pt$ bilayer devices (Hu et al., 2018). Dou et al. demonstrated remarkable improvement in performance by introducing a thin Si buffer layer into a CeO_2-based RS device (Dou et al., 2012). Banerjee et al. designed a high-k Al_2O_3/WO_x bilayer dielectric that has a significant resistance ratio of $>10^3$, good read endurance of 10^5 times at a read voltage of -0.5 V, and data retention of 10 years at 85°C (Banerjee et al., 2011).

12.8 High-density memory (crossbar memory)

Typically an RS memory device has a simple structure compared to flash memory (floating gate transistor). Therefore the fabrication process is much simple and more cost-effective with current semiconductor fabrication technologies. Future memory devices need to accommodate novel, highly scalable nanoelectronic structures to validate Moore's law. Many models have been proposed for nanoelectronics-based circuit design and fabrication. Because of their simple structure, high-density three-dimensional (3D) RRAM electronics are the most promising of all nanotechnologies (Ziegler and Stan, 2003). High-density crossbar memory was suggested for RRAM about a decade ago, and it is also used for custom configurable logic circuits (Strukov & Likharev, 2007). Fig. 12.12 shows a typical crossbar memory structure. Crossbar-based RS memory is among the most promising of all nanotechnologies, which enables an alternative to the von Neumann architecture (Ziegler and Stan, 2003). Compared to conventional solid-state devices, RRAM-based crossbar has many advantages. The 3D RRAM crossbar is very cost-effective, with about 20 times lower power

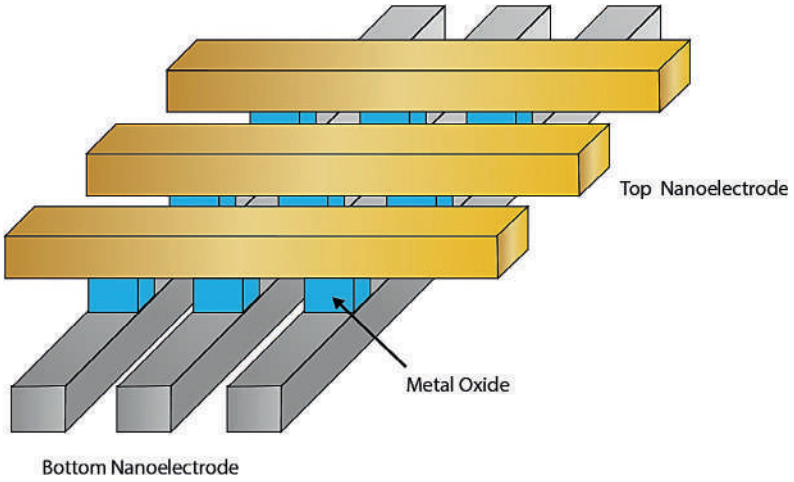

Figure 12.12. Schematic representation of the crossbar structure.

per bit. One of the main disadvantages of the crossbar structure is the sneak path (leakage current) issue (Kügeler et al., 2011). The sneak path current arises when we read a particular RS device in the crossbar, especially when it is in HRS. The read voltage (comparatively small voltage) applied to the device causes a small current through that device, but a significant current flows through the neighboring devices too, which also contributes to the read current. This issue mainly arises when all the surrounding RS devices are in LRS. Current flowing through neighboring RS devices other than the addressed one is called sneak current. This sneak current might lead to a wrong interpretation of the data. Linn et al. proposed an innovative method to address this sneak path issue by introducing a new RS device called complementary resistive switch (CRS). It is constructed by connecting two bipolar RS devices antiserially onto a single device (Fig. 12.13A) (Linn et al., 2010).

The RS devices integrated into crossbar arrays reduce the cell size to $4F^2$ (where F is the minimum feature size) per bit (Nauenheim et al., 2008). Top electrode lines and bottom electrode lines (interconnect lines) are connected to a multiplexer to address each RS device. The multiplexer selects the corresponding RS device

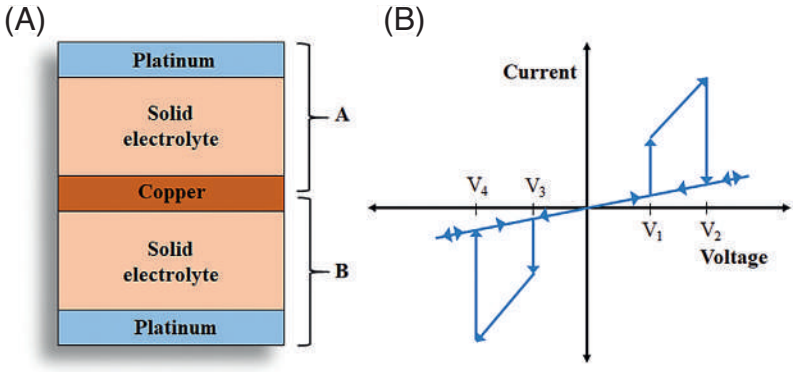

Figure 12.13. (A) Schematic of CRS (a combination of RS devices A and B). (B) I–V characteristic of a CRS (superimposed I–V characteristics of A and B).

with selector binary bits. An essential factor in the fabrication of the device is its uniformity. All the devices must have the same physical properties such as thickness, morphology, and crystallinity so that they probably have the same SET, RESET voltage, durability, and stability. Considering all these factors, conventional CMOS technology and photo/e-beam lithography are the most prominent methods for crossbar RS device fabrication. Nauenheim et al. fabricated a 64×64 bit nanocrossbar array with a feature size of 100 nm via electron beam lithography in combination with a lift-off process (Nauenheim et al., 2008).

CRS is composed of two RS devices, A and B, which are connected antiserially (Fig. 12.13A), resulting in superimposed I–V characteristics, as shown in Fig. 12.13B. Initially, both devices A and B are in HRS ("OFF" state); to change the state of CRS, a voltage has to be applied. An applied voltage of $V < 2V_3$ or $V > 2V_1$ is required for CRS to change the state from "OFF" to "1" or "0", respectively. Suppose devices A and B are in LRS and HRS, respectively (CRS state 1); then it acts like a potential divider and almost all voltage is dropped across device B for $V < V_1$. When the voltage reaches V_1, device B switches to LRS and device A continues to be in LRS (Fig. 12.13B) since the voltage drop across device B is far below the RESET voltage of device B. When both devices A and B are in LRS, the CRS state is defined as the ON state, which occurs only during read operation. If the voltage is further increased to V_2, device A switches to HRS, since this voltage is equivalent to the RESET voltage of device A and device B remains in the LRS. This state is defined as "0" i.e., device A in HRS and device B in LRS. Moving to the opposite polarity from 0 to V_3 volts, CRS remains in the state "0". At voltage V_3, device A changes its state to LRS. Now both the devices are in LRS (ON state) for the range $V_3 < V < V_4$. If the voltage exceeds V_4, device B changes its state to HRS and device A is in LRS, and the resulting state of CRS is termed "1". All the possible states of CRS are shown in Table 12.1.

12.9 In-memory digital computing

Conventional computers are based on the von Neumann architecture, in which data is processed in the processor and stored in the memory (Ielmini & Wong, 2018), where the processor and storage space are physically separated. In this architecture data stored in the memory unit must be transferred to the processing unit, and processed data has to be transferred back to the memory unit to store. This entire process takes up much time and energy; hence the speed of computing might be reduced. To address this issue, a new computer

Table 12.1 Possible states of a complementary resistive switch (CRS).

CRS state	RS device A	RS device B	Resistance CRS
0	HRS	LRS	HRS
1	LRS	HRS	HRS
ON	LRS	LRS	LRS + LRS; only during read operation
OFF	HRS	HRS	>>HRS; only in initial state

State "ON" occurs only during the read operation. State "OFF" is the initial state of the device. The states "0" and "1" are the memory states for which the overall resistance of the CRS is the same: $R_{CRS} = R_{LRS} + R_{HRS}$ (with $R_{LRS} << R_{HRS}$).

architecture called in-memory computing (IMC) has been proposed. IMC is a method that utilizes an architecture that is capable of computing within the memory, thus reducing time and energy consumption (Ielmini & Wong, 2018). RRAM is a novel nonvolatile memory that is able to compute within the memory. Fig. 12.14 shows the realization of an RRAM-based NAND logic gate. X_1 and X_2, indicated by red memory cells in Fig. 12.14, represent the resistance state of two RS devices. V_R and Y represent the input read voltage and output, respectively. Here logic values "0" and "1" are represented by the LRS and HRS (say, LRS ~1 kΩ and HRS ~1 MΩ), respectively; all processes are explained assuming negligible sneak path current. When X_1 and X_2 both set to the "0" state (LRS), a significant current flows through both devices. Then a measurable output voltage appears across the load resistor (R_L). When X_1 and X_2 both set to be in the "1" state (HRS), no significant current flows through the devices. Thus output Y becomes zero. When $X_1 = 0$ and $X_2 = 1$ or vice versa, a significant current flows through the device set to "0" and contributes to the output Y. Output Y can be stored in another location in the same array. Table 12.2 shows the truth table of the NAND gate realized by RRAM.

Also, NOT operation can be easily realized with the same configuration. Consider only the case of X_1 (forget about X_2), and if X_1 is set to LRS (logic value 0), then current flows through R_L; hence the output will be "1". If X_1 is set to HRS (logic value 1), then no current flows through R_L; hence the output will be "0". Therefore the output is NOT operation of X_1.

Figure 12.14. The realization of the NAND gate with the RRAM device.

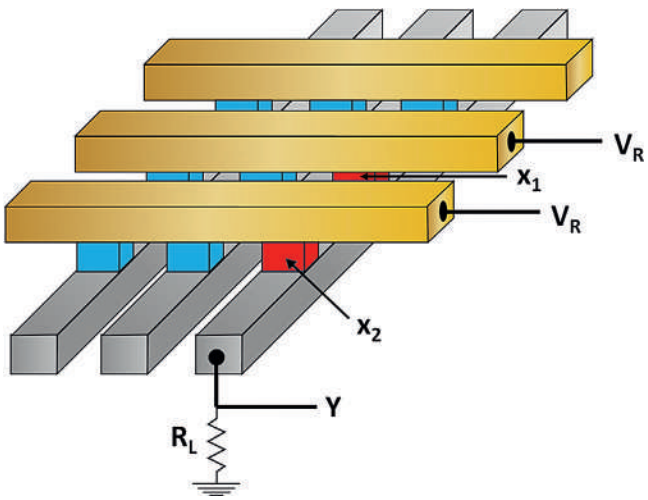

Table 12.2 The truth table of an RRAM-based NAND gate.

State of RS element X_1	Logic Value of X_1	State of RS element X_2	Logic Value of X_2	Output Y
LRS	0	LRS	0	1
LRS	0	HRS	1	1
HRS	1	LRS	0	1
HRS	1	HRS	1	0

Now, a small alteration in the circuit can lead to the formation of an XOR gate with RRAM; Fig. 12.15 shows the realization of the XOR gate. Suppose the red memory cells are initially in LRS (X_1, $X_2 = 0$); then the same current flows through both the RS devices; therefore the comparator output must be "0". The comparator gives an absolute output voltage corresponding to the input current difference, i.e., the output is high only for a large input difference and low otherwise. If $X_1 = 0$ and $X_2 = 1$, a large difference in current occurs at the inputs of the comparator, which leads to a high output (logic value "1"). If $X_1 = 1$ and $X_2 = 0$, the same thing happens again, since the comparator gives only absolute output proportional to the input difference. If X_1, $X_2 = 1$, then the difference in current must be negligible; hence the comparator output becomes "0". Table 12.3 shows the truth table of the

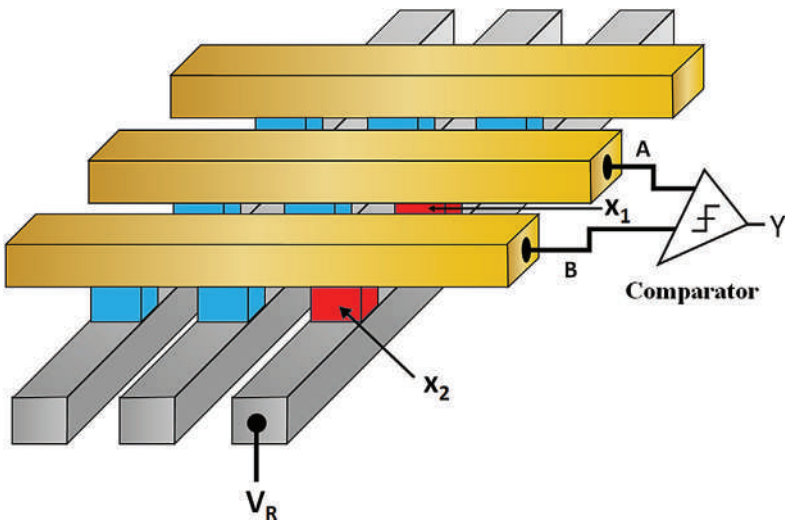

Figure 12.15. Realization of the XOR gate with the RRAM device.

Table 12.3 The truth table of an RRAM-based XOR gate.

State of RS element X_1	Logic value of X_1	State of RS element X_2	Logic value of X_2	Output Y
LRS	0	LRS	0	0
LRS	0	HRS	1	1
HRS	1	LRS	0	1
HRS	1	HRS	1	0

XOR gate realized by RRAM.

12.10 Neuromorphic computing with RS memory

Neuromorphic computing is a novel computing method inspired by human brain computation and thus is also called brain-inspired computing. Neuromorphic computing architectures enable in-memory analog computing technology; hence, memory and processor are not physically separated. This type of computation technology can address the drawbacks of the von Neumann architecture. Limitations, such as latency and power consumption, are usually described as the von Neumann bottleneck (Ielmini, 2018). RS memory, PCM, and Mott memristor can be used as an artificial synapse since the conductance can be tuned by applying a series of input pulses (Pickett et al., 2013; Tan et al., 2018; Tomas et al., 2016). Conductance change during the application of an electrical signal is analogous to the synaptic weight/connection alteration in neuroscience (Subin et al., 2021). An increase in conductance by applying a specific voltage stimulus is defined as the potentiation process, whereas a decrease in conductance is defined as depression. The conductance change of the artificial synapse (RS device) element depends upon the timing and amplitude of the input pulse. In the human brain memory is a result of the persistent strengthening of the connection between two neurons, and it is classified as short- and long-term plasticity, also called short-term memory (STM) and long-term memory (LTM), respectively, in the psychological model. According to Atkinson and Shiffrin, the transition from STM to LTM occurs due to a process called repeated rehearsal (Atkinson and Shiffrin, 1968). A similar process can be observed in an RS-based artificial

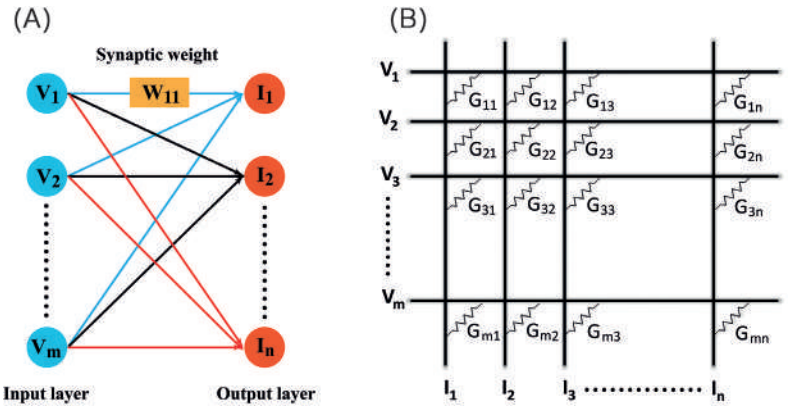

Figure 12.16. (A) Schematic illustration of a single-layer neural network. The input layer and output layer represent pre- and postsynaptic neurons, respectively, in which the depth of connection between the two neurons is denoted by a synaptic weight (W). (B) Crossbar array analogs to a neural network; here the conductance of the RS devices is equivalent to the synaptic weight.

synapse, in which the conductance of the device increases persistently as input pulse is applied repeatedly. Necessarily, an artificial synapse must exhibit this property in addition to potentiation and depression. Retention time is also tunable in some RS devices so that the sensory register (SR), STM, and LTM can be easily obtained. In order to implement artificial synapse for constructing artificial neural networks, it must exhibit synaptic plasticity with respect to spike timing (spike-timing-dependent plasticity [STDP]), spike rate (spike-rate-dependent plasticity [SRDP]), and transition from STM to LTM.

A simple single-layer neural network is shown in Fig. 12.16A, in which the input layer and output layer are connected through a synaptic weight. Here each synaptic weight (W) represents the conductance of individual RS devices having a specific conductance value. The inputs V_1, V_2, V_3,...V_m are the input voltages, and I_1, I_2, I_3,...I_n are the output currents (Fig. 12.16B). Here each output current strongly depends on the synaptic weights of the corresponding device. As mentioned earlier, the input layer and output layer are connected to the multiplexer to address each device in the crossbar. According to Kirchhoff's law, the output current can be represented by the equation (ignored sneak path issue),

$$I_j = \sum_{j}^{m} G_{ij} V_i \tag{12.1}$$

where G_{ij} is the conductance of the ij^{th} RS device.

Additionally, Eq. 12.1 can be represented in matrix form (Eq. 12.2). Thus by measuring the currents through each output line, we can solve

the vector-matrix multiplication:

$$\begin{bmatrix} I_1 \\ I_2 \\ . \\ . \\ . \\ I_n \end{bmatrix} = \begin{bmatrix} G_{11} & G_{21} & G_{31} & . & . & . & G_{m1} \\ G_{12} & G_{22} & G_{32} & . & . & . & G_{m1} \\ . & . & . & . & . & . & . \\ . & . & . & . & . & . & . \\ . & . & . & . & . & . & . \\ G_{1n} & G_{2n} & G_{3n} & . & . & . & G_{mn} \end{bmatrix} \times \begin{bmatrix} V_1 \\ V_2 \\ . \\ . \\ . \\ V_m \end{bmatrix} \tag{12.2}$$

Real-world physics problems are solvable via vector-matrix multiplication; thus they are solvable by artificial neural networks as well. The desired conductance matrix can be obtained by altering the conductance by applying pulses with a large voltage compared to the read voltage. The potentiation (increase in conductance) and depression (decrease in conductance) processes of the artificial synapse are usually achieved by applying positive and negative voltage pulses, respectively. Read voltage applied at each input line produces an output current through each RS device. The output current is the product of conductance and applied read voltage. The applied read voltage has some margin since the synaptic weight might be altered under the application of excess voltage.

Summary

RS devices are novel candidates for the realization of next-generation memory devices that are suitable for many applications. They are applicable in the fabrication of nonvolatile RRAM, artificial synapses, and advanced digital IMC. These applications are essential for artificial intelligence, deep learning, and energy-efficient computing. The RRAM device supports a 3D crossbar array structure capable of high-density memory fabrication since it has only two terminals. Fabrication processes are also simple because the active materials are simple TMOs. RRAM exhibits good endurance and retention as compared to conventional nonvolatile memories. As mentioned erlier, the RS devices are also suitable for artificial synapses, the basic building block of neuromorphic computing. This RS-based artificial synapse can emulate almost all characteristics of biological synapses, such as short-term plasticity, long-term potentiation, spike-timing–dependent plasticity (STDP), and paired-pulse facilitation (PPF). STM to LTM transition can also be realized in RS-based artificial synapse, which is essential for learning and memory. In digital computing IMC is feasible using RS devices by constructing essential logic gates. Logic gates are the fundamental units of a digital computer; many logic gates are practicable with RS, especially the universal NAND gate. In light

of these facts, RS-based devices are good candidates to fabricate high-density nonvolatile memory and artificial synapse for energy-efficient IMC and neuromorphic computing applications.

References

Atkinson, R.C., Shiffrin, R.M., 1968. Human Memory: A Proposed System and its Control Processes. Psychology of Learning and Motivation 2, 89–195. https://doi.org/10.1016/S0079-7421(08)60422-3.

Banerjee, W., Rahaman, S.Z., Prakash, A., Maikap, S., 2011. High-k Al_2O_3/WO_x bilayer dielectrics for low-power resistive switching memory applications. Japan. J. Appl. Phys. 50 (10). https://doi.org/10.1143/JJAP.50.10PH01.

Bertolazzi, S., Krasnozhon, D., Kis, A., 2013. Nonvolatile memory cells based on MoS_2/graphene heterostructures. ACS Nano 7 (4), 3246–3252. https://doi.org/10.1021/nn3059136.

Bogoslovskiy, N.A., Tsendin, K.D., 2012. Physics of switching and memory effects in chalcogenide glassy semiconductors. Semiconductors 46 (5), 559–590. https://doi.org/10.1134/S1063782612050065.

Boniardi, M., Ielmini, D., 2011. Physical origin of the resistance drift exponent in amorphous phase change materials. Appl. Phys. Lett. 98 (24). https://doi.org/10.1063/1.3599559.

Cabout, T., Vianello, E., Jalaguier, E., Grampeix, H., Molas, G., Blaise, P., Cueto, O., Guillermet, M., Nodin, J.F., Pemiola, L., Blonkowski, S., Jeannot, S., Denorme, S., Candelier, P., Bocquet, M., Muller, C., 2014. Effect of set temperature on data retention performances of HfO_2-based RRAM cells. 2014 IEEE 6th International Memory Workshop, IMW 2014. IEEE Computer Society. https://doi.org/10.1109/IMW.2014.6849355.

Cai, H., Ma, G., He, Y., Liu, C., Wang, H., 2018. A remarkable performance of $CH_3NH_3PbI_3$ perovskite memory based on passivated method. Org. Electron. 58, 301–305. https://doi.org/10.1016/j.orgel.2018.04.025.

Chen, S.W., Wu, J.M., 2010. Unipolar resistive switching behavior of $BiFeO_3$ thin films prepared by chemical solution deposition. Thin. Solid. Films 519 (1), 499–504. https://doi.org/10.1016/j.tsf.2010.08.004.

Chen, Y.-T., Chang, T.-C., Huang, J.-J., Tseng, H.-C., Yang, P.-C., Chu, A.-K., Yang, J.-B., Huang, H.-C., Gan, D.-S., Tsai, M.-J., Sze, S.M., 2013. Influence of molybdenum doping on the switching characteristic in silicon oxide-based resistive switching memory. Appl. Phys. Lett., 043508. https://doi.org/10.1063/1.4790277.

Chen, X., Hu, W., Wu, S., Bao, D., 2014. Stabilizing resistive switching performances of TiN/MgZnO/ZnO/Pt heterostructure memory devices by programming the proper compliance current. Appl. Phys. Lett. 104 (4). https://doi.org/10.1063/1.4863744.

Chen, Y., Tian, W., Li, H., Wang, X., Zhu, W., 2010. PCMO device with high switching stability. IEEE Electron Device Lett. 31 (8), 866–868. https://doi.org/10.1109/LED.2010.2050457.

Cheng, C.H., Chin, A., Yeh, F.S., 2010. Novel ultra-low power RRAM with good endurance and retention. In: Digest of Technical Papers—Symposium On VLSI Technology. IEEE, pp. 85–86. https://doi.org/10.1109/VLSIT.2010.5556180.

Cheng, X.F., Hou, X., Zhou, J., Gao, B.J., He, J.H., Li, H., Xu, Q.F., Li, N.J., Chen, D.Y., Lu, J.M., 2018. Pseudohalide-induced 2D $(CH_3NH_3)_2PbI_2(SCN)_2$ perovskite for ternary resistive memory with high performance. Small 14 (12). https://doi.org/10.1002/smll.201703667.

Choi, J.S., Kim, J.-S., Hwang, I.R., Hong, S.H., Jeon, S.H., Kang, S.-O., Park, B.H., Kim, D.C., Lee, M.J., Seo, S.S., 2009. Different resistance switching behaviors of NiO thin films deposited on Pt and $SrRuO_3$ electrodes. Appl. Phys. Lett., 022109. https://doi.org/10.1063/1.3173813.

Chu, D., Lin, X., Younis, A., Li, C.M., Dang, F., Li, S., 2014. Growth and self-assembly of $BaTiO_3$ nanocubes for resistive switching memory cells. J. Solid State Chem. 214, 38–41. https://doi.org/10.1016/j.jssc.2013.10.049.

Ciocchini, N., Laudato, M., Boniardi, M., Varesi, E., Fantini, P., Lacaita, A.L., Ielmini, D., 2016. Bipolar switching in chalcogenide phase change memory. Sci. Rep. 6. https://doi.org/10.1038/srep29162.

Dou, C., Kakushima, K., Ahmet, P., Tsutsui, K., Nishiyama, A., Sugii, N., Natori, K., Hattori, T., Iwai, H., 2012. Resistive switching behavior of a CeO_2 based ReRAM cell incorporated with Si buffer layer. Microelectron. Reliab. 52 (4), 688–691. https://doi.org/10.1016/j.microrel.2011.10.019.

Fujiwara, K., Nemoto, T., Rozenberg, M.J., Nakamura, Y., Takagi, H., 2008. Resistance switching and formation of a conductive bridge in metal/binary oxide/metal structure for memory devices. Japanese Journal of Applied Physics, Part 1: Regular Papers and Short Notes and Review Papers, 47 (8), 6266–6271. https://doi.org/10.1143/JJAP.47.6266.

He, C.L., Zhuge, F., Zhou, X.F., Li, M., Zhou, G.C., Liu, Y.W., Wang, J.Z., Chen, B., Su, W.J., Liu, Z.P., Wu, Y.H., Cui, P., Li, R.W., 2009. Nonvolatile resistive switching in graphene oxide thin films. Appl. Phys. Lett. 95 (23). https://doi.org/10.1063/1.3271177.

Hickmott, T.W., 1962. Low-frequency negative resistance in thin anodic oxide films. J. Appl. Phys. 33 (9), 2669–2682. https://doi.org/10.1063/1.1702530.

Hong, S.K., Kim, J.E., Kim, S.O., Cho, B.J., 2011. Analysis on switching mechanism of graphene oxide resistive memory device. J. Appl. Phys. 110 (4). https://doi.org/10.1063/1.3624947.

Hu, Q., Kang, T.S., Abbas, H., Lee, T.S., Lee, N.J., Park, M.R., Yoon, T.S., Kang, C.J., 2018. Resistive switching characteristics of $Ag/MnO/CeO_2/Pt$ heterostructures memory devices. Microelectron. Eng. 189, 28–32. https://doi.org/10.1016/j.mee.2017.12.014.

Ielmini, D., 2018. Brain-inspired computing with resistive switching memory (RRAM): devices, synapses and neural networks. Microelectron. Eng. 190, 44–53. https://doi.org/10.1016/j.mee.2018.01.009.

Ielmini, D., Wong, H.S.P., 2018. In-memory computing with resistive switching devices. Nat. Electron. 1 (6), 333–343. https://doi.org/10.1038/s41928-018-0092-2.

Jeong, D.S., Cheong, B.K., Kohlstedt, H., 2011. $Pt/Ti/Al_2O_3/Al$ tunnel junctions exhibiting electroforming-free bipolar resistive switching behavior. Solid State Electron. 63 (1), 1–4. https://doi.org/10.1016/j.sse.2011.05.028.

Jin-Yong, L., Yoon-Jae, B., Quanli, H., Young, J.C., Chi, J.K., Ho, L.H., Hyun-Mi, K., Ki-Bum, K., Tae-Sik, Y., 2013. Multimode threshold and bipolar resistive switching in bi-layered $Pt\text{-}Fe_2O_3$ core-shell and Fe_2O_3 nanoparticle assembly. Appl. Phys. Lett., 122111. https://doi.org/10.1063/1.4798534.

Ju, Y.C., Kim, S., Seong, T.G., Nahm, S., Chung, H., Hong, K., Kim, W., 2012. Resistance random access memory based on a thin film of CdS nanocrystals prepared via colloidal synthesis. Small 8 (18), 2849–2855. https://doi.org/10.1002/smll.201200488.

Kent, A.D., Worledge, D.C., 2015. A new spin on magnetic memories. Nat. Nanotechnol. 10 (3), 187–191. https://doi.org/10.1038/nnano.2015.24.

Kim, K.M., Choi, B.J., Koo, B.W., Choi, S., Jeong, D.S., Hwang, C.S., 2006. Resistive switching in $Pt/Al_2O_3/TiO_2/Ru$ stacked structures. Electrochem. Solid State Lett. 9 (12), 343–346. https://doi.org/10.1149/1.2353899.

Kim, K.M., Choi, B.J., Shin, Y.C., Choi, S., Hwang, C.S., 2007. Anode-interface localized filamentary mechanism in resistive switching of TiO_2 thin films. Appl. Phys. Lett. 91 (1). https://doi.org/10.1063/1.2749846.

Kim, K.M., Hwang, C.S., 2009. The conical shape filament growth model in unipolar resistance switching of TiO_2 thin film. Appl. Phys. Lett. 94 (12). https://doi.org/10.1063/1.3108088.

Kim, C.H., Jang, J.Y., Hwang, H.J., Sun, Z.H., Moon, H.B., Cho, J.H., 2009. Observation of bistable resistance memory switching in CuO thin films. Appl. Phys. Lett., 102107. https://doi.org/10.1063/1.3098071.

Koughia, K., Shakoor, Z., Kasap, S.O., Marshall, J.M., 2005. Density of localized electronic states in a-Se from electron time-of-flight photocurrent measurements. J. Appl. Phys. 97 (3). https://doi.org/10.1063/1.1835560.

Kügeler, C., Rosezin, R., Linn, E., Bruchhaus, R., Waser, R., 2011. Materials, technologies, and circuit concepts for nanocrossbar-based bipolar RRAM. Applied Physics A: Materials Science and Processing 102 (4), 791–809. https://doi.org/10.1007/s00339-011-6287-2.

Kumbhare, P., Chakraborty, I., Khanna, A., Ganguly, U., 2017. Memory performance of a simple $Pr_{0.7}Ca_{0.3}MnO_3$-based selectorless RRAM. IEEE Trans. Electron Devices 64 (9), 3967–3970. https://doi.org/10.1109/TED.2017.2725900.

Kwon, D.H., Kim, K.M., Jang, J.H., Jeon, J.M., Lee, M.H., Kim, G.H., Li, X.S., Park, G.S., Lee, B., Han, S., Kim, M., Hwang, C.S., 2010. Atomic structure of conducting nanofilaments in TiO_2 resistive switching memory. Nat. Nanotechnol. 5 (2), 148–153. https://doi.org/10.1038/nnano.2009.456.

Lee, H.Y., Chen, P.S., Wu, T.Y., Chen, Y.S., Wang, C.C., Tzeng, P.J., Lin, C.H., Chen, F., Lien, C.H., Tsai, M.J., 2008. Low power and high speed bipolar switching with a thin reactive Ti buffer layer in robust HfO_2 based RRAM. In: Technical Digest—International Electron Devices Meeting. IEDM. https://doi.org/10.1109/IEDM.2008.4796677.

Lee, J.S., Lee, S., Noh, T.W., 2015. Resistive switching phenomena: a review of statistical physics approaches. Appl. Phys. Rev. 2 (3). https://doi.org/10.1063/1.4929512.

Lee, J., Bourim, E.M., Lee, W., Park, J., Jo, M., Jung, S., Shin, J., Hwang, H., 2010. Effect of ZrO_x/HfO_x bilayer structure on switching uniformity and reliability in nonvolatile memory applications. Appl. Phys. Lett. 97 (17), 172105. https://doi.org/10.1063/1.3491803.

Lee, M.J., Park, Y., Ahn, S.E., Kang, B.S., Lee, C.B., Kim, K.H., Xianyu, W.X., Yoo, I.K., Lee, J.H., Chung, S.J., Kim, Y.H., Lee, C.S., Choi, K.N., Chung, K.S., 2008. Comparative structural and electrical analysis of NiO and Ti doped NiO as materials for resistance random access memory. J. Appl. Phys., 013706. https://doi.org/10.1063/1.2829814.

Lin, C.C., Lin, C.C., Tu, B.C., Yu, J.S., Lin, C.H., Tseng, T.Y., 2007. Resistive switching properties of $SrZrO_3$-based memory films. Japanese Journal of Applied Physics, Part 1: Regular Papers and Short Notes and Review Papers, 46 (4 B), 2153–2156. https://doi.org/10.1143/JJAP.46.2153.

Lin, C.C., Tu, B.C., Lin, C.C., Lin, C.H., Tseng, T.Y., 2006. Resistive switching mechanisms of V-doped $SrZrO_3$ memory films. IEEE Electron Device Lett. 27 (9), 725–727. https://doi.org/10.1109/LED.2006.880660.

Lin, C.Y., Lin, M.H., Wu, M.C., Lin, C.H., Tseng, T.Y., 2008. Improvement of resistive switching characteristics in $SrZrO_3$ thin films with embedded cr layer. IEEE Electron Device Lett. 29 (10), 1108–1111. https://doi.org/10.1109/LED.2008.2002879.

Linn, E., Rosezin, R., Kügeler, C., Waser, R., 2010. Complementary resistive switches for passive nanocrossbar memories. Nat. Mater. 9 (5), 403–406. https://doi.org/10.1038/nmat2748.

Liu, H., Wu, Y., Hu, Y., 2017. Reproducible switching effect of an all-inorganic halide perovskite $CsPbBr_3$ for memory applications. Ceram. Int. 43 (9), 7020–7025. https://doi.org/10.1016/j.ceramint.2017.02.128.

Liu, X., Sadaf, S.M., Son, M., Shin, J., Park, J., Lee, J., Park, S., Hwang, H., 2011. Diode-less bilayer oxide (WO_x-NbO_x) device for cross-point resistive memory applications. Nanotechnology 22 (47). https://doi.org/10.1088/0957-4484/22/47/475702.

Liu, Y., Li, F., Chen, Z., Guo, T., Wu, C., Kim, T.W., 2016. Resistive switching memory based on organic/inorganic hybrid perovskite materials. Vacuum 130, 109–112. https://doi.org/10.1016/j.vacuum.2016.05.010.

Mähne, H., Berger, L., Martin, D., Klemm, V., Slesazeck, S., Jakschik, S., Rafaja, D., Mikolajick, T., 2012. Filamentary resistive switching in amorphous and polycrystalline Nb_2O_5 thin films. Solid-State Electronics, 72, 73–77. https://doi.org/10.1016/j.sse.2012.01.005.

Maimon, J., Hunt, K., Rodgers, J., Burcin, L., Knowles, K., 2004. Progress on a new non-volatile memory for space based on chalcogenide glass. AIP Conference Proceedings, 699, 639–649. https://doi.org/10.1063/1.1649626.

Mehonic, A., Cueff, S., Wojdak, M., Hudziak, S., Jambois, O., Labbé, C., Garrido, B., Rizk, R., Kenyon, A.J., 2012. Resistive switching in silicon suboxide films. Journal of Applied Physics, 111 (7). https://doi.org/10.1063/1.3701581.

Meng-Han, L., Ming-Chi, W., Chen-Hsi, L., Tseung-Yuen, T., 2010. Resistive switching characteristics and mechanisms of pt-embedded $SrZrO_3$ memory devices. J. Appl. Phys., 124117. https://doi.org/10.1063/1.3437635.

Miracle, D.B., Egami, T., Flores, K.M., Kelton, K.F., 2007. Structural aspects of metallic glasses. MRS Bull. 32 (8), 629–634. https://doi.org/10.1557/mrs2007.124.

Muenstermann, R., Menke, T., Dittmann, R., Waser, R., 2010. Coexistence of filamentary and homogeneous resistive switching in Fe-doped $SrTiO_3$ thin-film memristive devices. Adv. Mater. 22 (43), 4819–4822. https://doi.org/10.1002/adma.201001872.

Muraoka, S., Osano, K., Kanzawa, Y., Mitani, S., Fujii, S., Katayama, K., Katoh, Y., Wei, Z., Mikawa, T., Arita, K., Kawashima, Y., Azuma, R., Kawai, K., Shimakawa, K., Odagawa, A., Takagi, T., 2007. Fast switching and long retention Fe-O ReRAM and its switching mechanism. In: Technical Digest—International Electron Devices Meeting, IEDM. IEEE, pp. 779–782.

Nardi, F., Cagli, C., Spiga, S., Ielmini, D., 2011. Reset instability in pulsed-operated unipolar resistive-switching random access memory devices. IEEE Electron Device Lett. 32 (6), 719–721. https://doi.org/10.1109/LED.2011.2131631.

Nauenheim, C., Kügeler, C., Rüdiger, A., Waser, R., Flocke, A., Noll, T.G., 2008. Nano-crossbar arrays for nonvolatile resistive ram (RRAM) applications. In: 2008 8th IEEE Conference on Nanotechnology, IEEE-NANO, pp. 464–467.

Niu, G., Calka, P., Auf Der Maur, M., Santoni, F., Guha, S., Fraschke, M., Hamoumou, P., Gautier, B., Perez, E., Walczyk, C., Wenger, C., Di Carlo, A., Alff, L., Schroeder, T., 2016. Geometric conductive filament confinement by nanotips for resistive switching of HfO2-RRAM devices with high performance. Sci. Rep. 6. https://doi.org/10.1038/srep25757.

Pan, R.K., Zhang, T.J., Wang, J.Y., Wang, J.Z., Wang, D.F., Duan, M.G., 2012. Mechanisms of current conduction in Pt/$BaTiO_3$/Pt resistive switching cell. Thin. Solid. Films 520 (11), 4016–4020. https://doi.org/10.1016/j.tsf.2012.01.013.

Panda, D., Tseng, T.Y., 2014. Perovskite oxides as resistive switching memories: a review. Ferroelectrics 471 (1), 23–64. https://doi.org/10.1080/00150193.2014.922389.

Pickett, M.D., Medeiros-Ribeiro, G., Williams, R.S., 2013. A scalable neuristor built with Mott memristors. Nat. Mater. 12 (2), 114–117. https://doi.org/10.1038/nmat3510.

Pradel, A., Frolet, N., Ramonda, M., Piarristeguy, A., Ribes, M., 2011. Bipolar resistance switching in chalcogenide materials. Physica Status Solidi (A) Applications and Materials Science 208 (10), 2303–2308. https://doi.org/10.1002/pssa.201000767.

Prakash, A., Maikap, S., Lai, C.S., Tien, T.C., Chen, W.S., Lee, H.Y., Chen, F.T., Kao, M.J., Tsai, M.J., 2012. Bipolar resistive switching memory using bilayer TaO_x/WO_x films. Solid State Electron. 77, 35–40. https://doi.org/10.1016/j.sse.2012.05.028.

Raoux, S., Wełnic, W., Lelmini, D., 2010. Phase change materials and their application to nonvolatile memories. Chem. Rev. 110 (1), 240–267. https://doi.org/10.1021/cr900040x.

Roorda, S., Sinke, W.C., Poate, J.M., Jacobson, D.C., Dierker, S., Dennis, B.S., Eaglesham, D.J., Spaepen, F., Fuoss, P., 1991. Structural relaxation and defect annihilation in pure amorphous silicon. Phys. Rev. B 44 (8), 3702–3725. https://doi.org/10.1103/PhysRevB.44.3702.

Sadaf, S.M., Liu, X., Son, M., Park, S., Choudhury, S.H., Cha, E., Siddik, M., Shin, J., Hwang, H., 2012. Highly uniform and reliable resistance switching properties in bilayer WO_x/NbO_x RRAM devices. Physica Status Solidi (A) Applications and Materials Science 209 (6), 1179–1183. https://doi.org/10.1002/pssa.201127659.

Sawa, A., 2008. Resistive switching in transition metal oxides. Mater. Today 11 (6), 28–36. https://doi.org/10.1016/S1369-7021(08)70119-6.

Scott, J.C., Bozano, L.D., 2007. Nonvolatile memory elements based on organic materials. Adv. Mater. 19 (11), 1452–1463. https://doi.org/10.1002/adma.200602564.

Seo, S., Lee, M.J., Seo, D.H., Jeoung, E.J., Suh, D.S., Joung, Y.S., Yoo, I.K., Hwang, I.R., Kim, S.H., Byun, I.S., Kim, J.S., Choi, J.S., Park, B.H., 2004. Reproducible resistance switching in polycrystalline NiO films. Appl. Phys. Lett. 85 (23), 5655–5657. https://doi.org/10.1063/1.1831560.

Shang, D.S., Shi, L., Sun, J.R., Shen, B.G., Zhuge, F., Li, R.W., Zhao, Y.G., 2010. Improvement of reproducible resistance switching in polycrystalline tungsten oxide films by *in situ* oxygen annealing. Appl. Phys. Lett., 072103. https://doi.org/10.1063/1.3300637.

Shuai, Y., Zhou, S., Brger, D., Helm, M., Schmidt, H., 2011. Nonvolatile bipolar resistive switching in $Au/BiFeO_3/Pt$. J. Appl. Phys. 109 (12). https://doi.org/10.1063/1.3601113.

Song, Min Yeong, Seo, Yujeong, Kim, Yeon Soo, Kim, Hee Dong, An, Ho-Myoung, Park, Bae Ho, Sung, Yun Mo, Kim, Tae Geun, 2012. Realization of One-Diode–Type Resistive-Switching Memory with $Cr–SrTiO_3$ Film. Applied Physics Express 5 (9), 91202. doi:10.1143/APEX.5.091202.

Strachan, J.P., Pickett, M.D., Yang, J.J., Aloni, S., Kilcoyne, A.L.D., Medeiros-Ribeiro, G., Williams, R.S., 2010. Direct identification of the conducting channels in a functioning memristive device. Adv. Mater. 22 (32), 3573–3577. https://doi.org/10.1002/adma.201000186.

Strukov, D.B., Likharev, K.K., 2007. Defect-tolerant architectures for nanoelectronic crossbar memories. J. Nanosci. Nanotechnol. 7 (1), 151–167.

Subin, P.S., Asha, A.S., Saji, K.J., Jayaraj, M.K., 2021. Spike-dependent plasticity modulation in TiO_2-based synaptic device. Journal of Materials Science: Materials in Electronics 13051–13061. doi:10.1007/s10854-021-05710-2.

Subin, P.S., Saji, K.J., Jayaraj, M.K., 2021. Plasticity and learning behavior emulated in a ZnO based transparent artificial synapse. Thin Solid Films 737, 138924. doi:10.1016/j.tsf.2021.138924.

Szot, K., Dittmann, R., Speier, W., Waser, R., 2007. Nanoscale resistive switching in $SrTiO_3$ thin films. Physica Status Solidi—Rapid Research Letters 1 (2), R86–R88. https://doi.org/10.1002/pssr.200701003.

Tan, T., Du, Y., Cao, A., Sun, Y., Zha, G., Lei, H., Zheng, X., 2018. The resistive switching characteristics of Ni-doped HfO_x film and its application as a synapse. J. Alloys Compd. 766, 918–924. https://doi.org/10.1016/j.jallcom.2018.07.044.

Tomas, T., Angeliki, P., Manuel, L.G., Abu, S., Evangelos, E., 2016. Stochastic phase-change neurons. Nat. Nanotechnol. 693–699. https://doi.org/10.1038/nnano.2016.70.

Varandani, D., Singh, B., Mehta, B.R., Singh, M., Singh, V.N., Gupta, D., 2010. Resistive switching mechanism in delafossite-transition metal oxide ($CuInO_2$-CuO) bilayer structure. J. Appl. Phys. 107 (10). https://doi.org/10.1063/1.3369436.

Vijila, C.V.M., Subin, P.S., Shaji, M., Kumar, K.R., Jayaraj, M.K., 2019. Perovskite quantum dot based resistive memory with very low operating power. AIP Conference Proceedings, 2082. American Institute of Physics Inc. https://doi.org/10.1063/1.5093879.

Wang, Y., Lv, Z., Liao, Q., Shan, H., Chen, J., Zhou, Y., Zhou, L., Chen, X., Roy, V.A.L., Wang, Z., Xu, Z., Zeng, Y.J., Han, S.T., 2018. Synergies of electrochemical metallization and valance change in all-inorganic perovskite quantum dots for resistive switching. Adv. Mater. 30 (28). https://doi.org/10.1002/adma.201800327.

Wang, X.P., Chen, Y.Y., Pantisano, L., Goux, L., Jurczak, M., Groeseneken, G., Wouters, D.J., 2010a. Effect of anodic interface layers on the unipolar switching of HfO_2-based resistive ram. Proceedings of 2010 International Symposium On VLSI Technology, System and Application, VLSI-TSA 2010. IEEE, pp. 140–141.

Wang, Z.Q., Li, X.H., Xu, H.Y., Wang, W., Yu, H., Zhang, X.T., Liu, Y.X., Liu, Y.C., 2010b. Effects of compliance currents on the formation and rupture of conducting filaments in unipolar resistive switching of CoO film. J. Phys. D Appl. Phys. 43 (38). https://doi.org/10.1088/0022-3727/43/38/385105.

Ziegler, M.M., Stan, M.R., 2003. CMOS/nano co-design for crossbar-based molecular electronic systems. IEEE Transactions on Nanotechnology 2, 217–230. https://doi.org/10.1109/TNANO.2003.820804.

Wang, Y.H., Zhao, K.H., Shi, X.L., Xie, G.L., Huang, S.Y., Zhang, L.W., 2013. Investigation of the resistance switching in Au/$SrTiO_3$:Nb heterojunctions. Appl. Phys. Lett, 031601. https://doi.org/10.1063/1.4813622.

Wei, Z., Kanzawa, Y., Arita, K., Katoh, Y., Kawai, K., Muraoka, S., Mitani, S., Fujii, S., Katayama, K., Iijima, M., Mikawa, T., Ninomiya, T., Miyanaga, R., Kawashima, Y., Tsuji, K., Himeno, A., Okada, T., Azuma, R., Shimakawa, K., Sugaya, H., Takagi, T., Yasuhara, R., Horiba, K., Kumigashira, H., Oshima, M., 2008. Highly reliable TaO_x ReRAM and direct evidence of redox reaction mechanism. 2008 IEEE International Electron Devices Meeting. IEEE, pp. 1–4.

Xin, G., 2012. Roles of schottky barrier and oxygen vacancies in the electroforming of $SrTiO_3$. Appl. Phys. Lett. 152903. https://doi.org/10.1063/1.4759030.

Y., S.J., Y.-H., S, 2008. Direct observation of conducting filaments on resistive switching of NiO thin films. Appl. Phys. Lett., 222106. https://doi.org/10.1063/1.2931087.

Yan, Z.B., Liu, J.M., 2015. Resistance switching memory in perovskite oxides. Ann. Phys. 358, 206–224. https://doi.org/10.1016/j.aop.2015.03.028.

Yan, Z., Guo, Y., Zhang, G., Liu, J.M., 2011. High-performance programmable memory devices based on Co-doped $BaTiO_3$. Adv. Mater. 23 (11), 1351–1355. https://doi.org/10.1002/adma.201004306.

Yang, J.J., Pickett, M.D., Li, X., Ohlberg, D.A.A., Stewart, D.R., Williams, R.S., 2008. Memristive switching mechanism for metal/oxide/metal nanodevices. Nat. Nanotechnol. 3 (7), 429–433. https://doi.org/10.1038/nnano.2008.160.

Yang, K., Li, F., Veeramalai, C.P., Guo, T., 2017. A facile synthesis of $CH_3NH_3PbBr_3$ perovskite quantum dots and their application in flexible nonvolatile memory. Appl. Phys. Lett. 110 (8). https://doi.org/10.1063/1.4976709.

Yang, M.K., Park, J.W., Ko, T.K., Lee, J.K., 2009. Bipolar resistive switching behavior in Ti/MnO_2/Pt structure for nonvolatile memory devices. Appl. Phys. Lett. 95 (4). https://doi.org/10.1063/1.3191674.

Yoo, E.J., Lyu, M., Yun, J.H., Kang, C.J., Choi, Y.J., Wang, L., 2015. Resistive switching behavior in organic-inorganic hybrid $CH_3NH_3PbI_{3-x}Cl_x$ perovskite for resistive random access memory devices. Adv. Mater. 27 (40), 6170–6175. https://doi.org/10.1002/adma.201502889.

Yoon, J., Choi, H., Lee, D., Park, J.B., Lee, J., Seong, D.J., Ju, Y., Chang, M., Jung, S., Hwang, H., 2009. Excellent switching uniformity of Cu-doped MoO_x/GdO_x bilayer

for nonvolatile memory applications. IEEE Electron Device Lett. 30 (5), 457–459. https://doi.org/10.1109/LED.2009.2015687.

Yoshida, C., Tsunoda, K., Noshiro, H., Sugiyama, Y., 2007. High speed resistive switching in Pt/TiO_2/TiN film for nonvolatile memory application. Appl. Phys. Lett. 91 (22). https://doi.org/10.1063/1.2818691.

Yu, B., Sun, X., Ju, S., Janes, D.B., Meyyappan, M., 2008. Chalcogenide-nanowire-based phase change memory. IEEE Trans. Nanotechnol. 7 (4), 496–502. https://doi.org/10.1109/TNANO.2008.926374.

Yu, S., Guan, X., Wong, H.S.P., 2011. Conduction mechanism of TiN/HfO_x/Pt resistive switching memory: a trap-assisted-tunneling model. Appl. Phys. Lett. 99 (6). https://doi.org/10.1063/1.3624472.

Zhang, Z., Gao, B., Fang, Z., Wang, X., Tang, Y., Sohn, J., Wong, H.S.P., Wong, S.S., Lo, G.Q., 2015. All-metal-nitride RRAM devices. IEEE Electron Device Lett. 36 (1), 29–31. https://doi.org/10.1109/LED.2014.2367542.

Zhuge, F., Dai, W., He, C.L., Wang, A.Y., Liu, Y.W., Li, M., Wu, Y.H., Cui, P., Li, Run-Wei, 2010. Nonvolatile resistive switching memory based on amorphous carbon. Appl. Phys. Lett., 163505. https://doi.org/10.1063/1.3406121.

Zhuge, F., Hu, B., He, C., Zhou, X., Liu, Z., Li, R.W., 2011. Mechanism of nonvolatile resistive switching in graphene oxide thin films. Carbon 49 (12), 3796–3802. https://doi.org/10.1016/j.carbon.2011.04.071.

13

Mechanical bottom-up nanoassembling and nanomanipulation using shape memory alloy nanogripper

V. Sampath [a], S. von Gratowski [b], A. Irzhak [c], P. Lega [d], Z. Song [e], M. Alonso Cotta [f] and V. Koledov [d]

[a] Indian Institute of Technology Madras, Chennai-600 036, India. [b] Laboratory of Spectroscopy and Millimeter and Submillimeter Wave Measurements, Kotelnikov Institute of Radio Engineering and Electronics, Russian Academy of Sciences, Fryazino Branch, FIRE RAS, Vvedenski Sq.1, Fryazino, Moscow Region, 141190, Russia. [c] Institute of Microelectronics Technology, Russian Academy of Sciences, Chernogolovka, 142432, Russia. [d] Magnetic Phenomena Laboratory, Kotelnikov Institute of Radio Engineering and Electronics, Russian Academy of Sciences, Mokhovaya 11-7, 125009, Moscow, Russia. [e] International Research Centre for Nano Handling & Manufacturing of China, Changchun University of Science and Technology, Changchun 130022, China. [f] Instituto de Física Gleb Wataghin, Universidade Estadual de Campinas, 13083-859 Campinas, São Paulo, Brazil.

13.1 Introduction

Miniaturization is one of the main global trends in modern science and technology. This trend is presented perfectly in nanotechnology and nanoscience in the matter of production and study of micro- and nanodevices, as well as micro-and nanoobjects. This branch of nanotechnology is divided into two paradigms: top-down technology (for example, silicon lithography) and bottom-up technology. In the top-down approach nanoobjects are created by processing objects that are larger in size. An important example of the top-down approach is the fabrication of integrated circuits. Nowadays, it has grown to the level of fabricating nanoelectromechanical system (NEMS), where tiny mechanical components, such as microfluidic channels along with electronic circuits, are embedded in a tiny chip. At the beginning of fabrication, relatively large structures, such as silicon crystals, are used.

Nanomaterials for Sensing and Optoelectronic Applications. DOI: https://doi.org/10.1016/B978-0-12-824008-3.00011-4

The main technology is nanolithography. This technology enabled the making of tiny chips. But these days, many types of nanolithography are used, such as photolithography, electron-beam lithography, and ion-beam lithography. The bottom-up approach in nanotechnology involves making larger nanostructures from smaller building blocks, such as clusters, molecules, and nanoobjects. The very rapid development of nanoscience and nanotechnology in the last few decades has provided the discovery of a wide range of individual zero-dimensional (0D), one-dimensional (1D), and two-dimensional (2D) nanoscale materials; for example, 0D: quantum dots, clusters (Alivisatos, 1996); 1D: structures like nanotubes and nanowires (NWs) (Avouris, 2002; Hongjie, 2002; Hu et al., 1999; Lieber & Wang, 2007; McEuen, 2000); and 2D: graphene, etc. of different materials.

Recently, individual nanomaterials are being intensively investigated in different ways, including the characterization of electrical, magnetic, mechanical, and biological properties and structure (Hongjie, 2002; Hu et al., 1999; Lieber & Wang, 2007). These studies show that individual nanoobjects have outstanding functional properties and have allowed/facilitated the construction of a wide range of nanodevices based on individual nanoobjects (Avouris, 2002; Collins et al., 1997; Duan et al., 2001; Huang et al., 2002; Li et al., 2006; Lieber & Wang, 2007; Wang, 2003). New promising spintronic nanodevices like spin-transfer torque microwave nanogenerators (Zeng et al., 2008, 2012, 2013a, 2013b); high-field superconductor-ferromagnet tunnel junctions (Kolenda et al., 2016); nanotransistors (Chaste et al., 2008), with their operating frequencies in the GHz region; nanolasers (Huang et al., 2001a; Johnson et al., 2002; Li et al., 2006; Wang, 2003); carbon nanotube (CNT)–based NEMSs (Andzane et al., 2009; Sazonova et al., 2004; Weldon et al., 2008); nanoantennae (Tong et al., 2013a); biomedical sensors based on NWs (Janissen et al., 2017; Sahoo et al., 2016); nanomotors (Mandal et al., 2015); and many other individual nanodevices (Huang et al., 2002; Li et al., 2006; Lieber & Wang, 2007) have been developed in recent times in laboratories around the globe. In principle, these nanomaterial-based devices possess unique functional properties, such as extremely high sensor sensitivity, and also cost less.

But for the real usage of the individual nanodevices mentioned above, depending on the individual nanoobjects, an effective as well as economical technology of assembling these nanodevices into micro- and then into macrodevices needs to be developed. It should be noted that in this case, it is also important that a reliable mechanical, and in many cases electrical and/or optical contact, needs to be established between nanocomponents. Such nanoassembling represents a “bottom-up” paradigm in nanotechnology. The bottom-up paradigm is an alternative to the mainstream “top-down” nanotechnology paradigm. “Top-down” nanotechnology is widely used for

fundamental and applied research in nanoscience and for industrial production at present. Equipment like nanolithography is very expensive and cumbersome.

In the meantime, for the large-scale "bottom-up" paradigm, such approaches as an electric field–directed assembly of NWs, fluid flow–directed assembly of NWs, and Langmuir–Blodgett assembling (Teo & Sun, 2006; Whang et al., 2004; Yu & Lieber, 2010) are used. All these technologies are based on liquids and have fundamental limitations that are related to the lack of a large-scale order in liquid media. But these methods currently cannot provide the required accuracy and reproducibility. As a result, the "bottom-up" technology cannot compete with the top-down paradigm, i.e., with nanolithography.

In this chapter we focus on the concept of the paradigm of bottom-up mechanical nanoassembling (MNA) that, in principle, can be competitive with a top-down paradigm in terms of accuracy and reproducibility. In the framework of this technology the original mechanical nanoassembly of individual nanoobjects into a single nano- and subsequently into meso-, micro-, and macrodevices and their integration with standard components of modern electronics, MEMS, devices for alternative energy, microbiosensors and lab-on-chip technology, telecommunications, instruments for fundamental and applied research, etc., are expected to be developed. The micro- and macro-devices produced using such paradigms will not only be cheaper but also make the equipment compact and inexpensive. These devices will be available for medium and small groups of scientists with a modest budget and also for small business enterprises. For the realization of MNA, the application of the new technology of three-dimensional (3D) manipulation is needed. The purpose of this chapter is to illustrate this concept by using some practical examples of the nanomanipulation of real nanoobjects using MNA.

13.2 Materials and methods

For the purpose of the development of the MNA bottom-up approach, we propose the methodology based on the new frontier nanomanipulation system with the world's smallest and fastest mechanical and optical nanotweezers (Amiri et al., 2012; Gratowski et al., 2017; Irzhak et al., 2010, 2014, 2017; Koledov et al., 2014a; Zakharov et al., 2012). The concept of the mechanical composite nanotools with shape memory effect (SME) is illustrated in Fig. 13.1.

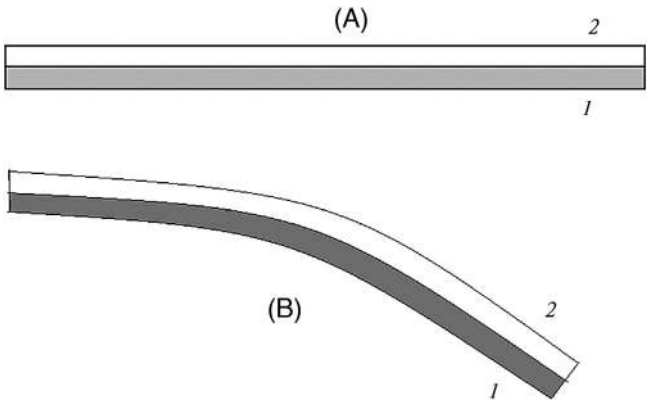

Figure 13.1. Concept of the layered prestrained composite with SME: (*1*) active layer with SME, (*2*) elastic metal layer; (A) composite in the martensitic (cold) state; (B) composite in the austenitic (hot) state.

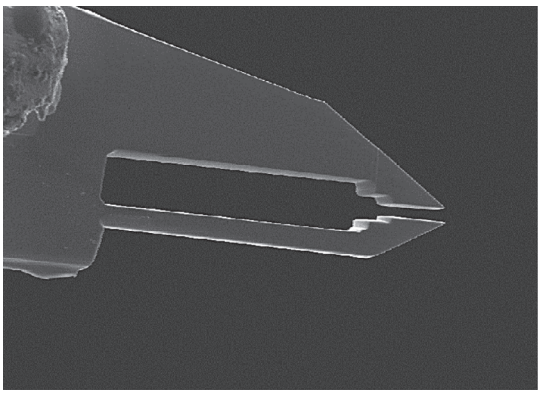

Figure 13.2. Microactuator on the base of Ti_2NiCu/Pt composite with SME, produced by FIB-CVD: actuation is controlled in the vacuum chamber of the ion scanning microscope via semiconductor laser radiation: microactuator in martensitic (cold) state.

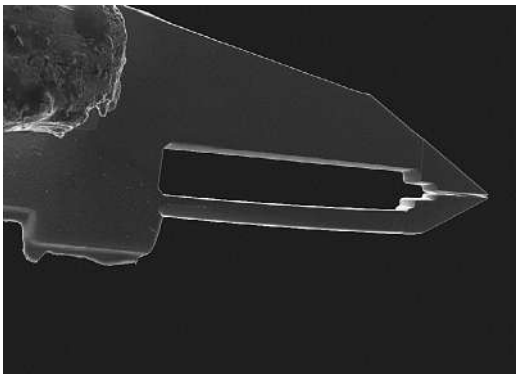

Figure 13.3. microactuator on the base of Ti_2NiCu/Pt composite with SME, produced by FIB-CVD: actuation is controlled in vacuum chamber of ion scanning microscope by semiconductor laser radiation: microactuator in martensitic (cold) state.

The active element of the composite micro- or nano-actuator consists of two layers: prestrained shape memory alloy, for example, Ti_2NiCu, and reliable elastic metal. Due to thermoelastic martensitic transition upon cooling/heating of the shape memory alloy, the bimetallic-layered composite demonstrates giant reversible deformation, whose magnitude is rather restricted by the reliability of the elastic layer than that of SME (Zakharov et al., 2012). Modern nanotechnologies like 3D ion nanolithography and FIB-CVD provide opportunities for the design and production of composite nanoactuators and nanomechanical devices like nanotweezers, as illustrated in Figs. 13.2 and 13.3 (Irzhak et al., 2010).

13.3 Experiment

Currently individual and mass production of the nano-tools based on composites exhibiting SME is possible [33–39]. The composite nano-tweezer system is fairly compatible with custom-made SEM and FIB systems. It can easily be connected to the standard manipulation devices, like OmniprobeR, Kleindieck, etc. and integrated into the environment of the custom electron and ion microscopes [33–39].

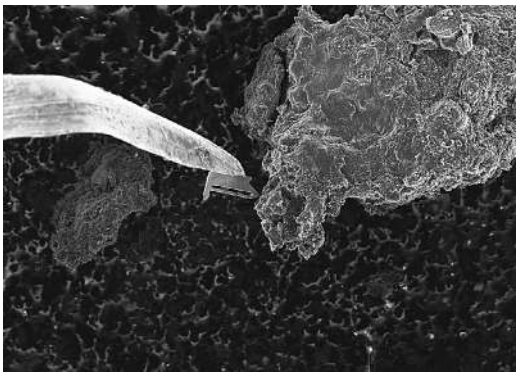

Figure 13.4. Ti_2NiCu/Pt shape memory composite nanotweezers produced by FIB-CVD: a tungsten microwire, connected to Omniprobe micromanipulator, is used as a carrier of the microtool with SME, connected to its tip by CVD.

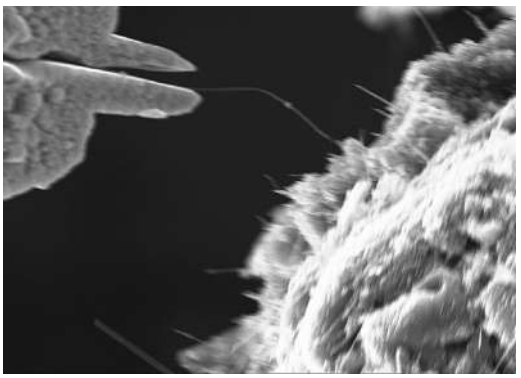

Figure 13.5. Ti_2NiCu/Pt shape memory composite nanotweezers produced by FIB-CVD: manipulation of individual CNTs by using the nanotweezers with SME controlled by the radiation of the semiconductor laser in the vacuum chamber of the scanning electron microscope.

13.4 Results and discussions

The solution to a task that can hardly be resolved by other methods but is successfully solved using composite nanotweezers with SME is illustrated in Figs. 13.4 and 13.5 (Gratowski et al., 2017; Irzhak et al., 2017; Koledov et al., 2014). Modern bionics considers the brain and sensor system of insects to be a model for future nanosensoric technology with attomolar sensitivity to chemicals and unique universality. A set of photographs in Figs. 13.4 and 13.5 demonstrates the different stages of the experiment relating to the manipulation of CNTs. The next example is the preparation of the submicron-sized fibers on the body of the insect (*Culex pipiens*). These fibers are, in fact, submicron chitinous tubules (sensilla), in which the nerve endings are located. The highly sensitive biosensors are located on the tips of the sensilla (Figs. 13.6 to 13.8). Figs. 13.9 to 13.14 illustrate an example of the 3D nanomanipulation of InP semiconductor NWs (Amiri et al., 2012). These NWs are produced in large quantities by using the standard technology and provide a unique model for nanophotonics and nanosensorics (Figs. 13.9 and 13.12). Both field-effect transistors and biological sensors can be designed on the basis of their applications in different fields, such as nanosensorics. Unfortunately, the selection, manipulation, and integration of individual NWs still remain a challenge. Figs. 13.9 to 13.14 illustrate the experimental study of the selected individual InP NWs, which involve grabbing them from the forest using composite

Figure 13.6. Manipulation of the biological micro-objects by Ti_2NiCu/Pt composite nanotweezers with SME in the vacuum chamber of the scanning electron microscope: comparison of the size of the composite nanotweezers with the leg-size of the insect (*Culex pipiens*).

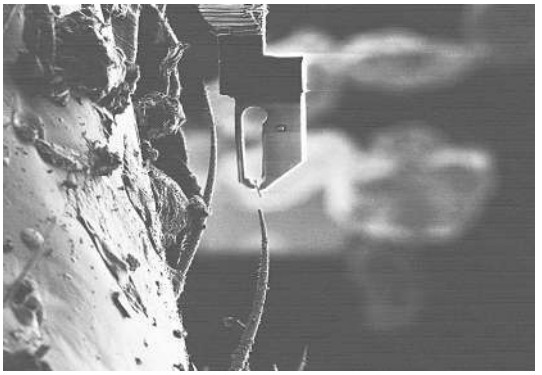

Figure 13.7. Manipulation of biological microobjects by using Ti_2NiCu/Pt composite nanotweezers with SME in the vacuum chamber of the scanning electron microscope: selection of the individual submicron bioobject (sensilla).

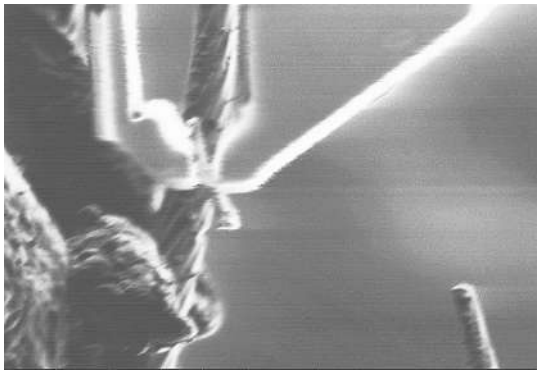

Figure 13.8. Manipulation of the biological microobjects by using Ti_2NiCu/Pt composite nanotweezers with SME in the vacuum chamber of the scanning electron microscope: processing of the selected submicron bioobject by FIB.

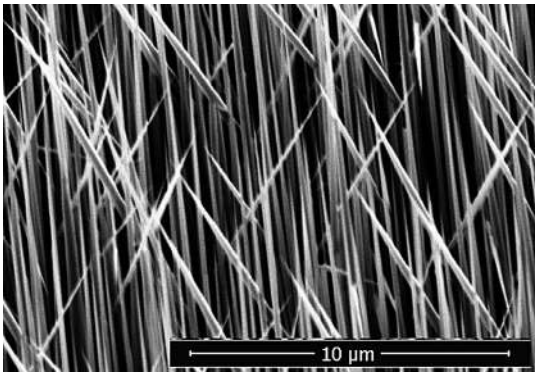

Figure 13.9. Manipulation and integration of the individual InP NWs using composite nanotweezers with SME and FIB-CVD: "forest" of InP.

nanotweezers (Fig. 13.10) and connecting to TEM copper contacts (Fig. 13.13), followed by a study of their electrical properties (Figs. 13.11 and 13.14).

Summary

The new SME-based technology of nanomanipulation presents a robust solution to large-scale (macroscale) and submicrometer-scale

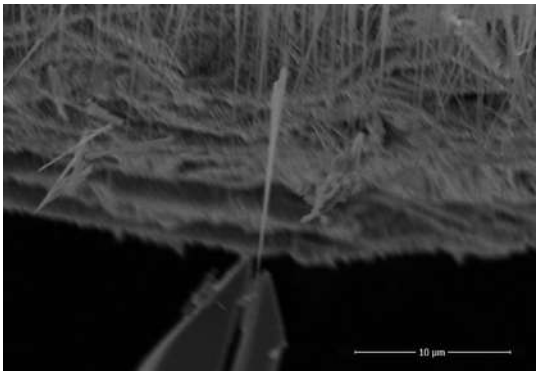

Figure 13.10. Manipulation and integration of the individual InP NWs using composite nanotweezers with SME and FIB-CVD: selection of the individual nanowire from the "forest."

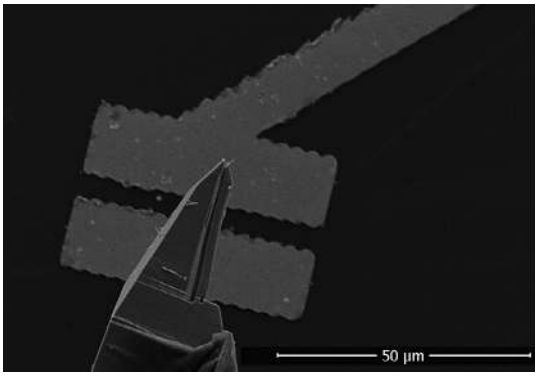

Figure 13.11. Manipulation and integration of the individual InP NWs using composite nanotweezers with SME and FIB-CVD: transportation and positioning of NW.

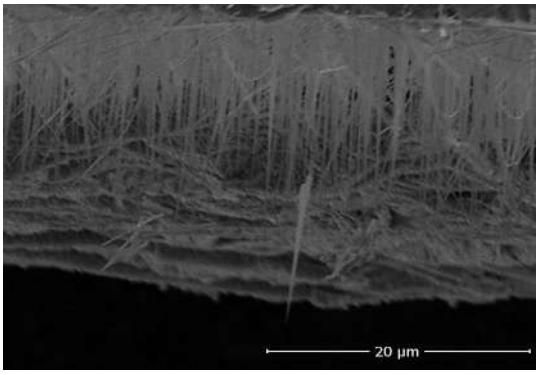

Figure 13.12. Manipulation and integration of the individual InP NWs using composite nanotweezers with SME and FIB-CVD: "forest" of InP nanowire.

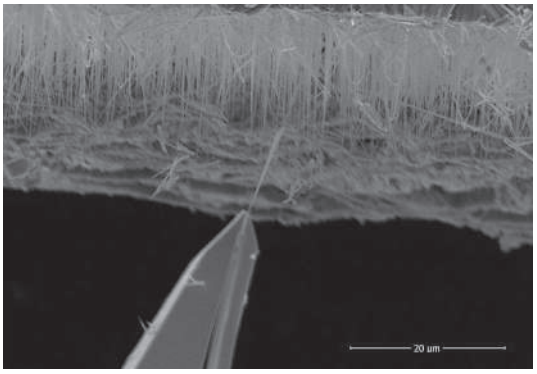

Figure 13.13. Manipulation and integration of the individual InP NWs using composite nanotweezers with SME and FIB-CVD: grabbing the nanoobject by using nanotweezers.

(nanoscale) easy-to-use nanoinstrument, consisting of a nanopositioning system and micron-size end-effectors controlled by semiconductor laser radiation or electric current for frontier nanomanipulation in a vacuum chamber or liquid environment in different microscopes. Further efforts are needed, particularly for the automation of the process of nanotweezer-assisted nanomanipulation, in order to achieve high output, low cost, and reliability of the new bottom-up nanointegration technology.

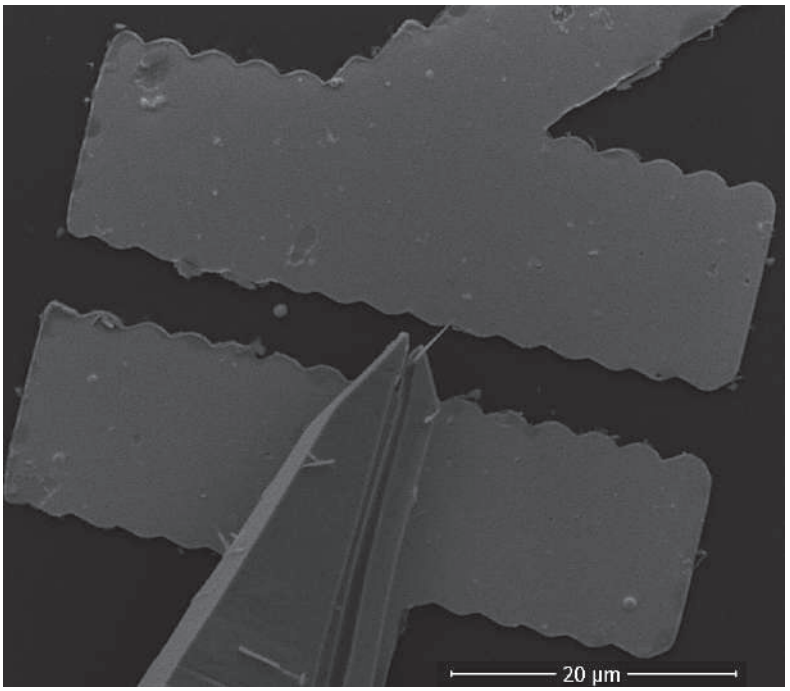

Figure 13.14. Manipulation and integration of the individual InP NWs using composite nanotweezers with SME and FIB-CVD: transportation and positioning of the NW on contacts.

Acknowledgments

The work is supported by RFBR-DST Grants No. 16-57-45066 and 17-57-80122. Dr. V. K. and Dr. S. V. G. are grateful for the financial support from RSF Grant No. 17-19-01748. Prof. V. Sampath gratefully acknowledges the help rendered by Ms. Poojalakshmi V and Ms. Bharathy J., Project Staff, IIT Madras, in the preparation of the text.

References

Alivisatos, A.P., 1996. Semiconductor clusters, nanocrystals, and quantum dots. Science 271 (5251), 933–937. https://doi.org/10.1126/science.271.5251.933.

Amiri, I.S., Ahsan, R., Shahidinejad, A., Ali, J., Yupapin, P.P, 2012. Characterisation of bifurcation and chaos in silicon microring resonator. IET Commun. 6 (16), 2671–2675.

Andzane, J., Petkov, N., Livshits, A.I., Boland, J.J., Holmes, J.D., Erts, D., 2009. Two-terminal nanoelectromechanical devices based on germanium nanowires. Nano Lett. 9 (5), 1824–1829. https://doi.org/10.1021/nl8037807.

Avouris, P., 2002. Molecular electronics with carbon nanotubes. Acc. Chem. Res. 35 (12), 1026–1034. https://doi.org/10.1021/ar010152e.

Chaste, J., Lechner, L., Morfin, P., Fève, G., Kontos, T., Berroir, J.M., Glattli, D.C., Happy, H., Hakonen, P., Plaçais, B., 2008. Single carbon nanotube transistor at GHz frequency. Nano Lett. 8 (2), 525–528. https://doi.org/10.1021/nl0727361.

Collins, P.G., Zettl, A., Bando, H., Thess, A., Smalley, R.E., 1997. Nanotube nanodevice. Science 278 (5335), 100. https://doi.org/10.1126/science.278.5335.100.

Duan, X., Huang, Y., Cui, Y., Wang, J., Lieber, C.M., 2001. Indium phosphide nanowires as building blocks for nanoscale electronic and optoelectronic devices. Nature 409 (6816), 66–69. https://doi.org/10.1038/35051047.

Gomez-Rojas, L., Bhattacharyya, S., Mendoza, E., Cox, D.C., Mauricio Rosolen, J., Silva, S.R.P., 2007. RF response of single-walled carbon nanotubes. Nano Lett. 7 (9), 2672–2675. https://doi.org/10.1021/nl0710598.

Gratowski, S., Koledov, V., Shavrov, V., Petrenko, S., Irzhak, A., Shelyakov, A., Jede, R., 2017. Frontiers in Materials Processing, Applications, Research and Technology, Springer (pp. 135–154). https://doi.org/10.1007/978-981-10-4819-7_13.

Hongjie, D., 2002. Carbon Nanotubes: Synthesis,Integration, and Properties, Acc. Chem. Res., 1035–1044, https://doi.org/10.1021/ar0101640.

Hu, J., Odom, T.W., Lieber, C.M., 1999. Chemistry and physics in one dimension: Synthesis and properties of nanowires and nanotubes. Acc. Chem. Res. 32 (5), 435–445. https://doi.org/10.1021/ar9700365.

Huang, M.H., Mao, S., Feick, H., Yan, H., Wu, Y., Kind, H., Weber, E., Russo, R., Yang, P., 2001. Room-temperature ultraviolet nanowire nanolasers. Science 292 (5523), 1897–1899. https://doi.org/10.1126/science.1060367.

Huang, Y., Duan, X., Cui, Y., Lauhon, L.J., Kim, K.H., Lieber, C.M., 2001. Logic gates and computation from assembled nanowire building blocks. Science 294 (5545), 1313–1317. https://doi.org/10.1126/science.1066192.

Huang, Y., Duan, X., Cui, Y., Lieber, C.M., 2002. Gallium nitride nanowire nanodevices. Nano Lett. 2 (2), 101–104. https://doi.org/10.1021/nl015667d.

Irzhak, A., Koledov, V., Zakharov, D., Lebedev, G., Mashirov, A., Afonina, V., Akatyeva, K., Kalashnikov, V., Sitnikov, N., Tabachkova, N., Shelyakov, A., Shavrov, V., 2014. Development of laminated nanocomposites on the bases of magnetic and non-magnetic shape memory alloys: Towards new tools for nanotechnology. J. Alloys Compd. 586 (1), S464–S468. https://doi.org/10.1016/j.jallcom.2012.10.119.

Irzhak, A.V., Lega, P.V., Zhikharev, A.M., Koledov, V.V., Orlov, A.P., Kuchin, D.S., Tabachkova, N.Y., Dikan, V.A., Shelyakov, A.V., Beresin, M.Y., Pushin, V.G., von Gratowski, S.V., Pokrovskiy, V.Y., Zybtsev, S.G., Shavrov, V.G., 2017. Shape memory effect in nanosized Ti_2NiCu alloy-based composites. Doklady Physics, 62 (1), 5–9. https://doi.org/10.1134/S1028335817010050.

Irzhak, A.V., Zakharov, D.I., Kalashnikov, V.S., Koledov, V.V., Kuchin, D.S., Lebedev, G.A., Lega, P.V., Perov, E.P., Pikhtin, N.A., Pushin, V.G., Tarasov, I.S., Khovailo, V.V., Shavrov, V.G., Shelyakov, A.V., 2010. Actuators based on composite material with shape-memory effect. J. Commun. Technol. Electron. 55 (7), 818–830. https://doi.org/10.1134/S1064226910070120.

J. W., K. J., A. Z., 2008. Nanomechanical radio transmitter. Phys. Status Solidi, 2323–2325. https://doi.org/10.1002/pssb.200879639.

Janissen, R., Sahoo, P.K., Santos, C.A., Da Silva, A.M., Von Zuben, A.A.G., Souto, D.E.P., Costa, A.D.T., Celedon, P., Zanchin, N.I.T., Almeida, D.B., Oliveira, D.S., Kubota, L.T., Cesar, C.L., Souza, A.P.D., Cotta, M.A., 2017. InP nanowire biosensor with tailored biofunctionalization: Ultrasensitive and highly selective disease biomarker detection. Nano Letters, 17 (10), 5938–5949. https://doi.org/10.1021/acs.nanolett.7b01803.

Johnson, J.C., Choi, H.J., Knutsen, K.P., Schaller, R.D., Yang, P., Saykally, R.J., 2002. Single gallium nitride nanowire lasers. Nat. Mater. 1 (2), 106–110. https://doi.org/10.1038/nmat728.

Koledov, V., Shavrov, V., Von Gratowski, S., Jede, R., Irzhak, A., Shelyakov, A., 2014. Ion beam nanofabrication for mass production of nanotweezers based on new composite functional material with shape memory. In: 2014 International Conference on Manipulation, Manufacturing and Measurement on the Nanoscale (3M-NANO). IEEE, pp. 321–325.

Kolenda, S., Wolf, M.J., Beckmann, D., 2016. Observation of thermoelectric currents in high-field superconductor-ferromagnet tunnel junctions. Physical Review Letters, 116 (9), 097001. https://doi.org/10.1103/PhysRevLett.116.097001.

Li, Y., Qian, F., Xiang, J., Lieber, C.M., 2006. Nanowire electronic and optoelectronic devices. Mater. Today 9 (10), 18–27. https://doi.org/10.1016/S1369-7021(06)71650-9.

Lieber, C.M., Wang, Z.L., 2007. Functional Nanowires. MRS Bull. 32 (2), 99–108. https://doi.org/10.1557/mrs2007.41.

Mandal, P., Chopra, V., Ghosh, A., 2015. Independent positioning of magnetic nanomotors. ACS Nano 9 (5), 4717–4725. https://doi.org/10.1021/acsnano.5b01518.

McEuen, P.L., 2000. Single-wall carbon nanotubes. Phys. World 13 (6), 31–36. https://doi.org/10.1088/2058-7058/13/6/26.

Sahoo, P.K., Janissen, R., Monteiro, M.P., Cavalli, A., Murillo, D.M., Merfa, M.V., Cesar, C.L., Carvalho, H.F., De Souza, A.A., Bakkers, E.P.A.M., Cotta, M.A., 2016. Nanowire arrays as cell force sensors to investigate adhesin-enhanced holdfast of single cell bacteria and biofilm stability. Nano Lett. 16 (7), 4656–4664. https://doi.org/10.1021/acs.nanolett.6b01998.

Santanu, T., Praveen, K., Rudra, P., 2016. Electrolithography—A new and versatile process for nano patterning. Sci. Rep. https://doi.org/10.1038/srep17753.

Sazonova, V., Yalsh, Y., Üstünel, I., Roundy, D., Arlas, T.A., McEuen, P.L., 2004. A tunable carbon nanotube electrochemical oscillator. Nature 431 (7006), 284–287. https://doi.org/10.1038/nature02905.

Shi, Z.Y., Wang, J., Wan, X.S., Shen, G.Z., Wang, X.Q., Zhang, J.L., 2007. Over-expression of rice *OsAGO7* gene induces upward curling of the leaf blade that enhanced erect-leaf habit. Planta 226 (1), 99–108. https://doi.org/10.1007/s00425-006-0472-0.

Teo, B.K., Sun, X.H., 2006. From top-down to bottom-up to hybrid nanotechnologies: Road to nanodevices. J. Cluster Sci. 17 (4), 529–540. https://doi.org/10.1007/s10876-006-0086-5.

Tong, L., Pakizeh, T., Feuz, L., Dmitriev, A., 2013a. Highly directional bottom-up 3D nanoantenna for visible light. Sci. Rep. 3 (1), 2311. https://doi.org/10.1038/srep02311.

Tong, Pakizeh T., Feuz, L., Dmitriev, A., 2013b. Highly directional bottom-up 3Dnanoantenna for visible light, Sci. Rep., 1-5, https://doi.org/10.1038/srep02311.

Wang, Z.L., 2003. Nanobelts, nanowires, and nanodiskettes of semiconducting oxides—From materials to nanodevices. Adv. Mater. 15 (5), 432–436. https://doi.org/10.1002/adma.200390100.

Wang, Y., Zeng, J., Wu, P.B., 2008. Dynamics simulation model of double united articulated container flat vehicle. Journal of Traffic and Transportation Engineering 8 (1), 1–4.

Weldon, J., Jensen, K., Zettl, A., 2008. Nanomechanical radio transmitter. Physica Status Solidi (b) 245 (10), 2323–2325. https://doi.org/10.1002/pssb.200879639.

Whang, D., Jin, S., Lieber, C.M., 2004. Large-scale hierarchical organization of nanowires for functional nanosystems. Japanese Journal of Applied Physics,, 43, pp. 4465–4470.

Yu, G., Lieber, C.M., 2010. Assembly and integration of semiconductor nanowires for functional nanosystems. Pure Appl. Chem. 82 (12), 2295–2314. https://doi.org/10.1351/PAC-CON-10-07-06.

Zakharov, D., Lebedev, G., Irzhak, A., Afonina, V., Mashirov, A., Kalashnikov, V., Koledov, V., Shelyakov, A., Podgorny, D., Tabachkova, N., Shavrov, V., 2012. Submicron-sized actuators based on enhanced shape memory composite material fabricated by FIB-CVD. Smart Mater. Struct. 21 (5). https://doi.org/10.1088/0964-1726/21/5/052001.

Zakharov, D., Lebedev, G., Koledov, V., Lega, P., Kuchin, D., Irzhak, A., Afonina, V., Perov, E., Shelyakov, A., Pushin, V., Shavrov, V., 2010. An enhanced composite

scheme of shape memory actuator for smart systems. Physics Procedia, 10. Elsevier B.V, pp. 58–64 Vol.

Zavarize, M., Martins, M.N., Von Zuben, A.A.G., Koledov, V., Gratowski, S.V., Cotta, M.A., 2020. Exploring fabrication methods to highly sensitive and selective InP nanowire biosensors. Journal of Physics: Conference Series, 1461. Institute of Physics Publishing Vol https://doi.org/10.1088/1742-6596/1461/1/012003.

Zeng, Z., Amiri, P.K., Krivorotov, I.N., Zhao, H., Finocchio, G., Wang, J.P., Katine, J.A., Huai, Y., Langer, J., Galatsis, K., Wang, K.L., Jiang, H., 2012. High-power coherent microwave emission from magnetic tunnel junction nano-oscillators with perpendicular anisotropy. ACS Nano 6 (7), 6115–6121. https://doi.org/10.1021/nn301222v.

Zeng, Z., Finocchio, G., Jiang, H., 2013a. Spin transfer nano-oscillators. Nanoscale 5 (6), 2219–2231. https://doi.org/10.1039/c2nr33407k.

Zeng, Z., Finocchio, G., Zhang, B., Amiri, P.K., Katine, J.A., Krivorotov, I.N., Huai, Y., Langer, J., Azzerboni, B., Wang, K.L., Jiang, H., 2013b. Ultralow-current-density and bias-field-free spin-transfer nano-oscillator. Sci. Rep. 3 (1), 1426. https://doi.org/10.1038/srep01426.

Zeng, Z., Wang, K., Zhang, Z., Chen, J., Zhou, W., 2008. The detection of H_2S at room temperature by using individual indium oxide nanowire transistors. Nanotechnology 20 (4).

14

Diamond deposition on WC–Co substrates with interlayers for engineering applications

Maneesh Chandran
Department of Physics, National Institute of Technology Calicut, Calicut, India

14.1 Introduction

Diamond is always a fascinating material for scientists because of its exceptional and extreme physical properties. Considering any physical property, diamond always comes out on top when compared to other materials. These exceptional physical properties can be utilized to fabricate outstanding devices for various engineering applications, and hence diamond is referred to as the "ultimate engineering material." The scarcity and high costs of natural diamond have led scientists to find alternative routes to make diamonds in the laboratory. It took more than a century to develop a technique to synthesize diamond artificially from carbon-containing compounds using the high-pressure, high-temperature technique (Bundy et al., 1955). Subsequently, the chemical vapor deposition (CVD) technique was developed, which facilitates the growth of diamond in the form of thin films on a wide variety of substrates at subatmospheric pressure and a temperature below 1000°C (Fedoseev et al., 1978; Kamo et al., 1983; Matsumoto et al., 1982). Recent developments have led to much higher growth rates with the ability to cover deposition areas of up to several square inches, which has generated an enormous interest in CVD diamond research. In this chapter the deposition of diamond films on tungsten carbide (WC–Co) substrates for various engineering applications is discussed. Rather than referring to other works, the research activities of the author (previously unpublished) are illustrated in this chapter. Further, this chapter is not meant to be an exhaustive review; hence the readers are referred to follow the references provided.

14.1.1 Crystal structure of diamond

Diamond is most frequently found in cubic form. The crystal structure of diamond can be considered two interpenetrating face-centered

Nanomaterials for Sensing and Optoelectronic Applications. DOI: https://doi.org/10.1016/B978-0-12-824008-3.00005-9

cubic lattices shifted along the body diagonally by (1/4, 1/4, 1/4) a, where a is the lattice constant. The lattice constant of the diamond is 3.56 Å at room temperature. In the diamond lattice each carbon atom is linked to four other carbon atoms by sigma (sp^3) bonds in a tetrahedral array. The density of diamond is 3.52 g cm^{-3} at room temperature. Diamond also exists in a minor hexagonal form, generally known as lonsdaleite. The density of lonsdaleite is the same as that of the cubic diamond. Diamond is kinetically stable but thermodynamically unstable at standard temperature and pressure. However, diamond still exists at normal temperature and pressure in its metastable state due to the very large activation energy barrier between diamond and graphite phases. This large activation barrier (0.4 eV per atom) inhibits the phase transformation (Asmussen & Reinhard, 2002; Sung & Lin, 2009).

14.1.2 Physical properties of diamond

Some of the remarkable physical properties of diamond are listed in Table 14.1 (Chandran & Hoffman, 2016). Apart from the listed physical properties, diamond is also highly resistant to chemical corrosion, which makes it suitable for electrochemistry applications. In addition, diamond is resistant to all kinds of radiation, including UV light, X-rays, γ-rays, and nuclear radiation. Moreover, diamond is biocompatible. All these exceptional properties of diamond arise from two basic facts: (1) carbon atoms are relatively small and light and (2) carbon atoms form very strong short-range covalent bonds in the diamond structure (Gracio et al., 2010).

The most renowned physical property of diamond is its extreme hardness. It is the hardest material found in nature. Diamond also has the highest elastic modulus and the lowest compressibility of any known material. The fundamental reason for the hardness is related to the high strength of the covalent bond (347 kJ mol^{-1}). This ensures that a large amount of energy is needed to remove a carbon atom from the diamond lattice, which makes the diamond very hard. In general, hard materials are wear resistant. It is impossible to scratch a diamond with any other materials. Or in other words, a diamond can only be scratched using another diamond. This makes diamond an ultimate wear-resistant material. The fundamental reason for the high elastic modulus (1050–1210 GPa) is associated with the chemical bonds of the diamond. The sigma bonds in a diamond are very stiff and have components in all spatial directions. Therefore a diamond crystal is very stiff in all directions. Single-crystal diamond possesses a hardness of 100 to 170 GPa. Microcrystalline diamond (MCD) films have hardness values of 60 to 100 GPa (Novikov & Dub, 1996). A diamond film having a grain size in the range of 10 to 100 nm is termed a nanocrystalline

Table 14.1 Physical properties of diamond.

Physical properties	Diamond
Hardness (GPa)	150
Young's modulus (GPa)	1150
Bulk modulus (N m^{-2})	1.2×10^{12}
Thermal conductivity (W cm^{-1} K^{-1})	20
Thermal expansion coefficient (K^{-1})	1.2×10^{-6}
Thermal diffusivity (cm^2 s^{-1})	12
Electrical resistivity (Ω cm)	1×10^{16}
Electron mobility (cm^2 V^{-1} s^{-1})	2500
Hole mobility (cm^2 V^{-1} s^{-1})	2100
Electric breakdown field (V cm^{-1})	2×10^7
Acoustic wave velocity (m s^{-1})	18,000

diamond (NCD), which possesses lower hardness compared to single-crystal or MCDs. However, the coefficient of friction is very low for NCD films (0.1), which makes NCD films attractive for various engineering applications. Doping could significantly influence the hardness of diamond. For instance, nitrogen doping was found to increase hardness by subjecting the lattice to compressive stress, thereby hindering the movement of lattice dislocations (Catledge & Vohra, 1999; Hess, 2012).

14.2 WC–Co substrates

Despite the fact that single-crystal diamond is the most wear-resistant material, it is not suitable for fabricating machining tools since it is difficult to fabricate with the desired geometry. In addition, single-crystal diamond tools have relatively poor chip resistance, leading to catastrophic failure under operation. On the other hand, cemented carbide (WC–Co) possesses relatively high fracture toughness. The trade-off between the wear resistance and fracture toughness of some common materials is shown in Fig. 14.1A. By depositing diamond films on WC–Co substrates, the hardness of diamond can be combined with the toughness of cemented carbide, resulting in excellent wear-resistant material. This would be ideal for various industrial applications. This possibility has directed great attention toward the growth of diamond films on WC–Co substrates using the CVD technique. Pertaining to this, a large number of papers have been published

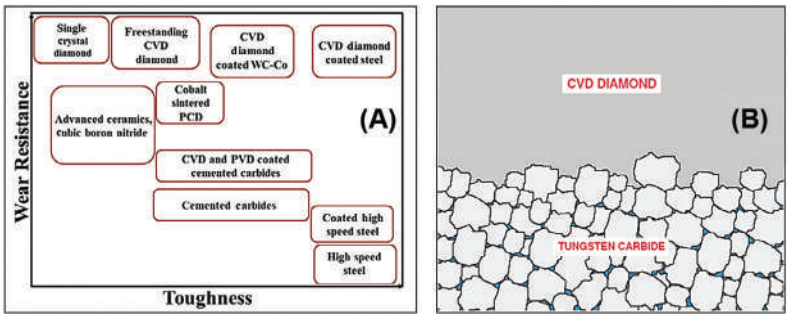

Figure 14.1. (A) Trade-offs between abrasive wear resistance and fracture toughness of common materials. (B) Schematic drawing of diamond thin films deposited on WC–Co substrates.

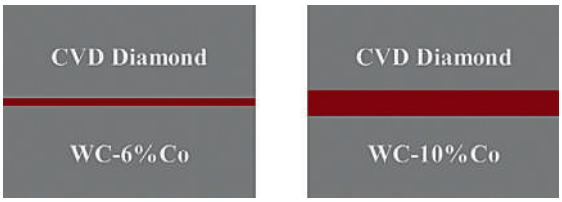

Figure 14.2. Thermal stress in diamond films increases with an increase in cobalt content. The *red line* represents the thermal stress generated at the diamond–tungsten carbide interface.

in this field due to their potential industrial applications (Cabral et al., 2008; Chandran et al., 2013; Perle et al., 2006). A schematic drawing of diamond films deposited on WC–Co substrates is shown in Fig. 14.1B.

One of the continuing challenges associated with the diamond coatings on WC–Co substrates is the lack of proper adhesion between the diamond film and the substrate. This leads to a shorter lifetime for diamond-coated tools than expected. The prime reason for the lack of proper adhesion is the presence of a cobalt binder, which promotes the preferential formation of a graphitic layer at the interface, thereby reducing the adhesion strength (Polini, 2006). This problem becomes much more severe if the cobalt content exceeds more than 6% (Hojman et al., 2012). In addition, interfacial residual stresses due to the difference in coefficient of thermal expansion (CTE) between the diamond coating and the substrate limits the adhesion. The CTE of the WC–Co substrate also increases with an increase in the cobalt content, which in turn increases the thermal stress in diamond coatings (schematically shown in Fig. 14.2). A large thermal stress at the film–substrate interface reduces the adhesion strength. Hence realizing adherent diamond coating on the WC–Co substrate is a great challenge, which requires the suppression, if possible complete elimination, of carbon–cobalt interactions, in addition to high nucleation density.

14.2.1 Chemical etching

The most commonly used method to remove the cobalt binder from the substrate surface is chemical etching (Oakes et al., 1991). Generally, a two-step chemical etching procedure is performed to remove the cobalt binder from the WC–Co substrate surface. The WC–Co substrates are initially dipped in Murakami's reagent (10 g $K_3[Fe(CN)_6]$ + 10 g KOH + 100 mL H_2O) for 30 min in an ultrasonicator, followed by a rinse with distilled water. Murakami's reagent attacks the WC grains

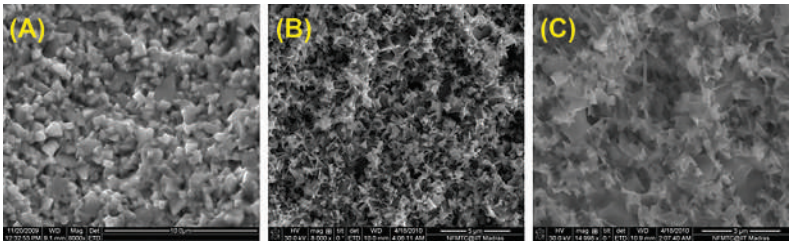

Figure 14.3. SEM images (A) of the as-received WC–Co substrate, (B) after etching with Murakami's reagent, and (C) after etching with Caro's acid.

and roughens the substrate surface. In fact, this process would help in improving the mechanical adhesion between the diamond coatings and the substrate through "mechanical interlocking." The second etching step is performed using Caro's acid (3 mL of 96 wt% H_2SO_4 + 88 mL of 30% w/v H_2O_2) for 15 s, followed by a rinse with ethanol. Caro's acid oxidizes the binder to a soluble Co^{2+} compound, thereby reducing the surface cobalt concentration (Kamiya et al., 2000). The chemical etching method is simple and cost-effective and performs well for the substrates with low cobalt (<6 wt%) content. Fig. 14.3A–C shows the SEM micrographs of the as-received WC–Co substrate after etching with Murakami's reagent and after etching with Caro's acid, respectively.

Despite some success, the chemical etching method did not allow a total suppression of graphitic layer formation during the deposition of diamond films. At high temperatures (800–850°C), cobalt can slowly diffuse through the etched layer and reach the substrate surface, and then interact with the incoming carbon radicals and form graphitic carbon. Moreover, the removal of cobalt binder from the surface/subsurface region may lead to a decrease in the mechanical strength of the subsurface region and it is against the present industrial trend to increase the cobalt content (>8%) for improving the toughness of the tools (Xu et al., 2013). For instance, for high-impact applications and cutting tools WC–Co composites with high cobalt content are generally preferred to improve the toughness.

14.2.2 Use of an interlayer

A possible alternative is to deposit an interlayer material on WC–Co substrates. The prime function of the interlayer is to act as a diffusion barrier against cobalt diffusion during the diamond deposition process. In addition, the interlayer should also be capable of relaxing the interfacial residual stresses to some extent. Thus the criteria for choosing interlayer are (1) low diffusion coefficients for carbon and cobalt, (2) good adhesion to both diamond coating and WC–Co substrate, and (3) intermediate CTE when compared to diamond and WC–Co. Needless to say, the melting point of the interlayer material should be higher than the typical diamond deposition temperature (~800°C).

Since there is no single material which fullfills all these requirements, numerous interlayer materials that may fullfills some of the foregoing attributes have been proposed and tested by various authors (Cui et al., 2015; Endler et al., 1996; Kupp et al., 1994; Polini & Barletta, 2008; Polini et al., 2006; W.D. et al., 1994). Despite this diversity, the performance comparison of different interlayer materials deposited on the WC–Co substrate is still missing in the literature. In fact, the performance of an interlayer as a diffusion barrier strongly depends on the chemical composition and microstructure of the interlayer material. In most of the studies different research groups have independently carried out diamond depositions on WC–Co substrates using the aforesaid interlayer materials under different conditions (Cui et al., 2015; Endler et al., 1996; Kupp et al., 1994; Manaud et al., 2007; O. et al., 1998; Polini & Barletta, 2008; Polini et al., 2006; W.D. et al., 1994). Hence a comparison study on the effect of the interlayer or multilayer on the growth of diamond films deposited under the same environment on WC–Co substrates is missing in the literature, which is the focus of the present chapter. Among various interlayer materials, diamond films deposited on WC–8 wt% Co substrates with (1) TiAlN and (2) TiCN interlayers and a multilayer of (3) TiN/Al_2O_3/TiCN are discussed in the present chapter.

14.3 Diamond deposition

In this section the preparation of interlayer/multilayer materials and subsequent diamond deposition using the hot filament CVD (HFCVD) technique are discussed. In general, the deposition of interlayer materials on the WC–Co substrate is carried out either by physical vapor deposition (PVD) or CVD techniques. In the present chapter both the interlayers, TiAlN, and TiCN, were deposited on WC–Co substrates using the PVD technique. The multilayer (TiN/Al_2O_3/TiCN) was deposited using the CVD technique. Details of the aforesaid experiments can be found elsewhere (H.G. et al., 1997; Santhanam et al., 1996). The thickness of both interlayers was 5 μm, whereas the thickness of each layer in the multilayer coatings, viz., TiN, Al_2O_3, and TiCN were 2 μm, 5 μm, and 15 μm, respectively. Our initial studies showed that diamond films deposited on the TiN multilayer were peeled off upon cooling down to room temperature. Thus TiN-coated WC–Co substrates were chemically pretreated, prior to diamond deposition, to improve the adhesion. TiN-coated WC–Co substrates were chemically pretreated with a solution of 0.5 mL sulfuric acid (H_2SO_4), 2 mL hydrofluoric acid (HF), 3 mL hydrogen peroxide (H_2O_2), 75 mL ethylene glycol, and 18 mL water at 250°C for 15 min. This modifies the TiN substrate surface, which leads to a better "mechanical interlocking" between the diamond film and the TiN layer. For the sake of comparison

studies, diamond films were deposited directly on a WC–Co substrate without any interlayer or multilayer. To ensure better adhesion, prior to diamond deposition, a two-step chemical etching procedure was performed to remove the cobalt binder from the WC–Co substrate surface. The WC–Co substrates were pretreated with Murakami's reagent (10 g $K_3[Fe(CN)_6]$ + 10 g KOH + 100 ml H_2O) for 30 min and then etched with Caro's acid (3 mL 96 wt% H_2SO_4 + 88 mL of 30% w/v H_2O_2) for 15 s and were cleaned with ethanol (Kamiya et al., 2000).

14.3.1 Seeding

Prior to diamond deposition, all the substrates were seeded with diamond nanoparticles, dispersed in dimethyl sulfoxide (DMSO), using a low-power ultrasonic bath for 10 min. The seeding process is inevitable in diamond deposition to realize a continuous film since diamond has very high surface energy (5.24 J m^{-2}), and hence nucleation from the gas phase is often difficult. The seeded substrates were again cleaned with ethanol using an ultrasonicator for 40 seconds to remove loosely bound diamond nanoparticles from the substrate surface. Typically, a seed density of $\sim 10^{10}$ cm^{-2} can be achieved on the substrate surface after the seeding process. The substrates were dried thoroughly using dry nitrogen and placed inside an HFCVD reactor for diamond deposition.

14.3.2 Hot filament CVD

In the present chapter diamond films were deposited using an HFCVD reactor since this technique has several advantages like adaptability to product geometries, uniformity over a large area, relatively simple setup, and ease of operation (Herlinger, 2006). A tungsten filament assembly, consisting of fine (0.12 mm diameter) tungsten filaments, with 12-mm wire-to-wire spacing, was placed above the samples. A rotary pump was used to evacuate the CVD chamber and the chamber pressure during deposition was carefully maintained using a throttle valve connected to the rotary pump. Methane (CH_4) and hydrogen (H_2) were used as precursor gases at a flow rate of 60 sccm and 3000 sccm, respectively. Diamond films were deposited at two different chamber pressures (10 and 50 Torr) in order to vary the grain size of the diamond from nanocrystalline to microcrystalline. The filament assembly was electrically heated using a DC power supply, which generated a uniform thermal energy distribution that ensures uniform diamond film deposition over the entire substrates. The filament temperature was measured using a two-color optical pyrometer (Electro-Optical Systems Inc., USA), which indicated 2200°C. The substrates were placed 15 mm away from the filament assembly and the thermocouples (Omega Inc., USA) located beneath the substrates indicated a temperature of ~800°C. The growth process was performed for 4 h

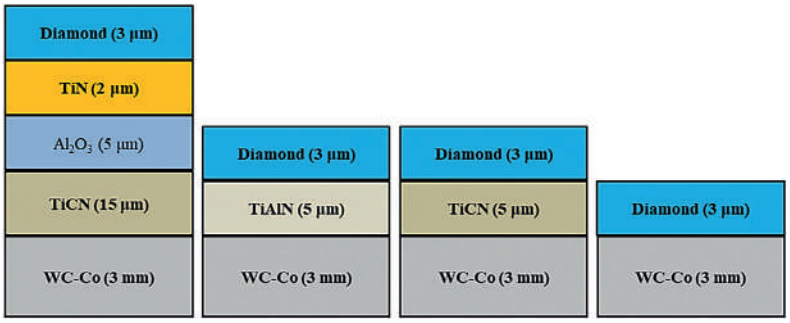

Figure 14.4. Schematic of diamond thin films deposited with a multilayer ($TiN/Al_2O_3/TiCN$), with interlayers (TiAlN and TiCN), and directly on WC–Co substrates using HFCVD. The thickness of each layer is mentioned in the bracket.

and the thickness of the deposited film for the same growth duration was estimated to be ~3 μm. The schematics of the deposited film with interlayer or multilayer are shown in Fig. 14.4.

As mentioned, the growth of CVD diamond requires CH_4 diluted in excess of H_2, typically at a ratio of 1–2% CH_4 in H_2. The process gases mix in the chamber and pass through the activation region (i.e., hot filament assembly), which dissociates H_2 molecule to atomic H_2 as well as CH_4 in fragments. These reactive fragments undergo a complex set of chemical reactions and physical processes, as schematically shown in Fig. 14.5A. For a detailed description of the growth chemistry of diamond, the readers are referred to follow the references provided: Butler & Woodin (1993) and May (2000). In general, the process of diamond film deposition involves (1) adsorption of arriving particles, (2) surface diffusion of adsorbed adatoms, (3) formation of nuclei, and (4) the growth of nuclei and their coalescence. But, the exact growth mechanism of CVD is dependent upon the reactor used, the gas-phase chemistry, process parameters, and the nature of the substrate surface (Holleck, 1986). A photograph of a HF CVD reactor is shown in Fig. 14.5B.

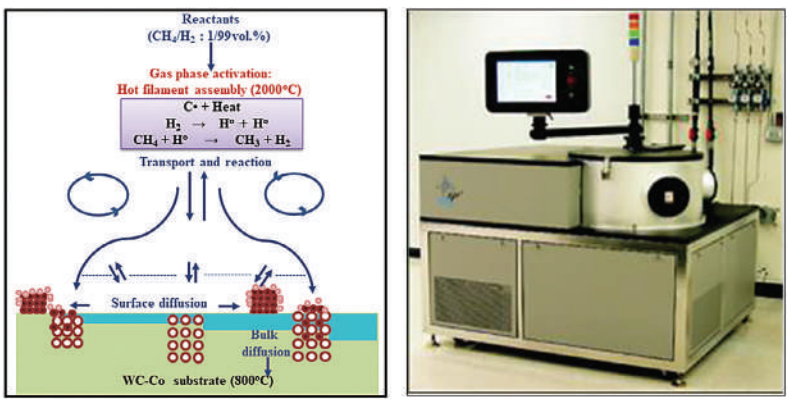

Figure 14.5. (A) Schematic of chemical reactions and physical processes occurring during the diamond CVD process and (B) the photograph of a hot filament CVD reactor.

14.4 Characterizations and analyses

In this section some of the most relevant analytical techniques that are used for characterizing diamond coatings are discussed. Literature reports indicate that the failure of diamond coatings arises mainly due to interfacial failure, owing to the residual stresses in the coating. Hence understanding the origin of residual stress is an important aspect since it strongly influences the adhesion property of diamond coatings. The basic characterization techniques, such as X-ray diffraction (XRD) and Raman spectroscopy, are essential to assess the residual stresses in diamond coatings.

14.4.1 X-ray diffraction

XRD is a very basic characterization technique to determine the crystal structure as well as to identify different phases present in a material. XRD technique has been widely used to determine the grain size as well as the residual stresses in diamond films. In the present chapter phase analyses of the deposited films were done using an X'pert Pro (PANalytical) diffractometer with Cu Kα radiation. XRD patterns of the diamond films deposited at 10 Torr and 50 Torr chamber pressures on WC–Co substrates with interlayers (D/TiAlN/WC–Co and D/TiCN/WC–Co) and a multilayer (D/TiN/Al_2O_3/TiCN/WC–Co) are shown in Fig. 14.6A and B, respectively. The XRD patterns exhibit peaks at 43.9 degrees and 75.3 degrees, indexed to the diffraction from (111) and (220) crystal planes of diamond, respectively. All the other peaks originated from the interlayer or multilayer. In addition, peaks obtained from the base WC–Co substrate can also be seen in the XRD pattern. For an Face centered cubic (FCC) lattice, the conditions for allowed Bragg diffraction are h,k,l all odd or all even. However, for a diamond lattice, if all are even and $h + k + l \neq 4n$, then the corresponding Bragg diffraction is absent. The grain size of the film as well as the strain in the film can be evaluated from the full width at half maximum (FWHM) of the diffraction peak using the Williamson–Hall method (Bachmann et al., 1994). The Williamson–Hall formula considers both

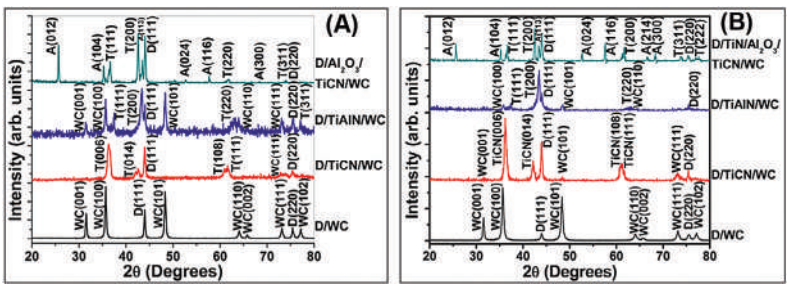

Figure 14.6. XRD patterns of diamond thin films deposited on WC–Co substrates with a multilayer (TiN/Al_2O_3/TiCN) and interlayers (TiCN and TiAlN) at (A) 10 Torr and (B) 50 Torr. The peaks D(111) at 43.9 degrees and D(220) at 75.3 degrees are the diffractions from the (111) and (220) crystal planes of the diamond, respectively.

size-induced broadening and strain-induced broadening, which often varies quite differently with respect to Bragg diffraction angle.

14.4.2 SEM analysis

Scanning electron microscopy (SEM) is widely used for observing the microstructure, morphology, and topological features in the submicrometer and nanometer range. In the present chapter the microstructure of the deposited diamond films was observed using a field emission SEM (Quanta 3D is the model, FEI, Netherlands is the manufacturer). Fig. 14.7A–D shows the SEM images of diamond films deposited at 50 Torr on the TiN multilayer (D/TiN/Al_2O_3/TiCN/WC–Co), TiAlN interlayer (D/TiAlN/WC–Co), TiCN interlayer (D/TiCN/WC–Co), and WC–Co substrates (D/WC–Co), respectively. Fig. 14.7E–H shows the corresponding SEM images of diamond films deposited at 10 Torr on the TiN multilayer (D/TiN/Al_2O_3/TiCN/WC–Co), TiAlN interlayer (D/TiAlN/WC–Co), TiCN interlayer (D/TiCN/WC–Co), and WC–Co substrates (D/WC–Co), respectively. Fig. 14.7E–H shows that diamond films deposited at 10 Torr resulted in the formation of NCD films. The average grain size of NCD films is estimated to be ~30 nm. On the other hand, Fig. 14.7A–D shows that diamond films deposited at 50 Torr resulted in the formation of well-faceted MCD films. The average grain size of MCD film is estimated to be ~500 nm.

This result showed that the grain size of the diamond film strongly depends on the chamber pressure. This is very significant as the physical properties of diamond films are strongly dependent on the grain size (Abreu et al., 2005). For instance, NCD films possess a lower hardness compared to MCD films. However, the surface roughness of NCD films is extremely low, which is desirable for wear-resistant coatings and other tribological applications (Fang et al., 2009). In the same manner diamond films with a larger grain size possess high hardness alongside high surface roughness, which are suitable for abrasive or machining applications. Thus by controlling the chamber pressure during deposition, grain size can be varied; thereby diamond films with desired physical properties can be produced. The possible reasons for the realization of NCD films at lower chamber pressure are explained in the subsequent section. It can also be noted that the surface morphologies of diamond films deposited on different interlayers and multilayers at the same chamber pressure (either 10 or 50 Torr) were also found to be slightly different. This is attributed to the differences in surface morphologies of the interlayer and/or multilayer. It is well known that the surface roughness of the deposited diamond thin film is strongly dependent on the initial roughness of the substrate surface (Chandran et al., 2012). Besides, the surface energy of the interlayer or

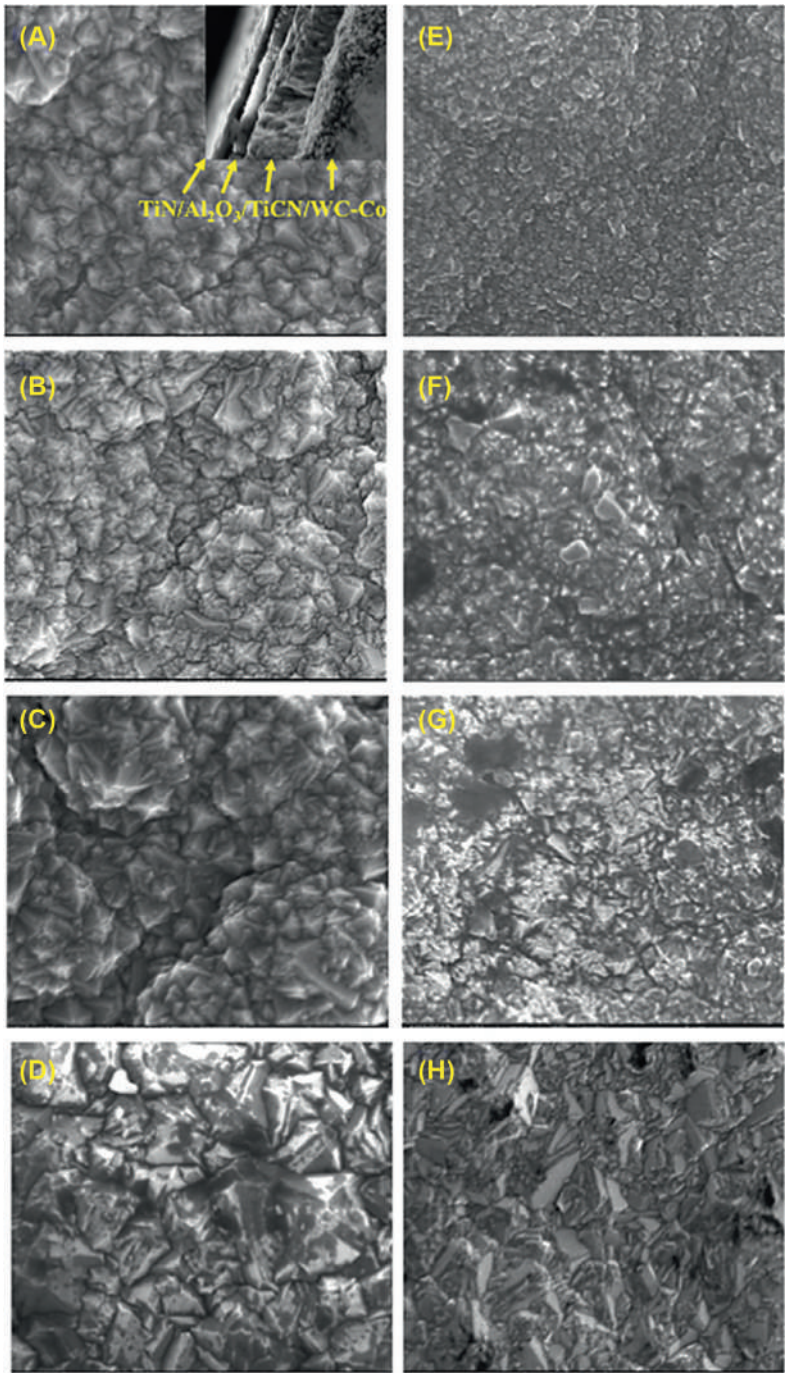

Figure 14.7. SEM images of diamond thin films deposited at 50 Torr on WC–Co substrates with (A) a TiN multilayer, (B) a TiAlN interlayer, and (C) a TiCN interlayer and (D) directly on WC–Co substrates. (E–H) The corresponding SEM images of diamond films deposited at 10 Torr.

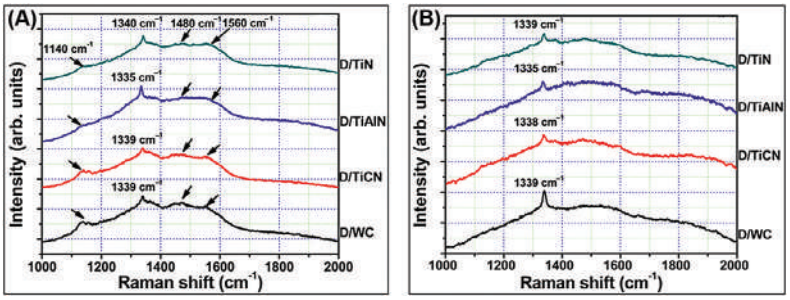

Figure 14.8. Raman spectra of diamond thin films deposited on WC–Co substrates with a multilayer ($TiN/Al_2O_3/TiCN$) and interlayers (TiAlN and TiCN) at (A) 10 Torr and (B) 50 Torr. The upshift (~1339 cm^{-1}) in the Raman spectrum was the result of the compressive stress in the diamond films.

multilayer may also influence the initial nucleation, as several complex surface reactions occur during the initial nucleation stage.

14.4.3 Raman spectroscopy

Raman spectroscopy is very commonly used to determine the phase analysis of carbon-based materials. This technique provides maximum structural and electronic information without any complicated sample preparation processes. The phase analysis of the deposited films was done using Raman spectroscopy (Alpha 300 is the model, WITec, Germany is the manufacturer). An excitation radiation of 532 nm of an Nd:YAG laser operated at <10 mW was used to excite the samples. The Raman spectra of the diamond films deposited on the WC–Co substrates with interlayers (D/TiAlN/WC–Co and D/TiCN/WC–Co) and multilayer (D/TiN/Al_2O_3/TiCN/WC–Co) at 10 Torr and 50 Torr chamber pressures are shown in Fig. 14.8A and B, respectively. Diamond has only one active phonon mode (F_{2g}), which gives a triply degenerate single peak at 1332 cm^{-1} (Knight & White, 1989). This phonon mode is due to the vibration of two interpenetrating cubic sublattices of diamond in opposite phases (Raman, 1962). The upshift in the Raman spectra (~1339 cm^{-1}) was a result of compressive thermal stress in the films. The thermal stress generated after deposition, during cooling down to room temperature, arises from the difference in the thermal expansion coefficients of diamond film and the substrate. Typically, the residual stress in diamond films is dominated by thermal stress, compared to epitaxial stress or intrinsic stress, due to a large thermal mismatch between diamond coating and the substrate. The broad peak near 1560 cm^{-1} corresponds to a minor amount of amorphous carbon present in the diamond film. However, the intensity of the peak at 1560 cm^{-1} cannot be taken into account for quantitatively evaluating the graphitic content of the deposited film because sp^2 hybridization has a large Raman scattering cross-section, typically about 50 to 230 times, compared to sp^3 hybridization (Ferrari & Robertson, 2000). It is interesting to note that diamond films grown

at 10 Torr showed additional peaks at ~1140 cm^{-1} and ~1480 cm^{-1}. These two peaks originate from the grain boundaries of NCD films and are assigned to the v_1 and v_3 modes of trans-polyacetylene (Ferrari & Robertson, 2001). Since these two peaks are only visible for NCD films and not for MCD films, it is widely used as a characteristic signature of NCD films. Thus the films deposited at 50 and 10 Torr, respectively, lead to the formation of MCD and NCD films, which is consistent with the SEM results shown in the previous section.

The formation of NCD films at a lower chamber pressure (10 Torr) is associated with the high rate of secondary nucleation of the diamond. Secondary nucleation is a process in which new growth centers are formed by inhibiting the continuous growth of diamond crystals before they can grow larger. Hence if the secondary nucleation rate is high, the "nucleation" process dominates over the "growth" process, which results in small crystallite films. Typically, secondary nucleation rate is enhanced by various techniques, viz., (1) incorporating an inert gas (Ar) in lieu of H_2; (2) applying a continuous bias during deposition; (3) increasing the ratio of CH_4/H_2 precursor gases; or (4) reducing the substrate temperature below 500°C (Chowdhury et al., 2006; Chu et al., 2014; Huang & Hong, 2006; Ihara et al., 1991; Kulisch et al., 2012; M., 1999; Mortet et al., 2012; Sun et al., 2000). In fact, in all these conditions we circumvent a narrow process parameter window for diamond growth. Or in other words, the simple technique to obtain a smooth NCD film is to leave the well-defined, narrow parameter window of diamond growth by selecting one parameter outside from the ideal growth conditions. Generally, diamond films are typically grown at a pressure in the range of 20 to 50 Torr, which often results in MCD. In the present chapter we reduced the pressure from 50 Torr to 10 Torr, which led to the dilution of precursor gases in the chamber. This induced a higher rate of secondary nucleation, leading to the formation of NCD films (Meng et al., 2008). The mean free path of activated species will be relatively high when diamond films are deposited at a lower chamber pressure (10 Torr). Thus the collision of atomic H_2 with the growing diamond faces was relatively at higher energy, which may produce many defects and that could increase the renucleation rates. This result showed that the reactant gas pressure has a very strong impact on the morphology and structural properties of diamond films.

Raman spectroscopy has also been extensively used to estimate the residual stresses in diamond coatings. Residual stress in diamond films is estimated by analyzing the peak position and FWHM of the Raman peak, located at 1332 cm^{-1}. The FWHM of the 1332 cm^{-1} peak reveals random stress present in the deposited film, whereas a shift or splitting of the line represents directional stress present in the film. In general, Raman peak shifts to a lower frequency when the film is under tensile

stress, whereas Raman peak shifts to a higher frequency when the film is under compressive stress. The stress σ in the diamond film was estimated from $\sigma = -0.348\ (v_m - v_0)$ (GPa) for the unsplit Raman peak at v_m, where $v_0 = 1332$ (Boppart et al., 1985). Thus the deposited diamond films accommodate compressive residual stresses varying from 0.696 to 2.78 GPa. This variation in residual stress was due to the difference in the thermal expansion coefficient of diamond film and the interlayer. The highest compressive residual stress (2.784 GPa) was found in the film deposited on the TiN multilayer (D/TiN/Al_2O_3/TiCN/WC–Co) coating, which is attributed to the high thermal expansion coefficient ($9 \times 10^{-6}\ K^{-1}$) of the TiN layer in comparison with diamond ($2 \times 10^{-6}\ K^{-1}$). The least compressive residual stress (0.696 GPa) was found in the film deposited on the TiAlN interlayer (D/TiAlN/WC–Co) due to the minimum thermal mismatch between the TiAlN ($7.3 \times 10^{-6}\ K^{-1}$) and diamond. This result is very significant as the residual stresses in the coated surfaces are crucial for their performance in tribological applications. For instance, compressive residual stress in the coatings inhibits crack initiation and propagation, which is beneficial for improving the wear resistance and hardness. However, a very high compressive residual stress reduces the adhesion strength and may result in interfacial failure (delamination) (Soroka et al., 2010). The present chapter showed that TiAlN would be a better choice compared to other interlayer materials or multilayer for diamond deposition. In fact, TiAlN-coated WC–Co inserts are commercially available. So a thin layer of the diamond coating on top of these commercially available TiAlN-coated WC–Co inserts could ensure an extended lifetime, owing to the excellent mechanical properties of diamond films.

14.5 Applications of CVD diamond

In this section some of the potential applications of diamond-coated WC–Co substrates are discussed. Diamond-coated WC–Co tools are used for machining fiber-reinforced composites (FRCs), hypereutectic Al-Si alloys, and metal matrix composites (MMCs), which are extensively used in aerospace and automobile industries nowadays. These materials are difficult to machine using conventional high-speed steel or WC–Co cutting tools (Oles et al., 1996; Polini et al., 2002; R.R. et al., 2015). Diamond-coated mechanical seals are already beginning to find their way into the marketplace since they are much superior to conventional WC–Co seals (Cline, 1999). Diamond-coated dental burrs have displayed superior performance over bare WC–Co burrs (Sein et al., 2003, 2004). Diamond-coated WC–Co riveting inserts showed improved performance and lifetime, which would be useful for chain manufacturing industries (Chandran et al., 2013). NCD-coated WC–Co drawing dies can be used for improving the working life of

tube drawing dies (Chandran et al., 2014; Sun et al., 2009). In short, CVD diamond is an ideal candidate for hard coatings and tribological applications.

14.6 Summary

In this chapter the deposition of diamond films on high-cobalt-content WC–Co substrates is discussed. Diamond thin films were deposited on WC–Co substrates with interlayers (TiAlN and TiCN) and a multilayer ($TiN/Al_2O_3/TiCN$) using an HFCVD system under similar chemical environments. Both the MCD and NCD films were prepared by changing the process parameters. The deposited films were characterized using XRD, Raman spectroscopy, and SEM. Residual stress in the deposited diamond thin films was estimated using Raman spectroscopy. The least residual compressive stress was found for the films deposited on TiAlN interlayer (D/TiAlN/WC–Co) and the highest for the films deposited on TiN multilayer ($D/TiN/Al_2O_3/TiCN/WC$). This showed that TiAlN would be a better choice compared to other interlayer materials or multilayer for diamond deposition. It is hoped that this chapter contributes to the progress of CVD diamond, in particular diamond coatings, on WC–Co substrates for various industrial applications.

References

Abreu, C.S., Oliveira, F.J., Belmonte, M., Fernandes, A.J.S., Silva, R.F., Gomes, J.R., 2005. Grain size effect on self-mated CVD diamond dry tribosystems. Wear 259 (1–6), 771–778. https://doi.org/10.1016/j.wear.2005.01.004.

Asmussen, J., Reinhard, D., 2002. Diamond Films Handbook. https://dx.doi.org/10.1002/9780470172551.ch42, CRC Press, ISBN 9780824795771 doi:https://doi.org/10.1201/9780203910603.

Bachmann, P.K., Bausen, H.D., Lade, H., Leers, D., Wiechert, D.U., Herres, N., Kohl, R., Koidl, P., 1994. Raman and X-ray studies of polycrystalline CVD diamond films. Diamond and Related Materials 3 (11–12), 1308–1314. https://doi.org/10.1016/0925-9635(94)90143-0.

Boppart, H., Van Straaten, J., Silvera, I.F., 1985. Raman spectra of diamond at high pressures. Physical Review B 32 (2), 1423–1425. https://doi.org/10.1103/PhysRevB.32.1423.

Boyer, R., Cotton, J., Mohaghegh, M., Schafrik, R., 2015. Materials considerations for aerospace applications. MRS Bulletin 40 (12), 1055–1066. https://doi.org/10.1557/mrs.2015.278.

Bundy, F.P., Hall, H.T., Strong, H.M., Wentorf, R.H., 1955. Man-made diamonds. Nature 176 (4471), 51–55. https://doi.org/10.1038/176051a0.

Butler, J.E., Woodin, R.L., 1993. Thin film diamond growth mechanisms. Philosophical Transactions of the Royal Society of London. Series A: Physical and Engineering Sciences 342 (1664), 209–224. https://doi.org/10.1098/rsta.1993.0015.

Cabral, G., Gäbler, J., Lindner, J., Grácio, J., Polini, R., 2008. A study of diamond film deposition on WC–Co inserts for graphite machining: Effectiveness of SiC

interlayers prepared by HFCVD. Diamond and Related Materials 17 (6), 1008–1014. https://doi.org/10.1016/j.diamond.2008.03.017.

Catledge, S.A., Vohra, Y.K., 1999. Effect of nitrogen addition on the microstructure and mechanical properties of diamond films grown using high-methane concentrations. Journal of Applied Physics 86 (1), 698–700. https://doi.org/10.1063/1.370787.

Chandran, M., Hoffman, A., 2016. Diamond film deposition on WC–Co and steel substrates with a CrN interlayer for tribological applications. Journal of Physics D: Applied Physics 49 (21). https://doi.org/10.1088/0022-3727/49/21/213002.

Chandran, M., Kumaran, C.R., Dumpala, R., Shanmugam, P., Natarajan, R., Bhattacharya, S.S., Rao, M., S.R, 2014. Nanocrystalline diamond coatings on the interior of WC–Co dies for drawing carbon steel tubes: Enhancement of tube properties. Diamond and Related Materials 50, 33–37. https://doi.org/10.1016/j.diamond.2014.09.002.

Chandran, M., Kumaran, C.R., Gowthama, S., Shanmugam, P., Natarajan, R., Bhattacharya, S.S., Rao, M., S.R, 2013. Chemical vapor deposition of diamond coatings on tungsten carbide (WC–Co) riveting inserts. International Journal of Refractory Metals and Hard Materials 37, 117–120. https://doi.org/10.1016/j.ijrmhm.2012.11.005.

Chandran, M., Kumaran, C.R., Vijayan, S., Bhattacharya, S.S., Rao, M., S.R, 2012. Adhesive microcrystalline diamond coating on surface modified non-carbide forming substrate using hot filament CVD. Materials Express 2 (2), 115–120. https://doi.org/10.1166/mex.2012.1061.

Chowdhury, S., Hillman, D.A., Catledge, S.A., Konovalov, V.V., Vohra, Y.K., 2006. Synthesis of ultrasmooth nanostructured diamond films by microwave plasma chemical vapor deposition using a $He/H_2/CH_4/N_2$ gas mixture. Journal of Materials Research 21 (10), 2675–2682. https://doi.org/10.1557/jmr.2006.0334.

Chu, Y.C., Tzeng, Y., Auciello, O., 2014. Microwave plasma enhanced chemical vapor deposition of nanocrystalline diamond films by bias-enhanced nucleation and bias-enhanced growth. Journal of Applied Physics 115 (2). https://doi.org/10.1063/1.4861417.

Cline, B.L., 1999. Mechanical applications for CVD diamond. In: Presented at Diamond 99 conference, Prague, Czech Republic.

Cui, Y.X., Wang, W.S., Shen, B., Sun, F.H., 2015. A study of CVD diamond deposition on cemented carbide ball-end milling tools with high cobalt content using amorphous ceramic interlayers. Diamond and Related Materials 59, 21–29. https://doi.org/10.1016/j.diamond.2015.09.002.

Endler, I., Leonhardt, A., Scheibe, H.J., Born, R., 1996. Interlayers for diamond deposition on tool materials. Diamond and Related Materials 5 (3–5), 299–303. https://doi.org/10.1016/0925-9635(95)00352-5.

Fan, W., Chen, X., Jagannadham, K., Narayan, J., 1994. Diamond-ceramic composite tool coatings. Journal of Materials Research 9 (11), 2850–2867. https://doi.org/10.1557/JMR.1994.2850.

Fang, Z.Z., Wang, X., Ryu, T., Hwang, K.S., Sohn, H.Y., 2009. Synthesis, sintering, and mechanical properties of nanocrystalline cemented tungsten carbide—A review. International Journal of Refractory Metals and Hard Materials 27 (2), 288–299. https://doi.org/10.1016/j.ijrmhm.2008.07.011.

Fedoseev, D.V., Deryagin, B.V., Bakul, V.N., Prikhna, A.I., Varnin, V.P., Vnukov, S.P., Gerasimenko, V.K., Nikitin, J.I., Tsypin, N.V., Hochko, A.V., 1978. Polycrystalline diamond member and method of preparing same, 1978. U.S. Patent 4, p. 104,441 issued August 1.

Ferrari, A.C., Robertson, J., 2001. Origin of the 1150 − cm^{-1} Raman mode in nanocrystalline diamond. Physical Review B—Condensed Matter and Materials Physics 63 (12). https://doi.org/10.1103/PhysRevB.63.121405.

Ferrari, A., Robertson, J., 2000. Interpretation of Raman spectra of disordered and amorphous carbon. Physical Review B—Condensed Matter and Materials Physics 61 (20), 14095–14107. https://doi.org/10.1103/PhysRevB.61.14095.

Glozman, O., Berner, A., Shechtman, D., Hoffman, A., 1998. Influence of Cr&N interlayer properties on the initial stages of CVD diamond growth on steel substrates. Diamond and Related Materials 7, 597–602. https://doi.org/10.1016/s0925-9635(97)00176-3.

Gracio, J.J., Fan, Q.H., Madaleno, J.C., 2010. Diamond growth by chemical vapour deposition. Journal of Physics D: Applied Physics 43 (37). https://doi.org/10.1088/0022-3727/43/37/374017.

Gruen, D.M., 1999. Nanocrystalline diamond films. Annual Review of Materials Science 29, 211–259. https://doi.org/10.1146/annurev.matsci.29.1.211.

Herlinger, J., 2006. sp3's experience using hot filament CVD reactors to grow diamond for an expanding set of applications. Thin Solid Films,, 501, pp. 65–69.

Hess, P., 2012. The mechanical properties of various chemical vapor deposition diamond structures compared to the ideal single crystal. Journal of Applied Physics 111 (5). https://doi.org/10.1063/1.3683544.

Hojman, E., Akhvlediani, R., Alagem, E., Hoffman, A., 2012. Cobalt out-diffusion and carbon phase composition at the WC-10%Co/diamond film interface investigated by XPS, SEM, Raman and SIMS. Physica Status Solidi (A) Applications and Materials Science 209 (9), 1726–1731. https://doi.org/10.1002/pssa.201200037.

Holleck, H., 1986. Material selection for hard coatings. Journal of Vacuum Science and Technology A: Vacuum, Surfaces and Films, 4 (6), 2661–2669. https://doi.org/10.1116/1.573700.

Huang, S.M., Hong, F.C.N., 2006. Low temperature growths of nanocrystalline diamond films by plasma-assisted hot filament chemical vapor deposition. Surface and Coatings Technology 200 (10), 3160–3165. https://doi.org/10.1016/j.surfcoat.2005.07.035.

Ihara, M., Maeno, H., Miyamoto, K., Komiyama, H., 1991. Diamond deposition on silicon surfaces heated to temperature as low as 135°C. Applied Physics Letters 59 (12), 1473–1475. https://doi.org/10.1063/1.106382.

Kamiya, S., Takahashi, H., Polini, R., Traversa, E., 2000. Quantitative determination of the adhesive fracture toughness of CVD diamond to WC–Co cemented carbide. Diamond and Related Materials 9 (2), 191–194. https://doi.org/10.1016/S0925-9635(00)00229-6.

Kamo, M., Sato, Y., Matsumoto, S., Setaka, N., 1983. Diamond synthesis from gas phase in microwave plasma. Journal of Crystal Growth 62 (3), 642–644. https://doi.org/10.1016/0022-0248(83)90411-6.

Knight, D.S., White, W.B., 1989. Characterization of diamond films by Raman spectroscopy. Journal of Materials Research 4 (2), 385–393. https://doi.org/10.1557/JMR.1989.0385.

Kulisch, W., Petkov, C., Petkov, E., Popov, C., Gibson, P.N., Veres, M., Merz, R., Merz, B., Reithmaier, J.P., 2012. Low temperature growth of nanocrystalline and ultrananocrystalline diamond films: A comparison. Physica Status Solidi (A) Applications and Materials Science 209 (9), 1664–1674. https://doi.org/10.1002/pssa.201228270.

Kupp, E.R., Drawl, W.R., Spear, K.E., 1994. Interlayers for diamond-coated cutting tools. Surface and Coatings Technology 68–69 (C), 378–383. https://doi.org/10.1016/0257-8972(94)90189-9.

Manaud, J.P., Poulon, A., Gomez, S., Petitcorps, Y.L., 2007. A comparative study of CrN, ZrN, NbN and TaN layers as cobalt diffusion barriers for CVD diamond deposition

on WC–Co tools. Surface and Coatings Technology 202 (2), 222–231. https://doi.org/10.1016/j.surfcoat.2007.05.024.

Matsumoto, S., Sato, Y., Tsutsumi, M., Setaka, N., 1982. Growth of diamond particles from methane-hydrogen gas. Journal of Materials Science 17 (11), 3106–3112. https://doi.org/10.1007/BF01203472.

May, P.W., 2000. Diamond thin films: A 21st-century material. Philosophical Transactions of the Royal Society A 358, 473–495. https://doi.org/10.1098/rsta.2000.0542.

Meng, X.M., Askari, S.J., Tang, W.Z., Hei, L.F., Wang, F.Y., Jiang, C.S., Lu, F.X., 2008. Nano-crystalline CVD diamond films deposited on cemented carbide using high current extended DC arc plasma process. Vacuum 82 (5), 543–546. https://doi.org/10.1016/j.vacuum.2007.06.005.

Mortet, V., Zhang, L., Eckert, M., D'Haen, J., Soltani, A., Moreau, M., Troadec, D., Neyts, E., De Jaeger, J.C., Verbeeck, J., Bogaerts, A., Van Tendeloo, G., Haenen, K., Wagner, P., 2012. Grain size tuning of nanocrystalline chemical vapor deposited diamond by continuous electrical bias growth: Experimental and theoretical study. Physica Status Solidi (A) Applications and Materials Science 209 (9), 1675–1682. https://doi.org/10.1002/pssa.201200581.

Novikov, N.V., Dub, S.N., 1996. Hardness and fracture toughness of CVD diamond film. Diamond and Related Materials 5 (9), 1026–1030. https://doi.org/10.1016/0925-9635(95)00346-0.

Oakes, J., Pan, X.X., Haubner, R., Lux, B., 1991. Chemical vapour deposition diamond coatings on cemented carbide tools. Surface and Coatings Technology 47 (1–3), 600–607. https://doi.org/10.1016/0257-8972(91)90330-Y.

Oles, E.J., Inspektor, A., Bauer, C.E., 1996. The new diamond-coated carbide cutting tools. Diamond and Related Materials 5 (6–8), 617–624. https://doi.org/10.1016/0925-9635(95)00347-9.

Perle, M., Bareiss, C., Rosiwal, S.M., Singer, R.F., 2006. Generation and oxidation of wear debris in dry running tests of diamond coated SiC bearings. Diamond and Related Materials 15 (4–8), 749–753. https://doi.org/10.1016/j.diamond.2005.10.069.

Polini, R., 2006. Chemically vapour deposited diamond coatings on cemented tungsten carbides: Substrate pretreatments, adhesion and cutting performance. Thin Solid Films 515 (1), 4–13. https://doi.org/10.1016/j.tsf.2005.12.042.

Polini, R., Barletta, M., 2008. On the use of CrN/Cr and CrN interlayers in hot filament chemical vapour deposition (HF-CVD) of diamond films onto WC–Co substrates. Diamond and Related Materials 17 (3), 325–335. https://doi.org/10.1016/j.diamond.2007.12.059.

Polini, R., Bravi, F., Casadei, F., D'Antonio, P., Traversa, E, 2002. Effect of substrate grain size and surface treatments on the cutting properties of diamond coated co-cemented tungsten carbide tools. Diamond and Related Materials 11 (3–6), 726–730. https://doi.org/10.1016/S0925-9635(02)00020-1.

Polini, R., Mantini, F.P., Barletta, M., Valle, R., Casadei, F., 2006. Hot filament chemical vapour deposition and wear resistance of diamond films on WC–Co substrates coated using PVD-arc deposition technique. Diamond and Related Materials 15 (9), 1284–1291. https://doi.org/10.1016/j.diamond.2005.09.045.

Prengel, H.G., Santhanam, A.T., Penich, R.M., Jindal, P.C., Wendt, K.H., 1997. Advanced PVD-TiAlN coatings on carbide and cermet cutting tools. Surface and Coatings Technology 94–95, 597–602. https://doi.org/10.1016/s0257-8972(97)00503-3.

Raman, C.V., 1962. The infra-red absorption by diamond and its significance—Part VI. The free vibrations of the structure. Proceedings of the Indian Academy of Sciences—Section A 55 (1), 24–29. https://doi.org/10.1557/mrs.2015.278.

Santhanam, A.T., Quinto, D.T., Grab, G.P., 1996. Comparison of the steel-milling performance of carbide inserts with MTCVD and PVD TiCN coatings. International

Journal of Refractory Metals and Hard Materials 14 (1–3), 31–40. https://doi.org/10.1016/0263-4368(96)83415-9.

Sein, H., Ahmed, W., Jackson, M., Woodwards, R., Polini, R., 2004. Performance and characterisation of CVD diamond coated, sintered diamond and WC–Co cutting tools for dental and micromachining applications. Thin Solid Films,, 447–448, pp. 455–461.

Sein, H., Ahmed, W., Rego, C.A., Jones, A.N., Amar, M., Jackson, M., Polini, R., 2003. Chemical vapour deposition diamond coating on tungsten carbide dental cutting tools. Journal of Physics Condensed Matter 15 (39), S2961–S2967. https://doi.org/10.1088/0953-8984/15/39/019.

Soroka, O.B., Klymenko, S.A., Kopeikina, M.Y., 2010. Evaluation of residual stresses in PVD-coatings. Part 2. Strength of Materials 42 (4), 450–458. https://doi.org/10.1007/s11223-010-9236-y.

Sun, F., Ma, Y., Shen, B., Zhang, Z., Chen, M., 2009. Fabrication and application of nano-microcrystalline composite diamond films on the interior hole surfaces of Co cemented tungsten carbide substrates. Diamond and Related Materials 18 (2–3), 276–282. https://doi.org/10.1016/j.diamond.2008.10.064.

Sun, Z., Shi, J.R., Tay, B.K., Lau, S.P., 2000. UV Raman characteristics of nanocrystalline diamond films with different grain size. Diamond and Related Materials 9 (12), 1979–1983. https://doi.org/10.1016/S0925-9635(00)00349-6.

Sung, J.C., Lin, J., 2009. Diamond nanotechnology: Synthesis and applications. Diamond Nanotechnology: Synthesis and Applications. Pan Stanford Publishing Pte. Ltd https://doi.org/10.4032/9789814241427.

Xu, F., Xu, J.H., Yuen, M.F., Zheng, L., Lu, W.Z., Zuo, D.W., 2013. Adhesion improvement of diamond coatings on cemented carbide with high cobalt content using PVD interlayer. Diamond and Related Materials 34, 70–75. https://doi.org/10.1016/j.diamond.2013.01.012.

Index

Page numbers followed by "*f*" and "*t*" indicate, figures and tables respectively.

NANOMATERIALS FOR SENSING AND OPTOELECTRONIC APPLICATIONS

Edited by M. K. Jayaraj, Subha P.P. and Shibi Thomas

Nanomaterials for Sensing and Optoelectronic Applications explores recent trends in nanomaterials and devices for chemical and biosensing applications. The synthesis, properties and applications of metal oxide nanostructures, as well as two-dimensional layered materials are covered, along with the fabrication of optoelectronic devices, such as chemical sensors based on 2D materials and oxide thin film transistors, biosensors, core-shell nanostructures-based surface-enhanced Raman spectroscopy (SERS) substrates, SERS substrates for monitoring biomarkers, luminescent nanoparticles, nanophotonic materials for disease diagnosis, precision nanoclusters for sensing and other optoelectronic applications, nanomaterial based flexible electrochemical sensors for health monitoring, artificial neural networks based on resistive switching devices, shape memory alloys and outstanding physical and chemical properties of diamond. Aiming at researchers in these respective areas, the fundamental principles and mechanisms of the optoelectronic phenomena behind every application mentioned are covered and comprehensively explored. The book is helpful in solving problems related to the synthesis and growth of various nanostructures, the application of these materials for various devices, and understanding how a specific synthesis route promotes a specific application.

Key Features

- Outlines the fundamental principles and mechanisms behind chemical sensing, bio-sensing, thin film transistor devices, SERS based substrates and memory devices.
- Offers a detailed description on the synthesis of 2D materials and oxide nanostructures and thin films.
- Details the health monitoring possibilities of SERS substrates, nanophotonic materials, flexible electrochemical sensors and precision nanoclusters for sensing and other optoelectronic applications.

About the Editors

M. K. Jayaraj is the Vice-Chancellor of the University of Calicut, Kerala, India. He was a Professor in the Department of Physics, Cochin University of Science and Technology, Kochi, India, and was also the founding Director of the Centre of Excellence in Advanced Materials, Cochin University of Science and Technology, Kochi, India. His specialization and research focus is in the area of optoelectronic materials and devices. His research expertise and interests include thin film and nanocomposite devices including sensors/detectors, especially transparent flexible electronic devices like thin film transistors, polycrystalline and domain matched epitaxial ferroelectric thin films devices, resistive switching devices, luminescent nanomaterials for bioimaging applications, and Surface Enhanced Raman Scattering (SERS).

Subha P. P. is a Post-doctoral research fellow at Department of Physics, Cochin University of Science and Technology, Kochi, India. Her research areas of interest are gas sensors based on metal oxide semiconductor nanostructures and two dimensional materials, colorimetric sensors based on gold nanoparticles, metal oxide gas sensors for breath analysis, upconversion phosphors, and luminescent nanoparticles.

Shibi Thomas is an Assistant Professor in the Department of Physics, Bharata Mata College, Thrikkakara, and Kochi, India. Her areas of research are pattern dynamics, reaction-diffusion systems, nanomaterials and biosensors.

ELSEVIER elsevier.com/books-and-journals

ISBN 978-0-12-824008-3

9 780128 240083